



UNIVERSITAT DE  
BARCELONA

## Photoswitchable allosteric ligands to modulate metabotropic glutamate receptors

Silvia Panarello

**ADVERTIMENT.** La consulta d'aquesta tesi queda condicionada a l'acceptació de les següents condicions d'ús: La difusió d'aquesta tesi per mitjà del servei TDX ([www.tdx.cat](http://www.tdx.cat)) i a través del Dipòsit Digital de la UB ([diposit.ub.edu](http://diposit.ub.edu)) ha estat autoritzada pels titulars dels drets de propietat intel·lectual únicament per a usos privats emmarcats en activitats d'investigació i docència. No s'autoritza la seva reproducció amb finalitats de lucre ni la seva difusió i posada a disposició des d'un lloc aliè al servei TDX ni al Dipòsit Digital de la UB. No s'autoritza la presentació del seu contingut en una finestra o marc aliè a TDX o al Dipòsit Digital de la UB (framing). Aquesta reserva de drets afecta tant al resum de presentació de la tesi com als seus continguts. En la utilització o cita de parts de la tesi és obligat indicar el nom de la persona autora.

**ADVERTENCIA.** La consulta de esta tesis queda condicionada a la aceptación de las siguientes condiciones de uso: La difusión de esta tesis por medio del servicio TDR ([www.tdx.cat](http://www.tdx.cat)) y a través del Repositorio Digital de la UB ([diposit.ub.edu](http://diposit.ub.edu)) ha sido autorizada por los titulares de los derechos de propiedad intelectual únicamente para usos privados enmarcados en actividades de investigación y docencia. No se autoriza su reproducción con finalidades de lucro ni su difusión y puesta a disposición desde un sitio ajeno al servicio TDR o al Repositorio Digital de la UB. No se autoriza la presentación de su contenido en una ventana o marco ajeno a TDR o al Repositorio Digital de la UB (framing). Esta reserva de derechos afecta tanto al resumen de presentación de la tesis como a sus contenidos. En la utilización o cita de partes de la tesis es obligado indicar el nombre de la persona autora.

**WARNING.** On having consulted this thesis you're accepting the following use conditions: Spreading this thesis by the TDX ([www.tdx.cat](http://www.tdx.cat)) service and by the UB Digital Repository ([diposit.ub.edu](http://diposit.ub.edu)) has been authorized by the titular of the intellectual property rights only for private uses placed in investigation and teaching activities. Reproduction with lucrative aims is not authorized nor its spreading and availability from a site foreign to the TDX service or to the UB Digital Repository. Introducing its content in a window or frame foreign to the TDX service or to the UB Digital Repository is not authorized (framing). Those rights affect to the presentation summary of the thesis as well as to its contents. In the using or citation of parts of the thesis it's obliged to indicate the name of the author.

# PHOTOSWITCHABLE ALLOSTERIC LIGANDS TO MODULATE METABOTROPIC GLUTAMATE RECEPTORS

## Tesi doctoral

Memòria presentada per Silvia Panarello per optar al títol de doctor per la  
Universitat de Barcelona

Aquesta Tesi ha estat realitzada en el Programa de Doctorat en Química Orgànica de  
la Universitat de Barcelona, a les instal·lacions de l'Institut de Química Avançada de  
Catalunya (IQAC-CSIC)

SILVIA  
PANARELLO -  
DNI Y4826914X

Firmato digitalmente  
da SILVIA PANARELLO  
- DNI Y4826914X  
Data: 2021.11.05  
12:42:34 +01'00'

Doctorant

**Silvia Panarello**

Director

**Dr. Amadeu Llebaria Soldevila**

Investigador científic

Departament de Química Biomèdica (IQAC-CSIC)

Codirector

**Dr. Xavier Gómez Santacana**

Investigador postdoctoral

Departament de Química

Biomèdica (IQAC-CSIC)

Tutor

**Dr. Vicente Marchán Sancho**

Professor Agregat

Departament de Química

Inorgànica i Orgànica (UB)



## Abbreviations

<b>7TMD</b>	Transmembrane domain
<b>Å</b>	Angstroms
<b>aAB</b>	Aminoazobenzene
<b>AB</b>	Azobenzene
<b>Abs</b>	Absorbance
<b>AC</b>	Adenylyl cyclase
<b>AcOH</b>	Acetic acid
<b>AM</b>	Allosteric modulator
<b>AMPA</b>	$\alpha$ -amino-3-hydroxy-5-methyl-4-isoxazolepropionic acid receptor
<b>ATP</b>	Adenosine triphosphate
<b>bAB</b>	Bridged azobenzene
<b>BG</b>	Benzylguanine
<b>BGAG</b>	Benzylguanine-azobenzene-glutamate
<b>br</b>	Broad
<b>BRET</b>	Bioluminescence resonance energy transfer
<b>°C</b>	Degree Celsius
<b><sup>13</sup>C</b>	Isotope carbon-13
<b>cAMP</b>	Cyclic adenosine monophosphate
<b>CaSR</b>	Calcium-sensing receptor
<b>Cat.</b>	Catalytic amount
<b>CDCl<sub>3</sub></b>	Deuterated chloroform
<b>(CD<sub>3</sub>)<sub>2</sub>CO</b>	Deuterated acetone
<b>CD<sub>3</sub>OD</b>	Deuterated methanol
<b>(CD<sub>3</sub>)<sub>2</sub>OS</b>	Deuterated dimethyl sulfoxide
<b>CFP</b>	Cyan fluorescent protein
<b>CL</b>	Caged ligands
<b>cGMP</b>	Cyclic guanosine monophosphate
<b>CNS</b>	Central Nervous system
<b>CRD</b>	Cystein-rich domain
<b>Cryo-EM</b>	Cryo-electron microscopy
<b>Cs<sub>2</sub>CO<sub>3</sub></b>	Cesium carbonate
<b>d</b>	Doublet
<b>dd</b>	Doublet of a doublet
<b>DCE</b>	1,2-dichloroethane
<b>DCM</b>	Dichloromethane
<b>DIPEA</b>	Diisopropylethylamine
<b>DMF</b>	Dimethyl formamide
<b>DMEM</b>	Dulbecco's modified Eagle's medium
<b>DMSO</b>	Dimethylsulphoxide
<b>DNA</b>	Deoxyribonucleic acid
<b>EC<sub>20</sub></b>	Effective concentration to induce 20% maximal response
<b>EC<sub>50</sub></b>	Half maximal effective concentration
<b>EC<sub>80</sub></b>	Effective concentration to induce 80% maximal response
<b>ECD</b>	Extracellular domain

<b>EDAM</b>	Extracellular domain allosteric modulator
<b>EDG</b>	Electron donating group
<b>e.g.</b>	Exempli gratia
<b>Eq.</b>	Equivalents
<b>EtOAc</b>	Ethyl acetate
<b>EtOH</b>	Ethanol
<b>Eu</b>	Europium
<b>EWG</b>	Electron withdrawing group
<b>FBDD</b>	Fragment-based drug discovery
<b>FRET</b>	Förster or fluorescence resonance energy transfer
<b>FXS</b>	Fragile X syndrome
<b>FZD</b>	Frizzled GPCRs
<b>GABA</b>	gamma-Aminobutyric acid
<b>GDP</b>	Guanosine diphosphate
<b>GFP</b>	Green fluorescent protein
<b>GPCR</b>	G protein-coupled receptor
<b>GTP</b>	Guanosine triphosphate
<b>h</b>	Hours
<b><sup>1</sup>H</b>	Isotope hydrogen-1
<b>H<sub>2</sub></b>	Hydrogen
<b>H<sub>2</sub>O</b>	Water
<b>HATU</b>	1-[Bis(dimethylamino)methylene]-1 <i>H</i> -1,2,3-triazolo[4,5- <i>b</i> ]pyridinium 3-oxid-hexafluorophosphate
<b>HBSS</b>	Hanks' Balanced Salt Solution
<b>HCl</b>	Hydrochloric acid
<b>HCOOH</b>	Formic acid
<b>HEPES</b>	<i>N</i> -(2-Hydroxyethyl)piperazine- <i>N'</i> -(2-ethanesulfonic acid) solution
<b>HEK293</b>	Human embryonic kidney cell line
<b>HOBt</b>	1-Hydroxybenzotriazole hydrate
<b>HPLC</b>	High performance liquid chromatography
<b>HRMS</b>	High resolution mass spectra
<b>HTRF</b>	Homogeneous time resolved fluorescence
<b>Hz</b>	Hertz
<b>i2</b>	Second intracellular loop
<b>IBMX</b>	3-isobutyl-1-methylxanthine
<b>IC<sub>50</sub></b>	Half maximal inhibitory concentration
<b>i.e.</b>	Id est
<b>iGluR</b>	Ionotropic glutamate receptor
<b>IP<sub>3</sub></b>	Inositol 1,4,5-trisphosphate
<b>IP</b>	Inositol monophosphate
<b>J</b>	J-coupling
<b>K<sub>2</sub>CO<sub>3</sub></b>	Potassium carbonate
<b>KA</b>	Kainate receptor
<b>KO</b>	Knock out (genetic technique)
<b>LC</b>	Liquid chromatography
<b>LED</b>	Light emitting diodes

<b>LGICs</b>	Ligand-gated ion channels
<b>m</b>	Multiplet
<b>MeCN</b>	Acetonitrile
<b>MeOH</b>	Methanol
<b>MgCl<sub>2</sub></b>	Magnesium chloride
<b>mGlu</b>	Metabotropic glutamate
<b>mGluR</b>	Metabotropic glutamate receptor
<b>MHz</b>	Megahertz
<b>MgSO<sub>4</sub></b>	Magnesium sulfate
<b>min</b>	Minute
<b>ml</b>	Milliliter
<b>mM</b>	Millimolar
<b>mm</b>	Millimeter
<b>MOPS</b>	(3-( <i>N</i> -morpholino)propanesulfonic acid) solution
<b>ms</b>	Millisecond
<b>MS</b>	Mass spectrometer
<b>m/z</b>	Mass-to-charge ratio
<b>NaCl</b>	Sodium chloride
<b>NAM</b>	Negative allosteric modulator
<b>Na<sub>2</sub>CO<sub>3</sub></b>	Sodium carbonate
<b>NaHCO<sub>3</sub></b>	Sodium bicarbonate
<b>NaNO<sub>2</sub></b>	Sodium nitrite
<b>NaOAc</b>	Sodium acetate
<b>NaOH</b>	Sodium hydroxide
<b>Na<sub>2</sub>HPO<sub>4</sub></b>	Disodium hydrogen phosphate
<b>Na<sub>2</sub>SO<sub>4</sub></b>	Sodium sulfate
<b>NH<sub>3</sub></b>	Ammonia
<b>NH<sub>4</sub>HCO<sub>3</sub></b>	Ammonium bicarbonate
<b>nHex</b>	Normal hexane
<b>NIR</b>	Near-infrared
<b>nm</b>	Nanometer
<b>NMDA</b>	<i>N</i> -methyl-D-aspartate receptor
<b>NMR</b>	Nuclear magnetic resonance
<b>pAB</b>	Protonated-azobenzene
<b>PAM</b>	Positive allosteric modulator
<b>PAS</b>	Photoinduced affinity shift
<b>PBS</b>	Phosphate buffered saline
<b>PCL</b>	Photochromic ligand
<b>Pd/C</b>	Palladium on carbon
<b>PD</b>	Parkinson's disease
<b>PDA</b>	Photodiode array
<b>PDE</b>	Photoinduced difference of efficacy
<b>PE</b>	Photon excitation
<b>PEG</b>	Polyethylene glycol
<b>PET</b>	Positron emission tomography
<b>PLO</b>	Poly-L-ornithine

<b>PNS</b>	Peripheral nervous system
<b>ppAB</b>	Push-pull azobenzene
<b>ppm</b>	Parts per million
<b>PPS</b>	Photoinduced potency shift
<b>pSB</b>	Pseudostilbene
<b>PSD</b>	Postsynaptic density
<b>psi</b>	pound per square inch
<b>PSS</b>	Photostationary state
<b>PTL</b>	Photochromic tethered ligand
<b>q</b>	quartet
<b>quant.</b>	Quantitatively
<b>RT</b>	Retention time
<b>rt</b>	Room temperature
<b>s</b>	Seconds
<b>s</b>	Singulet
<b>SAM</b>	Silent allosteric modulator
<b>SAR</b>	Structure-activity relationship
<b>SBDD</b>	Structure-based drug discovery
<b>SEM</b>	Standard error of the mean
<b>SMO</b>	Smoothened GPCRs
<b>t</b>	Triplet
<b>t<sub>0</sub></b>	Time zero
<b>t<sub>1/2</sub></b>	Half-life time
<b>Tb</b>	Terbium
<b>TEA</b>	Triethylamine
<b>THF</b>	Tetrahydrofuran
<b>toAB</b>	tetra- <i>o</i> -substituted azobenzene
<b>TR-FRET</b>	Time resolved Förster resonance energy transfer
<b>UV</b>	Ultra violet
<b>VFT</b>	Venus fly trap domain
<b>Vis</b>	Visible
<b>VGICs</b>	Voltage-gated ion channels
<b>VGLUT</b>	Vesicular glutamate transporters
<b>W</b>	Watt
<b>WT</b>	Wild type
<b>wt.</b>	Weight
<b>YFP</b>	Yellow fluorescent protein
<b>μM</b>	Micromolar
<b>μm</b>	Micrometer
<b>μs</b>	Microsecond
<b>μW</b>	Microwave

## Table of Contents

<b>General Introduction</b> .....	<b>3</b>
Photo-regulation of drug bioactivity: beyond proof of concept .....	9
G Protein-Coupled Receptors (GPCRs) .....	25
Photopharmacology of G Protein-Coupled Receptors .....	33
Class C GPCRs .....	49
Freely diffusible photoswitchable allosteric modulators for mGluRs .....	64
<b>Objectives</b> .....	<b>71</b>
<b>Results and discussion</b> .....	<b>75</b>
Chapter 1: mGlu <sub>5</sub> inhibition with <i>cis</i> -active photoswitchable NAMs .....	79
Chapter 2: Development of a selective photoswitchable PAM for mGlu <sub>4</sub> receptor .....	102
Chapter 3: A toolbox of photoswitchable PAMs to selectively modulate mGlu <sub>1</sub> .....	112
Chapter 4: A series of arylazothiazoles to control mGlu <sub>1</sub> function with light .....	125
<b>Summary of results and conclusions</b> .....	<b>151</b>
<b>Experimental section</b> .....	<b>155</b>
Synthetic chemistry .....	159
Photophysical and photochemical characterization .....	191
Pharmacological and biochemical characterization .....	198
<b>Bibliographic references</b> .....	<b>219</b>





## General Introduction

---

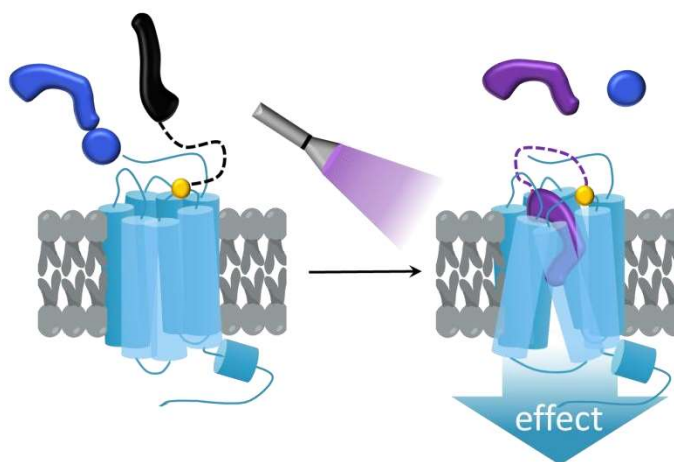
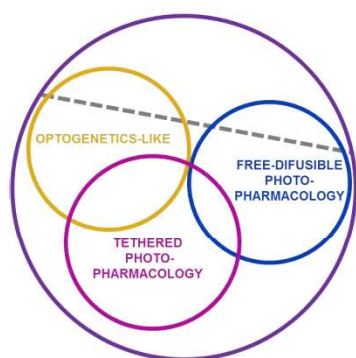
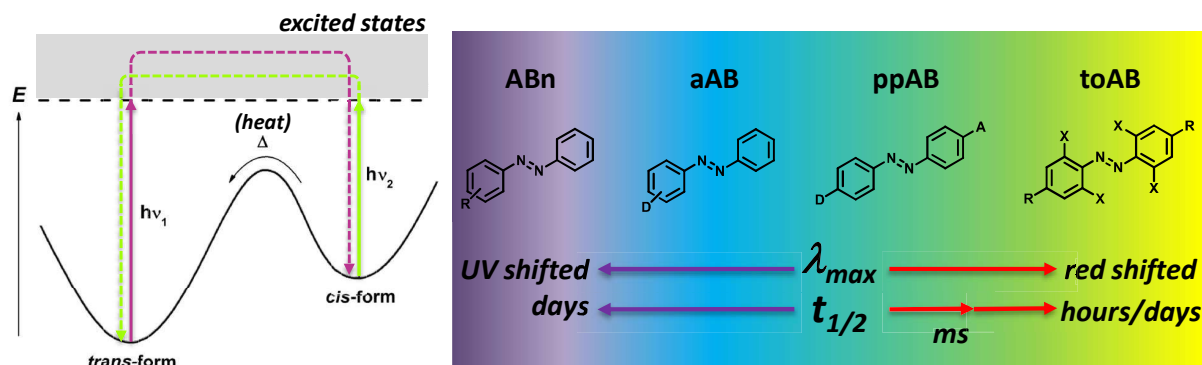


# General Introduction Contents

<b>Photo-regulation of drug bioactivity: beyond proof of concept</b> .....	<b>9</b>
Photoresponsive molecular switches .....	11
Azobenzene: probably the best molecular photoswitch .....	11
Photoisomerization of AB .....	13
Substituted Azobenzenes (ABs) .....	15
ABn derivatives.....	16
aAB derivatives.....	17
pAB derivatives (PSB family) .....	18
ppAB derivatives (PSB family) .....	19
toAB derivatives .....	21
bAB derivatives.....	23
<b>G Protein-Coupled Receptors (GPCRs)</b> .....	<b>25</b>
Guanine nucleotide-binding proteins (G Proteins) .....	26
Modification of GPCR function: orthosteric and allosteric ligands .....	28
Classification of human G protein-coupled receptors .....	30
<b>Photopharmacology of G Protein-Coupled Receptors</b> .....	<b>33</b>
Enabling light as an actuator for GPCR research.....	33
Optogenetics-like approaches .....	34
GPCR Photopharmacology approaches .....	34
Freely diffusible photopharmacology .....	35
Tethered photopharmacology .....	38
Characterization of GPCR photopharmacological tools .....	40
Photoisomerization and uncaging characterization .....	40
UV-Vis spectroscopy.....	40
LC-PDA-MS .....	40
NMR spectroscopy .....	41
Receptor photoswitching characterization .....	41
Kinetic functional assays .....	42
Endpoint functional assays.....	43
Conformational assays .....	44
Binding assays .....	44
T-on/ M-on photochromic ligands.....	46
Translation to <i>in vivo</i> and therapeutic prospects .....	48
<b>Class C GPCRs</b> .....	<b>49</b>
Topology and ligand recognition.....	49
Dimeric structure of class C GPCRs: a need for signal transduction .....	50
The 7TM domain activates G-protein stepwisely: mGlu receptors as archetypical examples .....	52
Glutamate as excitatory neurotransmitter .....	55
Classification of the mGlu receptors, functional anatomy and main biological roles.....	57
Group I mGluRs.....	58
Group II mGluRs.....	59
Group III mGluRs.....	59
Modulation of mGlu receptor activity .....	60
Ligands acting at the VFT .....	60

Ligands acting at the 7TMD .....	62
mGlu receptors as drug targets .....	63
<b>Freely diffusible photoswitchable allosteric modulators for mGluRs .....</b>	<b>64</b>
mGlu <sub>5</sub> ( <i>Group I</i> ) .....	64
mGlu <sub>2</sub> ( <i>Group II</i> ) .....	66
mGlu <sub>4/6/7/8</sub> ( <i>Group III</i> ).....	67

## General introduction



### Key points

- Light strategies currently described to control receptor activity
- G protein-coupled receptors: focus on class C GPCRs
- Characterization methods of GPCR photopharmacological tools
- Photoswitchable allosteric modulators developed so far for Metabotropic Glutamate Receptors

### Papers related to this chapter

- Silvia Panarello, Xavier Gómez-Santacana, Xavier Rovira and Amadeu Llebaria, "Photopharmacology of G protein-coupled receptors", *Molecular Photoswitches: Synthesis, Properties, and Applications*, Ed. Wiley-VCH Verlag GmbH by Pianowski, **2021**, ISBN/EAN: 3527347682/978-3527347681. Accepted for print.
- Xavier Gómez-Santacana, Silvia Panarello, Xavier Rovira and Amadeu Llebaria, "Photoswitchable allosteric modulators for Metabotropic Glutamate Receptor", *Current Opinion in Pharmacology*. In preparation.



## Photo-regulation of drug bioactivity: beyond proof of concept

Pharmacotherapy is the treatment of a disease using pharmaceutical drugs, as distinguished from therapy using surgery (surgical therapy), radiation (radiation therapy), movement (physical therapy) or other modes. It offers the possibility to cure diseases and alleviate symptoms through only the administration of drugs.<sup>1,2</sup> A drug is a chemical substance, usually a small molecule, used in the treatment, cure, prevention of disease or used to otherwise enhance physical or mental well-being. Thereby, pharmacotherapy has improved quality of life and has contributed to what our world is today. Clearly, the administration of a given drug represents the end point of a long, complex, and expensive previous process, characterized by several multidisciplinary steps.

In this regard, drug discovery represents the first pillar of the entire development process of a drug. It is a multifaceted process involving the identification of candidates as potential new medicines, synthesis, characterization, validation, optimization, screening and assays for therapeutic efficacy.<sup>3</sup> In the overall process, scientific disciplines such as biology, chemistry and pharmacology have a crucial role. In particular, pharmacology is often confused with pharmacotherapy but the subtle difference already lies in the word itself. "Pharmacology" is a word derived from Greek φάρμακον, *pharmakon*, "drug, poison" and -λογία, (or *-logia* in Medieval Latin) "study of", "knowledge of". Then, it is the scientific discipline that focuses on understanding the properties and actions of chemicals, usually drugs or compounds that could become drugs, emphasizing their therapeutic effects. Toxicology is instead another discipline regarding chemical's adverse effects and risk assessment. Hence, the complete pharmacological knowledge is important to guide pharmacotherapy in medicine and pharmacy.

However, if on the one hand pharmacotherapy wants to simplify access to treatments, deliver better health outcomes and enhance life quality, on the other hand it suffers from limitations due to drug-related problems. Classical pharmacotherapy, which benefits from high receptor specificity, is inadequate to address cellular processes with high spatio-temporal selectivity. In fact, once the drug is released in the body, through whichever of the possible routes of administration, it is spread in an imprecise fashion all over the body and the control of this substance is lost. At some point, it will reach and bind its target protein, wherever it is localized, regardless the kind of cell, tissue or system where it is expressed.<sup>4</sup> Moreover, poor drug selectivity can result also in toxicity-related side effects,<sup>5</sup> which means it lowers the threshold level of toxicity and thereby narrows the therapeutic window, leading to a decrease in allowable dose.<sup>6</sup> For this reason, many interesting drug candidates, which potentially could improve present pharmacotherapy or even treat currently untreatable conditions, are discarded solely due to insufficient selectivity.<sup>7</sup> Another major issue in modern pharmacotherapy is drug resistance.<sup>8,9</sup> In particular, the use of antibacterial agents is under pressure because of the emergence of many resistant bacterial strains. The main cause of antibiotic resistance is it is the use of the antibiotic itself. The overuse of antibiotics makes resistant bacteria more common. The more we use antibiotics, the more chances bacteria have to become resistant to them.<sup>9,10</sup>

At this point, in the search for novel molecular approaches to dynamically control drug activity and bypassing the aforementioned issues, it has been proposed a solution that lies in the use of light.<sup>11</sup> Light irradiation is an appealing phenomenon that interweaves together chemistry, biology, physics and engineering and the use of it opens new frontiers in science. More specifically, light helps in achieving new technologies through which it is possible to finely study the biological system in a real-time mode. Therefore, taking advantage of molecular probes and drugs with light-dependent properties (*i.e.* affinity and/or efficacy), crucial therapeutic challenges as control of the drug action site, time course of drug effect



and fine-tuning of effects on target protein could be solved (Figure 1).<sup>12-15</sup> From a medicinal chemistry perspective, photopharmaceuticals are developed by the incorporation of photoresponsive molecular switches (also called photoswitches) into existing drugs to enable alteration of their biological properties upon light irradiation, a process also known as photoswitching.<sup>15-18</sup> The photopharmaceutical in question exists in an inactive form, depicted in blue in Figure 1B, and in an active one (in purple, Figure 1B). The irradiation with light of suitable wavelengths allows to change the drug activity and, in most cases, in a reversible way. Moreover, light should make possible the investigation of fast processes that are confined to specific cellular compartments or specific subsets of cells<sup>19</sup> and it can also be regulated very precisely by adjusting the wavelength and the intensity.<sup>12</sup>

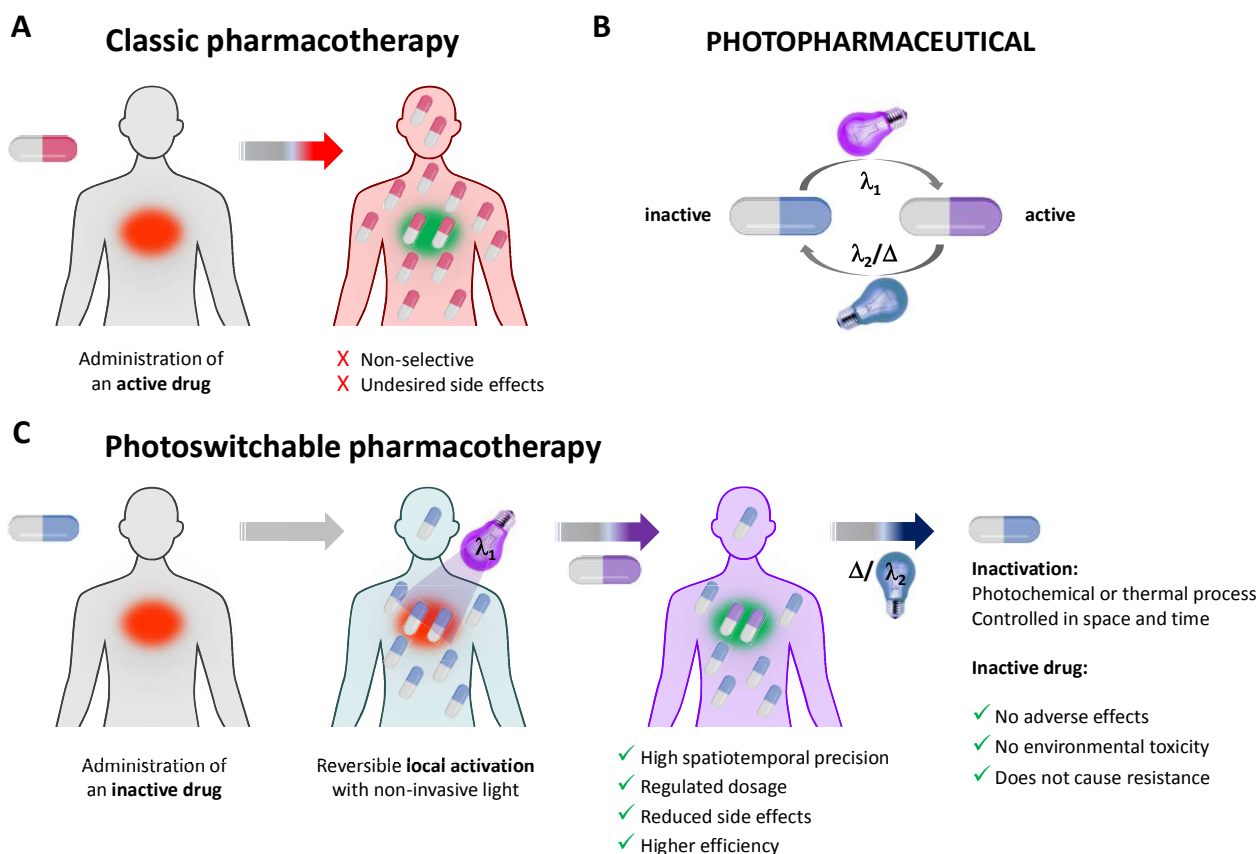


**Figure 1.** Comparison of the principles behind (A) classic pharmacotherapy and high-precision photoswitchable pharmacotherapy (B, C). The reversible photoswitching between the inactive (blue) and active (purple) therapeutic agent (B) allows for local activation of the drug and permits its use at lower concentrations, without systemic side effects (C). Pharmaceutical's inactivation limits environmental toxicity and drug resistance. (Adapted from Velema et al. and Szymanski et al.).<sup>12,18</sup>

Thereby, photoswitchable pharmacotherapy is ideally characterized by administration of an inactive drug first and reversible and local activation with non-invasive light later. This means that the photoswitchable drug could exert its function just in the area of the organism of interest when it is in its active form thanks to the use of light. The advantages of this approach are many: light can be delivered with very high spatiotemporal precision- thus we can reduce the dosage of the drug-, the effects on the rest of patient's body are very limited and the efficiency can be higher than using conventional drugs. Moreover, with a final inactivation step of the same compound, that can be achieved by irradiation with light of different wavelengths or after a thermal process,<sup>20</sup> the problems of environmental toxicity and antibiotic resistance could be limited (Figure 1C).<sup>12</sup> Examples of compounds with photoswitchable bioactivity include photocontrolled ion-channel blockers,<sup>21</sup> antibiotics,<sup>22</sup> enzyme inhibitors and GPCR ligands.<sup>23</sup>

## Photoresponsive molecular switches

In order to achieve a fine reversible control of a protein function with light, it is necessary to include a light-sensitive moiety containing a photochromic group covalently linked to either the target protein or a ligand. The chromophore absorbs a photon and produces a chemical transformation that may induce a change in the conformation of the attached protein. These light-activated processes are usually completely reversible, and the chromophores can switch between two or more isomeric forms, hence the commonly used term “photoswitches”.<sup>24</sup> In a certain way, there is nothing extraordinarily new about this strategy considering that several essential biological processes, such as vision<sup>25</sup> and photosynthesis are fueled by light.

An example could be retinal in opsin proteins (class A of GPCRs) that regulate the visual transduction (human rhodopsin), the trafficking of ions [channelrhodopsins (*Table 1*) and halorhodopsin]<sup>26</sup> and pump protons as a source of energy (bacteriorhodopsin).<sup>27</sup> However, retinal cannot be considered a formal photoswitch for monostable pigments, since this photoswitching is not reversible with a second light wavelength.<sup>28</sup> Anyhow, a variety of synthetic photoswitches have been designed (*Table 1*). These photocontrolled biomolecules, depending on their isomerization mechanism, can be interconverted upon light illumination between *cis* and *trans* isomers (azobenzenes, stilbenes and hemithioindigos) and open and closed forms (spiropyrans, diarylethenes and thiophenfulgides). This results in a change in geometry, flexibility, polarity and charge distribution of the compound (*Table 1*).<sup>15,29</sup> More precisely, these isomeric forms represent “metastable” and “thermodynamically stable” states. In physics and chemistry, a metastable state is a particular excited state of an atom, nucleus, or other system that has a longer life-time than the ordinary excited states and that generally has a shorter life-time than the lowest and more stable, energy state, called thermodynamically stable state.

### ***Azobenzene: probably the best molecular photoswitch***

Although chemistry has come up with a large number of synthetic photoswitches covering a vast number of structural types, azobenzene derivatives, including phenylazopyridines and azopyridines, are the molecules most extensively used for biological applications. This is due to the fact that they are considered pharmacologically promising as they fulfil many important criteria. First of all, both their synthesis and the chemical functionalization are relatively straightforward.<sup>30</sup> Both factors are crucial when it is desirable to change electronic and steric nature of the azobenzenes to fine tune the photophysical properties in terms of quantum yields and rate of isomerization. They are small-sized compounds characterized by an efficient photoswitching, which results in a large change in geometry. Other key factors are their high resistance to photodegradation with almost no photobleaching, their good stability under physiological conditions and photoisomerization rates faster than most biological processes.<sup>15</sup> All these properties make azobenzene a good candidate to replace several moieties with two aromatic rings found in bioactive molecules, such as biaryl amides, aryl phthalimides, biaryl acetylenes or biaryl ethers. This strategy is known as “azologization”<sup>31</sup> and the resulting analogs can be defined as “azologs”.

Azobenzene structure consists of two phenyl rings, joined by a -N=N- group, also called azo-bond or azo-bridge (*Figure 2A*). The *trans* isomer has a planar geometry with a dihedral angle of 180° and an extended delocalization of the  $\pi$ -electrons over the aromatic rings and the azo-bond. It also has a negligible dipolar moment. On the other hand, the *cis* isomer has a bent geometry, ~3.5 Å shorter than *trans* one (distance between the carbons at each *para* position of the rings), with its phenyl rings twisted 55° out of the plane and a dihedral angle of the azo-bond of 11° and a dipolar moment of 3.7 Debye.

Switch	Structure and isomerization	Change
Retinal (channelrhodopsin)		Geometry
Azobenzenes		Geometry and polarity
Stilbenes		Geometry
Hemithioindigos		Geometry and polarity
Spiroprans		Polarity, geometry and flexibility
Diarylethenes		Flexibility
Thiophenefulgides		Flexibility

**Table 1.** The natural photoswitch retinal binds covalently to a lysine of the channelrhodopsin through a Schiff base linkage. The relaxed state contains all-*trans*-retinal-iminium. The absorption of visible light favors the 13 *cis* configuration that induces a conformational change in proteins that allow ion flow. Relaxation to the all-*trans* configuration occurs spontaneously.<sup>29</sup> Apart from the natural retinal, the others are the most used synthetic photoswitches. *Trans* isomer and open form on the left whereas the *cis* isomer and closed form on the right (not for the spiroprans).

This geometry causes a rupture of the  $\pi$  delocalization on the azo-bond (*Figure 2B*). This rupture can be easily determined by  $^1\text{H-NMR}$  of the protons in *ortho* position. For *trans*-azobenzene (**1**), these protons are located in a clearly aromatic cone around 7.90 ppm ( $\text{CDCl}_3$ , 600 MHz),<sup>32</sup> whereas for *cis*-azobenzene (**1**) the same protons shift to the right till 6.83 ppm ( $\text{CDCl}_3$ , 600 MHz),<sup>32</sup> a nearly typical chemical shift for aniline (6.70 ppm,  $\text{CDCl}_3$ , 400 MHz).<sup>33</sup> This exactly means that the rupture of the delocalization of the  $\pi$ -electrons over the  $-\text{N}=\text{N}-$  leads to aniloid electronic properties.

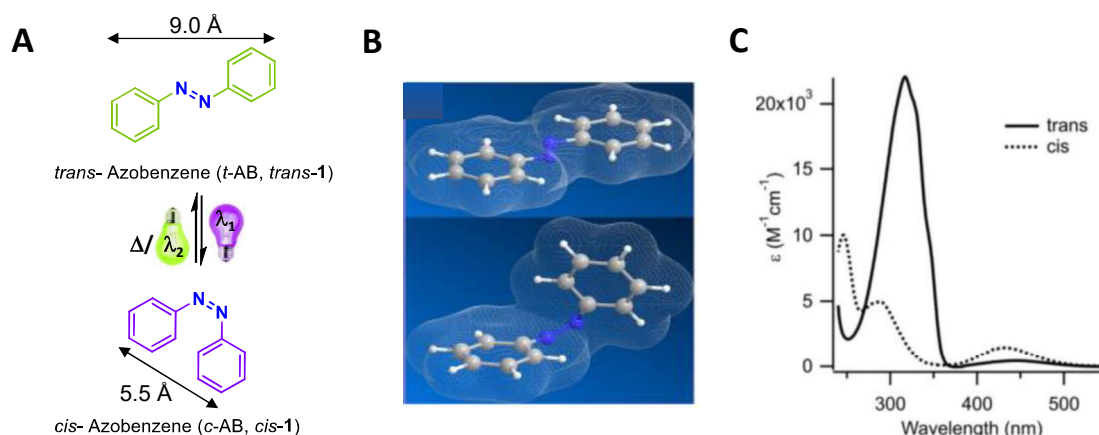


**Figure 2.** (A) Two-dimensional structure of *trans/cis* azobenzene (**1**) isomers; (B) 3D structure of both isomers with a total electron density surface after minimizing energy with MM2 (Chem3D 20.0); (C) UV-Vis absorption spectrum of *trans/cis* azobenzene (**1**).

The UV-Vis absorption spectra of *trans* and *cis*-azobenzene are distinct but overlapping (Figure 2C). The photoisomerization of azobenzene (AB, **1**) was reported for the first time in 1937, after observing a lack of reproducibility in absorbance measurements when a solution of azobenzene was exposed to light.<sup>34</sup> *Trans*-azobenzene displays a very weak  $n-\pi^*$  band near 440 nm, forbidden by symmetry, and a strong  $\pi-\pi^*$  transition near 320 nm. Alternatively, *cis*-azobenzene shows a stronger  $n-\pi^*$  band also near 440nm and shorter  $\pi-\pi^*$  bands at 280 nm and 250 nm. The *trans*-azobenzene is 10-12 Kcal/mol more stable than the *cis* one, resulting in a strong predominance of the *trans* isomer in equilibrium in the dark.<sup>15</sup> The *cis* isomer can be obtained under illumination with ultraviolet light ( $\sim 340$  nm) and it is possible to recover the initial state either thermally or by illumination with visible light ( $> 440$ nm).

### Photoisomerization of AB

More precisely, while in dark conditions only the *trans*-azobenzene is present, continuous irradiation of *t*-AB (**1**) with either 340 nm or 440 nm radiation results in a photostationary state (PSS) comprised of  $\sim 20\%$  or  $\sim 90\%$  of *t*-AB, respectively.<sup>20</sup> Indeed, the *trans* form of azobenzene is thermodynamically more stable than the *cis* form and hence the proportion of isomers at room temperature and dark conditions is characterized by a high population of *trans* isomer. However, upon irradiation with UV light, the equilibrium is shifted to a larger molar fraction of *cis* isomer. The *cis* isomer is stable in the dark and at low temperatures but slowly reverses to *trans* isomer according to a first-order kinetics. Irradiation with visible light or heating quickly shifts the isomeric equilibrium to the *trans* isomer (Figure 3).

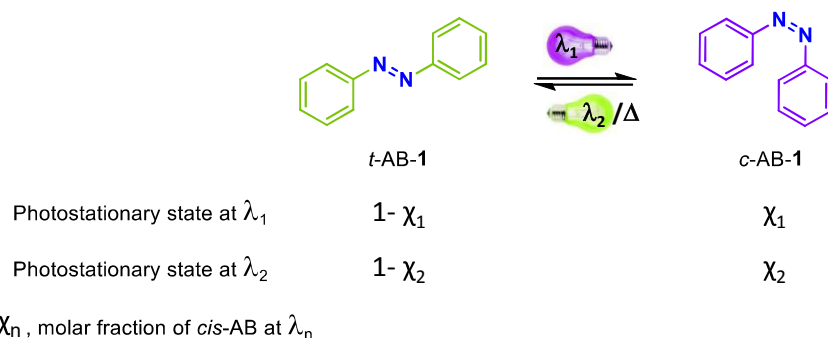
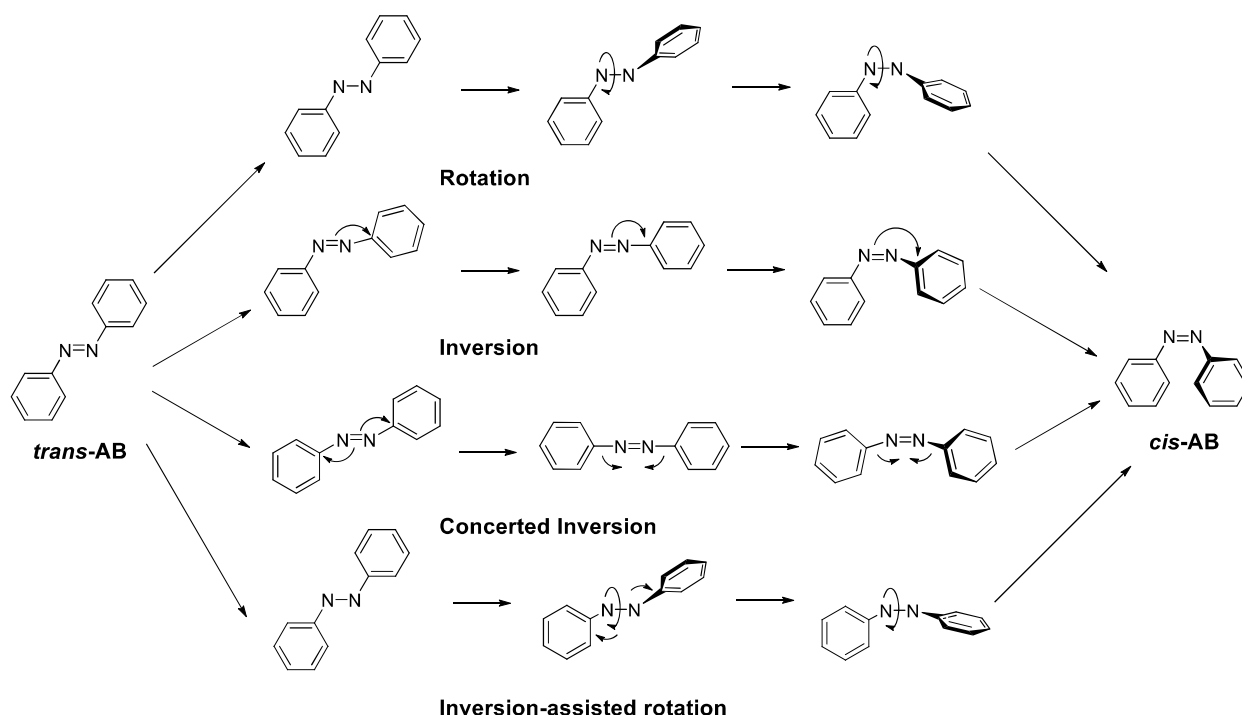


**Figure 3.** The illumination with a specific wavelength pulse induces a change of the populations of the azobenzene molecules in the *cis* and *trans* forms reaching the photostationary state (PSS) where a mixture of the two isomers can be detected. Each PSS is characterized by a different molar fraction of *cis*-AB.

Four mechanisms (rotation, inversion, concerted inversion, inversion-assisted rotation) have been proposed as possible pathways for AB photoisomerization (*Scheme 1*) depending on the different bonding movements and resulting changes in the C=N=N-C dihedral angle.<sup>20</sup> The rotational pathway involves rupture of the N=N  $\pi$ -bond to allow free rotation about the N-N bond. Rotation changes the C-N-N-C dihedral angle while the N-N-C angle remains fixed at  $\sim 120^\circ$ . In the inversion mechanism, one N=N-C angle increases to  $180^\circ$  while the C-N=N-C dihedral angle remains fixed at  $0^\circ$ . For isomerization by concerted inversion, both N=N-C bond angles increase to  $180^\circ$  generating a linear transition state. In inversion-assisted rotation, large changes in the C-N=N-C dihedral angle and smaller but significant changes in the N=N-C angles occur simultaneously. The transition state formed in concerted inversion has no net dipole moment, whereas the other three pathways possess polar transition states (*Scheme 1*). Multiple isomerization pathways have often been invoked to explain experimental observations.<sup>35</sup>



**Scheme 1.** Proposed mechanisms for the *trans*  $\rightarrow$  *cis* isomerization of AB.<sup>20</sup>

Therefore, this photoreaction simply causes the rearrangement of the electronic and nuclear structure of the molecule without any bond breaking. In the electronic ground state the *cis*-state is higher in energy than the *trans*-state by 0.6 eV and reaches the *trans*-state only via a barrier of 1.6 eV (*Figure 4A*).<sup>36,37</sup> For this reason, the two configurations can be interchanged easily by optical excitation with light at suitable wavelengths. However, regardless of the type of mechanism, the *trans*  $\rightarrow$  *cis* photoisomerization of azobenzene in solution occurs on the subpicosecond and picosecond time scale.<sup>36</sup> After exciting the *trans*-isomer and reaching the  $S_2$  state, the molecule leaves the Franck-Condon region and  $S_0 \leftarrow S_1$  relaxation takes place accompanied by isomerization of *t*-AB. Finally, vibrational cooling of the ground-state potential energy surface  $S_0$  and interconversion to the *cis*-configuration occur (*Figure 4B*).<sup>20</sup>

Ultrafast time-resolved spectroscopic studies confirmed that both  $S_1 \leftarrow S_2$  and  $S_0 \leftarrow S_1$  relaxation occur monomodally with time constants of 0.11–0.3 ps and 0.5–1.0 ps respectively following  $S_2 \leftarrow S_0$  excitation of *t*-AB.<sup>35</sup> Moreover, depending on the solvent polarity and viscosity the time constants could change but always remaining in the order of picoseconds (*Figure 4B*).<sup>20,35,36</sup>

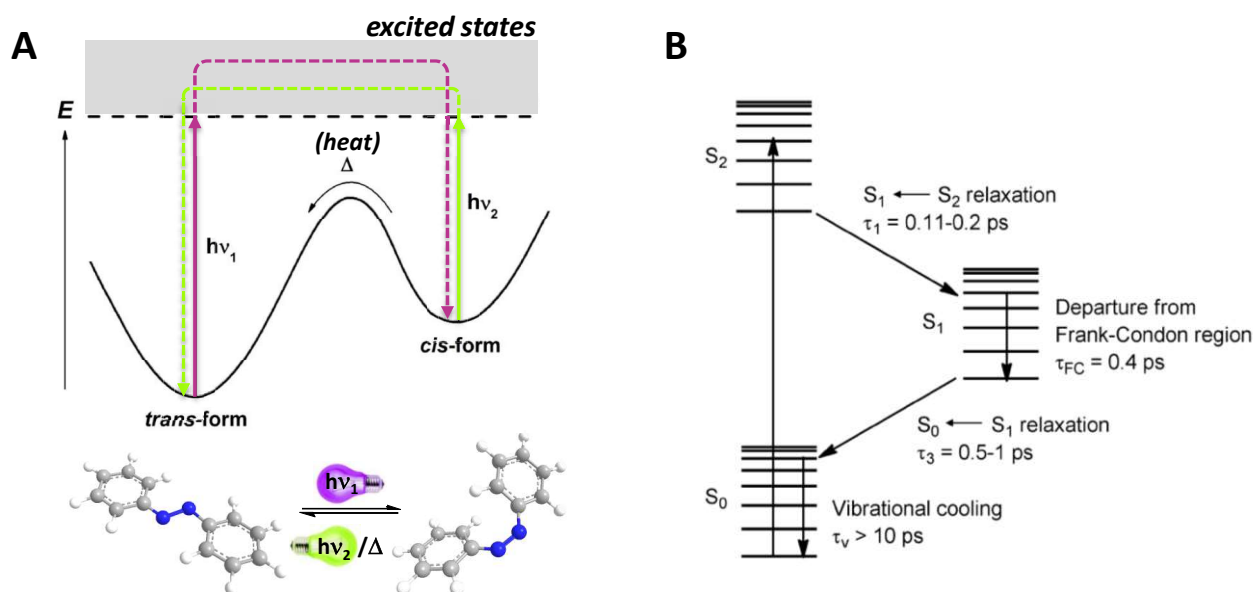
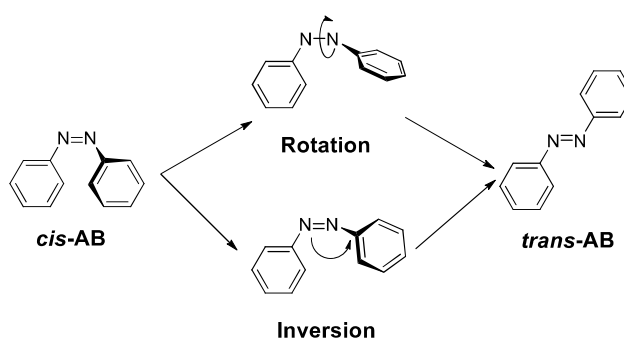


**Figure 4.** (A) Energetic profile for the switching process of azobenzene; (B) A simplified Jablonski diagram showing the  $S_0$ ,  $S_1$  and  $S_2$  states of *trans*-AB. (Adapted from Bandara/Burdette and García-Amorós/Velasco).<sup>20,37</sup>

The *cis*  $\rightarrow$  *trans* photoisomerization has not been investigated experimentally, so minimal information about its excited states lifetimes and conformations exists. However, it is very well known that it occurs ultrafast and with high quantum efficiency.<sup>36</sup> Instead, regarding the thermal *cis*  $\rightarrow$  *trans* isomerization, not only the polarity and viscosity of the solvent affect relaxation time constants but also the temperature and nature of the possible substituents on the aromatic rings.<sup>38</sup> The thermal half-life of unmodified *c*-AB is on the order of 3-4 days at room temperature and acids accelerate the isomerization process.<sup>20,39,40</sup> Rotation<sup>41</sup> and inversion<sup>42</sup> have been proposed as possible pathways for the thermal isomerization of *c*-AB (Scheme 2).



**Scheme 2.** Rotation and inversion mechanisms proposed for the thermal *cis*  $\rightarrow$  *trans* isomerization process of azobenzene. (Adapted from Asano and Okada).<sup>38</sup>

### Substituted Azobenzenes (ABs)

The conditions to isomerize the azobenzene from *trans* to *cis* isomer are not suitable for biological applications, since UV light is unable to penetrate into tissues and can cause severe damage to living cells.<sup>43</sup> Nevertheless, ring substituents can produce changes on the absorption profile and photochemical properties such as wavelengths shifting to longer biocompatible ranges and thermal relaxation times modification. Furthermore, new classes of azobenzene molecules were recently reported, which can be switched between *trans* and *cis* forms using visible light.<sup>16,44</sup> Historically, ABs have been divided into three main categories based on the relative energies of  $\pi$ - $\pi^*$  and  $n$ - $\pi^*$  transitions: azobenzenes (ABn),

aminoazobenzenes (aAB) and pseudostilbenes (pSB); the latter in turn including two subclasses more: the protonated-azobenzenes (pAB) and push-pull azobenzenes (ppAB). Additionally, thermal relaxation properties have also been considered, since some azoderivatives exhibit a fast thermal back reaction due to their capability to establish an azo-hydrazone tautomeric equilibrium.<sup>37</sup> All these are among the most common azobenzene approaches and are very well reviewed by Bandara and Burdette (Figure 5).<sup>20</sup> Moreover, the two new classes of azobenzenes mentioned above must also be considered and they are the tetra-*o*-substituted azobenzenes (toAB) and the bridged azobenzenes (bAB) (Figure 5).<sup>16,44</sup>

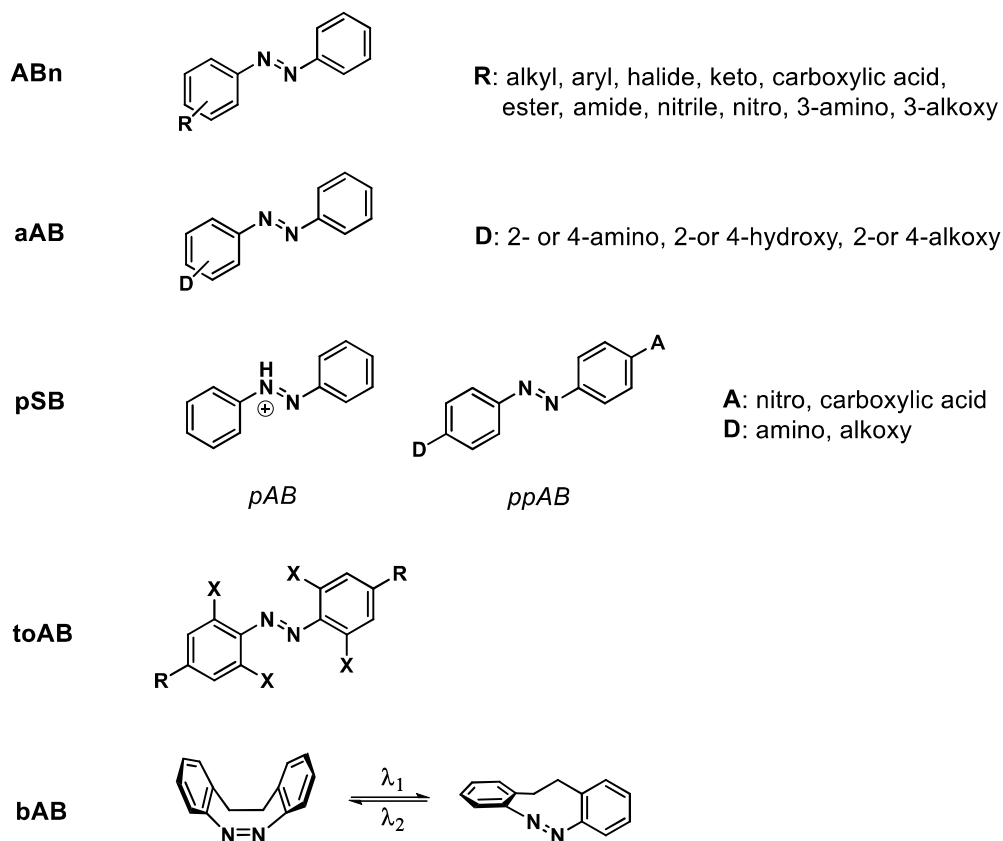
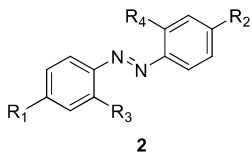


Figure 5. Types of substituted ABs.

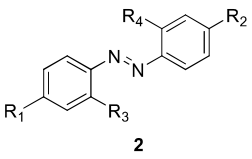
### ABn derivatives

ABn derivatives includes all azobenzenes (ABs) substituted with electro withdrawing groups (EWG) or mild electron donating group (EDG), such as alkyl, aryl, halide, carbonyl, amide, nitrile, ester, carboxylic acid or even amino and alkoxy in position 3. The family includes also azopyridines and phenylazopyridines. In all cases the absorption spectra is similar to the unsubstituted azobenzenes.<sup>45</sup> The two bands in ABns are well separated and the  $n-\pi^*$  transition absorbs much more weakly than the  $\pi-\pi^*$  transition. The thermal relaxation time of the *cis* isomer is generally slow but it can decrease depending on the number of substituents (Table 2). They are found in protein probes or molecular machines where fast thermal isomerization is undesirable.

Group	Comp.	R <sub>1</sub>	R <sub>2</sub>	R <sub>3</sub>	R <sub>4</sub>	$\lambda_{\max(\pi-\pi^*)}$ [nm]	t <sub>1/2</sub> [min]
<b>ABn</b>  <b>2</b>	<b>1</b>	H	H	H	H	315	-
	<b>2a</b>	Me	Me	H	H	330	401
	<b>2b</b>	Cl	Cl	H	H	331	431
	<b>2c</b>	NO <sub>2</sub>	H	H	H	330	94
	<b>2d</b>	NO <sub>2</sub>	H	Me	H	336	60
	<b>2e</b>	NO <sub>2</sub>	NO <sub>2</sub>	H	H	336	29

**Table 2.** Maximum of absorbance corresponding to the  $\pi$ - $\pi^*$  band and half-life times for thermal *cis*  $\rightarrow$  *trans* isomerization of different azobenzene derivatives belonging to the group ABn. The measurements were done in cyclohexane at 35°C. (Adapted from Gómez-Santacana).<sup>46</sup>

#### aAB derivatives

Group	Comp.	R <sub>1</sub>	R <sub>2</sub>	R <sub>3</sub>	R <sub>4</sub>	$\lambda_{\max(\pi-\pi^*)}$ [nm]	t <sub>1/2</sub> [min]
<b>aAB</b>  <b>2</b>	<b>2f</b>	OMe	H	H	H	342	357
	<b>2g</b>	Ome	Ome	H	H	353	221
	<b>2h</b>	Nme <sub>2</sub>	H	H	H	390	103
	<b>2i</b>	Nme <sub>2</sub>	Me	H	H	400	70
	<b>2j</b>	Nme <sub>2</sub>	Me	Me	Me	399	24
	<b>2k</b>	Nme <sub>2</sub>	Nme <sub>2</sub>	H	H	410	14.8
	<b>2l</b>	Net <sub>2</sub>	H	H	H	407	70
	<b>2m</b>	Net <sub>2</sub>	Net <sub>2</sub>	H	H	431	7.4

**Table 3.** Maximum of absorbance corresponding to the  $\pi$ - $\pi^*$  band and half-life times for thermal *cis*  $\rightarrow$  *trans* isomerization of different azobenzene derivatives belonging to the group aAB. The measurements were done in cyclohexane at 35°C. (Adapted from Gómez-Santacana).<sup>46,47</sup>

ABs with one or more amino, methoxy or hydroxy substituent in the 2 or 4 positions are classified as aABs. Due to the electron donating properties of these groups (EDG), the  $\pi$ - $\pi^*$  transition of aABs is shifted to higher wavelengths (also called red-shifting, *Table 3*) and overlaps or partially overlaps with the  $n$ - $\pi^*$  transition. The overlap between the two transitions depends on the number of amino substituents, degree of amine alkylation and solvent polarity. *N*-amides, *N*-carbamates and ureas may also be classified in this group since they also cause a red-shift of the  $\pi$ - $\pi^*$  band in compounds of general formula **3** depending on the electron donating properties of each group (*Figure 6*).<sup>48</sup>



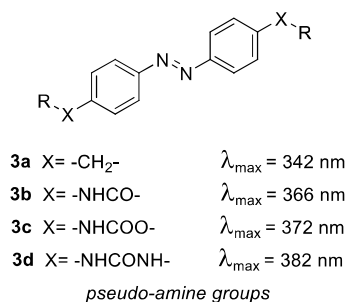


**Figure 6.** Comparison of the red-shifting effect of  $\pi$ - $\pi^*$  band of pseudo-amine groups such as amide, carbamate or urea.<sup>48</sup>

Electron donating substituents cause a modest decrease in the thermal isomerization barrier by increasing the electron density in  $\pi^*$  orbital and leading to higher rates of *cis*  $\rightarrow$  *trans* thermal isomerization than AB. Instead, substitution in *ortho* positions with bulky groups can make the relaxation slower due to a stabilization of the *cis* isomer.<sup>49</sup> Thermal isomerization rates in aABs are affected by solvent polarity but not by viscosity.<sup>20</sup> Additionally, when amines or hydroxyl groups are not alkylated, these aABs exhibit remarkably different properties from other ABs. More precisely, thermal relaxation half-life decreases due to an azo-hydrazone tautomeric equilibrium (*Figure 7A*), especially in polar solvents.<sup>37,46</sup>

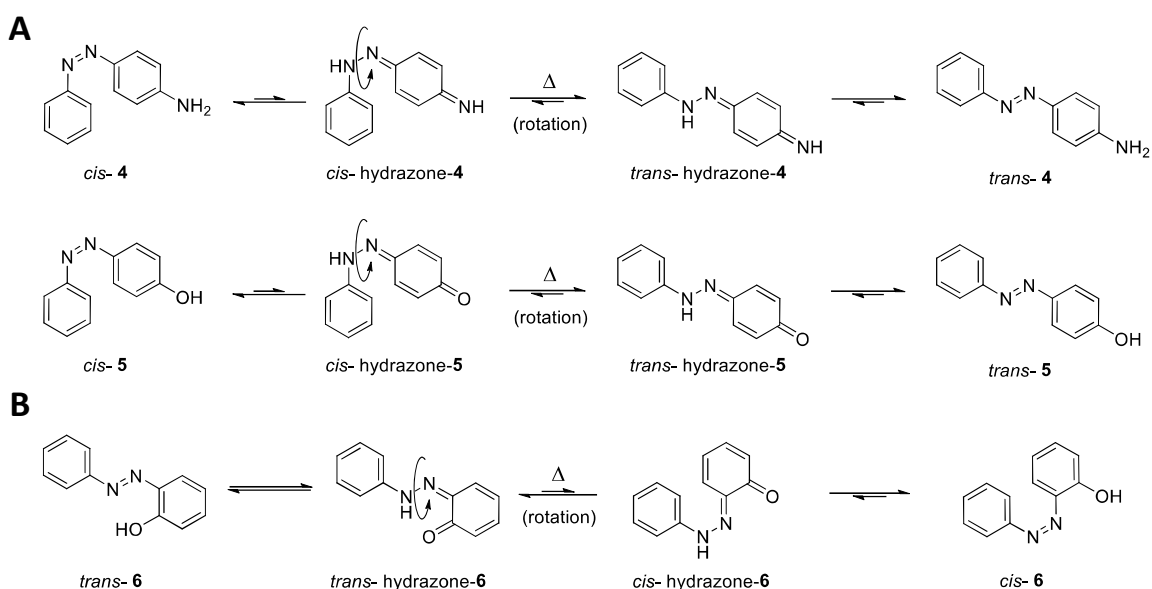


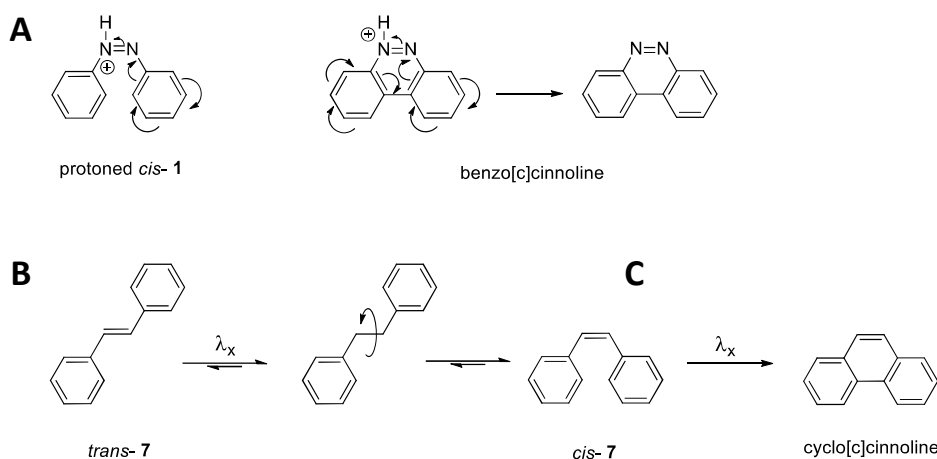
**Figure 7.** (A) Azo-hydrazone tautomeric equilibrium in non-*N*-substituted aminoazobenzenes (**4**) or non-*O*-substituted hydroxyazobenzenes (**5**);<sup>37,46</sup> (B) Tautomerization of 2-hydroxyAB (**6**). The hydrogen bond between the azo-nitrogen and -OH group is responsible for fast thermal isomerization of 2-hydroxyAB (**6**).<sup>20</sup>

Unlike 4-hydroxyAB (**5**), 2-hydroxyAB (**6**) does not readily undergo *trans*  $\rightarrow$  *cis* isomerization upon irradiation. This is because the tautomerization stabilizes the corresponding phenylhydrazone through intramolecular H-bonds. The tautomerization can be initiated by irradiation; therefore, 2-hydroxyAB (**6**) exhibits complex decay profile when excited with ultrafast pulses. Short-lived tautomers of 2-hydroxyABs (**6**) have been observed; however, intramolecular H-bonds in 2-hydroxyABs (**6**) are rarely strong enough to prevent isomerization.<sup>20</sup>

#### pAB derivatives (PSB family)

Pseudostilbenes (pSBs) include two classes of ABs: protonated-azobenzenes (pAB) and push-pull azobenzenes (ppAB). The  $n$ - $\pi^*$  and  $\pi$ - $\pi^*$  transitions of pSBs in general are nearly degenerate in energy and

occur in the visible region. The pKa values for *t*-AB and *c*-AB are -2.6 and -1.6 respectively,<sup>50</sup> so strong acids are required to protonate AB, such as 10% (v/v) ethanolic sulphuric acid.<sup>20,50</sup> Protonation raises the energy of the  $n-\pi^*$  state above that of the  $\pi-\pi^*$  state. Although protonation produces no significant effect on photoisomerization yields, it increases the rate of thermal back-isomerization. Additionally, the protonated *c*-AB slowly cyclizes to produce benzo[*c*]cinnoline in oxidative conditions and upon irradiation,<sup>51</sup> in a manner similar to the oxidative photocyclization, also known as Mallory reaction, of stilbenes (Figure 8).<sup>50,52,53</sup> This cyclization reaction seems to be enthalpically favored. In fact, comparing the electron shifts in the two structures, it is evident that the benzo[*c*]cinnoline ion has a considerably greater resonance energy than the conjugate acid of azobenzene (**1**) (Figure 8). Even if pABs have been classified as pSBs, the presumed shifting of the  $n-\pi^*$  above the  $\pi-\pi^*$  state has not been verified by rigorous theoretical and experimental analysis. It was thought that pseudostilbenes, like true stilbenes have a low-lying  $\pi-\pi^*$  state. True stilbene (**7**) consists of two phenyl rings separated by a C–C double bond (Figure 8). Its lowest energy excited state is  $\pi-\pi^*$  which appears  $\sim 300$  nm in *trans*-stilbene and  $\sim 280$  nm in *cis*-stilbene. Unlike AB, stilbene does not have an  $n-\pi^*$  transition. *Trans*-stilbene is thermodynamically more stable. However, the barrier to thermal isomerization is significantly larger than that of AB and the rate of thermal isomerization at room temperature is very slow. Moreover, its isomerization is dominated only by rotation (Figure 8).<sup>20</sup>

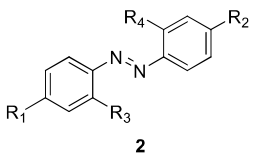


**Figure 8.** (A) Azobenzene (**1**) oxidatively cyclized to benzo[*c*]cinnoline when exposed to light in strongly acidic solutions;<sup>51</sup> (B) Stilbene (**7**) undergoes *trans*-*cis* isomerization exclusively by rotation; (C) Photocyclization of stilbene (**7**) after irradiation in the presence of a photosensitizer\* (Mallory reaction).<sup>50,52,53</sup>

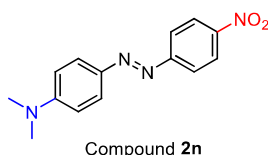
### ppAB derivatives (PSB family)

In push-pull ABs, usually a strong electron donor and a strong electron acceptor occupy the 4- and 4'-positions of the two phenyl rings, but also positions 2- and 2'- can display a strong effect. This lowers the energy of the  $\pi-\pi^*$  state, leading to a shift of the transition bands to visible ranges (red-shifting, Table 4). In addition to weak  $n-\pi^*$  and fully allowed  $\pi-\pi^*$  transitions, ppABs exhibit intramolecular charge transfer (ICT) bands that arise from electron transfer between donor and acceptor moieties.<sup>54</sup> Thermal isomerization of ppABs occurs extremely fast, and completes within milliseconds to seconds. The rate strongly depends on solvent polarity with an approximate 105-fold increase occurring in polar solvents over non-polar solvents (Table 5).<sup>38</sup>

\* A photosensitizer is a molecule that by absorbing light produces a physicochemical change in a neighboring molecule by either donating an electron to the substrate or by abstracting a hydrogen atom from the substrate.

Group	Comp.	R <sub>1</sub>	R <sub>2</sub>	R <sub>3</sub>	R <sub>4</sub>	$\lambda_{\max}(\pi-\pi^*)$ [nm]	$t_{1/2}$ [min]
ppAB  <b>2</b>	<b>2n</b>	NMe <sub>2</sub>	NO <sub>2</sub>	H	H	440	1.74
	<b>2o</b>	NMe <sub>2</sub>	NO <sub>2</sub>	Me	H	450	1.00
	<b>2p</b>	NMe <sub>2</sub>	NO <sub>2</sub>	H	Cl	459	0.21

**Table 4.** Maximum of absorbance corresponding to the  $\pi-\pi^*$  band and half-life times for thermal *cis*  $\rightarrow$  *trans* isomerization of different azobenzene derivatives belonging to the group ppAB. The measurements were done in hexane at 35°C. (Adapted from Gómez-Santacana).<sup>46</sup>



Solvent	$\epsilon_r$	$t_{1/2}$ [min]	Solvent	$\epsilon_r$	$t_{1/2}$ [min]	Solvent	$\epsilon_r$	$t_{1/2}$ [min]
pentane	1.84	255	C <sub>6</sub> H <sub>5</sub> Cl	5.62	4.2	acetone	20.7	0.072
hexane	1.89	344	THF	7.58	1.35	EtOH	24.55	0.038
1,4-dioxane	2.21	48	DCM	8.90	0.77	MeOH	32.7	0.0135
CCl <sub>4</sub>	2.23	293	o-C <sub>6</sub> H <sub>4</sub> Cl <sub>2</sub>	9.93	0.99	DMF	36.71	0.0083
benzene	2.27	64	cyclo-hexanone	18.3	0.083	DMSO	46.6	0.0023
Et <sub>2</sub> O	4.32	45	2-PrOH	19.92	0.084	formamide	111.0	0.00042
CHCl <sub>3</sub>	4.81	3.8						

**Table 5.** Half-life times of *cis*-**2n** at 25°C in different solvents with distinct polarity (expressed as a dielectric constant  $\epsilon_r$ ).<sup>38</sup>

Azoderivatives, bearing a pyridine ring or a pyridinium cation as an EWG (compounds **8c-e**, Figure 9), show a much stronger push-pull effect than the nitro-substituted compound **8b** or the cyano substituted **8a** (which is even weaker) and, thereafter, faster thermal isomerization rates were obtained. Moreover, if the donor allows azo-hydrazone tautomeric equilibrium, this relaxation rate can be radically increased (Figure 9).<sup>37</sup>

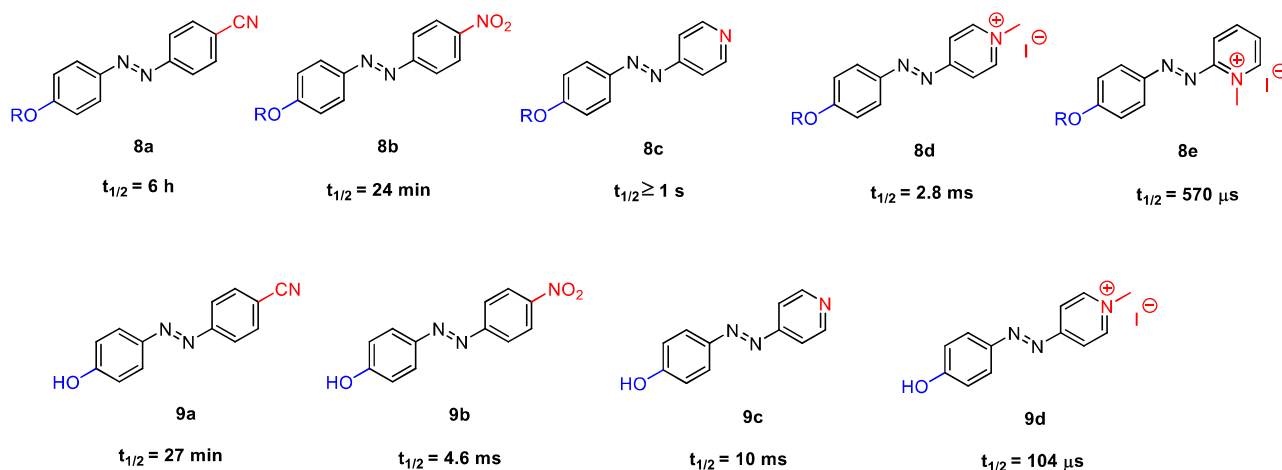


**Figure 9.** Effect of the presence of a pyridine ring or a positively charged nitrogen as an EWG group on the thermal relaxation time  $t_{1/2}$  at 25°C in ethanol for the ppABs **8c-e**. Comparison between EWG groups and *cis* isomer thermal relaxation times for push-pull compounds without (**8a-e**) and with azo-hydrazone tautomeric equilibrium (**9a-d**).<sup>37</sup>

ppABs are intensively colored and used as dyes in the industry or as pH and metal indicators. They are also useful for non-linear optical and photo-refractive materials, optical poling, holographic memory storage devices or as a fast information-transmitting photochromic switches.<sup>37</sup>

#### toAB derivatives

Most of the azobenzene-modified biomolecules developed to date require the use of UV light for photoisomerization. This can limit the use of this molecular switch *in vivo*. Azobenzene derivatives where photoisomerization can occur entirely in the visible region would therefore be desirable for *in vivo* applications. The ppAB derivatives would represent good candidates for fulfilling this requirement but they normally thermally relax very rapidly. Sometimes fast thermal relaxation is useful but an intense light source is usually required in order to maintain a considerable fraction of a short-lived *cis* isomer. This could be another undesirable limitation *in vivo*.

The incorporation of EDGs in *ortho* or *para* to the azo moiety can dramatically red-shift the photoswitching wavelength but it still does not reduce the rate of thermal *cis*  $\rightarrow$  *trans* relaxation.<sup>16</sup> The use of tetra-*o*-substituted azobenzenes (toAB) could represent a solution to this inconvenient. Beharry and colleagues based their study on the three azobenzene derivatives (**10a-c**) shown in Figure 10.<sup>16</sup> They found that substitution of all four *ortho* positions (2- and 2'-, 6- and 6'-) with methoxy groups in an amidoazobenzene derivative leads to a substantial red shift growth of the  $n-\pi^*$  band of the *trans*-isomer, separating it from the *cis*  $n-\pi^*$  transition (Figure 10). This red shift makes *trans*  $\rightarrow$  *cis* photoswitching possible using green-yellow light (530-560 nm).

The *cis* state usually shows high bistability\* with a half-life of  $\sim 2.4$  days in the dark in aqueous solution (Table 6). Reverse *cis*  $\rightarrow$  *trans* photoswitching can be accomplished with blue light (460 nm), so bidirectional photoswitching between thermally stable isomers is possible without the use of UV light.

\* In a dynamical system, bistability means the system has two stable equilibrium states. A compound that is bistable can be resting for quite a long time in either of two states. Usually, a long-lived *cis* isomer is considered a metastable state, which represents, as well as the thermodynamically stable state, one of the two stable states of an azo derivative.

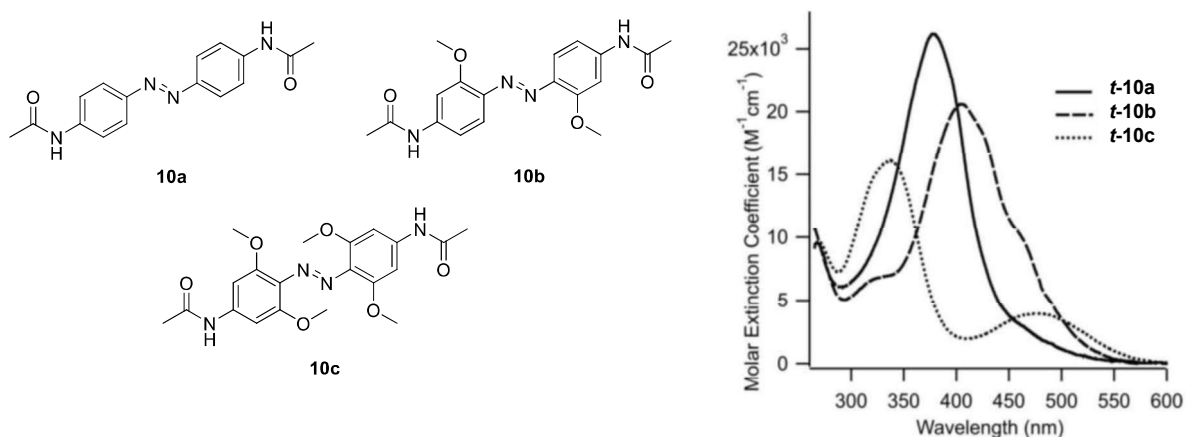


**Figure 10.** Structures of the azobenzene derivatives (**10a-c**) studied by Beharry and collaborators and the corresponding spectra of *trans*-**10a-c** isomers in DMSO at 25°C.<sup>16</sup>

T °C	$t_{1/2}$ <i>cis</i> - <b>10a</b> in DMSO	$t_{1/2}$ <i>cis</i> - <b>10b</b> in DMSO	$t_{1/2}$ <i>cis</i> - <b>10c</b> in DMSO	$t_{1/2}$ <i>cis</i> - <b>10c</b> in buffer
4	9 h	20 h	164 days	27 days
25	1.3 h	1.9 h	14 days	2.4 days
40	25 min	26 min	3 days	12 h

**Table 6.** *cis* half-lives of azobenzene derivatives **10a-c**.

Further studies demonstrated that not only bulky electron-rich substituents in all four positions *ortho* to the azo group, but also halides in the same positions, can provide azo compounds with red light photoswitching.<sup>55-58</sup> In particular, Bléger and co-workers discovered that the tetra-fluorination of the azobenzene core is well compatible for the design of two-way visible light-responsive systems.<sup>57</sup> Later, the same approach was used for the design of photoswitchable muscarinic ligands by Agnetta and collaborators.<sup>58</sup>

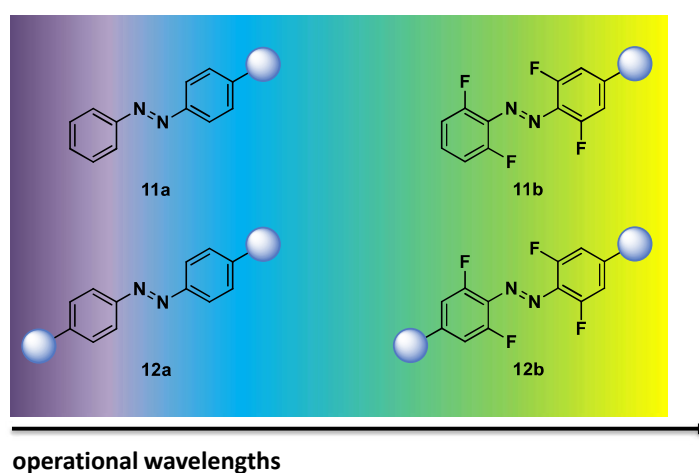


**Figure 11.** Structures of photoswitchable monovalent (**11a-b**) and homobivalent (**12a-b**) ligands. The tetra-fluorination of the azobenzene core alters the photochromic behavior offering two-way isomerization with visible light. (Adapted from Agnetta et al.)<sup>58</sup>

## bAB derivatives

Another remarkable type of azobenzenes are the bridged azobenzenes (bAB, *Figure 12* and *Figure 5*), which were first reported in 2009 by Siewertsen and collaborators.<sup>44</sup> This compound displays an “inverse photoisomerization”, since the bent *cis* isomer is the thermodynamically more stable compound. It isomerizes from *trans* to *cis* configuration with light between 450 and 500 nm and from *cis* to *trans* with 370-400 nm light. In fact, the photostationary state at  $\lambda = 385$  nm showed a clear predominancy of the *trans* isomer. By monitoring the absorption in the dark, its thermal half-life was found to be of 4.5 h at 28.5 °C. Samanta et al. made a bis-*p*-amido substituted (**13b**) and bis-*p*-amino substituted derivatives (**13c**) to allow conjugation to biomolecules (*Figure 12*).<sup>59</sup>

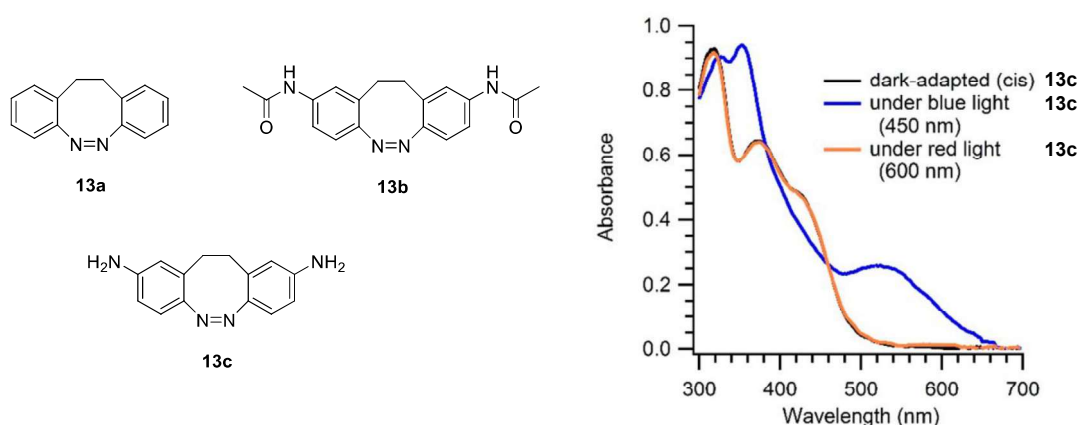
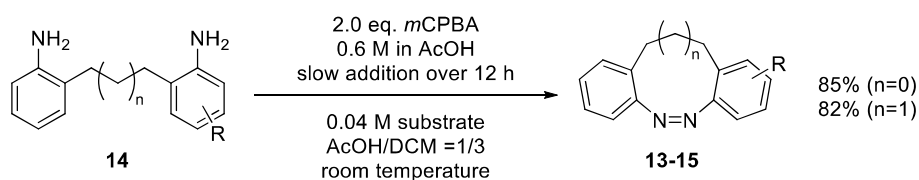


**Figure 12.** Amino-substituted bridged azobenzene photoswitches and UV-vis spectra of **13c** obtained in aqueous solution under dark conditions and under blue (445 nm) and red (600 nm) irradiation.

The molecule **13c** showed significant absorbance in the red region of the spectrum (*Figure 12*) in its *trans* isomeric form. Irradiation with red light (600 nm) produced full conversion to the *cis* isomer (*Figure 12*). The thermal relaxation rate at room temperature in aqueous solution was in the order of minutes. Recently, incorporation of these cyclic azobenzenes, so-called diazocines, into a variety of photopharmaceuticals could convert dark-active ligands into dark-inactive ligands, which is preferred in most biological applications.<sup>60</sup>

Although bAB derivatives (diazocines) have fascinating conformational and photophysical properties, their use has been limited by their synthetic accessibility. However, thanks to Maier and collaborators that provide a general, high yielding protocol relying on the oxidative cyclization of dianilines (*Scheme 3*), it has been possible to access to a wide variety of diazocines that are substituted on one or both aromatic rings.<sup>61</sup>



**Scheme 3.** Oxidative cyclization of substituted 2,2'-ethylenedianilines.<sup>61</sup>

The authors were also able to prepare a bAB with a nine-membered ring and another one substituted on the ethylene bridge, which could be considered as the vanguard of new types of photoswitches. In particular, they investigate the spectra and switching of the nine-membered diazocine **15**. Analogously to the eight-membered system, it could be isomerized to the *trans* isomer with 400 nm irradiation and back

to the *cis* isomer using 520 nm light (Figure 13). Interestingly, compared to that of the *trans* isomer of diazocine **13a**, the spectrum of the *trans* isomer of diazonine **15** exhibits a notably higher absorbance for the band corresponding to the  $\pi$ - $\pi^*$  transition, which also is found at a longer wavelength of 316 nm. Therefore, the spectrum of *trans* diazonine **15** resembles that of the regular *trans* azobenzene **1**, while the *cis* diazonine **15** spectrum is similar to that of *cis* diazocine **13a** (Figure 13).<sup>61</sup>

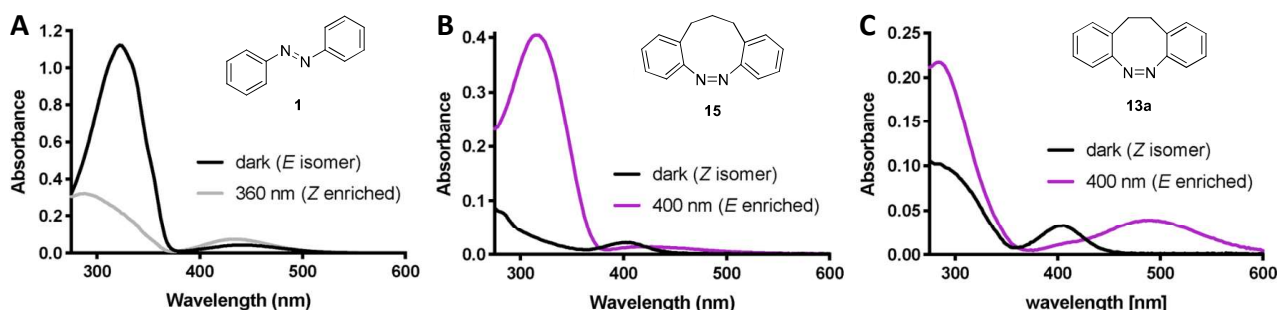


**Figure 13.** Comparison of UV-vis spectra of (A) azobenzene **1**, (B) diazonine **15** and (C) diazocine **13a** in the dark and under illumination. All spectra in DMSO, 50  $\mu$ M.

Summing up, azobenzene and its derivatives are the most versatile moieties for implementing photo-responsive properties in chemical systems to achieve a reversible control of a protein function with light. The main reasons of that are their facile synthesis and functionalization, and their predictable and highly tunable photophysical characteristics. In particular, the presence of substituents on the aromatic rings can induce radical changes on the absorption spectra and photochemical properties of azobenzene. According to their different spectroscopic characteristics, based on the relative energies of  $\pi$ - $\pi^*$  and  $n$ - $\pi^*$  transitions, the most widely used functionalized compounds can be schematized as in the following Figure 14.

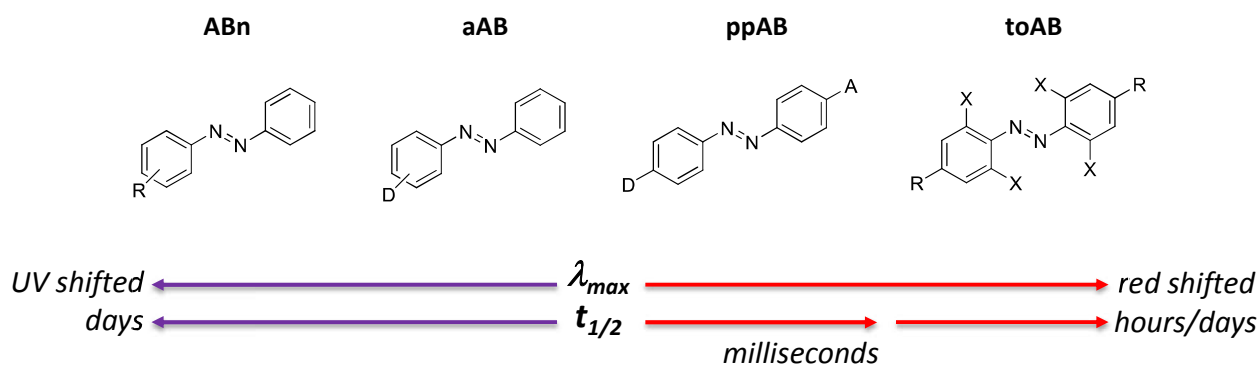


**Figure 14.** The mostly used classes of azobenzene and the corresponding variation of the absorption maximum of the *trans*-form ( $\lambda_{max}$ ) and the half-life at room temperature of the *cis*-form ( $t_{1/2}$ ).

Despite the abundance of application-driven research, ABs photochemistry and the isomerization mechanism remain topics of investigation. Figure 14 shows how additional substituents on the azobenzene ring system can drastically change the spectroscopic properties and isomerization mechanism. Thus, understanding the differences in photochemistry, which originate from substitution, is imperative in exploiting azobenzene derivatives in the desired applications.

## G Protein-Coupled Receptors (GPCRs)

The G protein-coupled receptor (GPCR) superfamily constitutes the largest collection of cell surface signaling proteins with approximately 800 members in the human genome.<sup>62</sup> GPCRs mediate biological responses to external stimuli by transducing signals across the plasma membrane to heterotrimeric G proteins and arrestins, which in turn activate cellular signaling cascades. GPCRs regulate many physiological processes and are sensitive to a wide variety of endogenous ligands including neurotransmitters, peptide and protein hormones, amino acids, ions, lipids, and several other bioactive molecules.<sup>63</sup> In addition, chemosensory GPCRs are responsible for our senses of sight, smell, and taste by responding to photons, organic odorants and taste stimulus.

G proteins may possibly exert cellular functions other than acting as signaling transducers. There is also increasing evidence for roles in different diseases including infections, inflammation, neurological diseases, cardiovascular diseases, cancer, and endocrine disorders. For this reason, GPCRs are important drug targets. In fact, it is estimated that ~35% of drugs on the market target a GPCR despite this superfamily only constitutes 4% of the human genome.<sup>64,65</sup> The non-stop breakthroughs in GPCR structural biology, obtained from X-ray crystallography, reveal the molecular basis for protein function and facilitate rational drug design. An excellent and relatively recent review focuses on GPCRs and GPCR-related proteins that are targets for approved drugs. The authors themselves presented a list of GPCRs currently targeted by approved drugs in order to account for discrepancies among the different sources. Their work was based on data integration from public databases (ChEMBL, Guide to PHARMACOLOGY (GtoPdb) and DrugBank) and from the Broad Institute Drug Repurposing Hub.<sup>65</sup> As of November 2017, 134 GPCRs are targets for drugs approved in the United States or European Union; 128 GPCRs are targets for drugs listed in the Food and Drug Administration Orange Book. As mentioned before, they estimated that ~700 approved drugs (~35% of approved drugs) target GPCRs. GPCRs and GPCR-related proteins, *i.e.*, those upstream of or downstream from GPCRs, represent ~17% of all protein targets for approved drugs, with GPCRs themselves accounting for ~12% (*Figure 15A*). All this makes GPCRs as the most relevant protein family for drug discovery. Additionally, approximately two-thirds of the drug-targeted receptors couple to either G<sub>s</sub> or G<sub>i</sub>, which are associated to signaling cascades related to cytosolic cAMP (*Figure 15B*) This highlights the importance of such GPCRs (and likely, the regulation by cAMP) of current therapeutic agents. This data indicate that not only GPCRs are still a mainstay for new and much improved drugs but also they may reveal novel clinically relevant therapeutic opportunities.<sup>65,66</sup>

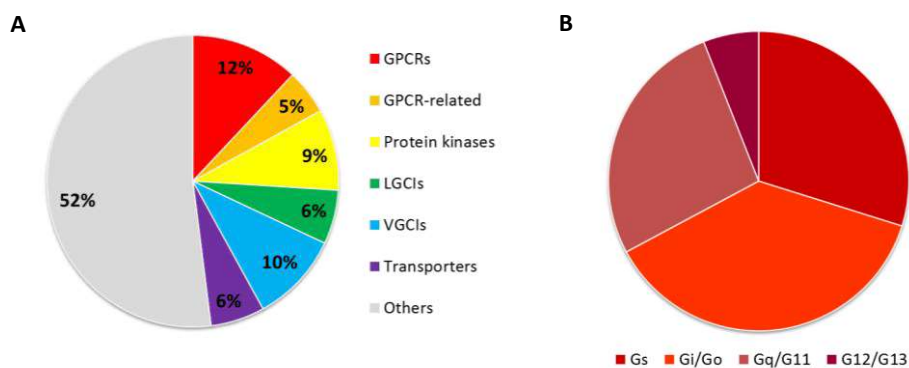


**Figure 15.** (A) The estimated proportion of different gene families that are targets for approved drugs. LGICs: ligand-gated ion channels; VGICs: voltage-gated ion channels; (B) Putative primary G $\alpha$  protein linkage, based on classification of GPCR signaling by GtoPdb, of the 134 curated GPCRs targeted by approved drugs. (Adapted from Sriram and Insel<sup>65</sup>).



The GPCR proteins are also characterized by a wide structural diversity.<sup>63</sup> Indeed, there are two main requirements for a protein to be included in the GPCR superfamily.<sup>62</sup>

The first requirement relates to seven sequence stretches of about 25 to 35 consecutive residues that show a relatively high degree of calculated hydrophobicity. These sequences are believed to represent seven  $\alpha$ -helices that pass through the plasma membrane, forming a receptor, or a recognition and connection unit, enabling an extracellular ligand to exert a specific effect into the cell (Figure 16). This is what it is named “seven transmembrane alpha helices domain” (7TMD), with an extracellular N-terminal and an intracellular C-terminal. The presence of other domains depends on the class/family and type of GPCRs.

The second main requirement is the ability of the receptor to interact with a G-protein after its own activation, which leads to the activation of the G Protein. In fact, as a general rule, GPCRs are activated by extracellular ligands, known as agonists, causing a conformational change of the 7TMD that makes possible the activation of the heterotrimeric G-protein and the modulation of downstream effector proteins in the cytosol face. However, interaction with G-proteins has not been demonstrated for most GPCRs, in particular for those whose genes have just recently been sequenced. It may therefore be more technically correct to term this superfamily “seven transmembrane receptors”, but the GPCR terminology is more established.

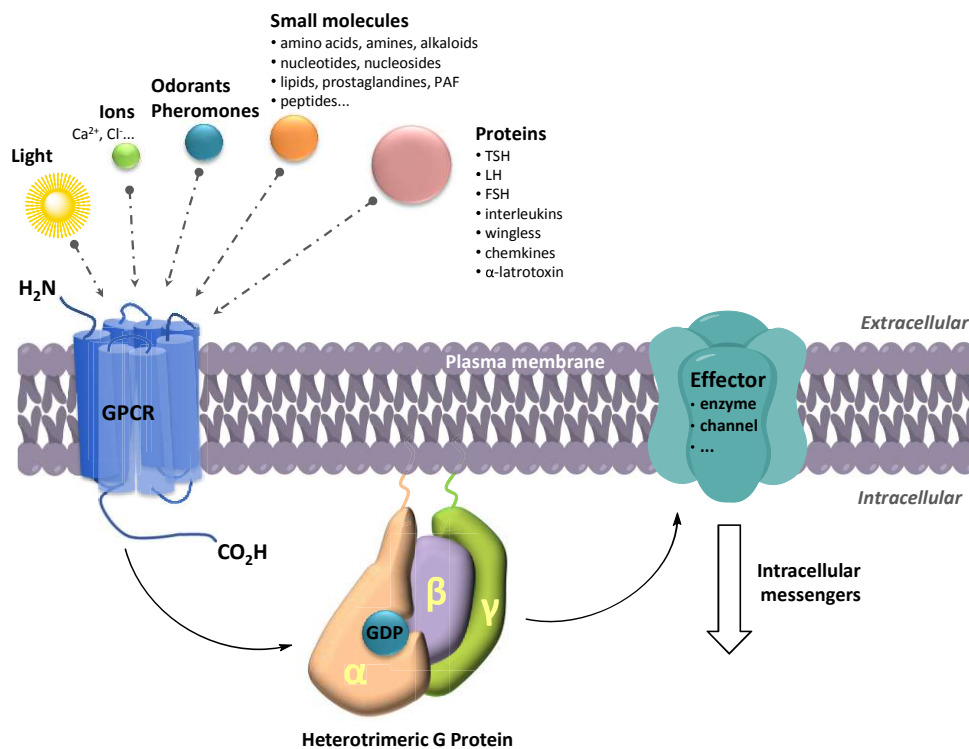


**Figure 16.** Topology and versatility of the GPCRs. All of them have a common signaling mode and topology with seven transmembrane alpha helices connected by three intracellular and three extracellular loops. Heterotrimeric G proteins are activated in response to stimulation of G protein-coupled receptors by numerous substances. (Adapted from Bockaert and Pin).<sup>67</sup>

### Guanine nucleotide-binding proteins (G Proteins)

G proteins, also known as guanine nucleotide-binding proteins, are a family of proteins that act as molecular switches inside cells. They are implicated in transmitting signals from a variety of stimuli outside a cell to its interior through their interaction with GPCRs. The G proteins are composed of an  $\alpha$ - (39–52 kDa),  $\beta$ - (35 kDa), and  $\gamma$ - (7–8 kDa) subunit. Altogether, 21 different G $\alpha$ -subunits (from 17 genes) have been described sharing ~20% conserved amino acids. Based on the amino acid sequence of the  $\alpha$ -subunits, the

heterotrimeric G proteins are divided into the four main families  $G_s$ ,  $G_i$ ,  $G_{q/11}$ , and  $G_{12/13}$ . Six  $\beta$ - and 12  $\gamma$ -subunits have been identified (Table 7).<sup>68,69</sup> The  $\beta$ - and  $\gamma$ -subunits form tightly bound functional dimers that only dissociate after denaturation. Whereas combinations of  $\beta$ - and  $\gamma$ -subunits assembling with specific  $\alpha$ -subunits have been defined in various cell types, there is still limited understanding with regard to the biological significance and regulation of G protein heterotrimeric composition.

G proteins, which are coupled to a given GPCR, bind guanosine triphosphate (GTP) and catalyze its hydrolysis to guanosine diphosphate (GDP) upon activation of the coupled GPCR. This GTPase activity is localized within the  $\alpha$ -subunit, which also includes a single guanine-nucleotide-binding site (Figure 17). In the resting and inactive state, the G protein exists as a heterotrimer with the  $\alpha$ -subunit in a GDP-bound form. Ligand binding to GPCR induces a change in receptor conformation triggering the coupling with the heterotrimeric G protein. The consequent activation of G protein is believed to involve two major events, a guanine-nucleotide exchange step ( $GDP \rightarrow GTP$ ) and the dissociation of the  $\alpha$ - and  $\beta\gamma$ -subunits.<sup>70</sup> Then the signaling cascade begins with the interaction of the  $G_\alpha$  or  $G_{\beta\gamma}$  with the corresponding effectors, which are summarized in Table 7. Once the reaction is finished, inactive  $G_\alpha$  is back-associated with  $G_{\beta\gamma}$  subunit (Figure 17).

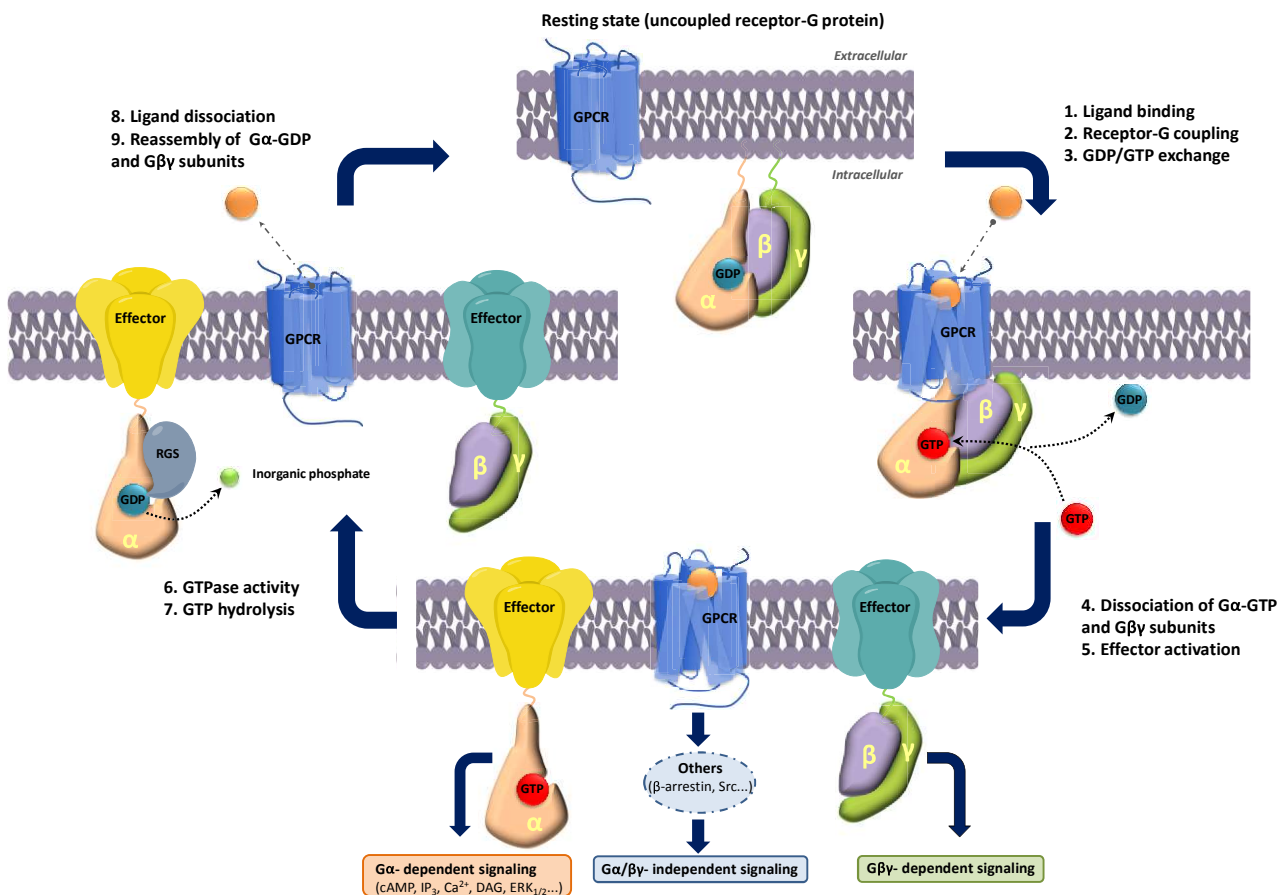


**Figure 17.** The classical GPCR-G protein activation/deactivation cycle. In the absence of activation, the  $G_\alpha$ -GDP and  $G_{\beta\gamma}$  subunits of the heterotrimeric G proteins are associated with each other without necessarily physically interacting with the receptor. Upon a ligand binding to its GPCR, conformational changes occur within the receptor leading to an intimate interaction and coupling with the heterotrimeric G protein. This results in G protein activation characterized by GDP/GTP exchange followed by the dissociation between  $G_\alpha$ -GTP complex from the  $G_{\beta\gamma}$  subunits. Each activated subunit is then able to interact with and modulate the function of its specific intracellular effectors leading to canonical  $G_\alpha$ - and  $G_{\beta\gamma}$ -dependent, but also  $G_\alpha/G_{\beta\gamma}$ -independent signaling pathways (e.g.  $\beta$ -arrestin, Src). As a regulation mechanism, the GTPase activity of  $G_\alpha$  hydrolyzes GTP to GDP and along with the involvement of selective regulators of G protein signaling (RGSs), this inactivates the  $G_\alpha$  subunit. Finally, the  $G_\alpha$ -GDP and  $G_{\beta\gamma}$  subunits re-associate to be ready for another GPCR-G protein activation cycle. (Adapted from Ayoub).<sup>70</sup>

Family	Subtype	Action	Effectors
G <sub>αs</sub>	G <sub>αs</sub>	Activation	Adenylyl cyclases, Maxi K channel and Src tyrosine kinases
	G <sub>αolf</sub>	Activation	Adenylyl cyclases from olfactory sensorial neurons and GTPase of tubulin
G <sub>αi/o</sub>	G <sub>αi</sub> , G <sub>αo</sub> , G <sub>αz</sub>	Inhibition	Adenylyl cyclases and Ca <sup>2+</sup> channels
		Activation	ERK/MAP kinases, K <sup>+</sup> channels, GTPase of tubulin, Src tyrosine kinases and GRIN1-mediated activation of Cdc42
	G <sub>αt</sub>	Activation	cGMP PDE (phosphodiesterase) in the photoreceptors
	G <sub>αgust</sub>	Activation	cGMP PDE in the gustative sensorial neurons
G <sub>αq</sub>	G <sub>αq</sub> , G <sub>α11</sub> , G <sub>α14</sub> , G <sub>α15</sub> , G <sub>α16</sub>	Activation	PLC-β (phospholipase C-β) isoforms, p63-RhoGEF (guanine nucleotide exchange factor), Bruton's tyrosine kinase and K <sup>+</sup> channels
G <sub>α12/13</sub>	G <sub>α12</sub> , G <sub>α13</sub>	Activation	Phospholipase D and Cε, NHE-1, iNOS, E-cadherin-mediated cell adhesion, p115RhoGEF, PDZ-RhoGEF, LARG (Leukaemia-associated RhoGEF), Radixin, PP5 (Protein phosphatase 5), AKAP110-mediated activation of PKA and HSP90
G <sub>βγ</sub>	β <sub>1-6</sub> , γ <sub>1-12</sub>	Inhibition	Adenylyl cyclases I and Ca <sup>2+</sup> channels
		Activation	PLC-β isoforms, adenylyl cyclases II, IV, VII, PI-3 kinases, K <sup>+</sup> channels, P-Rex1 (guanine nucleotide exchange factor for the small GTPase Rac), GTPase of tubulin, c-Jun N-terminal kinase (JNK) Src kinases, GPCR kinase recruitment to membrane, protein kinase D, Bruton's tyrosine kinase and p114-RhoGEF

**Table 7.** Summary of the human heterotrimeric G protein families and subtypes, with the main functions of each family. (Adapted from Milligan and Kostenis).<sup>68</sup>

### Modification of GPCR function: orthosteric and allosteric ligands

As stated above, GPCRs do not only couple to a wide range of signaling molecules and effector systems, but they are also activated by a large set of different ligands. The GPCRS ligands usually bind in the *orthosteric* site, which is a pocket located either on extracellular domains or embedded within the transmembrane domain. This binding causes a conformational change of the 7TMD that permits the activation of a G protein (*Figure 18A*). These orthosteric ligands can be endogenous (produced by the organism) or exogenous (uptaken substance or drug). However, a considerable number of important issues contribute to the difficulty of discovering small-molecule selective ligands acting on the orthosteric sites, despite the proven success of GPCRs as drug targets. For instance, the orthosteric binding sites across members of a single GPCR subfamily for a particular endogenous ligand are often highly conserved, making it difficult to achieve high selectivity for specific GPCR subtypes.<sup>71</sup> Furthermore, ligands at orthosteric sites for some GPCRs, such as peptides or proteins, have other physicochemical and pharmacokinetic properties that are incompatible with scaffolds that are useful for small-molecule drug discovery. An alternative and highly successful approach to overcome these issues is the development of selective *allosteric* modulators (AM) of the specific GPCR subtypes. These small molecules do not bind to the orthosteric ligand binding site but, they act in a binding site alternatively located (*allosteric* site), which is distinct from the orthosteric site. The

ligands binding in the *allosteric* site can either potentiate or inhibit activation of the receptor by its natural orthosteric ligand, which is binding in this *allosteric* side (Figure 18B and Figure 19A).

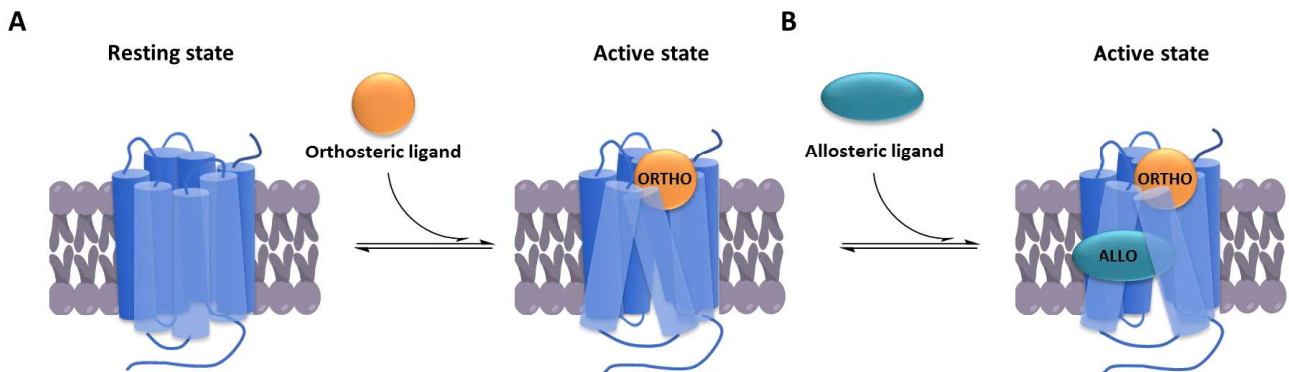
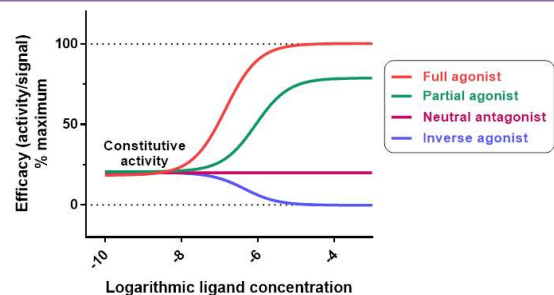


**Figure 18.** Modes of action of orthosteric and allosteric ligands. (A) Model of binding to a GPCR of an orthosteric modulator; (B) model of binding of allosteric ligand with no interference with endogenous orthosteric binding.\*

In recent years, remarkable progress has been made in the discovery, optimization and clinical development of allosteric modulators for multiple GPCR subtypes. These include positive, negative and silent allosteric modulators (named respectively PAMs, NAMs and SAMs) and offer novel action mode over all kinds of orthosteric ligand (full agonist, partial agonist, (neutral) antagonist and inverse agonist; see Box 1 for further details).<sup>72</sup> Allosteric modulators lead to a change in receptor conformation (Figure 18B) and therefore the properties of the GPCR can be modified in either a positive or negative direction. In essence, a receptor occupied by an allosteric ligand can be viewed as a “novel” receptor type, with unique behavior. Allosteric GPCR modulators exhibit one or more of the following pharmacological properties (Figure 19).<sup>73–75</sup>

- **Affinity modulation:** the AM-induced conformational change can have an impact on the orthosteric binding pocket leading to modify the association or dissociation rate (or both) of an orthosteric ligand.
- **Efficacy modulation:** the allosteric effect can change intracellular response, thus altering the signaling capacity or “intrinsic efficacy” of an orthosteric ligand.
- **Agonism/inverse agonism:** the AM can perturb receptor signaling in either a positive (agonism) or negative (inverse agonism) way, regardless of the presence or absence of an orthosteric ligand.

#### Box 1. Key Pharmacological Concepts



(Adapted from Wacker, Stevens and Roth)<sup>71</sup>

##### Constitutive activity

Receptor-mediated signaling in the absence of ligand due to spontaneous population of active receptor states

##### Full agonists

Ligands that elicit maximum signal at the interrogated pathway (endogenous ligands are, per definition, full agonists)

##### Partial agonists

Ligands that elicit activity below maximum level

##### Inverse agonists

Ligands that inhibit constitutive receptor activity

##### Neutral antagonists

Ligands that bind the receptor but do not affect constitutive receptor activity

##### PAMs and NAMs

PAMs increase and NAMs decrease a receptor's activity in response to an orthosteric ligand, while binding at a site distinct from the orthosteric site

##### Ago-allosteric modulators

Ligands that have potency of its own

##### Bitopic ligands

Ligands that possess both orthosteric and allosteric moieties

##### Bivalent ligands

Ligands that bridge a dimeric construct of GPCRs to bind simultaneously at binding sites of adjacent receptors<sup>75</sup>

\* Ligands are supersized for a better visualization of the figure.

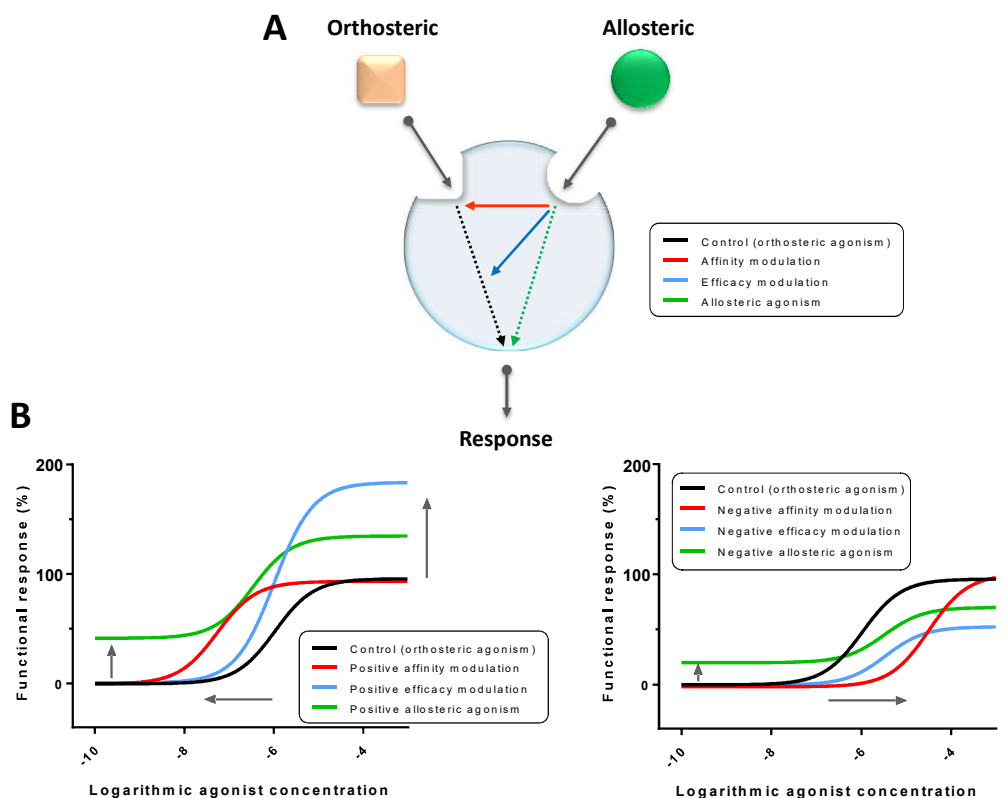


**Figure 19.** Modes of action of allosteric modulators. (A) Allosteric ligands bind to a topographically distinct site on a receptor to modulate orthosteric ligand affinity (red) and/or efficacy (blue). Some allosteric ligands can directly perturb signaling in their own right (green); (B) Simulations show the effects on the function of an orthosteric agonist mediated by six different allosteric modulators: the red ones enhance (left) or inhibit (right) orthosteric agonist affinity only; the blue ones enhance (left) or inhibit (right) orthosteric agonist efficacy only; the green ones modestly enhance (left) or inhibit (right) both affinity and efficacy, and also display allosteric agonism. (Adapted from Conn, Christopoulos and Lindsley).<sup>73</sup>

Modern chemical biology and drug discovery seek continuously to identify new small molecules that either as orthosteric or as allosteric ligands, can potently and selectively modulate the functions of target proteins. However, the power of drug discovery at GPCRs has been greatly enhanced by progress in structural biology unveiling the precise structures of the receptors. Indeed, several advances on crystallography and the advent of new techniques, such as the Cryo-electron microscopy (Cryo-EM), made possible the solution of many crystal structures of GPCRs, which helps the scientific community to understand the structural issues of these proteins and their binding with the corresponding ligands.<sup>76,77</sup> These advances are also of great importance for medicinal chemistry, allowing the design and synthesis of more selective and potent drug-like compounds.<sup>77</sup>

### Classification of human G protein-coupled receptors

Several classification systems have been used to sort out this superfamily, taking into consideration phylogeny, ligand features and binding modes. One of the most frequently exploited systems uses classes A, B, C, D, E, and F, and subclasses are assigned using roman number nomenclature. This A–F system is designed to cover all GPCRs, in both vertebrates and invertebrates. Human GPCRs were commonly classified in four main classes, A, B, C and F<sup>77–79</sup> or as five families, Rhodopsin, Adhesion, Secretin, Glutamate and Frizzled/Smoothed.<sup>62</sup> The two families, D and E, do not exist in human genome and represent fungal pheromone receptors and cAMP receptors. Furthermore, there are some subfamilies of

classes A-F that neither exist in humans, such as family IV in class A (invertebrate opsin receptors) or archaeobacterial opsins in class F.<sup>62</sup>

Class A GPCRs, the so called “rhodopsin-like family” consisting of 719 receptors in the human genome (Figure 20). In the GRAFS\* classification, the family was divided in four groups:  $\alpha$ ,  $\beta$ ,  $\gamma$  and  $\delta$  and can be activated by many different molecules, from small molecules to proteins. They can also bind many different G-proteins, depending on the receptors subtype.<sup>80</sup> Class B GPCRs is divided into two subfamilies: secretin (B1) and adhesion (B2), containing 15 and 33 members, respectively. The secretin family is activated by peptide ligands of intermediate size (30-40 amino acids residues), such as hormones and neuropeptides. The Adhesion Class is the second largest family of GPCRs and are a very peculiar family of GPCRs. The majority of them are orphans<sup>†</sup>, and recently only eight of them have been matched with natural ligands.<sup>80</sup> The class C/Glutamate family GPCRs comprise twenty two receptors in humans that are activated by small molecules such as amino acids and ions.<sup>62</sup> Class F GPCRs, or frizzled family or frizzled/smoothened GPCRs, comprise 11 receptors, 10 frizzled (FZD) and 1 smoothened (SMO), with no orphans.<sup>80</sup> The FZD are activated by lipoglycoproteins of the wingless/int1 family, whereas SMO is indirectly activated by the hedgehog family of proteins acting on the transmembrane protein patched.<sup>46</sup> Like the adhesion (B2), Taste 2 classes has atypical pharmacology. Indeed, they are not activated by an endogenous agonist.<sup>81</sup> According phylogenetic GRAFS classification, TAS2 receptors clustered together with the frizzled receptors, despite not having obvious similarities (Figure 20).

The last 21 years, and in particular the last five years, have seen an explosion in the solving of GPCR crystal structures and cryo-electronic microscopy (Cryo-EM) structures in multiple states. The result of this breakthrough in the understanding of GPCR structure and function has fostered an advance in the design of GPCR ligands through computational methods for better understanding ligand-receptor interactions. The class A/Rhodopsin family comprises the largest number of GPCRs and our structural understanding of these receptors is the most advanced. Rhodopsin was the first GPCR to have its structure determined by X-ray crystallography in 2000,<sup>82</sup> followed by the  $\beta_2$ -adrenergic receptor structure in 2007.<sup>83,84</sup> Further reports of other class A GPCR structures have been continually appearing in an nearly exponential fashion (reviewed in Yang et al. (2021)).<sup>85</sup> Moreover, new techniques such as the Cryo-EM has provided huge advances in the structural biology field. This technique has overcome the lack of high resolution offered by classical electron microscopy that did not allow a complete understanding of protein complexes, such as the crystal structure of a GPCR- $\beta$ -arrestin complex. Thereby, the Cryo-EM, achieving resolutions comparable to X-ray crystallography, has become a powerful tool for investigating the structures of proteins and other large biomolecules.<sup>86</sup> For example, in 2020 Cryo EM made possible the disclosure of the structures of full-length human neurotensin receptor 1 (NTSR1) in complex with truncated human  $\beta$ -arrestin 1 ( $\beta$ arr1( $\Delta$ CT))<sup>87</sup> and also the structure of  $\beta$ -arrestin 1 ( $\beta$ arr1) in complex with M<sub>2</sub> muscarinic receptor (M2R).<sup>88</sup> In 2013 the first 7TM domain structures of two class B/Secretin family GPCRs<sup>89,90</sup> and of the class F/Frizzled family smoothened GPCR were published.<sup>91</sup> In 2014 the first 7TM domain structures for two class C/Glutamate family GPCRs (mGluR5/1) were reported too.<sup>92,93</sup>

---

\* International Union of Basic and Clinical Pharmacology

† An orphan receptor is an apparent receptor that has a similar structure to other identified receptors but whose endogenous ligand has not been yet identified.

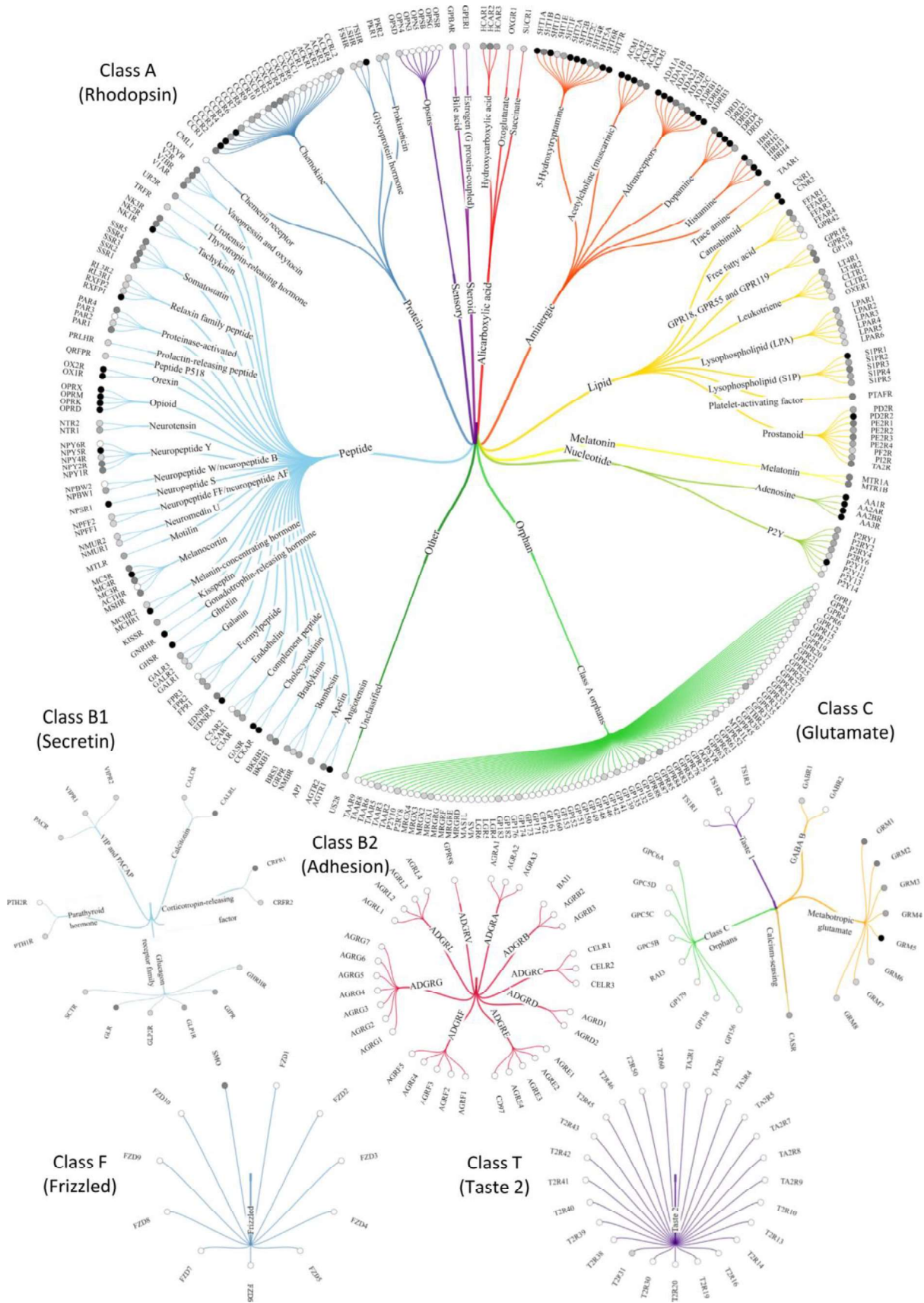


**Figure 20.** Trees showing the human GPCR classes (GRAFS family): A (Rhodopsin), B1 (Secretin), B2 (Adhesion), C (Glutamate), F (Frizzled) and T: Taste 2. Each tree is sorted alphabetically by ligand type (only class A) and receptor families which share the same physiological ligand. The tree branches are color-coded by ligand types, and the gray-scale circles before receptor names indicate their number of ligands (white: 0, light gray: >100, gray: >500 and black: >1000). (Figure from Pándy-Szekeres et al.)<sup>81</sup>

As mentioned at the beginning of this chapter, all GPCR members share a common seven transmembrane (7TM) architecture linked by three extracellular (ECL) and three intracellular (ICL) loops. However, they also include different extracellular *N*-terminal domains, which can be very large depending on the GPCR family and can also form ligand-binding pockets. For example, in case of class A GPCRs, the extracellular domains are small and the endogenous ligand is bound in a binding pocket located in the 7TM region. However, for class B GPCRs, the ligand is recognized by both extracellular and 7TM domains. Like the rest of GPCRs, both SMO and FZD receptors of class F GPCRs possess the 7TM domain with a *C*-terminus in the cytosol side, where the G-protein binds, and in the *N*-terminus have a cysteine rich domain of about 160 amino acids residues, that has been proposed to be the main ligand-binding region of the receptor.<sup>94</sup>

Class C GPCRs represent a family structurally more complex than other GPCRs. They are dimeric proteins composed of an extracellular ligand binding domain, where orthosteric agonists bind, and a 7TM domain responsible for G-protein activation. A detailed description of this family is presented in the section “Class C GPCRs” as the present PhD thesis is focused on this family of receptors.

## Photopharmacology of G Protein-Coupled Receptors

Although G protein-coupled receptors (GPCRs) are the largest family of membrane receptors targeted by small-molecule drugs, the proportion of new approved drugs targeting GPCRs is slowing down in the last years. This is in large part due to adverse effects or lack of efficacy found in clinical trials.<sup>95</sup> Many of these problems have been attributed to the lack of selectivity or the ubiquitous expression of receptors in non-targeted tissues and organs, thus eliciting undesired actions. Therefore, innovative research strategies are necessary to distinctly define the spatial and temporal action of GPCR drugs and this will help unravel the receptor function in physiologically relevant areas. To that aim, new chemical approaches are currently under development to confine a specific drug activity in a localized region during the right time period.<sup>96</sup> One of these strategies is photopharmacology, which represents an unprecedented opportunity inasmuch as light can be controlled with an unparalleled spatial and temporal precision. Indeed, as mentioned already in the first section of this introduction, driving the drug action through the use of light has demonstrated to allow for an accurate restriction of its effect to specific organs, tissues or even subcellular locations with strictly defined time applications.<sup>4,97</sup> This precision has permitted the study of the link between biological structures, a particular GPCR and the physiological responses elicited by its activation or inactivation.<sup>98,99</sup> The unique regulation of the receptor state offered by photopharmacology opens new opportunities to study the kinetic component of GPCRs mechanisms of activation and the underlying molecular processes. A comprehensive compilation and classification of the different photopharmacological strategies, the methods used to analyze and characterize light-regulated molecules and some examples of the impact that this field may have in drug discovery will be disclosed in this section.

### Enabling light as an actuator for GPCR research

When analysing the reported strategies to control GPCR activity with light, the following considerations are usually made:

- (1) Does the approach require genetic manipulation of the organism or can be applied to native receptors?
- (2) Is the light-induced reaction reversible (*i.e.* photoswitching)?



(3) Are the light-sensitive molecules freely diffusible or covalently bound to the GPCR protein?

Depending on these premises, light strategies to control biological function of GPCRs can be classified in three generic groups of approaches: **Optogenetics**, **Freely Diffusible Photopharmacology** and **Tethered Photopharmacology** (Figure 21). However, some approaches may have features of more than one group.

### **Optogenetics-like approaches**

**Optogenetic** approaches comprise a group of strategies that involve genetic modification to achieve light-control of well-defined biological events in specific cells that can be translated to living tissues and live animals.<sup>100</sup> Optogenetics was defined as “Nature Method of the Year 2010”<sup>101</sup> and was originally based on the use of genetically encoded photoreceptors already present in nature (rhodopsin,<sup>102</sup> channelrhodopsins,<sup>29,103</sup> halorhodopsin<sup>26</sup> and bacteriorhodopsin<sup>27</sup>) to excite a neuron upon illumination. These photoreceptors covalently bind to retinal and can be classified into two groups based on their photoisomerisation: bistable and monostable pigments. While monostable pigments (MSP) are only thermally stable before light application, bistable pigments are thermally stable in both isomers of retinal.<sup>28</sup>

Optogenetic approaches have evolved in the last years to include a broader variety of biological processes in neuroscience.<sup>104,105</sup> Among the large number of optogenetic tools currently developed, **opto-XRs** represents an interesting approach for the development of light-sensitive GPCRs. It is based on the development of chimeric GPCRs in which the extracellular part corresponds to that of the light-sensitive rhodopsin, whereas the intracellular component interacting with the G protein is derived from other GPCRs. A recent example is the opto- $\beta_2$ AR receptor, which is a chimeric rhodopsin/ $\beta_2$ -adrenergic receptor.<sup>106</sup> Opto- $\beta_2$ AR kinetically behaves similar to endogenous  $\beta_2$ AR in terms of G protein and MAP kinase activation, as well as receptor internalization. However, Opto- $\beta_2$ AR activity is triggered by light thanks to the light-sensitive region of rhodopsin. Of note, this construct demonstrated to be able to control  $G_s$  signalling *in vivo* after genetic modification of the animal and by the use optical fibres and wireless light application. Other receptor chimeras have been developed coupled to  $G_q$  and  $G_i$  proteins, based on  $\alpha_1$  adrenoceptors<sup>100</sup> and GPR37,<sup>107</sup> respectively, thus demonstrate in that this is a generalizable strategy for the different signaling pathways activated by GPCRs.

Optogenetic tools have become important to improve our understanding of biological processes, providing *fully reversible* photo-activation in most cases, with high specificity and fast temporal responses when compared with pharmacological methodologies using drugs. However, the presence of an exogenous protein can alter the cell physiology, thus hampering the possibility of drawing certain conclusions about the function of the endogenous biological system. Moreover, the need for genetic manipulation to introduce a photoactivable protein in the targeted organism implies ethical concerns and limits their therapeutic use in humans.

### **GPCR Photopharmacology approaches**

**GPCR Photopharmacology** offers an alternative to optogenetics based on the use of light-regulated small molecules, such as receptors agonists, antagonists or modulators.<sup>12</sup> Two general photopharmacological strategies have emerged by using small synthetic photoswitches: *freely diffusible photopharmacology*, based on non-covalent small molecules, and *tethered photopharmacology*, based on covalent molecules (Figure 21).

### Freely diffusible photopharmacology

Freely diffusible photopharmacology is applied on endogenous receptors and it in turn includes two different approaches depending on the nature of the photoswitching: the irreversible caged ligands (**CLs**) strategy and the reversible photochromic ligands (**PCLs**) one.

#### CLs strategy

Caged ligands (**CLs**) strategy is based on ligands equipped with a photolabile protecting group (*i.e.* cage) that prevents a correct ligand-receptor interaction, rendering the drug pharmacologically inactive. The cage can be photochemically cleaved under suitable light exposure to *irreversibly* release the biologically active ligand.<sup>108</sup> This approach has become a well-established approach for the study of cell physiology,<sup>109</sup> after being first used to study sodium/potassium channels in the seventies.<sup>110</sup> It has been later applied for the development of several photoactivable neurotransmitters acting on different GPCRs, such as glutamate, GABA, histamine and dopamine, or second messengers, such as cAMP, cGMP, Ca<sup>2+</sup>, IP<sub>3</sub>,<sup>111</sup> but it is not that common to develop photoactivable drug ligands with higher selectivity or optimized drug properties.

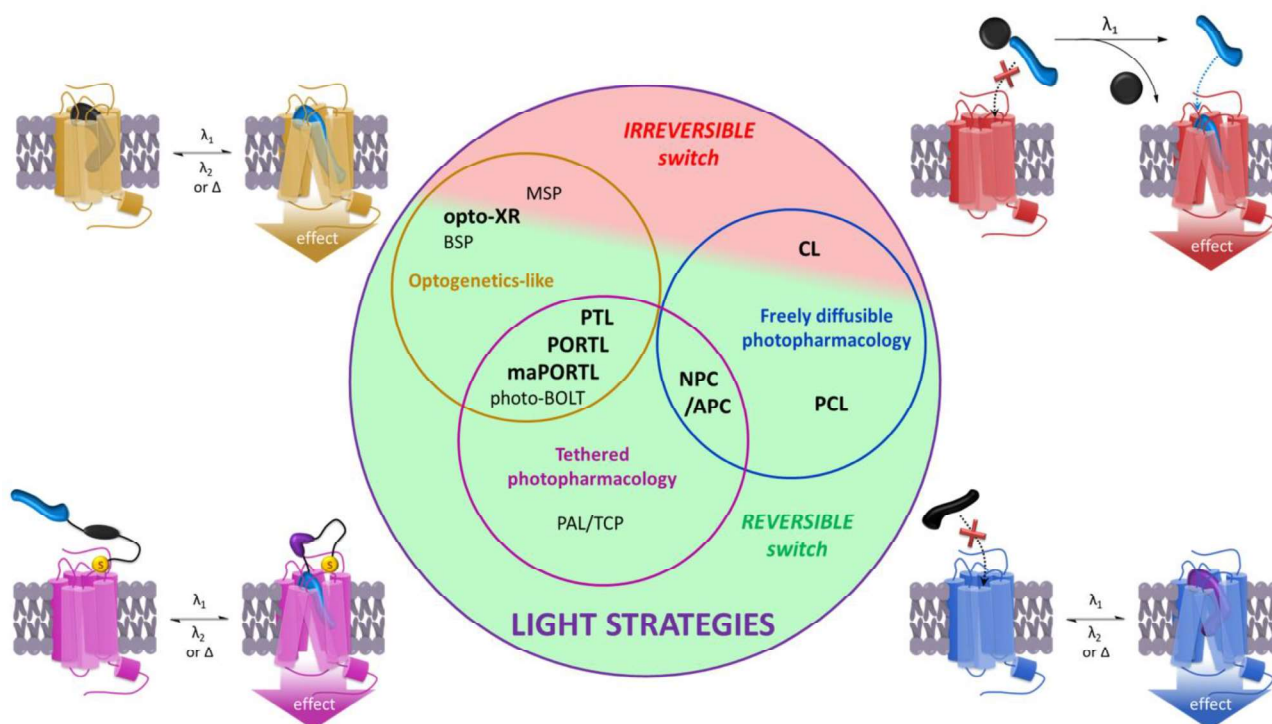


**Figure 21.** Venn diagram showing all relationships between light-technologies currently described to control GPCR function. Strategies are first classified depending on the nature of the photoswitching (reversible in green background or irreversible in red). The second classification depends on the following factors: (1) the target is a receptor genetically introduced or modified (optogenetics-like), (2) the ligand is free-diffusible or (3) the ligand covalently bound to the target protein (tethered). The strategies that have been developed for GPCRs are in bold. Side schematic depictions represent the following approaches: an optogenetic approach in yellow, a caged ligand (**CL**) in red, a photochromic ligand (**PCL**) in blue and a photochromic tethered ligand (**PTL**) in magenta.

For the design of caged ligands, several properties need to be considered. First, a negligible bioactivity of the caged compound is needed, including the presence of impurities from synthesis that often correspond to the bioactive ligand, which is usually very active. Purities above three orders of magnitude are desirable to have a good operativity window where no activity is found for the cage, whereas full activity is recovered upon illumination. Additionally, the drug photoreleasing (uncaging) reaction upon illumination has to be a

fast reaction and with a high yield. This can be achieved with the use of a suitable cage type and optimizing the illumination wavelength and intensity.<sup>111,112</sup> Importantly, the active compounds must be chemically and metabolically stable at these illumination conditions. That is, it does not degrade or promote a reaction that forms other molecules.

In the following example, the caged antagonist MG 307 (**16a**) selective for dopamine D<sub>2</sub>/D<sub>3</sub> receptor was described (Figure 22A).<sup>113</sup> Its design was based on the crystal structure of the dopamine D<sub>3</sub> receptor in complex with the widely used pharmacological agent eticlopride. The authors discovered that caging eticlopride provided compounds with unfavorable photochemical properties and decomposition even in the dark. For this reason, they tried to find a photostable analog of eticlopride by slight structural modifications of the antagonist that led them to the caged compounds based on the dechloroeticlopride (**18a**) pharmacophore. Therefore, not only dechloroeticlopride (**18a**) turned out to be a selective D<sub>2</sub>/D<sub>3</sub> receptor antagonist, with excellent receptor binding properties and photostability upon violet illumination, but also the 2-nitrobenzyl derivative MG 307 (**16a**) showed satisfactory photochemical stability, pharmacological behavior and uncaging properties when interacting with dopamine receptor-expressing cells.

The development of caged drugs for GPCRs in complex systems, such as *in vivo* studies, has been poorly developed, except for few examples. One of these examples is JF-NP-026 (**16b**) (Figure 22B), a caged analog of Raseglurant (**18b**), a negative allosteric modulator (NAM) selective for mGlu<sub>5</sub> receptor.<sup>99</sup> JF-NP-026 (**16b**) was proven inactive in rodent models but violet illumination either peripherally or in the CNS (thalamus) triggered Raseglurant uncaging and produced a highly significant analgesic behavior. Thanks to the spatio-temporal control offered by light, the authors could highlight the specific anatomic distribution of mGlu<sub>5</sub> receptors involved in pain transmission.

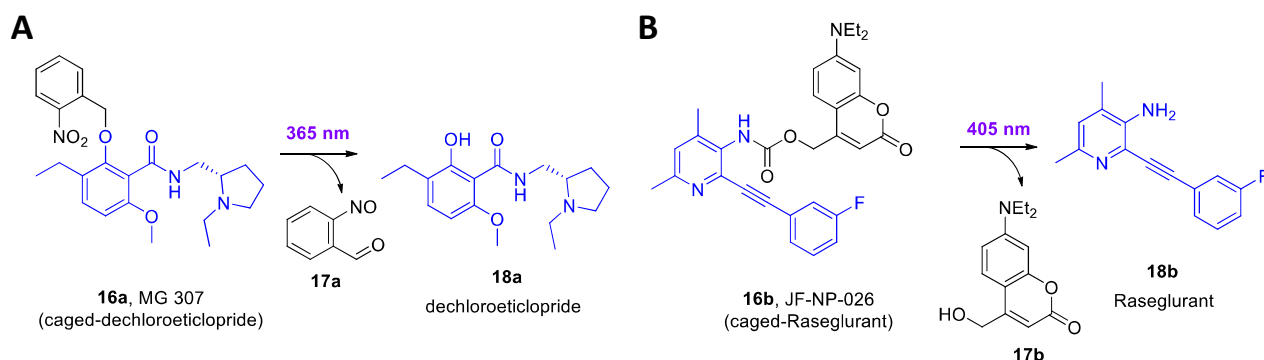


**Figure 22.** Structure and photochemistry of the photo-caged compounds (A) MG307 (**16a**) (caged-dechloroeticlopride) and (B) JF-NP-026 (**16b**) (caged-Raseglurant). Upon irradiation with 365 nm and 405 nm of light respectively the D<sub>2</sub>/D<sub>3</sub> receptor antagonist, (A) dechloroeticlopride (**18a**) and the mGlu<sub>5</sub> NAM, (B) Raseglurant (**18b**), are irreversibly released.

The strategies based on caged compounds are excellent approaches to release effective concentrations of active compounds at the site of action with precise control while avoiding undesired effects in other tissues. Moreover, the design and development of caged compounds can be simpler than using other light-controlled strategies since the photo-released drug is usually well characterized. However, uncaging is an irreversible process and, therefore, the drug cannot be inactivated once released, thus limiting a precise light control. Moreover, it is usually desirable that the ligand leaves the active area as quickly possible or is cancelled by a recovery pump or a deactivating enzyme. In addition, the released by-products from the cage can have off-target or toxic effects.<sup>114</sup> Ultimately, there is also to be considered the potential activity before the illumination that could generate off-target or on-target effects in undesired tissues.

## PCLs strategy

Some of these limitations can be overcome with the second freely diffusible photopharmacology approach: photochromic ligands (**PCLs**), which can be reversibly activated and inactivated upon illumination. Indeed, PCLs include a photochromic moiety in their molecular scaffold that can be reversibly switched between two isomers upon irradiation. If these isomers have different binding affinities or efficacies for the targeted GPCR, the PCL can be used to *reversibly* photoswitch the receptor associated biological effect. The design of this PCLs is generally more challenging than caged compounds since the ligand structure must include a photoswitch without compromising the affinity of the ligand. As extensively explained in the first section, there are several types of photocontrolled biomolecules (or photo switches) depending on the different isomerization mechanisms: *cis/Z* and *trans/E* isomers (azobenzenes, stilbenes and hemithioindigos) and open and closed forms (spiropyrans, diarylethenes and thiophenfulgides). These chemical transformations result in remarkable changes in geometry, flexibility, polarity and charge distribution of the compound.

Efforts in chemistry research have provided a large number of synthetic photoswitches for the regulation of GPCR biological processes, among which azobenzene derivatives are the most commonly used. This is due to the advantages offered by the physicochemical properties of azobenzenes, which are fulfilling many important requirements of photopharmacology. To date, freely-diffusible PCLs have been synthesized targeting all major GPCR classes acting at the orthosteric and allosteric sites or both at the same time, ligands named dualsteric (or bitopic, see *Box 1, Modification of GPCR function*).<sup>115</sup>

PCL photoisomerization usually affects binding properties of the ligand due to a lower affinity of one isomer. However, there are examples, where the photoswitching affects the intrinsic activity of the ligand without substantially modifying ligand affinity. A recent example of this last-mentioned type of PCL has been reported for chemokine receptor CXCR3.<sup>116</sup> In this study, a series of azobenzene based compounds was reported of which VUF16216 (**20a**) (*Figure 23*) demonstrated to perform as a real-time reversible efficacy trigger from antagonism to agonism.<sup>117</sup>

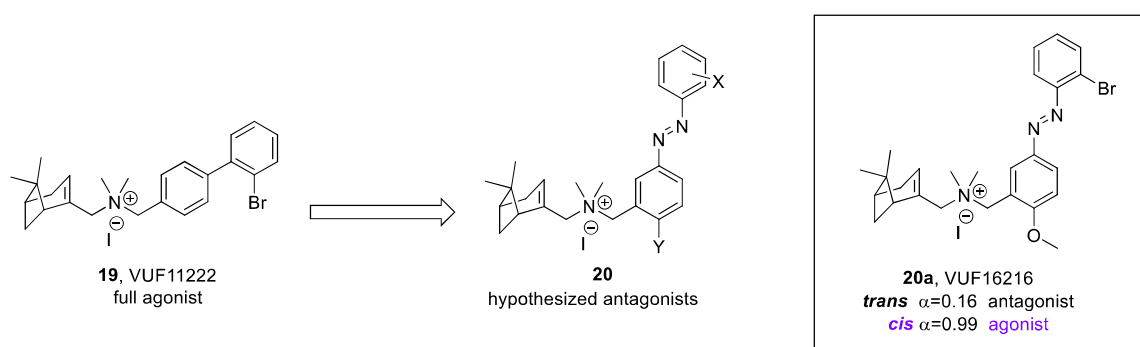


**Figure 23.** The compound VUF11222 (**19**) is an example of biaryl CXCR3 ligands. Azologization of the scaffold of VUF11222 (**19**) and proper Y and X groups gave rise to photoisomerizable analogs with efficacies depending on the Y substituents. Light at 360 nm promoted a switch from *trans* to *cis* configuration. Using [<sup>35</sup>S]-GTP $\gamma$ S functional assay the authors determined different efficacies for the *trans* and the *cis*. Among all molecules reported, VUF16216 (**20a**) represents the highest photoinduced efficacy switch for a GPCR azo-ligand reported to date.

PCLs are small-molecule drugs and therefore they are characterized by a certain ease of application as well as a fast distribution in tissues. As with all drugs, however, what might be a concern is the fact that their photoisomers show relatively small differences in efficacy. Although in our experience PCLs work remarkably well in complex systems and even small changes in the activity of a modulator could have dramatic effects on the output, there are situations where receptor-subtype selectivity and cellular

targeting is highly desirable. In this case then tethered photopharmacology comes into play that, after optogenetics and freely diffusible photopharmacology, represents the third approach with which, using light-operated ligands, it is possible to control receptor protein functions.

### *Tethered photopharmacology*

Tethered photopharmacology is based on photochromic ligands that are covalently bound to the target protein through a specific nucleophilic residue upon a bioconjugation reaction. The most frequent approach for GPCRs is based on the use of genetic engineering to introduce a residue (usually a cysteine) or a suicide enzyme-based tag (SNAP, CLIP, etc) to provide the receptor with an anchor point that allows the bioconjugation of the ligand.<sup>4,118</sup> Therefore, tethered photopharmacology could be considered as a merging strategy between optogenetics and PTL approaches, taking advantage of the best features of both, such as the receptor specificity provided by genetic manipulation (optogenetics), and the applicability of PCL photopharmacology (Figure 21). This allows the use of minimally modified receptors maintaining the biological functions of native ones. On the other hand, a few tethered pharmacology approaches have been used with wild-type proteins, but they are scarce in the GPCR field.

There are different tethered approaches reported in literature, with the common features above described. Depending on bioconjugation strategy and the anchor point placement, tethered photopharmacology can be divided in:

- Photoswitchable tethered ligands (PTLs) that will conjugate the receptor through a genetically introduced aminoacid.
- Photoswitchable bioorthogonal ligand tethering (photo-BOLTs) that conjugate to introduced unnatural aminoacid residues.
- Photoswitchable orthogonal remotely tethered ligands (PORTLs) or membrane anchored photoswitchable orthogonal remotely tethered ligands (maPORTLs) that conjugate to fused protein domains.
- Photoswitchable affinity labels (PALs) or targeted covalent photoswitches (TCPs) that react with nucleophiles of native/unmodified receptors.
- Antibody/nanobody-photoswitch conjugates (APCs/NPCs), which are based on tethering an antibody or a nanobody that binds the target receptor through a *strong* and specific non-covalent interaction.

Between these approaches, only PAL, PTLs, PORTLs, maPORTLs and NPC are described in the GPCR field and all them involving engineered proteins, except OptogluNAM4.1, which is a photoswitchable negative allosteric modulator of mGlu<sub>4</sub> that binds covalently.<sup>119</sup> In this PAL approach, the authors proved the covalently labeling of non-modified mGlu<sub>4</sub> receptor by pharmacological methodologies, but not at a molecular level.

**PTL** compounds are usually designed as maleimide-azobenzene ligand derivatives that react by affinity labeling with genetically engineered protein receptors, commonly introducing a cysteine amino acid. This single-point mutation must not alter the function of the protein or its membrane trafficking. The photoswitchable unit is generally located in the linker, close to the ligand moiety.<sup>120</sup> This approach has been applied to class A and class C GPCRs, as recently described for dopamine D<sub>1</sub>/D<sub>2</sub> receptors (DAR)<sup>121</sup> and mGlu<sub>2</sub> receptor.<sup>120</sup> This strategy has demonstrated to be very efficient due to the high selectivity of the ligand for the modified receptor but also possess some limitations. The presence of native cysteines on the

surface of the cells may reduce the bioconjugation selectivity. Moreover, maleimide stability is limited in cellular environments due to slow hydrolysis and possible reaction with cytosolic glutathione.<sup>118</sup>

To overcome those limitations, the **PORTL** strategy was developed as an evolution of PTLs for mGlu receptors. In this approach, the tether is a large chain that will covalently attach to a fusion protein tag based on suicide enzymes that covalently react with benzyl guanines, benzyl cytosines or haloalkanes (SNAP-,<sup>122</sup> CLIP-<sup>123</sup> and HALO<sup>124</sup>-tagged GPCRs). The complete tether is composed of a reactive moiety connected to a light-sensitive ligand by means a flexible linker (*i.e.* polyethylene glycol (PEG)). This linker is also water soluble and commercially available in several lengths so as to allow the ligand to tether distant domains. Using several wavelengths of light, the receptors could then be activated and disabled after the photoisomerization of the light-sensitive moiety of the tether (generally an azobenzene). This strategy provides an orthogonal bioconjugation with a very high selectivity.<sup>125–127</sup> However, the use of PORTLs is also limited. These ligands are often restricted to targeting points on a receptor that can only be accessed by the solvent. Additionally, the photoswitching between each isomer is often inefficient, which can lead to reduced activity and binding.<sup>128</sup> Some researchers are trying to overcome some of the limitations associated with this approach. For example, a recent work was based on the design of branched PORTLs to improve the efficiency of photoisomerization and the affinity of bound ligands.<sup>127</sup> Because the azobenzene glutamate head group is the pharmacologically active part of BGAGs (benzylguanine-azobenzene-glutamate compound), Acosta-Ruiz and colleagues hypothesized branched molecule containing two azobenzene-glutamates (*i.e.* *double* BGAG) would improve photoswitching efficiencies and, thus, the receptor activation across all photostationary states and also labeling efficiencies. They synthesized such molecules, demonstrated the previous hypotheses and proved their efficacy *in vivo*. Additionally, they postulated that these branched PORTL could contribute to know more about the role of group II mGluRs in working-memory-related behavior and in psychosis.<sup>127</sup>

In addition, PORTL approach can also work with unmodified receptors if the anchoring point is not located in the receptor. In this case, the tag (generally of the HALO and SNAP tag) can be fused to a protein in its vicinity. Here, a photoswitchable ligand is tethered through a very long PEG linker to a tag fused to a membrane anchor in the plasma membrane. Via lateral diffusion, the membrane anchor with the PORTL diffuses in the membrane to get in close in proximity to its target receptor and enable the interaction that can activate the receptor. Very recently, the maPORTL approach was used to target also mGlu<sub>2</sub>.<sup>129</sup> The resulting membrane anchored PORTL (**maPORTL**) is shown schematically in *Figure 24B*.

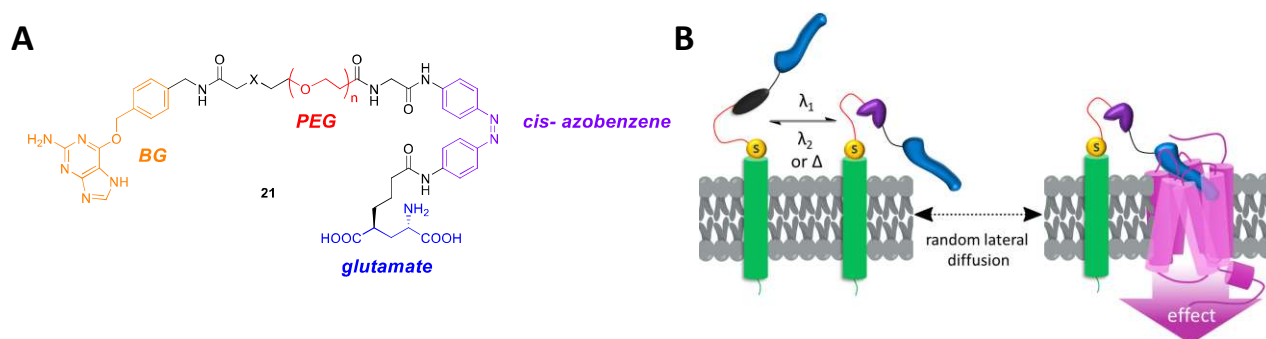


**Figure 24.** Targeting unmodified native mGluRs with BGAG. (A) SNAP-tag binding photoswitchable receptor agonist BGAG (**21**) in its *cis* active form upon 380 nm illumination, with PEG linker of different lengths between benzylguanine (BG) and azobenzene-glutamate. “X” indicates distinct spacer elements within the several analogs of BGAG. (B) The active isomer of BGAG, *cis*-BGAG (**21**), tethered to a SNAP-tag fused to a single-pass transmembrane segment (SNAP-TM) randomly approaches and photoactivates a native (unmodified) mGluR. (Adapted from Donthamsetti et al.).<sup>129</sup>

In this study, Donthamsetti and colleagues provide a tool box for controlling endogenous GPCRs and the photoactivation of wildtype mGlu<sub>2</sub> was optimized by tuning the chemical length of the BGAG linker, the position of the SNAP-tag relative to the plasma membrane and the surface density membrane anchored SNAP-tag.

## Characterization of GPCR photopharmacological tools

In the process of development of photopharmacological tools, such as caged or photochromic ligands (free diffusible or tethered), the characterization of compounds needs to be carefully addressed before testing them in physiologically relevant environments. However, since the biological activity of these compounds is illumination dependent, further considerations are necessary. First, the compound photoisomerization and photorelease (uncaging) under different light conditions have to be well determined. Subsequently, the translation of these light-induced molecular changes to biological activities requires to be fully addressed. Additionally, the intrinsic properties of compounds that make them sensitive to light must be carefully taken into consideration as they might interfere with the readout of the biological assay. All these theoretical and methodological considerations are covered in this section.

### *Photoisomerization and uncaging characterization*

The three most common methodologies to measure compound photoisomerization or photorelease are UV-Vis spectroscopy, liquid chromatography coupled to a photodiode array or mass spectroscopy (LC/PDA/MS), and nuclear magnetic resonance (NMR). These techniques allow the detection of photoisomers or caged compound components by their differential profile in the output (*i.e.* spectrum, chromatogram). Although these methods can provide complementary information, depending on the photosensitive compound it might not be amenable in some cases, as explained in the following subsections.

#### *UV-Vis spectroscopy*

The UV-Vis spectra of photochromic isomers are generally very different. Similarly, caged compounds and their photoreleased protecting groups often have a differential UV-Vis profile. This makes this technique one of the basic experimental procedures for photo-isomerization and photo-uncaging detection. Moreover, UV-Vis spectroscopy is a robust, unambiguous and inexpensive methodology that also allows monitoring different photoisomerization cycles, determining the thermal relaxation of the metastable isomer or measuring the photoreleasing rate of a caged compounds. On the other hand, evaluating the isomerization of photochromic compounds with low bistability might represent a challenge, but this technique allows to use a wide range of solvents that often modify the stability of the different isomeric forms. Usually, the concentrations needed to evaluate the UV-Vis spectrum ranges between 10 and 100  $\mu$ M. However, the main limitation of this methodology is that the quantitative detection of the amount of each isomer in a mixture is problematic. Some deconvolution methodologies have been described to overcome this issue. However, to apply these methods, the spectrum of a pure sample for each isomer is needed, which represents a methodological challenge with some photochromic compounds having low bistability.

#### *LC-PDA-MS*

Liquid chromatography (LC) is a powerful methodology that allows to quantitatively detect a mixture of molecules, such as caged compounds or photoisomers. If LC is coupled to a photodiode detector (PDA), the

UV-Vis absorption spectra of each of the separated peaks can be obtained to properly identify the isomer/compound. Moreover, if LC is subsequently coupled to a mass spectrometer (MS), it is possible to determine the mass of each molecular entity, which will be identical in the case of photoisomers. To quantify the isomeric ratio, the separated peaks must be integrated using the PDA channel at the wavelength of the isosbestic point (*i.e.* wavelength with equal absorbance of both species), which can be previously determined by UV-Vis spectroscopy. Methods based in LC have high sensitivity requiring small sample quantities (ca. 1 nmol) to quantify photoisomerization but are low throughput. Moreover, only bistable photochromic compounds can be analyzed using this method because the metastable isomer should not relax before or during the time of measurement (ca. 1-10 min), that would result in detecting only the thermodynamically stable isomer.

### *NMR spectroscopy*

Nuclear magnetic resonance (NMR) is a non-destructive technique that can be very useful to detect mixtures of isomers of a photochromic compound or a caged compound release. This technique allows a direct sample illumination with an optical fiber or a laser while measuring, what can be very useful for the characterization of photochromic compounds with low bistability. Using  $^1\text{H-NMR}$ , the hydrogen peaks of different species or isomers can be integrated and their ratio corresponds to the molar ratio. The main disadvantage of this technique is that it requires samples at high concentrations (>1 mM), at which some GPCR ligands may not be soluble in deuterated aqueous solutions.

### *Receptor photoswitching characterization*

The main objective of photopharmacological compounds is to gain control on the target protein activity through light. This activity switch is generally related to a molecular lysis or isomerization prompted by a specific light exposure. However, the effect of this chemical reaction is not always evident in biological experiments. Therefore, a proper pharmacological characterization is needed to correctly evaluate the differential activities of light-controllable molecules under different illumination conditions.

Many pharmacological and biochemical assays have been used to date in GPCR photopharmacology. Among these, only kinetic assays allow to measure real-time photoswitching. Indeed, when a spatiotemporally controllable molecular tool is evaluated, such as photopharmacological drugs, a time resolution of the method is an important parameter to be considered since in some assays long incubations are needed. Other relevant points to consider are the complexity of the set-up needed and the robustness of the data obtained since the application of light will likely alter the assay readout. Indeed, this is a very important point to contemplate since light-based assays (fluorescence, bioluminescence, etc.) may lead to artifacts due to ligand high absorbance resulting in signal quenching. Taking into consideration all these properties, the assays used for pharmacological characterization of these photopharmacological tools can be organized in three general categories:

- *Kinetic functional assays*, which are based on the measurement of a biological substance concentration variations (second messenger, ions, etc.) or on the interaction of two protein units that associate or dissociate upon a GPCR activation. These methods offer the possibility to perform dynamic measurements, including real-time measurement, while the system is being irradiated with different light wavelengths.
- *Endpoint functional assays*, which are based on the measurement of an accumulated biological substance (second messengers or proteins). These, usually provide good specific signal to noise



ratio. However, since the measurement is stopped at a certain time point, these methods do not allow a continuous dynamic measurement of biological events (including photoisomerization).

- *Binding assays*, which measure ligand binding to the target GPCR and can be kinetic or endpoint.
- *Conformational assays*, which are kinetic and measure a change of conformation of the target GPCR.

### *Kinetic functional assays*

#### *cAMP and Calcium Sensors (Figure 25 (1))*

A common strategy in photopharmacology is based on the use of second messenger sensors, which can be fluorescent, bioluminescent or produce FRET/BRET upon binding to a second messenger such as cAMP or  $\text{Ca}^{2+}$ . The kinetic nature of these sensors offers advantages such as the possibility of measuring the receptor photoswitching in real time. However, a possible interference in fluorescence or luminescence assay responses due to quenching by the photosensitive ligands can be a drawback. This involves the need to carefully consider the addition of control experiments to avoid assay interferences or subtract them from final results. Several assays with cAMP sensors in photopharmacology have been described, such as sensors fused with luciferase proteins<sup>130</sup> and cAMP EPAC FRET sensors.<sup>131</sup> Also cytosolic calcium concentration has been monitored upon GPCR photoswitching with chemical  $\text{Ca}^{2+}$  sensors (Fura-2, Fluo2, X-Rhod-5F)<sup>119,132-137</sup> or genetically encoded sensors (GCaMP, R-GECO, aequorin, OGB1AM ).<sup>127,138-142</sup>

#### *BRET to monitor G protein activation and $\beta$ -arrestin recruitment (Figure 25 (2))*

G protein activation methods based on bioluminescence resonance energy transfer (BRET) assays are cell-based assays in which different protein constructs have to be co-transfected:  $G_{\alpha}$  subunit fused to a luciferase and the  $G_{\beta}$  or  $G_{\gamma}$  fused to a fluorescent protein (GFP, YFP, Venus V1/V2). In proximity, the two elements, in presence of the luciferase substrate, give rise to resonance energy transfer from the bioluminescent luciferase to the fluorescent protein. Therefore, upon G protein activation  $G_{\alpha}$  and  $G_{\beta\gamma}$  subunits dissociate leading to a decrease of the BRET and an increased emission from the luciferase. Similar assay has been also applied to  $\beta$ -arrestin recruitment in which both, the receptor and  $\beta$ -arrestin, are labeled with BRET donors and acceptors.<sup>143</sup> BRET based assays are very common in GPCR pharmacology, however in the photopharmacology field has not been widely used, except in few reports.<sup>121</sup> The possible compatibility of luciferase substrates with an external illumination must be examined, since some are unstable and prone to photodegradation, such as coelenterazine. However, this assay is completely amenable for bistable photoswitchable compounds and caged molecules using pre-illumination protocols. Moreover, as an assay with bioluminescent and fluorescent components, the interference with photosensitive ligands must be assessed.

#### *Split luciferase complementation (Figure 25 (3))*

Split luciferase complementation assays are commonly used to measure protein-protein interactions. Both interacting proteins have a fragment that reconstitute into a functional luciferase when the complex is formed. This method can be applied to monitor interactions between  $G_{\alpha}$  and  $G_{\beta\gamma}$  subunits, G proteins and receptors, G proteins and effectors, and  $\beta$ -arrestin recruitment by GPCRs. However, photoregulated ligands could still quench luminescence from luciferase although it has been found to be less likely. In addition, as previously mentioned, external illumination might degrade the luciferase substrate thus limiting its use in photopharmacology protocols. Despite not being widely used, this method has been recently reported in GPCR photopharmacology.<sup>140,144</sup>

*GIRK channel activation (Figure 25 (4))*

One of the most common techniques to detect activity of a GPCR upon stimulation with light-controlled ligands is the measurement of a G protein-coupled inwardly-rectifying potassium channel (GIRK) opening, which is induced by its interaction with the  $G_{\beta\gamma}$  subunit after G protein activation and dissociation. This technique needs the co-transfection of the receptor of interest and the GIRK channel in cell cultures or in *xenopus tropicalis* oocytes. Channel opening is usually detected by electrophysiology experiments (*e.g.* voltage clamp, patch-clamp) using a buffer with high concentration of potassium to monitor depolarization upon GIRK channel opening. The main advantage of this technique is that the measurement is performed in a dynamic real-time mode. Moreover, the response recording is completely independent of the applied light, thus giving rise to robust results free of artifacts, which has promoted its wide use in GPCR photopharmacology.<sup>116,120,121,125–127,129,136,138,145–148</sup> These advantages has allowed the development of protocols with a variety of light conditions, thus making this method an excellent option to prove reversibility of a receptor photoswitching. However, the low throughput makes difficult testing large number of compounds.

*Endpoint functional assays**TR-FRET IP and cAMP accumulation (Figure 25 (5))*

One method to characterize GPCR light-regulated ligands is based on the measurement of the concentration of second messengers upon G protein activation. Second messengers accumulate when the natural degradation is inhibited. In the case of  $G_{\alpha q}$  activation, phospholipase C (PLC) activation produces an increase of inositol triphosphate ( $IP_3$ ), which is stepwise dephosphorylated to myo-inositol (Ins). However, the presence of lithium ions in the culture media inhibits the last dephosphorylation step, leading to an accumulation of inositol monophosphate (IP). Similarly,  $G_{\alpha s}$  activates the adenylyl cyclase (AC) and produces an increase in the concentration of cyclic AMP (cAMP), which is accumulated in the presence of a phosphodiesterase (PDE) inhibitors. In contrast,  $G_{\alpha i/o}$  and the other inhibitory G proteins inhibit the AC activity leading to a decrease of cAMP levels. A commonly used method in photopharmacology to quantify IP or cAMP accumulation in the cytosol is based on Homogeneous Time-resolved FRET (HTRF) using labeled antibodies and second messengers. In this method, during cell lysis it is used a buffer implemented with fluorescently labeled IP or cAMP with a FRET acceptor and an IP- or cAMP-recognising antibody labeled with a lanthanide cryptate/chelate. A competition between labeled and the endogenously produced IP or cAMP can be analyzed by time-resolved FRET signal after incubation of the cells using different light conditions.<sup>98,99,113,119,132–135,149–151</sup> The main limitation of this method is that photoswitches and photocages may interfere or quench the FRET signal between donor and acceptor molecules. However, since this is an endpoint assay, photoactive ligands can be washed out previous to the addition of the FRET fluorophores.

*Gene reporter assays (Figure 25 (6))*

Activation of GPCRs can promote gene expression through second messenger-responsive transcription factors. For instance, upon activation of  $G_{\alpha s}$  GPCRs, the activity of AC is enhanced resulting in an increase of the cAMP cytosolic concentration, which will subsequently promote the enzymatic activity of PKA. One of the PKA's reported actions is the phosphorylation of CREB transcription factor that will lead to an increase of the expression of CREB-target genes, such as secreted alkaline phosphatase (SEAP). Thus, a  $G_{\alpha s}$  GPCR activation can be monitored in cells transfected with SEAP adding a phosphorylated substrate that becomes fluorescent or chemiluminescent upon SEAP dephosphorylation. Other similar methods that detect cAMP-mediated expression of other CREB-target genes by immunofluorescence are also available. In GPCR

photopharmacology, this endpoint assay has been successfully used to characterize caged compounds.<sup>152-155</sup> However, these methods require long receptor stimulations of 24-48 h. Therefore, the use of these types of assay for the analysis of the activity of photochromic compounds that usually require high intensity and continuous illumination could result in cell phototoxicity or to light-induced biological effects that lead to activity biased measurements.

#### *[<sup>35</sup>S]-GTPγS binding (Figure 25 (7))*

[<sup>35</sup>S]-GTPγS binding assays are classical radiolabelling functional methods to quantify the activation of G proteins in cell membrane preparations. The assay, not specific for a G<sub>α</sub> subtype, is based on the non-hydrolysable analogue GTP with a radiolabelled sulphur in γ position binding, which will bind the G<sub>α</sub> subunit upon receptor and G protein activation. The ineffective hydrolysis results in a slow reversible binding of [<sup>35</sup>S]-GTPγS and its accumulation that can be measured by counting the amount of [<sup>35</sup>S]-label incorporated by G<sub>α</sub> subunits. The radioactive basis of these type of techniques has limited their use in GPCR photopharmacology. However, some remarkable examples have found in these methods several advantages, such as the low complexity of the protocols used and the lack of interference with light-regulated ligands.<sup>116,117,147,155</sup>

#### *Conformational assays*

##### *Conformational biosensors (Figure 25 (8))*

Although being a method of increasing interest to study activation mechanisms, GPCR conformational sensors have been only used in one photopharmacology study.<sup>156</sup> These sensors are based on FRET compatible fluorescent protein domains fused to in two regions of the receptor. A differential FRET can be measured upon conformational changes of the GPCR linked to the activation state. They were initially developed for mechanistic studies using pharmacology and microscopy and usually have a low signal/noise ratio although remarkable examples in class C GPCRs demonstrate very high accuracy and excellent robustness. Like many fluorescence-based assays, the possible interaction between the photosensitive ligands and the fluorophores needs to be explored. Nevertheless, they provide very useful information of the GPCR dynamics upon ligand binding, which may be different depending on the photoisomers regardless of their pharmacological activity.

#### *Binding assays*

##### *Radiolabelled ligand displacement (Figure 25 (9))*

This assay is the most common binding assay used for GPCRs. It is a straightforward method based on the competition of the assayed ligand with a radiolabelled tracer. Treating membranes containing the target GPCR, the bound ligand can be estimated by measuring the remaining radioactivity after a rapid and thorough washing. As an assay based in radiolabelled ligands, it is generally compatible with photopharmacological ligands if the photosensitive ligands do not quench scintillation processes. However, this method retains the major drawbacks of using radioactive isotopes (health and waste risks, need of appropriate infrastructure and equipment). Several reports in GPCR photopharmacology include binding information obtained by this type of assays.<sup>113,116,117,140,144,146,147,155,157</sup>

Fluorescent ligand displacement and HTRF binding (Figure 25 (10, 11))

These assays are based in similar principles to that of radiolabelled ligand displacement, with the difference that the ligand is fluorescently instead of radioactively labeled, thus avoiding the problems related to the use of radioactivity. They also offer the possibility to monitor kinetic measurements but the photosensitive ligands may interact with the components of the assay.<sup>149</sup> A related approach with fluorescent ligand displacement makes use of tagged GPCRs with an HTRF donor (Tb or Eu cryptates). This can induce time-resolved FRET with the fluorescent ligand bound, thus reducing the background signal.<sup>121</sup>

Mass spectrometry binding assay (Figure 25 (12))

This assay is based on the detection by MS/MS spectrometry of a ligand bound to the target receptor alone or in competition with another one.<sup>158</sup> Since the detection of the ligand does not require any irradiation or light detection, the assay is fully compatible with photopharmacological applications. However, the sensitivity of the assay can be variable due to the different capacities of ionization of the compounds and needs to be set-up for every ligand to be detected. It represents a powerful binding assay that has been used only very recently in the field of photopharmacology.<sup>159</sup>

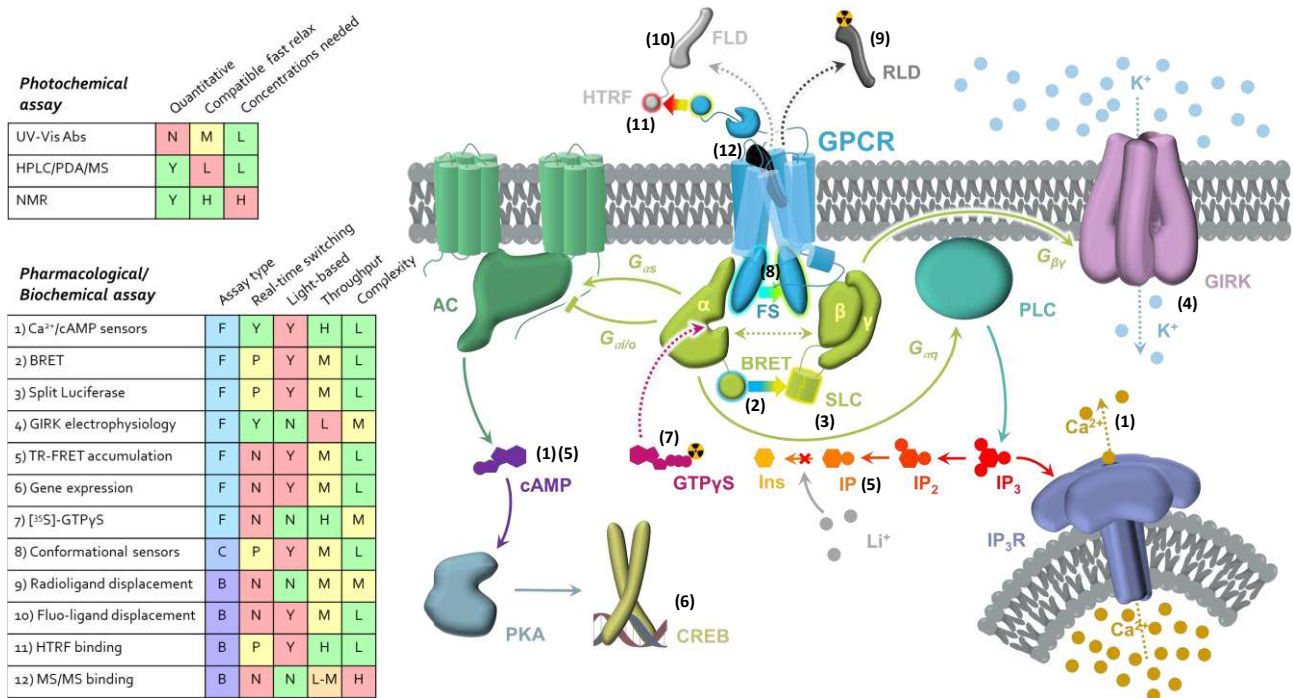


**Figure 25.** Summary of assays to characterize GPCR photopharmacological tools. (left) List of the different assays used in GPCR photopharmacology with a summary of the main features of each assay: assay type (F for functional, B for binding and C for conformational); ability to detect reversible photoswitching; if it is based on light; degree of throughput and complexity. The suitability of each feature to characterize photopharmacological tools responds to a color code: green for very good suitability, yellow for good or medium suitability and red for a lower suitability or a need for a careful examination. Letter codes are the following ones: Y for yes, N for no, H for high, M for medium, L for low, P for theoretically possible but not done in GPCR photopharmacology. (right) Graphic scheme of the different events present in GPCR signaling that can be object of measurement in different pharmacological/biochemical assays. The events are related to the assays listed on the left part with a number code from (1) to (12). β-arrestin recruitment assays are not represented in the scheme.

### ***T-on/ M-on photochromic ligands***

In the photopharmacology field, the term photoswitching refers to a change in the biological activity of a pharmacological target (in the case concerning here, a GPCR) due to a light-prompted ligand isomerization. This ligand isomerization may lead to a change in affinity that generally is translated in change of the receptor activity. Indeed, changes of ligand affinity are generally translated in changes on potency that is the dose of ligand needed to observe a specific functional effect. Most publications reporting on GPCR photochromic ligands describe a change of potency or affinity, usually expressed as a photoinduced shift (PAS or PPS, for affinity or potency, respectively).<sup>132,146</sup> The larger is this shift, the larger is the photoswitching resulting in higher chances to find a ligand dose to enable a complete *on/off* effect upon photoisomerization. However, the maximal effect that a ligand can produce upon binding, that is only related to the ligand efficacy, is also a relevant pharmacological parameter that can be differentially regulated by photoswitchable ligands. Depending on the intrinsic activity,<sup>\*</sup> a ligand can be described as a full agonist, partial agonist, neutral antagonist or inverse agonist (see *Box 1, Modification of GPCR function*), and two isomers of the same molecule may behave differently upon binding to the receptor.

With these assumptions, most of the GPCR directed photochromic ligands can be classified in following three main subgroups that we propose:

- **Affinity *T-on* ligands**, which are photochromic ligands, whose **T**hermodynamically more stable isomer is binding to the target GPCR with higher affinity. This would correspond to the *trans* isomers for common azobenzenes, *cis* isomers for cyclic azobenzenes, spiro isomer for spiropyrans or open isomer of dithienylethenes (*Figure 26A*).
- **Affinity *M-on* ligands**, which are photochromic ligands, whose **M**etastable isomer is binding to the target GPCR with higher affinity. This would correspond to the *cis* isomers in common azobenzenes, *trans* isomers in cyclic azobenzenes, merocyanine isomer for spiropyrans or closed isomer for dithienylethenes (*Figure 26B*).
- **Efficacy photoswitches**, which are photochromic ligands that bind to the target receptor both with the thermodynamically stable and the metastable isomer, but each photoisomer has different intrinsic activity (*i.e.* full agonist, partial agonist, antagonist, partial/full inverse agonist) (*Figure 26C*).

The *T-on* approach provides photochromic ligands that perform their biological activity in the dark and, by the illumination with a specific light wavelength, they lose their affinity. This affinity can also be eventually rescued with the use of another wavelength of illumination. Generally, the development of this type of ligands (especially using azobenzenes) is not arduous since, the azologization approaches<sup>31</sup> have good chances to be successful. The use of different illumination wavelengths can provide photostationary states (PSS) with different proportions of the two isomers. This allows adjusting the active ligand dose by means of light, therefore providing a spatiotemporal control of the GPCR activity. This makes *T-on* PCLs excellent tool compounds to control the activity of GPCRs in physiological studies, which is not possible with most of the currently available chemical biology tools. From the therapeutic point of view this approach is however

---

\* Intrinsic activity is a measure of the ability of a drug that is bound to the receptor to generate an activating stimulus and produce a change in cellular activity. Both agonists and antagonists can bind to a receptor. However, only agonist molecules can activate the receptor and, therefore, have intrinsic activity.

limited. Nonetheless, it could be designed to treat a disease which is spread throughout the organism whereas the drug activity is “disconnected” in specific regions of the body to prevent off-target side effects.

On the other hand, the use of the *M-on* approach for photochromic ligands can improve the previous therapeutic limitations of *T-on* ligands, since they show a lower activity in the dark and can be activated with a light of specific wavelengths in a precise time and location. Moreover, *T-on* ligands may be also advantageous in research applications to study the implication of a receptor activity with precision in cells, tissues and organs. The development of *T-on* ligands has been proved to be more challenging especially for *E-Z* photoswitches due to the particular angle between the aromatic rings of the isomers, such as *cis*-azobenzene, which is barely found in the binding mode of conventional GPCR drugs. Nonetheless, the spatiotemporal control of the ligand activity provides an extra local selectivity, which would prevent possible side effects if the GPCR is expressed in non-targeted regions of the body.

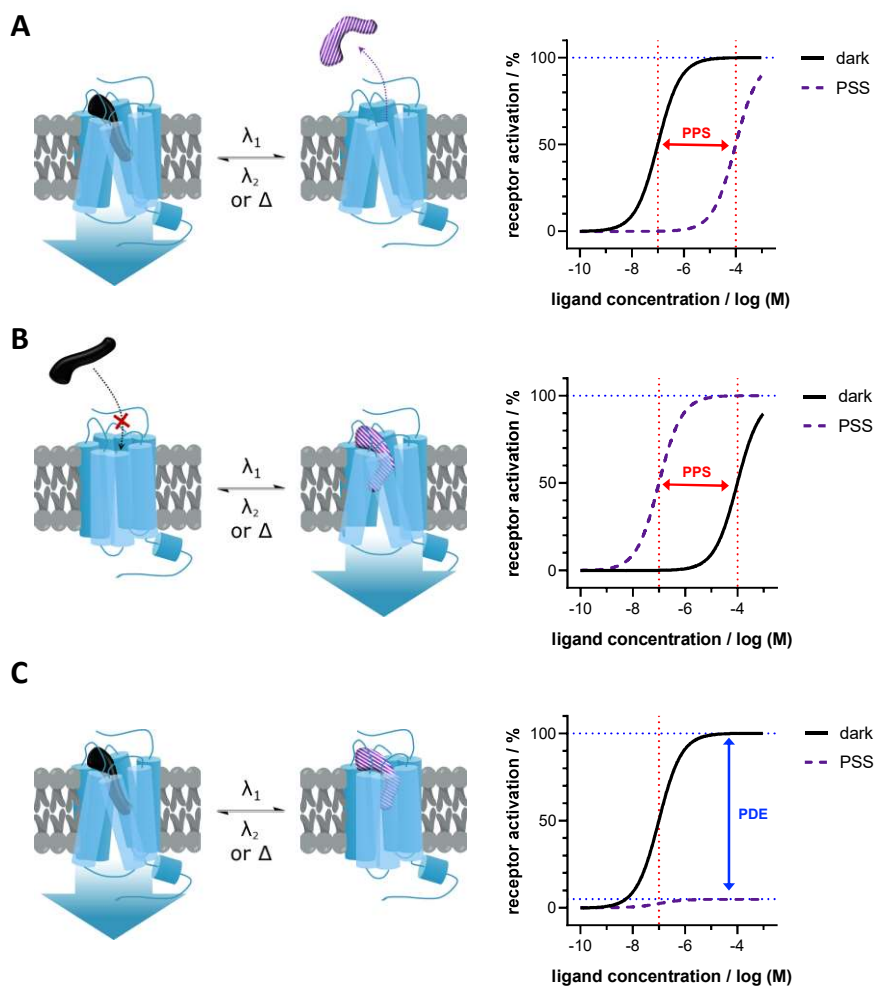


**Figure 26.** Pharmacological classification of GPCR photochromic ligands. Graphical scheme and model dose response curves of types of GPCR photoswitching ligands: (A) *M-on* Affinity switch, (B) *T-on* affinity switch, (C) Efficacy photoswitch from a *T-full* agonist to a *M-antagonist*.

The most prominent example of efficacy photoswitching in GPCRs is retinal. For this molecule, the *11-cis* isomer acts as an inverse agonist after covalently binding bistable pigments, such as paraptinopsin.<sup>28</sup> In contrast, after absorption of a photon, the ligand isomerizes to all-*trans*-retinal, which as an agonist, activates the receptor and initiates the transducing signaling cascades. However, retinal cannot be considered a formal photochromic ligand for monostable pigments, such as vertebrate rhodopsin, since this

photoswitching is not reversible with a second light wavelength.<sup>28</sup> Synthetic photochromic ligands have demonstrated differences of intrinsic efficacy between isomers and photoswitching from antagonism to full agonism (Figure 26C). These differences in intrinsic activity are usually expressed as PDE (photoinduced difference of efficacy).<sup>116,117,150</sup>

From the chemical biology point of view, light-regulated ligands controlling the receptor efficacy are excellent tool compounds to study the response of a particular GPCR. Indeed, the differential binding of photoisomers allows for a fine control of its functional activity, enabling a real *on/off* switch that is dependent on their relative ratio. However, this approach involves a continuous action of the ligand towards the targeted receptors regardless the isomer acting. This can be a limitation of the approach from the therapeutic point of view since the activity of receptors expressed in cells or tissues non-related to the treatment will be also altered.

### Translation to *in vivo* and therapeutic prospects

The translation of the photochemical and photophysical properties of a biologically active molecule to a precise control of biological activity constitutes the essence of photopharmacology. The use of light triggered stimulus to manipulate the molecular activation of GPCRs in living animals opens the opportunity to study of molecular and biological mechanisms with unprecedented spatial and temporal resolution. On one hand, *in vivo* photopharmacology allows to study a particular anatomical location of the receptor with a specific physiological response or stimulus at molecular and cellular levels, allowing to accurately establish the GPCR function, mechanism and dynamics in living organisms.<sup>97</sup> On the other hand, the high resolution of optical manipulation techniques offers the opportunity to develop light-regulated drugs acting on GPCRs with a degree of control unattainable with conventional drugs. This fine control allows therapeutically restoring specific receptor dysfunctional states, which are related to a defined pathophysiological situation.

A critical element for *in vivo* applications of photopharmacology is the existence of a suitable device to deliver light to a localized target tissue or organ to promote the photo-response of molecules and proteins.<sup>160,161</sup> Undoubtedly, there are organs where light delivery is relatively straightforward, for example in external organs such as skin, the auditory system and organs related to light transfer or light stimulus processing (*i.e.* eye and retina).<sup>162</sup> In contrast, some other locations present more difficulties because are deep and non-transparent tissues, such as the brain or the heart. Indeed, photopharmacological manipulation on these locations require invasive devices to transfer the light from the source.<sup>163</sup> The type of organism involved is also relevant and small animal models such as tadpoles or zebrafish, which are relatively transparent, offer advantages for light delivery over bigger organisms such as rodents or humans, which usually require implantable systems involving surgery. In addition, for specific applications, the light parameters (wavelengths, intensity, illumination time and area, tissue penetration) and the photomolecular properties define also the requirements of the illumination system. However, as a consequence of the advent of optogenetics, the development of bioelectronic devices and illumination systems for optical regulation and light delivery is in constant progress and can be applied into the photopharmacology field.

Therapeutic proofs of concept for GPCR photopharmacological pain control in wild type animals has been successful using mGlu photoswitchable azobenzenes,<sup>98,132</sup> caged allosteric modulators<sup>99</sup> or azobenzene lipids.<sup>136</sup> Photopharmacological approaches for visual impairment or blindness appear specially promising. A striking demonstration has been obtained using a white light photoswitchable azobenzene acting on ion

channels of retinal ganglion cells. In these reports, *on* and *off* responses were induced by utilizing intrinsic circuitry in mice blind retina showing promising effects in behavioral mice experiments.<sup>164,165</sup> However, the use of photoresponsive drugs to regulate the dynamic molecular architecture and cellular complexity of the vision machinery is an enormous challenge, which will require deep and sustained efforts for effective restoration of responses in damaged retina. Finally, among the excitement of many potential applications of light to improve drug effects, the control of bacterial growth with red-light operated antibiotics,<sup>166</sup> the regulation of pancreatic function for glucose homeostasis in anesthetized mice<sup>167</sup> or the development of molecules acting on cancer cells are particularly remarkable.

## Class C GPCRs

The class C/Glutamate family GPCRs comprise twenty two receptors in humans that are activated by small molecules such as amino acids and ions.<sup>62</sup> This family includes eight metabotropic receptors for the excitatory neurotransmitter glutamate (mGlu), which will be extensively described below. The family also includes two gamma-aminobutyric acid (GABA) type B receptors (*i.e.* GABA<sub>B1</sub>, which has two splice variants, a and b, and GABA<sub>B2</sub>) for the inhibitory neurotransmitter GABA. Several other GABA receptors are found in the human genome, but these are ion channels (GABA<sub>A</sub>). Additionally, a single calcium sensing receptor (CaS), three taste receptors (TAS1R1-3) and eight orphan GPCRs\* also belongs to family C GPCRs.<sup>80</sup>

This group basically corresponds to what has been called clan C receptors. They can bind several intracellular heterotrimeric G protein subtypes, depending on the receptor, activating them as we have already seen in the second section of this chapter. They are mainly expressed in the central nervous system (for GABA<sub>B</sub> and mGlu), in the tongue (TAS1) or in multiple tissues (CaS).

### Topology and ligand recognition

The distinctive features of class C GPCRs are the large extracellular domain (ECD) and the mandatory dimerization at the cell surface, either as homodimers (mGlu and CaS) or heterodimers (GABA<sub>B</sub> and T1R)<sup>168,169</sup> (Figure 27) In addition to homodimers, mGlu receptors have recently been reported to possibly form eleven different heterodimers in heterologous systems: the mGlu<sub>1</sub> and mGlu<sub>5</sub> receptors can only heteromerize between them, whereas all combinations are possible among five other mGlu receptors (mGlu<sub>2</sub>, mGlu<sub>3</sub>, mGlu<sub>4</sub>, mGlu<sub>7</sub> and mGlu<sub>8</sub>) (Figure 29).<sup>170</sup> Each protomer consists of two or three different main domains. Like the rest of GPCRs, they contain a transmembrane domain (7TMD) with seven transmembrane alpha helices with the C-terminus in the cytosol side, where the G proteins bind. At the N-terminus there is a large domain, called "Venus fly trap" (VFT) that contains the entire orthosteric ligand binding site.<sup>85</sup> In some class C GPCRs such as mGlu receptors, the VFT is linked to the 7TMD through a 70-amino-acid-long cysteine-rich domain (CRD) containing nine perfectly conserved cysteines (Figure 27). The CRD has the crucial role to transduce the signal from the VFT to the 7TMD.<sup>171</sup> The N-terminal of the GABA<sub>B</sub> receptors is long and form a VFT with the corresponding ligand-binding site but it is directly linked to the 7TMD without a cysteine-rich domain, as depicted in Figure 27. The GABA<sub>B2</sub> VFT domain is unable to bind ligands.<sup>172</sup> Moreover, the C-terminal regions of the two subunits are associated through a coiled coil interaction (Figure 27), indicating that mGlu and GABA<sub>B</sub> receptors may have different activation

---

\* An orphan receptor is an apparent receptor that has a similar structure to other identified receptors but whose endogenous ligand has not been yet identified.



mechanism.<sup>173</sup> The CaS receptor also has a long cysteine-rich *N*-terminus, but it is uncertain if it is involved in the binding of  $\text{Ca}^{2+}$ , even though it is important for mediating the signal of  $\text{Ca}^{2+}$ .

Each VFT domain consists in two opposing lobes separated by a cavity where the endogenous ligand is recognized. The mechanism by which agonist binding to the VFT results in activation of the 7TMD is complex and not yet fully understood.<sup>174,175</sup> However, it is very well known that the aforementioned two lobes fluctuate between open and close conformations, the agonists usually stabilize the closed one and the antagonists stabilize the open one.<sup>168,176</sup> Since 2000, many crystal and cryo-EM structures of class C GPCR dimeric VFTs have been solved, in close and open conformations, which helped to understand the activation of this class of receptors.<sup>173,176–179</sup> The most recent works concern the structures of mGlu<sub>5</sub>,<sup>180</sup> mGlu<sub>2</sub>,<sup>181,182</sup> mGlu<sub>4</sub>,<sup>181</sup> and mGlu<sub>7</sub>.<sup>182</sup>

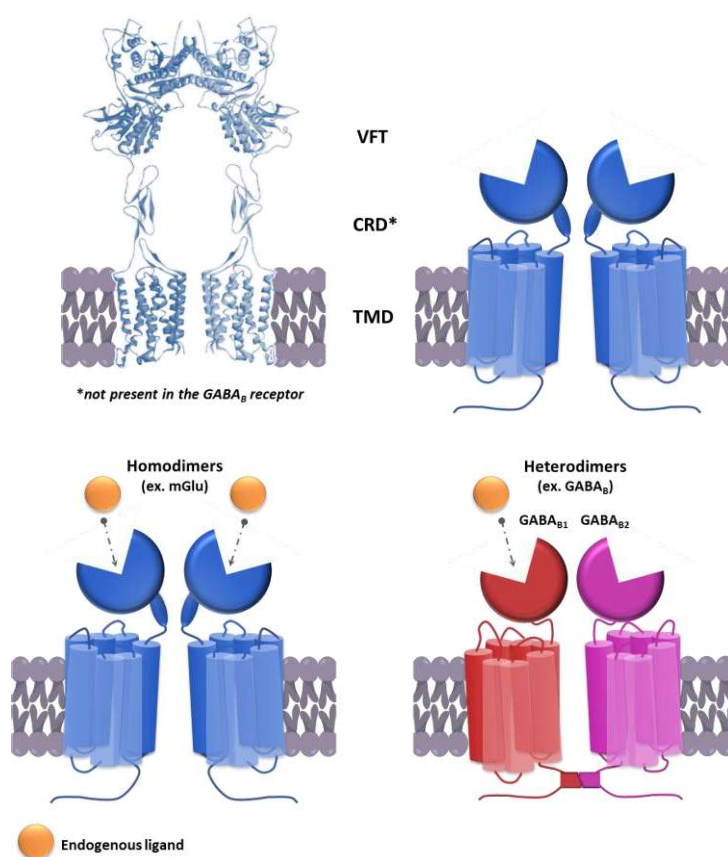


**Figure 27.** Structural model and schematic representation of class C GPCRs. Class C GPCRs are composed of a Venus flytrap (VFT) domain, a cysteine-rich domain (CRD) and a transmembrane (7TMD) domain. This class of receptors forms obligatory dimers, either homodimers (e.g. mGlu) or heterodimers (e.g. GABA<sub>B</sub>). The heterodimeric GABA<sub>B</sub> receptor is depicted with the subunit GABA<sub>B1</sub> in red and GABA<sub>B2</sub> in magenta. (Adapted from Møller et al.).<sup>175</sup>

### Dimeric structure of class C GPCRs: a need for signal transduction

mGlu and CaS receptors are prototypical homodimers that are stabilized by an inter-protomer disulfide bond, polar contacts between VFT domains and interactions between TM domains. The dimerization of these receptors is crucial for promoting the activation mechanism, leading from agonist binding to G protein activation. Indeed, different studies indicate that the conformation of one protomer is related to the changes of the other protomer upon activation, and this has been observed in all the structural domains found in class C GPCRs.<sup>183</sup> The dimer of VFT domains is in equilibrium between resting and active orientations, and agonist binding displaces the equilibrium towards the active states (*Figure 28*). In reality, when considering the conformations for the VFT and the VFT dimer, a total of six different conformations

are theoretically possible: Roo, Rco and Rcc and Aoo, Aco and Acc, where *A* and *R*, Active and Resting respectively, are indicative for the VFT dimer orientation and *c* and *o*, close and open, for the VFT conformation.<sup>168</sup> VFT crystal structures have been solved for several mGlu receptors in their open and closed conformations, without and with glutamate respectively.<sup>177–179,184</sup> These structures strongly support the theory that the lobes of the shell dynamically open and close in the absence of ligand and, when the agonist binds to at least one of the VFT, the closed conformation is stabilized. In fact, more stable contacts with glutamate were found in the closed conformation than in the open one and this represents a driving force that leads to the VFT dimer reorientation from *R* to *A*. More precisely, glutamate interacts with lobe 1 (the upper one) in the open form of the VFT and then stabilizes a closed form through the additional contacts made with lobe 2 (the lower one) (Figure 30).<sup>168</sup> In the end, glutamate binding to the VFT domains of both subunits is required for efficient signalling<sup>185</sup> (full activation), but only one of the two 7TMD subunits activates the G protein at a time (Figure 28A).<sup>186</sup> This means that upon receptor activation, the 7TMD of only one protomer adopts an active conformation, whereas the other one remains in the resting conformation.

The CRD has been shown to play a critical role in this process for mGlu receptors. This domain is highly rigid due to four intramolecular disulfide bonds.<sup>179</sup> In the active state, the two CRDs associate and are likely contacting each other; it is reported that a precise association of the two CRDs is sufficient for full mGlu receptor activation (Figure 28A and Figure 30).<sup>171,187</sup>

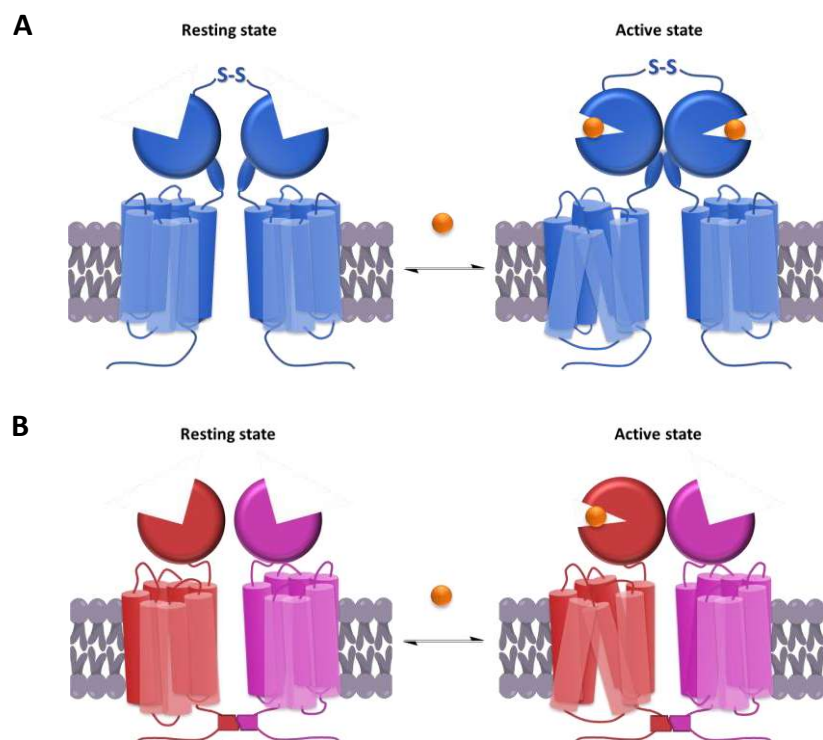


**Figure 28.** Mechanism of activation of (A) homodimers and (B) heterodimers. Both homodimers and heterodimers undergo conformational changes upon activation. The relative orientation of the VFT dimer is changed upon agonist binding; the CRDs (not in GABA<sub>B</sub>) are getting closer and the 7TMD dimer changes conformation. The heterodimeric GABA<sub>B</sub> receptor is depicted with the different subunits in red and magenta.

The GABA<sub>B</sub> and T1Rs receptors are prototypical class C heterodimers (Figure 28B).<sup>188</sup> Two different subunits are required to activate G proteins upon agonist binding.<sup>189</sup> This has been confirmed *in vivo* for the GABA<sub>B</sub> receptor by the disappearance of all physiological responses attributed to the heterodimer when either of

the two subunits is knocked out\*.<sup>190</sup> For the GABA<sub>B</sub> receptor, the GABA<sub>B1</sub> subunit contains the binding site for orthosteric ligands,<sup>172,189</sup> while the GABA<sub>B2</sub> subunit is necessary for G proteins activation being the only one coupled to them.<sup>191</sup>

In contrast to GABA<sub>B</sub> receptors, mGlu receptors were thought for a long time to exclusively form homodimers, owing to largely non-overlapping expression patterns in the brain. However, quantitative fluorescence resonance energy transfer (FRET) experiments revealed the existence of mGlu heterodimers in transfected cells, composed of either group I, or group II and group III subunits<sup>170</sup> (Figure 29). Experimental support for the existence of heterodimeric mGluRs in native tissue is still scarce, but pharmacological and proteomic evidence supports the existence of mGlu<sub>2</sub>–mGlu<sub>4</sub>, mGlu<sub>1</sub>–mGlu<sub>5</sub> and mGlu<sub>7</sub>–mGlu<sub>8</sub> heterodimers *in vivo*.<sup>192–194</sup> A remarkable step forward about mGluRs heterodimerization was instead made in a very recent work. It has been found that mGlu<sub>2</sub> can associate also with mGlu<sub>7</sub> in the hippocampus, which suggests a physiological relevance for this heterodimer.<sup>182</sup> The authors indeed reported four cryo-electron microscopy structures of the human mGlu subtypes mGlu<sub>2</sub> and mGlu<sub>7</sub>, including inactive mGlu<sub>2</sub> and mGlu<sub>7</sub> homodimers; mGlu<sub>2</sub> homodimer bound to an agonist and a positive allosteric modulator; and inactive mGlu<sub>2</sub>–mGlu<sub>7</sub> heterodimer. The existence of higher order oligomers of GPCRs is still a topic open for discussion, especially because most of the observations have been done in heterologous cells and not validated in native tissues.<sup>195</sup> However, increasing experimental evidence suggests that the GABA<sub>B</sub> receptor forms oligomers larger than heterodimers.

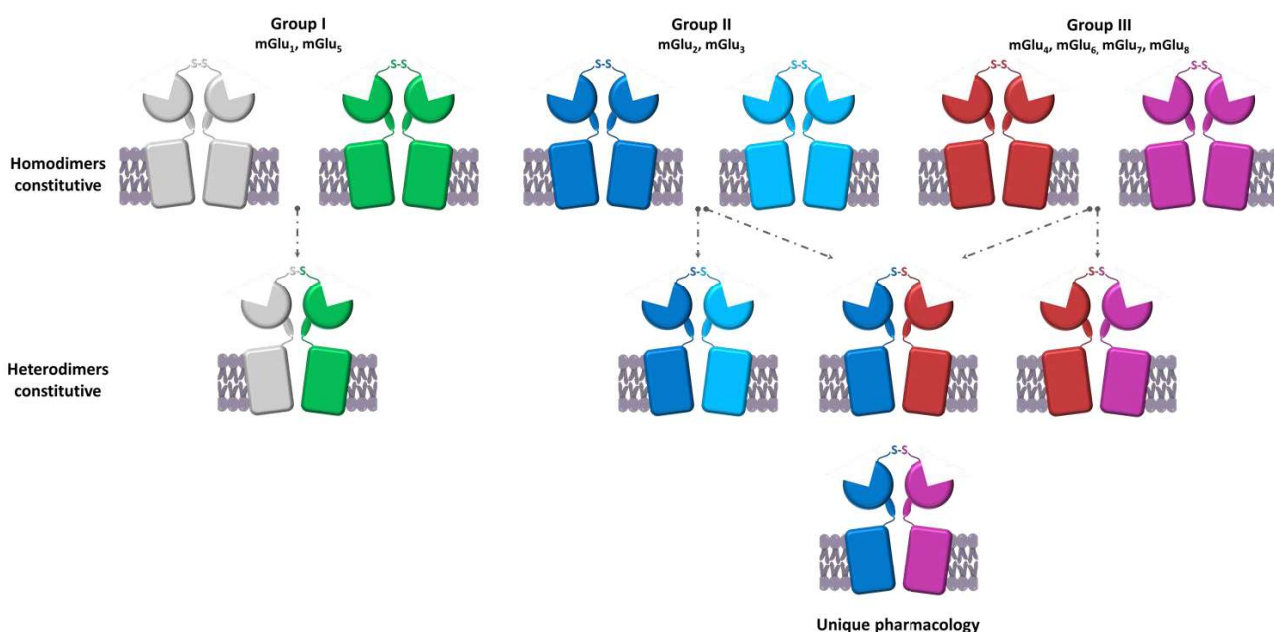


**Figure 29.** Oligomerization of mGluRs. mGluRs can form heterodimers within their classification groups and between group-II and -III in transfected cells. (Adapted from Pin and Bettler).<sup>183</sup>

### The 7TM domain activates G-protein stepwisely: mGlu receptors as archetypical examples

Since the reorientation of the VFT domain dimer is tightly linked to G protein activation, it can be inferred that this conformational change is somehow transmitted to the TM domains. The 7TMD of class C GPCR, common to all GPCRs, can adopt different conformations and they are responsible for G-protein activation. In 2019, Koehl and colleagues were able to propose a structural framework for mGlu<sub>5</sub> activation.<sup>180</sup> They confirmed that agonist binding at the Venus flytraps (VFT) leads to a compaction of the inter-subunit dimer

\* A gene knockout (KO) is a genetic technique in which one of an organism's genes is made inoperative.

interface, thereby bringing the cysteine-rich domains into close proximity (*Figure 30*). Then, the closeness of these bottom lobes is propagated through the CRDs to the 7TM domains. To be more precise, these are movements that all occur sequentially and immediately after the agonist binding at the VFT. From this work, it emerges that the closure of the lobes does not take place only two-dimensionally, but it is characterized by a contemporaneous axial rotation. Following the lobe's closure and their rotational movement, the CRDs are approaching each other and, due to the tight interactions between them and the second extracellular loops (ECL2) of the 7TMD, the rigid-body repositioning of the 7TMD occurs (*Figure 30* and *Figure 31A-C*).<sup>180</sup> In addition to moving closer to each other with a 20 Å translation, there is a 20° rotation of each 7TMD around TM4 upon activation (*Figure 31B-C*). Consequently, the TM1–TM1 distance decreases from 70 Å in the inactive state to 43 Å in the active state (*Figure 31C*). More importantly, the propagation of structural changes leads to a TM6–TM6 interface that appears to be a hallmark of activation (*Figure 31C*, right panel). Although these results did not fully explain how agonist binding at the VFT leads to G protein coupling and activation, they supported a model in which both inter- and intra-subunit rearrangements are required for full activity.<sup>196,197</sup> This work addresses the first of these conformational changes. Further studies were needed to elucidate the mechanism by which the establishment of a TM6–TM6 interface leads to 7TMD rearrangements that enable G protein coupling and signaling.

The activation mechanism explained above, from the agonist binding to the VFT, with consequent reorientation of the latter, to the association of CRDs takes ~30 ms in total and it is summarized in *Figure 30*. This initial conformational change is followed by the activation of the 7TMD of one of the two subunits. The totality of the conformational changes to activate the receptor, including those changes for VFT, CRD and 7TMD, were determined to take approximately 50 ms in total.<sup>187,196</sup>

While the photoreceptor rhodopsin has been shown to activate with a rearrangement of the 7TMD within ~1 ms,<sup>198</sup> all other GPCRs are thought to activate much slower.<sup>199,200</sup> To confirm the kinetic properties of the conformational changes of 7TMD level in class C GPCRs, Hlavackova and collaborators inserted yellow and cyan fluorescent proteins (YFP and CFP) in the second intracellular loop and at the C-terminus of mGlu<sub>1</sub> receptor to act as FRET sensors (intramolecular sensors).<sup>\*</sup> They also constructed a second mGlu<sub>1</sub> chimera with the fluorescent proteins fused to the second intracellular loop of each mGlu<sub>1</sub> protomer (intermolecular sensors<sup>\*</sup>). Thus, agonist-dependent activation of these mGlu<sub>1</sub> chimeras rapidly increased the inter-subunit FRET, suggesting rapid movement of the subunits relative to each other. After inter-subunit movement, the intra-subunit FRET decreased, reflecting conformational changes within a subunit (*Figure 30*).<sup>196</sup>

Very recently, Grushevskiy and colleagues were able to detect rhodopsin-like activation speeds for one step of 7TMD conformational changes. They used a technique that allows activation in the sub-millisecond range (*i.e.* UV light-triggered photoreleasing of caged glutamate in intact cells), and monitoring FRET between the same FRET sensor used by Hlavackova and collaborators.<sup>197</sup> They find that the first major activation step occurs within 1-2 ms and it consists in the rearrangement of the 7TMD of the two mGlu<sub>1</sub> subunits within the receptor dimer. This rapid change is followed by significantly slower conformational changes in each single mGlu<sub>1</sub> subunit (~20-25 ms).<sup>197</sup> This means that there is a loose coupling between the initial step and the real activation of the 7TMD. Moreover, the deactivation of the receptor finishes a cyclic pathway, including at least two metastable intermediate states in addition to the resting and active states. These conformational changes between metastable states consist of the inter- and intra-subunit conformational changes and have time constants of ~40 and ~900 ms, respectively (*Figure 30*).

---

<sup>\*</sup> See *Results and Discussion: Chapter 4* for further information.

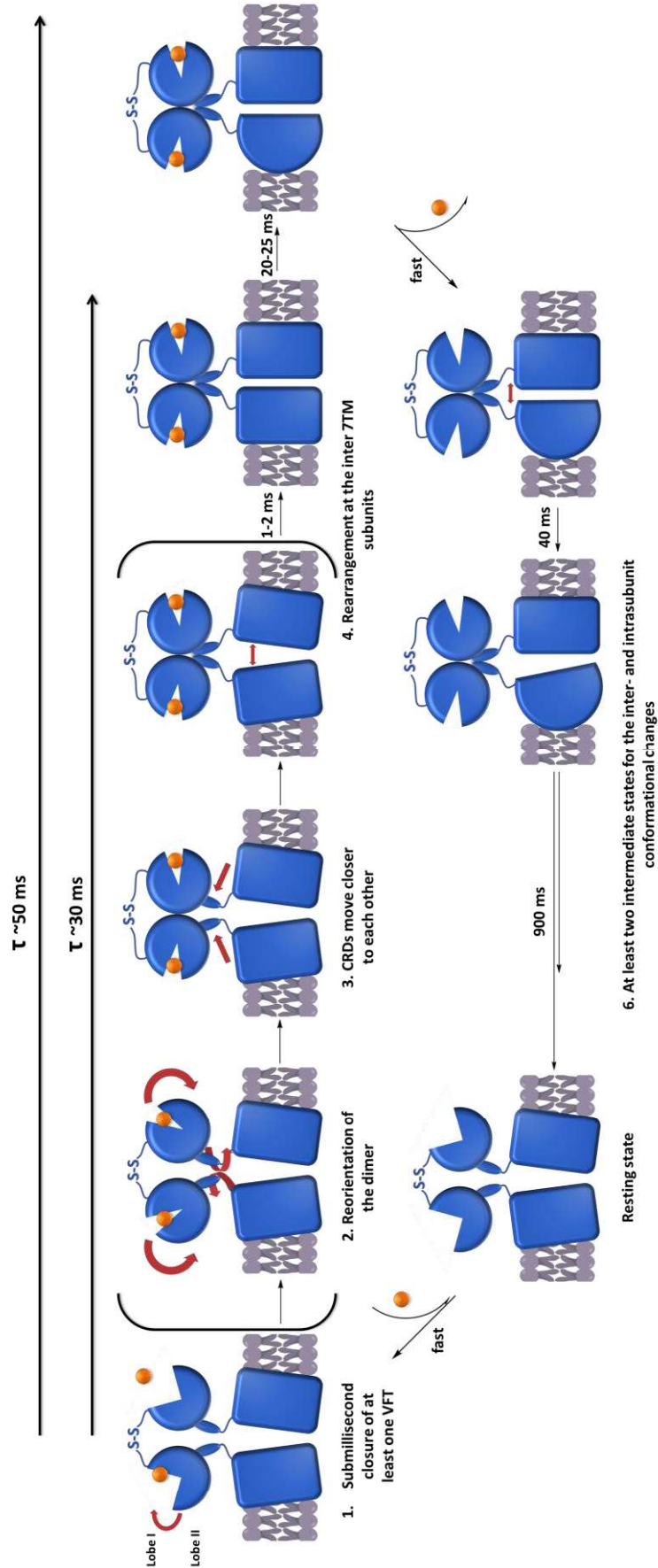


**Figure 30.** Schematic two-dimensional steps of activation and deactivation of mGlu receptors. The glutamate ligands are indicated in orange. (Adapted from Rondard/Pin and Grushevskiy et al.).<sup>187,197</sup> The steps in brackets occur sequentially<sup>180</sup> but they are represented separately here to facilitate the understanding of complete process.

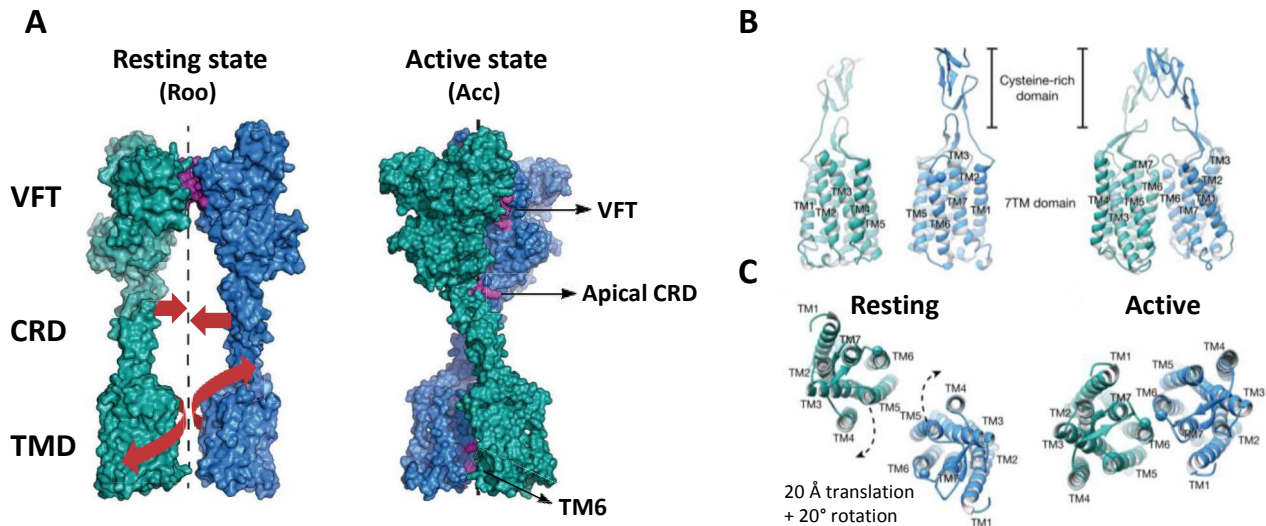


**Figure 31.** mGlu<sub>5</sub> activation. (A) Comparison of intersubunit interfaces in resting and active mGlu<sub>5</sub> are shown for resting (left) and active (right) mGlu<sub>5</sub>. Contact regions are shown in purple. Notably, resting mGlu<sub>5</sub> lacks any interactions beyond the VFT. (B-C) Activation leads to a rearrangement of the 7TM interface. (B) Side views of resting (left) and active (right) mGlu<sub>5</sub> CRD and 7TM domains. (C) Top views of resting (left) and active (right) mGlu<sub>5</sub> 7TM domains. Activation involves a 20 Å translation of the 7TM domains relative to each other, followed by a 20° rotation around TM4. (Figures from Koehl et al.).<sup>180</sup>

The second part of this study gives also confirmation of the full activation of mGlu<sub>1</sub> receptor as the result of the occupancy of both ligand binding sites. As mentioned above, only one of the 7TM domains needs to become active to activate a G protein, but the occupancy of both ligand binding sites is required for full activation.<sup>185,196</sup> To investigate more about binding site occupancy, Grushevskiy and co-workers generated binding-defective protomers by introducing mutations in lobe II of the ligand binding VFT domain, analogous to those described for the mGlu<sub>5</sub> receptor (termed YADA mutants).<sup>185</sup> The sensor mGlu<sub>1</sub> chimeras bore these mutations in only one (YADA:WT) or both protomers (YADA:YADA). Briefly, the YADA:YADA was completely unresponsive to glutamate, indicating that ligand binding was indeed suppressed. In contrast, the sensor mGlu<sub>1</sub> chimera bearing only one mutation (YADA:WT) showed a clear FRET response, but the kinetics were slowed down approximately six fold, with *on*- and *off*-time constants of  $7 \pm 2$  and  $295 \pm 16$  ms, respectively. This indicates that occupancy of both ligand binding sites in the mGlu<sub>1</sub> homodimer is required for full activation speed.

A more detailed description of fluorescence resonance energy transfer (FRET, also known as Förster resonance energy transfer)<sup>201</sup> and the possible mechanisms of action are explained in the Chapter 4 of the Results and Discussion section. In that chapter, mGlu<sub>1</sub> allosteric modulators are used as molecular tools to shed more light on the nature of those 7TMD intermediated states by means of fluorescence conformational dynamic studies.

### Glutamate as excitatory neurotransmitter

To understand the roles of class C GPCRs, and in particular mGlu receptors, it is important to have an appreciation of how fundamental their endogenous ligand is. In neuroscience, glutamate (**22a**, L-glutamate, *Figure 32A*) refers to the anion of L-glutamic acid (**22b**, *Figure 32B*) and its main role is to act as excitatory neurotransmitter: a chemical messenger that transmits a signal across the synapse\* from a neuron to a

\* In the nervous system, a synapse is a structure, a specialized connection, that permits a neuron (or nerve cell) to pass an electrical or chemical signal to another neuron or to the target effector cell; varieties of synapses are electrical and chemical (e.g. glutamatergic synapse).

target cell, which can be a different neuron, muscle cell or gland cell. L-Glutamic acid or (S)-2-aminopentanedioic acid or glutamate, as the conjugate base, is a non-essential amino acid. The side chain of glutamate corresponds to a propionic acid with a  $pK_a = 4.1$ , which results in deprotonation at physiologic pH ( $\sim 7.4$ ) and, therefore, it is considered a polar amino acid (Figure 32A). Although glutamate comprises 4 to 15% of all amino acids in natural proteins, plasma glutamate concentrations are rather low, ranging between 20 and 50  $\mu\text{M}$  in healthy humans. In contrast, the levels of glutamate in whole brain can locally reach 10000  $\mu\text{M}$ , although the concentrations in the extracellular fluid are very low, normally reaching less than 2  $\mu\text{M}$ . Therefore, glutamate must be locally synthesized in the central nervous system (CNS), because it does not cross the blood-brain barrier.<sup>202</sup> During the digestion process, glutamate is released to the lumen of the small intestine when dietary proteins are cleaved (Figure 32B). In addition, some food products contain significant amounts of free glutamate (*i.e.* not bound to a polypeptide). The major source of dietary free glutamate is the monosodium glutamate salt (MSG), which is used as a flavor-enhancing food additive. Glutamate is also responsible of “umami” taste; one of the five basic tastes and it is related to TAS1R1+3 receptor dimer (class C GPCR), which naturally binds glutamate and aspartate as ligands. As stated above, glutamate is synthesized from L-glutamine by presynaptic neurons and it is also the precursor of the synthesis of the inhibitory gamma-aminobutyric acid (GABA) neurotransmitter, which takes place in GABAergic neurons, through glutamate decarboxylase catalysis (Figure 32C).

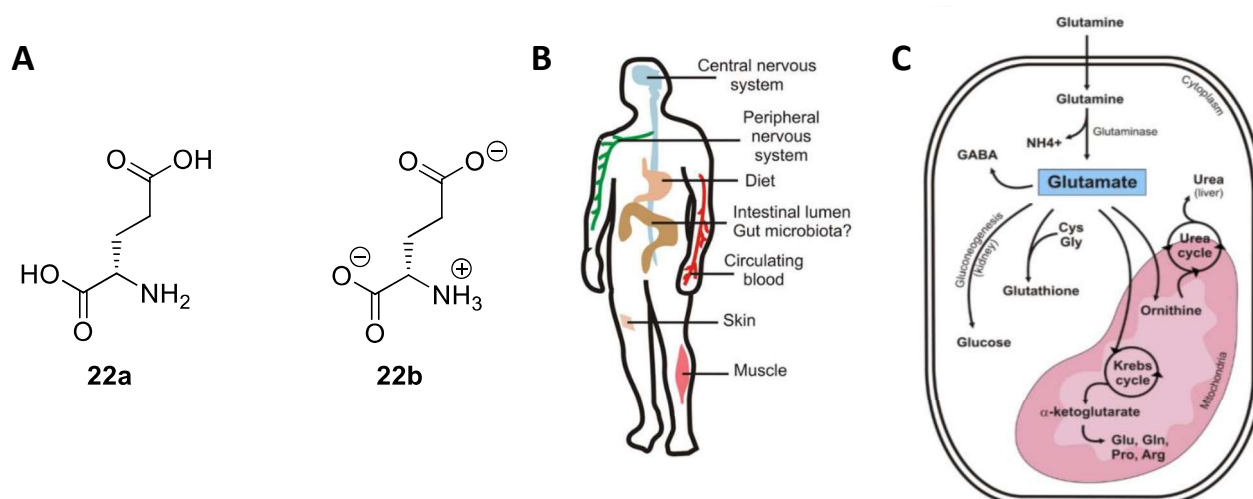


**Figure 32.** (A) Chemical structure of acid glutamic as a free base **22a** and its corresponding zwitterion form **22b** at physiological pH; (B) Physiological sources of glutamate. It is locally synthesized in the CNS. Peripheral nervous tissues contain glutamate too and it is also found in the intestinal contents, plasma, skeletal muscle and skin. (C) Metabolic fates of glutamate. Glutamate is a precursor for the neurotransmitter GABA and the endogenous antioxidant agent glutathione. It is also involved in various biochemical pathways relevant for energy production and nitrogen metabolism. (Adapted from Julio-Pieper et al.).<sup>202</sup>

Glutamate is also a key compound in cellular metabolism and, being primarily the major excitatory neurotransmitter in the vertebrate nervous system, its signaling is crucial for the majority of sensory processing and cognitive function.<sup>203</sup> In the glutamatergic synapse, glutamate is stored in vesicles in the presynaptic\* compartments through vesicular glutamate transporters (VGLUT). Upon calcium influx triggered by action potentials, these vesicles rapidly release the neurotransmitter from the nerve terminal. In addition, glutamate reuptake mechanism is activated, in both presynaptic terminals and in the adjacent astrocytes, for the long-term maintenance of low glutamate concentrations in the synaptic cleft.<sup>204</sup> Glutamate uptake is accomplished by means of glutamate transporter proteins (*i.e.*, glial excitatory GLT1

\* Presynaptic: relating to or denoting a nerve cell that releases a transmitter substance, through its axon terminal, into a synapse during transmission of an impulse.

and EAAC1) which use the electrochemical gradients across the plasma membranes as driving forces for uptake (Figure 33).<sup>205</sup>

Upon synapse process, glutamate reaches the postsynaptic\* terminal of a new cell, in the opposite side of the presynaptic terminal. Then, the machinery of the postsynaptic density (PSD) is activated and the signaling cascade continues (Figure 33). The PSD is an electron-dense region of scaffolding proteins, receptors and signaling molecules, localized at the postsynaptic sites, where the two types of glutamate receptors, ionotropic (AMPA or GluA, KA or GluK, and NMDA or GluN) and metabotropic (mGlu<sub>1</sub> and mGlu<sub>5</sub>) are clustered too (Figure 33).

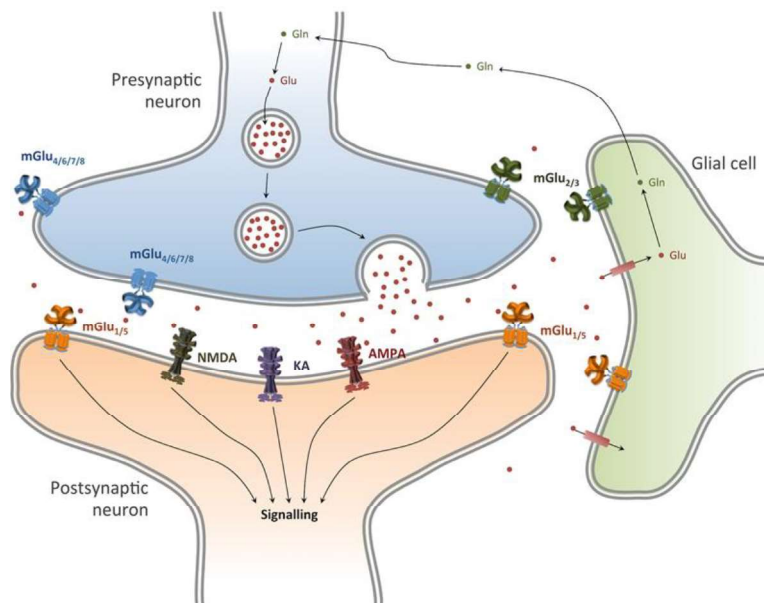


**Figure 33.** The Glutamate synapse. Glutamate (Glu) is accumulated in vesicles in presynaptic terminals through vesicular glutamate receptors (VGLUT). In the synapse these vesicles are fused with the neuron membrane, releasing glutamate. Then, this glutamate activates iGlu receptors (AMPA, NMDA and KA) and mGlu<sub>1</sub> and mGlu<sub>5</sub>, located in the postsynaptic terminal of a new neuron, triggering a signaling cascade. The uptake of glutamate is done by glial cells through glutamate transporters (GLT1 and EAAC1), where it is converted to glutamine (Gln) and released to enter again the presynaptic cell, where it is converted to glutamate and stored in glutamate vesicles. (Reprinted with permission from the reference.<sup>46</sup> Copyright 2016 Universitat de Barcelona).

More precisely, glutamate, the main excitatory neurotransmitter in the brain, produces fast synaptic responses (<10 ms) by activating cationic ligand-gated channels, the so-called ionotropic glutamate receptors. Additionally, glutamate influences neuronal and glial processes over a slower timescale (sub-seconds to minutes) by activating mGlu receptors. The latter, since they are, among the two types of glutamate receptors, the only ones belonging to class C GPCRs, will be the only ones discussed in this work.

### Classification of the mGlu receptors, functional anatomy and main biological roles

mGluRs comprise eight different subtypes, classified in three different groups on the bases of similarities in primary sequence, agonist pharmacology and G-protein effector coupling. Group I subtypes (mGlu<sub>1</sub> and mGlu<sub>5</sub>) are mainly postsynaptic and bind to G<sub>αq</sub> subunit, whereas group II (mGlu<sub>2</sub> and mGlu<sub>3</sub>) and group III (mGlu<sub>4</sub>, mGlu<sub>6</sub>, mGlu<sub>7</sub> and mGlu<sub>8</sub>) are mainly presynaptic and bind to G<sub>ai/o</sub> subunit (Table 8).

\* Postsynaptic: located on the distal side of a synapse.



Group	Subtype	Synaptic local.	Brain region	Glu EC <sub>50</sub>	Orth. ago	EC <sub>50</sub>	G-Protein	Effector	Main signaling
I	mGlu <sub>1</sub>	post/ glia	Cerebellum hippocampus	9-13	Quisqualic acid ( <b>23</b> )	0.1-1.0	G <sub>αq/11</sub> / G <sub>αs</sub>	↑PLC, ↑AC	↑IP <sub>3</sub> , ↑intracellular Ca <sup>2+</sup> , ↑DAG, PKC activation
	mGlu <sub>5</sub>		Cortex hippocampus	3-10		0.03-0.3	G <sub>αq/11</sub>	↑PLC	
II	mGlu <sub>2</sub>	pre/ post	low but widespread	4-20	LY 354740 ( <b>24</b> )	0.005	G <sub>αi/o</sub>	↓AC	↓cAMP, inhibit voltage gated Ca <sup>2+</sup> channels, activate K <sup>+</sup> channels, activate the MAPK and PtdIns-3-K pathways
	mGlu <sub>3</sub>	pre/ post/ glia	widespread	4-5		0.0034			
III	mGlu <sub>4</sub>		Cerebellum striatum	3-20	L-AP <sub>4</sub> ( <b>25</b> )	0.2-1.2	G <sub>αi/o</sub>	↓AC	↓cAMP, inhibit voltage gated Ca <sup>2+</sup> channels, activate K <sup>+</sup> channels, activate the MAPK and PtdIns-3-K pathways
	mGlu <sub>7</sub>	pre	widespread	1000		0.9			
	mGlu <sub>8</sub>		Uneven, widespread	16		160-500			
	mGlu <sub>6</sub>	post	Only retina	2.5-11		0.06-0.60			

\*PLC (phospholipase C), AC (adenyl cyclase), GC (guanylate cyclase), pre (presynaptic), post (postsynaptic), glia (glial cells).

**Table 8.** Classification of mGlu receptors in groups and sites of their expression in the CNS at cellular and brain region level. Glutamate potency for every subtype (EC<sub>50</sub> in μM units),<sup>206</sup> the most common agonists used for each group (Figure 34), with their potency as EC<sub>50</sub> in μM units with the main corresponding G-protein and the main signaling pathways that they activate.<sup>207</sup>

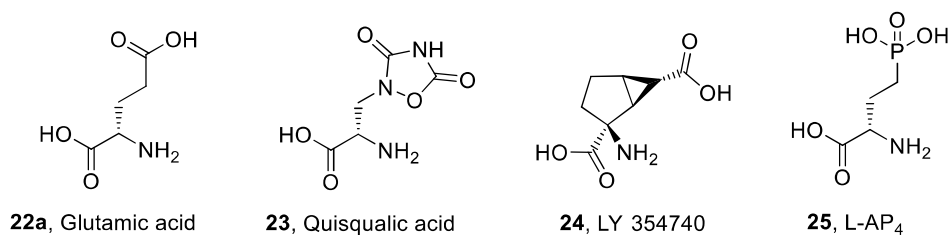


**Figure 34.** Structure of common group-selective orthosteric agonists

### Group I mGluRs

mGlu<sub>1</sub> and mGlu<sub>5</sub> are extensively expressed in the CNS, in neurons and also in glial cells. They are located predominantly in postsynaptic region, where the receptor appears to be concentrated in perisynaptic (near the synapse) and extrasynaptic (exterior to a synapse) areas. Thus, mGlu receptors are recruited by high concentrations of glutamate that escape the clearance mechanisms and spread to the sides of the synaptic cleft. They increase the neuronal excitability and, when found presynaptically, they can also modulate neurotransmitter release.<sup>207,208</sup>

Different studies suggested an involvement of mGlu<sub>1</sub> in learning and memory,<sup>209</sup> but also intellectual disability and autism.<sup>210</sup> Very recently, mGlu<sub>1</sub> was regarded as a major schizophrenia and bipolar disorder target too.<sup>211,212</sup> mGlu<sub>5</sub> turns out to be more related to cognition, drug addiction, anxiety, chronic pain and obesity.

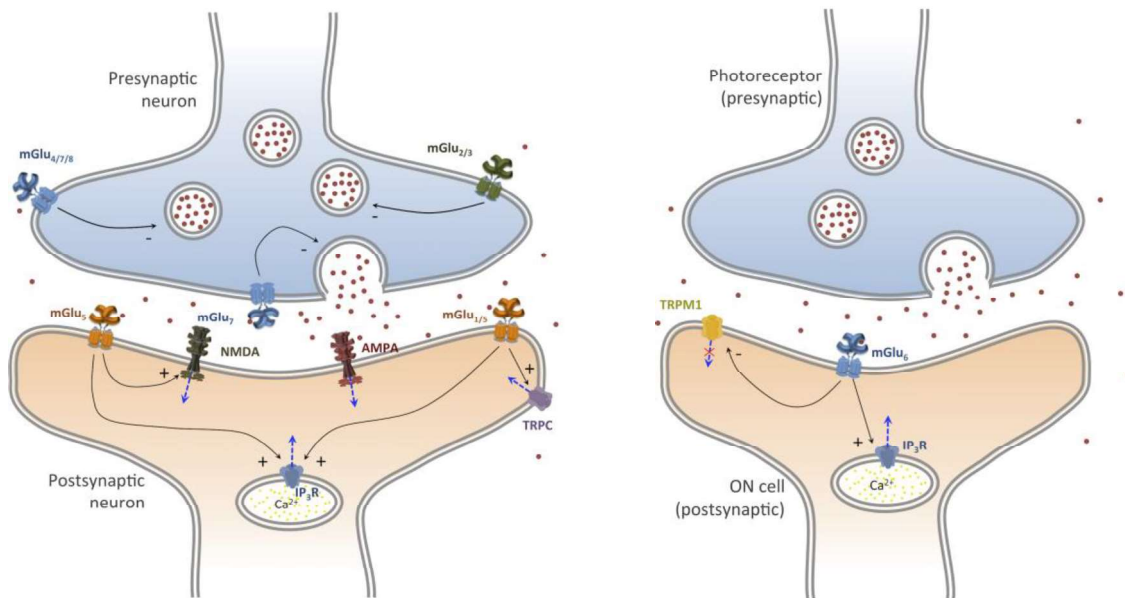


**Figure 35.** The glutamate synapse for glutamatergic neurons (left) and for photoreceptors/ON cells (right) with a representation of the localization of the different mGlu subtypes. (Reprinted with permission from the reference.<sup>46</sup> Copyright 2016 Universitat de Barcelona).

### Group II mGluRs

mGlu<sub>2</sub> and mGlu<sub>3</sub> are widely distributed in the central nervous system (CNS) and also in peripheral nervous system (PNS). Generally, they are located presynaptically in neurons, far from the neurotransmitter release zone, where they are activated by an excess of synaptic glutamate or by glutamate released from astrocytes. mGlu<sub>3</sub> can also be found in glial cells and in postsynaptic regions where they induce hyperpolarization. The major function of these two receptors in presynaptic terminals is to inhibit neurotransmitter release. They have an established role in regulation of synaptic plasticity\*.<sup>207,208</sup>

mGlu<sub>2</sub> and mGlu<sub>3</sub> knockout (KO)<sup>†</sup> mice have been heavily utilized in order to define the individual roles of the Group II mGluRs in a variety of physiologic processes. For example, mGlu<sub>2</sub> KO mice show a loss of the anxiolytic effects of mGlu<sub>2/3</sub> agonists, an enhanced responsiveness to cocaine, alterations in synaptic transmission in several regions of the brain, and loss of mGlu<sub>2/3</sub> agonists antipsychotic activity. mGlu<sub>3</sub> KO mice also show decreased efficacy of mGlu<sub>2/3</sub> agonists in anxiolytic models.<sup>208</sup>

### Group III mGluRs

Group III are widely distributed throughout the CNS in presynaptic regions of neurons, except mGlu<sub>6</sub> which is almost exclusively expressed in retina (Figure 35). Activation of these receptors negatively regulates the neurotransmitter release. Glutamate binds to mGlu<sub>4</sub>, mGlu<sub>6</sub> and mGlu<sub>8</sub> with a relative high affinity, but

\* In neuroscience, synaptic plasticity is the ability of synapses to strengthen or weaken over time, in response to increases or decreases in their activity.

<sup>†</sup> A gene knockout (KO) is a genetic technique in which one of an organism's genes is made inoperative.

displays a very low affinity for mGlu<sub>7</sub> (*Table 8*). Moreover, mGlu<sub>7</sub> receptor is localized at the active zones of the synapse. That is the reason why it has been proposed that it has glutamate-overstimulation-preventing role due to its localization and the high doses of glutamate needed for its activation. mGlu<sub>6</sub> receptor, which is involved in visual perception, is expressed postsynaptically in the dendrites of retinal ON bipolar cells and responds to glutamate released from rod and cone photoreceptor cells in the dark.<sup>207,208</sup>

Experiments with mGlu<sub>4</sub> KO mice showed an association of mGlu<sub>4</sub> with cerebellar synaptic plasticity, learning of complicated motor tasks and spatial memory performance. mGlu<sub>7</sub> has been related with epileptic phenotypes, memory and learning, anxiety and depression. Experiments with mGlu<sub>8</sub> KO mice revealed an association of the receptor with anxiety and weight control. Mice lacking mGlu<sub>6</sub> showed deficits in ON response to light stimulation.

### Modulation of mGlu receptor activity

According to their original structure and functioning, the mGlu receptors display different possible sites for ligand interaction. This offers a wide variety of possibilities for the development of drugs in order to modulate their activity by acting on precise steps during the activation process. These drugs are expected to be beneficial for the treatment of several hormonal, calcemic, neurological and psychiatric disorders, or improving the quality of food intake and obesity. Despite there are currently few drugs on the market that act directly on class C GPCRs (baclofen, cinacalcet<sup>®</sup>, sweet enhancers and umami receptor activators), there is none that act on mGlu receptors. Nevertheless, many mGlu drug candidates are in preclinical and clinical studies.

Most of the drug candidates for mGlu receptors (class C GPCRs) are small molecule ligands and they can be classified in two main groups: ligands binding at the VFT, which are usually orthosteric ligands, also named *competitive* with glutamate (*Figure 36A,B*); and ligands binding at the 7TMD, which are allosteric ligands or *non-competitive* (*Figure 36C*).

#### Ligands acting at the VFT

Based on the structure of glutamate and the structural studies on the VFT, many orthosteric compounds have been designed and screened.<sup>213</sup> They comprise full agonists, partial agonists, antagonists or inverse agonists and they are all competitive with glutamate (*Figure 36A*).<sup>206</sup> In the early years, group-selective orthosteric agonists, such as quisqualate (**23**) for group I, LY 354740 (**24**) for group II and L-AP<sub>4</sub> (**25**) for group III mGlu receptors (*Table 8, Figure 34*) were discovered. Recently, chloride ion was reported to act as a positive allosteric modulator, binding to at least two different sites of the VFT.<sup>214,215</sup> Thereby, this discovery allowed to find new allosteric modulators that bind to the extracellular domain (EDAM) acting on the chloride sites of the VFT or long agonists that binds simultaneously to the orthosteric site and also to the EDAM site (*i.e.* dualsteric/bitopic compounds, see *Box 1, Modification of GPCR function*), such as LSP4-2022 (**26**) for mGlu<sub>4</sub> (*Figure 36B*). However, achieving selectivity for a specific mGlu subtype is an arduous task, since glutamate binding site is highly conserved. That is the reason why the development of orthosteric ligands for mGlu receptors was excluded from the objectives of the present PhD thesis.

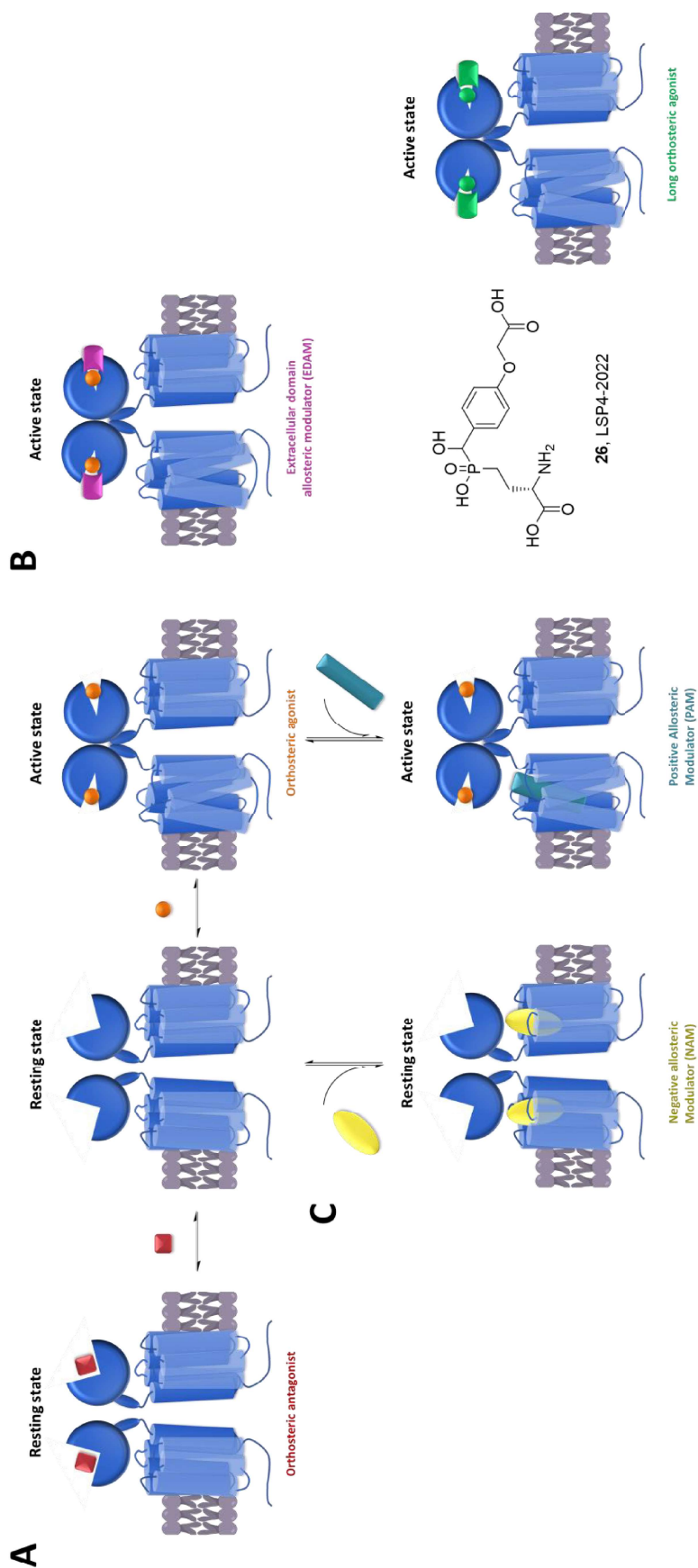


**Figure 36.** Representation of the mode of action of: (A) VFT orthosteric ligands (agonist and antagonist); (B) VFT extracellular domain allosteric modulators (EDAM) and long orthosteric agonists (or dualsteric agonists), such as LSPA-2022 (**26**); (C) 7TM allosteric modulators (NAM and PAM). (Adapted from Gómez-Santacana and Kniazeff).<sup>46,168</sup>

### Ligands acting at the 7TMD

An alternative and highly successful approach was the development of selective allosteric modulators of the specific receptor subtypes. In fact, most of mGlu allosteric modulators bind to a pocket located in the 7TMD, which may confer very different properties to these modulators compared to the orthosteric ligands. They can either enhance (positive allosteric modulators, PAMs, *Figure 36C*) or inhibit (negative allosteric modulators, NAMs, *Figure 36C*) the receptor activation, modulating the affinity of the orthosteric agonist and affecting the intrinsic efficacy of this agonist to trigger the signaling response.<sup>216</sup> They bind in a similar site than class A ligands, in which NAMs stabilize the inactive conformation of both 7TMDs and PAMs the active conformation of one 7TMD. In addition, another type of allosteric modulator exists, which is called silent allosteric modulator (SAM). These allosteric ligands bind to the 7TMD, but they do not preferentially stabilize a single conformation of the receptor (active or inactive), leading to no change of the functionality of the receptor.<sup>73</sup>

As mentioned above, the 7TMD is located inside the cellular membrane and this is possible due to hydrophobic residues that constitute the central part of this domain. Since class C GPCRs has no endogenous allosteric modulator, the allosteric binding site remained more hydrophobic than class A or B GPCRs. Therefore, the polarity of these allosteric modulators has to be low to afford binding in such a high hydrophobic environment. Their polarity is actually much lower than orthosteric ligands, which usually are charged amino acid analogs that bind to the highly hydrophilic VFT. Moreover, allosteric modulators that do not display any agonism are considered better drugs than orthosteric ligands because they are completely inactive under absence of orthosteric ligands. This means that they only potentiate or inhibit the response of the receptor in presence of a released endogenous orthosteric agonist in the synapsis. In contrast, orthosteric agonists and antagonists exert their effect independently of the neurotransmitter release. On the other hand, it is also possible to achieve allosteric partial antagonists, which reduce mGlu response to a new level, but not completely abrogated. Overall, these allosteric modulators offer a more “fine-tuning” approach, which is believed to confer a better and more controllable therapeutic profile.<sup>73,217</sup>

Despite the subtype selectivity of an allosteric modulator or the clear role as a PAM, NAM or SAM, very subtle modifications in their chemical structure can induce changes in their pharmacology, binding mode or subtype selectivity. This phenomenon is called “molecular switch” or “chemical switch” and it is very commonly found between allosteric modulators in mGlu receptors.<sup>218</sup> An example worth mentioning can be VU6004907 (**31**), found as potent positive allosteric modulator of mGlu<sub>1</sub> (*Figure 37*),<sup>219–224</sup> which was obtained from a previous series of “molecular switches” through which it was possible to dial-out mGlu<sub>4</sub> activity from the highly selective mGlu<sub>4</sub> PAM VU0400195 (**27**) (*Figure 37*). In particular, VU0400195 (**27**) was subject to a “molecular switch” by virtue of modification of the succinimide moiety, changing the subtype specificity from mGlu<sub>4</sub> to mGlu<sub>1</sub> and, thus, yielding a selective mGlu<sub>1</sub> NAM **28**. Based on these observations, a new optimization round was performed to identify the phthalimide analogs **29a** and **29b**. VU0405623 (**29a**) is a dual mGlu<sub>1</sub>/mGlu<sub>4</sub> PAM with comparable potency, whereas VU0483605 (**29b**) is a mGlu<sub>1</sub> PAM with remarkably improved selectivity over mGlu<sub>4</sub>. Both compounds were obtained via a NAM to PAM molecular switch from VU0465334 (**28**) but via a “double” molecular switch from compound **27**.<sup>219</sup> Subsequently, with only further optimization processes, the authors were able to obtain second and third generation of compounds with increasing selectivity over mGlu<sub>4</sub> (compounds **30** and **31**, *Figure 37*).<sup>221–224</sup>

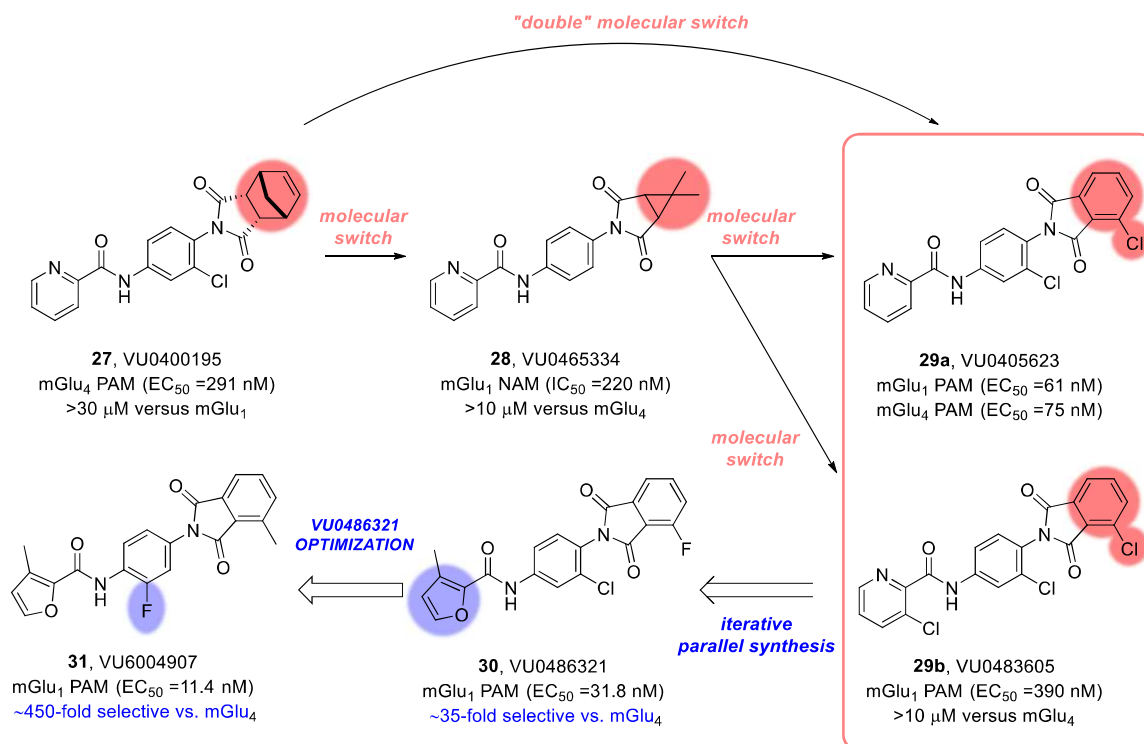


**Figure 37.** Modifications in the starting mGlu<sub>4</sub> PAM compound **27**, performed in Vanderbilt University, provide the potent and CNS penetrant positive allosteric modulator of group I mGlu receptors, VU6004907 (**31**).<sup>222,224</sup> The "molecular switches", modulating mGlu subtype selectivity and mode of pharmacology, are depicted in red. The optimization processes are depicted in blue.<sup>219–224</sup>

## mGlu receptors as drug targets

As stated above, mGlu receptors are widely distributed throughout the central and peripheral nervous system and each of the subtypes has singular roles that can be modulated with drug-like agonists, antagonists or allosteric modulators. For that reason, mGlu receptors represent excellent drug targets for a variety of psychiatric and neurodegenerative CNS disorders (*Table 9*) and knowledge regarding mGluRs has improved exponentially over the last several years. Treatments targeting iGlu receptors in the CNS have failed due to multiple side effects, including cognitive and motor impairment.<sup>225</sup> In general, targeting glutamatergic neurotransmission via the modulation of mGlu receptors holds great promise for the management of several CNS diseases, with the potential for fewer side effects. mGlu<sub>5</sub> and mGlu<sub>2</sub> are the main targets for drug development, but mGlu<sub>4</sub>, mGlu<sub>1</sub> and mGlu<sub>3</sub> are also promising targets. Group III receptors mGlu<sub>6</sub>, mGlu<sub>7</sub> and mGlu<sub>8</sub> are clearly undeveloped, although mGlu<sub>7</sub> and mGlu<sub>8</sub> could be proper targets for the treatment of stress-related diseases.<sup>217,226</sup>

Subtype	Mode of Action	CNS disease applications
mGlu <sub>1</sub>	PAM	Schizophrenia, bipolar disorders <sup>211,212,219,227</sup>
	NAM	Neuropathic pain, Fragile Syndrome X, anxiety/stress disorders, addiction
mGlu <sub>5</sub>	PAM	Anxiety disorders, Huntington's disease, schizophrenia, tuberous sclerosis complex
	NAM	Addiction, anxiety, chronic pain, depression, Fragile Syndrome X (autism spectrum disorders), migraine, Parkinson's disease-L-DOPA-induced dyskinesia
mGlu <sub>2</sub>	PAM	Addiction, anxiety disorders, depression, schizophrenia
	NAM	Depression
mGlu <sub>3</sub>	NAM	Depression
mGlu <sub>4</sub>	PAM	Neuropathic pain, neuroinflammation, neuroprotection, Parkinson's disease, schizophrenia
mGlu <sub>7</sub>	Agonist	Anxiety, depression, Parkinson's disease
	NAM	Anxiety, depression
mGlu <sub>8</sub>	Agonist	Parkinson's disease, anxiety

**Table 9.** Potential application of mGlu allosteric modulators in CNS diseases. (Adapted from Nickols).<sup>217</sup>

## Freely diffusible photoswitchable allosteric modulators for mGluRs

This PhD thesis was conceived with the main objective of designing and synthesizing freely diffusible azobenzene-based photoswitchable compounds with biological activity as allosteric modulators of metabotropic glutamate receptors. Therefore, an up-to-date list of reported photoswitchable AMs for mGluRs, in the field of freely diffusible photopharmacology, is presented below.

### mGlu<sub>5</sub> (Group I)

In the group I mGlu, Alloswitch-1 (**32a**) and analogs (**32**) are based on the phenylazopyridine scaffold and are potent and selective NAMs of mGlu<sub>5</sub> (Figure 38). They were the first allosteric modulators to be used in photopharmacology and the pharmacological properties of each photoisomer have been deeply characterized *in vitro* and *in vivo*.<sup>132,133</sup> All they behave as *trans* active compounds and exhibit significant differences on their pharmacological properties before and after violet light illumination.

Specifically, IC<sub>50</sub> for Alloswitch-1 (**32a**) shifts from a value of 297 nM in dark conditions to 1.5 μM under violet light. Afterwards, Pittolo and colleagues corroborated that 100 nM *trans*-Alloswitch-1 antagonized the orthosteric activation of the receptor and reduced its constitutive activity in the absence of the

agonist.<sup>133</sup> The activity profile of Alloswitch-1 across the eight members of the mGlu sub-family revealed a high mGlu<sub>5</sub> selectivity under either light conditions. Moreover, the ability of Alloswitch-1 to reversibly photoregulate mGlu<sub>5</sub> was also evaluated by monitoring the intracellular calcium concentration in individual HEK293 cells overexpressing the receptor. Agonist application induced cytosolic calcium oscillations, which were blocked by Alloswitch-1, in agreement with its NAM properties. Violet illumination restored receptor activity, and illumination with green light blocked calcium oscillations, indicating the recovery of Alloswitch-1-antagonistic action.<sup>133</sup> Also the phenylazopyridines (**32**) display IC<sub>50</sub>s in the range from nanomolar to micromolar in dark conditions and, as for Alloswitch-1 in the dark, they antagonized the calcium oscillations evoked by the activation of mGlu<sub>5</sub> with quisqualate.<sup>132</sup> Additionally, Gómez-Santacana and co-workers observed that, under 380 nm light, the frequency of calcium oscillations was increased compared to that observed with the orthosteric agonist alone, suggesting an over-activation or an increased signaling of mGlu<sub>5</sub> receptors in presence of the compounds. Remarkably, *in vivo* studies using tadpoles and zebrafish larvae showed important light regulated effects on the locomotion of the animals. In the absence of illumination, *trans*- Alloswitch-1 (**32a**) was found to exert an inhibitory action on the zebrafish motility compared to the untreated controls. Thereafter, Gómez-Santacana and collaborators noticed that not only Alloswitch-1 (**32a**), but also the others phenylazopyridines (**32**), showed analgesic effects in rodents, which can be regulated by peripheral violet illumination or directly in the CNS. This validates the potential usefulness of allosteric mGlu<sub>5</sub> photopharmacology *in vivo*.<sup>132,133</sup>

The authors associated the observed photo-induced loss of NAM activity to the photoisomerization of the *trans* isomers to the *cis* configuration, which displayed a reduced ligand binding to mGlu<sub>5</sub>. However, the authors wondered if this photoisomerization occurred outside of the binding pocket or inside. In the first hypothesis, the photoisomerisation would occur in the extracellular medium after the *trans* isomer unbinds and, after that, the *cis* isomer is not binding the receptor, inducing the loss of NAM activity observed. The second hypothesis was associated to photoisomerization inside the binding pocket that would involve a subtler effect such as a change in binding mode or a ligand-induced effect on receptor conformation. Computational docking and molecular dynamics simulations have shown that the *cis* isomer of Alloswitch-1 (**32a**) would have a different binding mode, reducing its binding affinity and stability. However, molecular simulations suggested that binding of the *cis* isomer might be possible, as well as a theoretical “instantaneous” photoswitching of the ligand while it is bound at the allosteric pocket of the mGlu<sub>5</sub> receptor.<sup>150,228</sup> Very recently, the work of Ricart-Ortega and colleagues answered this key question. They studied the mechanisms of action/modulation at mGlu<sub>5</sub> of two freely diffusible photoswitchable mGlu<sub>5</sub> NAMs, Alloswitch-1 (**32a**) and MCS0331 (**32b**, *Figure 38*) by means canonical G<sub>q/11</sub>-linked functional assays, Mass Spectrometry (MS) and radioligand binding assays.<sup>159</sup> Thereby, they were able to conclude that the observed differences in binding parameters of **32a** and **32b** between dark and 380 nm illumination conditions could be explained by a reduction in the available active *trans* isomers concentration under violet illumination and a lack of *cis* isomers receptor binding. They also associated these affinity changes to the loss of functional NAM activity. On the other hand, they observed that the dissociation rate constants of the ligands were significantly faster under irradiated conditions, suggesting that photoisomerization takes place also inside the ligand binding pocket. This means that *cis* isomer of ligands are capable of temporarily binding to the receptor, albeit with reduced affinity and a shorter residence time.<sup>159</sup> This represents an important confirmation of the hypothesis proposed by Dalton and co-workers stated above.<sup>228</sup>

Alloswitch-1 (**32a**) was used also to monitor and manipulate the activity of mGlu<sub>5</sub> receptors with 2-photon excitation illumination.<sup>229</sup> One major limitation of all current photopharmacological approaches is their



application in 3D tissues since the photo-responsive molecules can be selectively turned *on* and *off* using short and very energetic wavelength illumination by single-photon excitation (1PE). The mGlu<sub>5</sub>-expressing tissues are usually not permeable to the light wavelengths used for photoisomerization and the irradiation beams to stimulated mGlu<sub>5</sub> receptor usually cover a large volume in the microscopic scale. The photo-stimulated volume can be reduced using pulsed illumination with femtosecond near-infrared (NIR) lasers, which enable 2-photon excitation (2PE) of photosensitive molecules such as Alloswitch-1 (**32a**). Using 2P irradiation, this excitation can be constrained to physiologically relevant dimensions, such as dendritic spines or cell soma in circuits. Thus, Pittolo and collaborators demonstrated that Alloswitch-1 (**32a**) can be efficiently photoisomerized using 2PE determining the axial resolution of this method, and they established its feasibility in cultured cells and acute brain slices. In this way, the rapid and reversible silencing of neurotransmitter receptors, in rodent brain slices, by 2PE of an allosteric photoswitchable mGlu<sub>5</sub> NAM offered opportunities to study neuromodulation in intact neuronal circuits and 3D tissues with unprecedented pharmacological selectivity, tissue depth, and spatial resolution.<sup>229</sup>

Gómez-Santacana and collaborators also reported a new series of NAMs of mGlu<sub>5</sub> receptor, including four photoswitchable compounds based on phenylazopyridine as photoswitchable moieties. The first two compounds contained a 2-ethynylpyridine and a phenylazopyridine (**33a-b**) and the second ones were phenylbisazopyridines (**34a-b**, Figure 38)<sup>150</sup>. The authors demonstrated that the mGlu<sub>5</sub> NAM efficacy was depending on the substitution pattern of the central ring and this was supported by computational modelization. The authors also observed NAM potency or efficacy could be reduced upon photoisomerization of the compounds, but with low PPS or PDE, which make them weak candidates for further photopharmacological characterization.

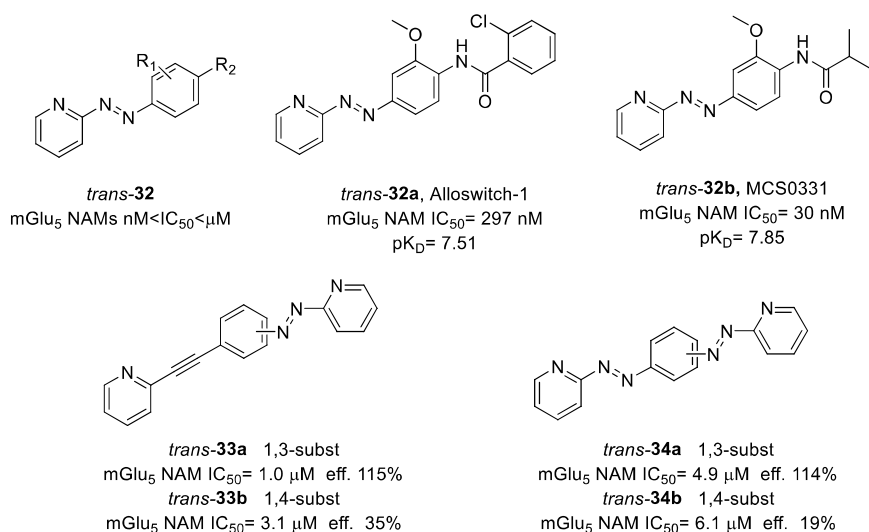


**Figure 38.** Structures of the current reported photoswitchable allosteric ligands for mGlu<sub>5</sub> receptor in their *trans* configurations with the corresponding potencies and affinities (EC<sub>50</sub>/IC<sub>50</sub> and pK<sub>D</sub>).<sup>132,133,150,159,228</sup>

## mGlu<sub>2</sub> (Group II)

Very recently, aBINA (**36**) has been reported as a photoswitchable allosteric agonist for mGlu<sub>2</sub> (group II) with activity in primary neuronal cultures (Figure 39).<sup>230</sup> Being an allosteric agonist, aBINA (**36**) represents the first example of a new class of precision drugs for GPCRs. Specifically, Donthamsetti and collaborators chose biphenyl-indanone A (**35**, BINA, Figure 39) as a parent compound for the development of a photoswitchable allosteric agonist applying the azologization strategy. BINA (**35**) is a highly mGlu<sub>2</sub>-selective

allosteric agonist that binds to the allosteric site and activate the receptor independently of the endogenous ligand. On the contrary, pure allosteric modulators generally have no effect on their own, but positively modulate the activity of an orthosteric agonist. aBINA (**36**) efficiently photoisomerized to its *cis* configuration with wavelengths ranging from 340 and 380 nm (UV) light and to its *trans* configuration with wavelengths ranging from 400 to 600 nm (visible) light.

To evaluate the effect of aBINA (**36**) on mGlu<sub>2</sub>, in comparison with the parent compound BINA (**35**), the authors used a mGlu<sub>2</sub>-mediated G protein-inwardly rectifying potassium channel (GIRK) activation assay. mGlu<sub>2</sub> and a homotetramerizing mutant of GIRK1 (F137S) were transiently transfected into HEK293 cells, whereby receptor activation results in G<sub>i/o</sub>-dependent GIRK activation and enhanced inward-current. The potency of the *trans* configuration of aBINA (**36**) was ~11-fold lower than that of the parent compound BINA (**35**), indicating that the replacement of benzyloxymethylbenzene with the *trans* isomer of azobenzene or the modifications introduced on the indanone ring would diminish agonist potency. Under 340 nm light, *cis*-aBINA (**36**) results 8.5-fold less active than its *trans* isomer. Thus, aBINA (**36**) is a photoswitchable allosteric agonist of mGlu<sub>2</sub> that activates the receptor in the *trans* configuration but not in the *cis* configuration. Moreover, since BINA (**35**) is also a PAM that potentiates the potency of glutamate at mGlu<sub>2</sub> by ~5–10 fold,<sup>231</sup> Donthamsetti and colleagues evaluated whether aBINA (**36**) performs also PAM activity, resulting in a positive effect as PAM on mGlu<sub>2</sub> but less dominant than the allosteric agonism.<sup>230</sup>

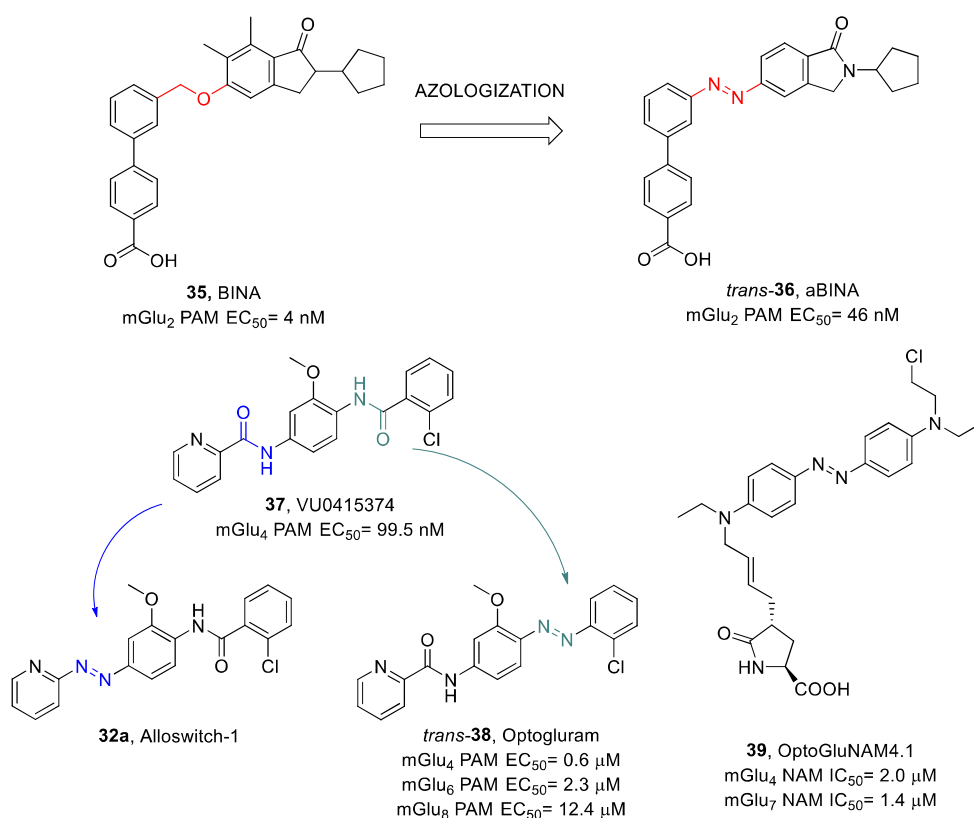


**Figure 39.** Structures of the current reported photoswitchable allosteric ligands for mGlu<sub>2</sub> and mGlu<sub>4</sub> receptors in their *trans* configurations with the corresponding potencies and affinities (EC<sub>50</sub>/IC<sub>50</sub> and pK<sub>D</sub>).<sup>46,98,119,230</sup>

### mGlu<sub>4/6/7/8</sub> (Group III)

Regarding group III mGlu receptors, a photoswitchable PAM and a NAM have been reported to date. Optogluram (**38**) is potent PAM of mGlu<sub>4</sub> and mGlu<sub>6</sub> with some residual PAM activity in mGlu<sub>8</sub> and was used

to control the pain behavior in rodents with illumination in the brain (Figure 39) and OptogluNAM4.1 (**39**) is the only reported NAM of mGlu<sub>4</sub>, which is also a photoswitchable NAM mGlu<sub>7</sub> (Figure 39).

Optogluram was originally designed from an azologization strategy based on VU0415374 (**37**, Figure 39), which is a positive allosteric modulator of mGlu<sub>4</sub> receptor resulting from a series of *N*-(4-acetamido)phenylpicolinamides.<sup>232</sup> VU0415374 (**37**) was not only selected as starting point due to the high potency as mGlu<sub>4</sub> PAM, but also for the two amide bonds flanked by aryl groups, which has a high structural homology to the Ar-N=N-Ar scaffold present in azobenzene. By replacing one of the amide bonds in **37** for a N=N double bond, the authors obtained the azobenzene derivatives **32a** and **38**. The compound **32a** is Alloswitch-1<sup>133</sup> that was found inactive in mGlu<sub>4</sub> while the **38** is Optogluram (Figure 39).<sup>98</sup> Optogluram (**38**) is the first photoswitchable positive allosteric modulator for the mGlu<sub>4</sub> receptor reported to date displaying nanomolar potency.<sup>98,133</sup> Its azobenzene molecular scaffold (Figure 39) allows a selective, reversible and repeated optical manipulation of mGlu<sub>4</sub> activity with light. Isomerization from *trans* to *cis*-configuration is rapidly achieved upon illumination with violet light (380 nm) and the *trans*-isomer could be quickly recovered from the *cis*-isomer upon green light illumination (500 nm) or by thermal relaxation in the dark.

With a cell-based IP accumulation in the dark, *trans*-Optogluram showed nanomolar mGlu<sub>4</sub> PAM potency (EC<sub>50</sub> = 0.6 μM), while upon 380 nm of illumination (high concentration of *cis* isomer) its potency is shifted to 1.9 μM.<sup>98</sup> Optogluram was found to be group III mGlu selective in both light conditions, but it was a PAM of mGlu<sub>6</sub> and mGlu<sub>8</sub> receptors with low micromolar potency in the dark (EC<sub>50</sub> = 2.3 μM and EC<sub>50</sub> = 12.4 μM respectively).<sup>46</sup> Concerning mGlu<sub>8</sub>, the logarithmic potency values were shifted around 1.5-log, which it is close to the 2-log threshold, considered for ideal selectivity. Regarding mGlu<sub>6</sub> potency, the values shifted in a lower extent.<sup>46</sup> However, expression of mGlu<sub>6</sub> is restricted to polar cells in retina,<sup>233</sup> whilst mGlu<sub>4</sub> is widely distributed through the CNS. Due to the different location of these receptor subtypes, Optogluram (**38**) was still considered as good candidate for *in vivo* testing. Subsequent *in vivo* studies using a murine model of persistent inflammatory pain showed that the combination of Optogluram (**38**) and different wavelengths of illumination allowed the optical “on/off” control of pain transmission associated with mGlu<sub>4</sub> receptors localized in the amygdala. Indeed, Optogluram (**38**) produced acute and reversible analgesic peripheral responses, as well as anxiolytic and anti-depressive effects in mice with persistent inflammatory pain in the dark, whereas those effects were significantly reduced upon illumination of the amygdala with 380 nm and subsequently restored with 500 nm light.<sup>98</sup>

As mentioned before, OptogluNAM4.1 (**39**, Figure 39) is the first reported photoswitchable NAM of mGlu<sub>4</sub>. It contains a blue-light-activated, fast-relaxing azobenzene group that allows reversible receptor activity photocontrol *in vitro* and *in vivo*.<sup>119</sup> The use of blue light to photoisomerize the compound represents a great advantage over the commonly used in photopharmacology UV light, which displays very reduced tissue penetration and potential cell damage. Therefore, the use of blue light represents a better paradigm for *in vivo* applications.

Rovira and collaborators demonstrated that the *trans* isomer blocked the mGlu<sub>4</sub> activation both with IP accumulation assays and single-cell calcium imaging experiments. In contrast, 430 nm light illumination induced the photoisomerization to obtain the *cis*-OptoGluNAM4.1, which was inactive and allowed the activation of mGlu<sub>4</sub> receptor. Additionally, OptoGluNAM4.1 (**39**) showed no PAM activity over any mGlu subtype at high concentrations, and, besides the mGlu<sub>4</sub> NAM activity, only a partial NAM effect on mGlu<sub>7</sub> was observed.

Remarkably, Rovira and collaborators suggested that OptoGluNAM4.1 (**39**) could be a covalent ligand considering that it contains a nitrogen mustard (2-chloroethyl aniline). This group is hypothesized to react with nucleophile residues of receptors (*e.g.* lysines and cysteines) after binding through a highly reactive aziridinium intermediate.<sup>234</sup> To confirm the ligand's conjugation, single-cell experiments were conducted in which a meticulous washing protocol was applied. Again, Rovira and collaborators observed that the antagonistic effect persisted and that this could be switched off after illumination and restored in the dark, indicating photoreversible receptor activation after removal of the ligand in solution. This effects after washout were not reproduced using a non-covalent closely related compound containing a hydroxyl group instead of the chlorine atom at the nitrogen substituent. The authors noticed through mouse behavioral studies that the compound was able to block the analgesic effect induced by an orthosteric agonist. Additionally, *in vivo* studies using zebrafish larvae also showed important light regulated effects on the locomotion of the animals. In the absence of illumination, *trans*-OptoGluNAM4.1 increased the free-swimming distance over untreated control animals, consistent with the effect of the *trans* isomer on mGlu<sub>4</sub>. The distance is reduced to a similar level to that of untreated controls upon illumination with blue light in accordance with the lack of effect of *cis*-OptoGluNAM4.1 on the receptor. The opposite effects found for OptoGluNAM4.1 (**39**) and Alloswitch-1 (**32a**) on animal behavior are consistent with the opposite synaptic roles of these receptors. Indeed, the activation of mGlu<sub>4</sub> (and also mGlu<sub>7</sub>) is known to inhibit synaptic glutamate release, whereas mGlu<sub>5</sub> has a positive modulatory effect on neuronal activity.<sup>98,207</sup>

In a later report, Bossi and co-workers studied OptoGluNAM4.1 (**39**) as a negative modulator of neurotransmission in rodent cerebellar slices at the parallel fiber-Purkinje cell synapse.<sup>235</sup> Using OptoGluNAM4.1 (**39**) as tool compound, they were able to demonstrate for the first time that, in brain slices from the rodent cerebellar cortex, mGlu<sub>4</sub> receptors are endogenously activated in excitotoxic conditions. These conditions could be the early phases of simulated cerebellar ischemia, which is associated with elevated levels of extracellular glutamate. These findings support OptoGluNAM4.1 (**39**) as a further photoswitchable tool for studying native mGlu<sub>4</sub> receptor activity under different physio-pathological conditions in brain tissue, without the need of genetic manipulation.



## Objectives

---



In the field of photopharmacology, many photoswitchable allosteric modulators have been developed. In the group I mGluRs, Alloswitch-1 and analogs are NAMs of mGlu<sub>5</sub> in their *trans* configuration and were the first allosteric modulators to be used in photopharmacology. Very recently, aBINA has been reported as an allosteric agonist for mGlu<sub>2</sub> (group II) with activity in primary neuronal cultures. Regarding group III mGluRs, a photoswitchable PAM and a NAM have been reported to date, Optogluram and OptogluNAM4.1, respectively. In particular, Optogluram is a potent PAM of mGlu<sub>4</sub> and mGlu<sub>6</sub> with some residual PAM activity in mGlu<sub>8</sub>. However, the other group I mGluR, the mGlu<sub>1</sub> receptor, has never been targeted in any photopharmacological approach.

According to what stated above the **main objective** of this thesis is:

**Design and synthesize azobenzene-containing photoisomerizable compounds with biological activity as allosteric modulators of metabotropic glutamate receptors. The aim of using these compounds is to control the *on/off* switching of the activity of mGlu receptors with visible light and obtain molecular tools for *in vivo* physiological applications with potential for pharmaceutical development.**

Taking into account the main objective, during the development of the present thesis and after gaining a further insight in the field, the following **specific objectives** were considered:

- I. To afford the first photoswitchable mGlu<sub>5</sub> NAM that only display pharmacological activity in its *cis* configuration, whilst the *trans* isomer remains inactive. The molecular design and *in vitro* characterization of three series of compounds are presented in **Chapter 1**.
- II. To enhance the PAM activity on mGlu<sub>4</sub> receptor and increase the selectivity over the other group III mGluRs of an azobenzene candidate with Optogluram-like structure. The optimization of a series of compounds driven by SAR is described in **Chapter 2**.
- III. To develop the first photoswitchable PAM to selectively enable the optical control of endogenous mGlu<sub>1</sub> receptor. The design, synthesis and characterization of two libraries of azo compounds are shown in **Chapter 3**.
- IV. To reversibly inactivate the mGlu<sub>1</sub> receptor function with the first photoswitchable NAM of this group I mGluR. The development and characterization of a family of novel azoheteroarene photoswitchable compounds are discussed in **Chapter 4**.
- V. To expand the knowledge about the nature of the agonist-induced intermediated states of mGlu receptors by using allosteric modulators as tools in fluorescence conformational dynamic studies. The analysis of mGlu<sub>1</sub> NAMs effect on receptor conformational changes is reported in **Chapter 4**.





## Results and discussion

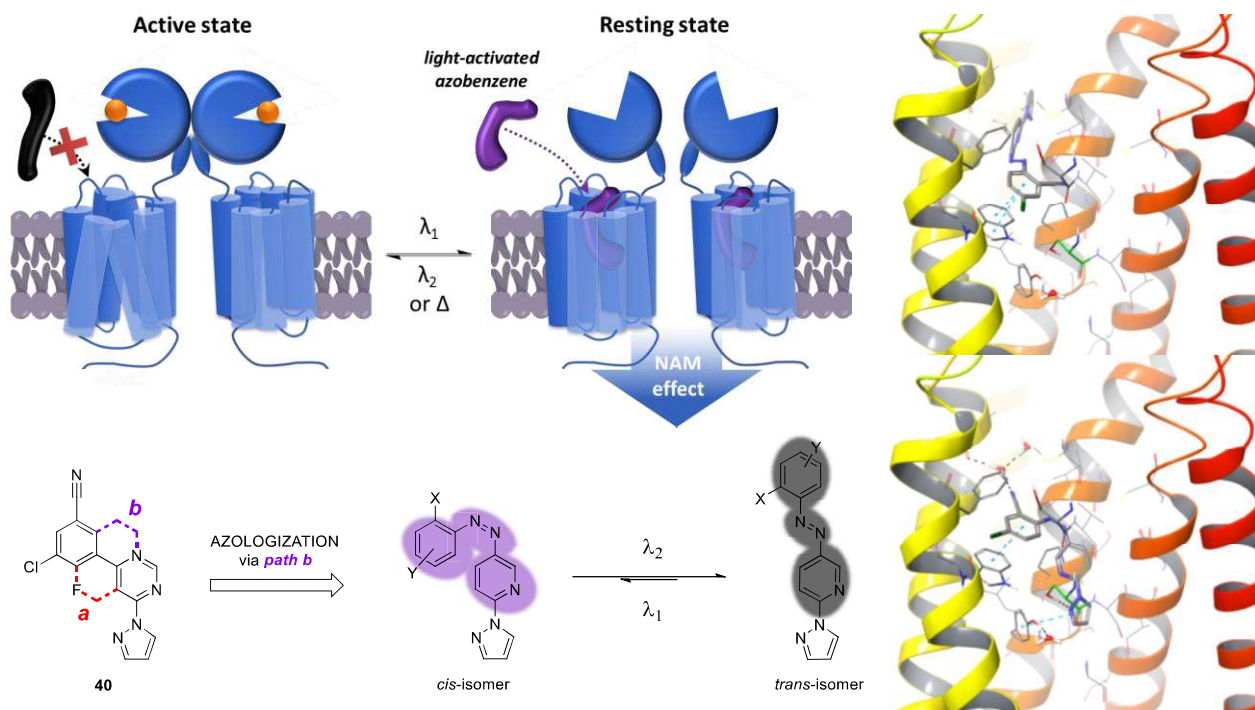
---



# Results and Discussion Contents

<b>Chapter 1: mGlu<sub>5</sub> inhibition with <i>cis</i>-active photoswitchable NAMs .....</b>	<b>79</b>
Design of an initial library of <i>cis</i> -on photoswitchable mGlu <sub>5</sub> NAMs .....	81
Synthesis of compounds 53, 55 and 59 .....	83
Photochemical and pharmacological characterization of the first series .....	84
UV-Vis absorption spectroscopy.....	84
In vitro functional assay: dose-response curves.....	86
Design and synthesis of a second library of <i>cis</i> -on photoswitchable mGlu <sub>5</sub> NAMs .....	87
Photoisomerization properties of compounds 62a-c .....	88
UV-Vis absorption spectroscopy.....	88
NMR spectroscopy.....	90
Determination of the most efficient illumination time .....	91
Confirmation of the optimal wavelengths for bidirectional photoisomerization .....	92
Measurement of thermal relaxation time .....	93
LC-PDA-MS.....	93
Pharmacological characterization of the putative <i>cis</i> -on compounds 62a-c .....	94
Design of a third series: the 5-phenylazo-2-pyrazol-pyridines 66a-f .....	95
In silico characterization of <i>trans</i> and <i>cis</i> configurations .....	96
Synthesis of analogs 66a-f.....	97
Photochemical and pharmacological characterization of the third series .....	98
UV-Vis absorption spectroscopy.....	98
In vitro endpoint functional assay: dose-response curves .....	99
Conclusions .....	100
<b>Chapter 2: Development of a selective photoswitchable PAM for mGlu<sub>4</sub> receptor .....</b>	<b>102</b>
Design of Optogluram analogs.....	103
Synthesis of compounds 71a-d and 74a-b .....	104
Photochemical characterization of compounds 71a-d and 74a-b .....	104
Pharmacological characterization of the putative mGlu <sub>4</sub> PAMs .....	106
Single dose screening .....	106
Dose-response curves.....	107
Selectivity of Optogluram-2 (74a).....	110
Conclusions .....	111
<b>Chapter 3: A toolbox of photoswitchable PAMs to selectively modulate mGlu<sub>1</sub>.....</b>	<b>112</b>
Design of an initial library of <i>trans</i> -on photoswitchable mGlu <sub>1</sub> PAMs.....	113
Synthesis of azologs 82a-b, 83a-b, 85 and 74b .....	114
Photochemical and pharmacological characterization: first series of compounds .....	116
UV-Vis absorption spectroscopy.....	116
In vitro functional assay: poor solubility of azologs 82a-b, 83a-b, 85 and 74b and protocol optimization.....	117
Optimization of the first hit Photoglurax-1 (83b) .....	120
Synthesis of azo compounds 89a-i.....	121
Photochemical and pharmacological characterization: second series of compounds .....	121
Conclusions .....	124
<b>Chapter 4: A series of arylazothiazoles to control mGlu<sub>1</sub> function with light .....</b>	<b>125</b>
Initial considerations and design of analog 103a.....	126
Solubility enhancement with R <sub>2</sub> groups.....	128

Covalent photoswitchable mGlu <sub>1</sub> ligands .....	130
Synthesis of compounds 101, 103a-h and 107 .....	130
Optimization of the diazotization/azo-coupling reaction .....	132
Photochemical characterization with UV-Vis absorption spectroscopy .....	134
Study of pH-dependent photoisomerization properties .....	135
Pharmacological characterization .....	137
Single dose screening .....	137
Dose-response curves.....	138
Analysis of mGlu <sub>1</sub> NAM effect on receptor conformational changes induced by agonist .....	139
Conclusions .....	148

Chapter 1: mGlu<sub>5</sub> inhibition with *cis*-active photoswitchable NAMs**Key points**

- A more suitable therapeutic approach: *cis*-on photoswitchable mGlu<sub>5</sub> NAMs
- Azologization strategy following two different pathways
- Three series of compounds with different photoisomerization properties
- *In silico* characterization of *trans* and *cis* configurations

Medicinal Chemistry and Synthesis group (MCS) in Barcelona has considerable expertise in the design and development of the photoswitchable allosteric modulators of mGlu receptors based on azobenzene photoswitches. The successful compounds obtained are bioactive in their elongated *trans* configuration, as shown for Alloswitch-1 (**32a**, mGlu<sub>5</sub> NAM), Optoglutram (**38**, mGlu<sub>4</sub> PAM) and OptogluNAM4.1 (**39**, mGlu<sub>4</sub> NAM).<sup>\*</sup> They are biologically active in their thermodynamically stable form and lose activity upon photoisomerization to their *cis* isomer (Figure 40A). This approach, also known *T*-on approach (or *trans*-on for azobenzene based compounds),<sup>†</sup> is not the most promising from the therapeutic point of view, since the switching-off of an already active drug with light has limited therapeutic applications. However, the major application of these *trans*-on photoswitchable compounds might be the use as tools to further investigate physiological processes with the possibility of *on/off* switching signaling cascades, induce over-activation of these cascades or study the unknown effects of intermittent activation by these photoswitchable compounds with *on/off* light pulses.

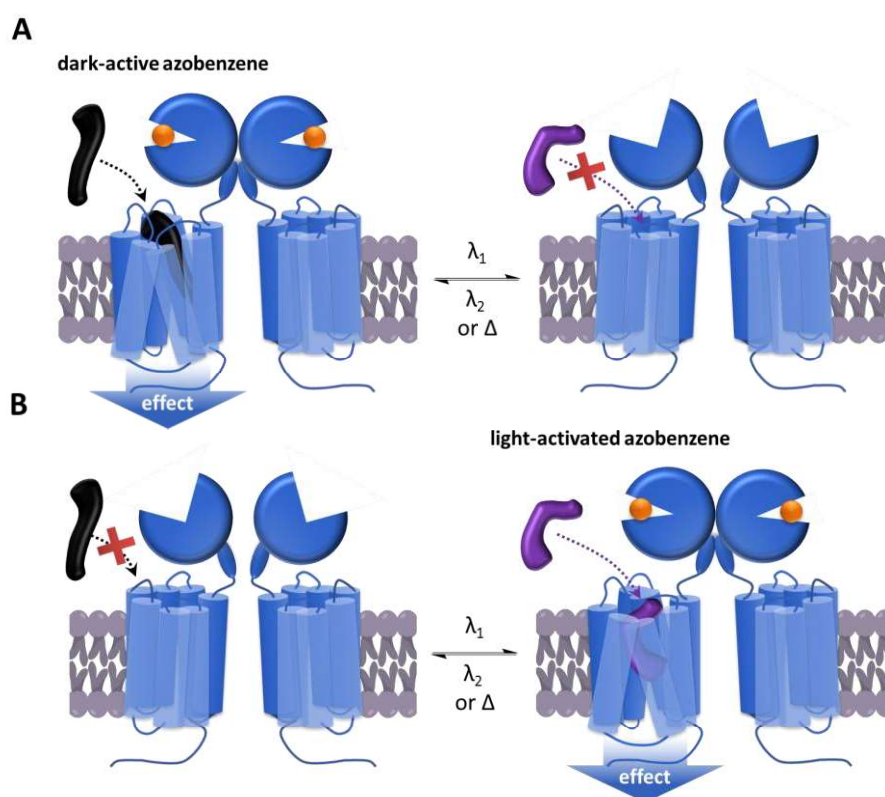


**Figure 40.** Schematic representation of the *trans*-on and *cis*-on approaches. (A) *trans*-on approach: Conventional dark-active azobenzenes are thermodynamically stable in their elongated *trans*-forms; (B) *cis*-on approach: the bent *cis*-forms of azobenzenes, bind to the target protein and induce the biological effect. Both types of ligands can be switched back and forth with a combination of irradiation and thermal relaxation. The wavelengths needed for photoisomerization and the kinetics of thermal relaxation can be tuned by modifying the substitution pattern of the azobenzene (See *General Introduction: Substituted Azobenzenes (ABs)*).

Alternatively, there is also a “inverted” approach known as “*M*-on” or “*cis*-on” approach for azobenzene based compound, which is based in *cis* isomers exerting a bioactive effect on the receptor, whereas the *trans* are devoid of any effect.<sup>†</sup> In other words, the application in the dark of these *trans* inactive compounds would ideally have no effect until a precise application of light in a specific region of the organism that would photoisomerize the azo compound. Thus, the resulting *cis* isomer would induce a pharmacological effect only in the regions irradiated (Figure 40B). The thermal relaxation of the *cis* isomers

<sup>\*</sup> See *General Introduction: Freely diffusible photoswitchable allosteric modulators for mGluRs*

<sup>†</sup> See *General Introduction: T-on/ M-on photochromic ligands*

would contribute to the inactivation of the compound while diffusing through the other regions of the organism. Overall, this approach is preferred in most biological and therapeutic applications since it benefits better from the high spatiotemporal precision that light offers.

In the present chapter, the rational design, synthesis and characterization of three new series of photoswitchable compounds using a *cis*-on approach are presented. Since Alloswitch-1 (**32a**) was the first photochromic ligand to allosterically target the endogenous mGlu<sub>5</sub> receptor with a *trans*-on approach, one of the aims of this thesis is to afford the first photoswitchable mGlu<sub>5</sub> NAM that only display pharmacological activity in its *cis* configuration, whilst the *trans* isomer remains inactive.

### Design of an initial library of *cis*-on photoswitchable mGlu<sub>5</sub> NAMs

Before any experimental work, we did an exhaustive bibliographic search of mGlu<sub>5</sub> NAMs focusing on molecules containing aromatic rings with a spacer susceptible to be replaced with a *cis*-azo-bond (/N=N\). This approach is known as “azologization strategy”.<sup>\*</sup> In this specific project, we sought compounds that fit in the allosteric binding site with a bent pose and mimic this active bent position with a *cis*-azo bond. Additionally, we also sought that the corresponding *trans* isomer with a straight disposition and higher length did not properly fit into the allosteric pocket, abolishing the effect on the receptor.

Therefore, we found the compound **40** developed by Heptares Therapeutics as a promising candidate compound that fulfilled our requirements.<sup>236,237</sup> In particular, we opted for this compound as starting point for our design for three main reasons: (a) it was a very potent mGlu<sub>5</sub> NAM with a pIC<sub>50</sub> of 8.6 and a pK<sub>i</sub> of 9.3;<sup>236,237</sup> (b) its structure included just a single bond between two aromatic rings, which gave it a bent geometry and was susceptible to be replaced with the azo group in *cis*-form, (c) the synthesis of the corresponding azo compounds apparently was not difficult and (d) the binding mode of compound **40** in the mGlu<sub>5</sub> allosteric site was very well determined since it was co-crystallized.<sup>236,237</sup>

Compound **40** (Figure 41 and Figure 42) was reported in 2015 as the first example of mGlu<sub>5</sub> NAM identified by tandem fragment- and structure-based drug discovery approaches (FBDD and SBDD).<sup>236</sup> A thermostabilized form of the mGlu<sub>5</sub> 7TMD (StaR<sup>®</sup> protein) demonstrated increased tolerance of high DMSO concentrations compared to wild-type receptor and enabled fragment screening in a high-concentration radioligand binding format. The radioligand used was the NAM [<sup>3</sup>H]-M-MPEP ([<sup>3</sup>H]-**42**), thus allowing identification of fragment hits that compete with the radioligand for the occupancy of the allosteric pocket. Compound **40** is part of a generation of non-acetylene compounds as mGlu<sub>5</sub> NAM. In contrast, Raseglurant (**18b**), MPEP (**41**), M-MPEP (**42**), Mavoglurant (**43**), Basimglurant (**44**) and MCS0593 (**45**)<sup>238</sup> are some examples of mGlu<sub>5</sub> NAM compounds containing a central acetylene flanked by two aromatic or aliphatic groups (Figure 41). It was demonstrated that the acetylene moiety is susceptible to metabolic activation<sup>239,240</sup> but at the same time the glutathione conjugation can be derisked by flanking the triple bond with only one EWG aryl ring as happened for Raseglurant (**18b**, Figure 41).<sup>241</sup> Additionally, when designing azobenzene based compounds, the presence of possible aromatic acetylene groups may interfere in the absorbance spectra in the near UV in both *trans* and *cis* isomers, possibly leading to a poor photostationary states upon UV irradiation.

<sup>\*</sup> Azologization or azo-replacement is based on the substitution of a bridge between two aromatic rings with an azo-bond; see *General Introduction: Photoresponsive molecular switches*.



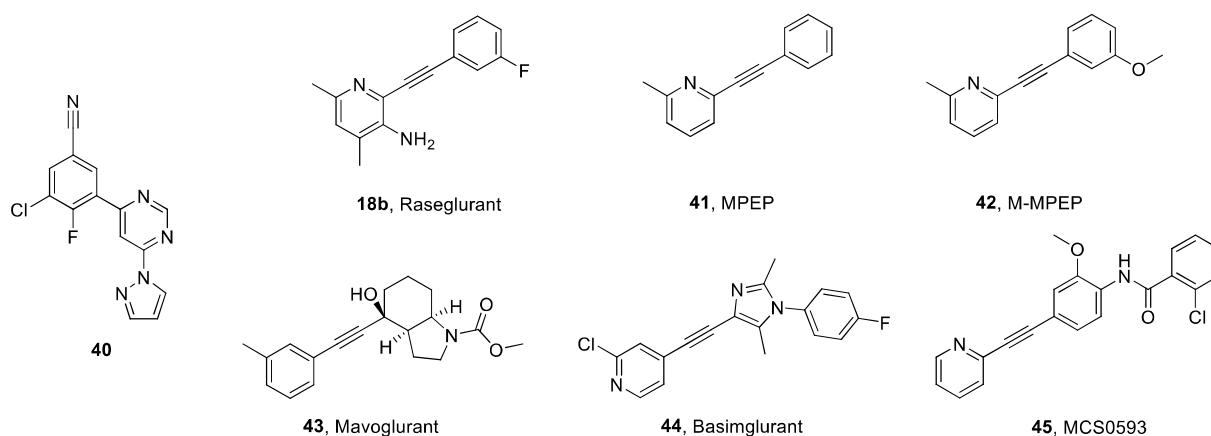


**Figure 41.** Chemical structure of the mGlu<sub>5</sub> NAM **40** and some examples of acetylene mGlu<sub>5</sub> NAMs from literature (**18b**, **41-45**).

The mGlu<sub>5</sub>-StaR crystal structure with **40** bound in the allosteric site was crystallized and solved through merging diffraction data from multiple crystals grown in lipidic cubic phase to give a structure with a resolution 3.1 Å (Figure 42A,B). In general, the protein backbone of the novel structure was in close agreement with the Mavoglurant co-structure: the ligand **40** was found in the allosteric pocket ~8 Å from the receptor surface and in a similar position to that observed previously for Mavoglurant (**43**).<sup>92</sup>

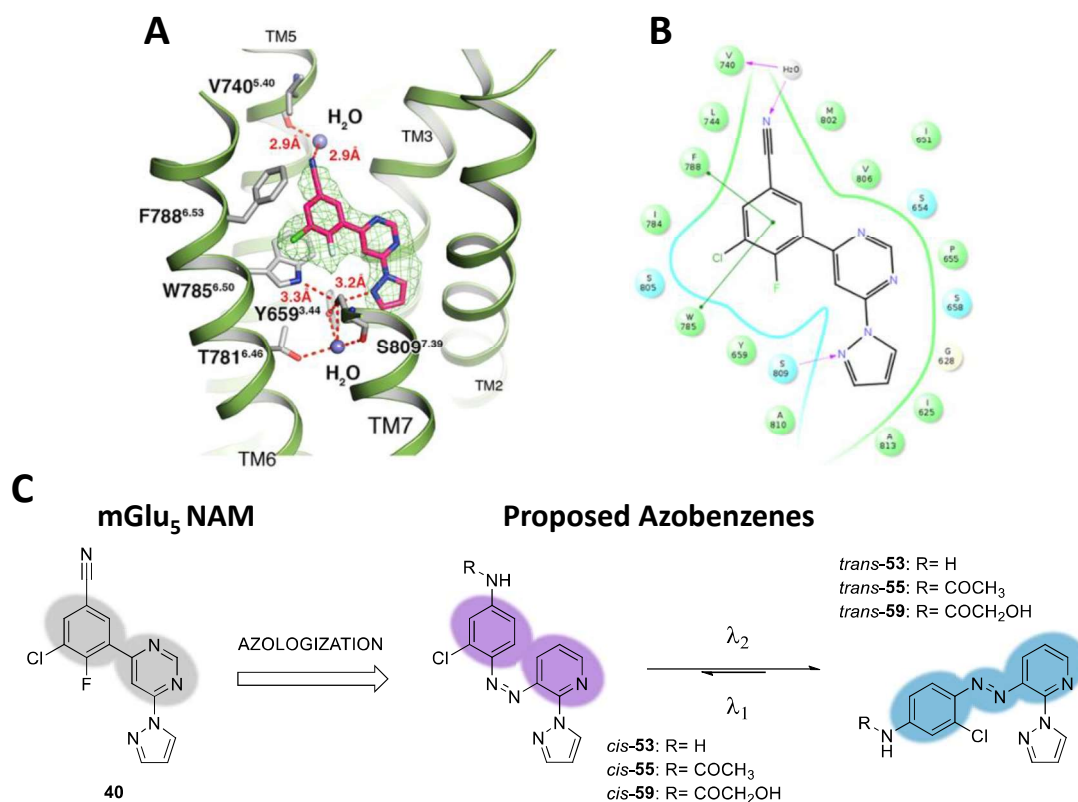


**Figure 42.** (A) Diagram of ligand interactions within the allosteric site of mGlu<sub>5</sub> with **40** bound (PDB code: 5CGC). mGlu<sub>5</sub> in ribbon representation colored green. **40** in stick representation with carbon, nitrogen, oxygen, chlorine, and fluorine atoms colored magenta, blue, red, green, and white, respectively. Selected residues from mGlu<sub>5</sub> in stick representation with carbon, nitrogen, and oxygen atoms colored gray, blue, and red, respectively. TM helices are labeled and selected hydrogen bonds depicted as dashed red lines with distances labeled in Å. (B) 2D diagram of **40** ligand interactions in the mGlu<sub>5</sub>-StaR allosteric pocket, respectively. Green lines denote π-stack interactions, dashed purple arrows denote hydrogen bonds (side chain), solid purple arrows denote hydrogen bonds (main chain), residues in cyan spheres denote polar interactions, and residues in green spheres denote hydrophobic interactions. (Figures from Christopher et al.).<sup>236</sup> (C) Azologization strategy from compound **40** to afford theoretically *cis*-on photoisomerizable compounds **53**, **55** and **59**.

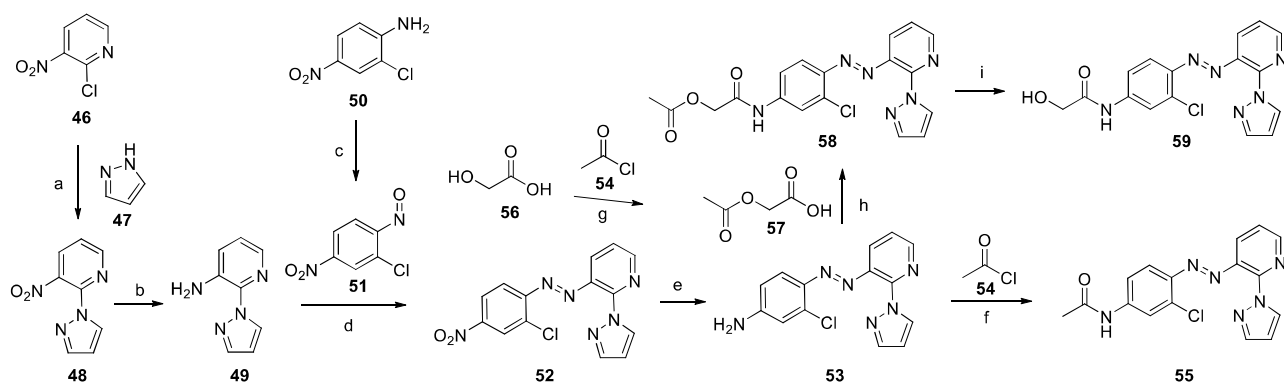
As mentioned above, compound **40** was used as reference compound on which applying the azologization strategy. We thought that the elimination of a single bond between two aromatic rings and the following insertion of an azo group, between the alpha position of each ring, would be suitable to successfully obtain photoswitchable mGlu<sub>5</sub> NAMs (Figure 42C) active in their *cis*-configuration. Applying this approach, the photoswitchable compounds should not display mGlu<sub>5</sub> NAM activity in their *trans* configuration since the resulting structure differs considerably from the parent compound **40**. After photoisomerization, the bent *cis* configurations would reproduce a similar geometry of the starting parent compound **40** without excessively altering the interactions inside the pocket.

In order to access an initial library of possible photoswitchable *cis*-on mGlu<sub>5</sub> NAMs we decided to maintain the pyrazole ring system in the molecular scaffold, important to stabilize polar interactions in the pocket, through hydrogen bond with the backbone carbonyl oxygen of Ser809<sup>7,39</sup> and the water molecule in the lower chamber of the allosteric pocket (Figure 42). The same pyrazole ring system was connected to a pyridine linker which we thought could traverse the narrow channel in the allosteric pocket formed between Tyr659<sup>3,44</sup>, Ser809<sup>7,39</sup>, Val806<sup>7,36</sup> and Pro655<sup>3,40</sup> like pyrimidine ring system of compound **40** did. Apparently, the presence of two nitrogen atoms in this area of the allosteric pocket did not seem to be so crucial for molecular interactions. Lastly, the upper chamber of the allosteric pocket for the three novel structures presented here could differ most significantly from that previously determined for mGlu<sub>5</sub> in complex with compound **40**. Indeed, it is well known that the overall properties of this upper region of the mGlu<sub>5</sub> allosteric pocket are mostly hydrophobic in nature and therefore it is very important to create a top ring system with the correct directional electronic character. Aware of this possible limitation, we decided anyway to initially replace the 5-cyano substituent with a 2-hydroxy-*N*-acetamide group in 4-position relative to the azo-bound (compound **59**, Figure 42C) for two main reasons: (a) obtaining a more red-shifted photoswitchable compound, since UV light is harmful for living system, and (b) keeping the possibility to replace the water mediated hydrogen bond of **40** (Figure 42A,B) with the backbone carbonyl of Val740<sup>5,40</sup> with a regular hydrogen bond, where the hydroxy group of *cis*-**59** would replace the water molecule. Additionally, we decided to also include in the library the compounds with other similar groups in this position such as amine and acetamide (compound **53** and **55**, respectively, Figure 42C).

### Synthesis of compounds **53**, **55** and **59**

The compound **59** was obtained after an eight-step synthetic route, whereas six steps were required to synthesize the compound **55**. The aniline **53** was a common intermediate for both compounds **55** and **59** and it was the third compound we wanted to test.

The synthetic routes developed are depicted in Scheme 4. The sequence began with a nucleophilic substitution of 2-chloro-3-nitropyridine (**46**) with 1*H*-pyrazole (**47**)<sup>242</sup> to obtain nitro compound **48**, which was reduced through palladium-catalyzed hydrogenation to give the aniline **49** in high yield. The nitro azo compound **52** was prepared via Mills reaction in good yields by reacting aniline **49** with nitroso derivative **51** in acidic media. The nitroso compound **51** was prepared by amine oxidation of the corresponding 2-chloro-4-nitroaniline (**50**) with Oxone<sup>®</sup> following the procedure described by Priewisch.<sup>243</sup> Then, the nitro functional group of **52** was reduced using sodium sulfide nonahydrate to give aniline **53** as common intermediate. A subsequent acylation with acetyl chloride (**54**) gave the second desired azo compound **55** in high yield. Alternatively, amide coupling of the intermediate **53** with freshly prepared glycolic acid **57** with HATU with TEA delivered the azo compound **58**. Finally, the third desired compound **59** was obtained by the ester hydrolysis of **58** with LiOH.



**Scheme 4.** Synthesis of compounds **53**, **55** and **59**. Reagents and conditions: (a)  $\text{Cs}_2\text{CO}_3$ , anhydrous MeCN, 85 °C, 16 h, 68%; (b)  $\text{H}_2$  (1 atm), Pd/C, EtOH, rt, 16 h, 98%; (c) Oxone<sup>®</sup>,  $\text{H}_2\text{O}$ , rt, 16 h, 94%; (d) AcOH excess, rt, DCM, 16 h, 84%; (e) sodium sulfide-  $9\text{H}_2\text{O}$ , 1-4, dioxane, 100 °C, 2 h, 83%; (f) TEA, THF, 60 °C, 48 h, 81 %; (g) no solvent, rt, 2 h, 39%; (h) HATU, TEA, THF, 60 °C, 16h, 80-90%; (i) LiOH/MeOH, THF, 0 °C, 30 min, 61%.

## Photochemical and pharmacological characterization of the first series

### UV-Vis absorption spectroscopy

To biologically take advantages of the azo compounds isomerization using light, it is important to previously obtain the UV-Vis absorption spectra of both *trans* and *cis* isomers of each compound. In this way, we can determine the wavelength where the maximum difference of absorption between the *trans* and *cis* isomer is found. This wavelength corresponds to the optimal one to illuminate the compound and isomerize from *trans* to *cis* disposition to reach a maximum fraction of *cis* isomer in the photostationary state. On the other hand, the wavelength located at the maximum difference of absorption between the *cis* and *trans* isomers would be the optimal one for the reverse isomerization. However, obtaining pure *cis* isomer samples is not straightforward, since it would require illuminating with a wavelength in which, the *trans* isomer absorbs but the *cis* isomer does not. Most of the times purification of the *cis* isomers would be required as well as minimizing its thermal decay. In conclusion, achieving a sample of *cis* isomer with very high purity is highly complicated and we have to consider that always there will be a fraction of the *trans* isomer upon illumination, though it can be very small for certain wavelengths. This *cis-trans* proportion is what we know as photostationary state (PSS).\*

Thus, we used UV-Vis absorption spectroscopy to determine the photochemical properties of azo compounds **53**, **55** and **59** in the dark after carefully protecting the compounds from ambient light to only obtain the UV-Vis spectrum of the *trans* isomers. Then we proceeded with the illumination of the samples with violet light (380 nm) to induce isomerization from *trans* to *cis* configuration, we collected the new spectra and we repeated the procedure after illuminating them with turquoise (455 nm), green (500 nm) and yellow (550 nm) light. While in the dark, the intense  $\pi\text{-}\pi^*$  band revealed the presences of only the *trans* isomers (Figure 43), a mixture of the *cis* and the *trans* isomers can be detected upon illumination.

Compound **53**, with the amino substituent in the 4-position, can be classified as aAB derivative.\* Due to the electron donating properties of this group, the  $\pi\text{-}\pi^*$  transition of **53** is shifted to higher wavelengths around 420 nm (Figure 43A, left panel) and overlaps with the  $n\text{-}\pi^*$  transition. However, the *trans* to *cis* isomerization can be induced with 380 nm more efficiently than with wavelengths at the blue range. Although the UV-Vis spectrum do not suggest that because 380 nm is located at a shoulder of the  $\pi\text{-}\pi^*$

\* See General Introduction: Photoresponsive molecular switches

transition band, the *cis* isomer has a minimum of absorbance around this wavelength, making it the most suitable wavelength for such isomerization (Figure 43A). On the other hand, 550 nm light is the suitable wavelength to back isomerize compound **53** to its thermodynamically stable *trans* isomer.

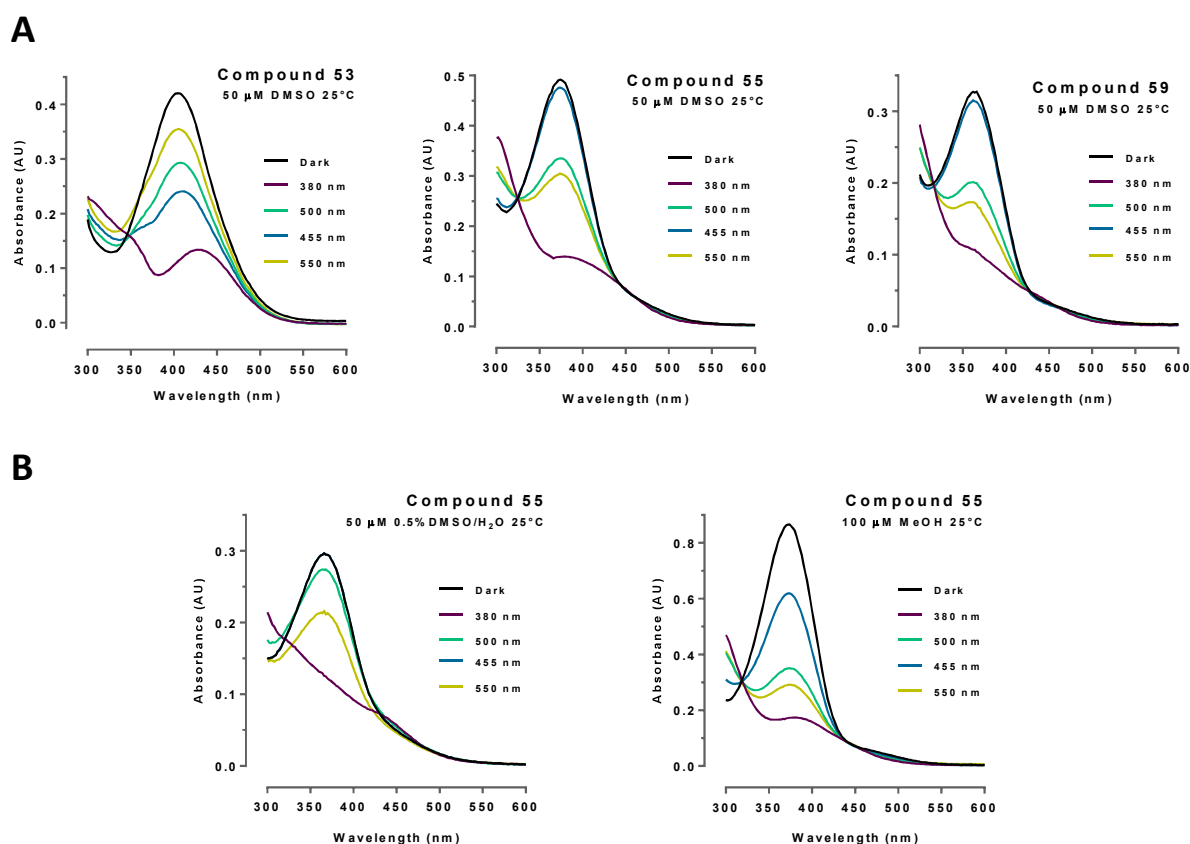


**Figure 43.** Photochemical properties of compounds **53**, **55** and **59**. (A) UV-Vis absorption spectra of the compounds 50 μM in DMSO at 25°C under dark (black) and different light conditions for 3 min; (B) UV-Vis absorption spectra of the compound **55** 50 μM in 0.5%DMSO/water (left panel) and 100 μM in MeOH (right panel) at 25°C under dark (black) and different light conditions for 3 min.

UV-Vis spectra showed general tendencies for the two acetamide substituted azobenzenes dissolved in DMSO. In fact, **55** and **59** can be considered aAB derivatives with pseudo-amine groups, such as amides, in 4-position relative to the azo-bond, although they also contain groups in two *ortho*-positions to the azo moiety. Hence, **55** and **59** showed the *trans*-azobenzene  $\pi$ - $\pi^*$  transition band at 360-370 nm under dark conditions; this maximum of absorbance is more red-shifted than that of derivatives belonging to the ABn group. Therefore, the *E/Z* isomerization could be achieved under illumination at this range of wavelengths (Figure 43A). After irradiating the samples with 380 nm light, mainly the *cis* isomers of the compounds were observed. Their absorption spectra were characterized by the stronger  $n$ - $\pi^*$  transition band around 445-455 nm, which is forbidden by the symmetry in *trans* azobenzenes. The two azo compounds **55** and **59** can be almost totally back-isomerized to their thermodynamically stable *trans* isomer using turquoise light (455 nm) because this region of the spectrum is where the *trans* compounds absorb less than the *cis* ones. This difference between absorption profiles of the two isomers is a little more evident with the spectrum of compound **55** dissolved in water (with 0.5% DMSO) and MeOH (Figure 43B). This underlines the fact that, not only the thermal relaxation, but also the absorption profiles of the azobenzene-based compounds can slightly change depending on the solvent (polarity, solvating power and viscosity).

The thermal relaxation of the *cis* isomers in aqueous media was also evaluated, showing a half-life of 8.8 minutes for *cis*-**53**, 67.0 minutes for *cis*-**55** and 77.5 minutes for *cis*-**59** (Figure 44). Those differences in relaxing times are attributable only to the type of substituent in *para* position relative to the azo-moiety. As explained in the General Introduction section, EDG substituents lead to higher rates of *cis* → *trans* thermal isomerization than the other AB derivatives more similar to unsubstituted AB. Additionally, when amine is not alkylated, as for **53**, the aAB derivative in question exhibits an even more reduced thermal relaxation half-life due to the azo-hydrazone tautomeric equilibrium, especially in polar solvents. This is why compound **53** back-isomerizes in aqueous media much faster than *cis*-**55** and *cis*-**59** (Figure 44). The two latter are characterized by a relatively slow thermal relaxation time (67.0 and 77.5 minutes), indicating a considerable bistable nature of this type of compounds.

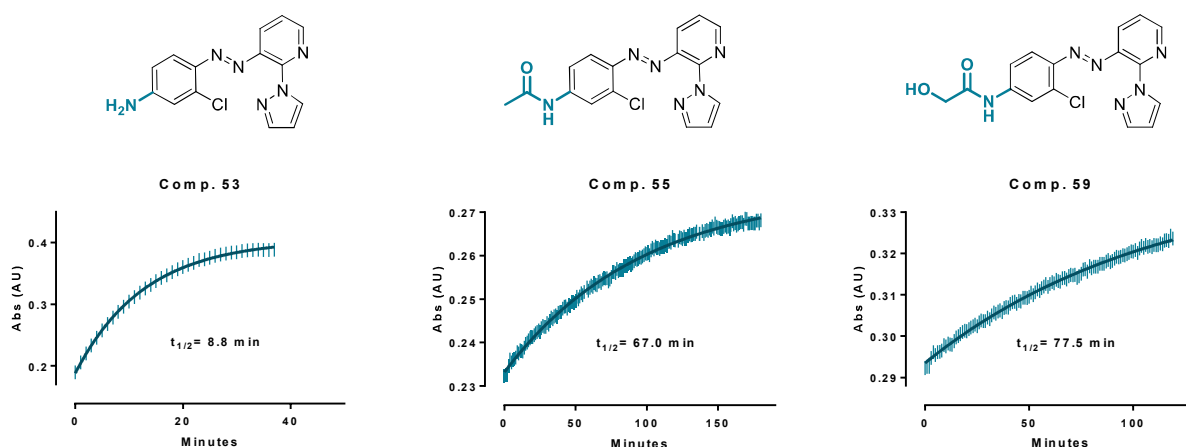


**Figure 44.** Thermal relaxation plot of the *cis* isomer of compounds **53**, **55** and **59** (50  $\mu$ M in H<sub>2</sub>O with 0.5% DMSO) after illumination with 380 nm. A significantly higher half-life for the *cis* isomers of compounds **55** and **59** was determined compared to their parent compound **53**. An exponential decay function was fitted according to a first-order equilibrium reaction formula.\*

### *In vitro* functional assay: dose-response curves

Fanny Malhaire- IGF, Institut de Génomique Fonctionnelle, CNRS, INSERM Montpellier

The pharmacological activity of compounds **53**, **55** and **59** as mGlu<sub>5</sub> NAMs were tested. Dose-response curves were generated with the azo compounds and 300 nM of the orthosteric agonist quisqualate in dark and 380-nm light conditions. An IP accumulation assay in HEK293 cells transiently transfected with mGlu<sub>5</sub> receptor was used, since mGlu<sub>5</sub> naturally couples to G<sub>q</sub> $\alpha$ . Alloswitch-1 (**32a**) was used as photoswitchable control compound for this assay.

Disappointingly, each of the three compounds displayed no activity as mGlu<sub>5</sub> NAMs neither in dark nor upon 380-nm illumination (Figure 45). On the other hand, a minimal *cis*-on effect as mGlu<sub>5</sub> PAMs was observed and it should be proved with a more appropriate assay. Nevertheless, we decided to move forward in the search for new compounds as putative *cis*-on mGlu<sub>5</sub> NAMs following a more rational design, which involved the addition of substituents in appropriate position on the chemical scaffold.

\* See Experimental Section: Thermal relaxation of *cis* isomers

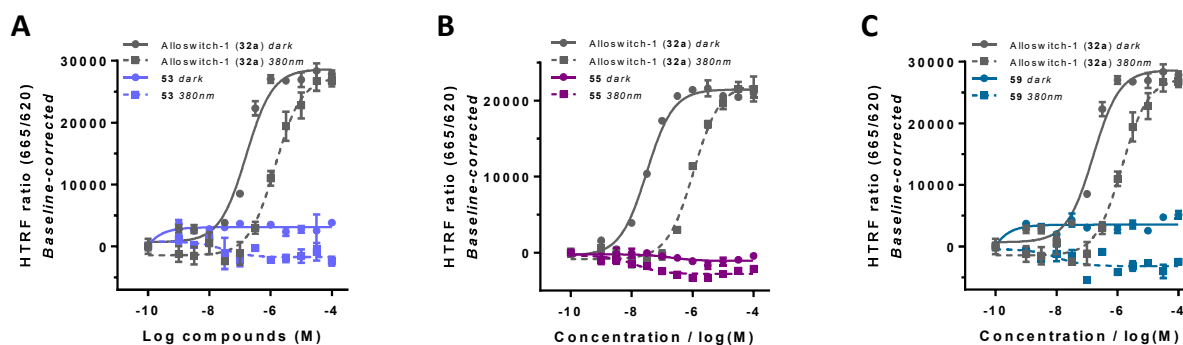


**Figure 45.** Pharmacological properties of compounds **53**, **55** and **59**. Dose-response curve of compound (A) **53** (violet), (B) **55** (magenta) and (C) **59** (turquoise) with a constant concentration of Quisqualate 300 nM in HEK293 cells overexpressing mGlu<sub>5</sub> in different conditions: in dark conditions (round dots and solid line), under illumination at 380 nm wavelength (square dots and dotted line). Alloswitch-1 (**32a**, grey lines) was used as a mGlu<sub>5</sub> NAM standard in dark conditions (round dots and solid line) and under illumination at 380 nm (square dots and dotted line). Each point corresponds to the mean of an experiment performed in duplo with the corresponding SEM as error bars.

### Design and synthesis of a second library of *cis*-on photoswitchable mGlu<sub>5</sub> NAMs

Three new azobenzene-based molecules (**62a-c**) were designed using a mGlu<sub>5</sub> NAM *cis*-on approach very similar to that one used for designing compounds **53**, **55** and **59**. We considered keeping the same chemical scaffold and trying not to introduce other bigger structural differences with the validated parent NAM compound **40**. Therefore, we decided to use the nitrile group as substituent in 4- and in 3 position relative to the azo-bond (Figure 46). Additionally, we also included in the library the non-functionalized phenyl ring, as a “naked” reference compound.

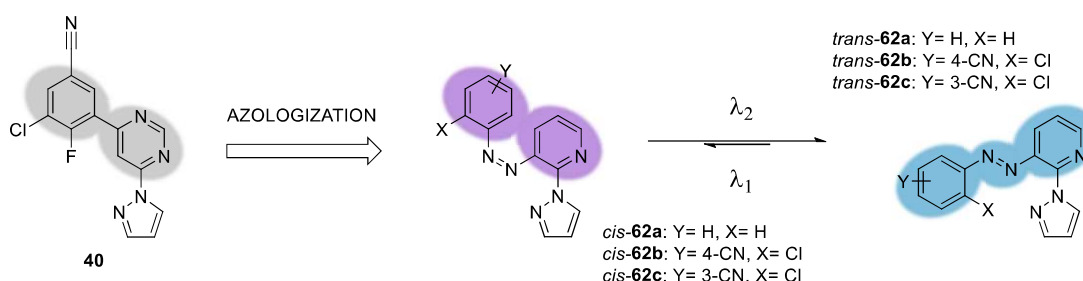
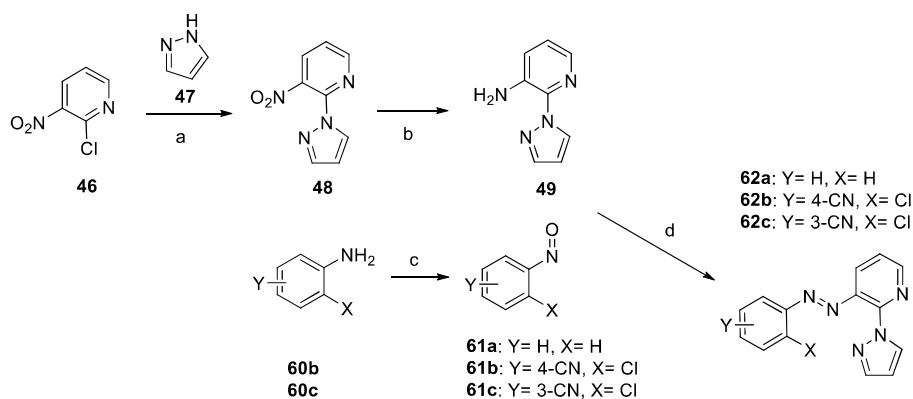


**Figure 46.** Azologization strategy from compound **40** to afford the second library of *cis*-on photoisomerizable compounds (**62a-c**). Compounds **62b** and **62c** include nitrile substitution in two different positions to probe the electronic properties of the compounds in the upper region of the allosteric pocket.

As mentioned above, the 5-cyano group of compound **40** is important to make electronic interactions within the allosteric pocket of the receptor and, in particular, a water mediated hydrogen bond with the backbone carbonyl of Val740<sup>5,40,236</sup>. However, when we started to design the first library of photoswitchable compounds we decided to replace this 5-cyano group because one of the requirements of photochromic compounds, capable of inducing a pharmacological photoswitching, is providing biocompatible wavelengths of illumination to be operated without producing toxicity. Despite azobenzenes (ABs) substituted with electro withdrawing groups such as alkyl, halide, carbonyl, nitrile etc.,\* are generally isomerizing with ultraviolet illumination, we decided that the new analogs **62a-c** were still a worthy option to explore.

\* See General Introduction: Photoresponsive molecular switches

Then, compounds **62a-c** were prepared following a synthetic strategy highly similar to that of the initial library with four steps of synthesis (*Scheme 5*). In fact, the compound **49** was common in both synthetic routes and its preparation was same. The anilines **60b-c** were converted into the nitroso compounds **61b-c**, but the non-functionalized nitroso benzene **61a** was obtained from commercial suppliers. Finally, the desired azo compounds **62a-c** were prepared via Mills reaction in good yields by reacting aniline **49** with the corresponding nitroso derivatives **61a-c** in acidic media.



**Scheme 5.** Synthesis of compounds **62a-c**. Reagents and conditions: (a) Cs<sub>2</sub>CO<sub>3</sub>, anhydrous MeCN, 85 °C, 16 h, 68%; (b) H<sub>2</sub> (1 atm), Pd/C, EtOH, rt, 16 h, 98%; (c) Oxone®, DCM/H<sub>2</sub>O 1:4, rt, 1.30 h, 87-96%; (d) AcOH excess, rt, DCM, 16 h, 54-82%.

## Photoisomerization properties of compounds **62a-c**

### UV-Vis absorption spectroscopy

As shown above, obtaining the UV-Vis absorption spectra of the *trans* isomers and the PSS after different wavelength illuminations is essential in order to evaluate the photoisomerization of the azo compounds. Then, we first measured UV-Vis absorption spectra of **62a-c**, which were in solution 50 μM in DMSO and in H<sub>2</sub>O with 1% DMSO. The measurements were performed in dark and after illuminating with different light conditions, as performed for compounds **53**, **55** and **59** of the first series: we obtained the spectra of the *trans* isomers in the dark and, then, we illuminated the samples with violet light (380 nm), lilac (405 nm), turquoise (455 nm), green (500 nm) and yellow (550 nm) light to obtain the spectra of the different PSSs as shown in *Figure 47.A* for **62b** in DMSO, which displays the general behavior common for all the three azobenzene derivatives.

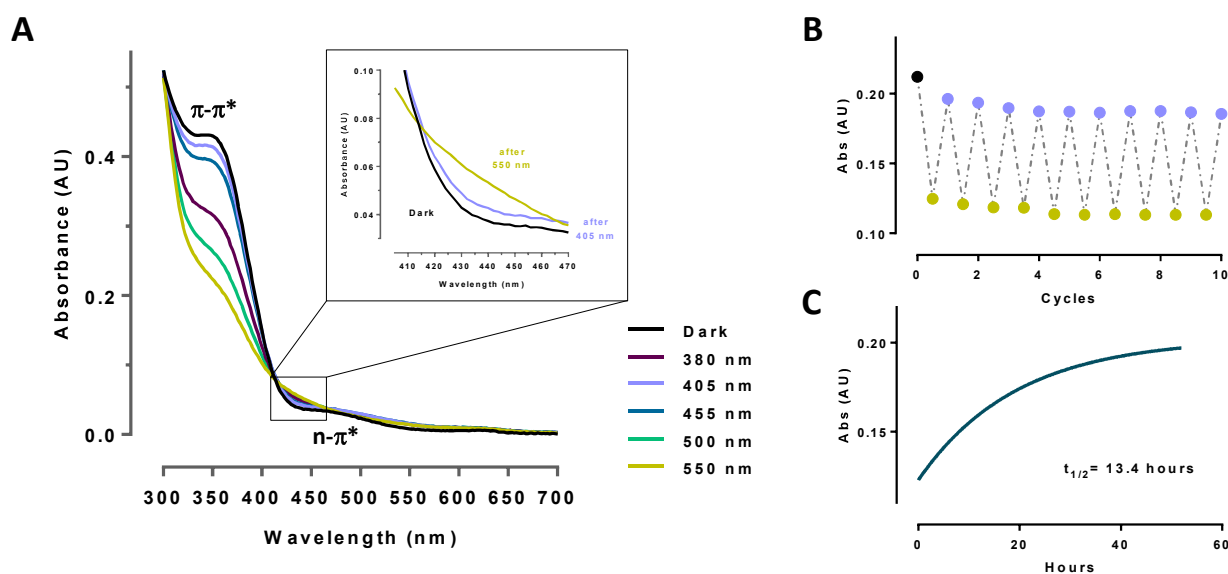
For analogs **62a-c**, the wavelength with the maximum difference of absorption between the two isomers is apparently 380 nm, as it could be expected for this kind of ABs. However, we obtained a very low amount of *cis* isomers after illuminating with 380-nm light. Surprisingly, 550 nm turned to be the optimal wavelength to achieve the maximum amount of *cis* isomer under illumination. This could be explained by the fact that a probable maximum of absorption of *trans* isomers, corresponding to the n-π\* band, and a much lower absorption of the *cis* isomers are located around 550 nm. Instead, the most suitable wavelengths to afford the reverse isomerization lie from 405 to 455 nm, since they are located close to a minimum of absorption of *trans* isomers between π-π\* and n-π\* bands (*Figure 47A*) and where the *cis* isomers have the maximum of absorption corresponding to the n-π\* band.

This “reverse” photochemical behavior of all three compounds of this series it is probably due to the incorporation of the bulky pyrazolyl substituent in the *ortho* position to the azo moiety, regardless of the presence or absence of chlorine and cyano groups in the phenyl group. We postulated that the bulky

pyrazolyl ring does not allow the *trans* isomer to adopt a completely planar conformation, leading to a growth of the red shift  $n\text{-}\pi^*$  band of the *trans*-isomer, which is forbidden by symmetry in regular ABs. This *trans*  $n\text{-}\pi^*$  is separated from the *cis*  $n\text{-}\pi^*$  transition, making it useful for *trans*  $\rightarrow$  *cis* photoisomerization using green light (530-560 nm). Reverse *cis*  $\rightarrow$  *trans* photoisomerization can be accomplished with blue light (430-460 nm), therefore, bidirectional photoisomerization between thermally stable isomers is possible without using UV light (Table 10).

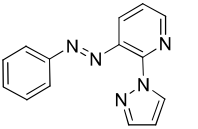
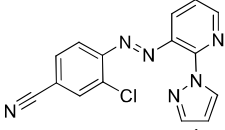
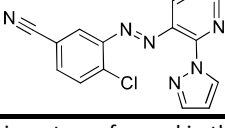
The photoisomerization after several light cycles was also determined with solutions of **62a-c** in DMSO and in H<sub>2</sub>O with 1% DMSO. Thus, the absorbance values were recorded after illuminating the samples at 550 nm and 405 nm per cycle. No considerable differences were observed between the absorbance values of three analogs **62a-c** upon several cycles of yellow and lilac light, showing convincing stability of the photoisomerization (Figure 47B).

The thermal relaxation of the *cis* isomers was also evaluated, showing that the *cis* state is thermally stable (*i.e.* bistable) with a half-life in the order of hours in aqueous solution. For example, the half-life of *cis*-**62b** was 13.4 and 72 hours in H<sub>2</sub>O with 1% DMSO and 100% DMSO, respectively (Figure 47C and Table 10). The thermal relaxation time of the *cis*-**62a** was extremely slow in both kind of solvents (> 6 days) whereas **62c** was not soluble in H<sub>2</sub>O with 1% DMSO and for that it was not possible to obtain an exponential decay function. Indeed, a fast *cis*  $\rightarrow$  *trans* relaxation of **62c** in aqueous medium was observed after irradiation with 550 nm, together with a decrease on the absorbance. This is hypothesized to be originated from compound precipitation, which was observed after the UV-Vis measurement. We believed that this was induced by a lower water solubility of the *trans* isomer respect the corresponding *cis* compound (Table 10), which, due a higher polarity, shows an increased solubility.



**Figure 47.** Photochemical properties of compound **62b**. (A) UV-Vis absorption spectra of **62b** 50  $\mu\text{M}$  in DMSO at 25°C under dark (black) and different light conditions for 3 min; inset graph highlights the absorption profile between 405 and 470 nm of **62b** under dark and 405 and 550 nm-light conditions; (B) UV-Vis absorption measurements of 25  $\mu\text{M}$  **62b** in H<sub>2</sub>O with 1% DMSO at  $\lambda_{\pi\text{-}\pi^*}$  max of *trans* isomer (342 nm) after repeated cycles of illumination with 550 (yellow) and 405 nm light (lilac); (C) Thermal relaxation plot of *cis*-**62b** in H<sub>2</sub>O with 1% DMSO at 25 °C. Absorbance at 342 nm was recorded for 52 h.



Photoisomerization properties			$t_{1/2}$ (h)	
Compound	<i>trans</i> <sup>[a]</sup>	<i>PSS</i> <sub>550</sub> <sup>[c]</sup>	DMSO	H <sub>2</sub> O/1%DMSO
	$\lambda_{\max}(\pi-\pi^*)$ <sup>[b]</sup> [nm]	$\lambda_{\max}(\pi-\pi^*)$ <sup>[b]</sup> [nm]		
<b>62a</b> 	334	420	> 6 days	> 6 days
<b>62b</b> 	350	416	72	13
<b>62c</b> 	346	416	61	ND <sup>[d]</sup>

[a] Experiments performed in the dark to characterize 100 % *trans* isomer.

[b] The absorbance maxima were extracted from UV-Vis spectra (50  $\mu$ M in DMSO at 25°C).

[c] Photostationary state upon illumination with 550 nm light to obtain a high % of *cis* isomer.

[d] ND= not determined because of solubility issue.

**Table 10.** Photoisomerization properties of analogs **62a-c** determined at 50  $\mu$ M in DMSO and water (+1% DMSO) at 25 °C.

### NMR spectroscopy

An interesting point to take into consideration is the real amount of *cis* and *trans* isomer that is afforded in the photostationary equilibrium under illumination, since its quantification by UV-Vis is complicated.\* A reasonable approach, previously described,<sup>244</sup> is the use of <sup>1</sup>H-NMR under continuous illumination to determine the photostationary states (PSSs), since the chemical shift of *cis* and *trans* configurations of the hydrogen atoms azo compounds are different and this allows a quantification of the relative amounts of the isomers. The optimal approach to have a high relevance would be performing this experiment in solution under the same conditions used in biological experiments. However, NMR spectroscopy has some limitations that we have to consider: solvents need to be deuterated to avoid interferences in the proton signals and to adjust the field-frequency lock. Moreover, NMR is a spectroscopy technique with a relatively low sensitivity, which involves using relatively concentrated solutions of the compound to be tested and accumulate several experiments to obtain a proper signal.

Due to the aforementioned limitations of the technique and the solubility issues of these compounds, we decided to perform these experiments with a solution 5 mM of compound **62b** in deuterated DMSO. Therefore, the purpose of this study is not to mimicking the physiological conditions for biological experiments, but rather to increase our knowledge about the properties of this family of compounds from a purely photochemical point of view. Because of the bistable nature of the *cis*-**62b** (low rate of *cis*  $\rightarrow$  *trans* isomerization) it was possible to perform the following <sup>1</sup>H-NMR experiments. The <sup>1</sup>H NMR acquisitions consisted in 32 scans with a total collecting time of 1 min and 54 s. All the obtained spectra were processed equally, integrating the most shielded proton of the pyrazole ring in the region 6.75- 6.60 ppm (Figure 48) and the resulting area relations were converted to a molar percentage of *cis* isomer.

\* See General Introduction: Characterization of GPCR photopharmacological tools

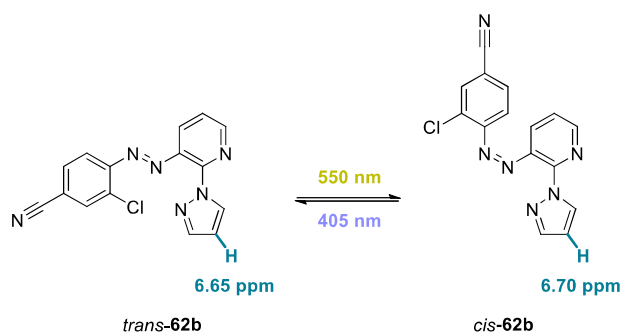


**Figure 48.** Two-dimensional chemical structures of the photoisomers of **62b**. Chemical shift variations on the most shielded proton of the pyrazole ring were followed under <sup>1</sup>H-NMR recording.

#### Determination of the most efficient illumination time

Before looking for the right molar fraction of *cis*-**62b** in the different photostationary states, it was necessary to know what illumination time was necessary to obtain the highest amount of *cis* isomer in such a concentrated sample (5 mM in DMSO). From the UV-Vis absorption spectroscopy experiments, we knew that 550 nm is the best wavelength to get a PSS with a high percentage of *cis* isomer. Therefore, a first <sup>1</sup>H NMR experiment was performed in dark conditions and, after that, the same sample was irradiated with 550 nm at several time lapses and new <sup>1</sup>H NMR acquisitions were taken at each lapse. The sample was first irradiated 1 minute with the power set at 50% of intensity (118.1 mW) and after 3 minutes at 100% power (181.9 mW).\*

From the results shown in *Table 11*, it was emerged that by illuminating the sample for 1 minute we obtained a low percentage of *cis* isomer. The sum of a high concentration of the sample, the intensity of light reaching the solution and the short period of illumination contributed to obtain an isomerization with a high percentage of *trans* isomer, which did not match the results obtained by UV-Vis spectroscopy. In a second effort, we expected to obtain a better isomerization increasing both the intensity of light and the time of illumination and, thus, get a higher fraction of *cis* compound. Effectively, we obtained an improved isomerization, as it can be observed in *Table 11*. Discouragingly, we obtained a percentage of *cis* isomer lower than 80%. This result was comparable to that obtained with UV-Vis spectroscopy since the two isomers of compound **62b** absorb practically all the same wavelengths in a different but still remarkable degree. For this reason, obtaining 80- 100% *cis* isomer samples is not easy. Later, illuminating the same sample with 550 nm for 30 minutes gave us the confirmation that the PSS was reached. Indeed, the PSS consisted of 35.7% of *trans* and 64.3% of *cis* isomers and it was already reached after 3 minutes of illumination.

Illumination Time (min)	Potency (mW)	Area <i>trans</i> - <b>62b</b>	Area <i>cis</i> - <b>62b</b>	% <i>cis</i> - <b>62b</b>
_[a]	-	1.00	0.00	0%
<b>1</b>	50%= 118.1	1.00	0.52	34.2%
<b>3</b>	100%= 181.9	1.00	1.80	64.3%
<b>30</b>	100%= 181.9	1.00	1.75	64.0%

[a] Measurement performed before illumination to characterize 100 % *trans* isomer in the dark

**Table 11.** Photoisomerization assay under <sup>1</sup>H-NMR recording. Illumination at 550 nm wavelength was achieved using the CoolLED pE-4000 Light Source. The studied sample (**62b**, 5 mM, DMSO-*d*<sub>6</sub>) was illuminated for 1, 3 and 30 min and <sup>1</sup>H NMR acquisitions were

\* See *Experimental Section*

taken each time. The photostationary state (PSS) with the highest percentage of *cis*-**62b** is characterized by 35.7% of *trans* and 64.3% of *cis* isomers and it was reached after 3 minutes of illumination in continuous mode.

#### Confirmation of the optimal wavelengths for bidirectional photoisomerization

Additionally, we determined the optimal wavelengths for bidirectional photoisomerization of compound **62b** screening all the illumination wavelengths available at that moment and quantifying the amount of *trans* and *cis* isomers once reached each photostationary state. Thus, we illuminated 3 minutes the sample in deuterated DMSO- $d_6$  with different light wavelengths and new  $^1\text{H}$  NMR acquisitions were taken each time. As explained before, we integrated the most shielded proton of the pyrazole ring (Figure 48) and converted the resulting area relations to a molar percentage of *cis* isomer. Then, we plotted the percentage of *cis*-**62b** versus the corresponding light wavelengths used (Figure 49). The results showed that the optimal wavelength of illumination to obtain the largest amount of *cis*-**62b** was 550 nm with 64.3% of *cis* isomer reached, together with 525 and 500 nm, which induced PSSs of 57.3% and 43.2% of *cis*-**62b**, respectively. Contextually, it was possible to determine the best wavelengths for the back isomerization *cis*→*trans*, that are 405 and 435 nm, reaching 88.7% and 88.5% of *trans*-**62b** respectively.

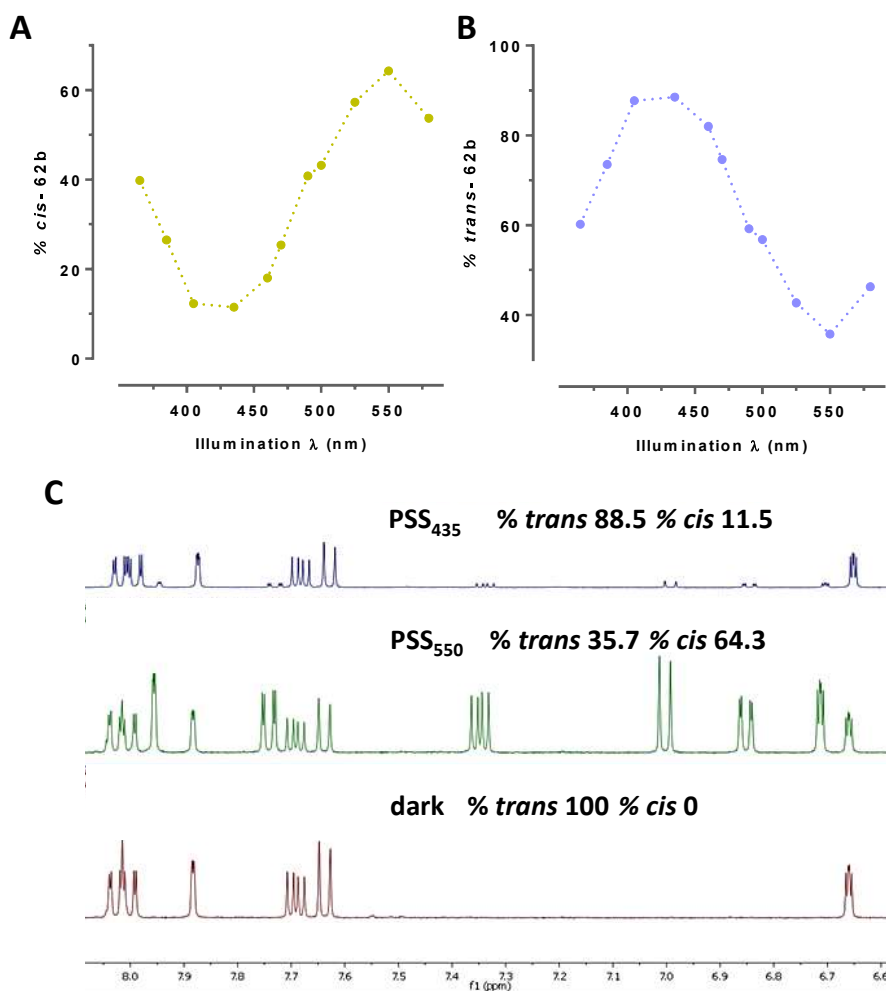


**Figure 49.** Photochemical properties of compound **62b** determined by  $^1\text{H}$  NMR spectroscopy. Maximum absorption values of compound **62b** (5 mM in DMSO) extracted from  $^1\text{H}$ -NMR spectra measured after illumination of the sample at wavelength indicated in the graphs for (A) *trans*→*cis* isomerization and (B) *cis*→*trans* isomerization; (C) Photostationary state (PSS) quantification. Samples were continuously illuminated using different light sources. Chemical shift variations on the most shielded proton of the pyrazole ring were followed.

### Measurement of thermal relaxation time

Finally, we used <sup>1</sup>H-NMR spectroscopy to measure the thermal relaxation rate of the *cis*-**62b** over the time. To do that, we illuminated the sample in DMSO-*d*<sub>6</sub> with 550 nm and new <sup>1</sup>H NMR acquisitions were taken over the time, while keeping the sample protected from ambient light. As shown before, we integrated the most shielded proton of the pyrazole ring (Figure 48 and Figure 49C) and converted the resulting area relations to a molar percentage of *cis* isomer. Then, we plotted the % of *cis*-**62b** versus the time of relaxation and we fitted an exponential decay function (Figure 50), according to a first order equilibrium reaction formula.\* In this way, we were able to calculate the half-life value (*t*<sub>1/2</sub>) of the *cis*-**62b** and the amount of the two isomers once reached the plateau (Figure 50).

From the results, we conclude that the *cis* isomer of compound **62b** is very stable over the time when it is dissolved in DMSO. After eleven days (264 h), there was a remarkable percentage of *cis* in the sample (~20%). Additionally, the half-life value (*t*<sub>1/2</sub>) of the *cis*-**62b** was found to be of ~68 hours in DMSO. This value is very close to that one extrapolated from the experiments carried out using UV-Vis absorption spectroscopy with 50 μM in DMSO samples (72 h, Table 10).

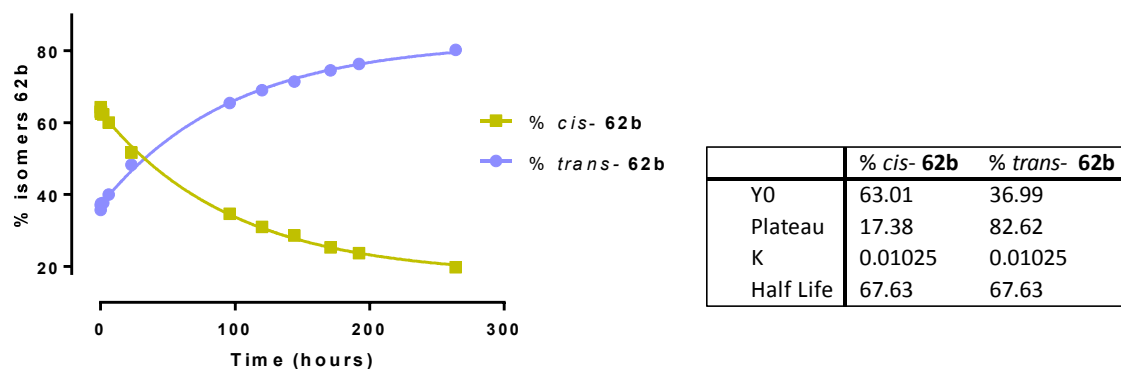


**Figure 50.** The one phase decay curve used to estimate the half-life of *cis*- **62b** 5 mM in DMSO at 25 °C. Several <sup>1</sup>H NMR acquisitions were taken over the time for eleven days.

### LC-PDA-MS

Photoisomerization of compound **62b** was also confirmed by liquid chromatography coupled to a photodiode array and a mass spectrometer detectors (LC-PDA-MS). Indeed, LC-PDA-MS allowed us to quantitatively detect a mixture of the two photoisomers by chromatographic separation and therefore to confirm the previously obtained results. The coupled photodiode detector (PDA) allowed to record the UV-Vis absorption spectra of each of the separated peaks and to properly identify each isomer. Moreover, the coupled mass spectrometer (MS) allowed to determine the mass of each molecular entity and verify that both *cis* and *trans* peaks had the identical mass. Clearly, this type of analysis was possible thanks to the bistable nature of the compound **62b** and therefore, it did not relax before or during the entire time of measurement (ca. 1-20 min); otherwise we would have detected only the thermodynamically stable isomer.

Then, we decided to use the compound **62b** in 100 μM solution of DMSO/MeCN (1:9) and analyze the PSS after illumination, comparing the results with those obtained by <sup>1</sup>H- NMR spectroscopy. The LC-PDA-MS measurements were performed in dark and after illuminating with 550 nm. To quantify the isomeric ratio,

\* See Experimental Section

the separated peaks were integrated using the PDA channel at the wavelength of the isosbestic point,\* in this specific case 414 nm, which was previously determined by UV-Vis spectroscopy.

In LC-MS analysis, only *trans*-**62b** was observed in the dark, whereas a PSS of ~64.5 % *cis*-**62b** after 550 nm illumination was identified (Figure 51). This isomeric ratio is exactly the same as that measured with <sup>1</sup>H-NMR spectroscopy (Table 12).

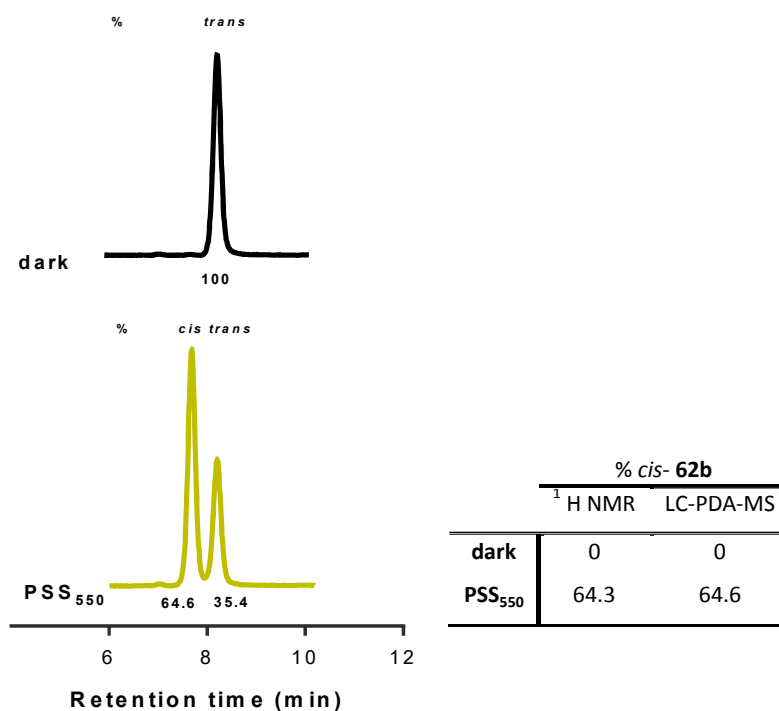


**Figure 51.** Identification of *trans*-**62b** in the dark (100 μM in DMSO/MeCN 1:9) and photostationary state (PSS) of **62b** analyzed by LC-PDA-MS after illumination with 550 nm.

**Table 12.** Photostationary states of the same compound **62b** in 5 mM in DMSO-*d*<sub>6</sub> determined by <sup>1</sup>H NMR and in 100 μM in DMSO/MeCN 1:9 measured by LC-PDA-MS after illumination with 550 nm.

## Pharmacological characterization of the putative *cis*-on compounds **62a-c**

Fanny Malhaire- IGF, Institut de Génomique Fonctionnelle, CNRS, INSERM Montpellier

To evaluate the possible *cis*-on mGlu<sub>5</sub> NAM activity for compounds **62a-c**, we generated dose-response curves extracted from IP accumulation assay with HEK293 cells transfected with mGlu<sub>5</sub> receptor. The assays were performed under illumination with 530 and 400 nm wavelengths to obtain a high percentage of *cis* and *trans* isomer respectively. Alloswitch-1 (**32a**) was used as photoswitchable control compound for this assay. However, the photoisomerization profile of Alloswitch-1 is different compared to the present series: illuminating with 400 nm would induce the *cis* form and *trans* active form is obtained upon illumination with 530 nm. Unfortunately, we could not find any *cis*-on profile in the dose-response curves (Figure 52) and all the three compounds displayed no activity as mGlu<sub>5</sub> NAMs neither in 530 nor upon 400-nm illumination.

\* In spectroscopy, an isosbestic point could be defined as a specific wavelength at which the total absorbance of a sample does not change during a physical change of the same sample. When the absorption spectra of two species are superimposed the isosbestic point corresponds to a wavelength at which these spectra cross each other and the two chemical species have identical molar absorption coefficients whose ratio, however, remains constant as the physical change proceeds.

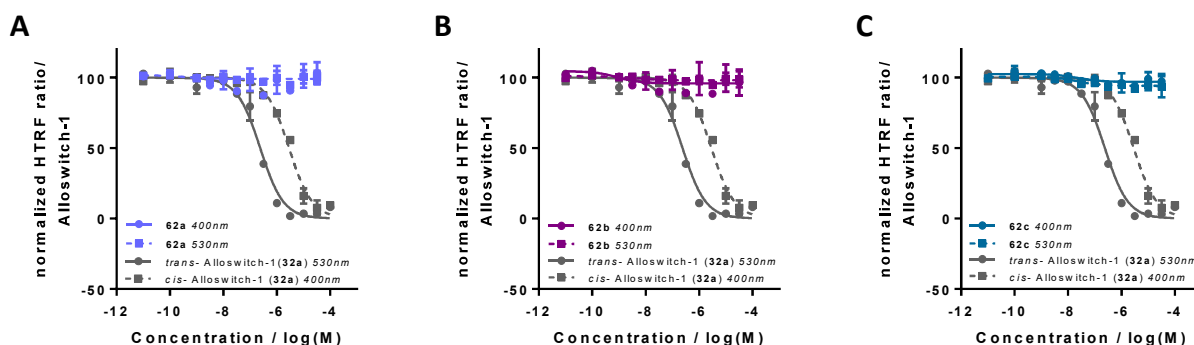


**Figure 52.** Pharmacological properties of compounds **62a-c**. Dose-response curve of compound (A) **62a** (violet), (B) **62b** (magenta) and (C) **62c** (turquoise) with a constant concentration of Quisqualate 100 nM in HEK293 cells overexpressing mGlu<sub>5</sub> in different conditions: under illumination at 400 nm (round dots and solid line), under illumination at 530 nm wavelength (square dots and dotted line). Alloswitch-1 (**32a**, grey lines) was used as a mGlu<sub>5</sub> NAM standard under illumination at 530 nm (round dots and solid line) and under illumination at 400 nm (square dots and dotted line). Each point corresponds to the mean of a minimum of two independent replicates with the corresponding SEM as error bars.

Despite the efforts in the design and photochemical characterization of the second series of compounds, we did not achieve our objective for the second time. However, the photochemical behavior, especially of the compounds **62a-c**, the relative simple chemical synthesis and the distinctive molecular structure led us to believe that changing the approach and accessing a third library of compounds to be tested as *cis*-on mGlu<sub>5</sub> NAMs, could be a worthy option to explore.

### Design of a third series: the 5-phenylazo-2-pyrazol-pyridines **66a-f**

To create a new library of *cis*-on mGlu<sub>5</sub> NAM candidates, we decided to re-apply the “azologization strategy” to compound **40** (Figure 53), still considered a good reference compound with a bent pose in the allosteric binding site. Again, our aim was to mimic this active bent position with a *cis*-azo bond in such a way that the corresponding *trans* isomer did not properly fit into the allosteric pocket due to its straight geometry and higher length. As already seen at the beginning of the chapter, the structure of **40** included just a single bond between two aromatic rings, which gave it a bent geometry and it was susceptible to be eliminated inserting an azo group in *cis*-form.

For the previous compounds **53**, **55**, **59** and **62a-c**, we inserted the azo group in *cis*-form in the molecular scaffold following *path a* (Figure 53). However, the same bent geometry could be achieved by inserting the azo group in *cis*-form via *path b* (Figure 53). Additionally, by including the *cis*- azo group in this second region, the difference in geometry between *trans* and *cis* isomers would be greater than that found in the pair of isomers of the two previous series. This led us to think that we might have had higher chances of obtaining photoswitchable compounds that do not exhibit mGlu<sub>5</sub> NAM activity in their *trans* configuration whereas, after illumination, their *cis* isomers do, due to the abrupt change in geometrical disposition.

To investigate better the influence of cyano and chlorine substituents in terms of electronic interactions within the allosteric pocket of the receptor, we inserted them in different positions in the phenyl ring. Thereby, the new analogs **66a-f** emerge from all these considerations (Figure 53).

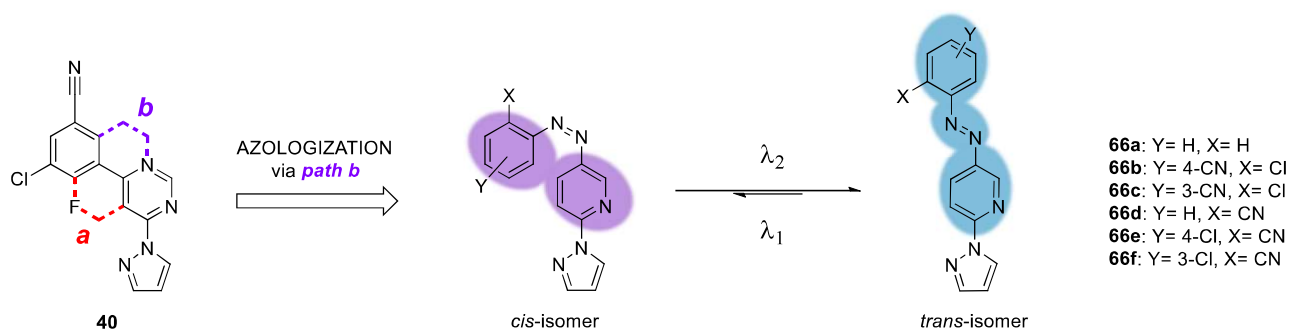


**Figure 53.** Azologization strategy following *path b* from compound **40** to afford the third library of *cis-on* photoisomerizable compounds (**66a-f**). The compounds include substitution by cyano and chlorine in three different positions of phenyl ring to probe the electronic properties of the compounds in the upper chamber of the allosteric pocket.

### *In silico* characterization of *trans* and *cis* configurations

Roser Borràs - MCS, Laboratory of Medicinal Chemistry and Synthesis, IQAC-CSIC, Barcelona

Before proceeding in the synthesis of the new compounds, we performed docking studies with the most promising compound of this new family in *trans* and *cis* configuration to check the suitability of the *cis-on* approach designed. Thus, we docked the parent compound **40** and M-MPEP (**42**) in the crystallized transmembrane domain of mGlu<sub>5</sub> receptor (PDB code: 5CGD, *Figure 54A*). These docked structures were compared with one compound from the past series that we already knew was not active (**62b**) and one from the new series (**66e**) (*Figure 54B,C*).<sup>92,236</sup>

In order to confirm the inactivity of the second series, we began the study with both isomers of compound **62b** docked in the receptor (*Figure 54B*). Indeed, **62b** in the *cis* configuration docked in a similar pose to compound **40** in the same model, whereas in the *trans* configuration the dockings did not result favorable from the very beginning (*Figure 54A* and *Figure 54B*). More precisely, the *trans* configuration of **62b** would not allow to occupy the lower space of the pocket, typically occupied by pyridine rings and involved in a series of hydrogen bonds with “Happy Water” and Ser809<sup>7,39</sup>. Concerning *cis*-**62b**, although it might adopt a similar binding-mode to the parent compound **40** at first sight, its azo moiety would rearrange in the same region as triple bond in M-MPEP (**42**) (*Figure 54A*) or Mavoglurant (**43**). This chamber of the receptor is known to be a narrow channel with critical polar interactions network (Tyr659<sup>3,44</sup>, Happy Water and Ser809<sup>7,39</sup>). The distortion of this narrow channel in the allosteric pocket by both isomers of **62b** could explain the lack of NAM activity of these series of compounds.

On the other hand, compound **66e** in its *cis* configuration showed a well-fitting docking very similar to that of **40** and M-MPEP (**42**) (*Figure 54C*) and its azo group would be located in an upper chamber of the allosteric pocket that would accept a higher degree of substitution. Instead, *trans*-**66e** could occupy a higher space in the allosteric pocket, displacing some water molecules, although these are not considered essential. However, this docking ended up with less attractive poses with a binding-mode far from that of **40** and M-MPEP (**42**) and therefore highly unlikely to be plausible.

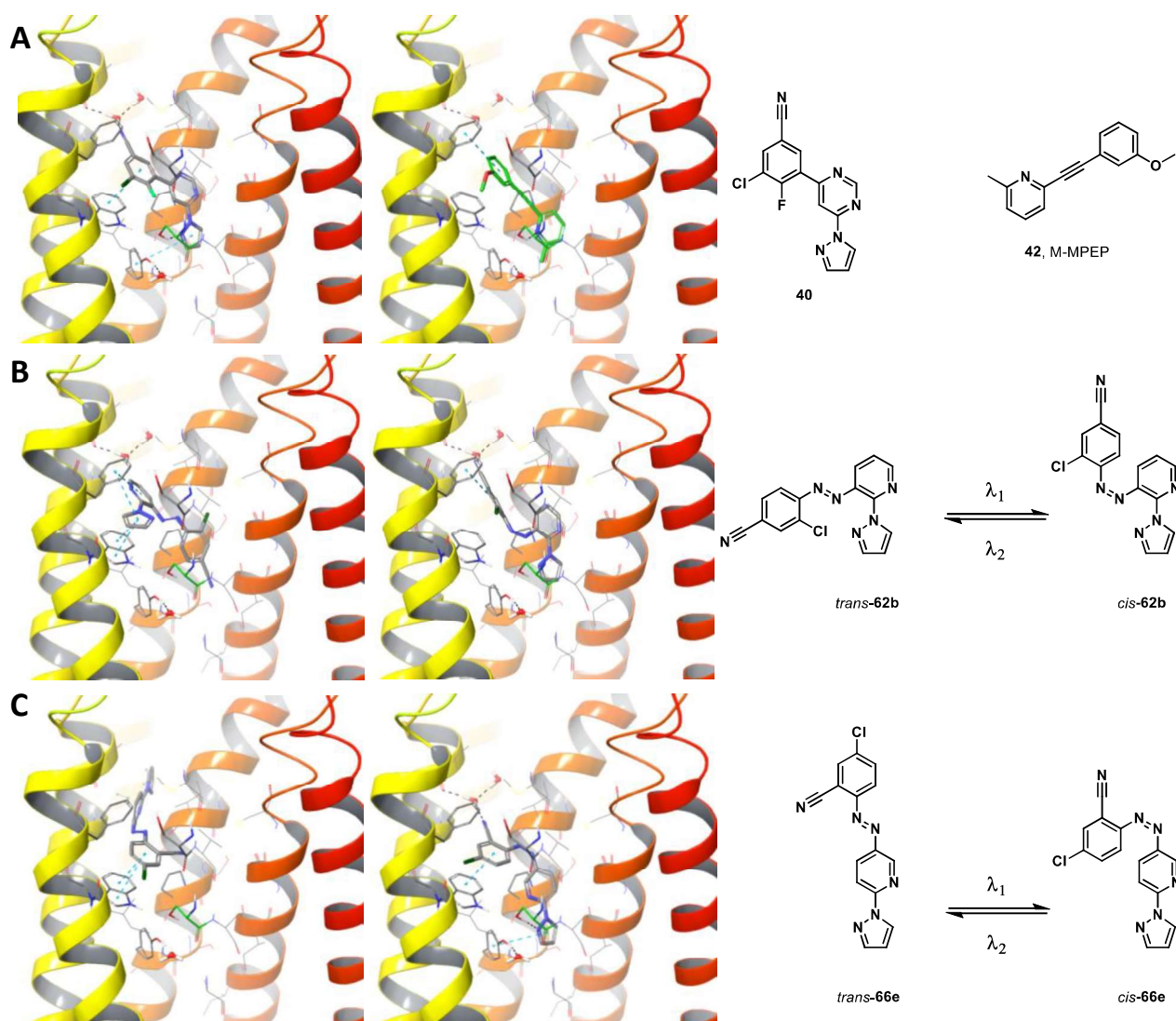


**Figure 54.** Compounds **40** (left) and M-MPEP (**42**) (right) (A), *trans* (left) and *cis* (right) isomers of **62b** (B) and *trans* (left) and *cis* (right) isomers of **66e** (C) docked in the crystal structure of mGlu<sub>5</sub> receptor (PDB code: 5CGD).<sup>92,236</sup> The allosteric binding pocket is shown from the side (TM7 has been removed for clarity). mGlu<sub>5</sub> in ribbon representation colored yellow, orange and red. Compounds in stick representation with carbon, nitrogen, oxygen, chlorine, fluorine atoms colored grey (green for M-MPEP (**42**)), blue, red, dark green, and green, respectively.

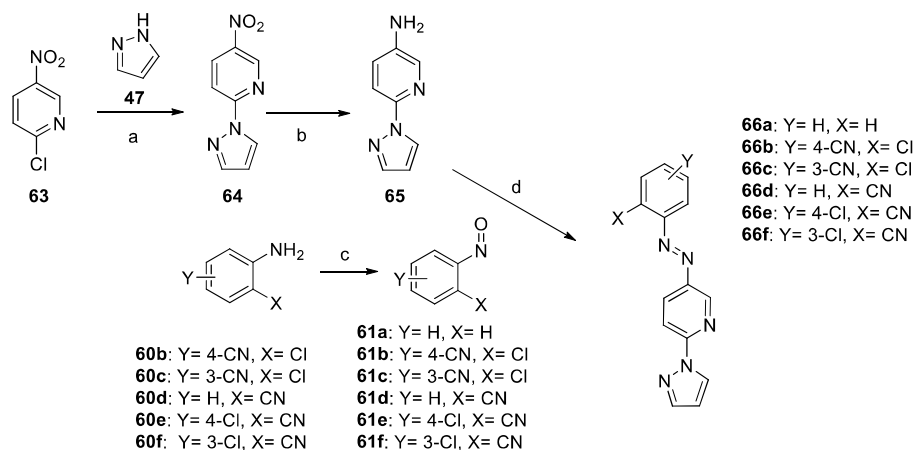
In the end, we were able to conclude from these dockings that the previous series of compounds are less likely to be successful as mGlu<sub>5</sub> NAMs because, despite the poses of the corresponding *cis* isomers are reasonable, the azo-bond is occupying a chamber that was reported to be sensitive for the receptor structure. This could explain the lack of pharmacological activity observed. Instead, compound **66e** within the third series constitutes a promising candidate for becoming *cis*-on photoswitchable mGlu<sub>5</sub> NAMs.

### Synthesis of analogs 66a-f

Compounds **66a-f** were prepared following a synthetic strategy similar to the previous two series and it is depicted in *Scheme 6*. The first step consisted of Cs<sub>2</sub>CO<sub>3</sub>-promoted nucleophilic substitution of 2-chloro-5-nitropyridine (**63**) with 1*H*-pyrazole (**47**). The obtained nitro compound (**64**) was reduced through palladium-catalyzed hydrogenation to give aniline **65** in high yield. The azo compound **66a-f** were prepared via Mills reaction in good yields by reacting aniline **65** with nitroso derivatives **61a-f** in acidic media. The



nitroso compounds **61a-f** were prepared by amine oxidation of the corresponding anilines (**60a-f**) with Oxone<sup>®</sup> following the procedure described by Priewisch.<sup>243</sup>



**Scheme 6.** Synthesis of compounds **66a-f**. Reagents and conditions: (a) Cs<sub>2</sub>CO<sub>3</sub>, anhydrous MeCN, 85 °C, 16 h, 87%; (b) H<sub>2</sub> (2 atm), Pd/C, EtOH, rt, 3 h, 81%; (c) Oxone<sup>®</sup>, DCM/H<sub>2</sub>O 1:4, rt, 1.30-16 h, 12-96%; (d) AcOH excess, rt, DCM, 2-4 days, 54-82%.

## Photochemical and pharmacological characterization of the third series

### UV-Vis absorption spectroscopy

As performed for the previous families, we measured UV-Vis absorption spectra of the *trans* isomers and the PSS after different wavelength illuminations to characterize the photoisomerization of the azo compounds. We first measured the UV-Vis absorption spectra of all the compounds within the family in a mixture of water and acetonitrile with 0.05% of formic acid by LC coupled simultaneously to a photodiodes array (PDA) and a mass spectrometer (MS). In contrast to the compounds of the second series, the new compounds **66a-f** include the bulky pyrazolyl substituent in the *para* position to the azo moiety. This substitution *para* conferred a more standard azobenzene photochemical behavior to the compounds: the *trans*-azobenzene  $\pi$ - $\pi^*$  transition band was found at 340-360 nm in dark conditions and the *cis*  $n$ - $\pi^*$  transition band around 430-450 nm.

After that, we tested the photoisomerization conditions with samples 50  $\mu$ M of the compounds **66a-f** in DMSO under different light conditions. Thus, we collected UV-Vis spectra in the dark and after 3 minutes of continuous illumination with 365, 380, 405, 455, 500 and 550 nm wavelengths to obtain the spectra corresponding to the PSS at each illumination wavelength. For all the compounds we obtained very similar photoisomerization properties. The optimal wavelengths to obtain the *cis* isomers were 365 and 380 nm, corresponding to the minimum of absorbance of the *cis* isomers, whereas upon 455 nm and even 500/550 nm we recovered a considerable fraction of the *trans* isomer (Figure 55). At these region (430-500 nm) of the spectra, the *trans* compounds absorb less than the *cis* ones, since the planarity of these long *trans* isomers makes the  $n$ - $\pi^*$  band forbidden by symmetry. For compounds **66e-f**, containing the cyano group in *ortho* position in combination with chlorine substituent in the same phenyl ring, the photoswitching *cis*  $\rightarrow$  *trans* with 455 nm and 500/550 nm was more effective.

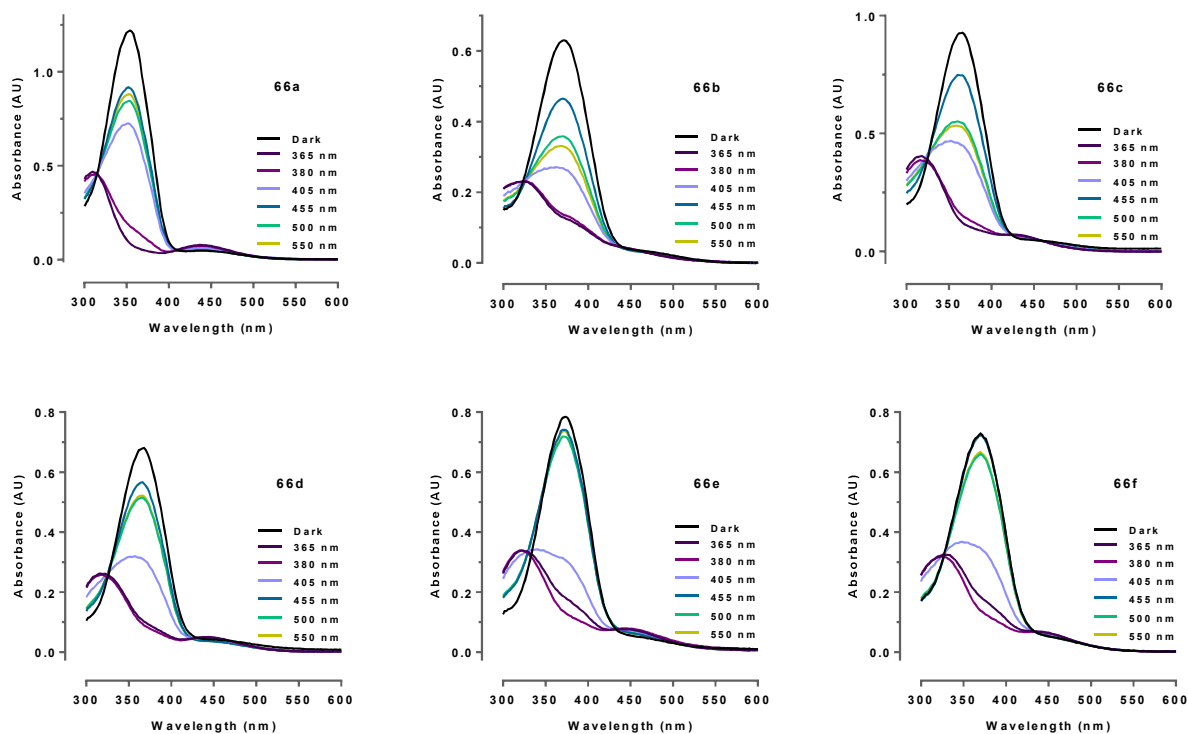


**Figure 55.** UV-Vis absorption spectra of the compounds **66a-f** 50  $\mu$ M in DMSO at 25°C in the dark (black) and different illumination conditions. Illumination with 365 and 380 nm wavelengths affords very similar profiles.

The thermal relaxation of the *cis* isomers in aqueous media was also evaluated. The preliminary results indicate that the six *cis*-**66a-f** show a high bistability both in DMSO and aqueous media (> 6 days). However, these compounds are very insoluble in aqueous media and show precipitation with time. For that reason, the absorption readings over time were decreasing in intensity and it was not possible to fit an exponential decay function. We believe that this low solubility is a consequence of the lack of polar groups in the molecular structure and the highly planar aromatic structure, that tends to form  $\pi$ - $\pi$  stacking and, thus, precipitation of the compounds.

#### ***In vitro* endpoint functional assay: dose-response curves**

Fanny Malhaire- IGF, Institut de Génomique Fonctionnelle, CNRS, INSERM Montpellier

To evaluate the possible *cis*-on mGlu<sub>5</sub> NAM activity for compounds **66a-f**, dose-response curves were extracted from IP accumulation assay with HEK293 cells transfected with mGlu<sub>5</sub> receptor. The assays were performed with 100 nM of the orthosteric agonist quisqualate in the dark and 380-nm light conditions. MCS0331 (**32b**) was used as photoswitchable NAM control compound for this assay. Unfortunately, all the six compounds displayed no activity as mGlu<sub>5</sub> NAMs neither in dark nor upon 380-nm illumination.

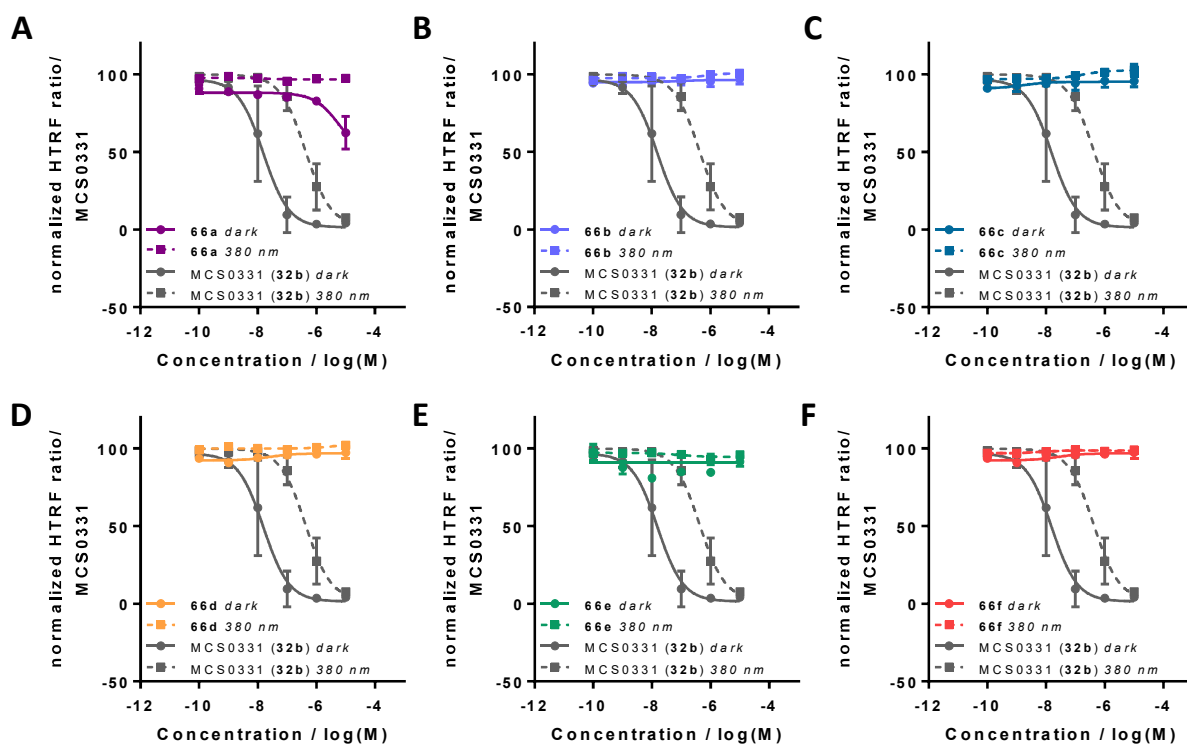


**Figure 56.** Pharmacological properties of compounds **66a-f**. Dose-response curve of compound (A) **66a**, (B) **66b**, (C) **66c**, (D) **66d**, (E) **66e** and (F) **66f** with a constant concentration of Quisqualate 100 nM in HEK293 cells overexpressing mGlu<sub>5</sub> in different conditions: in dark conditions (round dots and solid line) and under illumination at 380 nm wavelength (square dots and dotted line). MCS0331 (**32b**) was used as a mGlu<sub>5</sub> NAM standard in dark conditions (round dots and grey line) and under illumination at 380 nm (square dots and grey dotted line). Each point corresponds to the mean of a minimum of two independent replicates with the corresponding SEM as error bars.

## Conclusions

We designed compounds **53**, **55**, **59** and **62a-c** as candidates to display NAM activity in mGlu<sub>5</sub> receptors in their *cis* configuration and no activity in their *trans* configuration. This was based on a search in the literature for mGlu<sub>5</sub> NAMs with a bent disposition to mimic *cis* azobenzene geometry. Thus, the linear *trans* azo mimetic isomer would be too long to fit in the allosteric binding site of mGlu<sub>5</sub> receptor.

The compounds **53**, **55**, **59** and **62a-c** were synthesized and fully characterized photochemically using the three most common methodologies to measure photoisomerization: UV-Vis spectroscopy, nuclear magnetic resonance (NMR) and liquid chromatography coupled to a photodiode array and/or mass spectroscopy (LC/PDA/MS). While compounds **53**, **55** and **59** can be photoisomerized from *trans* to *cis* isomer with 380-nm light and from *cis* to *trans* isomers with 455nm, compounds **62a-c** display bidirectional photoswitching without using UV light (*trans* → *cis* with green light (530-560 nm) and *cis* → *trans* with blue light (430-460 nm)). Additionally, the *cis* isomers of this latter type of compounds are extremely stable over the time. All together, these are excellent characteristics for ideal *in vivo* applications.

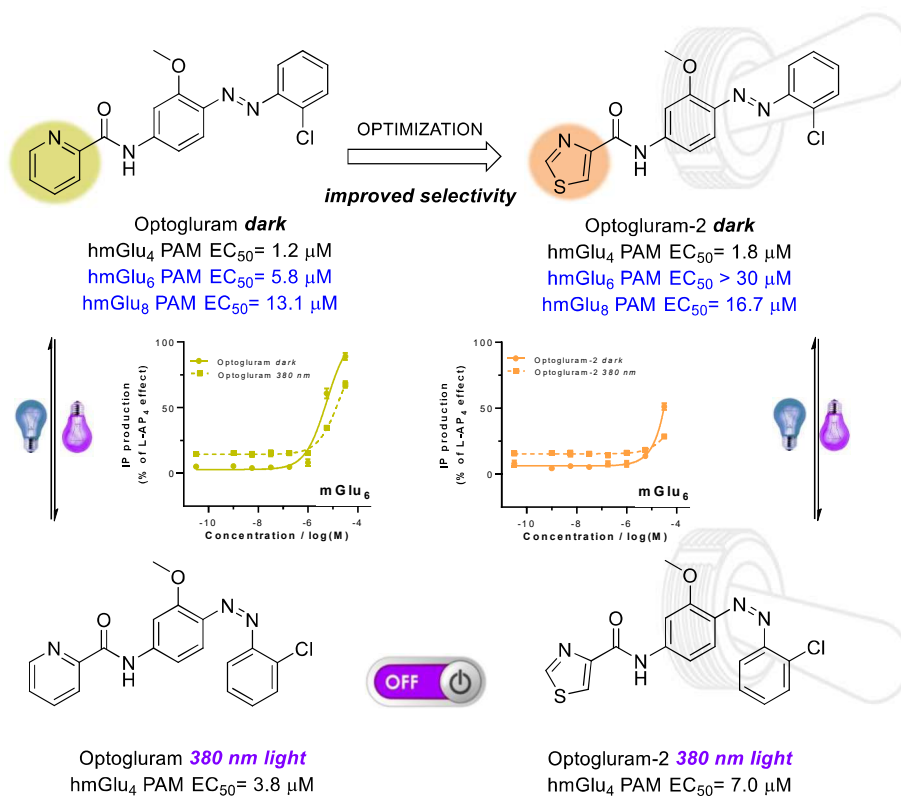
The compounds **53**, **55**, **59** and **62a-c** resulted inactive as mGlu<sub>5</sub> NAM in cell-based IP accumulation assays. A potential mGlu<sub>5</sub> PAM activity needs to be explored with the appropriate pharmacological assays.

Due to the inactivity shown both in dark and under illumination conditions, a third series of compounds was designed following a second azologization strategy and with computational support. The compounds were docked in the crystal structure of mGlu<sub>5</sub> receptor, showing promising results in their *cis* configuration.

The compounds **66a-f**, belonging to the third series, were synthesized and fully characterized photochemically with UV-Vis spectroscopy. These compounds have regular ABs photochemical behavior: they can be photoisomerized from *trans* to *cis* isomer with 365-nm or 380-nm light, from *cis* to *trans* isomers with 450 nm and the *cis* isomers were characterized by highly slow thermal relaxation times.

After the corresponding pharmacological evaluation in the dark and under 380 nm illumination, the analogs **66a-f** were found to display no activity as *cis*-on mGlu<sub>5</sub> NAMs. This leads us to the conclusion that we did not achieve our main objective for this project. Nevertheless, a potential mGlu<sub>5</sub> PAM activity should to be explored with the appropriate pharmacological assays.

## Chapter 2: Development of a selective photoswitchable PAM for mGlu<sub>4</sub> receptor



### Key points

- Photoswitchable mGlu<sub>4</sub> PAMs supporting the *trans*-on Optogluram-like approach
- Optimization of a series of compounds driven by SAR
- Improvement of selectivity over mGlu<sub>6/7/8</sub> receptors
- Very consistent *on/off* photoswitching of mGlu<sub>4</sub> activity

### Paper related to this chapter

- Silvia Panarello, Alice Berizzi, Fanny Malhaire, Carme Serra, Jean-Philippe Pin, Laurent Prézeau, Cyril Goudet, Amadeu Llebaria and Xavier Gómez-Santacana, “Development of a selective photoswitchable PAM for the metabotropic glutamate receptor subtype 4”. In preparation.

There is a growing interest in targeting the metabotropic glutamate receptor subtype 4 (mGlu<sub>4</sub>) due to its implication in a number of disease states, such as Parkinson's disease, epilepsy, anxiety and fear processing.<sup>245-248</sup> Selective activation of this receptor, via either subtype selective agonists or positive allosteric modulators (PAMs), has been shown to significantly reduce or eliminate motor symptoms in preclinical models of Parkinson's disease (PD).<sup>249</sup> Additionally, mGlu<sub>4</sub> PAMs have been proposed as potential novel therapeutics for the palliative treatment of some forms of epilepsy.<sup>250,251</sup>

Work from a number of laboratories has led to the development of more selective tools for the study of mGlu<sub>4</sub>, as well as refined models of the structure and function of this receptor. The increased understanding of the role of mGlu<sub>4</sub> combined with more detailed structural information are encouraging the development of better pharmacological tools, and ultimately to novel clinical therapies.

In the General Introduction section of the present thesis,<sup>\*</sup> we showed the design and development of Optogluram (**38**) as photoisomerizable allosteric modulator of mGlu<sub>4</sub>. After obtaining such outstanding results, we decided to use Optogluram as attractive starting point for optimization of the selectivity in order to obtain a possible improved *in vivo* tool compound. In the present chapter, we describe the first modifications to the structure of Optogluram (**38**) to generate a small library of azobenzene candidates with the aim of maintaining or enhancing the PAM activity on mGlu<sub>4</sub> receptor and decreasing that one over the other group III glutamate receptors.

### Design of Optogluram analogs

The chemical design of photoswitchable compounds targeting the metabotropic glutamate receptor subtype 4 (mGlu<sub>4</sub>) was based on Optogluram (**38**), the first photoswitchable positive allosteric modulator targeting mGlu<sub>4</sub> receptor, discovered in our research group.<sup>46,98,133</sup> During the optimization process, we decided to preserve the external 2-chlorophenyl ring and the 3-methoxy substituent in the central aromatic ring since both groups were important in the development of a series of *N*-(4-acetamido) phenylpicolinamides as positive allosteric modulators of mGlu<sub>4</sub> receptor (*e.g.* VU0416374 (**37**), *Figure 57A*).<sup>232</sup> In fact, the central phenyl ring containing a 3-methoxy moiety or 3-chloro and the 2-chlorophenyl amide resulted to be crucial to guarantee a nanomolar potency. Different substitutions in the central phenyl ring as well as in the aforementioned amide portion led to a significant decrease in activity.

Thus, we decided to focus our structure-activity relationship on key substituents on the picolinamide moiety and the central phenyl ring of Optogluram (**38**), as well as on two different five-membered heterocyclic amides to replace the aforementioned picolinamide group. These modifications provided analogs **71a-d** and **74a-b** (*Figure 57B*). Both structural modifications were designed to decrease activity at mGlu<sub>6/8</sub> hopefully maintaining intact mGlu<sub>4</sub> PAM activity.

---

\* See General Introduction: Freely diffusible photoswitchable allosteric modulators for mGluRs



				Photoisomerization	
Cpd.	het	X	Y	<i>trans</i> <sup>[a]</sup> $\lambda_{\max}(\pi-\pi^*)$ <sup>[b]</sup> [nm]	<i>PSS</i> <sub>380</sub> <sup>[c]</sup> $\lambda_{\max}(n-\pi^*)$ <sup>[b]</sup> [nm]
<b>71a</b>		Cl	H	385	434
<b>71b</b>		F	H	391	434
<b>71c</b>		Cl	Cl	391	436
<b>71d</b>		F	Cl	390	432
<b>74a</b>		-	H	385	433
<b>74b</b>		-	H	390	435

[a] Experiments performed in the dark to characterize 100% *trans* isomer.

[b] The absorbance maxima were extracted from UV/Vis spectra (25  $\mu$ M in DMSO at 25°C).

[c] Photostationary state upon illumination with 380 nm light to obtain a high % of *cis* isomer.

**Table 13.** Photoisomerization properties of analogs **71a-d** and **74a-b** determined at 25  $\mu$ M dimethyl sulfoxide (DMSO) at 25 °C.

The obtained UV-Vis spectra of compounds **71a-d** and **74a-b** showed the archetypical profile of *N*-amido azobenzenes.<sup>98,252</sup> In the dark, all six compounds showed the typical *trans*-azobenzene  $\pi-\pi^*$  transition band at 380-390 nm. The *E/Z* isomerization could be achieved under illumination at this range of wavelengths, as we did with 380 nm or 420 nm light to obtain a solution of mainly the *cis* isomers. We identified the *cis* isomers from a  $\pi-\pi^*$  transition band at 270-300 nm and a weaker  $n-\pi^*$  transition band near 430 nm, which is forbidden by the symmetry for *trans* azobenzenes. All the six azo compounds were back-isomerized to their thermodynamically stable *trans* isomer by using turquoise light (455-470 nm) (Figure 58B) or allowing them to thermally isomerize in the dark.

The photoisomerization properties of azo compound **74a** in DMSO were also examined by HPLC-MS analysis (Figure 58C). In the dark, 100% of *trans*-**74a** was observed, whereas a PSS of 64.5% *cis*-**74a** was detected after 380-nm illumination. Subsequent illumination with 470 nm wavelength afforded a PSS of 67.3% *trans*-**74a**. This ratio was calculated from the area of the corresponding peaks at 324 nm, since we determined that 324 nm was isobestic point in the UV-Vis spectra (Figure 58C).<sup>\*</sup> Additionally, the photoisomerization after several photoisomerization cycles was determined with a solution in DMSO recording the absorbance values after alternatively illuminating at 380 nm and 455 nm. No considerable differences were observed with the absorbance values under turquoise or violet light of the different cycle, showing robust photoisomerization process with no apparent degradation (Figure 58D).

\* In spectroscopy, an isobestic point could be defined as a specific wavelength at which the total absorbance of a sample does not change during a physical change of the same sample. When the absorption spectra of two species are superimposed the isobestic point corresponds to a wavelength at which these spectra cross each other and the two chemical species have identical molar absorption coefficients whose ratio, however, remains constant as the physical change proceeds.



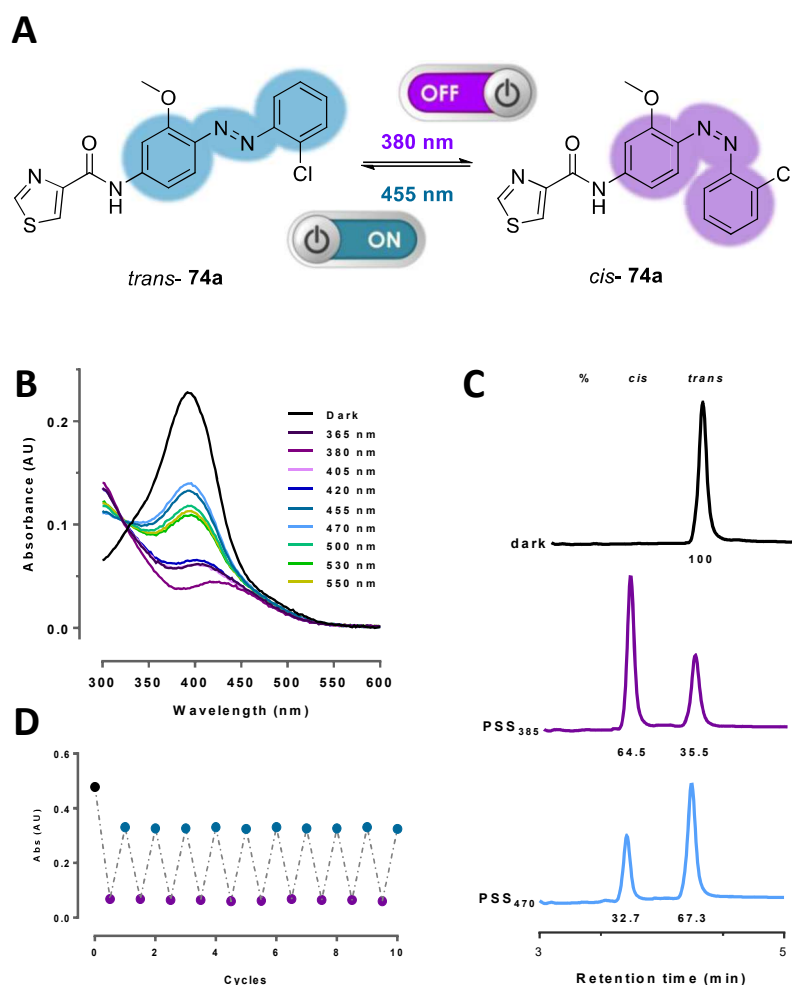


**Figure 58.** Photochemical properties of compound **74a**. (A) 2D structure of *trans/cis* isomers; (B) UV/Vis absorption spectra of **74a** 25  $\mu\text{M}$  in DMSO at 25°C under dark (black) and different light conditions for 3 min; (C) Photostationary state (PSS) quantification of **74a** 100  $\mu\text{M}$  in DMSO/MeCN 1:9 at 25°C by HPLC-MS. The measurement was performed in the dark and after illuminating the sample was for 3 min with 380 and 470 nm light sources; (D) UV/Vis absorption measurements of 25  $\mu\text{M}$  **74a** in DMSO at  $\lambda_{\pi-\pi^* \text{max}}$  of *trans* isomer (385 nm) after repeated cycles of illumination with 380 (violet) and 455 nm light (turquoise).

## Pharmacological characterization of the putative mGlu<sub>4</sub> PAMs

*In collaboration with Xavier Gómez Santacana and Alice Berizzi- IGF, Institut de Génomique Fonctionnelle, CNRS, INSERM Montpellier*

### Single dose screening

The azo compounds **71a-d** and **74a-b** were first screened at single dose (30  $\mu\text{M}$ ) in dark and under 380 nm illumination conditions simultaneously to their PAM activity as mGlu<sub>4</sub> and mGlu<sub>6</sub> PAMs using a constant concentration of an orthosteric agonist (*i.e.* L-AP<sub>4</sub>, 5 nM or 100 nM for mGlu<sub>4</sub> and for mGlu<sub>6</sub> respectively). We used a cell-based inositol phosphate (IP) accumulation assay with HEK293 cells transiently transfected with the corresponding mGlu receptor and a chimeric G<sub>αq</sub> protein that is able to bind all mGlu receptors.

Through this initial screening we were able to rapidly exclude from the study compounds **71c** and **71d**, which displayed no significant activity neither over mGlu<sub>4</sub> nor mGlu<sub>6</sub> receptor (Figure 59). Based on these data, we could state that the addition of a substituent in the 6-position of the central ring reduce drastically

the activity in both mGlu<sub>4</sub> and mGlu<sub>6</sub> receptor. In contrast, the rest of compounds at 30  $\mu$ M activated considerably mGlu<sub>4</sub> but minimally activated mGlu<sub>6</sub>, a welcomed departure for the next experiments.

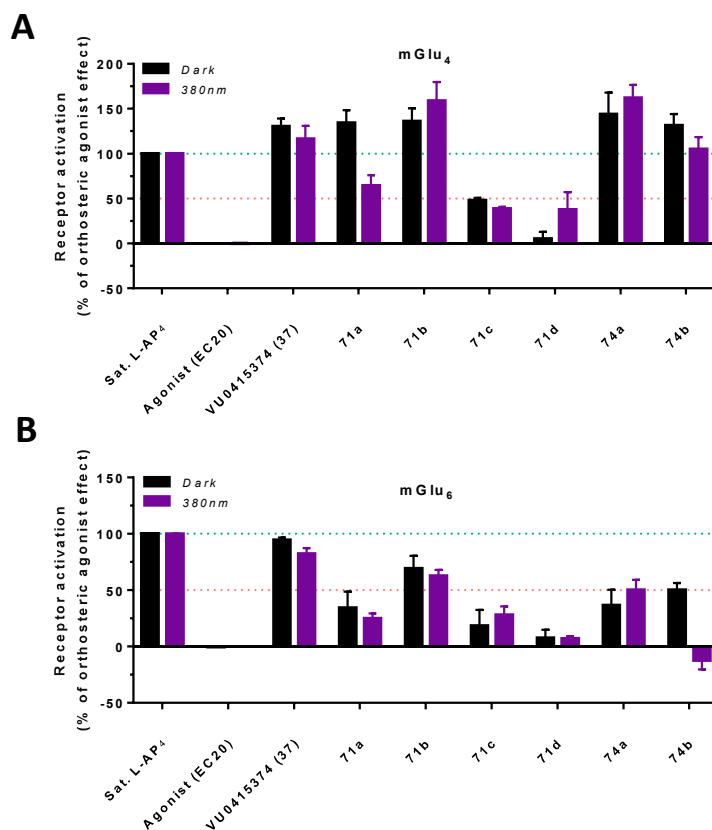


**Figure 59.** Screening of compounds **71a-d** and **74a-b** in mGlu<sub>4</sub> and mGlu<sub>6</sub>. Assay performed in mGlu<sub>4/6</sub> transiently transfected HEK293 cells with 5 nM or 100 nM of L-AP<sub>4</sub> respectively (EC<sub>20</sub>) and 30  $\mu$ M of each compound, in dark conditions (black bars) and under 380 nm-illumination (violet bars). Normalization is done between 0= agonist (EC<sub>20</sub>) and 100%= activation by L-AP<sub>4</sub>.

### Dose-response curves

The functional activity of **71a-b** and **74a-b** was further studied in mGlu<sub>4</sub>, mGlu<sub>6</sub> and mGlu<sub>8</sub> receptors. Thus we generated dose-response curves with the same IP accumulation assay in HEK293 cells transiently expressing the human isoform of the aforementioned mGlu receptors and the chimeric G<sub>αq</sub> protein. To evaluate the light-dependent effects, we simultaneously generated two curves for each compound, by incubating the cells with the azo compounds in the dark and under illumination at 380 nm. As a result, we obtained the potencies (EC<sub>50</sub>) for each compound under both conditions (*Table 14*).

Considering the activity on mGlu<sub>4</sub> receptor, we noted that the four compounds displayed an activity in a micromolar range in the dark, but only azo compounds **71b** and **74a** had potencies in line with Optogluram (**38**) (*Table 14*). From the assessment of their PAM activity in mGlu<sub>6</sub> and mGlu<sub>8</sub>, all compounds resulted practically inactive in mGlu<sub>6</sub>. In contrast, compound **71b** appeared to be the least active of all the library in mGlu<sub>8</sub>, while the rest of compounds displayed a similar potency than Optogluram (**38**).

When considering the assays performed under illumination, we noted that 380-nm irradiation induced a right shift of the dose-response curves when compared to the non-illuminated compounds, compatible with a loss of the PAM potency of the *cis* isomers. This confirms that the active isomers of these new azobenzene candidates are the *trans* isomers, supporting the *trans*-on Optogluram-like approach.

Additionally, the observed photoinduced potency shift is larger in the four azo compounds **71a-b** and **74a-b** than in Optogluram (**38**), which may induce an improved *on/off* photoswitching in coming more complex assays, such as *in vivo* assays (Table 15). Concerning all the results, we can conclude that **71b** and **74a** display a similar activity than Optogluram (**38**) but only compound **74a** displays a selectivity profile versus mGlu<sub>6</sub> and mGlu<sub>8</sub> satisfactory, since compound **71b** displays considerably PAM activity on mGlu<sub>6</sub> receptor. Added to the improved photoswitching properties above mentioned, all these results indicate that compound **74a** emerged as the mGlu<sub>4</sub> photoswitchable PAM with the best profile to date.

Pharmacological Characterization									
Cpd.	het	X	Y	hmGlu <sub>4</sub> <sup>[a]</sup> pEC <sub>50</sub> ± SEM		hmGlu <sub>6</sub> <sup>[a]</sup> pEC <sub>50</sub> ± SEM		hmGlu <sub>8</sub> <sup>[a]</sup> pEC <sub>50</sub> ± SEM	
				<i>trans</i> <sup>[b]</sup>	PSS <sub>380</sub> <sup>[c]</sup>	<i>trans</i> <sup>[b]</sup>	PSS <sub>380</sub> <sup>[c]</sup>	<i>trans</i> <sup>[b]</sup>	PSS <sub>380</sub> <sup>[c]</sup>
<b>38</b>		H	H	6.0 ± 0.1	5.5 ± 0.2	5.2 ± 0.0	4.7 ± 0.0	5.0 ± 0.2	4.5 ± 0.5
<b>71a</b>		Cl	H	5.2 ± 0.1	<4.5	<4.5	<4.5	5.0 ± 0.0	<4.5
<b>71b</b>		F	H	5.7 ± 0.1	4.9 ± 0.3	<4.5	<4.5	<4.5	<4.5
<b>74a</b>		-	H	5.7 ± 0.1	5.2 ± 0.1	<4.5	<4.5	4.8 ± 0.2	<4.5
<b>74b</b>		-	H	5.3 ± 0.1	<4.5	<4.5	<4.5	4.7 ± 0.2	<4.5

[a] HEK293 human cells transiently transfected with mGlu receptors.  
 [b] Experiments performed in the dark to characterize 100% *trans* isomer.  
 [c] Photostationary state upon illumination with 380 nm light to obtain a high % of *cis* isomer.

**Table 14.** Pharmacological characterization of analogs **71a-b**, **74a-b** and Optogluram (**38**) with IP accumulation assay. The measured pEC<sub>50</sub> in dark and light conditions are shown as the mean ± SEM of at least three independent experiments, each performed in duplicate.

However, the IP accumulation assays described make use of a G<sub>αq</sub> pathway, which is not the canonical pathway for the mGlu<sub>4</sub> receptor. Thus, we wanted to confirm the results obtained in mGlu<sub>4</sub> using a cyclic adenosine monophosphate (cAMP) accumulation assay to measure cAMP modulations in response to the G<sub>αi/o</sub>-activation, which is the canonical signaling pathway of group III mGlu receptors, including mGlu<sub>4</sub>. In this case, we used an inducible stable HEK293 cell line expressing the rat isoform of mGlu<sub>4</sub>. As performed before, the light-dependent effects were evaluated in parallel, simultaneously generating two curves for each azo compound, in the dark and under illumination at 380 nm.

When analyzing the results obtained with the cAMP canonical pathway, we obtained EC<sub>50</sub> in the nanomolar range (8.4 ≤ pEC<sub>50</sub> ≤ 6.6, Table 15). Those results were unexpected since the IP accumulation assays showed an activity of the same compounds in a micromolar range. As observed in the IP accumulation assays, compounds **71b** and **74a** had a potency in the dark more similar to Optogluram (**38**) than to **71a** and **74b**, which were visibly less active. From the four azo compounds, **74a** was the most potent and the one that shows a greater photoinduced potency shift (1.29 log-fold) after illuminating at 380 nm, which is larger than that for Optogluram (PPS=1.00 log-fold, Table 15).

Pharmacological Characterization												
	cAMP assay						IP assay					
	het											

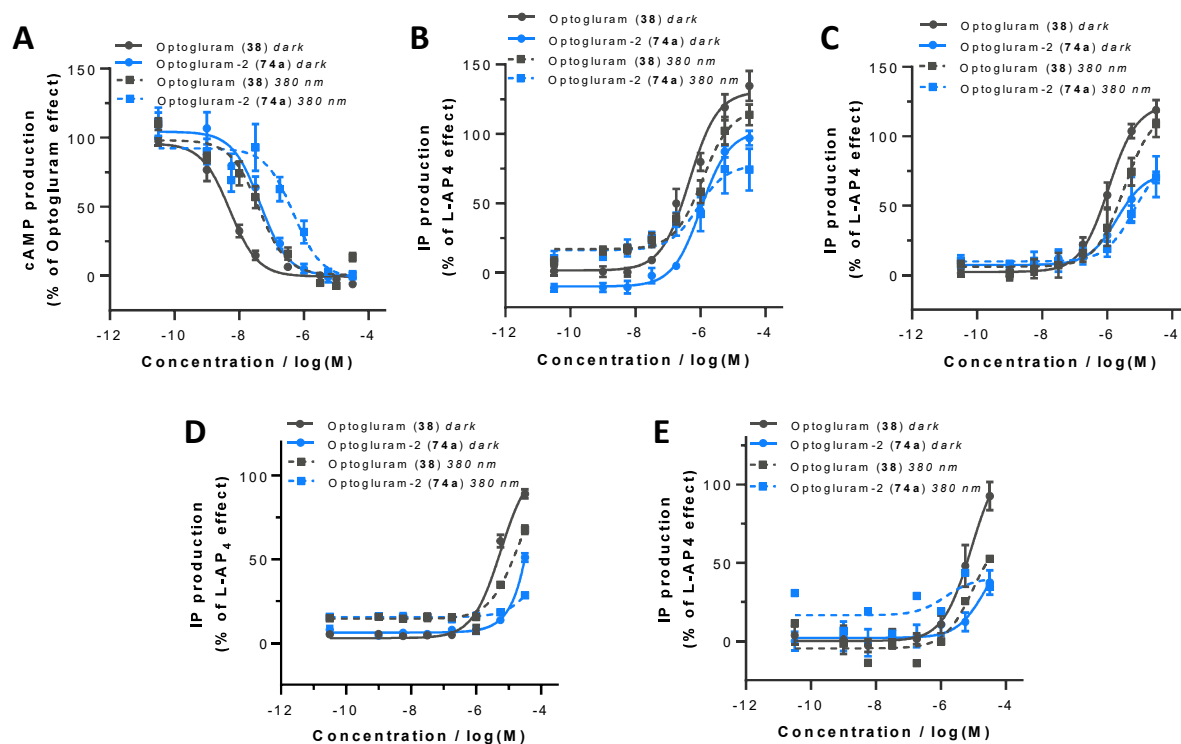


**Figure 60.** Pharmacological properties of Optoglutram-2 (**74a**). Dose-response curve of Optoglutram-2 (**74a**) with a constant concentration of L-AP<sub>4</sub> 5 nM in HEK293 stable mGlu<sub>4</sub> rat cell line with a cAMP assay (A) and in mGlu<sub>4</sub> transiently transfected rat cells with an IP assay (B) in dark conditions (rounded spots and blue solid line) and under illumination at 380 nm of wavelength (square dots and blue dotted line). Optoglutram (**38**) was used as a photoswitchable mGlu<sub>4</sub> PAM standard in dark conditions (round dots and grey solid line) and under illumination at 380 nm (square dots and grey dotted line). Dose-response curve of Optoglutram-2 (**74a**) with a constant concentration of L-AP<sub>4</sub> 5 nM in mGlu<sub>4</sub> transiently transfected human cells (C), 200 nM in mGlu<sub>6</sub> transiently transfected human cells (D) and 10 nM in mGlu<sub>8</sub> transiently transfected human cells (E) with an IP assay in dark conditions (rounded spots and blue solid line) and under illumination at 380 nm of wavelength (square dots and blue dotted line). Optoglutram (**38**) was used as a photoswitchable mGlu<sub>6/8</sub> PAM standard in dark conditions (round dots and grey solid line) and under illumination at 380 nm (square dots and grey dotted line).

### Selectivity of Optoglutram-2 (**74a**)

The selectivity of Optoglutram-2 (**74a**) was also studied over the remaining mGlu subtypes at a single dose of 30  $\mu$ M with different concentrations of agonists, depending on the mGlu subtype and the desired effect to measure: PAM or NAM activity (Figure 61A,B respectively). Additionally, it was compared with the selectivity of Optoglutram (**38**).

We used the IP accumulation assay in HEK293 cell overexpressing the corresponding receptors. Despite being slightly less potent than Optoglutram (**38**) as mGlu<sub>4</sub> PAM, Optoglutram-2 (**74a**) was found to be selective among all the mGlu receptors with a very negligent PAM activity over mGlu<sub>6</sub> and mGlu<sub>8</sub> (Figure 61A,B)

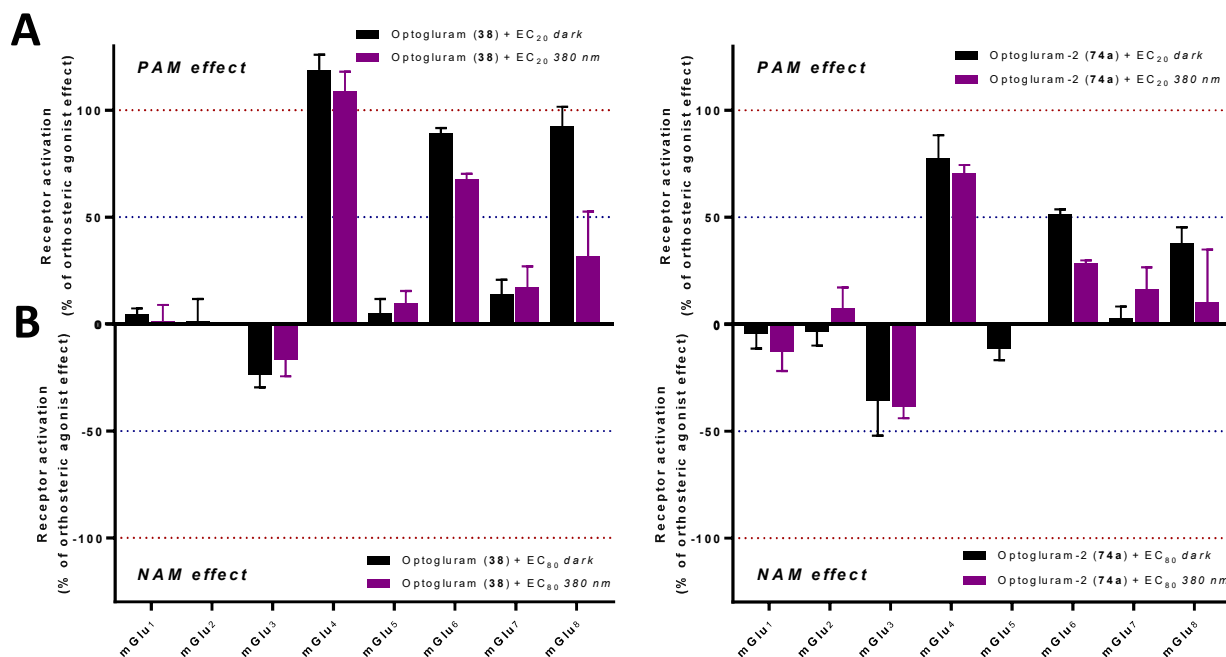


**Figure 61.** Selectivity profile of Optogluram-2 (**74a**) and Optogluram (**38**) among all the mGlu subtypes as PAM (A) and as NAM (B) in dark conditions (black bars) and 380 nm-illumination (violet bars).

## Conclusions

With this work, we present an initial library of photoswitchable mGlu<sub>4</sub> PAMs exploring a little SAR based on the Optogluram structure. Optogluram (**38**) was reported as the first photoswitchable mGlu<sub>4</sub> and is able to control persistent pain-related symptoms in a temporally and spatially restricted manner. However, Optogluram is also a PAM of mGlu<sub>6</sub>, with a slightly lower potency.<sup>46</sup>

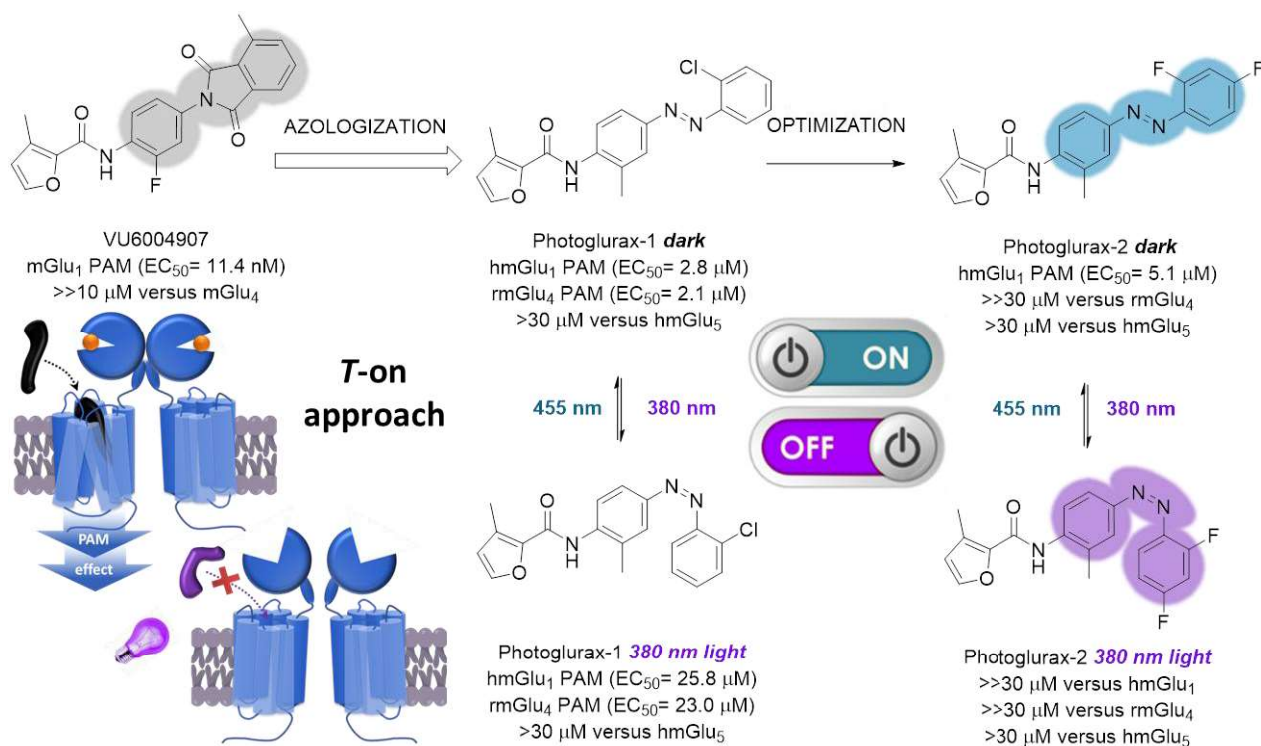
From the present generation of new mGlu<sub>4</sub> PAM candidates, compounds **71b** and Optogluram-2 (**74a**) emerged as potent mGlu<sub>4</sub> PAMs in the *trans* isomer, both in human and rat mGlu<sub>4</sub> isoform, likewise to Optogluram. However, only Optogluram-2 (**74a**) emerged as the mGlu<sub>4</sub> PAM with a full mGlu<sub>4</sub> selectivity profile over the other group III glutamate receptors.

Under 380 nm light the potency of Optogluram-2 (**74a**) is significantly reduced. The observed photoinduced potency shift is larger in Optogluram-2 (**74a**) than in Optogluram (**38**), which may induce an improved *on/off* photoswitching in coming more complex assays, such as *in vivo* assays.

Overall, the results here disclosed present Optogluram-2 (**74a**) as an improved small diffusible drug-like photoswitchable ligand that can be used to regulate behavior in a disease model based in mGlu<sub>4</sub> receptor, such as neuropathic pain, but also to other models such as Parkinson disease.

Added to the possibilities that photopharmacology offers, such as the spatiotemporal control of the compound activities, Optogluram-2 (**74a**) is an excellent tool that opens new avenues for understanding the role of mGlu<sub>4</sub> in the central nervous system and unraveling its implications in the development of neurologic disorders with prospects to find innovative therapeutic strategies.

## Chapter 3: A toolbox of photoswitchable PAMs to selectively modulate mGlu<sub>1</sub>



### Key points

- First photoswitchable mGlu<sub>1</sub> PAMs
- Two libraries of compounds for structure–activity relationship studies
- Gain in selectivity over mGlu<sub>4/5</sub> receptors
- Very consistent *on/off* photoswitching of mGlu<sub>1</sub> activity

### Paper related to this chapter

- Silvia Panarello, Alice Berizzi, Fanny Malhaire, Carme Serra, Jean-Philippe Pin, Laurent Prézeau, Cyril Goudet, Amadeu Llebaria and Xavier Gómez-Santacana, “A toolbox of photoswitchable PAMs to selectively modulate mGlu<sub>1</sub> with light”.  
In preparation.

The therapeutic potential of selective mGlu<sub>1</sub> activation is still vastly unexplored, in comparison with the other group I mGluR (mGlu<sub>5</sub>). It has been widely discussed that mGlu<sub>1</sub> may be a drug target for the treatment of diseases such as stroke, epilepsy, cerebellar ataxia, Parkinson's disease, anxiety and mood disorders.<sup>209,210,217,253,254</sup> Additionally, mGlu<sub>1</sub> receptor has been associated with synaptic plasticity and the absence or dysregulation of mGlu<sub>1</sub> can be associated with severe motor coordination, learning deficits, intellectual disability and autism.<sup>255</sup> Some mutations found in GRM1 gene (encoding mGlu<sub>1</sub>) reduce mGlu<sub>1</sub> receptor signaling and are associated with schizophrenia.<sup>211,212,227</sup> However, a normal function of some of these mutated receptors can be achieved with the use of mGlu<sub>1</sub> PAMs.<sup>219</sup> Lastly, the activation of only thalamostriatal mGlu<sub>1</sub> with PAMs is reported to show antipsychotic-like activity in rodents.<sup>256</sup>

In any case, conventional mGlu<sub>1</sub> PAMs would activate all mGlu<sub>1</sub> receptors, which are expressed in many locations of the CNS. Autoradiographic studies showed a large distribution of mGlu<sub>1</sub> in brain, including a high level in the cerebellum, moderate or low level in the thalamus, striatum and cerebral cortex, and a very low level in the brainstem.<sup>257</sup> However, photoswitchable PAMs can be activated and inactivated with light with a high local and temporal precision. This gives the possibility to selectively activate only the mGlu<sub>1</sub> receptor in the site of action desired, which could be the case of striatum to obtain an antipsychotic effect.

Since mGlu<sub>1</sub> receptor has never been targeted in any photopharmacological approach, except on engineered mGlu<sub>2/1</sub> chimera, in which only the mGlu<sub>2</sub> part is binding a photochromic tethered ligand, one of the aims of this thesis is to afford photoswitchable mGlu<sub>1</sub> PAMs. In the present chapter, we show the first family of photoswitchable allosteric modulators for mGlu<sub>1</sub> receptors up to date. The design was based in the scaffold of the known positive allosteric modulator VU6004907 (**31**, *Figure 62*),<sup>222,224</sup> which emerged after the optimization of a series of mGlu<sub>4</sub> PAMs and was extensively discussed in the General Introduction section of the present thesis.\*

### Design of an initial library of *trans*-on photoswitchable mGlu<sub>1</sub> PAMs

The chemical design of photoswitchable compounds targeting the metabotropic glutamate receptor subtype 1 (mGlu<sub>1</sub>) was based on the azologization an *N*-(2-fluoro-4-(4-methyl-1,3-dioxoisindolin-2-yl)phenyl)-3-methylfuran-2-carboxamide scaffold recently found as potent and CNS penetrant allosteric modulator of group I mGlu receptors (**31**, *Figure 62*).

Specifically, VU6004907 (**31**) emerged from the optimization of the VU0486321 (**30**) series of mGlu<sub>1</sub> PAM, driven by a robust SAR and leading to an increased selectivity versus mGlu<sub>4</sub> and mGlu<sub>5</sub> (*Figure 62*).<sup>219-224</sup> Both molecules include a furyl amide with a 3-methyl group, which is deputed to enhance mGlu<sub>1</sub> PAM potency, compared to other rings such as pyridines, unsubstituted five-membered heterocycles or different substituted furylamides.<sup>220,222,224</sup> However, VU6004907 (**31**) includes a fluorine atom in the 2-position (relative to the amide moiety) of the central phenyl core preventing mGlu<sub>4</sub> activity while maintaining mGlu<sub>1</sub> PAM potency.<sup>221</sup> On the other hand, the phthalimide moiety admits certain variations in being substituted in 3- or 4- position with both electron donating and electron withdrawing substituents.<sup>222,224</sup>

Consequently, we considered the phthalimide core as suitable moiety for the azologization strategy,<sup>31</sup> considering especially its rigidity due to the planar structure and the delocalization of  $\pi$ -electrons. This properties are rather similar to the *trans*-azobenzene structure.<sup>20,258</sup> Therefore, we thought that the replacement of the *N*-phenylphthalimide for an azobenzene group would be suitable to successfully obtain photoswitchable mGlu<sub>1</sub> PAMs (*Figure 62*) in their *trans*-configuration.

\* See *Modulation of mGlu receptor activity: Ligands acting at the 7TMD*.



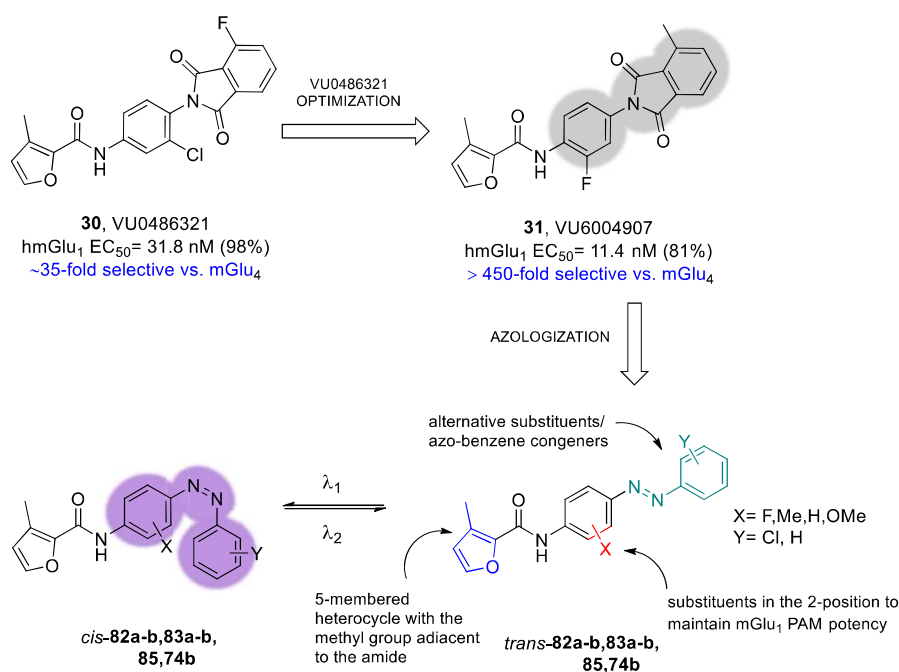


**Figure 62.** Structures of reported mGlu<sub>1</sub> PAMs **30-31** and designed *trans*-on photoisomerizable molecules, following the azologization strategy starting from VU6004907 (**31**), with chemical optimization plan to access multi-dimensional SAR around analogs **82a-b**, **83a-b**, **85** and **74b**.

In order to access an initial library of possible photoswitchable mGlu<sub>1</sub> PAMs and survey the SAR for the three regions above explained (Figure 62), we decided to maintain the 3-methylfuranlyl amide as 5-membered heterocycle in the molecular scaffold present in the VU series and explore the functional substitution of the azobenzene moiety. These modifications included the F and Me in the 2-position relative to the amide; and the Cl in the 2- or 3-position in the external ring.

Introducing a photochromic moiety within the compound structure was thought to minimally modify the steric occupancy, binding determinants and physicochemical properties. However, the pharmacological properties of the new ligand could be significantly changed in relation to the parent compound. For this reason, we decided to also include in the library the compound with both non-functionalized phenyl rings, as a “naked” reference compound. Additionally, we included another analog with OMe in the 3-position relative to the amide, while maintaining the 2-Cl in the external phenyl group. This azobenzene substitution was particularly successful when it was applied to PAMs of mGlu<sub>4</sub> in previous studies<sup>98</sup> and, given the structural similarities between reported PAMs of mGlu<sub>1</sub> and mGlu<sub>4</sub>,<sup>219,232</sup> we considered including the compound **74b**\* as a worthy option to explore.

Overall, applying the postulated azologization approach, the photocontrolled analogs **82a-b**, **83a-b**, **85** and **74b** were expected to display mGlu<sub>1</sub> PAM activity in their *trans* configuration and, after illumination, the *cis* isomers should not be active due to the abrupt change of geometrical disposition (Figure 62). This constitutes a *trans*-on approach.

### Synthesis of azologs **82a-b**, **83a-b**, **85** and **74b**

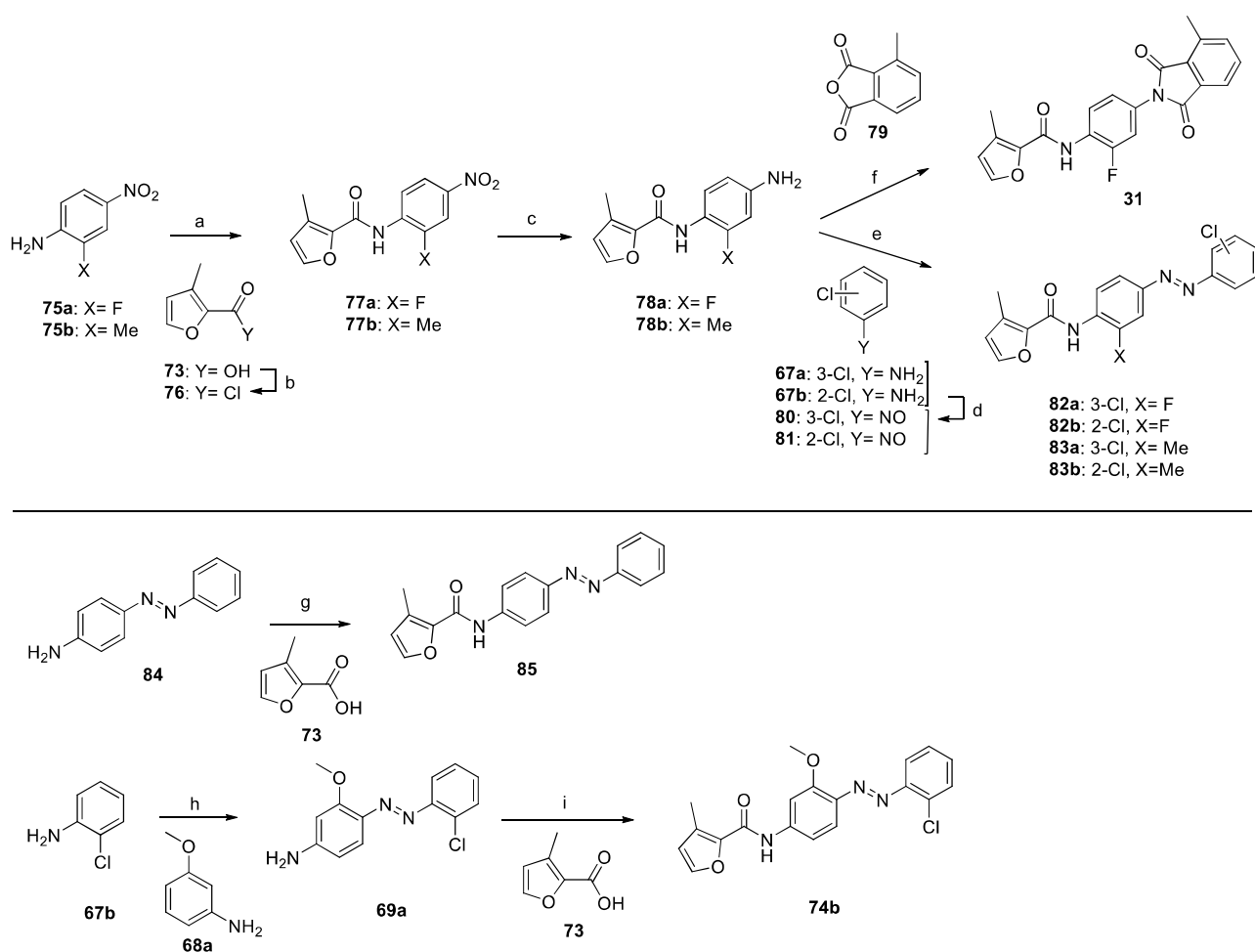
The synthetic routes developed to produce the six photoisomerizable mGlu<sub>1</sub> allosteric modulators and the compound **31** (VU6004907) are depicted in Scheme 8. A general five step synthetic route was used to

\* See Chapter 2: Development of a selective photoswitchable PAM for mGlu<sub>4</sub> receptor.

afford analogs **82a-b** and **83a-b**. The sequence began with the microwave-assisted acylation of the corresponding aniline **75a** and **75b** with 3-methylfuran-carbonyl chloride (**76**), which was previously obtained through conversion of 3-methylfuran-2-carboxylic acid (**73**) with thionyl chloride in quantitative yields. The aforementioned acylation gave furylamide **77a** and **77b** in good yield. Then, the nitro functional groups were reduced through palladium-catalyzed hydrogenation to give a quantitative yield of aniline **78a** and **78b**. Finally, the desired azo compounds **82a-b** and **83a-b** were prepared via Mills reaction in good yields by reacting **78a** with nitroso derivatives **80** and **81** in acidic media to obtain respectively **82a-b** and aniline **78b** with **80** and **81** to afford **83a-b**. Both nitroso compounds **80** and **81** were prepared by amine oxidation of the corresponding 3- and 2-chloroaniline (**67a** and **67b**) with Oxone<sup>®</sup> following the procedure described by Priewisch.<sup>243</sup> The mGlu<sub>1</sub> PAM VU6004907 (**31**) was obtained by condensation of the aniline **78a** with 3-methylphthalic anhydride **79** in reflux of acetic acid in good yield.

The non-functionalized azo compound **85** was yielded by a direct acylation of the commercially obtained (*E*)-4-(phenyldiazenyl)aniline (**84**) and 3-methylfuran-2-carboxylic acid (**73**) with good yields.

Compound **74b** was prepared following the two-step synthesis depicted in *Scheme 8* and also reported in Chapter 2 of the Results and Discussion section. First, direct diazotization of the 2-chloroaniline (**67b**) followed by an azo-coupling with 3-methoxyaniline (**68a**) yielded aminoazobenzene **69a** as intermediate for the next amide coupling reaction with 3-methylfuran-2-carboxylic acid (**73**) to give the last azo compound **74b** of this first series of photoregulated mGlu<sub>1</sub> PAMs.



**Scheme 8.** Synthesis of compounds **82a-b**, **83a-b**, **85** and **74b**. Reagents and conditions: (a) DIPEA, DCE,  $\mu$ W, 120 °C, 150 psi, 150 W, 30 min, 57-61%; (b) SOCl<sub>2</sub>, 76 °C, 2 h, quant.; (c) H<sub>2</sub> (2 atm), Pd/Ct, EtOH, rt, 16 h; (d) Oxone<sup>®</sup>, DCM/H<sub>2</sub>O 1:4, rt, 2 h, 87-100%; (e)

AcOH cat., rt, DCM, 48 h, 60–76%; (f) AcOH, 118 °C, 16 h, 70%; (g) HATU, DIPEA, DMF, 40 °C, 5 h, 72%; (h) (I) HCl, NaNO<sub>2</sub>, 0 °C, 20 min; (II) NaOAc, 0 °C, 30 min, 57%; (i) 3-methylfuran-2-carboxylic acid, HATU, TEA, DMF, 60 °C, 16h, 49%.

## Photochemical and pharmacological characterization: first series of compounds

### UV-Vis absorption spectroscopy

Next, we determined the photochemical properties of azo compounds **82a-b**, **83a-b**, **85** and **74b** by the UV/Vis absorption spectroscopy, in the dark and after illumination with different wavelengths. While in the dark, only the *trans* isomers is present (Table 16), upon illumination, a mixture of the *cis* and the *trans* isomers can be detected, which is known as photostationary state (PSS).

UV-Vis spectra showed general tendencies for five of the six azobenzenes. **82a-b**, **83a-b** and **85** showed the typical *trans*-azobenzene  $\pi$ - $\pi^*$  transition band at 360-370 nm under dark conditions and therefore the *E/Z* isomerization could be achieved under illumination at this range of wavelengths. In fact, after irradiating the samples with 380 nm light, mainly the *cis* isomers of the compounds were observed. This was characterized by the  $n$ - $\pi^*$  transition band around 445-450 nm, which is forbidden by the symmetry in *trans* azobenzenes. The photochemical characteristics of the compound **74b** are slightly different. The presence of a mild electron-donating methoxy group in *ortho* position relative to the azo unit produces a small redshift of the band corresponding to the  $\pi$ - $\pi^*$  transition of the *trans* isomer. In contrast, the  $n$ - $\pi^*$  transition band of the corresponding *cis* isomer is at lower wavelength than the other analogs.

Photoisomerization					
Cpd.	X	Y	<i>trans</i> <sup>[a]</sup>	<i>PSS</i> <sub>380</sub> <sup>[c]</sup>	
			$\lambda_{\max}(\pi-\pi^*)$ <sup>[b]</sup> [nm]	$\lambda_{\max}(n-\pi^*)$ <sup>[b]</sup> [nm]	
<b>82a</b>	2-F	3-Cl	370	450	
<b>82b</b>	2-F	2-Cl	365	445	
<b>83a</b>	2-Me	3-Cl	365	450	
<b>83b</b>	2-Me	2-Cl	360	450	
<b>85</b>	H	H	365	445	
<b>74b</b>	3-OMe	2-Cl	390	418	

[a] Experiments performed in the dark to characterize 100% *trans* isomer.

[b] The absorbance maxima were extracted from UV/Vis spectra (25  $\mu$ M in DMSO at 25°C).

[c] Photostationary state upon illumination with 380 nm light to obtain a high % of *cis* isomer.

**Table 16.** Photoisomerization properties of analogs **82a-b**, **83a-b**, **85** and **74b**.

All the six azo compounds can be back-isomerized to their thermodynamically stable *trans* isomer by using turquoise light (455 nm) (Figure 63B) or allowing them to thermally isomerize in the dark. The photoisomerization properties of azo compound **83b** in DMSO were also examined by HPLC-MS analysis (Figure 63C). 100% of *trans*-**83b** was observed in the dark, whereas a PSS of 71.9% *cis*-**83b** after 385-nm illumination was detected. Subsequent illumination with 455-460 nm wavelength afforded a PSS of 71.1% *trans*-**83b**. This ratio was calculated from the area of the corresponding peaks at 310 nm, since we determined that 310 nm was isosbestic point in the UV-Vis spectra (Figure 63B).\*

\* In spectroscopy, an isosbestic point could be defined as a specific wavelength at which the total absorbance of a sample does not change during a physical change of the same sample. When the absorption spectra of two species are superimposed the isosbestic point corresponds to a wavelength at which these spectra cross each other and the two chemical species have identical molar absorption coefficients whose ratio, however, remains constant as the physical change proceeds.

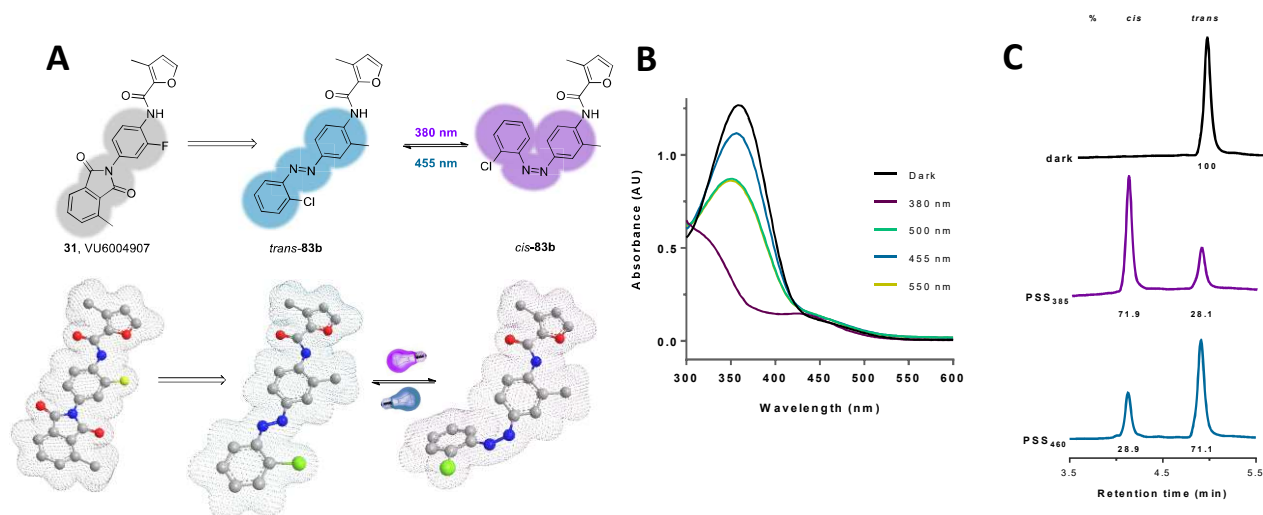


**Figure 63.** Photochemical properties of compound **83b**. (A) 2D structure of *trans/cis* isomers compared with that of the VU6004907 (**31**) and their 3D structure with a total electron density surface after minimizing energy with MM2 (Chem3D 20.0); (B) UV/Vis absorption spectra of **83b** 100 μM in DMSO at 25°C under dark (black) and different light conditions for 3 min; (C) Photostationary state (PSS) quantification of **83b** 100 μM in DMSO/MeCN 1:9 at 25°C by HPLC-MS. The measurement was performed in the dark and after illuminating the sample was for 3 min with 380 and 455 nm light sources.

#### ***In vitro functional assay: poor solubility of azologs 82a-b, 83a-b, 85 and 74b and protocol optimization***

*In collaboration with Xavier Gómez Santacana - IGF, Institut de Génomique Fonctionnelle, CNRS, INSERM Montpellier*

The pharmacological activity of compounds **82a-b**, **83a-b**, **85** and **74b** as mGlu<sub>1</sub> PAMs were tested using an IP accumulation assay in HEK293 cells transiently transfected with mGlu<sub>1</sub> receptor, which under activation naturally couples to G<sub>αq</sub>. Thus, dose–response curves were generated with the azo compounds and 50 nM of the orthosteric agonist quisqualate in dark and 380-nm light conditions.

Disappointingly, we obtained not only a minimal *trans*-on effect for all the azo compounds tested but also a much lower potency of the parent compound VU6004907 (**31**) than that reported in literature. Differences in EC<sub>50</sub> values of dose–response curves extracted from different types of assay may exist but are generally small. In the present case, we thought that there was a problem in the procedure of the assay that did not make the obtained results reliable. One possible explanation for this issue could be related to the low water solubility of compounds **31**, **82a-b**, **83a-b**, **85** and **74b** that can be troublesome when working with aqueous buffers.

To prove that the origin of the problem was the poor solubility while performing the cascade solutions of the compounds in the assay stimulation buffer, we changed the protocol modifying the order of mixing the dilutions before the incubation of the cells. Thus, the cascade dilutions of the compounds were performed in DMSO, subsequently diluted 1:100 with the orthosteric agonist solution just before adding them to the cells.\* Finally, we obtained different dose–response curves for VU6004907 (**31**) and compound **83b** tested in dark conditions and using the aforementioned new protocol (*Figure 64* and *Table 17*) and the obtained results were more in line with those reported in the literature. Therefore, the results confirmed the theory that, following the classical protocol the compounds **31**, **82a-b**, **83a-b**, **85** and **74b** were sticking at the end

\* See *Experimental section: Detailed procedure for dose–response curves in dark and light conditions: new protocol, DMSO “microdilutions”*.

of the plastic tubes used to prepare the eight concentrations predilutions, significantly decreasing the real concentration of compounds of each dilution.

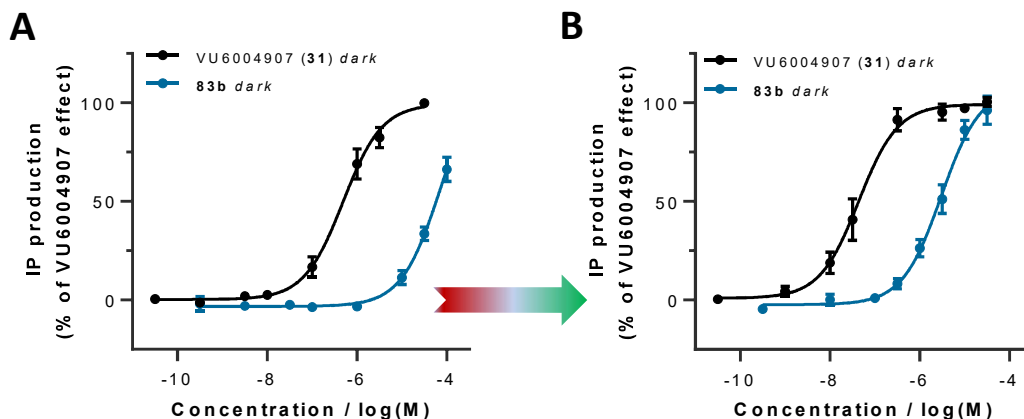


**Figure 64.** Comparison of dose-response curves of the parent compound VU6004907 (**31**) and azo compound **83b** in dark conditions following the classical (A) or new protocol (B). Each point of the curves are the mean of three independent replicates and the error bars are corresponding SEM.

Compound	Classical protocol				New protocol			
	pEC <sub>50</sub>	SEM	EC <sub>50</sub> (μM)	SEM (μM)	pEC <sub>50</sub>	SEM	EC <sub>50</sub> (μM)	SEM (μM)
VU6004907 ( <b>31</b> )	6.3	0.1	0.54	0.18	7.2	0.1	0.07	0.01
<b>83b</b> dark	4.1	0.3	120	78	5.6	0.1	2.76	0.50

**Table 17.** Comparison of EC<sub>50</sub>s of the parent compound VU6004907 (**31**) and azo compound **83b** obtained from dose-response curves from IP accumulation assays using the classical and the new protocol.

Furthermore, we decided to test all the compounds again with this new protocol to obtain more reliable and consistent results, especially on the photoswitching efficiency. Thus, we could also establish a robust comparison of the compound series, since they would share the same pharmacological profile.

From this set of azologs, the three compounds **83a-b** and **85** provided the most relevant results highlighting compound **83b** as the best with moderate activity as mGlu<sub>1</sub> PAM in dark conditions (EC<sub>50</sub>= 2.7 μM, pEC<sub>50</sub>= 5.6 ± 0.1, Table 18). Compound **83b** also displayed the highest light-induced shift on the PAM activity, with 1 log fold shift of the potency measured for the compound in dark conditions (Table 18 and Figure 65A). Those experiments showed a very consistent photoswitching of PAM activity, not described for the metabotropic glutamate receptor 1 before.

Then, in order to understand any undesired off-target activity we also assessed selectivity of the six analogs versus the key anti-targets for this chemotype, the other group I mGlu receptor, mGlu<sub>5</sub>, and mGlu<sub>4</sub>. We considered to assess the possible PAM or NAM activity of the analogs **82a-b**, **83a-b**, **85** and **74b** in mGlu<sub>5</sub>, not only because both mGlu<sub>5</sub> and mGlu<sub>1</sub> are from the same group I mGlu receptors but also because all these analogs structurally can be related to many PAMs and NAMs of mGlu<sub>5</sub>.<sup>238</sup>

Pharmacological Characterization								
Cpd.	X	Y	hmGlu <sub>1</sub> pEC <sub>50</sub> ± SEM <sup>[a]</sup>			rmGlu <sub>4</sub> pEC <sub>50</sub> ± SEM <sup>[b]</sup>		
			<i>trans</i> <sup>[c]</sup>	PSS <sub>380</sub> <sup>[d]</sup>	PPS <sup>[e]</sup>	<i>trans</i> <sup>[c]</sup>	PSS <sub>380</sub> <sup>[d]</sup>	PPS <sup>[e]</sup>
<b>82a</b>	2-F	3-Cl	<4.5	<4.5	-	<4.5	<4.5	-
<b>82b</b>	2-F	2-Cl	<4.5	<4.5	-	<4.5	<4.5	-
<b>83a</b>	2-Me	3-Cl	4.9 ± 0.2	4.6 ± 0.2	0.3	5.5 ± 0.2	<4.5	-
<b>83b</b>	2-Me	2-Cl	5.6 ± 0.1	4.6 ± 0.1	1.0	5.8 ± 0.1	<4.5	-
<b>85</b>	H	H	4.5 ± 0.3	<4.5	-	5.4 ± 0.1	<4.5	-
<b>74b</b>	3-OMe	2-Cl	<4.5	<4.5	-	7.1 ± 0.4	5.9 ± 0.1	1.2

[a] Extracted from dose-response curves with a constant concentration of quisqualate 50 nM using TR-FRET IP accumulation assay.

[b] Extracted from dose-response curves with a constant concentration of L-AP<sub>4</sub> 5 nM using TR-FRET cAMP accumulation assay.

[c] Experiments performed in the dark to characterize 100% *trans* isomer.

[d] Photostationary state upon illumination with 380 nm light to obtain a high % of *cis* isomer.

[e] PPS corresponds to photoinduced potency shift (log-fold) between the measured pEC<sub>50</sub> in light and dark conditions.

**Table 18.** Pharmacological characterization of analogs **82a-b**, **83a-b**, **85** and **74b**. The pEC<sub>50</sub>-values are extracted from dose-response curves considering the *trans* isomers in the dark or upon illumination at 380 nm wavelength (PSS<sub>380</sub>) to obtain a high *cis* isomer concentration. Values are shown as the mean ± SEM of at least three independent experiments, each performed in duplicate.

Additionally, it seemed prudent to also characterize the series in mGlu<sub>4</sub> receptor. This especially because the parent compounds, VU0486321 series of mGlu<sub>1</sub> PAMs, were optimized from a mGlu<sub>4</sub> PAM series through several “molecular switches”<sup>\* 218–220</sup>. Moreover, the azo compounds **82a-b**, **83a-b**, **85** and **74b** structurally resemble to Optogluram<sup>98</sup> and other Optogluram-like photoswitchable mGlu<sub>4</sub> PAMs.<sup>†</sup>

The possible interaction of the compounds with mGlu<sub>5</sub> was tested with IP accumulation assay in HEK293 cell overexpressing mGlu<sub>5</sub> receptor with different concentrations of orthosteric agonist quisqualate, depending on the type of allosteric modulation to measure (*i.e.* PAM or NAM), and a single dose of 33 μM of the azo-derivatives. Thus, we found the azo compounds **82a-b**, **83a-b**, **85** and **74b** were all uniformly inactive on mGlu<sub>5</sub>, both as PAM or NAM (*Figure 65C*). In particular, **83b** was unable to activate or inhibit the receptor if compared with the corresponding reference standards VU0424465 or VU0409106.

As mentioned before, these compounds were also tested in mGlu<sub>4</sub> subtype but, in this case, we used a stable HEK293 cell line expressing mGlu<sub>4</sub> and a cAMP accumulation assay to measure cAMP concentration modulation in response to Gi-activation, since the mGlu<sub>4</sub>, like other group III mGlu receptor, binds to G<sub>i/o</sub>α subunit.

Surprisingly, except the first two compounds in the series, all the others showed considerable allosteric agonism on mGlu<sub>4</sub> receptor in dark. Upon illumination, the less thermodynamically stable configuration of the analogs was found to be clearly less potent (*Table 18*). In particular, the most potent mGlu<sub>1</sub> PAM, compound **83b**, turned out to be an equipotent mGlu<sub>4</sub> PAM. However, it displayed a remarkable photo-induced potency shift in both receptors (*Table 18* and *Figure 65B*).

\* See *Modulation of mGlu receptor activity: Ligands acting at the 7TMD*

† See *Chapter 2: Design of Optogluram analogs*

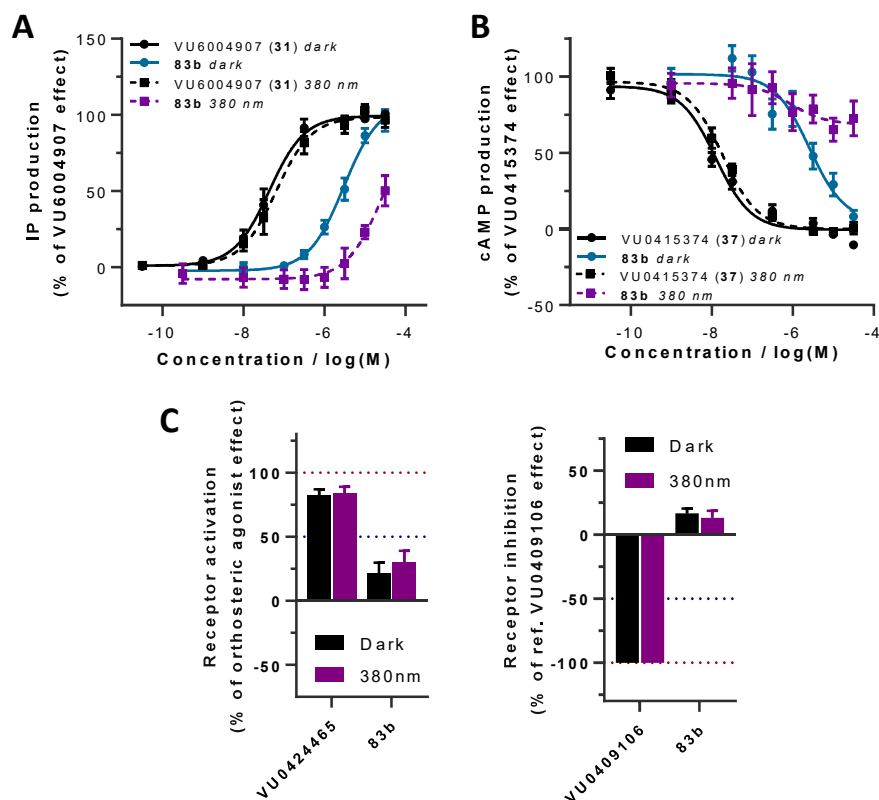


**Figure 65.** Pharmacological properties of compound **83b**. (A) Dose-response curve of compound **83b** with a constant concentration of quisqualate 50 nM in HEK293 cells overexpressing mGlu<sub>1</sub> in different conditions: in dark conditions (rounded dots and turquoise solid line), under illumination at 380 nm of wavelength (square dots and violet dotted line). VU6004907 (**31**) was used as a mGlu<sub>1</sub> PAM standard in dark conditions (round spots and black solid line) and under illumination at 380 nm (square dots and dotted line); (B) Dose-response curve of compound **83b** with a constant concentration of L-AP<sub>4</sub> 5 nM in HEK293 stable mGlu<sub>4</sub> cell line in dark conditions (rounded spots and turquoise solid line) and under illumination at 380 nm of wavelength (square dots and violet dotted line). VU0415374 was used as a mGlu<sub>4</sub> PAM standard in dark conditions (round dots and black solid line) and under illumination at 380 nm (square dots and black dotted line); (C) Single dose experiments of **83b** at 30 μM on mGlu<sub>5</sub> receptor as PAM (left) and as NAM (right) in dark conditions (black bars) and under illumination at 380 nm of wavelength (violet bars). All the data represent normalized receptor activation for at least 3 independent experiments, performed in duplicate or triplicate. Dots are represented as mean ±SEM.

In summary, while mGlu<sub>1</sub> potency could be attractive for a proof of concept for the precise control of mGlu<sub>1</sub> receptor with light, the overall profile and selectivity versus mGlu<sub>4</sub> were not appropriate for an *in vivo* translation of possible mGlu<sub>1</sub> PAM tool compound. However, a dual mGlu<sub>1</sub>/mGlu<sub>4</sub> PAM activity could be intriguing for an antipsychotic agent,<sup>212</sup> as mGlu<sub>4</sub> PAM activity can alleviate catalepsy,<sup>249,259,260</sup> a major adverse event with the standard treatment with antipsychotic drugs.<sup>261</sup>

In the end, we were pleased to verify that our azologization strategy for a reversible mGlu<sub>1</sub> receptor photopharmacological approach was successful, even those analogs were still suboptimal as *in vivo* tools. However, achieving these first results led us to further explore the structure-activity relationships (SAR) around **83b**, after named Photoglurax-1, to obtain reversible photoswitchable and selective mGlu<sub>1</sub> PAM activity.

### Optimization of the first hit Photoglurax-1 (**83b**)

Since our azologization strategy of VU6004907 (**31**) to get a photoswitchable mGlu<sub>1</sub> PAM was plagued by crossover activity at mGlu<sub>4</sub>, we considered to focus the second round of optimization on the best hit,

Photoglurax-1 (**83b**), obtained in the previous library. To survey alternatives in the molecular scaffold, we decide to keep the 3-methylfuran-2-yl amide as it was the heterocycle that gave the best results in previous optimizations.<sup>220,222</sup> We also decide to keep the methyl in 2-position of the central aryl of Photoglurax-1 (**83b**) because compounds including F or H in the same 2-position and OMe in the 3-position did not provide the expected mGlu<sub>1</sub> activity (Table 18).

Therefore, we synthesized analogs **89a-i** (Figure 66) to examine the impact of the substitution of the external aromatic ring on both mGlu<sub>1</sub> and mGlu<sub>4</sub> activity. Thus, we first explored different substituents in the 2-position and later double substitutions in 2- or 3- position together with 5-Cl or 4-F. These structural modifications were designed to decrease activity at mGlu<sub>4</sub> trying not to impact negatively on that of mGlu<sub>1</sub>.

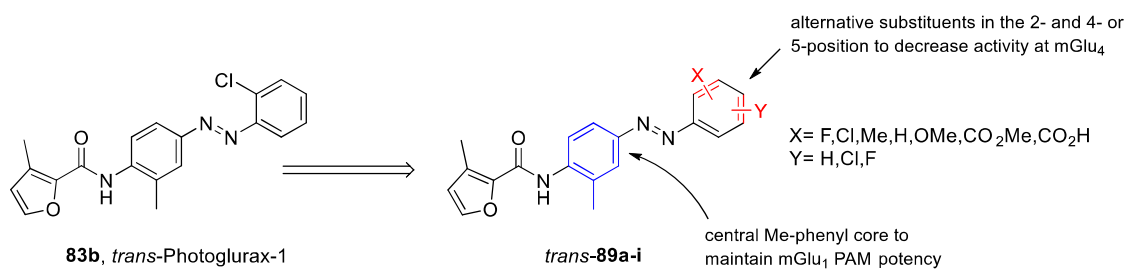
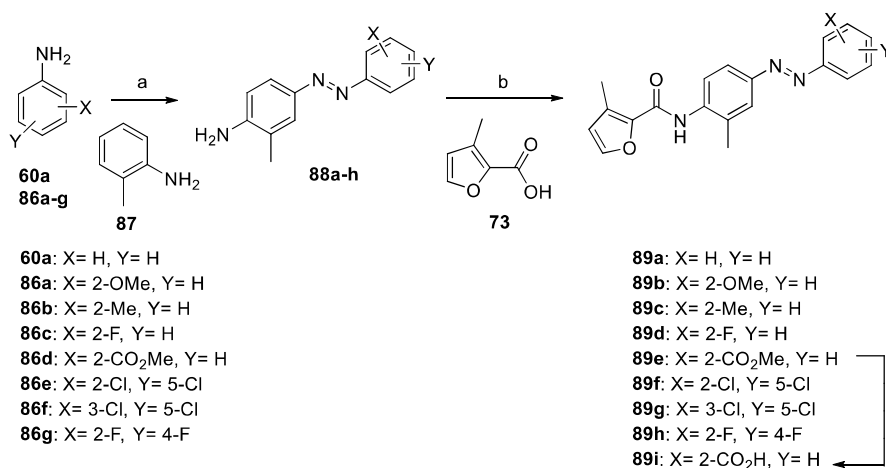


Figure 66. Optimization of mGlu<sub>1</sub> PAM **83b** (Photoglurax-1) to decrease potency at mGlu<sub>4</sub> and/or enhance mGlu<sub>1</sub> activity.

### Synthesis of azo compounds **89a-i**

As shown in Scheme 9, the new putative photoisomerizable mGlu<sub>1</sub> allosteric modulators (**89a-i**) were readily prepared in two steps and in good overall yields. The sequence started with the direct diazotization of anilines **60a** and **86a-g** followed by an azocoupling with *o*-toluidine (**87**) to yield aminoazobenzenes **88a-h**. The following amide coupling of the intermediates **88a-h** with 3-methylfuran-2-carboxylic acid **73**, delivered the azo compounds **89a-h** of this second series of photoregulated mGlu<sub>1</sub> PAMs. The compound **89i** was obtained by a basic hydrolysis of the methyl benzoate **89e**.



Scheme 9. Synthesis of compounds **89a-i**. Reagents and conditions: (a) (I) HCl, NaNO<sub>2</sub>, 0°C, 20 min; (II) NaOAc, 0°C, 30 min, 9-32%; (b) HATU, TEA, DMF, 40-60°C, 16-24h, 21-68%; (c) LiOH (1M aq), MeOH, 60°C, 2h, 45%.

### Photochemical and pharmacological characterization: second series of compounds

The photoisomerization of azo compounds **89a-i** was examined by recording the UV/Vis absorption spectra in the dark and after illumination with different wavelengths between 365 and 500 nm, as performed with



the previous series (Table 19 and Figure 67A). The results showed that mainly the *cis* isomers of **89a-i** were observed upon illumination with 365 or 380 nm light (Figure 67A) and after subsequent illumination of the samples with 455 nm light, mostly the *trans* isomers of **89a-i** were detected (Figure 67A). This behavior was exactly in line with that of the first series of compounds.

Additionally, compound **89h** displayed high photostability over the application of multiple light cycles (Figure 67B) and the long thermal relaxation half-life of *cis*-**89h** made it a suitable tool compound since G protein activation occurs on the second time scale.<sup>262</sup>

Cpd.	Photoisomerization		Photopharmacological Characterization						
			Photoisomerization		hmGlu <sub>1</sub>		rmGlu <sub>4</sub>		
			X	Y	<i>trans</i> <sup>[a]</sup> $\lambda_{\max}(\pi-\pi^*)$ <sup>[b]</sup> [nm]	<i>PSS</i> <sub>380</sub> <sup>[c]</sup> $\lambda_{\max}(n-\pi^*)$ <sup>[b]</sup> [nm]	<i>trans</i> <sup>[a]</sup>	<i>PSS</i> <sub>380</sub> <sup>[c]</sup>	<i>trans</i> <sup>[a]</sup>
<b>89a</b>	H	H	370	430	5.0 ± 0.0	<4.5	5.8 ± 0.2	<4.5	
<b>89b</b>	2-OMe	H	374	428	4.9 ± 0.2	<4.5	5.9 ± 0.2	<4.5	
<b>89c</b>	2-Me	H	356	436	5.3 ± 0.1	<4.5	6.0 ± 0.3	<4.5	
<b>89d</b>	2-F	H	358	436	5.3 ± 0.1	<4.5	6.0 ± 0.2	<4.5	
<b>89e</b>	2-CO <sub>2</sub> Me	H	340	430	<4.5	<4.5	-	-	
<b>89f</b>	2-Cl	5-Cl	370	450	<4.5	<4.5	-	-	
<b>89g</b>	3-Cl	5-Cl	366	448	<4.5	<4.5	-	-	
<b>89h</b>	2-F	4-F	358	436	5.3 ± 0.1	<4.5	<4.5	<4.5	
<b>89i</b>	2-CO <sub>2</sub> H	H	338	426	<4.5	<4.5	-	-	

[a] Experiments performed in the dark to characterize 100% *trans* isomer.

[b] The absorbance maxima were extracted from UV/Vis spectra (25 μM in DMSO at 25°C).

[c] Photostationary state upon illumination with 380 nm light to obtain a high % of *cis* isomer.

[d] Extracted from dose-response curves with a constant concentration of quisqualate 50 nM using TR-FRET IP accumulation assay.

[e] Extracted from dose-response curves with a constant concentration of L-AP<sub>4</sub> 5 nM using TR-FRET cAMP accumulation assay.

**Table 19.** Photoisomerization properties and photopharmacological characterization of analogs **89a-i**. The measured pEC<sub>50</sub> in light and dark conditions are shown as the mean ± SEM of at least three independent experiments, each performed in triplicate.

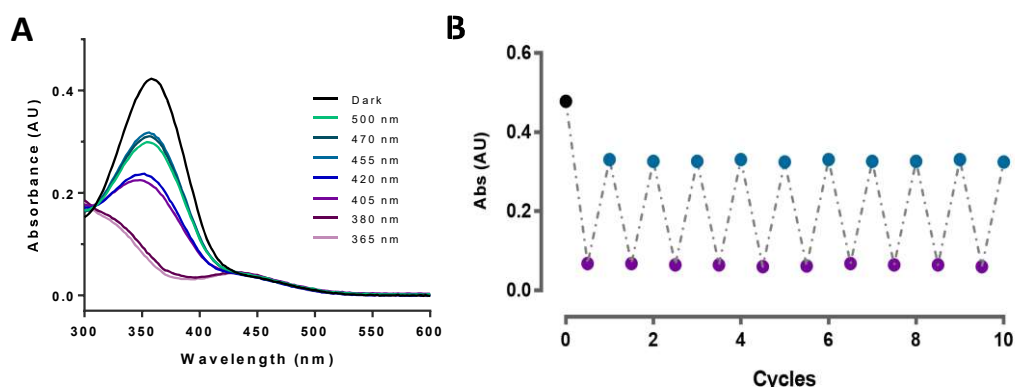


**Figure 67.** Photochemical properties of compound **89h**. (A) UV/Vis absorption spectra of **89h** 25 μM in DMSO at 25°C under dark (black) and different light conditions for 3 min; (B) UV-Vis absorption measurements of **89h** 25 μM in DMSO at 25°C at  $\lambda_{\pi-\pi^*}$ -max of *trans* isomer (358 nm) after repeated cycles of illumination with 380 (violet) and 455 nm light (turquoise).

The functional activity of the analogs **89a-i** was examined as mGlu<sub>1</sub> and mGlu<sub>4</sub> PAMs, in the dark and after illumination with 380 nm, with exactly the same optimized methodology used for the first series of compounds. Regarding the PAM activity in mGlu<sub>1</sub> receptor, the 2-position in the external ring emerged as the most fruitful, since the substitution with small sized functional groups, including even a single hydrogen atom, (**89a-d**, Table 19) provided the best results in the dark. These four compounds showed comparable

mGlu<sub>1</sub> potency as the previous *trans* azo compound Photoglurax-1 (**83b**). However, those compounds also showed analogous potency towards the mGlu<sub>4</sub> receptor in the dark.

When the functional group in 2-position in the external ring is a methoxycarbonyl or a carboxyl (**89e** and **89i** respectively), the mGlu<sub>1</sub> potency is negligible. Therefore, these compounds were excluded for the mGlu<sub>4</sub> characterization. Poor mGlu<sub>1</sub> activities in dark conditions were also found for those compounds containing a second functional group in 5-position such as a chlorine (**89f-g**).

Remarkably, when the double substitution concerned a fluorine atom in both 2- and 4- position in the external ring, the compound appeared to be a mGlu<sub>1</sub> PAM (**89h**, Table 19 and Figure 68B) with a potency comparable to those of compounds **89a-d** or Photoglurax-1 (**83b**). However, compound **89h** was practically inactive as an mGlu<sub>4</sub> PAM in the dark, affording the greatest mGlu<sub>1</sub>/mGlu<sub>4</sub> selectivity within the series (Table 19 and Figure 68C).

All the compounds were tested in parallel in the dark and upon illumination with 380 nm light. As the previous series, the active compounds **89a-d** and **89h** (in mGlu<sub>1</sub> and/or mGlu<sub>4</sub> receptor) loss their activity in different degrees upon 380 nm illumination, which indicates that the less thermodynamically stable isomer is clearly less potent. Indeed, the compounds within this second family and especially **89h** show a complete and very consistent *on/off* photoswitching of mGlu<sub>1</sub> activity at 10 μM (Figure 68B) that leads to a higher photoinduced potency shift than the Photoglurax-1 (**83b**). These results define the compound **89h** as the first highly specific mGlu<sub>1</sub> PAM and we decided to name it Photoglurax-2.

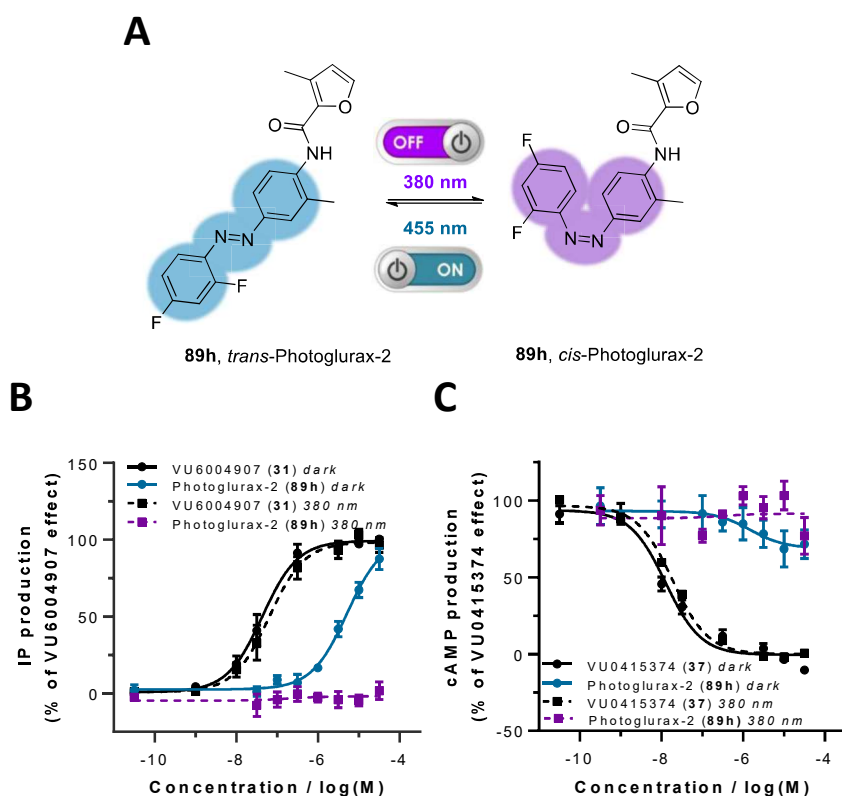


**Figure 68.** Pharmacological properties of Photoglurax-2 (**89h**). (A) Chemical structures of the photoisomers of compound **89h** and their distinct pharmacological behaviors towards the mGlu<sub>1</sub> receptor; (B) Dose-response curve of Photoglurax-2 (**89h**) in HEK293 cells overexpressing mGlu<sub>1</sub> receptor, with a constant concentration of quisqualate 50 nM, in different conditions: in dark conditions (rounded dots and turquoise solid line), under illumination at 380 nm wavelength (square dots and violet dotted line). VU6004907 (**31**) was used as a mGlu<sub>1</sub> PAM standard in dark conditions (round dots and black solid line) and under illumination at 380 nm wavelength (square dots and dotted line); (C) Dose-response curve of Photoglurax-2 (**89h**) in HEK293 overexpressing mGlu<sub>4</sub>

receptor with a constant concentration of L-AP4 5 nM in dark conditions (rounded dots and turquoise solid line) and under illumination at 380 nm wavelength (square dots and violet dotted line). VU0415374 was used as a mGlu<sub>4</sub> PAM standard in dark conditions (round spots and black solid line) and under illumination at 380 nm wavelength (square dots and dotted line).

## Conclusions

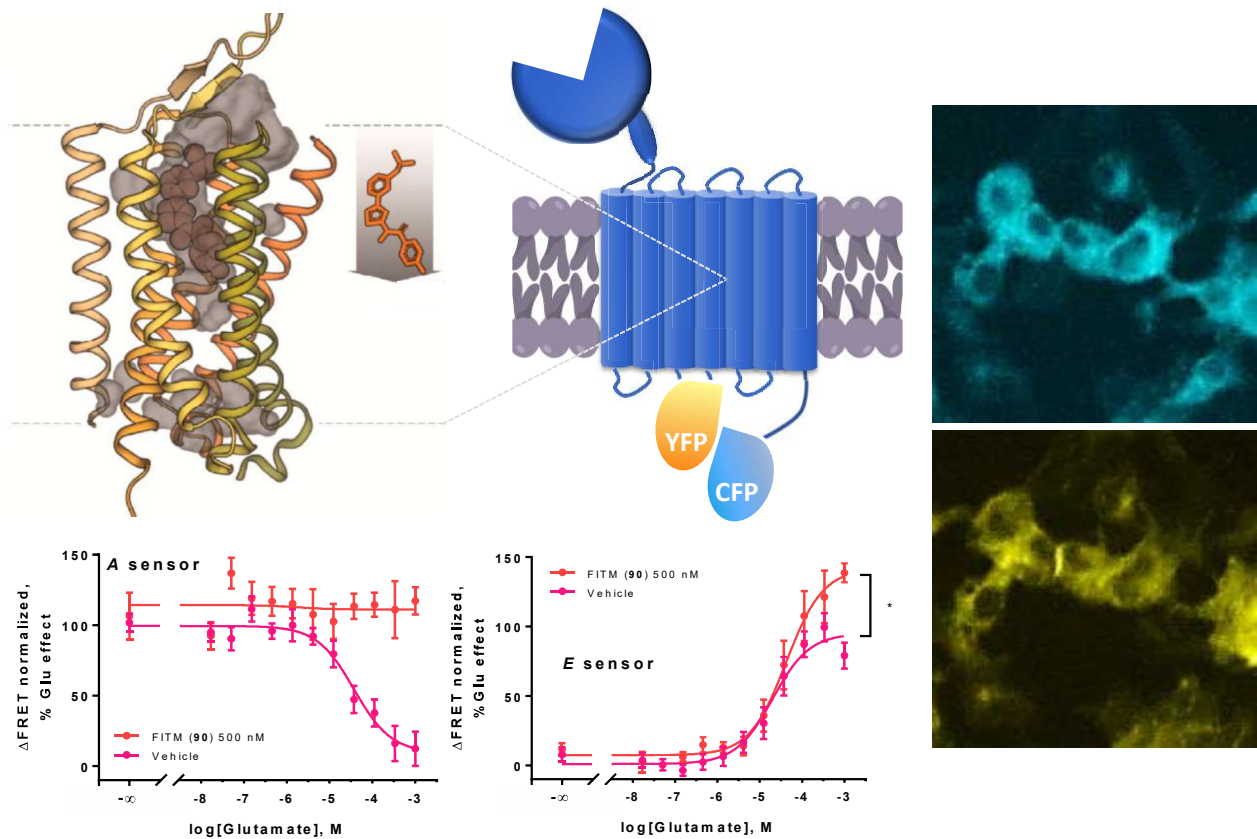
In summary, the proposed azologization approach was proven successful. VU6004907 (**31**) was a good candidate for engineering an initial library of photosensitive mGlu<sub>1</sub> PAMs by converting the phthalimide core with an azobenzene moiety.

Photogluxurax-1 (**83b**), emerged as a mGlu<sub>1</sub> PAM with micromolar potency in the *trans* isomer. Under 380 nm light the potency is significantly reduced. Unfortunately Photogluxurax-1 (**83b**) displays comparable potency as mGlu<sub>4</sub> PAM. Based on these data, we decided to optimize this first series of photoswitchable compounds driven by SAR studies, identifying key substituents and thereby engendering improved selectivity as well as a larger photo-induced potency shift.

Photogluxurax-2 (**89h**) acts like a mGlu<sub>1</sub> PAM and does not show any observable allosteric effect in mGlu<sub>4</sub> as well as no activity at mGlu<sub>5</sub>. Surprisingly, it is characterized by a modest potency on mGlu<sub>1</sub>, highlighting once again the structure-activity relationship challenges with allosteric ligands. However, our first explorations of central and external phenyl rings in the photosensitive molecular structure open new avenues for further optimization.

Nevertheless, the strength of Photogluxurax-2 (**89h**) is its activity that can be switched on and off by means of different wavelength illumination. From this effort, indeed, Photogluxurax-2 (**89h**) emerged as the first proof of concept for a reversible metabotropic glutamate receptor subtype 1 photopharmacological approach. These are very exciting findings overall because, due to the lack of activity at mGlu<sub>4</sub>, Photogluxurax-2 (**89h**) represents a potential *in vivo* photoswitchable mGlu<sub>1</sub> PAM tool compound. The obtained reversible control of mGlu<sub>1</sub> activity with light may be highly advantageous to study the pharmacological and physiological implications of mGlu<sub>1</sub> in many diseases with an unprecedented precision.

## Chapter 4: A series of arylazothiazoles to control mGlu<sub>1</sub> function with light



### Key points

- First photoswitchable *trans*-on mGlu<sub>1</sub> NAMs
- Water soluble series of arylazothiazoles and pH-dependent bistability of *cis* isomers
- Use of extra and intracellular sensors: 3 receptor levels explored with conformational assays
- Allosteric effect of mGlu<sub>1</sub> NAMs on receptor conformational changes induced by agonist

In the present chapter, we discuss the design, synthesis and characterization of a small library of photoswitchable arylazothiazole analogs. These compounds are hypothesized to be noncompetitive antagonists or so-called negative allosteric modulators of mGlu<sub>1</sub> receptor, in contrast to Photoglutax-1 (**83b**) and Photoglutax-2 (**89h**), which are the first PAMs that can modulate mGlu<sub>1</sub> activity with light.

Experiments with mGlu<sub>1</sub> knockout mice showed decreased pain sensitivity and administration of selective mGlu<sub>1</sub> NAMs or antagonists were reported to show efficacy in neuropathic pain animal models.<sup>217</sup> mGlu<sub>1</sub> NAMs are reported to have a robust efficacy in Fragile X syndrome (FXS)<sup>\*</sup> animal models too.<sup>217</sup> Finally, mGlu<sub>1</sub> antagonists are also potential therapeutic agents for the treatment of addiction, since they show efficacy in rodent models of cocaine addiction.<sup>226</sup> Besides the extensive potential of mGlu<sub>1</sub> NAMs, obtaining a reversible and efficient spatiotemporal control of mGlu<sub>1</sub> activity would be advantageous to selectively inactivate only the mGlu<sub>1</sub> receptors expressed in one determined tissue and this control finally can be highly relevant for both research and clinical applications.

### Initial considerations and design of analog 103a

The study of group I mGlu receptors has benefited greatly from the publication of FITM (**90**) (*Figure 69A*) as novel full NAM of the wild-type human mGlu<sub>1</sub> receptor. Indeed, since its discovery in 2009 by Satoh and colleagues<sup>263</sup> there have been a series of studies that have seen an intensive use of the FITM and derivatives.<sup>93,264–266</sup>

Since FITM (**90**) inhibits the functional response of human mGlu<sub>1</sub> with an IC<sub>50</sub> value of 5.1 nM and displays excellent selectivity for mGlu<sub>1</sub> over other subtypes (IC<sub>50</sub> values were 7,000 nM for mGlu<sub>5</sub>, >10,000 nM for mGlu<sub>2</sub> and >10,000 nM for mGlu<sub>8</sub>).<sup>263</sup> Yamasaki and co-workers also synthesized <sup>18</sup>F-labelled FITM and demonstrated specific binding of [<sup>18</sup>F]-FITM to mGlu<sub>1</sub> using *in vitro* and *ex vivo* autoradiography of rat brain sections.<sup>264</sup> Subsequently, they used [<sup>18</sup>F]-FITM for PET (positron emission tomography)<sup>†</sup> imaging of mGlu<sub>1</sub> in rodent and primate brains. PET using [<sup>18</sup>F]-FITM showed significant signals in rat and monkey brain regions, not only in the cerebellum, which is rich in mGlu<sub>1</sub> receptor, but also in regions with moderate or low mGlu<sub>1</sub> expression, such as the thalamus, striatum and cortex.<sup>265</sup> Inspired by these results, Fujinaga and collaborators wanted to develop new <sup>11</sup>C or <sup>18</sup>F-labeled PET ligands with improved kinetics over [<sup>18</sup>F]-FITM to quantitatively determine mGlu<sub>1</sub> in the brain. Thus, they opted to introduce a methoxy group into the compound, instead of the fluorine atom in [<sup>18</sup>F]-FITM, in order to obtain the compound [<sup>11</sup>C]-**91** (*Figure 69A*), which resulted to maintain a high specific binding for mGlu<sub>1</sub> in the brain, but it has faster kinetics in rat and monkey brains than the lead compound [<sup>18</sup>F]-FITM.<sup>266</sup>

Additionally, Wu and colleagues reported the first crystal structure of the human mGlu<sub>1</sub> 7TMD bound to the negative allosteric modulator FITM (**90**) at a resolution of 2.8 Å.<sup>93</sup> It was found that the mGlu<sub>1</sub> NAM FITM (**90**) binds within a pocket formed by the 7TMD bundle in inactive conformation close to the extracellular side (*Figure 69B*), a region that partially overlaps with the orthosteric binding sites observed in class A GPCRs crystal structures.<sup>267</sup> Later, it was demonstrated that FITM binding site is in a higher position compared to the NAM binding pocket of mGlu<sub>5</sub>, such as that of M-MPEP (**42**) (*Figure 69C*).<sup>268</sup>

---

\* FXS is the most common form of human inherited intellectual disability and inherited cause of autism.

† PET with radioligands is a molecular imaging technique that enables study of the living human brain and in particular of specific proteins involved in pathophysiology or as targets for therapeutic interventions.

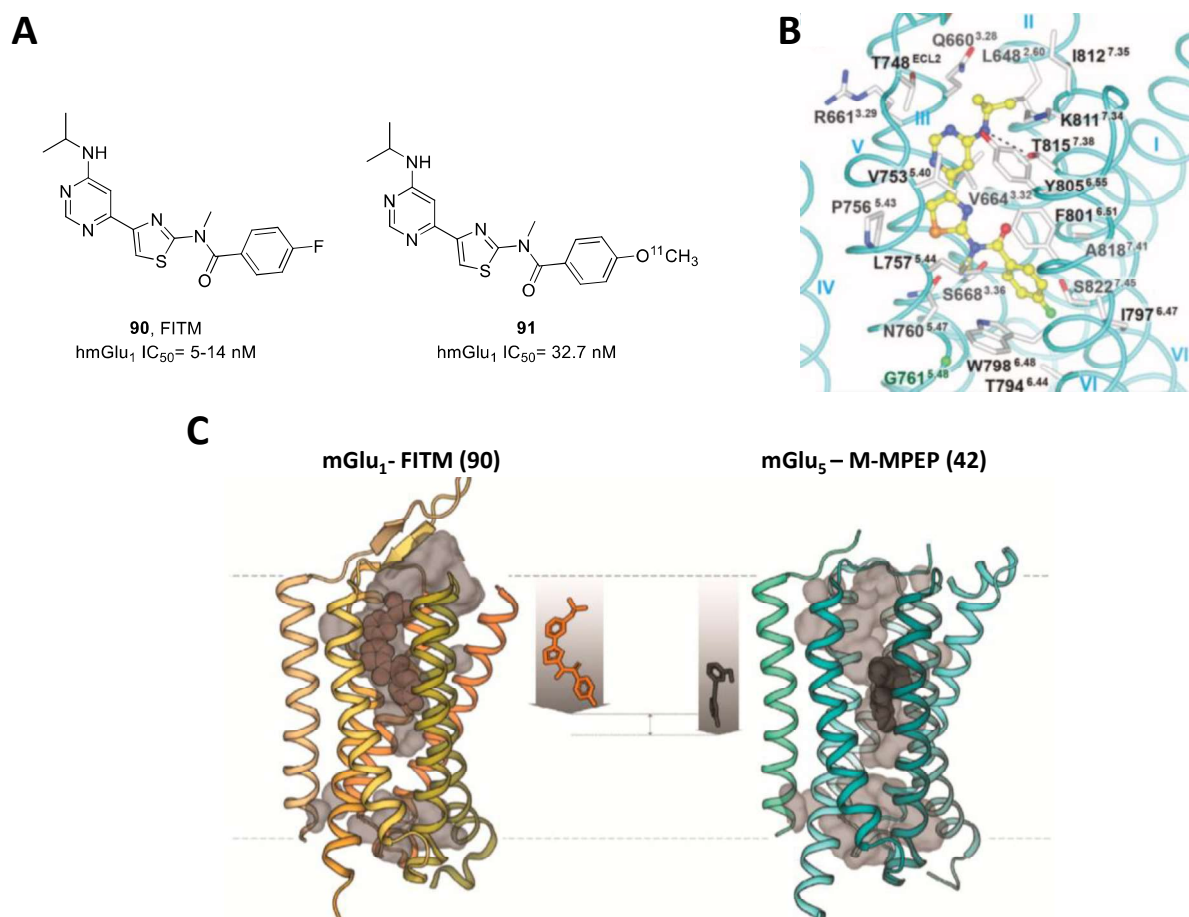


**Figure 69.** (A) Chemical structures of FITM (**90**) and labeled **91** with values of functional IC<sub>50</sub>s; (B) Structure of mGlu<sub>1</sub> 7TMD co-crystallized with FITM bound (NAM) (PDB code: 4OR2). Side chains of the FITM (**90**) binding pocket residues are shown as white carbons. Hydrogen bond interaction between the NAM and Thr815<sup>7,38</sup> is shown as a dashed line. The C $\alpha$  carbon of Gly761<sup>5,48</sup> is shown as a green ball. The ligand FITM (**90**) is shown as yellow carbons; (C) X-ray structures of mGlu<sub>1</sub> and mGlu<sub>5</sub> receptor 7TMs showing the different depth of binding pockets for NAMs. (Figure 69C from Llinas del Torrent et al.).<sup>268</sup>

Considering all this information about FITM (**90**) and compound **91**, we thought that we could obtain promising photoswitchable compounds applying an azologization strategy based on the replacement of the amide flanked by the thiazolyl and phenyl aromatic rings with azo group. We considered this replacement convenient to afford photoswitchable mGlu<sub>1</sub> NAMs because aromatic amides are characterized to display an unusual rigidity, due to the delocalization of  $\pi$ -electrons over the aromatic rings and the amide, giving a highly planar structure. This delocalization is very similar to that found in azobenzenes, making the shape of the new azo compound very similar to the parent one. Therefore, the azolog **103a** is expected to have binding affinity similar to that of compound **91** and display NAM activity in its *trans* configuration. After illumination, the binding of the corresponding *cis* isomer is not expected due to the abrupt change of geometrical disposition (Figure 70). We only considered the azologization of compound **91** (with a OMe) because the bioactivity properties did not significantly differ from FITM (**90**) and the synthesis of the corresponding azo compounds through a phenol-directed azo-coupling was more accessible.

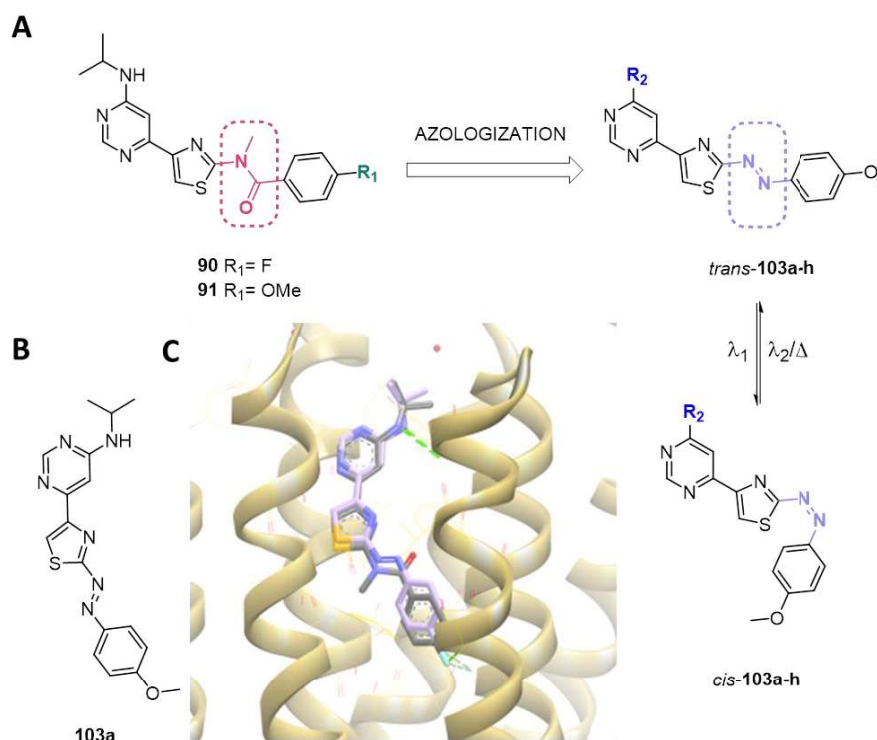


**Figure 70.** (A) Azo-replacement *trans-on* approach of **91** to afford theoretically photoswitchable compounds **103a-h**; (B) Two-dimensional chemical structure of the first azo derivative **103a**; (C) Compounds **103a** and FITM (**90**) aligned in the crystal structure of mGlu<sub>1</sub> receptor (PDB code: 4OR2).<sup>93</sup> The allosteric binding pocket is shown from the side. mGlu<sub>1</sub> in ribbon representation colored slight yellow. Compound **103a** in stick representation with carbon, nitrogen, oxygen, sulfur, fluorine atoms colored lilac, blue, red, yellow and slight green, respectively. A molecule of water is shown as a red ball.

Additionally, the azo compound **103a** may constitute the first example of a family of novel azoheteroarene photoswitchable compounds, since there are only a few examples of five membered azo photoswitches in the literature and they are mostly phenylazoimidazoles and arylazopyrazoles.<sup>157,269–271</sup> However, these heterocyclic azo compounds were studied mainly from a photochemical point of view. It was seen that they provide quantitative isomerization and long thermal half-lives,<sup>270</sup> and their photoisomerization performance can be easily tuned.<sup>271</sup>

Before proceeding in the synthesis, we studied the binding pose of compound **103a** in *trans* configuration in the crystal structure of mGlu<sub>1</sub> (PDB 4OR2) in order to check the suitability of our approach in the designed series. Thus, we aligned the parent compound **90** and **103a** (Figure 70B,C) and its *trans* configuration showed a well-fitting docking very similar to that of **90**. The amide group replacement for an azo bond does not alter the fitting of the ligand within the narrow binding pocket. Most of the hydrophobic ligand-receptor interactions observed in the crystal structure are maintained even with the compound **103a**, as well as the hydrogen bond of the pyrimidine-amine group with the Thr815<sup>7,38, 93</sup>. Additionally, the oxygen of the *p*-methoxyphenyl moiety of the ligand **103a** seems to have polar contacts at the bottom of the pocket with Trp798<sup>6,48</sup>, in a similar fashion to those of the fluorine of the ligand **90** (Figure 69B and Figure 70C)<sup>93</sup>. All these conserved interactions between **90** and **103a** suggested that both compounds would have a similar binding properties and, therefore, similar functional activity as mGlu<sub>1</sub> NAMs.

### Solubility enhancement with R<sub>2</sub> groups

Once the azologization strategy to obtain the compound **103a** seemed to be reliable from the model shown in Figure 70B, we decided to create a series of derivatives to improve the water solubility. The solubility of

the new compounds was considered a critical point since they were supposed to be tool compounds to study the conformational changes of mGlu<sub>1</sub> receptors and a limited solubility may lead to erroneous conclusions, as seen in previous series of mGlu<sub>1</sub> PAMs.\* Indeed, inserting an azo moiety into a molecular structure may frequently result in compounds that have a considerably lower solubility in aqueous media than the parent compounds.

Therefore, we planned to obtain the small library of possible photoswitchable *trans*-on mGlu<sub>1</sub> NAMs. To minimally modify the pharmacological properties of **103a**, keeping a binding affinity similar to that of compound **91**, we decided to maintain both heterocycles in the molecular scaffold of the parent compounds and also to keep the OMe group in the 4-position of the phenyl (*Figure 70A*). Indeed, it was demonstrated that the FITM analogs containing a pyrimidine as the left ring showed the most potent antagonist activity among different heteroaromatic groups<sup>263</sup> and the fluorine replacement by methoxy group was very well tolerated.<sup>266</sup> Then, we opted for the replacement of the isopropyl group in **103a** with more polar R<sub>2</sub> groups (*Figure 71*) trying to occupy a chamber where a water molecule is found and, thus, minimally disturb the binding affinity to the protein receptor, as stated above. Additionally, Wu and colleagues attributed the high potency observed for FITM (**90**) to the polar interaction between Thr815<sup>7,38</sup> and the amine derivative on the 6-position of the pyrimidine ring, after comparing the binding of FITM (**90**) with those of other non-alkylated pyridyl and pyrimidyl analogs.<sup>93</sup> For this reason, the more polar R<sub>2</sub> groups were all amino groups on the 6-position of the pyrimidine ring with some change in term of chain length and presence of nitrogen and oxygen atoms (derivatives **103b-g**, *Figure 71*).

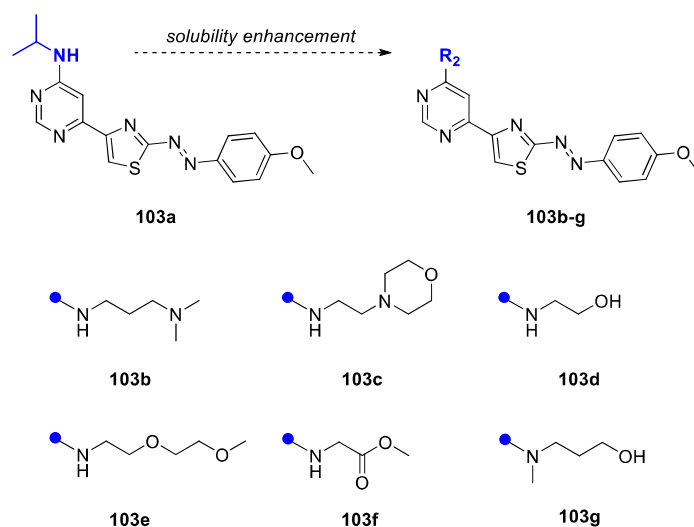


**Figure 71.** Structures of the compounds **103a-g** constituting a library of arylazothiazoles hypothesized to be mGlu<sub>1</sub> NAMs.

Ideally, this library of arylazothiazoles should be capable of inducing a pharmacological photoswitching in the activity of mGlu<sub>1</sub> fulfilling four main requirements:

- Biocompatible wavelengths of absorption for photoswitching,
- A different isomers population between dark and light conditions,
- A considerable difference of activity/affinity on mGlu<sub>1</sub> between *trans* and *cis* isomers,
- A suitable water solubility.

\* See Chapter 3: Photochemical and pharmacological characterization: first series of compounds



## Covalent photoswitchable mGlu<sub>1</sub> ligands

Finally, we explored the possibility to add covalent photoswitchable mGlu<sub>1</sub> ligands to this series of arylazothiazoles and circumvent an eventual poor affinity of this class of compounds to the mGlu<sub>1</sub> receptor. These ligands typically comprise a pharmacophore that generates affinity for a given GPCR and contain a reactive functional group that may form a covalent bond with a suitably positioned amino acid residue in the allosteric pocket of mGlu<sub>1</sub> receptor. Then, after detecting that the lysine K811<sup>7,34</sup> is close to the FITM (**90**) in the mGlu<sub>1</sub> crystal structure (Figure 69B and Figure 72A),<sup>93</sup> we designed the possible covalent analog **103h** (Figure 72A,B). Compound **103h** contains a nitrogen mustard (2-chloroethyl aniline) that was hypothesized to react with the aforementioned K811<sup>7,34</sup> after binding through the highly reactive aziridinium ion formed in aqueous solution (Figure 72B).<sup>234</sup> Moreover, it was seen that K811<sup>7,34</sup> is also quite close to the non-alkylated pyridyl and pyrimidyl compounds.<sup>93</sup> This led us to think that even the compound with just the choropyrimidine (**101**) could be a good candidate for covalently binding with the receptor via a nucleophilic aromatic substitution (Figure 72A,C).

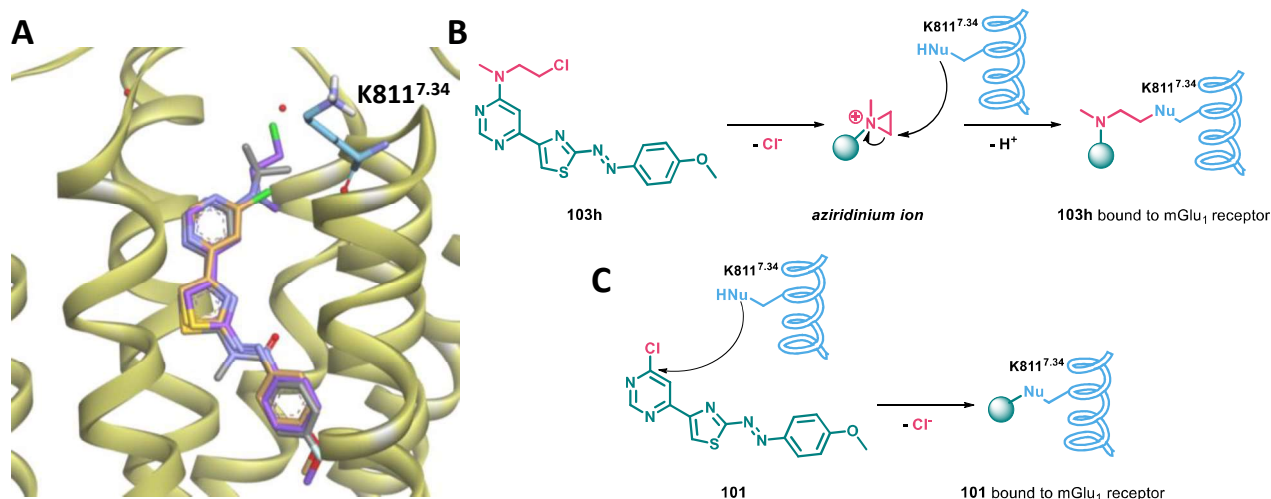


**Figure 72.** (A) Compounds **101**, **103h** and FITM (**90**) aligned in the crystal structure of mGlu<sub>1</sub> receptor (PDB code: 4OR2).<sup>93</sup> The allosteric binding pocket is shown from the side. mGlu<sub>1</sub> in ribbon representation colored yellow. Compounds **101**, **103h** and FITM (**90**) in stick representation with carbon colored orange (**101**), purple (**103h**) and grey (**90**), nitrogen, oxygen, sulfur, chlorine and fluorine atoms colored blue, red, yellow, green and cyan, respectively. K811<sup>7,34</sup> in stick representation with carbon, nitrogen, oxygen and hydrogen colored light blue, blue, red and white, respectively. A molecule of water is shown as a red ball; (B) The 2-chloroethylamine moiety (red) of the possible irreversible mGlu<sub>1</sub> NAM (**103h**) forming an aziridinium ion in solution. This reactive species ligates with the nucleophilic lysine residue (K811<sup>7,34</sup>) in the mGlu<sub>1</sub> receptor; (C) Possible nucleophilic aromatic substitution in which the nucleophilic lysine residue (K811<sup>7,34</sup>) displaces the chlorine on the pyrimidyl ring.

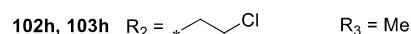
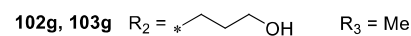
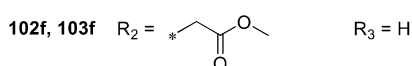
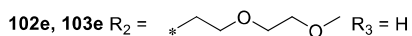
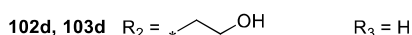
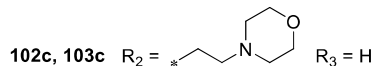
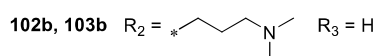
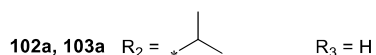
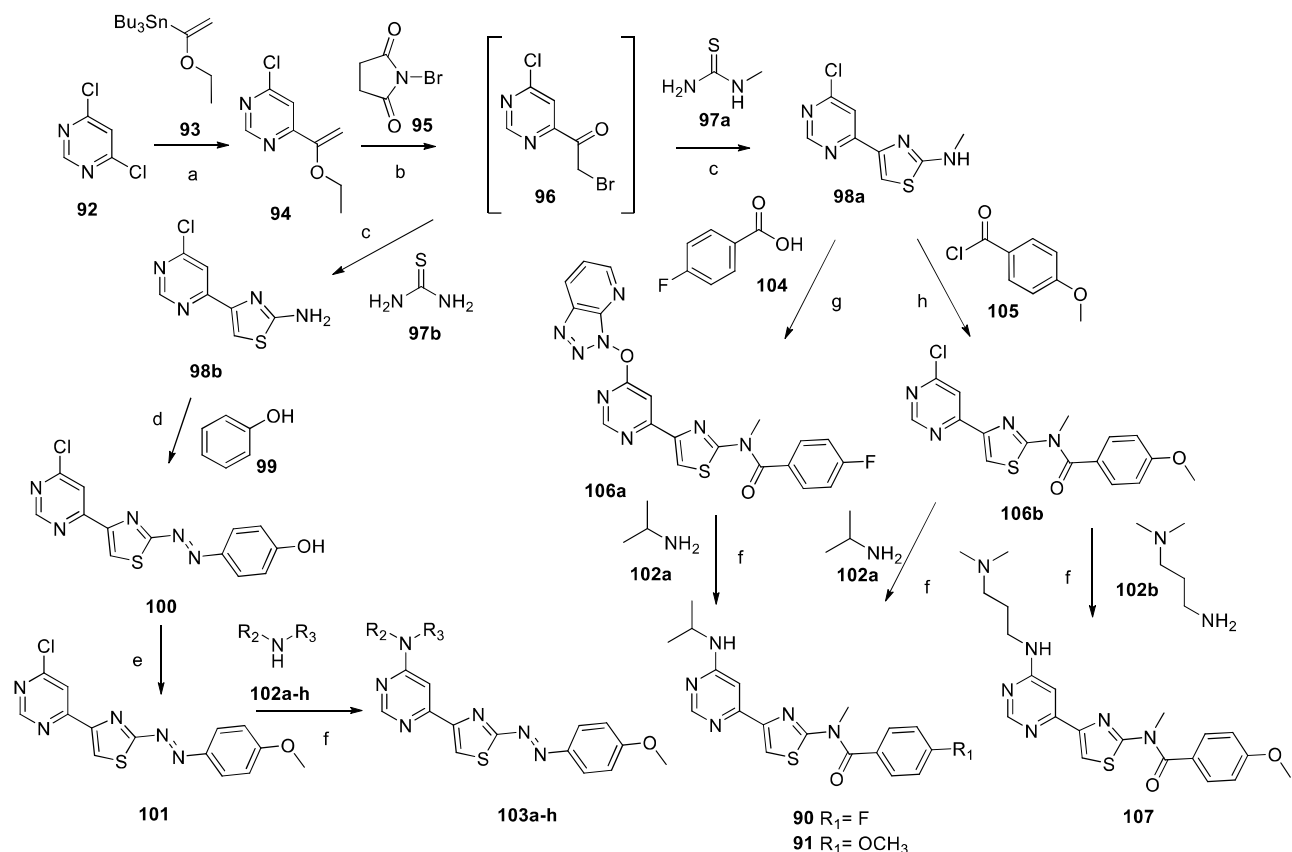
## Synthesis of compounds **101**, **103a-h** and **107**

The novel azo compounds **101** and **103a-h**, and the parent compounds **90** and **91** together with compound **107**, as a non-azobenzene analog of compound **103b**, were synthesized according to reaction sequences depicted in Scheme 10. Ethoxyvinylpyrimidine **94** was synthesized by a Stille coupling of 4,6-dichloropyrimidine (**92**) with tributyl(1-ethoxyvinyl)-stannane (**93**) in the presence of tetrakis(triphenylphosphine)-palladium(0) (Pd(PPh<sub>3</sub>)<sub>4</sub>). The bromination of **94** with *N*-bromosuccinimide (**95**), followed by bromine substitution with *N*-methylthiourea (**97a**) and thiourea (**97b**) induce a thiazole formation to give 4-(6-chloropyrimidin-4-yl)-*N*-methylthiazol-2-amine (**98a**) and 4-(6-chloropyrimidin-4-yl)thiazol-2-amine (**98b**), respectively.<sup>263,266</sup> At this point two parallel synthetic paths were considered: the

one leading to the synthesis of the azo compounds **101** and **103a-h** and the one concerning the synthesis of the parent compounds with the amide group instead of the azo bond (**90**, **91** and **107**).

The intermediate azo compound **100** was prepared from amine **98b** through a two-step preparation, previously reported for similar compounds.<sup>272</sup> It started with the diazotization of the 4-(6-chloropyrimidin-4-yl)thiazol-2-amine (**98b**) followed by an azo-coupling with phenol (**99**) to yield **100** as first azo-intermediate. Methylation of the phenol azo compound **100** with Me<sub>2</sub>SO<sub>4</sub><sup>273</sup> furnished the compound **101**. Next, the chloropyrimidine moiety of **101** was reacted with the different amines **102a-h** to obtain the series of azo compounds **103a-h**.

Aminothiazole derivative **98a** was acylated with 4-fluorobenzoic acid (**104**) and HATU/TEA as an acylating agent to obtain the corresponding *N*-methylamide. This compound reacted spontaneously with the azabenzotriazole oxide byproduct through an aromatic nucleophilic substitution in the position 6 of the pyrimidine ring to give the intermediate **106a**. The acylation the amine **98a** with 4-methoxybenzoyl chloride (**105**) gave the expected **106b**. The electrophilic reactivity of the pyrimidine 6-position of compounds **106a** and **106b** resulted similar and allowed the substitution with amines **102a** and **102b** to give the compounds **90**, **91** and **107** that will be used as reference non-photoswitchable standards.

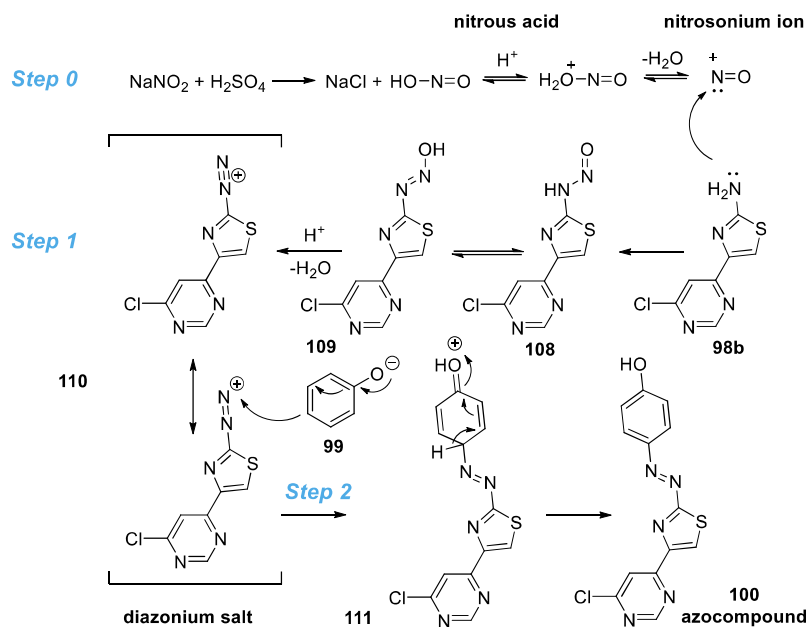


**Scheme 10.** Synthesis of compounds **101**, **103a-h**, **90**, **91** and **107**. Reagents and conditions: (a) Pd(PPh<sub>3</sub>)<sub>4</sub>, DMF, 80 °C, 4 h, 66%; (b) THF, H<sub>2</sub>O, rt, 2 h; (c) rt, 2 h, 85- 96% (two-steps); (d) (I) H<sub>2</sub>SO<sub>4</sub>, NaNO<sub>2</sub>, -5 °C, 1 h; (II) NaOH, -5 °C, 30 min, 64%; (e) K<sub>2</sub>CO<sub>3</sub>, Me<sub>2</sub>SO<sub>4</sub>, DMF, rt, 16 h, 76%; (f) base<sup>\*</sup>, 1,4-dioxane, 40-80 °C, 2-16 h, 20-67%; (g) HATU, TEA, DMF, 65 °C, 16 h, 37%; (h) TEA, toluene, 100 °C, 16 h, 71%.

### Optimization of the diazotization/azo-coupling reaction

The general synthetic route to yield the compounds **101**, **103a-h**, **90**, **91** and **107** (Scheme 10) is not characterized by a high complexity. However, the reaction corresponding to the *step d* were not straightforward and needed a process of optimization. The synthetic step included the diazotization reaction of the amine **98b** followed by an azo-coupling with phenol (**99**) to obtain the azo compound **100**, which can be conceived as the "bottleneck" two-step reaction of the whole synthetic strategy.

Azo compounds can be synthesized following different procedures, such as the Mills reaction (reaction between aromatic nitroso derivatives and anilines),<sup>243</sup> the oxidation of arylhydrazines and anilines<sup>30</sup> and the reductive coupling of aromatic nitro derivatives,<sup>30</sup> among others. Nonetheless, the most common reaction to synthesize azobenzenes is the azo-coupling reaction and it was used to synthesize the azo compound **100**.<sup>30,272</sup> The methodology is based on the initial liberation *in situ* of nitrous acid from NaNO<sub>2</sub>. Further protonation and H<sub>2</sub>O elimination provides the nitrosating agent (nitrosonium ion, NO<sup>+</sup>, Step "0", Scheme 11), which is attacked by the amine **98b** to form the *N*-nitroso derivative **108**, a tautomer of the diazohydroxide **109**. A second protonation and H<sub>2</sub>O elimination affords the diazonium salt **110** stabilized by resonance (Step "1", Scheme 11). After that, phenol **99** at controlled pH is coupled with the electrophilic nitrogen of the diazonium salt **110**, through electrophilic aromatic substitution, to finally provide azo compound **100** (Step "2", Scheme 11).



**Scheme 11.** Diazotization and azo-coupling reactions. Diazotization is composed by Steps "0" and "1" to afford nitrosonium ion and diazonium salt **110**, respectively. The final azo-coupling represents Step "2" of the synthesis providing azo compound **100**.

There are several aspects in this reaction that are considered critical and must be considered. One of these is the reaction temperature in the preparation of the diazonium salts. Indeed, a number of salts derived from primary aromatic amines are relatively stable if the reaction temperature is maintained between 0

\* See Experimental Section: Synthetic procedures

and 5 °C, whereas other amines decompose even at this temperature. Furthermore, isolation of these compounds is not advisable since they are potentially explosive. Generally, diazonium salts are weak electrophiles that react with electron rich species, such as substituted arenes having electron donor groups like amine or hydroxyl, to give azobenzenes. Normally, such a substitution reaction takes place at the *para* position to the electron donor group on the activated aromatic ring, acting as a nucleophile. This reaction is highly pH dependent, making the pH another aspect of utmost importance for the success of the azo-coupling reaction. For example, it has been established that phenols are successfully coupled in alkaline conditions. In these conditions, a phenolate ion is formed, which is more soluble in water than the phenol itself. This in turn readily provides the desired electron releasing group, thus, facilitating the electrophilic substitution reaction to afford the azo compound. However, highly alkaline conditions are usually avoided as they lead to diazonium salt decomposition.<sup>274</sup>

Then, aware of the very high instability of the specific diazonium salt **110**, we considered all the critical aspects of this reaction and carried out an optimization process focusing on number of equivalents of reagents, order of addition of the different reaction mixtures, holding times and temperature in order to increase the yield for the synthesis of the intermediate azo compound **100**. The synthesis was conducted using water and methanol in appropriate ratio and in different conditions and temperatures, providing the desired compound in poor yields. On the contrary, the use of small quantities of acetic acid as solvent to initially solubilize the amine **98b** avoided the formation of the by-product **112** as result of nucleophilic substitution by methoxide ion in highly basic conditions (Figure 73). All the mentioned parameters are reported in Table 20.

The best results were obtained when we replaced methanol for acetic acid to solubilize the starting amine **98b** with the next diazonium salt **110** formation at -5 °C and the resulting solution (at -5 °C) was slowly added to the phenolate, maintaining very carefully the temperature at 0°C and the pH of the resulting mixture constantly at 10, adding NaOH 5M solution when necessary. Indeed, we noticed that very small changes in pH drastically reduced the yield. For this reason, we decided to use the same deprotonated azo compound **100** as *in situ* pH indicator as soon as gradually formed, taking advantage of the fact that this deprotonated compound is extremely red, due to its large  $\pi$  electron conjugation. Therefore, each time we added the acidic solution of the diazonium salt **110** to the basic phenolate dropwise, we paid attention on the color change of the resulting mixture, adding NaOH (2 or 5M) solution to keep it continuously red (*i.e.* at  $\text{pH} \geq 10$ ). This allowed us to have a constant amount of phenolate ready to react as soon as the highly unstable and pH-sensitive diazonium salt **110** was added to the mixture.

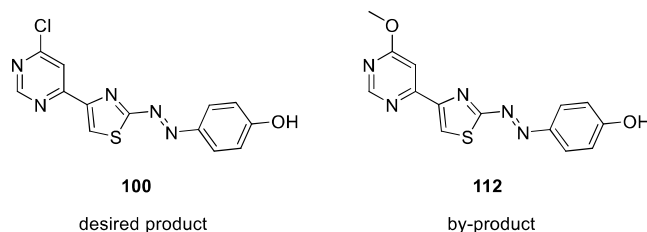


**Figure 73.** Structures of desired azo compound **100** and major by-product **112**.

Entry	NaNO <sub>2</sub> <sup>[a]</sup>	H <sub>2</sub> SO <sub>4</sub> <sup>[a]</sup>	NaOH <sup>[a,b]</sup>	phenol (99) <sup>[a]</sup>	Solvent	Order of addition to form 110	Order of addition to form 100	Holding time + temp. of 110 <sup>[c]</sup>	Yield %
1	1.0	177	180+ 2M sol.	1.0	MeOH/H <sub>2</sub> O	Nitrous solution over 98b	99+ NaOH over 110.	2 h at 0± 5°C	2.3
2	1.0	190	1.0+ 5M sol.	1.0	MeOH/H <sub>2</sub> O	98b over nitrous solution	110 over 99+ NaOH.	2 h at 0± 5°C	4.7
3	1.2	190	2.0+ 5M sol.	2.0	MeOH/H <sub>2</sub> O	98b over nitrous solution	99+ NaOH over 110	30 min at 0± 5°C	0.0
4	1.2	500	1.2+ 5M sol.	1.2	MeOH/H <sub>2</sub> O	98b over nitrous solution	110 over 99+ NaOH	2 h at 0± 5°C	15.4
5	1.2	90	4.0 +5M sol.	1.2	MeOH/H <sub>2</sub> O	98b over nitrous solution	110 over 99+ NaOH	2 h at -10°C	16.0
6	1.2	70	90+5M sol.	1.2	AcOH/H <sub>2</sub> O	98b over nitrous solution	110 over 99+ NaOH	1.5 h at -5°C	64.0%

[a] Number of equivalents.

[b] (X M) NaOH solution added to keep the pH of the mixture at 10.

[c] Reaction mixture containing 110 held to stir during the dropwise addition in order to obtain the azo compound 100.

**Table 20.** Diazotization reaction optimization. Impact of number of equivalents of NaNO<sub>2</sub>, H<sub>2</sub>SO<sub>4</sub>, NaOH and phenol (99); order of addition of the reaction mixtures, holding times and temperature in synthesis of the intermediate azo compound 100.

### Photochemical characterization with UV-Vis absorption spectroscopy

As done for the Chapters 1-3 of the present thesis, we used UV-Vis absorption spectroscopy to determine the photochemical properties of samples of the azo compounds **101** and **103a-h** 50 μM in H<sub>2</sub>O with 0.5% DMSO, which were carefully protected from ambient light. In the dark, we obtained the UV-Vis spectrum of the *trans* isomers and we proceeded with the illumination of the samples with violet light (380 nm) to induce isomerization from *trans* to *cis* configuration. We collected the new spectra and we repeated the procedure after illuminating them with lilac (405 nm), turquoise (455 nm), green (500 nm), slight green (532 nm) and yellow (550 nm) light to obtain the spectra of the different PSSs, as shown in *Figure 74A* for **103b**, which displays the general behavior common for all the arylazothiazoles derivatives.

The *trans*→*cis* isomerization can be induced with 405 nm more efficiently than with wavelengths at the violet range. Indeed, the *cis* isomer has a minimum of absorbance around this wavelength (*Figure 74A*), making it the most suitable wavelength for such isomerization. 420 nm gave very equivalent results (*Figure 74B*). On the other hand, 532 and 550 nm light are the suitable wavelength to back isomerize compound **103b** to its thermodynamically stable *trans* isomer, since they are in the same region as the minimum of absorbance of *trans* isomer.

The photoisomerization after several photoisomerization cycles was also determined with the same compound solutions using 405-nm and 550-nm illumination wavelengths per cycle. No differences were observed between the absorbance values of all the analogs upon several cycles of yellow and lilac light, showing convincing stability of the photoisomerization of the arylazothiazole photoswitches and high

solubility of both isomers in aqueous medium (Figure 74D). The thermal relaxation of the *cis*-**103b** in aqueous medium was also evaluated, showing a half-life of 14 min (Figure 74E,F).

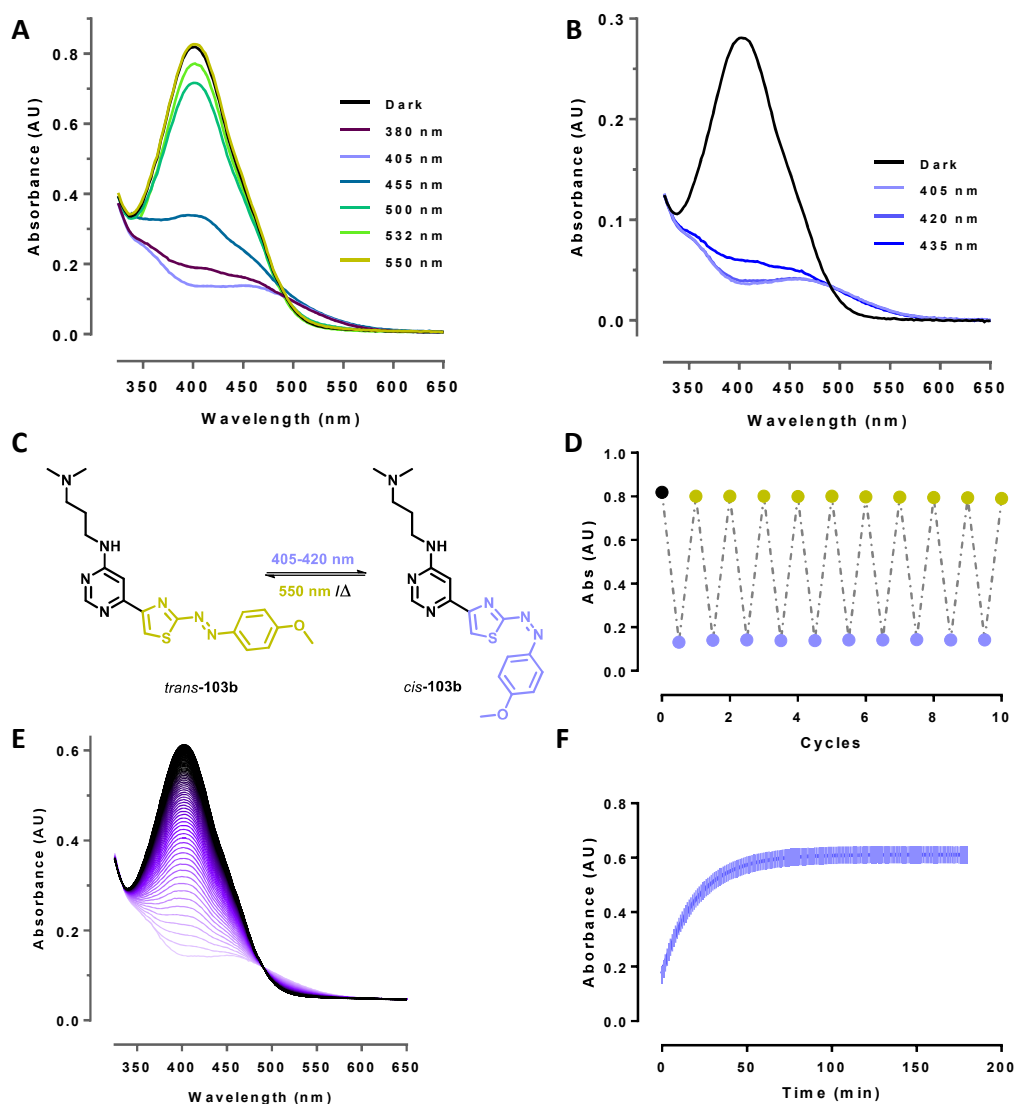


**Figure 74.** Photochemical properties of compound **103b**. (A) UV-Vis absorption spectra of **103b** 50  $\mu\text{M}$  in  $\text{H}_2\text{O}$  with 0.5% DMSO at 25  $^\circ\text{C}$  under dark (black) and different light conditions for 3 min; (B) UV-Vis absorption spectra of **103b** 40  $\mu\text{M}$  in  $\text{H}_2\text{O}$  with 0.5% DMSO at 25  $^\circ\text{C}$  under dark (black) and 405-435 nm light range for 3 min; (C) Chemical structures of the photoisomers of **103b**; (D) UV-Vis absorption measurements of 50  $\mu\text{M}$  **103b** in  $\text{H}_2\text{O}$  with 0.5% DMSO at  $\lambda_{\pi-\pi^*}\text{max}$  of *trans* isomer (400-402 nm) after repeated cycles of illumination with 550 (yellow) and 405 nm light (lilac); (E) UV-Vis absorption spectra of **103b** in  $\text{H}_2\text{O}$  with 0.5% DMSO after attainment of the PSS, measured every minute for 3 hours at 25  $^\circ\text{C}$ ; (F) Thermal relaxation plot of *cis*-**103b** in  $\text{H}_2\text{O}$  with 0.5% DMSO at 25  $^\circ\text{C}$ . Absorbance at 400 nm was recorded for 3 h.

### Study of pH-dependent photoisomerization properties

After studying the photochemical properties of this series of arylazothiazoles, we decided to explore also their photoisomerization in different pH conditions. Then, we selected the azo compound **103b**, shown in Figure 74C, as the prototypical example of this azobenzene family, taking advantage of its remarkable water solubility observed in the previous experiments. Certainly, the study of the possible pH dependence may be more relevant from a chemical rather than a biological point of view, although there are some cellular compartments that have a pH lower than 6.8-7.4 (e.g. cell organelles, such as lysosomes, have a pH of around 4.5). Thus, we studied the photoisomerization and relaxation kinetics of **103b**, 50  $\mu\text{M}$  at 25  $^\circ\text{C}$ , in

several buffer solutions, with 0.5% DMSO, covering a pH range from 3.5 to 10.6. For the first study, we collected UV-Vis absorption spectra of **103b** under dark and different light conditions for 3 min whereas for the second one we obtained relaxation plots of *cis*-**103b** at 25 °C after illumination with 405 nm light.\*

The change in pH provided no significant effect on its absorption spectra, but rather a variation in the rate of thermal *cis* → *trans* isomerization (Figure 75). This led us to think that the pH and therefore the protonation only concerns the *cis* isomer, which is known to be the isomer with more basic behavior (the 1<sup>st</sup> pK<sub>a</sub> value for *t*-AB (**1**) and *c*-AB (**1**) are -2.6 and -1.6, respectively).<sup>20</sup> More precisely, the arylazothiazole **103b** has four types of nitrogen atoms that can be subject to protonation. The secondary aliphatic amine is the one that protonates more easily in both photoisomers and even at high pH (pH ≤ 8-9, Figure 76), followed by the two nitrogen atoms of the pyrimidine ring, which have similar properties due to the amino group in *ortho* and *para* position respectively (pH ≤ 5-6, Figure 76).<sup>275,276</sup> At a more acidic pH it might be possible both the thiazole (the pK<sub>a</sub> value of the only thiazole is 2.5)<sup>277</sup> and azo protonation (Figure 76).

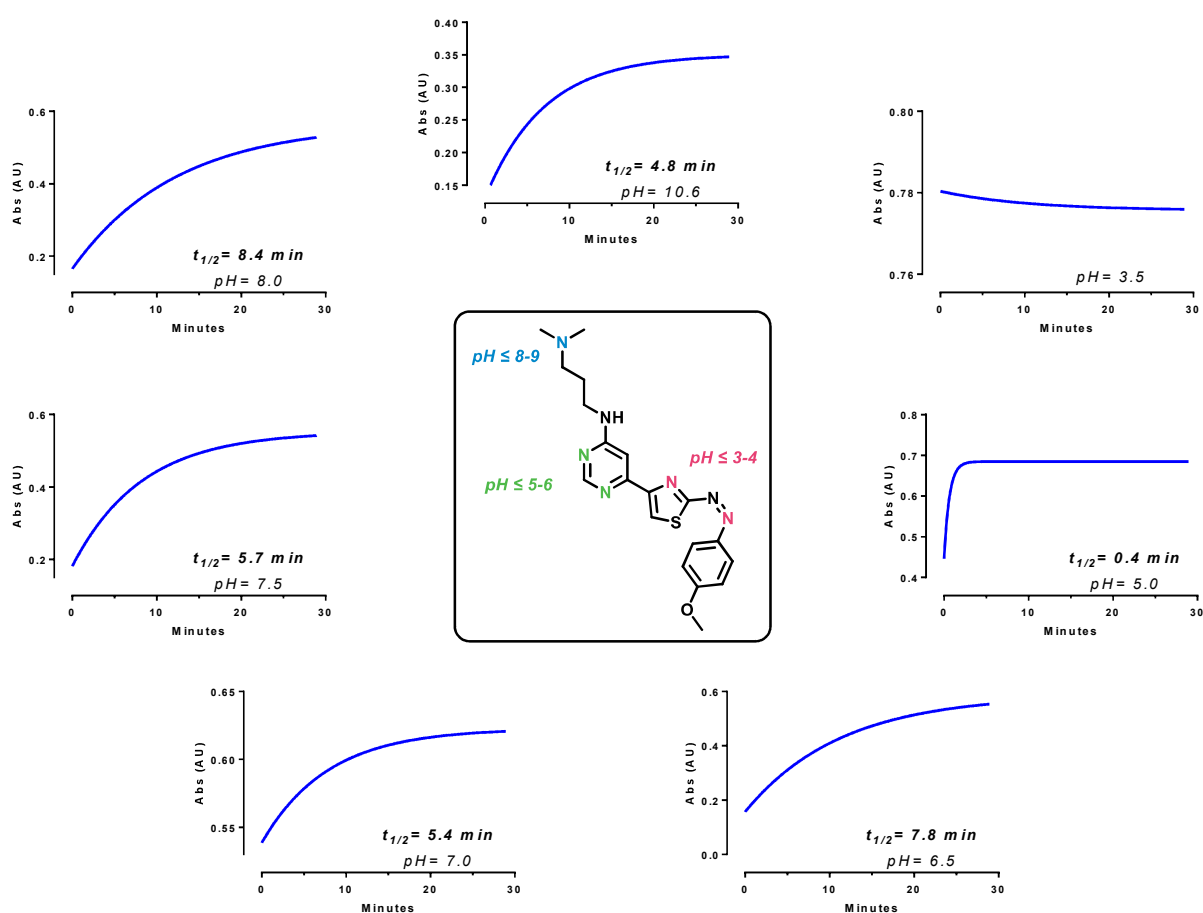


**Figure 75.** Cycle showing the pH-induced change of rate of thermal *cis* → *trans* isomerization of **103b** 50 μM at 25 °C in different buffer solutions. In the center, the structure of *cis*-**103b** and its protonable nitrogen atoms depending on pHs. Both N atoms of the pyrimidine ring are subject to protonation at pH ≤ 5-6 equivalently.

Thermal *cis* → *trans* isomerization rates are of the order of 5-8 minutes at pHs from 6 to 10 (Figure 75). This would be explained by the fact that for the protonated species at these pHs the positive charge is delocalized on the molecule without directly affecting the conjugation of arylazothiazole. On the other hand, the nitrogen of the thiazole or the azo bond could be also protonated at a more acidic pH. In this case

\* See Experimental section

the positive charge will be distributed throughout the arylazothiazole system affecting negatively the delocalization of  $\pi$  electrons on N-N double bond and facilitating the rotation of this bond (Figure 76). Therefore, the rotation mechanism should dominate the relaxation pathway of *cis*-**103b** at pH  $\leq$  3-4, leading to much higher rates of thermal *cis*  $\rightarrow$  *trans* isomerization. This could explain the fact that we can only observed the *trans* isomer and no *cis*  $\rightarrow$  *trans* relaxation at pH= 3.5, probably due to a fast relaxation in the order of milliseconds (Figure 75).

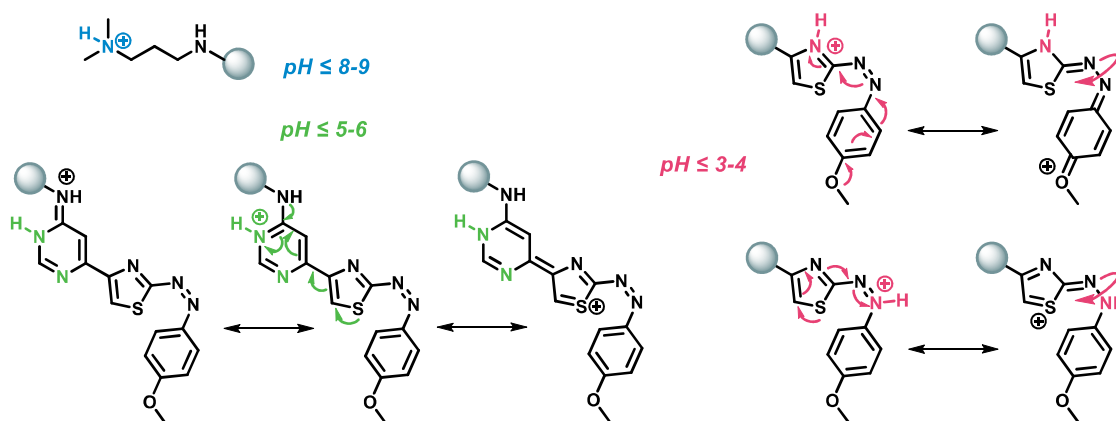


**Figure 76.** *cis*-**103b** and the possible four protonation points to which it would be subject based on the pH. Both N atoms of the pyrimidine ring are subject to protonation at pH  $\leq$  5-6 equivalently. The rupture of the N=N double bond in the resonance structures at pH  $\leq$  3-4 facilitates rotation increasing the thermal *cis*  $\rightarrow$  *trans* isomerization rates of **103b**.

## Pharmacological characterization

### Single dose screening

In order to evaluate the pharmacological activity of all the arylazothiazoles of the series, we first screened them in HEK293 cells transiently transfected with human mGlu<sub>1</sub> using an inositol phosphate (IP) accumulation assay based on homogeneous time-resolved fluorescence (HTRF) assay.\* We measured the capacity of the compounds at a 10  $\mu$ M single concentration to antagonize the activity induced by an orthosteric agonist. The experiments were performed in dark and 400-nm light conditions. Gratifyingly, analogs **103a-e** and the non-photoisomerizable compound **107** showed with a very promising activity as mGlu<sub>1</sub> NAMs when compared with the reference FITM (**90**) or compound **91** (Figure 77). The active azo compounds **103a-e** loss their inhibitory activity upon 400 nm illumination, which indicates that the less thermodynamically stable isomer is clearly less potent. Compound **107** is not photoisomerizable and, as FITM (**90**) and **91**, shows the same activity both in dark and under light conditions. Disappointingly, **103f-g** and the putative covalent photoswitchable ligands **103h** and **101** did not even reach the threshold of 50% inhibitory effect on the receptor (Figure 77). Therefore, we decided to exclude those compounds for further characterization, and focus the study of the activity in mGlu<sub>1</sub> receptor only of the compounds **103a-e** and **107**.

\* See Experimental Section: Homogeneous Time-Resolved FRET (HTRF) technology



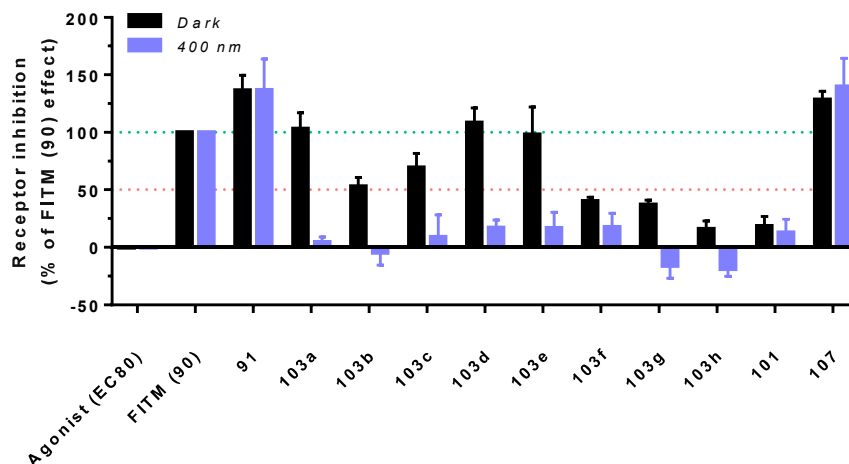


**Figure 77.** Screening of compounds **101**, **103a-h** and **107** in mGlu<sub>1</sub>. Assay performed in mGlu<sub>1</sub> transiently transfected HEK293 cells with 100  $\mu$ M of Glutamate (EC<sub>80</sub>) and 10  $\mu$ M of each compound, in dark conditions (black bars) and under 400 nm-illumination (lilac bars). Normalization is done between 0= agonist (EC<sub>80</sub>) and 100%= inhibition by FITM (**90**).

### Dose-response curves

As single concentration assays revealed antagonism of compounds **103a-e** and **107**, we needed to further evaluate their *trans*-on NAM activity. Therefore, we generated dose-response curves from IP accumulation assay with HEK293 cells transfected with mGlu<sub>1</sub> receptor. The assays were performed under dark and illumination with 400 nm wavelength conditions to obtain a high percentage of *trans* and *cis* isomer respectively. FITM (**90**) was used as non-photoswitchable reference NAM for this assay. As expected, both FITM (**90**) and the arylazothiazoles **103a-e** antagonized the IP production evoked by the activation of mGlu<sub>1</sub> with quisqualate. The azo compounds **103a-e** and non-photoisomerizable **107** displayed IC<sub>50</sub>s in the micromolar range in dark conditions, which correspond to  $\sim 1.5/2$  log-fold lower than that of the parent compound FITM (**90**). This indicates that the replacement of the methyl amide moiety with the *trans* azo bond or the modification introduced in the aliphatic chain of the molecule would reduce considerably the antagonistic activity (Figure 78).

Unfortunately, we obtained some artifacts under 400 nm light conditions that did not allow us to obtain reliable dose-response curves and therefore, they are not shown in Figure 78. One possible explanation could be related to some kind of toxicity exhibited by the azo compounds in their *cis* configuration, after light illumination, and leading to *in vitro* cell death.

At this point, we decided to suspend these assays looking forward to performing a better analysis of the photopharmacological properties of azo compounds **103a-e**. Indeed, new experiments are programmed with azo compounds **103a-e** under dark and light conditions using mock\* HEK293 cells or HEK293 cells transiently transfected with another receptor such as mGlu<sub>5</sub>. In addition, eventual toxicity should be corroborated in presence of other light wavelengths and also delivered by a different light system.

\* Mock transfection is treatment of cells without DNA and with only the delivery agent (e.g. transfection reagent alone or empty vector) to control for cellular effects due to transfection reagent exposure or transduction. This control is important because transfection reagents or transduction can easily alter gene expression.

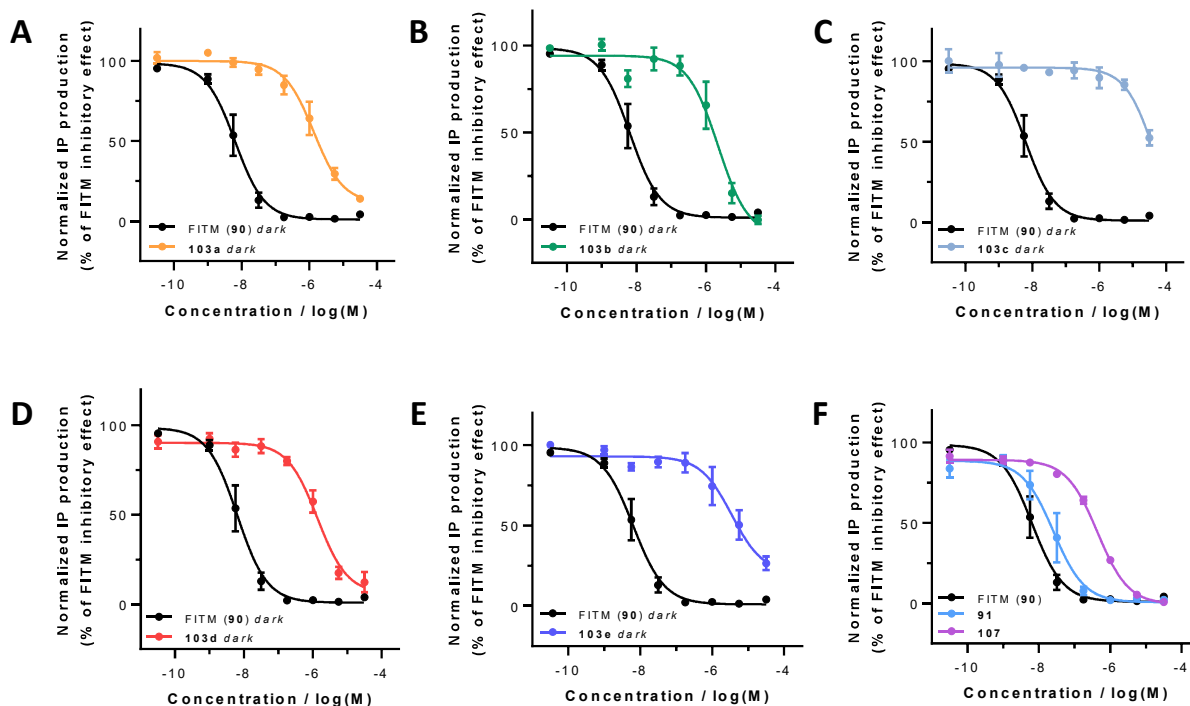


**Figure 78.** Pharmacological properties of compounds **103a-e** and **107**. Dose-response curve of compound (A) **103a**, (B) **103b**, (C) **103c**, (D) **103d**, (E) **103e** and (F) **107** with a constant concentration of Quisqualate 1  $\mu$ M in HEK293 cells overexpressing mGlu<sub>1</sub> in dark conditions only. FITM (**90**) was used as a mGlu<sub>1</sub> NAM standard (round dots and black line). Compound **91** was tested as well in the same conditions (F, round dots and blue line). Each point corresponds to the mean of at least three independent experiments, performed in duplicate, with the corresponding SEM as error bars.

### Analysis of mGlu<sub>1</sub> NAM effect on receptor conformational changes induced by agonist

As mentioned in the General Introduction section of this PhD thesis, there is an increasing interest in GPCR conformational biosensor assays as methods to study activation mechanisms. These sensors are based on FRET compatible fluorescent protein domains fused into two regions of the receptor. These protein domains are fluorescent because they are natural fluorescent protein analogs (*e.g.* GFP or YFP) or because they have been labeled with a fluorescent probe (*e.g.* SNAP-tag, HALO-tag), which has been demonstrated not to affect the receptor function.<sup>170</sup> Thus, a differential FRET can be measured upon conformational changes of the GPCR linked to the activation state.

Therefore, we decided to explore the allosteric effect of mGlu<sub>1</sub> NAMs on the several conformational changes that characterize the entire mGlu receptor activation process, from VFT to 7TMD, using the aforementioned FRET-based biosensors. We used glutamate or quisqualate as orthosteric agonists to activate mGlu<sub>1</sub> receptor, which was monitored in absence or in presence of a NAM with three different types of FRET biosensors:

- VFT sensors (*V* sensors; reporting movements between VFT domains, *Figure 79A*),
- IntErmolecular sensors (*E* sensors; reporting movements between the protomers, *Figure 79B*)
- IntrAmolecular sensors (*A* sensors; reporting movements in the 7TMD, *Figure 79C*).

The *V* sensors consist in SNAP protein tag domains fused at the *N* termini of both mGlu subunits labelled with time-resolved FRET-compatible fluorophores, which allow us to measure the distance variation between VFT domains of the receptor.<sup>170,278</sup> In mGlu receptors, agonist binding induces a closure of the VFT domain, which in turn induces a reorientation of the VFT protomers, resulting in an increased distance between the *N* termini and a decrease of TR-FRET (*Figure 79A*).<sup>170,278</sup> In the past, this method allowed the analysis of the effect of orthosteric and allosteric ligands on the receptor, notably the ability of PAMs to enhance the affinity and efficacy of agonists and stabilize the active conformation of the VFT dimer.<sup>279</sup> Additionally, Rovira and colleagues used these biosensors with mGlu<sub>4</sub> receptor to show that all PAMs enhance agonist action on the receptor through different degrees of allosteric agonism and positive cooperativity.<sup>280</sup> Very recently, the effect of a PAM on the structural dynamics of mGlu<sub>2</sub> using single molecule FRET at sub-millisecond timescales was also explored. The authors were able to demonstrate that glutamate alone partially stabilizes the extracellular domains in the active state while full activation is only observed in the presence of a PAM or the G<sub>i</sub> protein. Moreover, positive allosteric modulators enhance agonist efficacy by increasing the residence time of a GPCR in the active state.<sup>281</sup> However, these *V* sensors have not been used yet to investigate the negative cooperativity of a NAM on the structural dynamics of mGlu receptors.

To study the conformational changes at 7TMD level, we used the intermolecular and intramolecular FRET sensors previously reported by Hlavackova and Grushevskiy.<sup>\*,196,197</sup> The *E* sensors include a fluorescent protein domain fused in the second intracellular (i2) loop, between Ile<sup>685</sup> and Leu<sup>686</sup>. Indeed, one protomer includes a CFP (FRET donor) and the other a YFP (FRET acceptor) that allow the FRET production when the mGlu<sub>1</sub> dimer is formed at the cell surface. This FRET can be detected by microscopy (*Figure 80A*) and increases upon the addition of agonists as a result of the 7TMD rearrangement (*Figure 79B*) in which the two protomers move toward each other. In fact, when the protein domains were fused in the *C*-termini, the FRET increase upon receptor activation was much lower than that of receptors with the fluorescent domains fused at i2 loop, indicating that the latter constituted better biosensors.<sup>196</sup> To control the subunit composition of mGlu<sub>1</sub> dimers, Hlavackova and collaborators used the *C*-terminal “quality control system” of the GABA<sub>B</sub> receptor. They replaced the *C* termini of the mGlu<sub>1</sub> subunits with the last 87 *C*-terminal amino acids of GABA<sub>B1</sub> (c1) and the last 181 *C*-terminal amino acids of GABA<sub>B2</sub> (c2), such that only heterodimers containing two different longer *C*-terminal tails (a c1 version and a c2 version) reached the cell surface.<sup>196,197</sup>

While the *E* sensors consist in a fluorescent protein domain in each protomer, the *A* sensors involve the fusion of two fluorescent proteins in each of the two mGlu<sub>1</sub> protomers. Thus, they are labeled with a YFP in the i2 loop and a CFP at the *C* terminus (*Figure 79C* and *Figure 80B*). To control the subunit composition of mGlu<sub>1</sub> dimers, a *C*-terminal “quality control system” of the GABA<sub>B</sub> receptor similar to that for the *E* sensors was used. In this case, only the *A* sensor which have the short *C*-terminal tails (c1sh and c2sh versions) reached the cell surface.<sup>196,197</sup> After activation of the receptor and consequent conformational changes within a single transmembrane domain, FRET between *A* sensors decreased. This result is compatible with the notion of an outward movement of TM6 on activation and resultant distancing of the sensors.<sup>196,197,282</sup> Due to the activation of class C GPCRs, FRET signal comes only from one of the two protomers.

---

\* See *General Introduction: The 7TM domain activates G-protein stepwisely*.

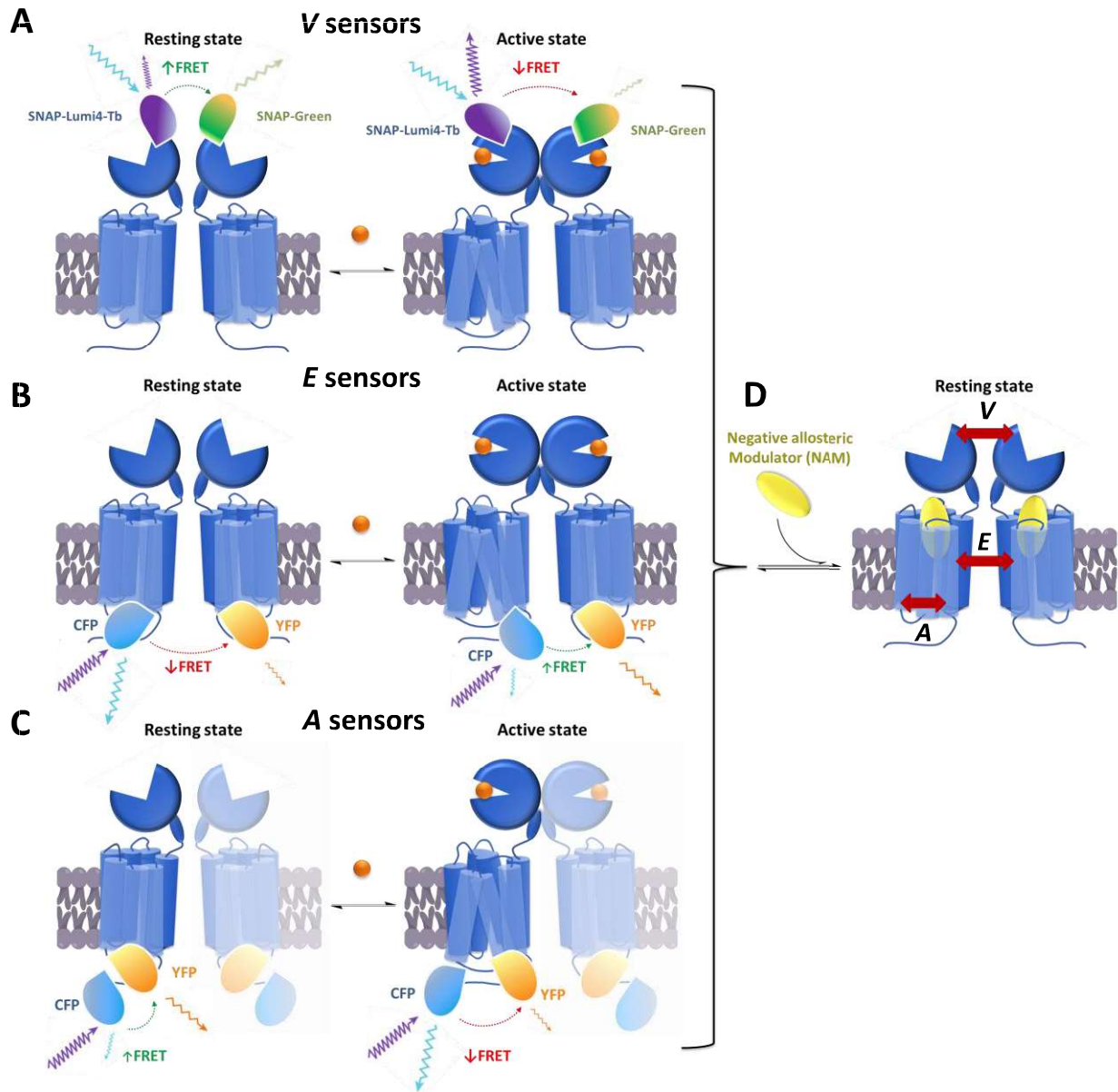


**Figure 79.** Schematic representation of FRET-based mGlu sensors. (A) *V* sensors report movements between VFT domains. These sensors consist in mGlu receptor modified 20-kDa SNAP-tag suicide enzyme, which is labelled with a TR-FRET acceptor (SNAP-Green (Fluorescein)) and donor (SNAP-Lumi4-Tb). The SNAP-tags are positioned strategically to sense the change of conformation occurring on receptor activation. In the open resting conformation (basal) or in the inactive conformation stabilized by a competitive antagonist, the fluorophores are in close proximity and the measured FRET is high. In the active closed conformation, stabilized by agonists, the FRET is low. (B,C) *E* sensors (B) and *A* sensors (C) reporting intermolecular and intramolecular movements of the mGlu<sub>1</sub> receptor, respectively. The *E* sensor is composed of one mGlu<sub>1</sub> protomer labeled with a CFP and one labeled with a YFP. Both protein domains are inserted in the second intracellular loop. A C-terminal tail from the GABA<sub>B1</sub> and GABA<sub>B2</sub> receptors, respectively, assures that only dimers carrying two different labels reach the cell surface. The *A* sensor contains two mGlu<sub>1</sub> protomers, each labeled with a YFP in the second intracellular loop and a CFP at the C terminus. Due to the activation of class C GPCRs, FRET signal comes only from one of the two protomers and, that is why, only one protomer labeled with CFP and YFP is highlighted. (D) Cartoon illustration of eventual effects of the 7TM-targeting mGlu<sub>1</sub> NAM on the conformational dynamics of the receptor at the three different levels and how such events can be monitor with the presented sensors. (Adapted from Scholler et al. and Grushevskiy et al.).<sup>197,278</sup>

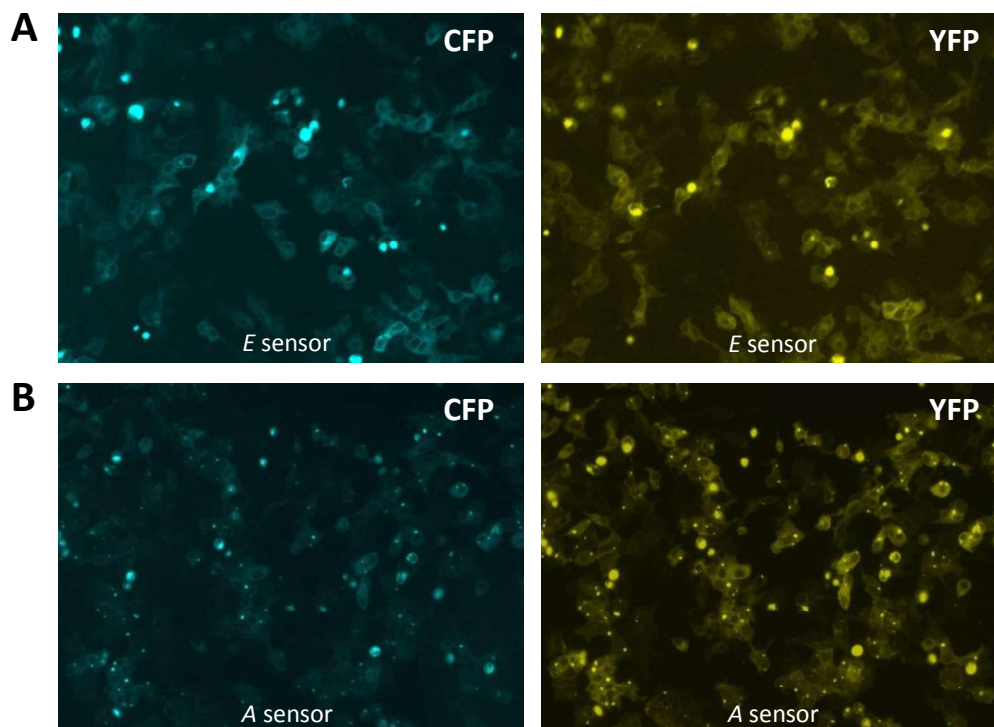


**Figure 80.** HEK293 cells transfected with (A) *E* sensor or (B) *A* sensor constructs and imaged in the CFP channel (left panels) and the YFP channel (right panels).

To identify the possible relationship between the allosteric effect of a ligand on the several conformational changes during the stepwise activation of mGlu<sub>1</sub> receptor, we chose a set of four mGlu<sub>1</sub> NAMs with similar chemical scaffold but with different functional groups capable of modifying their mode of action. We have already proven that compounds **91**, **103b**, and **107** and FITM (**90**), which binding mode in the mGlu<sub>1</sub> allosteric site was very well determined in its crystal structure with mGlu<sub>1</sub> 7TMD,<sup>93</sup> decrease the effect of the prototypical mGlu<sub>1</sub> agonist (quisqualate) with potencies ranging from 6.4 nM (**90**) to 2.2 μM (**103b**) (Figure 78 and Table 21).

Cpd.	R <sub>1</sub>	R <sub>2</sub>		hmGlu <sub>1</sub> <sup>[a]</sup> pIC <sub>50</sub> ± SEM <sup>[b]</sup>
<b>90</b>	F		MeNC=O	8.1 ± 0.2
<b>91</b>	OMe		MeNC=O	7.6 ± 0.3
<b>103b</b> <sup>[c]</sup>	OMe		N=N	5.5 ± 0.0
<b>107</b>	OMe		MeNC=O	6.4 ± 0.1

[a] HEK293 human cells transiently transfected with mGlu<sub>1</sub> receptor.

[b] Extracted from DR curves using TR-FRET IP accumulation assay.

[c] 100 % *trans*-**103b**. Compound tested only under dark conditions.

**Table 21.** Pharmacological characteristics of mGlu<sub>1</sub> NAMs **90**, **91**, **103b** and **107**.

In the following experiments, we chose FITM (**90**) as first mGlu<sub>1</sub> NAM probe with a concentration that exhibits a maximal inhibitory effect on agonist activity (500 nM). The compounds **91**, **103b** and **107** were

tested with a concentration of 300 nM, since preliminary experiments suggested it was a good concentration to use. Compound **103b** is characterized by a N=N bond instead of an amide flanked by two aromatic rings, which makes it the only photoisomerizable compound of the series. However, in this preliminary study **103b** was included in the small library as an additional analog with a different core functional group, which possible effect on the intermediate states of the receptor we wanted to explore. Therefore, it was tested only under dark conditions, exactly as done for the other compounds.

The influence of FITM (**90**, *Figure 81A*) on the conformational changes upon mGlu<sub>1</sub> activation was first assessed by studying the conformational movements of the VFT in presence of orthosteric agonists (glutamate and quisqualate) with *V* sensor. In the open resting conformation, the fluorophores are in close proximity and the measured FRET is high, whereas in active closed conformation, the FRET is low (*Figure 79A*). The mGlu<sub>1</sub> NAM FITM (**90**) elicited no significant effect on the *V* mGlu<sub>1</sub> sensors (*Figure 81B,C*), demonstrating that its antagonist activity is not associated with any change in the VFT dimer conformation. Indeed, this was a confirmation of what we already expected since FITM (**90**) is an allosteric modulator acting at 7TMD and it is non-competitive with orthosteric ligands.\*

The results changed when the effect of the same FITM (**90**) on glutamate was tested with mGlu<sub>1</sub> equipped with *E* sensors and *A* sensors. The compound, binding into the 7TMD allosteric pocket of the receptor, did not seem to exert a negative effect on the glutamate-induced rearrangement of the 7TMD of the two mGlu<sub>1</sub> subunits. On the contrary, FITM (**90**) seems to produce a significant increase in the saturating FRET effect compared to that produced with the orthosteric ligand alone (*Figure 81D,E*). These initial movements between the two protomers within the receptor dimer were detected by *E* sensors. In this case, fluorophores are approaching each other after release of glutamate and FRET increases (*Figure 79B*). A possible explanation for the enhanced FRET, reported after intermolecular movements of the mGlu<sub>1</sub> receptor, could be that the glutamate-induced rotation of the 7TMD with FITM (**90**) bound is slightly different leading to a conformation where the i2 loops get in closer proximity (*Figure 81D,E*).

Finally, we tested FITM (**90**) using mGlu<sub>1</sub> equipped with *A* sensors to obtain a further insight on the conformational changes within a single 7TMD, since sensors are fused to the same subunit of the receptor (*Figure 79C*). In this case, a FRET decrease has been observed for *A* sensors constructs reporting intramolecular conformational changes of GPCRs on activation. In the resting conformation (with the VFT open), the fluorophores are in close proximity and the measured FRET is high, whereas in active conformation (with the VFT closed), the FRET is low due to a conformational change in the 7TMD of one protomer. This new conformation is thought to be the responsible of binding and activating a G protein. In contrast, when FITM (**90**) was added in the presence of increasing concentrations of agonist, it completely blocked the action of glutamate on mGlu<sub>1</sub> equipped with *A* sensors regardless of the agonist concentration (*Figure 81F*). In other words, there was no change in FRET when FITM (**90**) was applied because it fully inhibited the glutamate-induced decrease in FRET, thus behaving as a negative allosteric modulator since it stabilizes the inactive conformation of each single 7TMD.

---

\* See *General Introduction: Modulation of mGlu receptor activity*

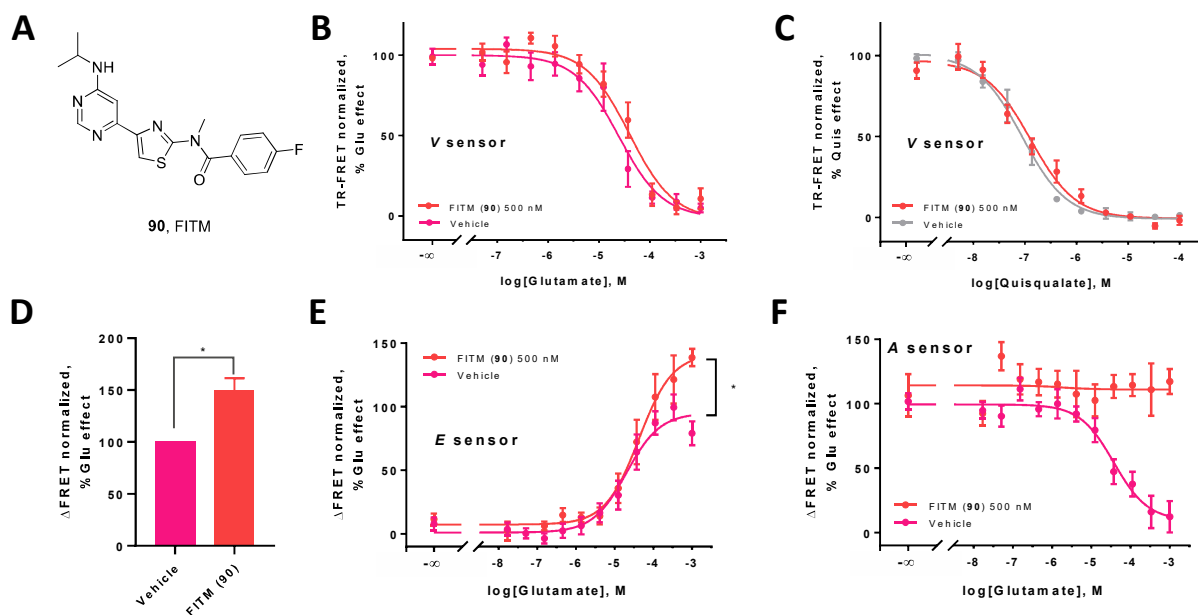


**Figure 81.** Dose-response curve of orthosteric agonists in the presence of (A) FITM (**90**) on the mGlu<sub>1</sub> equipped with (B, C) V sensors, reporting movements between VFT domains; (E) E sensors, reporting intermolecular movements between 7TMD protomers and (F) A sensors, reporting intramolecular movements in the same transmembrane domain. Data shows the mean curve  $\pm$  S.E.M. of three or four independent experiments, each performed in triplicate. (D) Percentage of glutamate maximal  $\Delta$ FRET on the mGlu<sub>1</sub> receptor using E sensors constructs in absence and in presence of 500 nM FITM (**90**). Statistical calculations were performed with two-tailed paired t test with 95% of confidence level and statistical significance \* $p < 0.05$ .

Then, a plausible explanation for FITM (**90**)-induced increase of FRET observed with the E sensors may be related to the results observed with the A sensors. The E sensors measure the difference of inter-subunit distance (on the i2 loop) and the obtained results imply that this distance is slightly larger when the FITM (**90**) is not bound in the allosteric pocket (Figure 81E). Upon glutamate application, there is also an intra-subunit increase of distance between i2 loop and the C-terminus (observed with the A sensors), which may consequentially slightly increase the distance between the two i2 loops (observed with E sensors). In presence of a NAM, the intra-subunit activation is not produced and the distance between i2 loops of each protomer may be slightly shorter with resulting increase of FRET when the E sensors are used (Figure 81E Figure 82A).

Afterwards, we decided to repeat the assays with another NAM reported in the literature, *i.e.* compound **91**, whose only structural difference with FITM (**90**) is the methoxy group instead of the fluorine atom (Figure 83C), which is common to the rest of the compounds of the mGlu<sub>1</sub> NAM series. Due to the slight structural change, we did not expect highly different results from those obtained previously with FITM (**90**).

Surprisingly, compound **91** exhibited a different response with the V sensors. It seems that **91** considerably reduces by itself the FRET in presence of low concentration or also in absence of orthosteric ligands (glutamate or quisqualate, Figure 83A,B). This decrease of the basal FRET and the consequent stabilization of a possible closed conformation of the VFTs of a considerable population of mGlu<sub>1</sub> receptors, or the stabilization of an intermediate conformation between the closed and the open conformations, could be considered as result of a high degree of cooperativity between the allosteric ligand acting at 7TMD and VFT dimer conformation.

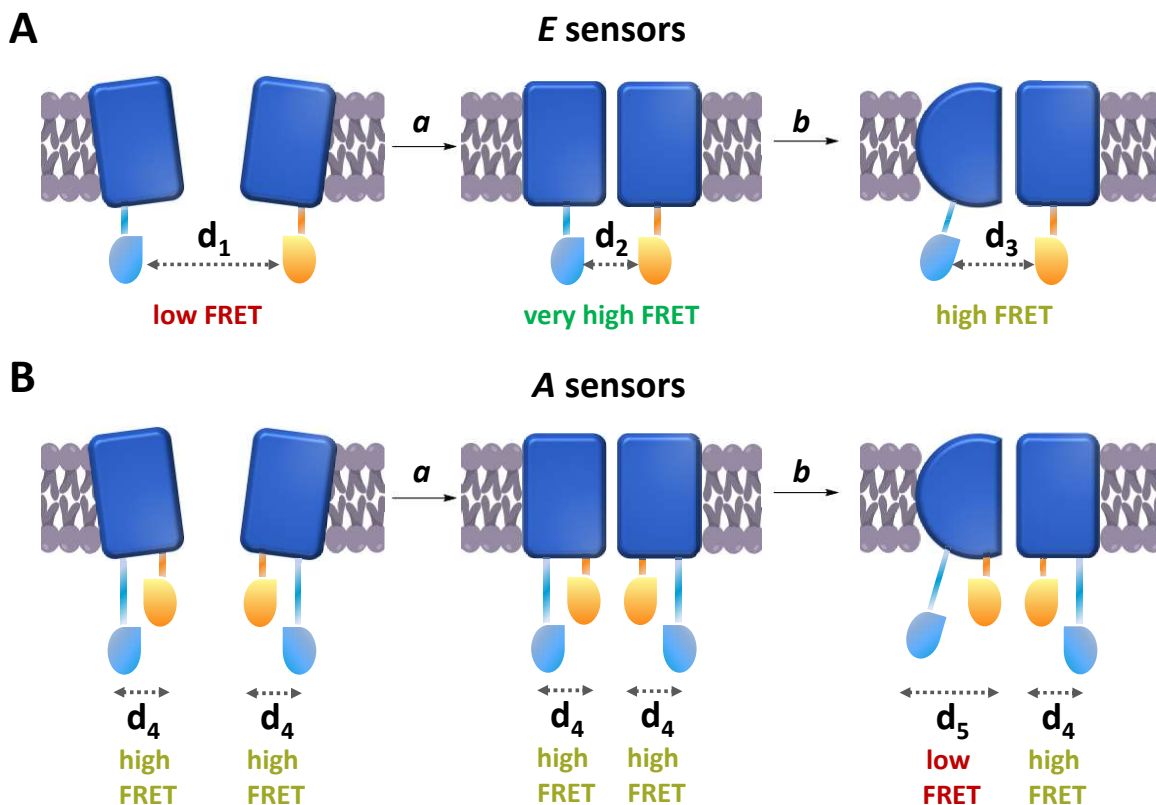


**Figure 82.** Schematic illustration of the 7TM agonist-induced activation steps (the initial inter-subunits rearrangement, *a*, and the intra-subunit conformational change, *b*) in mGlu<sub>1</sub> monitored by *E* (A) and *A* sensors (B). When the mGlu<sub>1</sub> is equipped with *E* sensors in each protomer (A), the FRET is very high upon the addition of agonist as result of the first rearrangement in which the two protomers move toward each other, passing from an initial distance  $d_1$  to a smaller one  $d_2$  (step *a*). Later, the subsequent conformational change of a single protomer induces a slight displacement of only one sensor and the resulting FRET decreases a little (step *b*) compared to that of step *a*. The distance between the two sensors is now  $d_3$ , barely greater than  $d_2$  but less than the initial  $d_1$ . In presence of a NAM, the step *b* is not produced and the distance between each protomer is stopped to  $d_2$  with resulting increase of FRET (Figure 81D,E). When the mGlu<sub>1</sub> is equipped with *A* sensors, both in each protomer (B), upon the addition of agonist the FRET decreases only in step *b*, the intra-subunit conformational change, due to the greater distance  $d_5$  than the initial  $d_4$ . In presence of a NAM, the step *b* is not produced and the distance between each pair of sensors does not change throughout the kinetic process (Figure 81F). VFT domain has been removed from the illustration for clarity.

This eventual direct connection, as well as any allosteric agonist behavior assumed by **91**, should be explored with a more appropriate assay. Additionally, while the NAM effect of **91** on the EC<sub>50</sub> of glutamate is negligible, its effect on quisqualate is not. Indeed, compound **91** inhibits the EC<sub>50</sub> of quisqualate, shifting it to the right. That means that compound **91** is subject to probe dependence,\* meaning that as the orthosteric ligand changes, so does the behavior of the allosteric modulator (Figure 83B).

The effect that compound **91** on the glutamate-induced rearrangement of the 7TMD of a mGlu<sub>1</sub> dimer was also explored using the *E* sensors, as performed with FITM (**90**). Also in this case, it seems that compound **91** produces a significant increase in the maximal FRET of the orthosteric ligand (Figure 83D,E) providing further confirmation of the effects on the conformational rearrangement observed with FITM (**90**) (Figure 82).

\* Probe dependence is one of the features of allostery. The same allosteric ligand, which can modulate different orthosteric ligands to different extents, is subject to probe dependence.



Due to the similar effects observed with FITM (**90**) and **91** at the 7TMD level with the *E* Sensors, knowing that the NAM potency of both compounds is also similar and complexity of the assay with the *A* sensors, it was assumed that compound **91** exhibits an inhibitory effect such as that of FITM (**90**) with the *A* sensors.

Having observed that small structural changes between FITM (**90**) and **91** (F/OMe) can lead to different conformational changes, we also decided to test the compounds **103b** and **107** with the same sensors. Thus, we could explore how a larger structural variation to the molecular scaffold could modify the allosteric effect of the ligands on the three types of conformational change of mGlu<sub>1</sub> receptor. These structural changes respect compound **91** consist of replacing the isopropyl with a dimethylaminopropyl (**107**) and replacing the N-methyl amide with an azo-bond (**103b**).

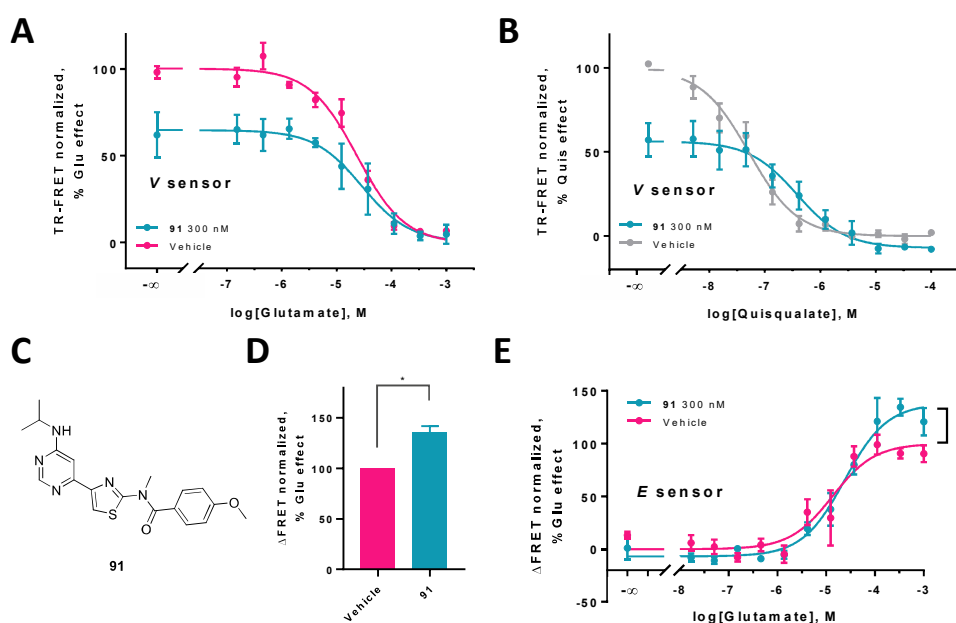


**Figure 83.** Dose-response curve of orthosteric agonists in the presence of (C) compound **91** on the mGlu<sub>1</sub> (A, B) equipped with *V* sensors, reporting movements between VFT domains and (E) *E* sensors, reporting intermolecular movements between 7TMD protomers. Data shows the mean curve  $\pm$  S.E.M. of three to four independent experiments, each performed in triplicate. (D) Percentage of glutamate efficacy on the mGlu<sub>1</sub> receptor using *E* sensors constructs in absence and in presence of 300 nM **91**. Statistical calculations were performed with two-tailed paired t test with 95% of confidence level and statistical significance \* $p < 0.05$ .

On the *V* sensor system applied to mGlu<sub>1</sub> receptor, the replacement of the methyl amide moiety with the *trans* azo bond and/or the modification introduced in the aliphatic chain of the molecule (compounds **103b** and **107**, *Figure 84A* and *Figure 85C*, respectively) did not produce significant effect on the *V* mGlu<sub>1</sub> sensors (*Figure 84B,C* and *Figure 85A,B*) as for FITM (**90**). This demonstrates that their allosteric activity could be not associated with any change in the VFT dimer conformation, despite having the methoxy group in *para* position relative to the azo-moiety as compound **91**. It is important to note that the concentration used for compounds **91**, **103b** and **107** was 300 nM, but the potency observed for **91** in the IP accumulation assays was higher than that for **103b** and **107**. In such functional assays, 300 nM of **91** induced high inhibition of the signaling but, for compounds **103b** and **107**, 300 nM was the beginning of the inhibition curve. That suggests that higher concentrations of **103b** and **107** (such as 3-10  $\mu$ M) might produce an effect on the conformation of the VFT similar to that observed with compounds **91**. However, with the present data it is not possible to draw conclusions and further experiments should be performed.

Both compound **103b** and **107** were tested using the *E* sensors-system to explore the rearrangement of the dimeric mGlu<sub>1</sub> 7TMDs. Their binding into the 7TMD allosteric pocket of the receptor, did not seem to exert any kind of effect on the glutamate action during this rearrangement of the 7TMD of the two mGlu<sub>1</sub> subunits, unlike the two previous compounds **90** and **91** (Figure 84D,E and Figure 85D,E). Again, it is difficult to explain these results without further information, such as new assays with a higher concentration of the allosteric modulators. Thus, we would be able to discuss whether this lack of effect is due to an inadequate concentration of the allosteric modulators or to the presence of a longer and ionic aliphatic chain in the molecule that is also binding the receptor.

Finally, compound **103b** was tested also using mGlu<sub>1</sub> equipped with the *A* sensors. using a 300 nM concentration in the presence of increasing concentrations of agonist. In such conditions, compound **103b** apparently blocked the conformational change induced by glutamate at a single 7TMD level. Since the glutamate-induced decrease in FRET was cut off when **103b** was added, it is possible to assert that both compounds **103b** and **107** promote a stabilization of the inactive conformation of each single 7TMD of mGlu<sub>1</sub> receptor, despite the concentration used in such conformational assays is not the most effective to observe mGlu<sub>1</sub> functional inhibition.

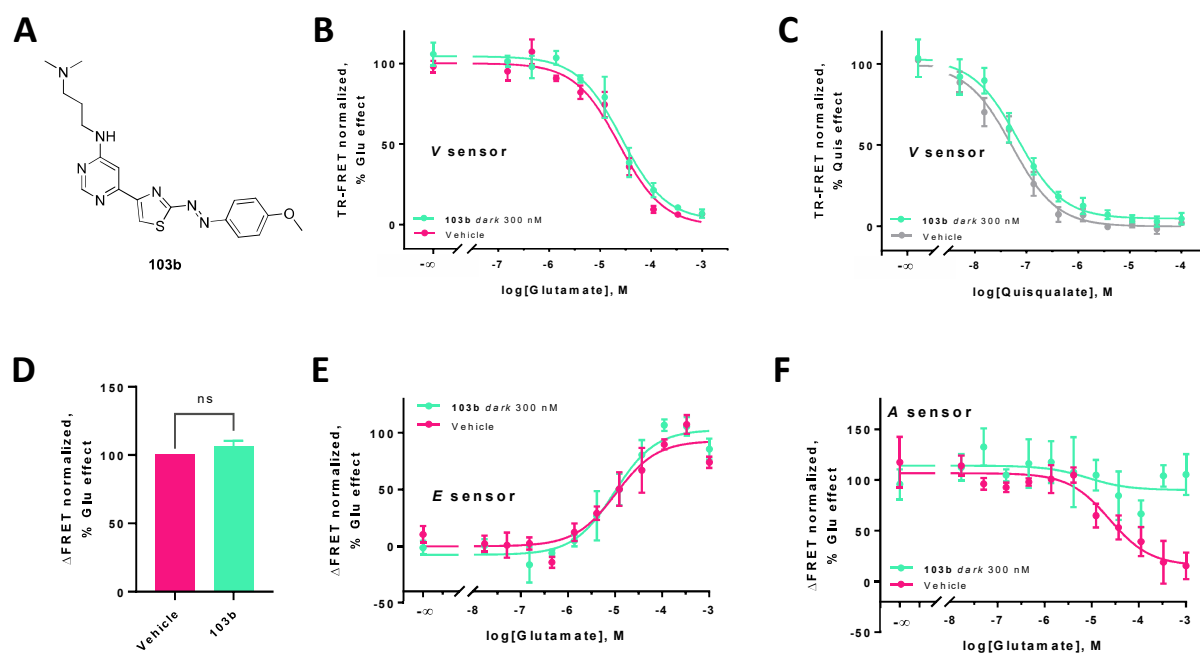


**Figure 84.** Dose-response curve of orthosteric agonists in the presence of (A) compound **103b** on the mGlu<sub>1</sub> equipped with (B, C) *V* sensors, reporting movements between VFT domains; (E) *E* sensors, reporting intermolecular movements between 7TMD protomers and (F) *A* sensors, reporting intramolecular movements in the same transmembrane domain. Data shows the mean curve  $\pm$  S.E.M. of three to four independent experiments, each performed in triplicate. (D) Percentage of glutamate efficacy on the mGlu<sub>1</sub> receptor using *E* sensors constructs in absence and in presence of 300 nM **103b**. Statistical calculations were performed with two-tailed paired t test with 95% of confidence level and statistical significance \* $p < 0.05$ .

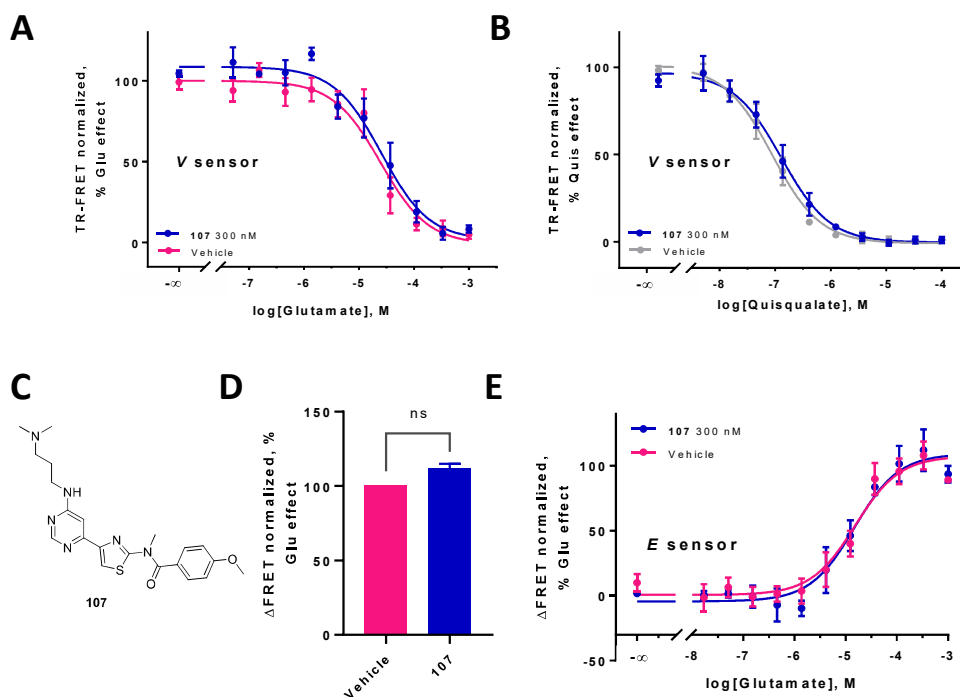


**Figure 85.** Dose-response curve of orthosteric agonists in the presence of (C) compound **107** on the mGlu<sub>1</sub> (A, B) equipped V sensors, reporting movements between VFT domains and (E) E sensors, reporting intermolecular movements between 7TMD protomers. Data shows the mean curve  $\pm$  S.E.M. of three to four independent experiments, each performed in triplicate. (D) Percentage of glutamate efficacy on the mGlu<sub>1</sub> receptor using E sensors constructs in absence and in presence of 300 nM **91**. Statistical calculations were performed with two-tailed paired t test with 95% of confidence level and statistical significance \* $p < 0.05$ .

## Conclusions

FITM (**90**) was an appropriate candidate for engineering novel mGlu<sub>1</sub> NAMs by replacing an amide with an azo-bond. We obtained a series of photoswitchable allosteric modulators based on arylazothiazole scaffold and able to display NAM activity in mGlu<sub>1</sub> receptor in their *trans* configuration and no activity in their *cis* configuration.

Six compounds displayed inhibitory functional activity on mGlu<sub>1</sub> in cell-based assays. The potencies of the *trans* configurations of **103a-e** and the non-photoswitchable **107** were  $\sim 1.5/2$  log-fold lower than that of the parent compound FITM (**90**). Unfortunately, dose-response curves of **103a-e** upon 400-nm illumination gave inconclusive results due to artifacts that might be originated from a possible toxicity of *cis* azo compounds. Further experiments should be done with cells non-expressing mGlu<sub>1</sub> and changing the light system.

The mGlu<sub>1</sub> allosteric modulators FITM (**90**), **91**, **103b** and **107** were used as molecular tools to shed more light on the nature of agonist-induced conformational dynamics involving the VFT and 7TMD of mGlu<sub>1</sub> receptor. This involved the exploration of the allosteric effect of those mGlu<sub>1</sub> NAMs on different conformational changes that characterize the entire mGlu<sub>1</sub> receptor activation process.

The V sensor assays demonstrated that mGlu<sub>1</sub> NAM FITM (**90**) produces no significant effect on the agonist-induced VFT movements, revealing that its antagonist activity is not associated with any change in the VFT dimer conformation. On the contrary, compound **91** considerably stabilizes a closed conformation of the VFTs of a considerable population of mGlu<sub>1</sub> receptors or stabilizes an intermediate conformation between

the closed and the open conformations. This highlights the existence of a high degree of cooperativity between the allosteric ligand acting at 7TMD and VFT dimer conformation. This connection, as well as any allosteric agonist behavior assumed by **91**, should be explored in the future with a more appropriate assay. Additionally, compound **91** could be subject to probe dependence, since its allosteric behavior changes depending on the orthosteric ligand.

On the assays with the *E* sensors, we observed that FITM (**90**) and **91** induced a significantly different rearrangement of the 7TMD of the two mGlu<sub>1</sub> subunits upon orthosteric ligand application. This rearrangement involves a shorter distance between the inter-subunits intracellular loops 2, compared to the receptor activated without any allosteric ligand. Additionally, with the *A* sensor assays, we observed that FITM (**90**) blocks the conformational change of one of the protomers upon glutamate application. A possible explanation for the difference of inter-subunits distance (on the i2 loop) observed may be the difference of distance between the i2 loop and the C-terminus observed with the *A* sensors, which may put a bit more apart the two i2 loops. In presence of a NAM, the intra-subunit activation is not produced and the distance between the i2 loops may be slightly shorter.

The other two compounds **103b** and **107**, with different molecular structures, seem to act on the mGlu<sub>1</sub> receptor exactly like FITM (**90**). The only difference is that they do not induce a 7TMD rearrangement with a shorter distance upon the orthosteric ligand application. However, the NAM concentrations used may not be appropriate to observe a significant effect with this assay. On the contrary, compound **103b** partially block the conformational change of one of the protomers upon glutamate application, despite the concentrations used.

The work here presented represents a starting point for a conformational study of mGlu<sub>1</sub> receptor upon activation and will be continued in the future. We will certainly need to perform computational studies and binding assays to support our preliminary conclusions. It would also be interesting to compare this results with experiments performed with conformational biosensors in presence of NAM<sub>5</sub> structurally different from FITM (**90**).



## Summary of results and conclusions

---



The results in **Chapter 1** indicate that the two azo-replacement approaches in compound **40** were not successful to obtain candidates displaying NAM activity in mGlu<sub>5</sub> receptors in their *cis* configuration and no activity in their *trans* configuration. However, a potential *trans*-on mGlu<sub>5</sub> PAM activity of the first two series of compounds needs to be explored with the appropriate pharmacological assays.

In **Chapter 2** we reported the design and synthesis of a series of compounds based on Optogluram structure with the aim to improve PAM activity at the mGlu<sub>4</sub> receptor and increase selectivity over the other group III mGluRs.

We obtained Optogluram-2 (**74a**) with good pharmacological potency, improved photoisomerization properties and specially a full mGlu<sub>4</sub> selectivity profile over the other group III glutamate receptors. The observed photoinduced potency shift is larger in Optogluram-2 (**74a**) than in Optogluram (**38**), which may induce an improved *on/off* photoswitching in coming more complex assays, such as *in vivo* assays.

In **Chapter 3** we showed the synthesis of two series of compounds in order to find the first photoswitchable compound to selectively enable optical control of the endogenous mGlu<sub>1</sub> receptor. Photoglurax-1 (**83b**) arose as a PAM of mGlu<sub>1</sub> with micromolar potency in the *trans* isomer. Under 380nm light, the potency is significantly reduced.

Photoglurax-1 (**83b**) turned out to be an equipotent mGlu<sub>4</sub> PAM and therefore its general profile is not suitable for *in vivo* translation as a possible mGlu<sub>1</sub> PAM tool compound. However, a dual mGlu<sub>1</sub>/mGlu<sub>4</sub> PAM activity could be intriguing for an antipsychotic agent, since mGlu<sub>4</sub> PAM activity can alleviate catalepsy, a major adverse event with standard antipsychotic drug treatment.

In contrast, Photoglurax-2 (**89h**) acts as a mGlu<sub>1</sub> PAM and does not show any observable allosteric effect on mGlu<sub>4</sub> or mGlu<sub>5</sub>, and therefore Photoglurax-2 (**89h**) represents a potential *in vivo* photoswitchable PAM mGlu<sub>1</sub> tool compound.

In **Chapter 4**, we designed and synthesized a family of novel photoswitchable azoheteroarenes as mGlu<sub>1</sub> NAMs with an active *trans* isomer and an inactive *cis* isomer to reversibly inactivate the function of the mGlu<sub>1</sub> receptor. The potencies of the *trans* configurations of some compounds are in the micromolar range. Unfortunately, after 400 nm illumination the results were inconclusive due to artifacts that could originate from a possible toxicity of *cis* azo compounds. More experiments should be done with cells that do not express mGlu<sub>1</sub> and also changing the light system to corroborate eventual toxicity.

However, we use some of these mGlu<sub>1</sub> NAMs in their *trans* form, therefore without applying light, as tools in fluorescence conformational dynamic studies to expand the knowledge about the nature of the intermediate states induced by mGlu receptor agonists.

It was demonstrated that mGlu<sub>1</sub> NAM FITM (**90**) produces no significant effect on the agonist-induced VFT movements, revealing that its antagonist activity is not associated with any change in the VFT dimer conformation. On the contrary, compound **91** considerably stabilizes a closed conformation of the VFTs of a considerable population of mGlu<sub>1</sub> receptors or stabilizes an intermediate conformation between the closed and the open conformations.

Additionally, we observed that FITM (**90**) and **91** induced a significantly different rearrangement of the 7TMD of the two mGlu<sub>1</sub> subunits upon orthosteric ligand application and FITM (**90**) also blocked the conformational change of one of the protomers upon glutamate application.



The other two compounds **103b** and **107**, with different molecular structures, seem to act on the mGlu<sub>1</sub> receptor exactly like FITM (**90**). The only difference is that they do not induce a 7TMD rearrangement with a shorter distance upon the orthosteric ligand application. However, the NAM concentrations used may not be appropriate to observe a significant effect with this assay. On the contrary, compound **103b** partially block the conformational change of one of the protomers upon glutamate application, despite the concentrations used.

The work presented in **Chapter 4** represents a starting point for a conformational study of mGlu<sub>1</sub> receptor upon activation and will be continued in the future. We will certainly need to perform computational studies and binding assays to support our preliminary conclusions.

## Experimental section

---



## Experimental section Contents

<b>Synthetic chemistry</b> .....	<b>159</b>
Materials and general methods.....	159
Chemical and solvents.....	159
Reaction monitoring.....	159
Microwave reactor.....	159
Purification of compounds.....	159
Nuclear Magnetic Resonance (NMR).....	159
High Performance Liquid Chromatography (HPLC) and Mass Spectrometry (MS).....	159
High Resolution Mass Spectrometry (HRMS).....	160
Synthetic procedures.....	160
Chapter 1: cis-on mGlu <sub>5</sub> NAMs.....	160
Chapter 2: trans-on mGlu <sub>4</sub> PAMs.....	169
Chapter 3: trans-on mGlu <sub>1</sub> PAMs.....	172
Chapter 4: trans-on mGlu <sub>1</sub> NAMs.....	183
<b>Photophysical and photochemical characterization</b> .....	<b>191</b>
Materials and general methods.....	191
Light source.....	191
UV-Vis spectroscopy.....	192
Determination of optimal wavelengths.....	192
Stability of the photoisomerization.....	192
Thermal relaxation of cis isomers.....	192
Study of pH-dependent photoisomerization properties of compound <b>103b</b> .....	193
Nuclear magnetic resonance (NMR).....	193
Determination of the most efficient illumination time.....	194
Confirmation of the optimal wavelengths for bidirectional photoisomerization.....	194
Measurement of thermal relaxation time.....	195
Photoisomerization analyzed by LC-PDA-MS.....	197
<b>Pharmacological and biochemical characterization</b> .....	<b>198</b>
Cell cultures and types of transfection.....	198
Materials and methods for transient transfections.....	198
Procedure for transfection by electroporation.....	198
Procedure for lipofectamine transfection.....	200
Procedure for induction of rat mGlu <sub>4</sub> in HEK293 cells.....	201
Procedure for labeling of SNAP-tag with VFT FRET-based biosensors on adherent mGlu <sub>1</sub> cells.....	202
Procedure for effectene transfection with E and A biosensor mGlu <sub>1</sub> constructs.....	202
Pharmacological and biochemical assays.....	203
Endpoint functional assays.....	204
Homogeneous Time-Resolved FRET (HTRF) technology.....	204
TR-FRET Inositol phosphate one (IP1) accumulation assay.....	207
TR-FRET Cyclic adenosine monophosphate (cAMP) accumulation assay.....	211
Conformational biosensor assays.....	213
Conformational VFT FRET-based biosensors (V sensors) assay.....	213
Conformational intermolecular and intramolecular-FRET-based biosensors (E/A sensors) assays.....	215



## Synthetic chemistry

MCS, Laboratory of Medicinal Chemistry and Synthesis, IQAC-CSIC, Barcelona

### Materials and general methods

#### Chemical and solvents

All the chemicals and solvents were provided from commercial suppliers and used without purification, except the anhydrous solvents, which were treated previously through a system of solvent purification (*PureSolv*), degasified with inert gases and dried over alumina or molecular sieves (DMF).

#### Reaction monitoring

All the reactions described below were monitored by thin layer chromatography (60F, 0.2 mm, *Macherey-Nagel*) by visualization under 254 and/or 365 nm lamp.

#### Microwave reactor

Reactions under microwave irradiation ( $\mu\text{W}$ ) were carried out in a CEM Discover Focused Microwave reactor in 10 ml sealed glass.

#### Purification of compounds

Flash column chromatography was performed using silica gel 60 (*Panreac*, 40-63  $\mu\text{m}$  mesh) or by means of SNAP KP-Sil 50  $\mu\text{m}$  (*Biotage*) and/or SNAP KP-C18-HS 50  $\mu\text{m}$  (*Biotage*) columns, automated with Isolera One with UV-Vis detection (*Biotage*).

#### Nuclear Magnetic Resonance (NMR)

Nuclear magnetic resonance (NMR) spectra were recorded on a 400 MHz Variant Mercury (*Agilent Technologies*) and on a 400 MHz Brüker Avance NEO instrument. Data were processed using *Mestre Nova V. 8.1* software (*Mestrelab Research*).  $^1\text{H}$  and  $^{13}\text{C}$  chemical shifts are reported in parts per million (ppm) against the reference compound using the signal of the residual non-deuterated solvent [Chloroform ( $\text{CDCl}_3$ )  $\delta = 7.26, 1.56$  ppm ( $^1\text{H}$ ),  $\delta = 77.16$  ppm ( $^{13}\text{C}$ ); DMSO ( $(\text{CD}_3)_2\text{OS}$ )  $\delta = 3.3, 2.5$  ppm ( $^1\text{H}$ ),  $\delta = 39.52$  ppm ( $^{13}\text{C}$ ); Methanol ( $\text{CD}_3\text{OD}$ )  $\delta = 4.87, 3.31$  ppm ( $^1\text{H}$ ),  $\delta = 49.00$  ppm ( $^{13}\text{C}$ ); Acetone ( $(\text{CD}_3)_2\text{CO}$ )  $\delta = 2.84, 2.05$  ppm ( $^1\text{H}$ ),  $\delta = 206.26$  ppm, 29.94 ppm ( $^{13}\text{C}$ )].

#### High Performance Liquid Chromatography (HPLC) and Mass Spectrometry (MS)

Purity determination and absorption UV-Vis spectra were determined with High-Performance Liquid Chromatography Thermo Ultimate 3000SD (*Thermo Scientific Dionex*) coupled to a PDA detector and an LTQ XL ESI-ion trap mass spectrometer (*Thermo Scientific*) or with a Waters 2795 Alliance coupled to a DAD detector (*Agilent 1100*) and an ESI Quattro Micro MS detector (*Waters*). Data from mass and UV-Vis spectra were analyzed using *Xcalibur 2.2 SP1* software (Thermo) or *MassLynx 4.1* software (Waters) HPLC columns used were ZORBAX Eclipse Plus C18 (4.6  $\times$  150 mm; 3.5  $\mu\text{m}$ ) and ZORBAX Extend-C18 (2.1  $\times$  50 mm, 3.5  $\mu\text{m}$ ).

HPLC purity was determined using the following binary solvent system as general method: 0.05% formic acid in 5% MeCN and 0.05% formic acid in 95% water for 0.5 min, from 5 to 100% MeCN in 5 min, 100%

MeCN for 1.5 min, from 100 to 5% MeCN in 2 min and 5% MeCN for 2 min. The use of different methods than the general one is detailed in the corresponding specific synthetic procedures.

The flow rate was 0.5 ml/ min, the column temperature was fixed to 35 °C, and wavelengths from 210 to 600 nm were registered. Compound purities were calculated as the percentage peak area of the analyzed compound by UV detection at 254 nm. For the only photoswitchable compounds the isomeric ratio is given considering the % of absorbance at the isosbestic point of the two species.

### High Resolution Mass Spectrometry (HRMS)

All high-resolution mass spectra (HRMS) and elemental compositions were performed on a FIA (flux injected analysis) with ultrahigh-performance liquid chromatography (UPLC) *Aquity* (Waters) coupled to LCT Premier Orthogonal Accelerated Time of Flight Mass Spectrometer (TOF) (Waters). The following binary solvent system is used: from 10% MeCN in 20 mM formic acid to 100% MeCN in 5 min. Data from mass spectra was analyzed by electrospray ionization in positive and negative modes using *MassLynx* 4.1 software (Waters). Given calculated masses are calculated with Chemdraw 20.0. Spectra were scanned between 50 and 1500 Da with values every 0.2 s and peaks are reported as m/z.

## Synthetic procedures

### Chapter 1: *cis-on* mGlu<sub>5</sub> NAMs

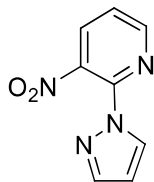
*General synthetic procedure A for compounds 48 and 64:* A suspension of the 1*H*-pyrazole (**47**) (1.5 eq) and Cs<sub>2</sub>CO<sub>3</sub> (1.1 eq) in anhydrous MeCN was stirred for 30 min at rt and under an inert atmosphere. The 2-chloro-3-nitropyridine (**46**) or 2-chloro-5-nitropyridine (**63**) (1.0 eq) was then added to give a red/brown suspension that was stirred under reflux (82 °C) for 16 h. The purification of the obtained residues is detailed in the corresponding specific synthetic procedures for compounds **48** and **64**.

*General synthetic procedure B for compounds 49 and 65:* In a tube, the corresponding nitrocompounds **48** or **64** (1.0 eq) and Pd/C (10% wt, 0.025-0.05 eq) were suspended in ethanol and a hydrogen atmosphere of 2-3 bar was applied for 3-16 h at rt. The mixture was thereafter filtered through Celite and washed with EtOH. Concentration *in vacuo* gave the resulting compounds **49** and **65**, which were used without further purification.

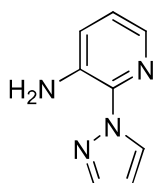
*General synthetic procedure C for compounds 51 and 61b-f:* Neat aniline **50** or the yellow/green suspensions of the anilines (**60b-f**) (1.0 eq) in DCM were added to a solution of Oxone® (2.0 eq) in water. The resulting mixture was stirred vigorously at rt for 1.5-16 h. The reaction mixture containing **51** and no DCM was filtered through Gooch funnel and the solid washed with cold water (3 times). The orange powder was dried under pump vacuum and used without further purification. To the reaction mixtures containing **61b-f**, water and DCM were added and the layers were separated. The aqueous layer was extracted with DCM, the green organic layer was washed with 1M HCl, sat. aq. NaHCO<sub>3</sub>, water and sat. NaCl, and dried over Na<sub>2</sub>SO<sub>4</sub>. Evaporation of the solvent *in vacuo* afforded the desired products as greenish-yellow solids, which were used without further purification, except **61d-f**, which were purified by *flash* column chromatography (elution with n-Hexane/DCM 1:3).

*General synthetic procedure D for compounds 52, 62a-c and 66a-f:* An excess AcOH was added to a suspension of aniline **49** or **65** (1.0 eq) and the corresponding nitrosobenzene **51** or **61b-f** (1.5 eq) in DCM. The resulting suspension was stirred protected from light at rt for 16h-4 days. After the addition of DCM

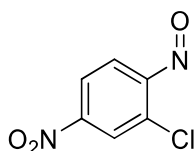
and water, the organic phase was washed twice with sat. NaCl, dried over anhydrous Na<sub>2</sub>SO<sub>4</sub> and filtered. The solvent were removed *in vacuo* and the resulting dark residue was purified by automated *flash* reverse phase chromatography (from H<sub>2</sub>O/MeCN 95:5 to MeCN 100% + 0.1% HCOOH) to give the expected product as an orange solid.



**3-nitro-2-(1H-pyrazol-1-yl)pyridine (48):** The general synthetic procedure A was used with 2-chloro-3-nitropyridine (**46**) (1.0 g, 6.3 mmol), 1H-pyrazole (**47**) (644 mg, 9.5 mmol) and Cs<sub>2</sub>CO<sub>3</sub> (2.3 g, 6.9 mmol) in MeCN (25 ml) to give a mixture that was filtered to remove any trace of Cs<sub>2</sub>CO<sub>3</sub> and then diluted in water/EtOAc (1:1). The aqueous phase was extracted twice with EtOAc. The joined organic layers were washed twice with water, dried over MgSO<sub>4</sub>, filtered and concentrated. The resulting residue was purified by *flash* column chromatography (nHex/EtOAc 5:2) to give the expected nitrocompound **48** as a white powder (813 mg, 68% yield). <sup>1</sup>H NMR (400 MHz, CDCl<sub>3</sub>) δ 8.55 (dd, *J* = 4.7, 1.6 Hz, 1H), 8.37 (dd, *J* = 2.7, 0.7 Hz, 1H), 7.99 (dd, *J* = 8.0, 1.6 Hz, 1H), 7.71 (d, *J* = 2.1 Hz, 1H), 7.34 (dd, *J* = 8.0, 4.8 Hz, 1H), 6.48 (dd, *J* = 2.7, 1.7 Hz, 1H). <sup>13</sup>C NMR (101 MHz, CDCl<sub>3</sub>) δ 150.4, 143.5, 142.4, 138.5, 133.6, 128.8, 121.8, 108.6. The described NMR spectra are in good agreement with the data reported in the literature.<sup>242</sup> HPLC-PDA-MS: RT= 2.80 min, [M+H]<sup>+</sup>= 191.02, purity (254 nm): 86%.

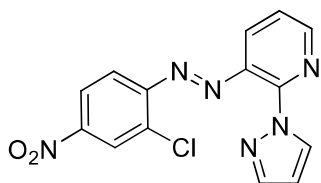


**2-(1H-pyrazol-1-yl)pyridin-3-amine (49):** The general synthetic procedure B was used with nitrocompound **48** (766 mg, 4.0 mmol) and Pd/C (214 mg, 0.20 mmol) in ethanol (40 ml) to give the amine **49** as an oil after stirring 16 h at 2 bar (635 mg, 98% yield). <sup>1</sup>H NMR (400 MHz, CDCl<sub>3</sub>) δ 8.53 (dd, *J* = 2.7, 0.8 Hz, 1H), 7.82 (dd, *J* = 4.5, 1.5 Hz, 1H), 7.71 (d, *J* = 1.5 Hz, 1H), 7.12 (dd, *J* = 8.0, 1.5 Hz, 1H), 7.02 (dd, *J* = 8.0, 4.5 Hz, 1H), 6.45 (dd, *J* = 2.6, 1.8 Hz, 1H), 5.60 (br, 2H). <sup>13</sup>C NMR (101 MHz, CDCl<sub>3</sub>) δ 140.2, 137.2, 136.4, 134.76, 128.6, 125.3, 122.6, 106.3. HPLC-PDA-MS: RT= 2.34 min, [M+H]<sup>+</sup>= 161.06, purity (254 nm): 88%.

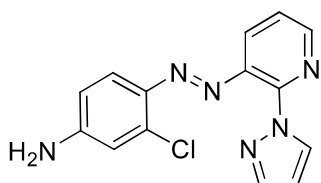


**2-chloro-4-nitro-1-nitrosobenzene (51):** The general synthetic procedure C was used with 2-chloro-4-nitroaniline (**50**) (2.0 g, 11.6 mmol) and Oxone<sup>®</sup> (14.3 g, 23 mmol) in water (80 ml) to form the corresponding nitroso compound **51** after stirring for 16 h (2.0 g, 94% yield). <sup>1</sup>H NMR (400 MHz, CDCl<sub>3</sub>) δ 8.69 (d, *J* = 2.2 Hz, 1H), 8.10 (dd, *J* = 8.8, 2.2 Hz, 1H), 6.30 (d, *J* = 8.8 Hz, 1H). <sup>13</sup>C NMR (101 MHz, CDCl<sub>3</sub>) δ 158.0, 150.8, 142.6, 128.5, 122.6, 109.9. HPLC-PDA-MS: RT= 3.35 min, purity (254 nm): 88%. Poor ionization of product **51** in the MS prevents the detection of the molecular ion.

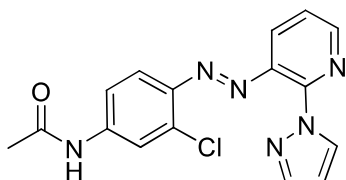




**(E)-3-((2-chloro-4-nitrophenyl)diazenyl)-2-(1H-pyrazol-1-yl)pyridine (52):** The general synthetic procedure D was used with pyridin-3-amine (**49**) (42 mg, 0.26 mmol) and 2-chloro-4-nitro-1-nitrosobenzene (**51**) (73 mg, 0.39 mmol) in DCM (1.0 ml) and AcOH (1.0 ml) to obtain nitro azo compound **52** (72 mg, 84% yield) as an orange solid.  $^1\text{H}$  NMR (400 MHz,  $\text{CDCl}_3$ )  $\delta$  8.70 (s, 1H), 8.45 (d,  $J = 2.3$  Hz, 1H), 8.39 (d,  $J = 2.7$  Hz, 1H), 8.21 (dd,  $J = 8.8, 2.4$  Hz, 1H), 8.12 (dd,  $J = 8.0, 1.7$  Hz, 1H), 7.87 (d,  $J = 1.6$  Hz, 1H), 7.79 (d,  $J = 8.8$  Hz, 1H), 7.46 (dd,  $J = 8.0, 4.6$  Hz, 1H), 6.60 – 6.57 (m, 1H). HPLC-PDA-MS: *cis* isomer RT= 3.58 min,  $\lambda_{\text{max}} = 412$  nm,  $[\text{M}+\text{H}]^+ = 329.10$ ; *trans* isomer RT= 3.64 min,  $\lambda_{\text{max}} = 355$  nm,  $[\text{M}+\text{H}]^+ = 329.07$ ; purity (254 nm): 96% (*trans* + *cis* isomer). The overlapping peaks of *cis* and *trans*-**52** makes impossible to individually measure the purity of each isomer.

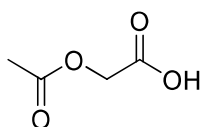


**(E)-4-((2-(1H-pyrazol-1-yl)pyridin-3-yl)diazenyl)-3-chloroaniline (53):** The 3-((2-chloro-4-nitrophenyl)diazenyl)-2-(1H-pyrazol-1-yl)pyridine (**52**) (337 mg, 1.0 mmol) and sodium sulfide nonahydrate (1.2 g, 5.1 mmol) were dissolved in 1,4-dioxane/water (11 ml, 10:1). The reaction mixture was stirred for 2 h at 100 °C and then poured on water. The resulting mixture was extracted with EtOAc (3x 40 ml). The joined organic layers were dried over anhydrous  $\text{MgSO}_4$  and the solvent was removed under vacuum to give a dark residue, which later was purified with automated *flash* reverse phase chromatography (from  $\text{H}_2\text{O}/\text{MeCN}$  95:5 to  $\text{MeCN}$  100%+ 0.1%  $\text{HCOOH}$ ) to give the expected product as a dark orange solid (254 mg, 83% yield).  $^1\text{H}$  NMR (400 MHz,  $\text{CDCl}_3$ )  $\delta$  8.61 (dd,  $J = 4.6, 1.7$  Hz, 1H), 8.19 – 8.16 (m, 2H), 7.86 (dd,  $J = 1.6, 0.7$  Hz, 1H), 7.59 (d,  $J = 8.9$  Hz, 1H), 7.39 (dd,  $J = 8.0, 4.6$  Hz, 1H), 6.82 (d,  $J = 2.5$  Hz, 1H), 6.57 (dd,  $J = 8.9, 2.5$  Hz, 1H), 6.51 (dd,  $J = 2.6, 1.7$  Hz, 1H). HPLC-PDA-MS: *trans* isomer RT= 2.41 min,  $\lambda_{\text{max}} = 409$  nm,  $[\text{M}+\text{H}]^+ = 299.14$ ; purity (254 nm): 100 % *trans* isomer. HRMS ( $m/z$ ):  $[\text{M}+\text{H}]^+$  calcd for  $\text{C}_{14}\text{H}_{12}\text{ClN}_6^+$  299.0807, found 299.0799.

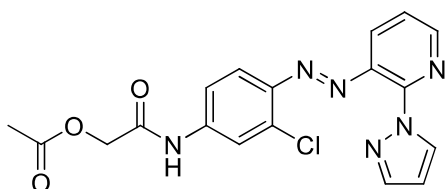


**(E)-N-(4-((2-(1H-pyrazol-1-yl)pyridin-3-yl)diazenyl)-3-chlorophenyl)acetamide (55):** The amino azo compound **53** (32 mg, 0.11 mmol) was dissolved in THF (2.0 ml) and acetyl chloride (**54**) (12.5 mg, 0.16 mmol) and TEA (60  $\mu\text{l}$ , 0.42 mmol) were subsequently added. The reaction mixture was stirred for 48 h at 60°C in an inert atmosphere. The solution was cooled and EtOAc and satd. aq.  $\text{NaHCO}_3$  were added. the layers were separated and the organic layer was washed with satd. aq.  $\text{Na}_2\text{CO}_3$  and sat.  $\text{NaCl}$  twice. The organic phase was dried over  $\text{MgSO}_4$ , filtered and concentrated *in vacuo* to give a residue that was purified by *flash* column chromatography (elution with  $n\text{Hex}/\text{EtOAc}$  1:4) to give the expected azo compound **55** as a

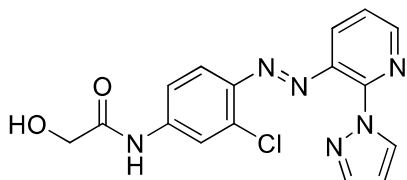
yellow solid (29 mg, 81% yield).  $^1\text{H}$  NMR (400 MHz, MeOD)  $\delta$  8.68 – 8.66 (m, 1H), 8.34 (d,  $J$  = 2.6 Hz, 1H), 8.23 (dd,  $J$  = 8.1, 1.7 Hz, 1H), 8.10 (d,  $J$  = 2.2 Hz, 1H), 7.87 (d,  $J$  = 1.7 Hz, 1H), 7.63 – 7.58 (m, 2H), 7.47 (dd,  $J$  = 8.9, 2.2 Hz, 1H), 6.64 (d,  $J$  = 3.0 Hz, 1H), 2.18 (s, 3H). HPLC-PDA-MS: *trans* isomer RT= 3.01 min,  $\lambda_{\text{max}}$ = 369 nm,  $[\text{M}+\text{H}]^+$  = 341.04; purity (254 nm): 95.3 % *trans* isomer. HRMS (m/z):  $[\text{M}+\text{H}]^+$  calcd for  $\text{C}_{16}\text{H}_{14}\text{ClN}_6\text{O}^+$  341.0913, found 341.0911.



**2-acetoxyacetic acid (57):** A mixture of 2-hydroxyacetic acid (56) (3.8 g, 50 mmol) and acetyl chloride (54) in excess (6.4 ml, 90 mmol) was stirred at rt for 2 h. The unreacted acetyl chloride was removed *in vacuo* and to the resulting oil was added water. Then, the solution was extracted three times with DCM. The combined organic phases were dried over  $\text{Na}_2\text{SO}_4$ , filtered and concentrated *in vacuo* to afford the product **57** as an oily product (29.3 mg, 81% yield). It was used without further purification.  $^1\text{H}$  NMR (400 MHz,  $\text{CDCl}_3$ )  $\delta$  9.62 (br, 1H), 4.66 (s, 2H), 2.17 (s, 3H). The described NMR spectrum is in good agreement with the data reported for the commercial glycolic acid (CAS number: 79-14-1).

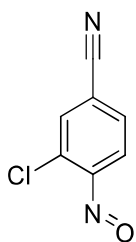


**(E)-2-((4-((2-(1H-pyrazol-1-yl)pyridin-3-yl)diazenyl)-3-chlorophenyl)amino)-2-oxoethyl acetate (58):** 2-acetoxyacetic acid (57) (18 mg, 0.15 mmol), aminoazobenzene **53** (30 mg, 0.10 mmol), HATU (115 mg, 0.30 mmol) were suspended in THF (2.0 ml) and anhydrous TEA (70  $\mu\text{l}$ , 0.50 mmol) was added. The resulting mixture was stirred in an inert atmosphere at 60°C for 16 h. EtOAc and satd. aq.  $\text{NaHCO}_3$  were added and the layers were separated. The organic layer was washed with satd. aq.  $\text{Na}_2\text{CO}_3$  and sat. NaCl twice. The organic phase was dried over  $\text{MgSO}_4$ , filtered and concentrated *in vacuo* to give a residue that was purified by *flash* column chromatography (Hex/EtOAc 1:3) to give the expected azo compound **58** as an orange powder (40 mg, quantitative yield).  $^1\text{H}$  NMR (400 MHz,  $\text{CD}_3\text{OD}$ )  $\delta$  8.64 (dd,  $J$  = 4.6, 1.7 Hz, 1H), 8.31 (d,  $J$  = 2.8 Hz, 1H), 8.17 (dd,  $J$  = 8.1, 1.7 Hz, 1H), 8.04 (d,  $J$  = 2.2 Hz, 1H), 7.87 (d,  $J$  = 1.7 Hz, 1H), 7.60 – 7.53 (m, 2H), 7.47 (dd,  $J$  = 9.0, 2.3, 0.7 Hz, 1H), 6.64 – 6.58 (m, 1H), 4.72 (s, 2H), 2.20 (s, 3H). HPLC-PDA-MS: *trans* isomer RT= 2.48 min,  $\lambda_{\text{max}}$ = 365 nm,  $[\text{M}+\text{H}]^+$  = 399.23; purity (254 nm): 91.5 %.

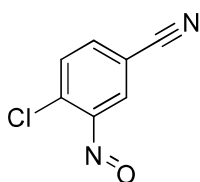


**(E)-N-(4-((2-(1H-pyrazol-1-yl)pyridin-3-yl)diazenyl)-3-chlorophenyl)-2-hydroxyacetamide (59):** The corresponding azobenzoate **58** (20 mg, 0.05 mmol) was suspended in THF (1.0 ml). In a separate tube lithium hydroxide (2.4 mg, 0.10 mmol) was dissolved in MeOH (0.5 ml). Both mixtures were cooled to 0°C and the solution of LiOH was added dropwise to form a dark red solution. After stirring 30 min, HCl 1M (3.0 ml) was added and the mixture was allowed to warm up to room temperature. Following the addition of

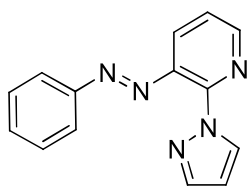
satd. aq. NaCl solution, the mixture was extracted with EtOAc three times and the combined organic layers were dried over MgSO<sub>4</sub>, filtered and concentrated *in vacuo* to give a residue, which was purified with automated *flash* reversed-phase chromatography (from H<sub>2</sub>O/MeCN 95:5 to MeCN 100%+ 0.1% HCOOH) to give compound **59**. <sup>1</sup>H NMR (400 MHz, (CD<sub>3</sub>)<sub>2</sub>CO) δ 9.59 (br, 1H), 8.65 (dd, *J* = 4.7, 1.7 Hz, 1H), 8.49 (dd, *J* = 2.7, 0.7 Hz, 1H), 8.33 (d, *J* = 2.3 Hz, 1H), 8.07 (dd, *J* = 8.0, 1.7 Hz, 1H), 7.81 – 7.73 (m, 2H), 7.70 (d, *J* = 8.9 Hz, 1H), 7.61 (dd, *J* = 8.0, 4.7 Hz, 1H), 6.59 (dd, *J* = 2.6, 1.6 Hz, 1H), 5.01 (br, 1H), 4.16 (s, 2H). HPLC-PDA-MS: *trans* isomer RT= 2.23 min, λ<sub>max</sub>= 365 nm, [M+H]<sup>+</sup>= 357.23; purity (254 nm): 99.29 % *trans* isomer. HRMS (m/z): [M+H]<sup>+</sup> calcd for C<sub>16</sub>H<sub>14</sub>ClN<sub>6</sub>O<sub>2</sub><sup>+</sup> 357.0862, found 357.0852.



**3-chloro-4-nitrosobenzonitrile (61b)**: The general synthetic procedure C was used with 4-amino-3-chlorobenzonitrile (**60b**) (1.0 g, 6.5 mmol) in DCM (12.5 ml) and Oxone® (8.1 g, 13.1 mmol) in water (50 ml) to form the corresponding nitroso compound **61b** after stirring 1.5 h (1.1 g, 96% yield). <sup>1</sup>H NMR (400 MHz, (CD<sub>3</sub>)<sub>2</sub>CO) δ 8.50 (d, *J* = 1.5 Hz, 1H), 7.86 (dd, *J* = 8.3, 1.6 Hz, 1H), 6.39 (d, *J* = 8.3 Hz, 1H).

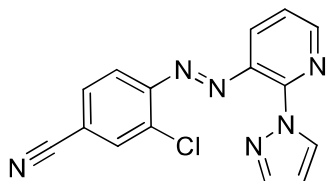


**4-chloro-3-nitrosobenzonitrile (61c)**: The general synthetic procedure C was used with 4-amino-3-chlorobenzonitrile (**60c**) (1.0 g, 6.5 mmol) in DCM (12.5 ml) and Oxone® (8.1 g, 13.1 mmol) in water (50 ml) to form the corresponding nitroso compound **61c** after stirring 1.5 h (952 mg, 87% yield). <sup>1</sup>H NMR (400 MHz, CDCl<sub>3</sub>) δ 7.96 (d, *J* = 8.3 Hz, 1H), 7.87 (ddd, *J* = 8.4, 2.0, 0.8 Hz, 1H), 6.49 (d, *J* = 2.0 Hz, 1H).

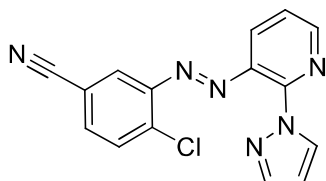


**(E)-3-(phenyldiazenyl)-2-(1H-pyrazol-1-yl)pyridine (62a)**: The general synthetic procedure D was used with pyridin-3-amine (**49**) (30 mg, 0.19 mmol) and nitrosobenzene (**61a**) (30 mg, 0.28 mmol) in DCM (1.0 ml) and AcOH (1.0 ml) to obtain the azo compound **62a** (25 mg, 54% yield) as an orange solid. <sup>1</sup>H NMR (400 MHz, CDCl<sub>3</sub>) δ 8.67 (dd, *J* = 4.6, 1.7 Hz, 1H), 8.22 (dd, *J* = 2.6, 0.7 Hz, 1H), 8.10 (dd, *J* = 8.0, 1.7 Hz, 1H), 7.92 – 7.88 (m, 2H), 7.86 (d, *J* = 1.6 Hz, 1H), 7.53 (dd, *J* = 5.2, 2.0 Hz, 3H), 7.41 (dd, *J* = 8.0, 4.6 Hz, 1H), 6.53 (dd, *J* = 2.6, 1.7 Hz, 1H). <sup>13</sup>C NMR (400 MHz, CDCl<sub>3</sub>) δ 152.9, 150.6, 148.8, 142.6, 139.6, 132.4, 132.1, 129.4, 126.4, 123.7, 123.0, 107.8. Purity determination and absorption UV-Vis spectra were determined using the following binary solvent system: 0.05% formic acid in 5% MeCN and 0.05% formic acid in 95% water for 0.5 min, from 5 to 40% MeCN in 20 min, from 40 to 100% MeCN in 2 min, then from 100 to 5% MeCN in 3 min and 5% MeCN for 5 min. HPLC-PDA-MS: *cis* isomer RT= 10.73 min, λ<sub>max</sub>= 288, 420 nm, [M+H]<sup>+</sup>= 250.19;

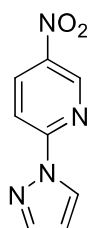
*trans* isomer RT= 12.43 min,  $\lambda_{\max}$ = 334, 446 nm,  $[M+H]^+$ = 250.15; purity (254 nm): 94.8 % *trans* isomer (5.2% *cis* isomer). HRMS (m/z):  $[M+H]^+$  calcd for  $C_{14}H_{12}N_5^+$  250.1088, found 250.1082.



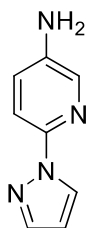
**(E)-4-((2-(1H-pyrazol-1-yl)pyridin-3-yl)diazenyl)-3-chlorobenzonitrile (62b):** The general synthetic procedure D was used with pyridin-3-amine **49** (30 mg, 0.19 mmol) and 3-chloro-4-nitrosobenzonitrile (**61b**) (47 mg, 0.28 mmol) in DCM (1.0 ml) and AcOH (1.0 ml) to obtain the azo compound **62b** (41 mg, 71% yield) as an orange solid.  $^1H$  NMR (400 MHz,  $CDCl_3$ )  $\delta$  8.68 (dd,  $J$  = 4.6, 1.7 Hz, 1H), 8.37 (d,  $J$  = 3.3 Hz, 1H), 8.10 (dd,  $J$  = 8.0, 1.7 Hz, 1H), 7.87 (d,  $J$  = 1.7 Hz, 1H), 7.85 (d,  $J$  = 1.3 Hz, 1H), 7.74 (d,  $J$  = 8.4 Hz, 1H), 7.63 (dd,  $J$  = 8.3, 1.7 Hz, 1H), 7.44 (dd,  $J$  = 8.0, 4.7 Hz, 1H), 6.56 (dd,  $J$  = 2.6, 1.7 Hz, 1H).  $^{13}C$  NMR (400 MHz,  $CDCl_3$ )  $\delta$  151.4, 151.3, 149.0, 143.3, 139.7, 135.9, 134.4, 131.4, 131.3, 127.0, 123.0, 119.6, 117.2, 115.6, 108.2. Purity determination and absorption UV-Vis spectra were determined using the following binary solvent system: 0.05% formic acid in 5% MeCN and 0.05% formic acid in 95% water for 0.5 min, from 5 to 40% MeCN in 20 min, from 40 to 100% MeCN in 2 min, then from 100 to 5% MeCN in 3 min and 5% MeCN for 5 min. HPLC-PDA-MS: *trans* isomer RT= 15.03 min,  $\lambda_{\max}$ = 350, 440 nm,  $[M+H]^+$ = 309.12; purity (254 nm): 94.8% *trans* isomer. HRMS (m/z):  $[M+H]^+$  calcd for  $C_{15}H_{10}ClN_6^+$  309.0650, found 309.0647.



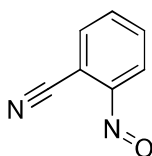
**(E)-3-((2-(1H-pyrazol-1-yl)pyridin-3-yl)diazenyl)-4-chlorobenzonitrile (62c):** The general synthetic procedure D was used with pyridin-3-amine (**49**) (30 mg, 0.19 mmol) and 4-chloro-3-nitrosobenzonitrile (**61c**) (47 mg, 0.28 mmol) in DCM (1.0 ml) and AcOH (1.0 ml) to obtain the azo compound **62c** (48 mg, 82% yield) as an orange solid.  $^1H$  NMR (400 MHz,  $CDCl_3$ )  $\delta$  8.66 (dd,  $J$  = 4.7, 1.7 Hz, 1H), 8.39 (dd,  $J$  = 2.7, 0.7 Hz, 1H), 8.07 (dd,  $J$  = 8.0, 1.7 Hz, 1H), 7.96 (dd,  $J$  = 1.6, 0.8 Hz, 1H), 7.88 (dd,  $J$  = 1.6, 0.7 Hz, 1H), 7.73 – 7.63 (m, 2H), 7.42 (dd,  $J$  = 8.0, 4.6 Hz, 1H), 6.58 (dd,  $J$  = 2.6, 1.7 Hz, 1H).  $^{13}C$  NMR (400 MHz,  $CDCl_3$ )  $\delta$  151.2, 149.2, 148.8, 143.5, 140.2, 139.6, 134.6, 131.9, 131.0, 127.0, 123.0, 122.8, 117.5, 111.9, 108.3. Purity determination and absorption UV-Vis spectra were determined using the following binary solvent system: 0.05% formic acid in 5% MeCN and 0.05% formic acid in 95% water for 0.5 min, from 5 to 40% MeCN in 20 min, from 40 to 100% MeCN in 2 min, then from 100 to 5% MeCN in 3 min and 5% MeCN for 5 min. HPLC-PDA-MS: *trans* isomer RT= 14.63 min,  $\lambda_{\max}$ = 346, 446 nm,  $[M+H]^+$ = 309.12; purity (254 nm): 98.8% *trans* isomer. HRMS (m/z):  $[M+H]^+$  calcd for  $C_{15}H_{10}ClN_6^+$  309.0650, found 309.06344.



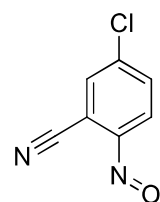
**5-nitro-2-(1H-pyrazol-1-yl)pyridine (64):** The general synthetic procedure A was used with 2-chloro-5-nitropyridine (**63**) (3.2 g, 20 mmol), 1H-pyrazole (**47**) (2.0 g, 30 mmol) and Cs<sub>2</sub>CO<sub>3</sub> (7.2 g, 22 mmol) in MeCN (56 ml) to give a precipitate that was filtered to give the nitrocompound **64** as a yellow solid (3.3 g, 87% yield). <sup>1</sup>H NMR (400 MHz, CDCl<sub>3</sub>) δ 9.26 (d, *J* = 2.7 Hz, 1H), 8.62 (d, *J* = 2.7 Hz, 1H), 8.59 (dd, *J* = 9.3, 2.9 Hz, 1H), 8.15 (d, *J* = 9.1 Hz, 1H), 7.82 (s, 1H), 6.54 (dd, 1H). HPLC-PDA-MS: RT= 3.30 min, [M+H]<sup>+</sup> = 191.02, purity (254 nm): 99.7%.



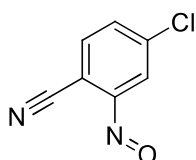
**6-(1H-pyrazol-1-yl)pyridin-3-amine (65):** The general synthetic procedure B was used with nitrocompound **64** (3.2 g, 17 mmol) and Pd/C (442 mg, 0.41 mmol) in ethanol (50 ml) to give pyridin-3-amine **65** as a green/yellow powder after stirring 3 h at 3 bar (2.2 g, 81% yield). <sup>1</sup>H NMR (400 MHz, CDCl<sub>3</sub>) δ 8.40 (d, *J* = 2.5 Hz, 1H), 7.87 (d, *J* = 2.8 Hz, 1H), 7.76 (d, *J* = 8.7 Hz, 1H), 7.67 (d, *J* = 1.0 Hz, 1H), 7.13 (dd, *J* = 8.7, 2.8 Hz, 1H), 6.42 (dd, *J* = 2.1 Hz, 1H), 3.72 (br, 2H). <sup>13</sup>C NMR (101 MHz, CDCl<sub>3</sub>) δ 144.6, 141.1, 134.5, 126.4, 124.9, 113.2, 110.2, 107.2. HPLC-PDA-MS: RT= 2.30 min, [M+H]<sup>+</sup> = 161.06, purity (254 nm): 96%.



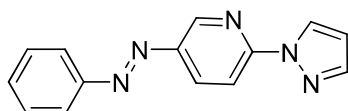
**2-nitrosobenzonitrile (61d):** The general synthetic procedure C was used with 2-aminobenzonitrile (**60d**) (1.0 g, 8.6 mmol) in DCM (12.5 ml) and Oxone<sup>®</sup> (11 g, 18 mmol) in water (50 ml) to form the corresponding nitroso compound **61d** after stirring 16 h (714 mg, 61% yield). <sup>1</sup>H NMR (400 MHz, CDCl<sub>3</sub>) δ 8.06 (dd, *J* = 7.6, 1.3 Hz, 1H), 7.85 (td, *J* = 7.4, 0.8 Hz, 1H), 7.76 (td, *J* = 7.8, 0.9 Hz, 1H), 6.99 (d, *J* = 8.0 Hz, 1H). <sup>13</sup>C NMR (400 MHz, CDCl<sub>3</sub>) δ 161.9, 135.4, 134.5, 133.5, 116.7, 114.1, 112.3.



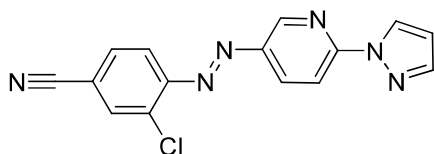
**5-chloro-2-nitrosobenzonitrile (61e):** The general synthetic procedure C was used with 2-amino-5-chlorobenzonitrile (**60e**) (1.0 g, 6.6 mmol) in DCM (12.5 ml) and Oxone<sup>®</sup> (8.3 g, 14 mmol) in water (50 ml) to form the corresponding nitroso compound **61e** after stirring 16 h (313 mg, 28% yield). <sup>1</sup>H NMR (400 MHz, CDCl<sub>3</sub>) δ 8.03 (d, *J* = 2.1 Hz, 1H), 7.71 (dd, *J* = 8.7, 2.1 Hz, 1H), 6.91 (d, *J* = 8.6 Hz, 1H). <sup>13</sup>C NMR (400 MHz, CDCl<sub>3</sub>) δ 159.9, 142.6, 134.2, 133.9, 115.9, 115.4, 113.3.



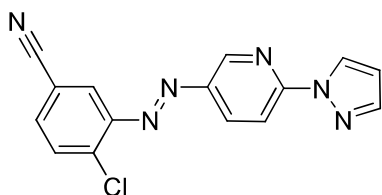
**4-chloro-2-nitrosobenzonitrile (61f):** The general synthetic procedure C was used with 2-amino-4-chlorobenzonitrile (**60f**) (1.0 g, 6.6 mmol) in DCM (12.5 ml) and Oxone® (8.3 g, 14 mmol) in water (50 ml) to form the corresponding nitroso compound **61f** after stirring 16 h (134 mg, 12% yield). <sup>1</sup>H NMR (400 MHz, CDCl<sub>3</sub>) δ 8.03 (d, *J* = 8.2 Hz, 1H), 7.82 (dd, *J* = 8.2, 2.1 Hz, 1H), 6.83 (d, *J* = 1.9 Hz, 1H).



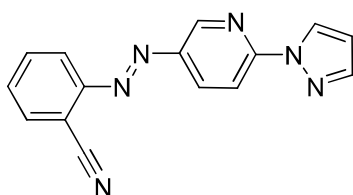
**(E)-5-(phenyldiazenyl)-2-(1H-pyrazol-1-yl)pyridine (66a):** The general synthetic procedure D was used with 6-(1H-pyrazol-1-yl)pyridin-3-amine (**65**) (35 mg, 0.22 mmol) and nitrosobenzene (**61a**) (35 mg, 0.32 mmol) in DCM (1.0 ml) and AcOH (1.0 ml) stirring 48 h to obtain the azo compound (**66a**) (44 mg, 82% yield) as an orange solid. <sup>1</sup>H NMR (400 MHz, CDCl<sub>3</sub>) δ 9.02 (d, *J* = 2.4 Hz, 1H), 8.65 (d, *J* = 2.6 Hz, 1H), 8.31 (dd, *J* = 8.9, 2.4 Hz, 1H), 8.13 (d, *J* = 8.8 Hz, 1H), 7.95 (dd, *J* = 8.1, 1.6 Hz, 2H), 7.79 (d, *J* = 1.6 Hz, 1H), 7.59 – 7.45 (m, 3H), 6.52 (dd, *J* = 2.6, 1.6 Hz, 1H). <sup>13</sup>C NMR (400 MHz, CDCl<sub>3</sub>) δ 152.7, 147.2, 146.5, 142.9, 131.7, 129.3, 129.3, 127.7, 123.1, 112.9, 108.6. HPLC-PDA-MS: *cis* isomer RT= 2.63 min, λ<sub>max</sub>= 434 nm, [M+H]<sup>+</sup> = 250.04; *trans* isomer RT= 3.35 min, λ<sub>max</sub>= 347 nm, [M+H]<sup>+</sup> = 250.16; purity (254 nm): 83.4 % *trans* isomer (16.6 % *cis* isomer). HRMS (*m/z*): [M+H]<sup>+</sup> calcd for C<sub>14</sub>H<sub>12</sub>N<sub>5</sub><sup>+</sup> 250.1088, found 250.1088.



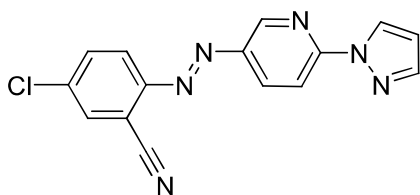
**(E)-4-((6-(1H-pyrazol-1-yl)pyridin-3-yl)diazenyl)-3-chlorobenzonitrile (66b):** The general synthetic procedure D was used with 6-(1H-pyrazol-1-yl)pyridin-3-amine (**65**) (33 mg, 0.21 mmol) and 3-chloro-4-nitrosobenzonitrile (**61b**) (52 mg, 0.31 mmol) in DCM (1.0 ml) and AcOH (1.0 ml) stirring for 3 days to obtain the azo compound **66b** (50 mg, 78% yield) as an orange solid. <sup>1</sup>H NMR (400 MHz, CDCl<sub>3</sub>) δ 9.10 (d, *J* = 2.0 Hz, 1H), 8.67 (d, *J* = 2.7 Hz, 1H), 8.36 (dd, *J* = 8.9, 2.4 Hz, 1H), 8.17 (d, *J* = 8.9 Hz, 1H), 7.89 (d, *J* = 1.7 Hz, 1H), 7.82 (d, *J* = 3.3 Hz, 1H), 7.81 (d, *J* = 4.2 Hz, 1H), 7.66 (dd, *J* = 8.3, 1.7 Hz, 1H), 6.54 (dd, *J* = 2.7, 1.6 Hz, 1H). <sup>13</sup>C NMR (400 MHz, CDCl<sub>3</sub>) δ 153.7, 151.0, 148.8, 146.6, 143.5, 136.1, 134.6, 131.2, 129.7, 128.0, 118.5, 117.3, 115.4, 113.2, 109.1. HPLC-PDA-MS: *cis* isomer RT= 2.79 min, λ<sub>max</sub>= 430 nm, [M+H]<sup>+</sup> = 309.11; *trans* isomer RT= 3.32 min, λ<sub>max</sub>= 361 nm, [M+H]<sup>+</sup> = 309.08; purity (254 nm): 93.6 % *trans* isomer (5.8 % *cis* isomer). HRMS (*m/z*): [M+H]<sup>+</sup> calcd for C<sub>15</sub>H<sub>10</sub>ClN<sub>6</sub><sup>+</sup> 309.0650, found 309.0654.



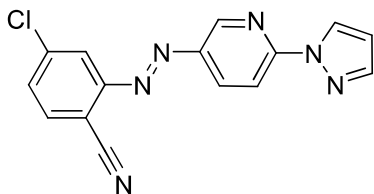
**(E)-3-((6-(1H-pyrazol-1-yl)pyridin-3-yl)diazenyl)-4-chlorobenzonitrile (66c):** The general synthetic procedure D was used with 6-(1H-pyrazol-1-yl)pyridin-3-amine (**65**) (33 mg, 0.20 mmol) and 4-chloro-3-nitrosobenzonitrile (**61c**) (52 mg, 0.31 mmol) in DCM (1.0 ml) and AcOH (1.0 ml) stirring 4 days to obtain the azo compound **66c** (39 mg, 62% yield) as an orange solid.  $^1\text{H}$  NMR (400 MHz,  $\text{CDCl}_3$ )  $\delta$  9.10 (dd,  $J = 2.4, 0.7$  Hz, 1H), 8.67 (dd,  $J = 2.7, 0.8$  Hz, 1H), 8.36 (dd,  $J = 8.9, 2.4$  Hz, 1H), 8.17 (dd,  $J = 8.8, 0.8$  Hz, 1H), 8.06 (d,  $J = 1.8$  Hz, 1H), 7.81 (d,  $J = 0.8$  Hz, 1H), 7.73 – 7.66 (m, 2H), 6.54 (dd,  $J = 2.7, 1.6$  Hz, 1H).  $^{13}\text{C}$  NMR (400 MHz,  $\text{CDCl}_3$ )  $\delta$  153.7, 148.8, 148.7, 146.4, 143.5, 140.5, 134.4, 132.2, 129.7, 128.0, 121.7, 117.6, 113.1, 111.9, 109.1. HPLC-PDA-MS: *cis* isomer RT= 2.77 min,  $\lambda_{\text{max}} = 429$  nm,  $[\text{M}+\text{H}]^+ = 309.15$ ; *trans* isomer RT= 3.31 min,  $\lambda_{\text{max}} = 356$  nm,  $[\text{M}+\text{H}]^+ = 309.14$ ; purity (254 nm): 85.8 % *trans* isomer (14.2 % *cis* isomer). HRMS (m/z):  $[\text{M}+\text{H}]^+$  calcd for  $\text{C}_{15}\text{H}_{10}\text{ClN}_6^+$  309.0650, found 309.0652.



**(E)-2-((6-(1H-pyrazol-1-yl)pyridin-3-yl)diazenyl)benzonitrile (66d):** The general synthetic procedure D was used with 6-(1H-pyrazol-1-yl)pyridin-3-amine (**65**) (32 mg, 0.20 mmol) and 2-nitrosobenzonitrile (**61d**) (40 mg, 0.30 mmol) in DCM (1.0 ml) and AcOH (1.0 ml) stirring 4 days to obtain the azo compound **66d** (43 mg, 78% yield) as an orange solid.  $^1\text{H}$  NMR (400 MHz,  $\text{CDCl}_3$ )  $\delta$  9.11 (d,  $J = 2.6$  Hz, 1H), 8.66 (d,  $J = 2.6$  Hz, 1H), 8.41 (dd,  $J = 8.9, 2.4$  Hz, 1H), 8.15 (d,  $J = 8.9$  Hz, 1H), 7.94 (dd,  $J = 8.8, 0.9$  Hz, 1H), 7.87 (dd,  $J = 7.7, 1.4$  Hz, 1H), 7.81 (d,  $J = 1.1$  Hz, 1H), 7.73 (ddd,  $J = 8.3, 7.4, 1.4$  Hz, 1H), 7.59 (td,  $J = 7.6, 1.2$  Hz, 1H), 6.53 (dd,  $J = 2.7, 1.6$  Hz, 1H).  $^{13}\text{C}$  NMR (400 MHz,  $\text{CDCl}_3$ )  $\delta$  153.6, 153.1, 148.8, 146.3, 143.4, 133.9, 133.6, 131.5, 129.5, 127.9, 117.1, 116.8, 113.6, 113.2, 109.0. HPLC-PDA-MS: *cis* isomer RT= 2.55 min,  $\lambda_{\text{max}} = 437$  nm,  $[\text{M}+\text{H}]^+ = 275.11$ ; *trans* isomer RT= 3.02 min,  $\lambda_{\text{max}} = 355$  nm,  $[\text{M}+\text{H}]^+ = 275.18$ ; purity (254 nm): 91.5 % *trans* isomer (8.5 % *cis* isomer). HRMS (m/z): HRMS (m/z):  $[\text{M}+\text{H}]^+$  calcd for  $\text{C}_{15}\text{H}_{11}\text{N}_6^+$  275.1040, found 275.1048.



**(E)-2-((6-(1H-pyrazol-1-yl)pyridin-3-yl)diazenyl)-5-chlorobenzonitrile (66e):** The general synthetic procedure D was used with 6-(1H-pyrazol-1-yl)pyridin-3-amine (**65**) (31 mg, 0.19 mmol) and 5-chloro-2-nitrosobenzonitrile (**61d**) (48 mg, 0.29 mmol) in DCM (1.0 ml) and AcOH (1.0 ml) stirring 4 days to obtain the azo compound **66e** (45 mg, 76% yield) as an orange solid.  $^1\text{H}$  NMR (400 MHz,  $\text{CDCl}_3$ )  $\delta$  9.10 (d,  $J = 2.4$  Hz, 1H), 8.67 (d,  $J = 2.7$  Hz, 1H), 8.41 (dd,  $J = 8.9, 2.4$  Hz, 1H), 8.16 (d,  $J = 8.9$  Hz, 1H), 7.92 (d,  $J = 8.8$  Hz, 1H), 7.85 (d,  $J = 2.2$  Hz, 1H), 7.81 (d,  $J = 1.7$  Hz, 1H), 7.69 (dd,  $J = 8.8, 2.3$  Hz, 1H), 6.54 (dd,  $J = 2.7, 1.6$  Hz, 1H).  $^{13}\text{C}$  NMR (400 MHz,  $\text{CDCl}_3$ )  $\delta$  151.6, 149.0, 146.2, 143.5, 139.0, 137.7, 134.0, 133.4, 129.5, 128.0, 118.4, 115.6, 115.0, 113.2, 109.1. HPLC-PDA-MS: *cis* isomer RT= 2.81 min,  $\lambda_{\text{max}} = 440$  nm,  $[\text{M}+\text{H}]^+ = 309.11$ ; *trans* isomer RT= 3.32 min,  $\lambda_{\text{max}} = 364$  nm,  $[\text{M}+\text{H}]^+ = 309.10$ ; purity (254 nm): 91.6 % *trans* isomer (8.4 % *cis* isomer). HRMS (m/z):  $[\text{M}+\text{H}]^+$  calcd for  $\text{C}_{15}\text{H}_{10}\text{ClN}_6^+$  309.0650, found= 309.0655.

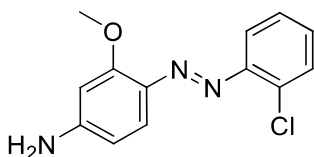


**(E)-2-((6-(1H-pyrazol-1-yl)pyridin-3-yl)diazenyl)-4-chlorobenzonitrile (66f):** The general synthetic procedure D was used with 6-(1H-pyrazol-1-yl)pyridin-3-amine (**65**) (31 mg, 0.19 mmol) and 4-chloro-2-nitrosobenzonitrile (**61f**) (48 mg, 0.29 mmol) in DCM (1.0 ml) and AcOH (1.0 ml) stirring 4 days to obtain the azo compound **66f** (39 mg, 65% yield) as an orange solid.  $^1\text{H}$  NMR (400 MHz,  $\text{CDCl}_3$ )  $\delta$  9.12 (d,  $J = 2.3$  Hz, 1H), 8.67 (dd,  $J = 2.7, 0.8$  Hz, 1H), 8.41 (dd,  $J = 9.0, 2.4$  Hz, 1H), 8.17 (d,  $J = 9.0$  Hz, 1H), 7.94 (d,  $J = 2.0$  Hz, 1H), 7.84 – 7.77 (m, 2H), 7.57 (dd,  $J = 8.3, 2.1$  Hz, 1H), 6.54 (dd,  $J = 2.7, 1.6$  Hz, 1H).  $^{13}\text{C}$  NMR (400 MHz,  $\text{CDCl}_3$ )  $\delta$  153.9, 153.8, 149.3, 146.1, 143.6, 140.5, 134.6, 131.5, 129.5, 128.0, 117.6, 116.1, 113.3, 112.1, 109.1. HPLC-PDA-MS: *cis* isomer RT= 2.79 min,  $\lambda_{\text{max}} = 437$  nm,  $[\text{M}+\text{H}]^+ = 309.12$ ; *trans* isomer RT= 3.35 min,  $\lambda_{\text{max}} = 361$  nm,  $[\text{M}+\text{H}]^+ = 309.06$ ; purity (254 nm): 92.6 % *trans* isomer (7.4 % *cis* isomer). HRMS (m/z):  $[\text{M}+\text{H}]^+$  calcd for  $\text{C}_{15}\text{H}_{10}\text{ClN}_6^+ = 309.0650$ , found= 309.0642.

## Chapter 2: *trans-on mGlu<sub>4</sub>* PAMs

**General synthetic procedure A for compounds 69a and 69b:** HCl (37% aq., 3.1-5.2 eq) was added slowly to a stirred solution of 2-chloroaniline **67** (1.0 eq) in MeOH and the resulting mixture was stirred at 0-5 °C for 5 min. An aqueous solution of sodium nitrite (1.2 eq) was added dropwise to generate the corresponding diazonium salt, keeping the temperature between below 5 °C. The mixture was left stirring for 20 min at 0-5 °C. In parallel, a solution of 3-methoxyaniline **68a** or 2-chloro-5-methoxyaniline **68b** (1.2 eq) and sodium acetate (3.1-5.2 eq) in MeOH/H<sub>2</sub>O (2:1, v/v) was prepared in a separate reaction flask and stirred in an ice bath. The freshly prepared diazonium salt solution was kept at 0-5 °C to avoid degradation and was added dropwise onto the solution of the corresponding aniline **68a-b** and sodium acetate, while keeping the temperature of the reaction at 0-5°C. The resulting mixture was stirred at 0-5°C for 30 min and cold water was subsequently added to induce the precipitation of the product **69a-b**, which was filtered, washed with precooled water and dried. If the precipitation did not occur, the mixture was extracted twice with EtOAc. The joined organic layers were washed with sat.  $\text{Na}_2\text{CO}_3$ , sat.  $\text{NaHCO}_3$  and sat. NaCl (x2), dried over anhydrous  $\text{MgSO}_4$ , filtered and concentrated *in vacuo*. The obtained residue was purified with automated *flash* direct-phase chromatography (n-Hexane/Ethyl acetate 3:1).

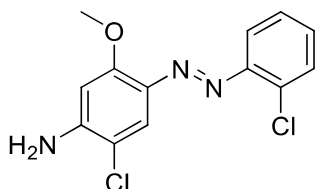
**General synthetic procedure B for compounds 71a-d and 74a-b:** The corresponding aromatic carboxylic acid **70a-b**, **72** or **73** (1.5-2.0 eq) with the corresponding aminoazobenzenes **69a-b** (1.0 eq), HATU (3.0 eq) were dissolved in DMF. TEA (5-7.0 eq) was added and the mixture was stirred in an inert atmosphere at 40-60°C for 16-48 h. The reaction crude was diluted with EtOAc and was washed with sat.  $\text{Na}_2\text{CO}_3$ , sat.  $\text{NaHCO}_3$  and sat. NaCl (x2), dried over  $\text{MgSO}_4$ , filtered and concentrated *in vacuo*. The residue was purified with automated *flash* reverse phase chromatography (from H<sub>2</sub>O/MeCN 95:5 to MeCN 100%+ 0.1% HCOOH).



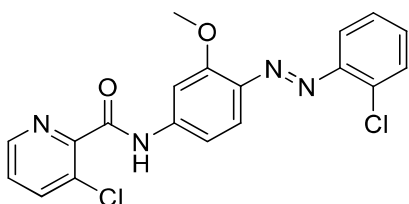
**(E)-4-((2-chlorophenyl)diazenyl)-3-methoxyaniline (69a):** The general synthetic procedure A was used with 2-chloroaniline (**67**) (500 mg, 3.9 mmol) in MeOH (7.5 ml), HCl (37% aq) (1.0 ml, 33 mmol), sodium nitrite



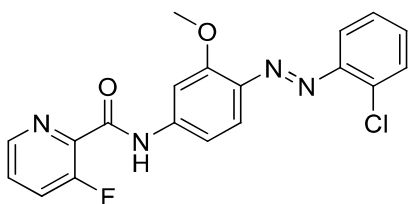
(325 mg, 4.7 mmol) in water (1.8 ml). The second solution was prepared with 3-methoxyaniline (**68a**) (579 mg, 4.7 mmol) and sodium acetate (2.7 g, 33 mmol) in MeOH/H<sub>2</sub>O (2:1, v/v; 11.5 ml). Pre-cooled water (150 ml) was added slowly to induce the precipitation of the aminoazobenzene **69a** as an orange solid (587 mg, 57% yield). <sup>1</sup>H NMR (400 MHz, CDCl<sub>3</sub>) δ 7.78 (d, *J* = 9.3 Hz, 1H), 7.68 – 7.61 (m, 1H), 7.53 – 7.45 (m, 1H), 7.30 – 7.26 (m, 2H), 6.32 – 6.27 (m, 2H), 4.15 (br, 2H), 3.98 (s, 3H). <sup>13</sup>C NMR (101 MHz, CDCl<sub>3</sub>) δ 159.8, 152.2, 149.8, 135.7, 133.9, 130.4, 130.0, 127.4, 119.4, 118.3, 107.8, 97.8, 56.3. HPLC-PDA-MS: RT= 2.35 min, λ<sub>max</sub>= 478 nm, [M+H]<sup>+</sup> = 262.14; purity (254 nm): 91%



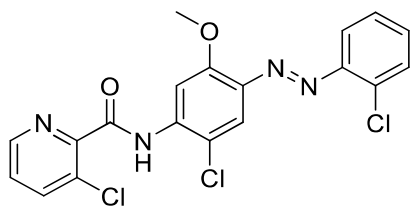
**(E)-2-chloro-4-((2-chlorophenyl)diazenyl)-5-methoxyaniline (69b)**: The general synthetic procedure A was used with 2-chloroaniline (**67**) (300 mg, 2.4 mmol) in MeOH (5 ml), conc. HCl (1.0 ml, 12.2 mmol), sodium nitrite (195 mg, 2.8 mmol) in water (1.0 ml). The second solution was prepared with 2-chloro-5-methoxyaniline (**68b**) (445 mg, 2.8 mmol) and sodium acetate (1.0 g, 12.2 mmol) in MeOH/H<sub>2</sub>O (2:1, v/v; 7.5 ml). The aminoazobenzene **69b** was obtained as an orange solid (592 mg, 85% yield). <sup>1</sup>H NMR (400 MHz, CDCl<sub>3</sub>) δ 7.86 (s, 1H), 7.63 (dd, *J* = 6.2, 3.5 Hz, 1H), 7.53 – 7.46 (m, 1H), 7.29 (dd, *J* = 6.0, 3.6 Hz, 2H), 6.40 (s, 1H), 4.56 (br, 2H), 3.97 (s, 3H). HPLC-PDA-MS: RT= 3.10 min, λ<sub>max</sub>= 420 nm, [M+H]<sup>+</sup> = 296.18; purity (254 nm): 99.5%



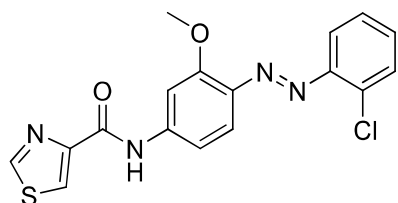
**(E)-3-chloro-N-(4-((2-chlorophenyl)diazenyl)-3-methoxyphenyl)picolinamide (71a)**: The general synthetic procedure B was used with the aminoazobenzene **69a** (30 mg, 0.11 mmol), 3-chloropicolinic acid (**70a**) (27 mg, 0.17 mmol), HATU (131 mg, 0.34 mmol) and anhydrous TEA (80 μl, 0.57 mmol) in DMF (2.0 ml) at 40°C for 16 h to give the azo compound **71a** (10 mg, 22% yield). <sup>1</sup>H NMR (400 MHz, CDCl<sub>3</sub>) δ 10.25 (br, 1H), 8.55 (dd, *J* = 4.5, 1.4 Hz, 1H), 8.14 (d, *J* = 2.1 Hz, 1H), 7.90 (dd, *J* = 8.2, 1.4 Hz, 1H), 7.83 (d, *J* = 8.7 Hz, 1H), 7.71 – 7.65 (m, 1H), 7.54 – 7.50 (m, 1H), 7.46 (dd, *J* = 8.2, 4.5 Hz, 1H), 7.36 – 7.29 (m, 2H), 7.00 (dd, *J* = 8.8, 2.1 Hz, 1H), 4.11 (s, 3H). <sup>13</sup>C NMR (101 MHz, CDCl<sub>3</sub>) δ 161.0, 158.8, 149.6, 146.0, 144.9, 142.6, 141.3, 138.9, 134.7, 133.0, 131.1, 130.6, 127.5, 127.3, 118.3, 118.2, 111.8, 103.5, 56.6. HPLC-PDA-MS: *cis* isomer RT= 2.78 min, λ<sub>max</sub>= 434 nm, [M+H]<sup>+</sup> = 401.22; *trans* isomer RT= 3.21 min, λ<sub>max</sub>= 385 nm, [M+H]<sup>+</sup> = 401.17; purity (254 nm): 91.6% *trans* isomer (4.6% *cis* isomer). HRMS (*m/z*): [M+H]<sup>+</sup> calcd for C<sub>19</sub>H<sub>15</sub>Cl<sub>2</sub>N<sub>4</sub>O<sub>2</sub><sup>+</sup> 401.0567, found 401.0565.



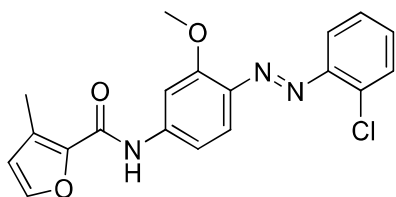
**(E)-N-(4-((2-chlorophenyl)diazenyl)-3-methoxyphenyl)-3-fluoropicolinamide (71b):** The general synthetic procedure B was used with the aminoazobenzene **69a** (30.0 mg, 0.11 mmol), 3-fluoropicolinic acid (**70b**) (24 mg, 0.17 mmol), HATU (131 mg, 0.34 mmol) and anhydrous TEA (80  $\mu$ l, 0.57 mmol) in DMF (2.0 ml) at 40°C for 16 h to give the azo compound **71b** (35 mg, 79% yield).  $^1\text{H}$  NMR (400 MHz,  $\text{CDCl}_3$ )  $\delta$  10.11 (br, 1H), 8.47 (ddd,  $J = 4.4, 1.4$  Hz, 1H), 8.18 (d,  $J = 2.1$  Hz, 1H), 7.83 (d,  $J = 8.7$  Hz, 1H), 7.72 – 7.66 (m, 1H), 7.65 – 7.61 (m, 1H), 7.58 (ddd,  $J = 8.4, 4.4, 3.7$  Hz, 1H), 7.54 – 7.49 (m, 1H), 7.36 – 7.29 (m, 2H), 7.00 (dd,  $J = 8.8, 2.2$  Hz, 1H), 4.10 (s, 3H).  $^{13}\text{C}$  NMR (101 MHz,  $\text{CDCl}_3$ )  $\delta$  161.3, 160.1, 160.0, 158.6, 149.4, 143.8, 143.7, 142.3, 138.8, 136.8, 136.8, 134.6, 130.9, 130.4, 128.8, 128.8, 127.3, 127.0, 126.8, 118.1, 118.1, 111.6, 103.4, 56.4.  $^{19}\text{F}$  NMR (376 MHz,  $\text{CDCl}_3$ )  $\delta$  -118.19 – -118.28 (m). HPLC-PDA-MS: *cis* isomer RT= 2.72 min,  $\lambda_{\text{max}}$ = 434 nm,  $[\text{M}+\text{H}]^+ = 385.20$ ; *trans* isomer RT= 3.13 min,  $\lambda_{\text{max}}$ = 391 nm,  $[\text{M}+\text{H}]^+ = 385.07$ ; purity (254 nm): 90% *trans* isomer (5% *cis* isomer). HRMS (m/z):  $[\text{M}+\text{H}]^+$  calcd for  $\text{C}_{19}\text{H}_{15}\text{ClFN}_4\text{O}_2^+$  385.0863, found 385.0873.



**(E)-3-chloro-N-(2-chloro-4-((2-chlorophenyl)diazenyl)-5-methoxyphenyl)picolinamide (71c):** The general synthetic procedure B was used with the aminoazobenzene **69b** (30 mg, 0.10 mmol), 3-chloropicolinic acid (**70a**) (24 mg, 0.15 mmol), HATU (116 mg, 0.30 mmol) and anhydrous TEA (100  $\mu$ l, 0.70 mmol) in DMF (2.0 ml) at 60°C for 48 h to give the azo compound **71c** (9.4 mg, 21% yield).  $^1\text{H}$  NMR (400 MHz,  $\text{CDCl}_3$ )  $\delta$  11.00 (br, 1H), 8.69 (s, 1H), 8.62 (dd,  $J = 4.5, 1.4$  Hz, 1H), 7.97 – 7.89 (m, 2H), 7.69 (dd,  $J = 7.5, 2.2$  Hz, 1H), 7.54 (dd,  $J = 7.5, 1.9$  Hz, 1H), 7.50 (dd,  $J = 8.2, 4.5$  Hz, 1H), 7.39 – 7.30 (m, 2H), 4.13 (s, 3H). HPLC-PDA-MS: *cis* isomer RT= 3.29 min,  $\lambda_{\text{max}}$ = 436 nm,  $[\text{M}+\text{H}]^+ = 435.13$ ; *trans* isomer RT= 3.84 min,  $\lambda_{\text{max}}$ = 391 nm,  $[\text{M}+\text{H}]^+ = 435.18$ ; purity (254 nm): 81.3% *trans* isomer (18.2% *cis* isomer). HRMS (m/z):  $[\text{M}+\text{H}]^+$  calcd for  $\text{C}_{19}\text{H}_{14}\text{Cl}_3\text{N}_4\text{O}_2^+$  435.0177, found 435.0178.



**(E)-N-(4-((2-chlorophenyl)diazenyl)-3-methoxyphenyl)thiazole-4-carboxamide (74a):** The general synthetic procedure B was used with the aminoazobenzene **69a** (30 mg, 0.11 mmol), the thiazole-4-carboxylic acid (**72**) (22 mg, 0.17 mmol), HATU (131 mg, 0.34 mmol) and anhydrous TEA (80  $\mu$ l, 0.57 mmol) in DMF (2.0 ml) at 40°C for 16 h to give azo compound **74a** (33 mg, 78% yield).  $^1\text{H}$  NMR (400 MHz,  $\text{CDCl}_3$ )  $\delta$  9.46 (br, 1H), 8.84 (d,  $J = 2.1$  Hz, 1H), 8.31 (d,  $J = 2.1$  Hz, 1H), 8.03 (d,  $J = 2.1$  Hz, 1H), 7.84 (d,  $J = 8.7$  Hz, 1H), 7.71 – 7.66 (m, 1H), 7.55 – 7.49 (m, 1H), 7.37 – 7.28 (m, 2H), 7.04 (dd,  $J = 8.8, 2.2$  Hz, 1H), 4.10 (s, 3H).  $^{13}\text{C}$  NMR (101 MHz,  $\text{CDCl}_3$ )  $\delta$  159.0, 158.7, 153.1, 150.9, 149.6, 142.6, 139.0, 134.8, 131.2, 130.6, 127.5, 124.6, 118.3, 118.3, 111.8, 103.7, 56.5. HPLC-PDA-MS: *cis* isomer RT= 2.64 min,  $\lambda_{\text{max}}$ = 433 nm,  $[\text{M}+\text{H}]^+ = 373.03$ ; *trans* isomer RT= 3.06 min,  $\lambda_{\text{max}}$ = 385 nm,  $[\text{M}+\text{H}]^+ = 373.22$ ; purity (254 nm): 92.7% *trans* isomer (2.9% *cis* isomer). HRMS (m/z):  $[\text{M}+\text{H}]^+$  calcd for  $\text{C}_{17}\text{H}_{14}\text{ClFN}_4\text{O}_2\text{S}^+$  373.0521, found 373.0518.



**(E)-N-(4-((2-chlorophenyl)diazenyl)-3-methoxyphenyl)-3-methylfuran-2-carboxamide (74b):** The general synthetic procedure B was used with the aminoazobenzene **69a** (30 mg, 0.12 mmol), the 3-methylfuran-2-carboxylic acid (**73**) (29 mg, 0.23 mmol), HATU (131 mg, 0.34 mmol) and anhydrous TEA (80  $\mu$ l, 0.57 mmol) in DMF (2.0 ml) at 60°C for 16 h to give azo compound **74b** (21 mg, 49% yield).  $^1\text{H}$  NMR (400 MHz, Chloroform-*d*)  $\delta$  8.24 (br, 1H), 8.03 (d,  $J$  = 2.1 Hz, 1H), 7.81 (d,  $J$  = 8.7 Hz, 1H), 7.72 – 7.64 (m, 1H), 7.56 – 7.48 (m, 1H), 7.40 (d,  $J$  = 1.7 Hz, 1H), 7.37 – 7.27 (m, 2H), 6.89 (dd,  $J$  = 8.8, 2.2 Hz, 1H), 6.43 (d,  $J$  = 1.7 Hz, 1H), 4.09 (s, 3H), 2.48 (s, 3H).  $^{13}\text{C}$  NMR (101 MHz,  $\text{CDCl}_3$ )  $\delta$  158.7, 157.5, 149.6, 143.0, 142.8, 141.8, 138.8, 134.7, 131.1, 130.6, 130.0, 127.5, 118.3, 118.2, 116.3, 111.5, 103.5, 56.6, 11.5. HPLC-PDA-MS: *cis* isomer RT= 2.85 min,  $\lambda_{\text{max}}$ = 286, 435 nm,  $[\text{M}+\text{H}]^+$ = 370.11; *trans* isomer RT= 3.25 min,  $\lambda_{\text{max}}$ = 390 nm,  $[\text{M}+\text{H}]^+$ = 370.19; purity (254 nm): 96.6% *trans* isomer (2.2% *cis* isomer). HRMS ( $m/z$ ):  $[\text{M}+\text{H}]^+$  calcd for  $\text{C}_{19}\text{H}_{17}\text{N}_3\text{O}_3^+$  370.0953, found 370.0955.

### Chapter 3: *trans*-on mGlu<sub>1</sub> PAMs

**General synthetic procedure A for compounds 77a and 77b:** The 3-methylfuran-2-carbonyl chloride (**76**) (1.0 eq) and the corresponding nitroaniline **75a-b** (1.2 eq) were dissolved in DCE. Then, DIPEA (2.8 eq) was added and microwave radiation was applied to the mixture for 30 min (120°C, 150 psi, 150 W). After the addition of EtOAc the resulting solution was washed with  $\text{Na}_2\text{CO}_3$  (1M aq),  $\text{NaHCO}_3$  and later with sat. NaCl and water. Finally, the organic layer was dried over anhydrous  $\text{MgSO}_4$ , filtered and concentrated *in vacuo* to give a residue which was purified with automated *flash* chromatography (nHex/EtOAc 2:1).

**General synthetic procedure B for compounds 78a and 78b:** In a tube were added the corresponding nitrophenylfuran-carboxamide **77a-b** (1.0 eq) and Pd/C (10% wt, 0.05 eq) in ethanol and a hydrogen atmosphere of 3 bar was applied for 16 h at rt. The mixture was thereafter filtered through Celite and washed with EtOH. After concentration *in vacuo*, the resulting compounds **78a** and **78b** were used without further purification.

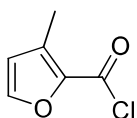
**General synthetic procedure C for compounds 80 and 81:** A solution of Oxone® (2.0 eq) in water was added to a solution of chloroaniline **67a-b** (1.0 eq) in DCM. The resulting mixture was stirred vigorously at rt during 2 h. Water and DCM were added and the layers were separated. The aqueous layer was backextracted with DCM. Then, the green organic layer was washed with water and dried over  $\text{Na}_2\text{SO}_4$  and concentrated under reduced pressure. The crude products were used without further purification.

**General synthetic procedure D for compounds 82a-b and 83a-b:** A suspension of nitrosobenzene **80** or **81** (1.5 eq) and the corresponding aniline **78a** or **78b** (1.0 eq) in DCM was prepared. Two drops of AcOH were added and the resulting solution was left to stir at rt for 2 days protected from light. Subsequently, the solvents were removed *in vacuo* and the resulting dark residue was purified with automated *flash* reversed-phase chromatography (from  $\text{H}_2\text{O}/\text{MeCN}$  95:5 to MeCN 100%).

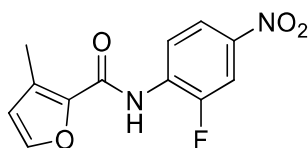
**General synthetic procedure E for compounds 85, 74b and 89a-h:** 3-methylfuran-2-carboxylic acid (**73**) (1.5-2.0 eq), the corresponding aminoazobenzenes **84**, **69a** or **88a-h** (1.0 eq), HATU (3.0 eq) were suspended in DMF and anhydrous DIPEA (3.10 eq) or anhydrous TEA (5-7.5 eq) was added. The resulting mixture was

stirred in an inert atmosphere at 40-60°C for 5-24 h. EtOAc and satd. aq. Na<sub>2</sub>CO<sub>3</sub> were added and the layers were separated. The organic layer was washed with satd. aq. NaHCO<sub>3</sub> and sat. NaCl twice. The organic phase was dried over MgSO<sub>4</sub>, filtered and concentrated *in vacuo*. The residue was purified with automated *flash* reversed-phase chromatography (from H<sub>2</sub>O/MeCN 95:5 to MeCN 100% + 0.1% HCOOH).

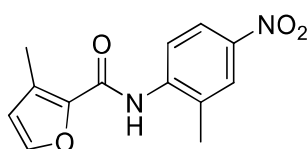
**General synthetic procedure F for compounds 69a and 88a-h:** Conc. HCl (3.11-8.5 eq) was added slowly to a solution of aniline **67b** or **60a** or **86a-g** (1.0 eq) in MeOH and the resulting mixture was stirred at 0-5°C for 5 min. An aqueous solution of sodium nitrite (1.2 eq) was added dropwise to generate the azonium intermediate, keeping the temperature between below 5°C. The mixture was left stirring for 20 min at 0-5°C. In parallel, a solution of 3-methoxyaniline (**68a**) or *o*-toluidine (**87**) (1.2 eq) and sodium acetate (0.5-8.5 eq) in a mixture MeOH/H<sub>2</sub>O (2:1, v/v) was prepared in a separate reaction vessel and stirred in an ice bath. The freshly prepared diazonium solution was kept cold (0-5°C) to avoid degradation and was added dropwise to the flask with the aniline solution with sodium acetate at 0-5°C. During the addition, the temperature was constantly kept at 0-5°C and the reaction mixture was stirred for 30 min at the same temperature. The subsequent addition of cold water caused precipitation of the products **69a** and **88b**, which were filtered, washed with precooled water and dried. If the product did not precipitate, the mixture was extracted twice with EtOAc. The combined organic layers were washed with sat. Na<sub>2</sub>CO<sub>3</sub>, sat. NaHCO<sub>3</sub> (sat) and sat. NaCl (2x ml), dried over anhydrous MgSO<sub>4</sub>, filtered and concentrated *in vacuo*. The resulting residues were purified with automated *flash* reversed-phase chromatography (from H<sub>2</sub>O/MeCN 95:5 to MeCN 100% + 0.1% HCOOH) to give the compounds **88a-h** as red and orange oils.



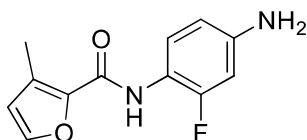
**3-methylfuran-2-carbonyl chloride (76):** The 3-methylfuran-2-carboxylic acid (**73**) (50 mg, 0.39 mmol) was dissolved in thionyl chloride (2.0 ml) to give a yellow solution. The reaction mixture was left stirring for 2 h at reflux (75°C) in an inert atmosphere. Subsequently, the solution was cooled and the thionyl chloride removed under vacuum. 100% yield was assumed and the crude product was directly used for the next synthetic steps.



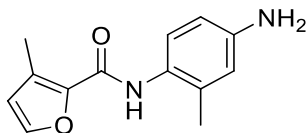
**N-(2-fluoro-4-nitrophenyl)-3-methylfuran-2-carboxamide (77a):** The general synthetic procedure A was used with 2-fluoro-4-aniline (**75a**) (133 mg, 0.86 mmol), 3-methylfuran-2-carbonyl chloride (**76**) (103 mg, 0.71 mmol) and DIPEA (350 μl, 2.0 mmol) in DCE (2.0 ml) to give nitrocompound **77a** as a **white(?)** powder (107 mg, 57% yield). <sup>1</sup>H NMR (400 MHz, CDCl<sub>3</sub>) δ 8.76 (dd, *J* = 9.1, 7.8 Hz, 1H), 8.53 (br, 1H), 8.10 (ddd, *J* = 9.1, 2.4, 1.3 Hz, 1H), 8.03 (dd, *J* = 10.8, 2.5 Hz, 1H), 7.44 (d, *J* = 1.7 Hz, 1H), 6.45 (d, 1H), 2.46 (s, 3H). <sup>13</sup>C NMR (101 MHz, CDCl<sub>3</sub>) δ 157.1, 152.1, 149.6, 143.8, 142.8, 142.7, 141.3, 133.0, 132.9, 131.4, 121.0, 121.0, 120.0, 120.0, 116.4, 111.2, 111.0, 11.5.



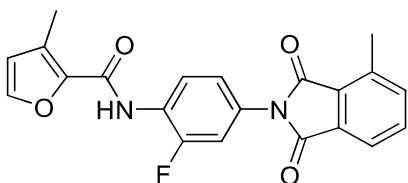
**3-methyl-*N*-(2-methyl-4-nitrophenyl)furan-2-carboxamide (77b)**: The general synthetic procedure A was used with 2-methyl-4-nitroaniline (**75b**) (130 mg, 0.86 mmol), 3-methylfuran-2-carbonyl chloride (**76**) (103 mg, 0.71 mmol) and DIPEA (350  $\mu$ l, 2.0 mmol) in DCE (2.0 ml) to give nitrocompound **77b** as a white powder (114 mg, 61% yield).  $^1\text{H}$  NMR (400 MHz,  $\text{CDCl}_3$ )  $\delta$  8.55 (d,  $J$  = 8.8 Hz, 1H), 8.22 (br, 1H), 8.17 – 8.07 (m, 2H), 7.42 (d,  $J$  = 1.5 Hz, 1H), 6.45 (d,  $J$  = 1.4 Hz, 1H), 2.47 (s, 3H), 2.45 (s, 3H).  $^{13}\text{C}$  NMR (101 MHz,  $\text{CDCl}_3$ )  $\delta$  157.2, 143.4, 143.3, 142.0, 141.7, 130.7, 126.9, 125.8, 123.2, 120.0, 116.4, 17.7, 11.5.



***N*-(4-amino-2-fluorophenyl)-3-methylfuran-2-carboxamide (78a)**: The general synthetic procedure B was used with nitrocompound **77a** (99 mg, 0.34 mmol) and Pd/C (20 mg, 0.02 mmol) in ethanol (2.0 ml) to give aniline **78a** as an oil (88 mg, quantitative yield).  $^1\text{H}$  NMR (400 MHz,  $\text{CDCl}_3$ )  $\delta$  8.04 (dd,  $J$  = 9.5, 8.1 Hz, 1H), 8.00 (br, 1H), 7.36 (d,  $J$  = 1.7 Hz, 1H), 6.50 – 6.41 (m, 2H), 6.37 (d,  $J$  = 1.7 Hz, 1H), 3.69 (br, 2H), 2.44 (s, 3H).

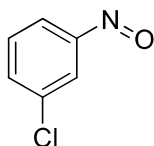


***N*-(4-amino-2-methylphenyl)-3-methylfuran-2-carboxamide (78b)**: The general synthetic procedure B was used with nitrocompound **77b** (88 mg, 0.34 mmol) and Pd/C (18 mg, 0.02 mmol) in ethanol (2.0 ml) to give aniline **78b** as an oil (78 mg, quantitative yield).  $^1\text{H}$  NMR (400 MHz,  $\text{CDCl}_3$ )  $\delta$  7.72 (br, 1H), 7.57 (d,  $J$  = 9.2 Hz, 1H), 7.35 (d,  $J$  = 1.7 Hz, 1H), 6.58 – 6.51 (m, 2H), 6.38 (d,  $J$  = 1.7 Hz, 1H), 3.58 (br, 2H), 2.43 (s, 3H), 2.23 (s, 3H).

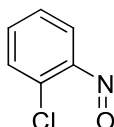


***N*-(2-fluoro-4-(4-methyl-1,3-dioxoisindolin-2-yl)phenyl)-3-methylfuran-2-carboxamide (31)**:

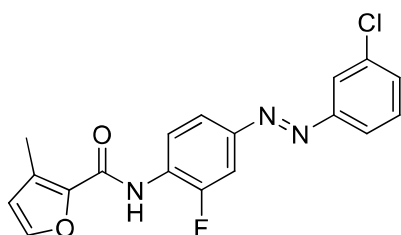
A suspension of aniline **78a** (20 mg, 0.08 mmol) and the 3-methylphthalic anhydride (**79**) (14 mg, 0.09 mmol) in AcOH (1.0 ml) was prepared. The mixture was left to stir at 120°C and under an argon atmosphere overnight. A pale yellow precipitate was formed, then it was filtered, washed with water and dried under vacuum. The desired product **31** (VU6004907) was isolated as a white solid and used without further purification (22 mg, 70% yield).  $^1\text{H}$  NMR (400 MHz,  $\text{DMSO}-d_6$ )  $\delta$  9.87 (br, 1H), 7.83 (d,  $J$  = 1.7 Hz, 1H), 7.80 – 7.65 (m, 4H), 7.44 (dd,  $J$  = 11.3, 2.2 Hz, 1H), 7.30 (dd, 1H), 6.61 (d,  $J$  = 1.9 Hz, 1H), 2.67 (s, 3H), 2.34 (s, 3H).  $^{13}\text{C}$  NMR (101 MHz,  $\text{DMSO}-d_6$ )  $\delta$  167.4, 166.6, 157.4, 156.2, 153.7, 144.1, 141.5, 137.6, 136.8, 134.3, 131.9, 129.8, 129.7, 128.3, 128.1, 126.5, 126.5, 124.9, 124.8, 123.5, 123.4, 121.2, 115.6, 115.3, 115.0, 17.2, 11.0.  $^{19}\text{F}$  NMR (376 MHz,  $\text{DMSO}-d_6$ )  $\delta$  -120.16 (ddd,  $J$  = 8.4 Hz). The described NMR spectra are in good agreement with the data reported in the literature.<sup>222,224</sup> HPLC-PDA-MS: RT= 3.69 min,  $[\text{M}+\text{H}]^+$  = 379.13; purity (254 nm): 97.0%.



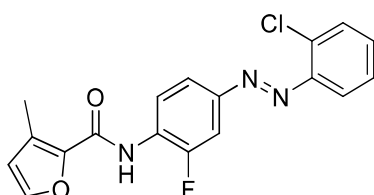
**1-chloro-3-nitrosobenzene (80):** The general synthetic procedure C was used with 3-chloroaniline (**67a**) (100 mg, 0.78 mmol) in DCM (1.0 ml) and Oxone® (969 mg, 1.6 mmol) in water (4.0 ml) to form the corresponding nitroso compound **80** (96 mg, 87% yield) which was previously described.<sup>283</sup> <sup>1</sup>H NMR (400 MHz, CDCl<sub>3</sub>) δ 8.06 (dt, *J* = 7.8, 1.5 Hz, 1H), 7.69 (ddd, *J* = 7.8, 2.2, 1.3 Hz, 1H), 7.66 – 7.60 (m, 2H). The described NMR spectra are in good agreement with the data reported in the literature.<sup>283</sup>



**1-chloro-2-nitrosobenzene (81):** The general synthetic procedure C was used with 2-chloroaniline (**67b**) (100 mg, 0.78 mmol) in DCM (1.0 ml) and Oxone® (969 mg, 1.6 mmol) in water (4.0 ml) to form the corresponding nitroso compound **81** (111 mg, quantitative yield). <sup>1</sup>H NMR (400 MHz, CDCl<sub>3</sub>) δ 7.80 (dd, *J* = 8.0, 1.2 Hz, 1H), 7.63 (ddd, *J* = 8.1, 7.2, 1.7 Hz, 1H), 7.26 – 7.21 (m, 1H), 6.24 (dd, *J* = 8.1, 1.6 Hz, 1H). The described NMR spectra are in good agreement with the data reported in the literature.<sup>284</sup>

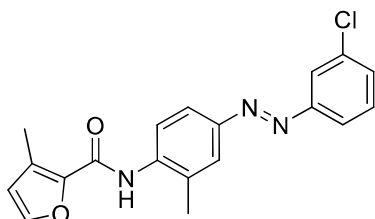


**(E)-N-(4-((3-chlorophenyl)diazenyl)-2-fluorophenyl)-3-methylfuran-2-carboxamide (82a):** The general synthetic procedure D was used with aniline **78a** (27 mg, 0.12 mmol) and 1-chloro-3-nitrosobenzene (**80**) (24 mg, 0.17 mmol) in DCM (1.0 ml) to obtain azo compound **82a** (31 mg, 76% yield) as an orange solid. <sup>1</sup>H NMR (400 MHz, CDCl<sub>3</sub>) δ 8.71 (t, *J* = 8.4 Hz, 1H), 8.46 (d, *J* = 3.6 Hz, 1H), 7.87 (d, *J* = 0.9 Hz, 1H), 7.84 (d, *J* = 8.8 Hz, 1H), 7.81 (dt, *J* = 6.8, 2.2 Hz, 1H), 7.71 (dd, *J* = 12.0, 2.1 Hz, 1H), 7.47 – 7.43 (m, 2H), 7.42 (d, *J* = 1.7 Hz, 1H), 6.43 (d, *J* = 1.7 Hz, 1H), 2.47 (s, 3H). <sup>13</sup>C NMR (101 MHz, cdcl<sub>3</sub>) δ 156.9, 153.5, 153.0, 151.1, 148.0, 148.0, 143.0, 141.4, 135.0, 130.6, 130.0, 130.0, 129.4, 129.2, 122.9, 122.9, 122.2, 121.6, 120.3, 120.3, 115.9, 106.7, 106.5, 11.2. <sup>19</sup>F NMR (376 MHz, CDCl<sub>3</sub>) δ -130.20 – -130.40 (m). HPLC-PDA-MS: *cis* isomer RT = 3.08 min, λ<sub>max</sub> = 273, 434 nm, [M+H]<sup>+</sup> = 358.08; *trans* isomer RT = 3.81 min, λ<sub>max</sub> = 352 nm, [M+H]<sup>+</sup> = 358.23; purity (254 nm): 93.5% *trans* isomer (5.2% *cis* isomer). HRMS (*m/z*): [M+H]<sup>+</sup> calcd for C<sub>18</sub>H<sub>14</sub>ClFN<sub>3</sub>O<sub>2</sub><sup>+</sup> 358.0754, found 358.0754.

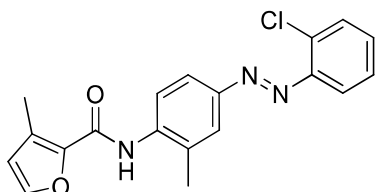


**(E)-N-(4-((2-chlorophenyl)diazenyl)-2-fluorophenyl)-3-methylfuran-2-carboxamide (82b):** The general synthetic procedure D was used with aniline **78a** (25 mg, 0.11 mmol) and 1-chloro-2-nitrosobenzene (**81**)

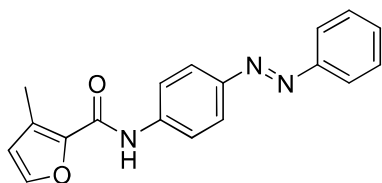
(22 mg, 0.16 mmol) in DCM (1.0 ml) to give azo compound **82b** (23 mg, 60% yield) as an orange solid.  $^1\text{H}$  NMR (400 MHz,  $\text{CDCl}_3$ )  $\delta$  8.72 (t,  $J = 8.4$  Hz, 1H), 8.48 (d,  $J = 4.1$  Hz, 1H), 7.89 (ddd,  $J = 8.7, 2.1, 1.1$  Hz, 1H), 7.76 (dd,  $J = 12.0, 2.1$  Hz, 1H), 7.70 (dd,  $J = 7.9, 1.8$  Hz, 1H), 7.55 (dd,  $J = 7.7, 1.6$  Hz, 1H), 7.42 (d,  $J = 1.7$  Hz, 1H), 7.38 (dd,  $J = 7.8, 1.9$  Hz, 1H), 7.34 (dd,  $J = 7.9, 1.4$  Hz, 1H), 6.43 (d,  $J = 1.7$  Hz, 1H), 2.48 (s, 3H).  $^{13}\text{C}$  NMR (101 MHz,  $\text{CDCl}_3$ )  $\delta$  157.2, 153.8, 151.4, 148.8, 148.7, 148.5, 143.3, 141.7, 135.6, 131.8, 130.8, 130.2, 129.7, 129.6, 127.3, 123.9, 123.9, 120.5, 120.5, 117.6, 116.1, 106.8, 106.6, 11.4.  $^{19}\text{F}$  NMR (376 MHz,  $\text{CDCl}_3$ )  $\delta$  -130.28 (ddd,  $J = 12.0, 8.0, 3.9$  Hz). HPLC-PDA-MS: *cis* isomer RT= 3.07 min,  $\lambda_{\text{max}} = 273, 429$  nm,  $[\text{M}+\text{H}]^+ = 358.15$ ; *trans* isomer RT= 3.69 min,  $\lambda_{\text{max}} = 354$  nm,  $[\text{M}+\text{H}]^+ = 358.13$ ; purity (254 nm): 82.6% *trans* isomer (17.4% *cis* isomer). HRMS (m/z):  $[\text{M}+\text{H}]^+$  calcd for  $\text{C}_{18}\text{H}_{14}\text{ClFN}_3\text{O}_2^+$  358.0754, found 358.0755.



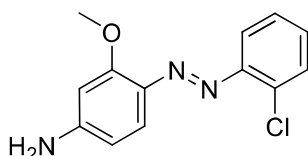
**(E)-N-(4-((3-chlorophenyl)diazenyl)-2-methylphenyl)-3-methylfuran-2-carboxamide (83a)**: The general synthetic procedure D was used with aniline **78b** (25 mg, 0.11 mmol) and 1-chloro-3-nitrosobenzene (**80**) (23 mg, 0.16 mmol) in DCM (1.0 ml) to form azo compound **83a** (27 mg, 71% yield) as an orange solid.  $^1\text{H}$  NMR (400 MHz,  $\text{CDCl}_3$ )  $\delta$  8.47 (d,  $J = 8.7$  Hz, 1H), 8.15 (br, 1H), 7.92 – 7.76 (m, 4H), 7.49 – 7.42 (m, 2H), 7.41 (d,  $J = 1.8$  Hz, 1H), 6.43 (d,  $J = 1.7$  Hz, 1H), 2.48 (s, 3H), 2.45 (s, 3H).  $^{13}\text{C}$  NMR (101 MHz,  $\text{CDCl}_3$ )  $\delta$  157.3, 153.7, 148.6, 143.0, 142.2, 139.2, 135.2, 130.5, 130.2, 129.7, 127.5, 124.6, 123.2, 122.4, 121.8, 121.1, 116.2, 17.8, 11.5. HPLC-PDA-MS: *cis* isomer RT= 3.00 min,  $\lambda_{\text{max}} = 274, 434$  nm,  $[\text{M}+\text{H}]^+ = 354.23$ ; *trans* isomer RT= 3.64 min,  $\lambda_{\text{max}} = 353$  nm,  $[\text{M}+\text{H}]^+ = 354.25$ ; purity (254 nm): 96.8% *trans* isomer (3.2% *cis* isomer). HRMS (m/z):  $[\text{M}+\text{H}]^+$  calcd for  $\text{C}_{19}\text{H}_{17}\text{ClN}_3\text{O}_2^+$  354.1004, found 354.1010.



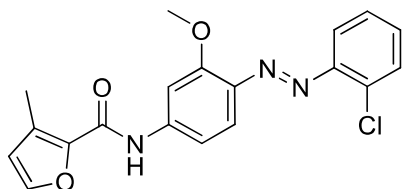
**(E)-N-(4-((2-chlorophenyl)diazenyl)-2-methylphenyl)-3-methylfuran-2-carboxamide (83b)**: The general synthetic procedure D was used with aniline **78b** (25 mg, 0.11 mmol) and 1-chloro-2-nitrosobenzene (**81**) (23 mg, 0.16 mmol) in DCM (1.0 ml) to obtain azo compound **83b** (28 mg, 73% yield).  $^1\text{H}$  NMR (400 MHz,  $\text{CDCl}_3$ )  $\delta$  8.47 (d,  $J = 8.7$  Hz, 1H), 8.16 (br, 1H), 7.90 (dd,  $J = 8.7, 2.3$  Hz, 1H), 7.84 (d,  $J = 1.7$  Hz, 1H), 7.68 (dd,  $J = 7.7, 2.0$  Hz, 1H), 7.54 (dd,  $J = 7.3, 2.0$  Hz, 1H), 7.40 (d,  $J = 1.6$  Hz, 1H), 7.35 (app. td,  $J = 7.3, 1.9$  Hz, 2H), 6.42 (d,  $J = 1.6$  Hz, 1H), 2.48 (s, 3H), 2.45 (s, 3H).  $^{13}\text{C}$  NMR (101 MHz,  $\text{CDCl}_3$ )  $\delta$  157.3, 149.0, 149.0, 143.0, 142.2, 139.2, 135.1, 131.4, 130.7, 129.7, 127.5, 127.4, 124.3, 124.0, 121.0, 117.7, 116.2, 17.9, 11.5. HPLC-PDA-MS: *cis* isomer RT= 2.98 min,  $\lambda_{\text{max}} = 323, 428$  nm,  $[\text{M}+\text{H}]^+ = 354.11$ ; *trans* isomer RT= 3.53 min,  $\lambda_{\text{max}} = 355$  nm,  $[\text{M}+\text{H}]^+ = 354.14$ ; purity (254 nm): 75.1% *trans* isomer (24.4% *cis* isomer). HRMS (m/z):  $[\text{M}+\text{H}]^+$  calcd for  $\text{C}_{19}\text{H}_{17}\text{ClN}_3\text{O}_2^+$  354.1004, found 354.1010.



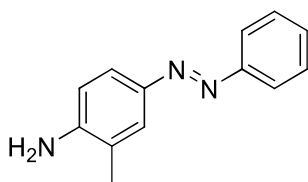
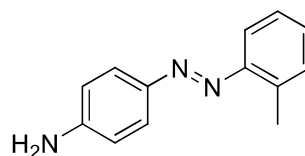
**(E)-3-methyl-N-(4-(phenyldiazenyl)phenyl)furan-2-carboxamide (85):** The general synthetic procedure E was used with aminoazobenzene (**84**) (23 mg, 0.12 mmol), the 3-methylfuran-2-carboxylic acid (**73**) (21 mg, 0.17 mmol), HATU (127 mg, 0.33 mmol) and anhydrous DIPEA (60  $\mu$ l, 0.33 mmol) in DMF (1.0 ml) at 40 °C for 5 h to give azo compound **85** (24.5 mg, 72% yield) as an orange solid.  $^1\text{H}$  NMR (400 MHz,  $\text{CDCl}_3$ )  $\delta$  8.22 (br, 1H), 7.96 (d,  $J$  = 8.9 Hz, 2H), 7.94 – 7.87 (m, 2H), 7.82 (d,  $J$  = 8.9 Hz, 2H), 7.56 – 7.47 (m, 2H), 7.50 – 7.42 (m, 1H), 7.40 (d,  $J$  = 1.4 Hz, 1H), 6.43 (d,  $J$  = 1.7 Hz, 1H), 2.48 (s, 3H).  $^{13}\text{C}$  NMR (101 MHz,  $\text{CDCl}_3$ )  $\delta$  157.4, 152.9, 149.1, 142.9, 141.9, 140.4, 130.9, 129.8, 129.2, 124.2, 122.9, 119.8, 116.2, 11.5. HPLC-PDA-MS: *cis* isomer RT= 2.69 min,  $\lambda_{\text{max}}$ = 286, 434 nm,  $[\text{M}+\text{H}]^+$ = 306.19; *trans* isomer RT= 3.23 min,  $\lambda_{\text{max}}$ = 351 nm,  $[\text{M}+\text{H}]^+$ = 306.19; purity (254 nm): 96.0% *trans* isomer (4.0% *cis* isomer). HRMS ( $m/z$ ):  $[\text{M}+\text{H}]^+$  calcd for  $\text{C}_{18}\text{H}_{16}\text{N}_3\text{O}_2^+$  306.1238, found 306.1239.



**(E)-4-((2-chlorophenyl)diazenyl)-3-methoxyaniline (69a):** The general synthetic procedure F was used. See *Synthetic procedures: Chapter 2* for further information.



**(E)-N-(4-((2-chlorophenyl)diazenyl)-3-methoxyphenyl)-3-methylfuran-2-carboxamide (74b):** The general synthetic procedure E was used. See *Synthetic procedures: Chapter 2* for further information.

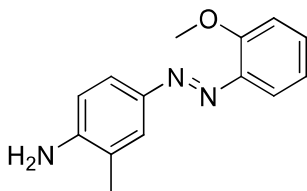
**88a****88i**

**(E)-2-methyl-4-(phenyldiazenyl)aniline (88a):** The general synthetic procedure F was used with aniline (**60a**) (300 mg, 3.2 mmol) in MeOH (5.0 ml), conc. HCl (823  $\mu$ l, 10.0 mmol), sodium nitrite (267 mg, 3.9 mmol) in water (1.5 ml). The second solution was prepared with *o*-toluidine (**87**) (414 mg, 3.9 mmol) and sodium acetate (132 mg, 1.6 mmol) in MeOH/ $\text{H}_2\text{O}$  (2:1, v/v; 8.5 ml). The aminoazobenzene **88a** was obtained as a red oil (152 mg, 22% yield). Purity ( $^1\text{H}$  NMR): 62.9% (37.1% of (*E*)-4-(*o*-tolyldiazenyl)aniline **88i** as by-product).  $^1\text{H}$  NMR (400 MHz,  $\text{CDCl}_3$ )  $\delta$  7.85 (d,  $J$  = 7.0 Hz, 2H), 7.74 – 7.70 (m, 2H), 7.49 (dd,  $J$  = 7.7 Hz, 2H), 7.44 – 7.36 (m, 1H), 6.79 – 6.72 (m, 1H), 4.04 (br, 2H), 2.25 (s, 3H).  $^{13}\text{C}$  NMR (101 MHz,  $\text{CDCl}_3$ )  $\delta$  153.0,

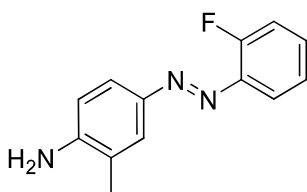


148.1, 145.6, 129.8, 129.1, 125.3, 123.9, 122.4, 122.2, 114.6, 17.5. HPLC-PDA-MS: RT= 3.88 min,  $\lambda_{\max}$ = 396 nm,  $[M+H]^+$ = 212.35.

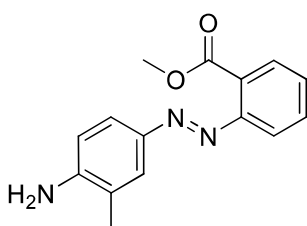
**(E)-4-(*o*-toluidiazenyl)aniline (88i):**  $^1\text{H}$  NMR (400 MHz,  $\text{CDCl}_3$ )  $\delta$  7.82 (d,  $J$  = 8.7 Hz, 2H), 7.59 (d,  $J$  = 8.0 Hz, 1H), 7.32 – 7.29 (m, 2H), 7.28 – 7.22 (m, 1H), 6.79 – 6.72 (m, 2H), 4.04 (br, 2H), 2.69 (s, 3H).  $^{13}\text{C}$  NMR (101 MHz,  $\text{CDCl}_3$ )  $\delta$  151.1, 149.4, 146.2, 137.2, 131.2, 129.8, 126.5, 125.2, 115.5, 114.8, 17.7. HPLC-PDA-MS: RT=3.93 min,  $\lambda_{\max}$ = 382 nm,  $[M+H]^+$ = 212.35.



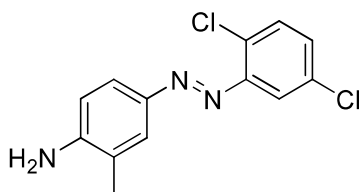
**(E)-4-((2-methoxyphenyl)diazenyl)-2-methylaniline (88b):** The general synthetic procedure F was used with 2-methoxyaniline **86a** (300 mg, 2.4 mmol) in MeOH (5.0 ml), conc. HCl (622  $\mu\text{l}$ , 7.6 mmol), sodium nitrite (202 mg, 2.9 mmol) in water (1.5 ml). The second solution was prepared with *o*-toluidine (**87**) (313 mg, 2.9 mmol) and sodium acetate (621 mg, 7.6 mmol) in MeOH/ $\text{H}_2\text{O}$  (2:1, v/v; 8.5 ml). 100 ml of water were added slowly delivering the aminoazobenzene **88b** precipitated (55 mg, 9.4% yield) as a red oil.  $^1\text{H}$  NMR (400 MHz,  $\text{CDCl}_3$ )  $\delta$  7.74 – 7.67 (m, 2H), 7.62 (dd,  $J$  = 8.0, 1.7 Hz, 1H), 7.37 (ddd,  $J$  = 8.0, 7.3, 1.6 Hz, 1H), 7.06 (dd,  $J$  = 8.4, 1.1 Hz, 1H), 7.05 – 6.96 (m, 1H), 6.76 – 6.69 (m, 1H), 4.01 (s, 3H), 2.23 (s, 3H).  $^{13}\text{C}$  NMR (101 MHz,  $\text{CDCl}_3$ )  $\delta$  156.3, 148.0, 146.2, 142.8, 131.1, 125.0, 124.4, 122.1, 121.0, 117.1, 114.5, 112.6, 56.4, 17.4. HPLC-PDA-MS: RT= 3.61 min,  $\lambda_{\max}$ = 394 nm,  $[M+H]^+$ = 242.34; purity (254 nm): 94.2%



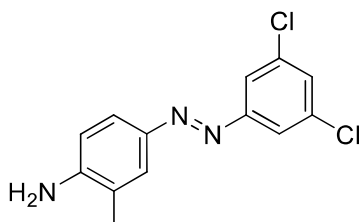
**(E)-4-((2-fluorophenyl)diazenyl)-2-methylaniline (88d):** The general synthetic procedure F was used with 2-fluoroaniline (**86c**) (300 mg, 2.7 mmol) in MeOH (5.0 ml), conc. HCl (690  $\mu\text{l}$ , 8.4 mmol), sodium nitrite (224 mg, 3.2 mmol) in water (1.5 ml). The second solution was prepared with *o*-toluidine (**87**) (347 mg, 3.2 mmol) and sodium acetate (111 mg, 1.35 mmol) in MeOH/ $\text{H}_2\text{O}$  (2:1, v/v; 8.5 ml). The aminoazobenzene **88d** was obtained as an orange solid (71 mg, 11.5% yield).  $^1\text{H}$  NMR (400 MHz,  $\text{CDCl}_3$ )  $\delta$  7.78 – 7.69 (m, 3H), 7.41 – 7.33 (m, 1H), 7.25 – 7.16 (m, 2H), 6.75 (dd,  $J$  = 7.7, 1.1 Hz, 1H), 3.92 (br, 2H), 2.25 (s, 3H).  $^{13}\text{C}$  NMR (101 MHz,  $\text{CDCl}_3$ )  $\delta$  160.9, 158.4, 148.2, 146.1, 141.2, 141.1, 131.1, 131.0, 125.5, 124.4, 124.4, 124.3, 122.3, 117.9, 117.0, 116.8, 114.7, 17.5.  $^{19}\text{F}$  NMR (376 MHz,  $\text{CDCl}_3$ )  $\delta$  -125.7. HPLC-PDA-MS: RT= 3.91 min,  $\lambda_{\max}$ = 396 nm,  $[M+H]^+$ = 230.28; purity (254 nm): 98.1%



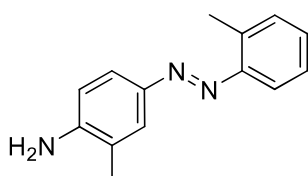
**(E)-methyl 2-((4-amino-3-methylphenyl)diazenyl)benzoate (88e):** The general synthetic procedure F was used with methyl 2-aminobenzoate (**86d**) (300 mg, 2.0 mmol) in MeOH (5.0 ml), conc. HCl (1.0 ml, 12.2 mmol), sodium nitrite (164 mg, 2.4 mmol) in water (1.5 ml). The second solution was prepared with *o*-toluidine (**87**) (255 mg, 2.4 mmol) and sodium acetate (81 mg, 0.99 mmol) in MeOH/H<sub>2</sub>O (2:1, v/v; 8.5 ml). The aminoazobenzene **88e** was obtained as a red oil (9.5 mg, 1.8% yield). <sup>1</sup>H NMR (400 MHz, CDCl<sub>3</sub>) δ 7.76 (dd, *J* = 7.4, 1.2 Hz, 1H), 7.71 – 7.66 (m, 2H), 7.60 (dd, *J* = 8.0, 1.9 Hz, 1H), 7.55 (ddd, *J* = 8.0, 7.6, 1.4 Hz, 1H), 7.41 (ddd, *J* = 7.5, 1.4 Hz, 1H), 6.73 (d, *J* = 8.2 Hz, 1H), 3.89 (s, 3H), 2.24 (s, 3H). <sup>13</sup>C NMR (101 MHz, CDCl<sub>3</sub>) δ 168.7, 152.5, 148.6, 145.7, 131.9, 129.7, 128.7, 127.9, 125.9, 124.1, 122.1, 119.6, 114.5, 52.4, 17.5. HPLC-PDA-MS: RT= 3.61 min, λ<sub>max</sub>= 394 nm, [M+H]<sup>+</sup>= 270.25; purity (254 nm): 93%.



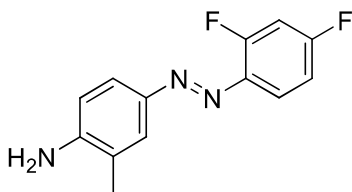
**(E)-4-((2,5-dichlorophenyl)diazenyl)-2-methylaniline (88f):** The general synthetic procedure F was used with 2,5-dichloroaniline (**86e**) (334 mg, 2.1 mmol) in MeOH (5.0 ml), conc. HCl (526 μl, 6.4 mmol), sodium nitrite (171 mg, 2.5 mmol) in water (1.5 ml). The second solution was prepared with *o*-toluidine (**87**) (265 mg, 2.5 mmol) and sodium acetate (85 mg, 1.03 mmol) in MeOH/H<sub>2</sub>O (2:1, v/v; 8.5 ml). The aminoazobenzene **88f** was obtained as a red oil (17 mg, 2.9% yield). <sup>1</sup>H NMR (400 MHz, CDCl<sub>3</sub>) δ 7.79 – 7.72 (m, 2H), 7.67 (d, *J* = 2.5 Hz, 1H), 7.44 (d, *J* = 8.5 Hz, 1H), 7.27 (dd, 1H), 6.74 (d, *J* = 9.1 Hz, 1H), 4.07 (br, 2H), 2.25 (s, 3H). <sup>13</sup>C NMR (101 MHz, CDCl<sub>3</sub>) δ 149.6, 149.1, 145.8, 133.5, 132.5, 131.4, 129.9, 126.2, 124.9, 122.2, 118.0, 114.5, 17.5. HPLC-PDA-MS: RT= 4.61 min, λ<sub>max</sub>= 414 nm, [M+H]<sup>+</sup>= 280.23; purity (254 nm): 99%.



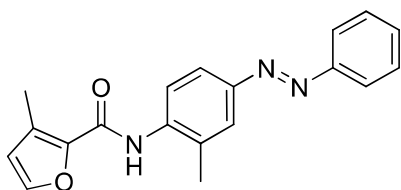
**(E)-4-((3,5-dichlorophenyl)diazenyl)-2-methylaniline (88g):** The general synthetic procedure F was used with 3,5-dichloroaniline (**86f**) (300 mg, 1.9 mmol) in MeOH (5.0 ml), conc. HCl (473 μl, 5.8 mmol), sodium nitrite (153 mg, 2.2 mmol) in water (1.5 ml). The second solution was prepared with *o*-toluidine (**87**) (238 mg, 2.2 mmol) and sodium acetate (228 mg, 2.8 mmol) in MeOH/H<sub>2</sub>O (2:1, v/v; 8.5 ml). The aminoazobenzene **88g** was obtained as a red oil (43 mg, 8.4% yield). <sup>1</sup>H NMR (400 MHz, CDCl<sub>3</sub>) δ 7.76 – 7.66 (m, 4H), 7.36 (t, *J* = 1.9 Hz, 1H), 6.78 – 6.72 (m, 1H), 4.07 (br, 2H), 2.24 (s, 3H). <sup>13</sup>C NMR (101 MHz, CDCl<sub>3</sub>) δ 154.4, 149.1, 145.2, 135.5, 129.0, 125.8, 124.5, 122.1, 121.1, 114.5, 17.5. HPLC-PDA-MS: RT= 4.95 min, λ<sub>max</sub>= 406 nm, [M+H]<sup>+</sup>= 280.23; purity (254 nm): 98.3%.



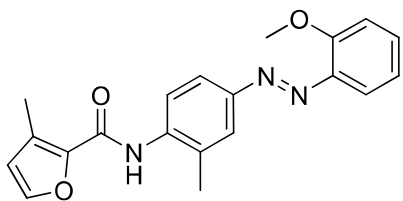
**(E)-2-methyl-4-(o-tolyldiazenyl)aniline (88c):** The synthetic pathway used for the compound **88c** was the general synthetic procedure F for aminoazobenzene **88g** and it was obtained as a by-product of the aforementioned reaction. The aminoazobenzene **88c** was obtained as an orange solid (132 mg, 32% yield).  $^1\text{H}$  NMR (400 MHz,  $\text{CDCl}_3$ )  $\delta$  7.72 (d,  $J = 6.9$  Hz, 2H), 7.58 (d,  $J = 8.7$  Hz, 1H), 7.34 – 7.29 (m, 2H), 7.30 – 7.21 (m, 1H), 6.74 (d,  $J = 9.1$  Hz, 1H), 3.90 (br, 2H), 2.70 (s, 3H), 2.26 (s, 3H).  $^{13}\text{C}$  NMR (101 MHz,  $\text{CDCl}_3$ )  $\delta$  151.2, 147.8, 146.1, 137.0, 131.1, 129.7, 126.5, 125.6, 123.5, 122.1, 115.5, 114.5, 17.7, 17.5. HPLC-PDA-MS: RT= 4.14 min,  $\lambda_{\text{max}} = 390$  nm,  $[\text{M}+\text{H}]^+ = 226.37$ ; purity (254 nm): 100%.



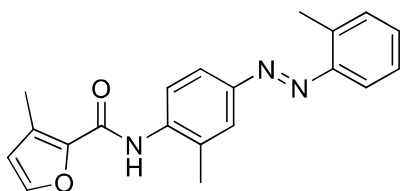
**(E)-4-((2,4-difluorophenyl)diazenyl)-2-methylaniline (88h):** The general synthetic procedure F was used with 2,4-difluoroaniline (**86g**) (300 mg, 2.3 mmol) in MeOH (5.0 ml), conc. HCl (1.0 ml, 12.3 mmol), sodium nitrite (192 mg, 2.8 mmol) in water (1.5 ml). The second solution was prepared with *o*-toluidine (**87**) (299 mg, 2.8 mmol) and sodium acetate (95 mg, 1.2 mmol) in MeOH/ $\text{H}_2\text{O}$  (2:1, v/v; 8.5 ml). The aminoazobenzene **88h** was obtained as a red oil (51 mg, 8.8% yield).  $^1\text{H}$  NMR (400 MHz,  $\text{CDCl}_3$ )  $\delta$  7.81 – 7.68 (m, 3H), 7.05 – 6.86 (m, 2H), 6.74 (d,  $J = 8.5$  Hz, 1H), 4.07 (br, 2H), 2.24 (s, 3H).  $^{13}\text{C}$  NMR (101 MHz,  $\text{CDCl}_3$ )  $\delta$  165.0, 164.9, 162.5, 162.4, 158.7, 158.5, 148.5, 145.8, 125.4, 124.3, 122.2, 119.1, 119.0, 119.0, 118.9, 114.5, 111.9, 111.8, 111.6, 111.6, 105.2, 105.0, 105.0, 104.7, 17.5.  $^{19}\text{F}$  NMR (376 MHz,  $\text{CDCl}_3$ )  $\delta$  -107.84 – -107.96 (m), -120.97 – -121.09 (m). Purity determination and absorption UV-Vis spectra were determined using the following binary solvent system: 0.05% formic acid in 5% MeCN and 0.05% formic acid in 95% water as starting mobile phase, from 5 to 25% MeCN in 0.5 min and constant for 1.5 min, from 25 to 60% MeCN in 10 min, from 60 to 100% MeCN in 2 min, from 100 to 5% MeCN in 3 min and 5% MeCN for 3 min. HPLC-PDA-MS: RT= 8.15 min,  $\lambda_{\text{max}} = 394$  nm,  $[\text{M}+\text{H}]^+ = 248.27$ ; purity (254 nm): 95%.



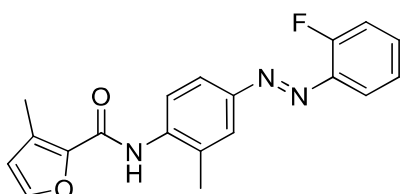
**(E)-3-methyl-N-(2-methyl-4-(phenyldiazenyl)phenyl)furan-2-carboxamide (89a):** The general synthetic procedure E was used with aminoazobenzene **88a** (27 mg, 0.13 mmol), the 3-methylfuran-2-carboxylic acid (**73**) (32 mg, 0.26 mmol), HATU (145 mg, 0.38 mmol) and anhydrous TEA (89  $\mu\text{l}$ , 0.64 mmol) in DMF (1.0 ml) at 60  $^\circ\text{C}$  for 16 h to give azo compound **89a** (13 mg, 33% yield) as an orange solid.  $^1\text{H}$  NMR (400 MHz,  $\text{CDCl}_3$ )  $\delta$  8.45 (d,  $J = 8.7$  Hz, 1H), 8.15 (br, 1H), 7.92 – 7.89 (m, 2H), 7.86 (dd,  $J = 8.6, 2.3$  Hz, 1H), 7.81 (d,  $J = 1.8$  Hz, 1H), 7.52 (ddd,  $J = 7.8, 6.5, 1.5$  Hz, 2H), 7.49 – 7.44 (m, 1H), 7.42 (d,  $J = 1.8$  Hz, 1H), 6.44 (d,  $J = 1.8$  Hz, 1H), 2.48 (s, 3H), 2.46 (s, 3H). HPLC-PDA-MS: *cis* isomer RT= 3.76 min,  $\lambda_{\text{max}} = 436$  nm,  $[\text{M}+\text{H}]^+ = 320.34$ ; *trans* isomer RT=4.53 min,  $\lambda_{\text{max}} = 348$  nm,  $[\text{M}+\text{H}]^+ = 320.34$ ; purity (254 nm): 88.6% *trans* isomer (7.5% *cis* isomer).



**(E)-N-(4-((2-methoxyphenyl)diazenyl)-2-methylphenyl)-3-methylfuran-2-carboxamide (89b):** The general synthetic procedure E was used with aminoazobenzene **88b** (29 mg, 0.12 mmol), the 3-methylfuran-2-carboxylic acid (**73**) (31 mg, 0.24 mmol), HATU (139 mg, 0.37 mmol) and anhydrous TEA (85  $\mu$ l, 0.61 mmol) in DMF (1.0 ml) at 40 °C for 16 h to give azo compound **89b** (9.2 mg, 22% yield) as an orange solid.  $^1\text{H}$  NMR (400 MHz,  $\text{CDCl}_3$ )  $\delta$  8.44 (d,  $J = 8.7$  Hz, 1H), 8.14 (br, 1H), 7.86 (dd,  $J = 8.7, 2.3$  Hz, 1H), 7.80 (d,  $J = 1.4$  Hz, 1H), 7.66 (dd,  $J = 8.0, 1.7$  Hz, 1H), 7.47 – 7.39 (m, 2H), 7.09 (dd,  $J = 8.4, 1.2$  Hz, 1H), 7.02 (ddd,  $J = 8.3, 7.3, 1.2$  Hz, 1H), 6.43 (d,  $J = 1.7$  Hz, 1H), 4.04 (s, 3H), 2.48 (s, 3H), 2.45 (s, 3H).  $^{13}\text{C}$  NMR (101 MHz,  $\text{CDCl}_3$ )  $\delta$  157.3, 156.9, 149.4, 142.9, 142.5, 142.2, 138.5, 132.3, 129.6, 127.5, 123.9, 123.7, 121.1, 120.9, 117.1, 116.2, 112.7, 56.5, 17.8, 11.5. HPLC-PDA-MS: *cis* isomer RT= 3.71 min,  $\lambda_{\text{max}} = 430$  nm,  $[\text{M}+\text{H}]^+ = 350.35$ ; *trans* isomer RT= 4.20 min,  $\lambda_{\text{max}} = 366$  nm,  $[\text{M}+\text{H}]^+ = 350.35$ ; purity (254 nm): 79.2% *trans* isomer (20.8% *cis* isomer).

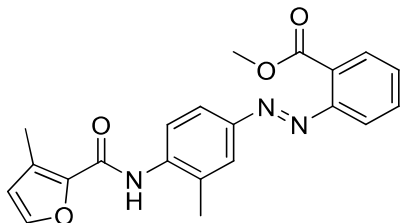


**(E)-3-methyl-N-(2-methyl-4-(o-tolyldiazenyl)phenyl)furan-2-carboxamide (89c):** The general synthetic procedure E was used with aminoazobenzene **88c** (30 mg, 0.13 mmol), the 3-methylfuran-2-carboxylic acid (**73**) (33 mg, 0.26 mmol), HATU (151 mg, 0.40 mmol) and anhydrous TEA (138  $\mu$ l, 0.99 mmol) in DMF (1.0 ml) at 50 °C for 24 h to give azo compound **89c** (27 mg, 62% yield) as an orange solid.  $^1\text{H}$  NMR (400 MHz,  $\text{CDCl}_3$ )  $\delta$  8.42 (d,  $J = 8.7$  Hz, 1H), 8.13 (br, 1H), 7.85 (dd,  $J = 8.6, 2.3$  Hz, 1H), 7.80 (d,  $J = 2.2$  Hz, 1H), 7.67 – 7.56 (m, 1H), 7.41 (d,  $J = 1.7$  Hz, 1H), 7.38 – 7.29 (m, 2H), 7.30 – 7.22 (m, 1H), 6.43 (d,  $J = 1.7$  Hz, 1H), 2.73 (s, 3H), 2.48 (s, 3H), 2.46 (s, 3H).  $^{13}\text{C}$  NMR (101 MHz,  $\text{CDCl}_3$ )  $\delta$  157.3, 151.0, 149.3, 142.9, 142.2, 138.4, 138.0, 131.3, 130.7, 129.6, 127.6, 126.5, 124.7, 122.7, 121.3, 116.2, 115.6, 17.9, 17.7, 11.5. HPLC-PDA-MS: *cis* isomer RT= 3.94 min,  $\lambda_{\text{max}} = 438$  nm,  $[\text{M}+\text{H}]^+ = 334.30$ ; *trans* isomer RT= 4.78 min,  $\lambda_{\text{max}} = 350$  nm,  $[\text{M}+\text{H}]^+ = 334.37$ ; purity (254 nm): 87.9% *trans* isomer (12.1% *cis* isomer).

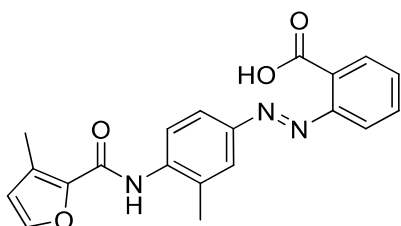


**(E)-N-(4-((2-fluorophenyl)diazenyl)-2-methylphenyl)-3-methylfuran-2-carboxamide (89d):** The general synthetic procedure E was used with aminoazobenzene **88d** (26 mg, 0.11 mmol), the 3-methylfuran-2-carboxylic acid (**73**) (28.6 mg, 0.23 mmol), HATU (129 mg, 0.34 mmol) and anhydrous TEA (119  $\mu$ l, 0.85 mmol) in DMF (1.0 ml) at 50 °C for 24 h to give azo compound **89d** (24 mg, 62% yield) as an orange solid.  $^1\text{H}$  NMR (400 MHz,  $\text{CDCl}_3$ )  $\delta$  8.47 (d,  $J = 8.7$  Hz, 1H), 8.16 (br, 1H), 7.89 (dd,  $J = 8.7, 2.3$  Hz, 1H), 7.83 (d,  $J = 2.2$  Hz, 1H), 7.75 (ddd,  $J = 7.9, 1.7$  Hz, 1H), 7.47 – 7.39 (m, 2H), 7.31 – 7.17 (m, 2H), 6.43 (d,  $J = 1.7$  Hz, 1H), 2.48 (s, 3H), 2.45 (s, 3H).  $^{13}\text{C}$  NMR (101 MHz,  $\text{CDCl}_3$ )  $\delta$  161.4, 158.8, 157.3, 149.0, 143.0, 142.2, 140.9, 140.9,

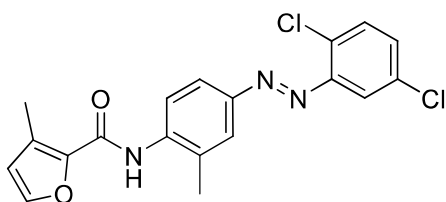
139.1, 132.2, 132.2, 129.7, 127.5, 124.4, 124.4, 124.1, 123.9, 121.0, 117.9, 117.2, 117.0, 116.2, 17.8, 11.5.  $^{19}\text{F}$  NMR (376 MHz,  $\text{CDCl}_3$ )  $\delta$  -124.78 (d,  $J$  = 1.7 Hz). HPLC-PDA-MS: *cis* isomer RT= 3.84 min,  $\lambda_{\text{max}}$ = 430 nm,  $[\text{M}+\text{H}]^+$  = 338.28; *trans* isomer RT= 4.49 min,  $\lambda_{\text{max}}$ = 356 nm,  $[\text{M}+\text{H}]^+$  = 338.28; purity (254 nm): 81.6% *trans* isomer (18.4% *cis* isomer).



**(E)-methyl 2-((3-methyl-4-(3-methylfuran-2-carboxamido)phenyl)diazenyl)benzoate (89e):** The general synthetic procedure E was used with aminoazobenzene **88e** (21 mg, 0.08 mmol), the 3-methylfuran-2-carboxylic acid (**73**) (20 mg, 0.16 mmol), HATU (89 mg, 0.23 mmol) and anhydrous TEA (54  $\mu\text{l}$ , 0.40 mmol) in DMF (700  $\mu\text{l}$ ) at 60  $^\circ\text{C}$  for 16 h to give azo compound **89e** (2.5 mg, 8.5% yield) as an orange solid.  $^1\text{H}$  NMR (400 MHz,  $\text{CDCl}_3$ )  $\delta$  8.46 (d,  $J$  = 8.7 Hz, 1H), 8.16 (br, 1H), 7.90 – 7.76 (m, 3H), 7.66 – 7.55 (m, 2H), 7.47 (ddd,  $J$  = 7.6, 6.9, 1.9 Hz, 1H), 7.42 (d,  $J$  = 1.8 Hz, 1H), 6.44 (d,  $J$  = 1.7 Hz, 1H), 3.91 (s, 3H), 2.48 (s, 3H), 2.46 (s, 3H). HPLC-PDA-MS: *cis* isomer RT= 3.70 min,  $\lambda_{\text{max}}$ = 424 nm,  $[\text{M}+\text{H}]^+$  = 378.34; *trans* isomer RT= 4.20 min,  $\lambda_{\text{max}}$ = 350 nm,  $[\text{M}+\text{H}]^+$  = 378.27; purity (254 nm): 91.0% *trans* isomer (9.0% *cis* isomer).

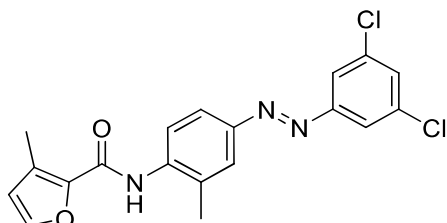


**(E)-2-((3-methyl-4-(3-methylfuran-2-carboxamido)phenyl)diazenyl)benzoic acid (89i):** The corresponding azobenzoate **89e** (5.3 mg, 0.014 mmol) was dissolved in MeOH (140  $\mu\text{l}$ ). LiOH (1M aq, 41.7  $\mu\text{l}$ ) was added and the reaction mixture was warmed to 60 $^\circ\text{C}$  and stirred for 2 h. The reaction mixture was quenched with HCl (1M aq) and DCM was added. The layers were separated and the organic layer was washed with water, dried over anhydrous  $\text{Na}_2\text{SO}_4$ , filtered and concentrated *in vacuo*. The obtained residue was purified with automated *flash* reversed-phase chromatography (ACN/ $\text{H}_2\text{O}$  + 0.1% HCOOH) to give compound **89i** (2.3 mg, 45% yield) as an orange solid. HPLC-PDA-MS: *cis* isomer RT= 3.32 min,  $\lambda_{\text{max}}$ = nm,  $[\text{M}+\text{H}]^+$  = 364.31; *trans* isomer RT= 3.84 min,  $\lambda_{\text{max}}$ = 352 nm,  $[\text{M}+\text{H}]^+$  = 364.31; purity (254 nm): 86.5% *trans* isomer (13.5% *cis* isomer).

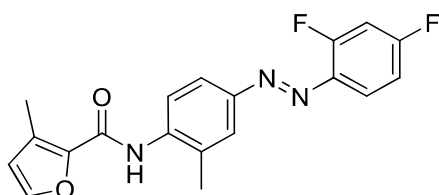


**(E)-N-(4-((2,5-dichlorophenyl)diazenyl)-2-methylphenyl)-3-methylfuran-2-carboxamide (89f):** The general synthetic procedure E was used with aminoazobenzene **88f** (16 mg, 0.06 mmol), the 3-methylfuran-2-carboxylic acid (**73**) (14 mg, 0.11 mmol), HATU (64 mg, 0.17 mmol) and anhydrous TEA (58  $\mu\text{l}$ , 0.42 mmol) in

DMF (500  $\mu$ l) at 50 °C for 24 h to give azo compound **89f** (13 mg, 62% yield) as an orange solid.  $^1\text{H}$  NMR (400 MHz,  $\text{CDCl}_3$ )  $\delta$  8.50 (d,  $J$  = 8.7 Hz, 1H), 8.18 (br, 1H), 7.91 (dd,  $J$  = 8.7, 2.3 Hz, 1H), 7.85 (dd,  $J$  = 2.3, 0.9 Hz, 1H), 7.70 (d,  $J$  = 2.5 Hz, 1H), 7.48 (d,  $J$  = 8.5 Hz, 1H), 7.42 (d,  $J$  = 1.8 Hz, 1H), 7.33 (dd,  $J$  = 8.5, 2.5 Hz, 1H), 6.44 (d,  $J$  = 1.8 Hz, 1H), 2.48 (s, 3H), 2.46 (s, 3H).  $^{13}\text{C}$  NMR (101 MHz,  $\text{CDCl}_3$ )  $\delta$  157.3, 149.3, 148.7, 143.0, 142.1, 139.8, 133.6, 133.4, 131.6, 131.0, 129.9, 127.5, 124.7, 124.3, 120.9, 117.9, 116.3, 17.9, 11.5. HPLC-PDA-MS: *cis* isomer RT= 4.28 min,  $\lambda_{\text{max}}$ = 432 nm,  $[\text{M}+\text{H}]^+$ = 388.18; *trans* isomer RT= 5.28 min,  $\lambda_{\text{max}}$ = 364 nm,  $[\text{M}+\text{H}]^+$ = 388.18; purity (254 nm): 89.5% *trans* isomer (9.8% *cis* isomer).



**(E)-N-(4-((3,5-dichlorophenyl)diazenyl)-2-methylphenyl)-3-methylfuran-2-carboxamide (89g):** The general synthetic procedure E was used with aminoazobenzene **88g** (34 mg, 0.12 mmol), the 3-methylfuran-2-carboxylic acid (**73**) (30 mg, 0.24 mmol), HATU (137 mg, 0.36 mmol) and anhydrous TEA (126  $\mu$ l, 0.90 mmol) in DMF (1.0 ml) at 50 °C for 24 h to give azo compound **89g** (32 mg, 68% yield) as an orange solid.  $^1\text{H}$  NMR (400 MHz,  $\text{CDCl}_3$ )  $\delta$  8.49 (d,  $J$  = 8.7 Hz, 1H), 8.17 (br, 1H), 7.85 (dd,  $J$  = 8.7, 2.3 Hz, 1H), 7.82 – 7.76 (m, 3H), 7.48 – 7.37 (m, 2H), 6.44 (d,  $J$  = 1.7 Hz, 1H), 2.48 (s, 3H), 2.45 (s, 3H).  $^{13}\text{C}$  NMR (101 MHz,  $\text{CDCl}_3$ )  $\delta$  157.3, 154.0, 148.3, 143.0, 142.1, 139.7, 135.7, 130.0, 129.9, 127.4, 124.9, 123.5, 121.5, 121.0, 116.3, 17.8, 11.5. HPLC-PDA-MS: *cis* isomer RT= 4.39 min,  $\lambda_{\text{max}}$ = 436 nm,  $[\text{M}+\text{H}]^+$ = 388.25; *trans* isomer RT= 5.67 min,  $\lambda_{\text{max}}$ = 362 nm,  $[\text{M}+\text{H}]^+$ = 388.18; purity (254 nm): 76.3% *trans* isomer (16.8% *cis* isomer).



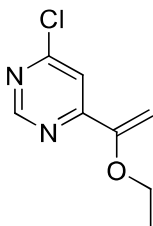
**(E)-N-(4-((2,4-difluorophenyl)diazenyl)-2-methylphenyl)-3-methylfuran-2-carboxamide (89h):** The general synthetic procedure E was used with aminoazobenzene **88h** (18 mg, 0.07 mmol), the 3-methylfuran-2-carboxylic acid (**73**) (18 mg, 0.15 mmol), HATU (83 mg, 0.22 mmol) and anhydrous TEA (51  $\mu$ l, 0.36 mmol) in DMF (700  $\mu$ l) at 60 °C for 16 h to give azo compound **89h** (13 mg, 50% yield) as an orange solid.  $^1\text{H}$  NMR (400 MHz,  $\text{CDCl}_3$ )  $\delta$  8.47 (d,  $J$  = 8.7 Hz, 1H), 8.16 (br, 1H), 7.87 (dd,  $J$  = 8.7, 2.3 Hz, 1H), 7.85 – 7.75 (m, 2H), 7.41 (d,  $J$  = 1.7 Hz, 1H), 7.00 (ddd,  $J$  = 10.8, 8.6, 2.6 Hz, 1H), 6.95 (dddd,  $J$  = 9.1, 7.8, 2.7, 1.3 Hz, 1H), 6.43 (d,  $J$  = 1.8 Hz, 1H), 2.48 (s, 3H), 2.45 (s, 3H).  $^{13}\text{C}$  NMR (101 MHz,  $\text{CDCl}_3$ )  $\delta$  165.7, 165.6, 163.2, 163.1, 161.8, 161.7, 159.3, 159.1, 157.3, 148.9, 143.0, 142.1, 139.1, 137.8, 137.8, 137.8, 137.7, 129.7, 127.5, 124.1, 123.8, 121.0, 119.2, 119.1, 119.0, 119.0, 116.2, 112.0, 112.0, 111.8, 111.8, 105.4, 105.2, 105.2, 104.9, 17.8, 11.5.  $^{19}\text{F}$  NMR (376 MHz, Chloroform-*d*)  $\delta$  -105.41 – -106.90 (m), -119.33 – -120.93 (m). HPLC-PDA-MS: *cis* isomer RT= 3.91 min,  $\lambda_{\text{max}}$ = 432 nm,  $[\text{M}+\text{H}]^+$ = 356.28; *trans* isomer RT= 4.60 min,  $\lambda_{\text{max}}$ = 354 nm,  $[\text{M}+\text{H}]^+$ = 356.28; purity (254 nm): 79.2% *trans* isomer (14.5% *cis* isomer).

#### Chapter 4: *trans*-on *mGlu*<sub>1</sub> NAMs

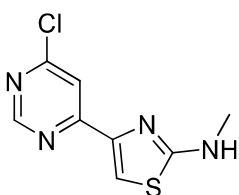
**General synthetic procedure A for compounds 98a and 98b:** To a solution of **94** (1.0 eq) in THF/water (1:1) was added *N*-bromosuccinimide (**95**) (1.1 eq) at room temperature and stirred for 2 h. Methylthiourea

(**97a**) or thiourea (**97b**) (1.0 eq) was directly added to the reaction mixture containing the intermediate **96** and the mixture was stirred at room temperature for further 2 h. The reaction mixture was diluted with EtOAc/water (1:1) and after back-extraction of aqueous phase, the organic layers were washed with sat. NaCl, dried over MgSO<sub>4</sub>, filtered and concentrated to give **98a** or **98b** as yellow solids.

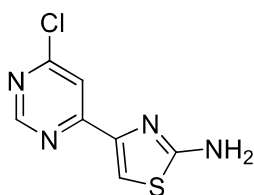
*General synthetic procedure B for compounds 90, 91, 103a-h and 107:* To a solution of **106a-b** or **101** (1.0 eq) and potassium carbonate (2.0 eq) or TEA (3.0 eq) in 1,4-dioxane was added the corresponding amine **102a-h** (1-16.7 eq) at room temperature. The reaction mixture was heated at 40-100°C for 2-16 h. The mixture was quenched with water and extracted with EtOAc. The organic layer was washed with sat. NaCl, dried over MgSO<sub>4</sub> and evaporated under reduced pressure. The residue was purified by automated *flash* direct or reverse phase chromatography to give the expected products in good yields.



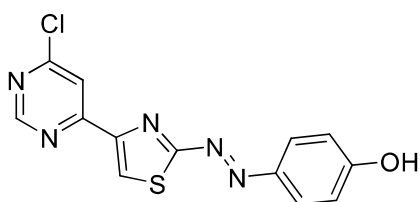
**4-chloro-6-(1-ethoxyvinyl)pyrimidine (94):** A mixture of 4,6-dichloropyrimidine (**92**) (500 mg, 3.4 mmol), Pd(PPh<sub>3</sub>)<sub>4</sub> (194 mg, 0.17 mmol), cesium fluoride (1.0 g, 6.7 mmol) and copper(I) iodide (128 mg, 0.67 mmol) in DMF (6 ml) was stirred at rt and under strict argon atmosphere while tributyl(1-ethoxyvinyl)stannane (**93**) (1.2 ml, 3.5 mmol) in DMF (4 ml) was added. Then the reaction mixture was stirred at 80 °C for 4 h. After that, it was quenched with DCM/water (1:1, v/v), and the suspension was filtered through Celite with DCM. After back-extraction of aqueous phase, the organic layers were washed 3 times with sat. NaCl, dried over Na<sub>2</sub>SO<sub>4</sub> and evaporated under reduced pressure. The residue was purified by *flash* column chromatography using nHex/EtOAc (15:1, v/v) to give **94** (273 mg, 44% yield) as a colorless solid. <sup>1</sup>H NMR (400 MHz, CDCl<sub>3</sub>) δ 8.87 (d, *J* = 1.1 Hz, 1H), 7.64 (d, *J* = 1.1 Hz, 1H), 5.69 (d, *J* = 2.4 Hz, 1H), 4.55 (d, *J* = 2.4 Hz, 1H), 3.95 (q, *J* = 7.0 Hz, 2H), 1.43 (t, *J* = 7.0 Hz, 3H). <sup>13</sup>C NMR (101 MHz, CDCl<sub>3</sub>) δ 162.4, 162.1, 158.1, 155.7, 116.4, 89.6, 64.0, 14.5. The described NMR spectra are in good agreement with the data reported in the literature.<sup>266</sup> HPLC-PDA-MS: RT= 3.77 min, [M+H]<sup>+</sup> = 185.05, purity (254 nm): 94.3%



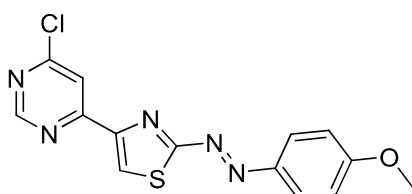
**4-(6-chloropyrimidin-4-yl)-N-methylthiazol-2-amine (98a):** The general synthetic procedure A was used with 4-chloro-6-(1-ethoxyvinyl)pyrimidine (**94**) (27.5 mg, 0.15 mmol), *N*-bromosuccinimide (**95**) (30 mg, 0.17 mmol) and methylthiourea (**97a**) (14 mg, 0.15 mmol) in THF/water (1:1, 2.0 ml) to give the expected product **98a** as a slight yellow powder without further purification (30 mg, 85% yield). <sup>1</sup>H NMR (400 MHz, CDCl<sub>3</sub>) δ 8.89 (s, 1H), 7.91 (s, 1H), 7.61 (s, 1H), 5.25 (br, 1H), 3.06 (d, *J* = 5.0 Hz, 3H). The described NMR spectrum is in good agreement with the data reported in the literature.<sup>266</sup> HPLC-PDA-MS: RT= 3.09 min, [M+H]<sup>+</sup> = 227.02, purity (254 nm): 84.5%



**4-(6-chloropyrimidin-4-yl)thiazol-2-amine (98b):** The general synthetic procedure A was used with 4-chloro-6-(1-ethoxyvinyl)pyrimidine (**94**) (300 mg, 1.6 mmol), *N*-bromosuccinimide (**95**) (318 mg, 1.8 mmol) and thiourea (**97b**) (124 mg, 1.62 mmol) in THF/water (1:1, 6 ml) to give the expected product **98b** as a yellow powder without further purification (333 mg, 96% yield).  $^1\text{H}$  NMR (400 MHz,  $\text{CD}_3\text{OD}$ )  $\delta$  8.88 (d,  $J = 1.1$  Hz, 1H), 7.95 (d,  $J = 1.1$  Hz, 1H), 7.70 (s, 1H).  $^{13}\text{C}$  NMR (101 MHz,  $\text{CD}_3\text{OD}$ )  $\delta$  181.5, 171.5, 163.2, 161.3, 159.7, 118.2, 113.5. HPLC-PDA-MS: RT= 2.73 min,  $[\text{M}+\text{H}]^+ = 213.0$ , purity (254 nm): 95.5%



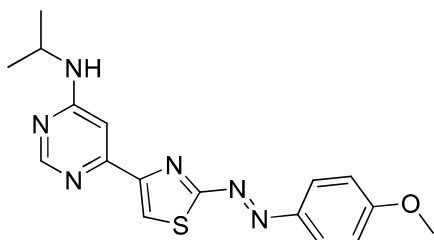
**(E)-4-((4-(6-chloropyrimidin-4-yl)thiazol-2-yl)diazenyl)phenol (100):** Nitrosyl sulphuric acid was prepared by dissolving sodium nitrite (78 mg, 1.13 mmol) in sulphuric acid (3.5 ml, 65.8 mmol) at 0 °C and the suspension obtained was stirred for 10-15 min at 20 °C. The mixture was cooled to -7 °C and a cold solution of 4-(6-chloropyrimidin-4-yl)thiazol-2-amine (**98b**) in water/AcOH (3:1, 4 ml) (200 mg, 0.94 mmol) was carefully added in portions in 1 hour maintaining -5°C. Phenol (**99**) (106 mg, 1.13 mmol) was dissolved in NaOH (3.4 g, 85 mmol) in water (10 ml) and the cold solution of the diazonium salt **110** (-5 °C) was added dropwise. The temperature was kept at 0-5°C and the pH of the mixture was kept at 10 adding 5M NaOH when its color changed from red to brown/green. The bloody red mixture was stirred continuously at room temperature for 1 hour. The color of solution was red at pH= 10, brown/green at pH= 4-5 and yellow/orange at pH= 1. Then, the reaction mixture was diluted with HCl 1M/EtOAc (1:1). After back-extraction of aqueous phase, the organic layers were reunited and washed with sat. NaCl, dried over  $\text{MgSO}_4$ , filtered and concentrated. The residue was purified by column chromatography using nHex/EtOAc (2:1, v/v) to give **100** (191 mg, 64% yield) as a red solid.  $^1\text{H}$  NMR (400 MHz,  $\text{CD}_3\text{OD}$ )  $\delta$  9.00 (d,  $J = 1.1$  Hz, 1H), 8.59 (s, 1H), 8.24 (d,  $J = 1.1$  Hz, 1H), 7.95 (d,  $J = 8.9$  Hz, 2H), 7.00 (d,  $J = 8.9$  Hz, 2H).  $^{13}\text{C}$  NMR (101 MHz,  $\text{CD}_3\text{OD}$ )  $\delta$  179.6, 165.3, 163.6, 161.4, 160.0, 152.6, 146.4, 127.9, 125.2, 118.5, 117.5. HPLC-PDA-MS: *trans* isomer RT= 3.75 min,  $\lambda_{\text{max}} = 402$  nm,  $[\text{M}+\text{H}]^+ = 318.01$ ; purity (254 nm): 98.3%.



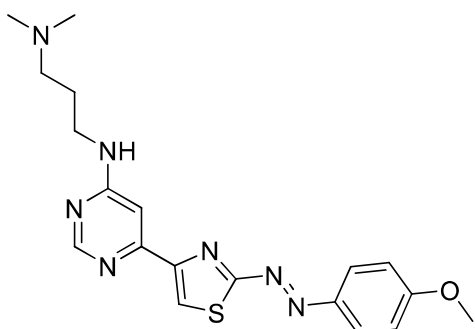
**(E)-4-(6-chloropyrimidin-4-yl)-2-((4-methoxyphenyl)diazenyl)thiazole (101):** A solution of (E)-4-((4-(6-chloropyrimidin-4-yl)thiazol-2-yl)diazenyl)phenol (**100**) (160 mg, 0.50 mmol) and potassium carbonate (139 mg, 1.01 mmol) in anhydrous DMF (10 ml) was stirred for 30 minutes under inert atmosphere. Then, dimethyl sulfate (95 mg, 0.75 mmol) was added. The solution was stirred at room temperature 48 h. After, the reaction mixture was diluted with water and the product was extracted with EtOAc. The organic extract



was washed with sat. NaCl, dried over  $\text{MgSO}_4$ , filtered and the solvent was distilled off under reduced pressure. The crude was purified by *flash* column chromatography using a mixture of nHex/EtOAc (3:1 v/v) as eluent. **101** was obtained as an orange solid (127 mg, 76% yield).  $^1\text{H}$  NMR (400 MHz,  $\text{CDCl}_3$ )  $\delta$  8.98 (d,  $J$  = 1.1 Hz, 1H), 8.41 (s, 1H), 8.31 (d,  $J$  = 1.1 Hz, 1H), 8.06 (d,  $J$  = 9.1 Hz, 2H), 7.06 (d,  $J$  = 9.0 Hz, 2H), 3.94 (s, 3H).  $^{13}\text{C}$  NMR (101 MHz,  $\text{CDCl}_3$ )  $\delta$  178.0, 164.6, 162.8, 159.9, 158.9, 152.0, 146.0, 126.8, 123.5, 118.0, 114.9, 77.2, 76.8, 56.0. HPLC-PDA-MS: *trans* isomer RT= 4.55 min,  $\lambda_{\text{max}}$ = 398 nm,  $[\text{M}+\text{H}]^+$  = 332.03; purity (254 nm): 100%. HRMS (m/z):  $[\text{M}+\text{H}]^+$  calcd for  $\text{C}_{14}\text{H}_{11}\text{ClN}_5\text{OS}^+$  332.0368, found 332.0377.

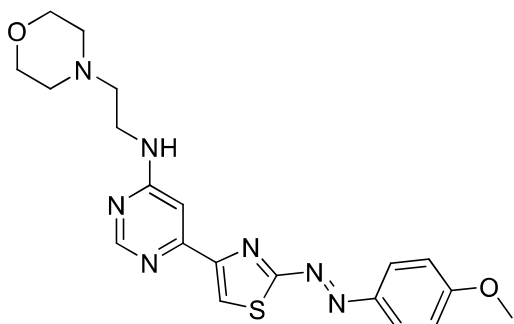


**(E)-N-isopropyl-6-(2-((4-methoxyphenyl)diazenyl)thiazol-4-yl)pyrimidin-4-amine (103a):** The general synthetic procedure B was used with azo compound **101** (16.3 mg, 0.05 mmol),  $\text{K}_2\text{CO}_3$  (13.6 mg, 0.09 mmol), HOBt (2.3 mg, 0.015 mmol) and isopropylamine (**102a**) (70  $\mu\text{l}$ , 0.8 mmol) in 1,4-dioxane (1.0 ml). The reaction mixture was heated at  $80^\circ\text{C}$  for 16 h. The residue was purified by automated *flash* reverse phase chromatography (from  $\text{H}_2\text{O}/\text{MeCN}$  95:5 to MeCN 100%) to give **103a** as a yellow powder (11 mg, 64% yield).  $^1\text{H}$  NMR (400 MHz,  $\text{CDCl}_3$ )  $\delta$  8.56 (s, 1H), 8.26 (s, 1H), 8.05 (d,  $J$  = 9.0 Hz, 2H), 7.28 (s, 1H), 7.04 (d,  $J$  = 9.0 Hz, 2H), 5.09 (br, 1H), 4.09 (br, 1H), 3.93 (s, 3H), 1.30 (d,  $J$  = 6.4 Hz, 6H).  $^{13}\text{C}$  NMR (101 MHz,  $\text{CDCl}_3$ )  $\delta$  177.5, 164.2, 162.7, 161.4, 158.5, 154.1, 146.0, 126.6, 121.2, 114.8, 110.2, 55.9, 43.1, 23.0. HPLC-PDA-MS: *trans* isomer RT= 2.96 min,  $\lambda_{\text{max}}$ = 401 nm,  $[\text{M}+\text{H}]^+$  = 355.11; purity (254 nm): 99.4%. HRMS (m/z):  $[\text{M}+\text{H}]^+$  calcd for  $\text{C}_{17}\text{H}_{19}\text{N}_6\text{OS}^+$  355.1336, found 355.1331.

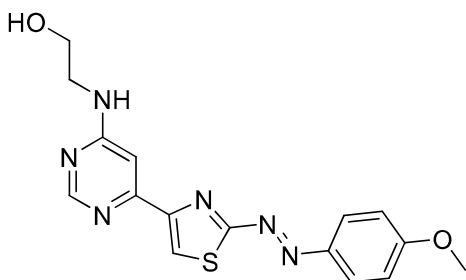


**(E)-N1-(6-(2-((4-methoxyphenyl)diazenyl)thiazol-4-yl)pyrimidin-4-yl)-N3,N3-dimethylpropane-1,3-diamine (103b):** The general synthetic procedure B was used with azo compound **101** (20 mg, 0.06 mmol) and a solution 1M of *N1,N1*-dimethylpropane-1,3-diamine (**102b**) (60  $\mu\text{l}$ , 0.06 mmol) in 1,4-dioxane (0.5 ml). The reaction mixture was heated at  $80^\circ\text{C}$  for 16 h. The residue was purified by automated *flash* reverse phase chromatography (from  $\text{H}_2\text{O}/\text{MeCN}$  95:5 to MeCN 100% + 0.1%  $\text{NH}_3$ ) to give **103b** as an orange powder (16 mg, 67% yield).  $^1\text{H}$  NMR (400 MHz,  $\text{CDCl}_3$ )  $\delta$  8.57 (s, 1H), 8.23 (s, 1H), 8.04 (d,  $J$  = 9.0 Hz, 2H), 7.29 (s, 1H), 7.04 (d,  $J$  = 9.0 Hz, 2H), 6.66 (br, 1H), 3.92 (s, 3H), 3.58 – 3.48 (m, 2H), 2.53 (m, 2H), 2.33 (s, 6H), 1.85 (m, 2H).  $^{13}\text{C}$  NMR (101 MHz,  $\text{CDCl}_3$ )  $\delta$  177.4, 174.4, 164.2, 163.4, 161.8, 158.7, 152.1, 146.0, 126.6, 120.8, 114.8, 58.5, 55.9, 45.4, 41.3, 25.6. Purity determination and absorption UV-Vis spectra were determined using the following binary solvent system: 0.05% ammonia solution 33% in 5% MeCN and 0.05% ammonia solution 33% in 95% water for 0.5 min, from 5 to 100% MeCN in 5 min, 100% MeCN for 1.5 min, from 100 to 5%

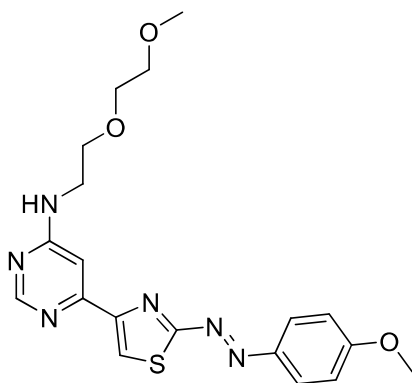
MeCN in 2 min and 5% MeCN for 2 min. HPLC-PDA-MS: *trans* isomer RT= 3.24 min,  $\lambda_{\max}$ = 399 nm,  $[M+H]^+$ = 398.17; purity (254 nm): 98.5%. HRMS (m/z):  $[M+H]^+$  calcd for  $C_{19}H_{24}N_7OS^+$  398.1758, found 398.1760.



**(E)-6-(2-((4-methoxyphenyl)diazenyl)thiazol-4-yl)-N-(2-morpholinoethyl)pyrimidin-4-amine (103c):** The general synthetic procedure B was used with azo compound **101** (13 mg, 0.04 mmol) and a solution 1M of 2-morpholinoethanamine (**102c**) (39  $\mu$ l, 0.04 mmol) in 1,4-dioxane (0.4 ml). The reaction mixture was heated at 80°C for 16 h and later it was directly concentrated, without any additional work up. The residue was purified by automated *flash* reverse phase chromatography (from H<sub>2</sub>O/MeCN 95:5 to MeCN 100%) to give **103c** as an orange powder (11 mg, 67% yield). <sup>1</sup>H NMR (400 MHz, CDCl<sub>3</sub>)  $\delta$  8.59 (s, 1H), 8.24 (s, 1H), 8.04 (d, *J* = 9.0 Hz, 2H), 7.34 (s, 1H), 7.04 (d, *J* = 9.0 Hz, 2H), 5.80 (br, 1H), 3.93 (s, 3H), 3.77 – 3.73 (m, 4H), 3.51 (br, 2H), 2.69 – 2.64 (m, 2H), 2.54 – 2.51 (m, 4H). Purity determination and absorption UV-Vis spectra were determined using the following binary solvent system: 0.05% ammonia solution 33% in 5% MeCN and 0.05% ammonia solution 33% in 95% water for 0.5 min, from 5 to 100% MeCN in 5 min, 100% MeCN for 1.5 min, from 100 to 5% MeCN in 2 min and 5% MeCN for 2 min. HPLC-PDA-MS: *trans* isomer RT= 2.61 min,  $\lambda_{\max}$ = 401 nm,  $[M+H]^+$ = 426.33; purity (254 nm): 98.5%. HRMS (m/z):  $[M+H]^+$  calcd for  $C_{20}H_{24}N_7O_2S^+$  426.1707, found 426.1713.

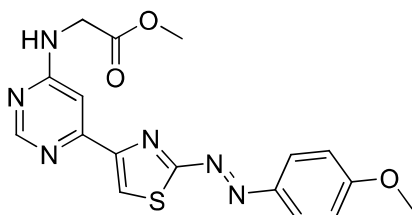


**(E)-2-((6-(2-((4-methoxyphenyl)diazenyl)thiazol-4-yl)pyrimidin-4-yl)amino)ethanol (103d):** The general synthetic procedure B was used with azo compound **101** (14 mg, 0.04 mmol), TEA (18  $\mu$ l, 0.13 mmol) and a solution 1M of 2-aminoethanol (**102d**) (62  $\mu$ l, 0.04 mmol) in 1,4-dioxane (0.4 ml). The reaction mixture was heated at 80°C for 16 h and later it was directly concentrated, without any additional work up. The residue was purified by automated *flash* direct-phase chromatography (DCM +10% MeOH) to give **103d** as an orange powder (8.2 mg, 54.6% yield). <sup>1</sup>H NMR (400 MHz, CDCl<sub>3</sub>)  $\delta$  8.59 (s, 1H), 8.31 (s, 1H), 8.04 (d, *J* = 8.8 Hz, 2H), 7.37 (s, 1H), 7.04 (d, *J* = 8.8 Hz, 2H), 5.56 (br, 1H), 3.93 (s, 3H), 3.89 (t, *J* = 4.8 Hz, 2H), 3.66 (br, 2H). Purity determination and absorption UV-Vis spectra were determined using the following binary solvent system: 0.05% ammonia solution 33% in 5% MeCN and 0.05% ammonia solution 33% in 95% water for 0.5 min, from 5 to 100% MeCN in 5 min, 100% MeCN for 1.5 min, from 100 to 5% MeCN in 2 min and 5% MeCN for 2 min. HPLC-PDA-MS: *trans* isomer RT= 2.38 min,  $\lambda_{\max}$ = 401 nm,  $[M+H]^+$ = 357.20; purity (254 nm): 97.9%. HRMS (m/z):  $[M+H]^+$  calcd for  $C_{16}H_{17}N_6O_2S^+$  357.1129, found 357.1129.

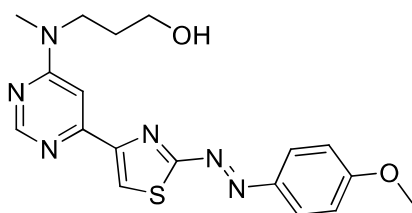


**(E)-N-(2-(2-methoxyethoxy)ethyl)-6-(2-((4-methoxyphenyl)diazenyl)thiazol-4-yl)pyrimidin-4-amine**

**(103e):** The general synthetic procedure B was used with azo compound **101** (10 mg, 0.03 mmol),  $K_2CO_3$  (8.3 mg, 0.06 mmol) and 2-(2-methoxyethoxy)ethanamine (**102e**) (21.5 mg, 0.18 mmol) in 1,4-dioxane (0.4 ml). The reaction mixture was heated at 40°C for 16 h. Then, it was decided to evaporate the solvent after filtration of  $K_2CO_3$ . The residue was purified by automated *flash* direct-phase chromatography (DCM +4% MeOH) to give **103e** as an orange powder (2.4 mg, 19.5% yield).  $^1H$  NMR (400 MHz,  $CDCl_3$ )  $\delta$  8.60 (s, 1H), 8.31 (br,  $J = 12.1$  Hz, 1H), 8.05 (d,  $J = 9.0$  Hz, 2H), 7.33 (d,  $J = 1.2$  Hz, 1H), 7.05 (d,  $J = 9.0$  Hz, 2H), 5.70 (br, 1H), 3.93 (s, 3H), 3.75 – 3.70 (m, 3H), 3.69 – 3.65 (m, 3H), 3.59 – 3.55 (m, 2H), 3.42 (s, 3H). HPLC-PDA-MS: *trans* isomer RT= 2.35 min,  $\lambda_{max}$ = 402 nm,  $[M+H]^+$  = 415.37; purity (254 nm): 97.0%. HRMS (m/z):  $[M+H]^+$  calcd for  $C_{19}H_{23}N_6O_3S^+$  415.1547, found 415.1547.



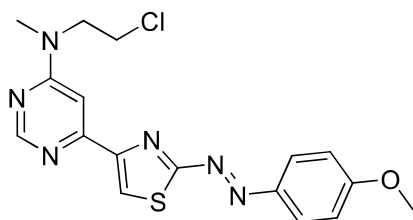
**(E)-methyl 2-((6-(2-((4-methoxyphenyl)diazenyl)thiazol-4-yl)pyrimidin-4-yl)amino)acetate (103f):** The general synthetic procedure B was used with azo compound **101** (16 mg, 0.05 mmol), TEA (20  $\mu$ l, 0.14 mmol) and methyl 2-aminoacetate hydrochloride (**102f**) (12 mg, 0.09 mmol) in 1,4-dioxane (0.5 ml). The reaction mixture was heated at 80°C for 16 h. The residue was purified by automated *flash* direct-phase chromatography (DCM +5% MeOH) to give **103f** as an orange powder (8.5 mg, 46% yield).  $^1H$  NMR (400 MHz,  $CDCl_3$ )  $^1H$  NMR (400 MHz, Chloroform-*d*)  $\delta$  8.65 (d,  $J = 1.1$  Hz, 1H), 8.43 (br, 1H), 8.04 (d,  $J = 9.0$  Hz, 2H), 7.41 (s, 1H), 7.04 (d,  $J = 9.0$  Hz, 2H), 5.74 (br, 1H), 4.28 (d,  $J = 5.2$  Hz, 2H), 3.93 (s, 3H), 3.82 (s, 3H). HPLC-PDA-MS: *cis* isomer RT= 3.08 min,  $\lambda_{max}$ = 306, 450 nm,  $[M+H]^+$  = 385.10; *trans* isomer RT= 3.37 min,  $\lambda_{max}$ = 402 nm,  $[M+H]^+$  = 385.0; purity (254 nm): *trans* isomer 91.0% (*cis* isomer 7.0%). HRMS (m/z):  $[M+H]^+$  calcd for  $C_{17}H_{17}N_6O_3S^+$  385.1078, found 385.1086.



**(E)-3-((6-(2-((4-methoxyphenyl)diazenyl)thiazol-4-yl)pyrimidin-4-yl)(methyl)amino)propan-1-ol (103g):**

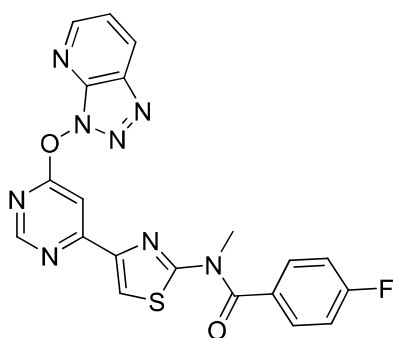
The general synthetic procedure B was used with azo compound **101** (19.7 mg, 0.06 mmol), TEA (25  $\mu$ l, 0.18

mmol) and a solution 1M of 3-(methylamino)propan-1-ol (**102g**) (119  $\mu$ l, 0.12 mmol) in 1,4-dioxane (0.5 ml). The reaction mixture was heated at 80°C for 16 h and later it was directly concentrated, without any additional work up. The residue was purified by automated *flash* reverse phase chromatography (from H<sub>2</sub>O/MeCN 95:5 to MeCN 100% +0.1% HCOOH) to give **103g** as an orange powder (13.7 mg, 60% yield). <sup>1</sup>H NMR (400 MHz, CDCl<sub>3</sub>)  $\delta$  8.61 (s, 1H), 8.04 (d, *J* = 9.0 Hz, 2H), 7.46 (br, 1H), 7.04 (d, *J* = 9.0 Hz, 2H), 3.93 (s, 3H), 3.89 – 3.85 (m, 2H), 3.59 (br, 2H), 3.20 (br, 3H), 1.92 – 1.84 (m, 2H). HPLC-PDA-MS: *trans* isomer RT=2.95 min,  $\lambda_{\max}$ = 390 nm, [M+H]<sup>+</sup>= 385.14; purity (254 nm): *trans* isomer 97.5% (*cis* isomer 0%). HRMS (m/z): [M+H]<sup>+</sup> calcd for C<sub>18</sub>H<sub>21</sub>N<sub>6</sub>O<sub>2</sub>S<sup>+</sup> 385.1442, found 385.1450.



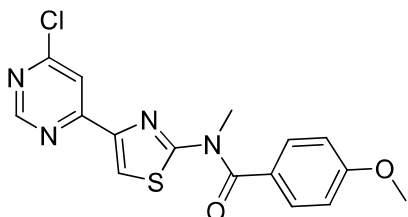
**(E)-N-(2-chloroethyl)-6-(2-((4-methoxyphenyl)diazenyl)thiazol-4-yl)-N-methylpyrimidin-4-amine (103h):**

The general synthetic procedure B was used with azo compound **101** (16 mg, 0.05 mmol), TEA (26  $\mu$ L, 0.19 mmol) and 2-chloro-*N*-methylethanamine hydrochloride (**102h**) (12.3 mg, 0.09 mmol) in 1,4-dioxane (0.5 ml). The reaction mixture was heated at 80°C for 16 h and later it was directly concentrated, without any additional work up. The residue was purified by automated *flash* reverse phase chromatography (from H<sub>2</sub>O/MeCN 95:5 to MeCN 100% +0.1% HCOOH) to give **103h** as an orange powder (9 mg, 49% yield). <sup>1</sup>H NMR (400 MHz, CDCl<sub>3</sub>)  $\delta$  8.64 (s, 1H), 8.26 (s, 1H), 8.05 (d, *J* = 8.9 Hz, 2H), 7.53 (s, 1H), 7.04 (d, *J* = 9.0 Hz, 2H), 3.93 (s, 3H), 3.90 (br, 2H), 2.63 (br, 2H), 2.44 (s, 3H). <sup>13</sup>C NMR (101 MHz, CDCl<sub>3</sub>)  $\delta$  177.5, 164.3, 162.7, 158.4, 157.4, 154.2, 146.0, 126.6, 121.1, 114.8, 99.2, 55.9, 54.5, 45.9, 43.5. Purity determination and absorption UV-Vis spectra were determined considering the adduct that the desired compound **103h** forms in acid medium with MeCN used as solvent for HPLC and HRMS analysis. HPLC-PDA-MS: *trans* isomer RT= 2.86 min,  $\lambda_{\max}$ = 402 nm, [M+H]<sup>+</sup>= 396.16; purity (254 nm): *trans* isomer 100%. HRMS (m/z): [M+H]<sup>+</sup> calcd for C<sub>19</sub>H<sub>22</sub>N<sub>7</sub>O<sub>2</sub>S<sup>+</sup> 396.1602, found 396.1600.

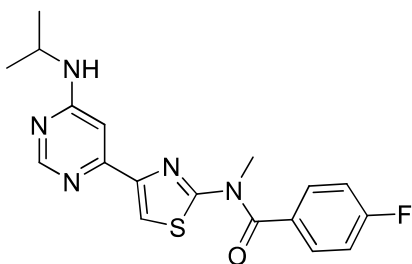


**N-(4-(6-((3H-[1,2,3]triazolo[4,5-b]pyridin-3-yl)oxy)pyrimidin-4-yl)thiazol-2-yl)-4-fluoro-N-methylbenzamide (106a):** 4-fluorobenzoic acid (**104**) (50 mg, 0.36 mmol), 4-(6-chloropyrimidin-4-yl)-*N*-methylthiazol-2-amine **98a** (40.5 mg, 0.18 mmol), HATU (136 mg, 0.36 mmol) were suspended in DMF (2.0 ml) and anhydrous TEA (124  $\mu$ l, 0.89 mmol) was added. The resulting mixture was stirred in an inert atmosphere at 65°C for 16 h. EtOAc and satd. aq. Na<sub>2</sub>CO<sub>3</sub> were added and the layers were separated. The organic layer was washed with satd. aq. NaHCO<sub>3</sub> and sat. NaCl twice. The organic phase was dried over MgSO<sub>4</sub>, filtered and concentrated *in vacuo*. The residue was purified with automated *flash* reversed-phase chromatography

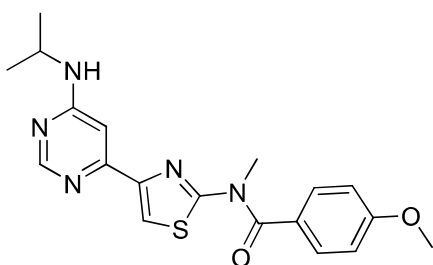
(from H<sub>2</sub>O/MeCN 95:5 to MeCN 100%). The main product obtained is the HATU-adduct **106a** (29.3 mg, 37% yield).



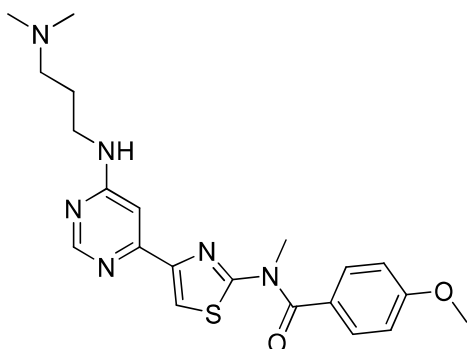
***N*-(4-(6-chloropyrimidin-4-yl)thiazol-2-yl)-4-methoxy-*N*-methylbenzamide (106b)**: To a solution of 4-(6-chloropyrimidin-4-yl)-*N*-methylthiazol-2-amine (**98a**) (44 mg, 0.19 mmol) and TEA (162  $\mu$ l, 1.16 mmol) in toluene (1.5 ml) was added 4-methoxybenzoyl chloride (**105**) (39  $\mu$ l, 0.29 mmol) at room temperature under N<sub>2</sub> atmosphere. The reaction mixture was heated at 100 °C for 12h. This mixture was quenched with water and extracted with DCM. The organic layer was dried over Na<sub>2</sub>SO<sub>4</sub> and evaporated under reduced pressure. The residue was purified by *flash* silica gel column chromatography using DCM/EtOAc/TEA (4:1:0.005, v/v/v) to give **106b** (50 mg, 71% yield) as a colorless solid. <sup>1</sup>H NMR (400 MHz, CDCl<sub>3</sub>)  $\delta$  8.95 (d, *J* = 1.1 Hz, 1H), 8.11 (s, 1H), 8.07 (d, *J* = 1.1 Hz, 1H), 7.60 (d, *J* = 8.7 Hz, 2H), 7.01 (d, *J* = 8.7 Hz, 2H), 3.89 (s, 3H), 3.80 (s, 3H). <sup>13</sup>C NMR (101 MHz, CDCl<sub>3</sub>)  $\delta$  170.6, 162.4, 162.2, 161.4, 160.7, 158.8, 146.2, 130.2, 126.0, 118.8, 117.5, 114.1, 55.7, 39.0. The described NMR spectra are in good agreement with the data reported in the literature.<sup>266</sup> HPLC-PDA-MS: RT= 4.13 min, [M+H]<sup>+</sup> = 361.04; purity (254 nm): 92.5%



**4-fluoro-*N*-(4-(6-(isopropylamino)pyrimidin-4-yl)thiazol-2-yl)-*N*-methylbenzamide (90)**: The general synthetic procedure B was used with intermediate **106a** (18 mg, 0.04 mmol), K<sub>2</sub>CO<sub>3</sub> (11.1 mg, 0.08 mmol) and isopropylamine (**102a**) (57  $\mu$ l, 0.67 mmol) in 1,4-dioxane (1.0 ml). The reaction mixture was heated at 100°C for 2 h. The residue was purified by automated *flash* reverse phase chromatography (from H<sub>2</sub>O/MeCN 95:5 to MeCN 100%) to give **90** as a white powder (12 mg, 80% yield). <sup>1</sup>H NMR (400 MHz, CDCl<sub>3</sub>)  $\delta$  8.57 (s, 1H), 8.16 (s, 1H), 7.61 (dd, *J* = 8.8, 5.2 Hz, 2H), 7.20 (t, *J* = 8.6 Hz, 2H), 7.10 (s, 1H), 5.56 (br, 1H), 4.15 (br, 1H), 3.74 (s, 3H), 1.31 (d, *J* = 6.4 Hz, 6H). The described NMR spectra are in good agreement with the data reported in the literature.<sup>263,266</sup> HPLC-PDA-MS: RT= 2.67 min, [M+H]<sup>+</sup> = 372.21; purity (254 nm): 95.0%.



***N*-(4-(6-(isopropylamino)pyrimidin-4-yl)thiazol-2-yl)-4-methoxy-*N*-methylbenzamide (91):** The general synthetic procedure B was used with intermediate **106b** (10 mg, 0.03 mmol), K<sub>2</sub>CO<sub>3</sub> (7.7 mg, 0.06 mmol) and isopropylamine (**102a**) (40 μl, 0.46 mmol) in 1,4-dioxane (0.3 ml). The reaction mixture was heated at 80°C for 16 h. The residue was purified by automated *flash* direct-phase chromatography (nHex/EtOAc 2:5, v/v) to give **91** as a white powder (4.1 mg, 39% yield). <sup>1</sup>H NMR (400 MHz, CDCl<sub>3</sub>) δ 8.57 (s, 1H), 7.91 (s, 1H), 7.58 (d, *J* = 8.7 Hz, 2H), 7.07 (s, 1H), 7.00 (d, *J* = 8.7 Hz, 2H), 4.96 (br, 1H), 4.10 (br, 1H), 3.88 (s, 3H), 3.78 (s, 3H), 1.29 (d, *J* = 6.4 Hz, 6H). The described NMR spectra are in good agreement with the data reported in the literature.<sup>266</sup> HPLC-PDA-MS: RT= 2.29 min, [M+H]<sup>+</sup> = 384.28; purity (254 nm): 96.5%.



***N*-(4-(6-((3-(dimethylamino)propyl)amino)pyrimidin-4-yl)thiazol-2-yl)-4-methoxy-*N*-methylbenzamide (107):** The general synthetic procedure B was used with intermediate **106b** (10 mg, 0.03 mmol) and a solution 1M of *N*1,*N*1-dimethylpropane-1,3-diamine (**102b**) (83 μl, 0.08 mmol) in 1,4-dioxane (0.3 ml). The reaction mixture was heated at 80°C for 16 h and later it was directly concentrated, without any additional work up. The residue was purified by automated *flash* direct-phase chromatography (DCM/MeOH 9:1, v/v +1% NH<sub>3</sub>) to give **107** as a white powder (8.3 mg, 70.2% yield). <sup>1</sup>H NMR (400 MHz, CDCl<sub>3</sub>) δ 8.56 (s, 1H), 7.89 (s, 1H), 7.58 (d, *J* = 8.7 Hz, 2H), 7.06 (s, 1H), 6.99 (d, *J* = 8.7 Hz, 2H), 6.17 (br, 1H), 3.88 (s, 3H), 3.78 (s, 3H), 3.55 – 3.45 (m, 2H), 2.48 (m, 2H), 2.30 (s, 6H), 1.83 (m, 2H). <sup>13</sup>C NMR (101 MHz, CDCl<sub>3</sub>) δ 170.4, 163.4, 162.0, 161.0, 158.7, 153.3, 148.2, 130.2, 126.4, 122.2, 115.8, 114.0, 58.2, 55.6, 45.5, 40.8, 38.9, 26.3. HPLC-PDA-MS: RT= 2.62 min, [M+H]<sup>+</sup> = 427.0; purity (254 nm): 100%. HRMS (*m/z*): [M+H]<sup>+</sup> calcd for C<sub>21</sub>H<sub>27</sub>N<sub>6</sub>O<sub>2</sub>S<sup>+</sup> 427.1911, found 427.1910.

## Photophysical and photochemical characterization

*MCS, Laboratory of Medicinal Chemistry and Synthesis, IQAC-CSIC, Barcelona*

### Materials and general methods

#### Light source

Two different LED illumination systems were used as light sources: Teleopto and CoolLED.

The *Teleopto light system* consists of single or dual wavelength LED Array (model LEDA-X and LEDA2-By respectively) connected to a LED Array Driver (model LAD-1). By the mode switch of LAD-1 LED Array Driver is it possible to choose constant or trigger mode, the latter by means a stimulator (STO mkII, version 1.6) which enables time-controlled pulsed stimulation. The light was delivered from the bottom to the solutions since the LED Array perfectly fits for 96 well-plates and each LED element comes just under each well.

Teleopto system set at 12 V intensity and in continuous mode corresponds to 0.09 mW/mm<sup>2</sup> for 365 nm, 0.09 mW/mm<sup>2</sup> for 380 nm, 0.19 mW/mm<sup>2</sup> for 405 nm, 0.13 mW/mm<sup>2</sup> for 420 nm, 0.17 mW/mm<sup>2</sup> for 455 nm, 0.14 mW/mm<sup>2</sup> for 470 nm, 0.10 mW/mm<sup>2</sup> for 500 nm, 0.09 mW/mm<sup>2</sup> for 530 nm and 0.14 mW/mm<sup>2</sup> for 550 nm wavelength.

The *CoolLED light system* consists of a liquid light guide accessory (pE-1906, CoolLed) connected to a LED light source (pE-4000, CoolLed). For the photochemical characterization of the samples, the liquid light guide accessory was pointed directly toward each sample placed in transparent 96-well plates so that the light was delivered from the top to the solutions and for three minutes in continuous mode. CoolLED set at 50% intensity corresponds to 1.04 mW/mm<sup>2</sup> for 365 nm, 2.60 mW/mm<sup>2</sup> for 385 nm, 2.10 mW/mm<sup>2</sup> for 405 nm, 0.72 mW/mm<sup>2</sup> for 435 nm, 2.17 mW/mm<sup>2</sup> for 460nm, 1.02 mW/mm<sup>2</sup> for 470 nm, 0.95 mW/mm<sup>2</sup> for 490 nm, 0.3 mW/mm<sup>2</sup> for 500 nm, 0.36 mW/mm<sup>2</sup> for 525 nm, and 1.57 mW/mm<sup>2</sup> for 550 nm light.

Potencies were measured using a Thorlabs PM100D power energy meter connected with a standard photodiode power sensor (S120VC).

### **UV-Vis spectroscopy**

The absorption spectra of the photoisomerizable compounds were obtained with solutions 10-50  $\mu$ M in DMSO, MeCN, water or in a buffer (PBS or a determined pH buffer) with 0.5-10% DMSO (200  $\mu$ L of compound solution/well) using a Tecan's Spark 20M Multimode Microplate reader. The samples were measured between 800 and 300 nm with an average time of 50 ms at 2 nm fixed intervals to achieve the full absorption spectra.

### **Determination of optimal wavelengths**

To evaluate the photoisomerization of the samples and obtain the optimal illumination wavelengths to photoisomerize from *trans* to *cis* configuration by UV-Vis, a continuous illumination for a minimum of three minutes was applied with the corresponding light source mentioned above, on the sample solutions placed in black clear-bottom (Greiner Bio-one) or transparent (Greiner CELLSTAR<sup>®</sup>) 96-well plates (200  $\mu$ L of compound solution/well). Immediately after the illumination, the samples were read as indicated above with Tecan's Spark 20M Multimode Microplate reader.

### **Stability of the photoisomerization**

The effect of repeated light cycles to sample of 10-50  $\mu$ M of the compounds in DMSO and PBS, HEPES buffer solution or water was evaluated in order to assess the stability of the photoisomerization. Therefore, multiple *trans/cis* isomerization cycles were registered by measuring absorbance at a determined single wavelength with Tecan's Spark 20M Multimode Microplate reader in the dark and after three minutes of constant illumination with the optimal isomerization wavelengths.

### **Thermal relaxation of *cis* isomers**

To determine the thermal relaxation rate of the *cis* isomers of the compounds, 25-50  $\mu$ M solutions in PBS or HEPES buffer solution with 0.5-10% DMSO and in DMSO 100% were prepared and illuminated with a determined wavelength for three minutes. After prolonged absorbance recording at 25°C, the relaxation half-life of the compounds was calculated by plotting absorbance readings at a given wavelength (around the maximum of the  $\pi$ - $\pi^*$  band of the *trans* isomer) versus time and by fitting the obtained curve to an

exponential decay function with *GraphPad Prism 8.1.1* software, corresponding to a first order equilibrium reaction formula (Equation 1).

*cis*-azo compound → *trans*-azo compound

$$A(t) = A_0 \cdot e^{-\lambda t} \text{ with } \lambda = \frac{1}{\tau}$$

**Equation 1.** Formula for the thermal relaxation from *cis* to *trans* isomers corresponding to a direct first order reaction.<sup>46</sup>

$A(t)$  is the absorbance at time  $t$ ,  $A_0 = A(0)$  is the initial absorbance, that is, the absorbance at time  $t = 0$ , and the constant  $\lambda$  is called the decay constant, which relates to the exponential time constant  $\tau$ , so-called mean lifetime. A more intuitive characteristic of exponential decay is the time required for the decaying quantity to fall to one half of its initial value. This time is called the half-life, and often denoted by the symbol  $t_{1/2}$ . The half-life can be written in terms of the decay constant as shown below (Equation 2). Therefore, the mean lifetime is equal to the half-life divided by the natural log of 2 (Equation 2).

$$t_{1/2} = \frac{\ln(2)}{\lambda} = \tau \cdot \ln(2) \rightarrow \tau = \frac{t_{1/2}}{\ln(2)} \approx 1.44 \cdot t_{1/2}$$

**Equation 2.** Formula for the half-life in exponential decay highlighting the relation between the three parameters  $t_{1/2}$ ,  $\tau$  and  $\lambda$ .

### Study of pH-dependent photoisomerization properties of compound **103b**

To explore the photoisomerization properties of the arylazothiazoles series in different pH conditions, we selected the azo compound **103b** as the prototypical example of this azobenzene family, taking advantage of its remarkable water solubility. We studied the photoisomerization and relaxation kinetics of **103b**, 50  $\mu\text{M}$  at 25 °C, in several buffer solutions, with 0.5% DMSO, covering a pH range from 3.5 to 10.6.\* The pH buffer solutions used are the following:

- \* MOPS 0.5 M sol. acidified with HCOOH, pH 3.5,
- \* HEPES 1M buffer soln., pH 5.0,
- \*  $\text{NH}_4\text{HCO}_3$  50 mM buffer soln. acidified with HCOOH, pH 6.5,
- \* Mcilvaine (citrate-phosphate) buffer soln. (18.2 mM citric acid+ 163.7 mM  $\text{Na}_2\text{HPO}_4$ ), pH 7.0,
- \* Binding Buffer soln. (25 mM HEPES+ 100 mM NaCl+ 2.5 mM  $\text{MgCl}_2$ + NaOH 1M), pH 7.5,
- \*  $\text{NH}_4\text{HCO}_3$  50 mM buffer soln., pH 8.0,
- \* Glycine-Sodium Hydroxide buffer soln. (50 mM Glycine+ 45.5 mM NaOH), pH 10.6.

We collected UV-Vis absorption spectra of **103b** with Tecan's Spark 20M Multimode Microplate reader under dark and different light conditions for 3 min whereas we obtained relaxation plots of *cis*-**103b** at 25 °C after illumination with 405 nm light, the optimal illumination wavelengths to photoisomerize from *trans* to *cis* configuration.

### Nuclear magnetic resonance (NMR)

To quantitatively determine the photostationary states (PSSs) by nuclear magnetic resonance (NMR), we performed  $^1\text{H}$  NMR experiments with 700  $\mu\text{l}$  of a solution 5 mM of compound **62b** in deuterated DMSO and placed in a Norell® 3 mm NMR tube. The spectra of the same sample were recorded on a 400 MHz Variant Mercury (Agilent Technologies) in dark conditions and after irradiation with several wavelengths and new

\* See Chapter 4: A series of arylazothiazoles to control *mGlu<sub>1</sub>* function with light.



$^1\text{H}$  NMR acquisitions were taken each time. The  $^1\text{H}$  NMR acquisitions consisted in 32 scans with a total collecting time of 1 min and 54 s. All the obtained spectra were processed equally, integrating the most shielded proton of the pyrazole ring in the region 6.75- 6.60 ppm and the resulting area relations were converted to a molar percentage of *cis* isomer.\*

#### Determination of the most efficient illumination time

To know what illumination time was necessary to obtain the highest amount of *cis* isomer in such a concentrated sample, a first  $^1\text{H}$  NMR experiment was performed in dark conditions and, after that, the same sample was irradiated with 550 nm, the best wavelength to get a high percentage of *cis* isomer, at several time lapses and new  $^1\text{H}$  NMR acquisitions were taken at each lapse. The *CoolLED light system* was used as light source for this experiment. The sample was first irradiated 1 minute with the power of the LED light source set at 50% of intensity (118.1 mW) and after 3 minutes at 100% power (181.9 mW). The illumination system was built in such a way as to ensure a homogeneous light delivery from the LED light source to the NMR tube at the same distance each time we repeated the illumination (*Figure 86*).

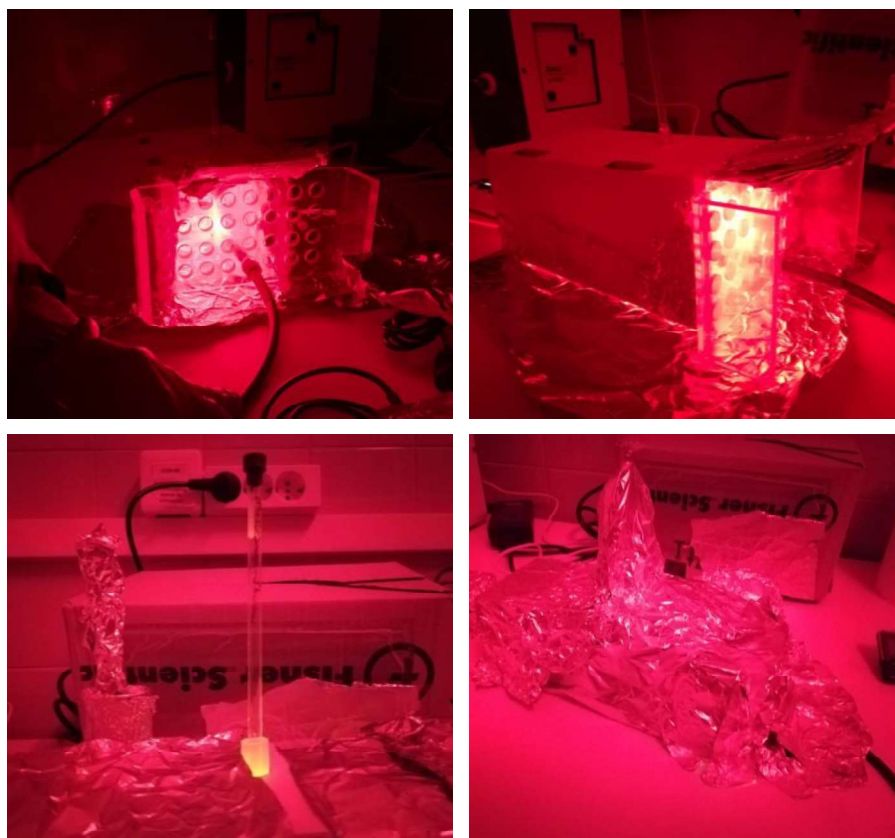


**Figure 86.** Customed system built to allow a direct illumination of the sample in NMR tube with an optical fiber.

#### Confirmation of the optimal wavelengths for bidirectional photoisomerization

To determine the optimal wavelengths for bidirectional photoisomerization of compound **62b** we screened several illumination wavelengths and quantified the amount of *trans* and *cis* isomers once reached each photostationary state. Thus, we illuminated 3 minutes the sample in deuterated DMSO- $d_6$  with different light wavelengths using the illumination system explained above and new  $^1\text{H}$  NMR acquisitions were taken each time. The results showed that the optimal wavelength of illumination to obtain the largest amount of

---

\* See Chapter 1: Photoisomerization properties of compounds **62a-c**.

*cis-62b* was 550 nm with 64.3% of *cis* isomer reached. Contextually, it was possible to determine the best wavelengths for the back isomerization *cis*→*trans*, that are 405 and 435 nm, which induced PSSs of 12.3% and 11.5% of *cis-62b*, respectively (Table 22).

$\lambda$ (nm)	Potency (mW)- 100%	Area <i>trans- 62b</i>	Area <i>cis- 62b</i>	% <i>cis- 62b</i>
[a]	-	1.00	0.00	0%
580	242.1	1.00	1.16	53.7%
550	181.9	1.00	1.80	64.3%
525	67.1	1.00	1.34	57.3%
500	63.9	1.00	0.76	43.2%
490	176.6	1.00	0.69	40.8%
470	152.2	1.00	0.34	25.4%
460	HIGH	1.00	0.22	18.0%
435	147.4	1.00	0.13	11.5%
405	252.5	1.00	0.14	12.3%
385	HIGH	1.00	0.36	26.5%
365	206.8	1.00	0.66	39.8%

[a] Measurement performed before illumination to characterize 100 % *trans* isomer in the dark

**Table 22.** Photoisomerization assay under  $^1\text{H-NMR}$  recording. Illumination at several wavelengths was achieved using the CoolLED pE-4000 Light Source. The studied sample (**62b**, 5 mM,  $\text{DMSO-}d_6$ ) was illuminated for 3 min in continuous mode and  $^1\text{H NMR}$  acquisitions were taken each time. The photostationary state (PSS) with the highest percentage of *cis-62b* is characterized by 35.7% of *trans* and 64.3% of *cis* isomers.

Potencies were measured using a Thorlabs PM100D power energy meter connected with a standard photodiode power sensor (S120VC) at a distance of 0.5 cm (Figure 87).

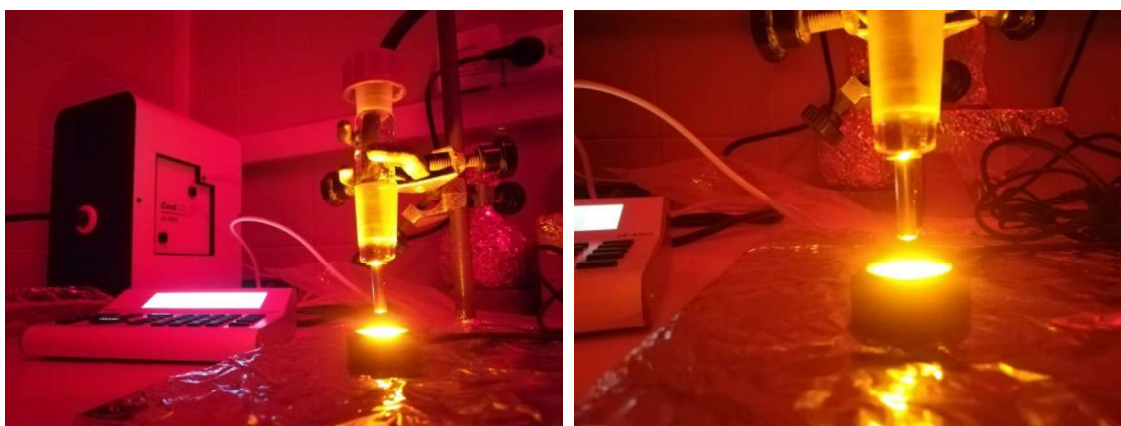


**Figure 87.** Illumination system built to ensure a homogeneous light delivery from the LED light source to the power sensor (S120VC, Thorlabs) at the same distance each time we repeated the measurement of wavelengths potency.

#### Measurement of thermal relaxation time

To measure the thermal relaxation rate of the *cis-62b* over the time, we illuminated the sample in  $\text{DMSO-}d_6$  with 550 nm and new  $^1\text{H NMR}$  acquisitions were taken over the time, while keeping the sample protected from ambient light (Table 23).

Time of acquisition	Area <i>trans</i> - <b>62b</b>	Area <i>cis</i> - <b>62b</b>	% <i>cis</i> - <b>62b</b>
<sub>[a]</sub>	1.00	0.00	0%
$t_0$			
5 min	1.00	1.70	63.0%
15 min	1.00	1.70	63.0%
30 min	1.00	1.66	62.5%
2 h	1.00	1.65	62.3%
6 h	1.00	1.50	60.0%
23 h	1.00	1.07	51.7%
96 h	1.00	0.53	34.6%
120 h	1.00	0.45	31.0%
144 h	1.00	0.40	28.6%
171 h	1.00	0.34	25.4%
192 h	1.00	0.31	23.7%
264 h	1.00	0.24	19.8%

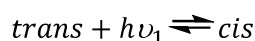
[a] Measurement performed before illumination to characterize 100 % *trans* isomer in the dark

**Table 23.** Several photostationary states of the **62b** 5 mM in DMSO- $d_6$  comparing  $^1\text{H}$  NMR recordings over the time. Identification of *trans*-**62b** in the dark and after illumination with 550 nm, starting from  $t_0$  considered the time zero of measurements until the eleventh day (264 h).

We plotted the % of *cis*-**62b** versus the time of relaxation and we fitted an exponential decay function, according to a first order equilibrium reaction formula (Equation 3).

$$Y = (Y_0 - \text{Plateau}) * e^{-K \cdot X} + \text{Plateau}$$

concerning bidirectional reaction *trans/cis* azo-compounds and back isomerization *cis*  $\rightarrow$  *trans*:



$$[\text{cis}] = [\text{cis}]_{\infty} + [\text{cis}]_{\infty} \cdot e^{-(k'_d + k_i) \cdot t}$$

**Equation 3.** One phase decay equation<sup>285</sup> and formula for bidirectional reaction of *trans/cis* to reach the photostationary equilibrium corresponding to a pseudo-first order reaction, as light intensity remains constant.<sup>46</sup>

X is the time, Y represents isomers level, starting at  $Y_0$  (when X (time) is zero) and decaying (with one phase) down to plateau and K is the rate constant, expressed in reciprocal of the X axis time units. The derivative of an exponential decay equals  $-K \cdot Y$ . So the initial rate equals  $-K \cdot Y_0$ . Plateau is the Y value at infinite times, expressed in the same units as Y.

In this way, we were able to calculate the half-life value ( $t_{1/2}$ ) of the *cis*-**62b** and the amount of the two isomers once reached the plateau.

**Photoisomerization analyzed by LC-PDA-MS**

The photoisomerization of compound **62b**, **74a** and **83b** was also determined by liquid chromatography coupled to a photodiode array and a mass spectrometer detectors (LC-PDA-MS). Through the analysis of LC-PDA-MS spectra we quantified the amount of *trans* and *cis* isomers in the dark and upon illumination once reached the photostationary state. The separated peaks were integrated using the PDA channel at the wavelength of the isosbestic point which was previously determined by UV-Vis spectroscopy for each pair of isomers.

Illuminations were performed with *CoolLED light system* in microcentrifuge tube containing 150  $\mu$ L of 1 mM DMSO solution of each compound for 3 min. Then, 10  $\mu$ l of the stock solution were taken each time and diluted with 90  $\mu$ l of MeCN in Amber Glass 9 mm Screw Neck Vial to obtain the final 100  $\mu$ M sample to be analyzed by LC-PDA-MS.

## Pharmacological and biochemical characterization

IGF, Institut de Génomique Fonctionnelle, CNRS, INSERM Montpellier  
Max Delbrück Center for Molecular Medicine (MDC), Berlin

### Cell cultures and types of transfection

#### **Materials and methods for transient transfections**

IGF-CNRS Montpellier

The HEK293 (ATCC, CRL-1573) cells were cultured in Dulbecco's modified Eagle's medium (*Gibco* DMEM; *Thermo Fisher Scientific*) supplemented with 10% fetal bovine serum (FBS, *Merck-Aldrich*) and maintained at 37°C in a humidified atmosphere with 5% CO<sub>2</sub>. Then the cells were transfected with human mGlu receptor by electroporation or lipofectamine transfection following the manufacturer's protocol (*Invitrogen* Lipofectamine 2000, *Thermo Fisher Scientific*) (see below). For those mGlu receptors that are not naturally linked to the phospholipase C (PLC) signaling pathway (mGlu<sub>4,6,8</sub>), a chimeric G<sub>q/i</sub>-protein (G<sub>q</sub> top) was transfected in order to couple receptor activation to the PLC pathway and obtain IP production.<sup>286</sup> We also co-transfected the Excitatory Amino Acid Transporter 3 (EAAC1) to remove the glutamate from the extracellular space, and therefore keep its levels low. Thus, we avoid excessive amounts of glutamate that can over-activate most mGlu receptors and may be toxic in certain cell cultures (such as neurons). The mGlu receptor constructs contained a Flag and SNAP tag to enable the measurement of cell surface receptor expression. Once transfected, the cells were seeded in black clear-bottom 96-well plates at a concentration of 1x10<sup>6</sup> cells/well. At least 2 h before the experiment, the medium was changed to preheated DMEM Glutamax (*Gibco*, *Thermo Fisher Scientific*), which does not include L-glutamine but contains Glutamax<sup>TM</sup> supplement. Glutamax<sup>TM</sup> supplement is a dipeptide, L-alanine-L-glutamine, which is more stable in aqueous solutions than L-glutamine and does not spontaneously degrade, releasing otherwise an excess of L-glutamate into the culture media that could interfere in the assays.

MDC Berlin

HEK293 cells were cultured in DMEM (*PAN Biotech*) supplemented with 10% FBS (*Biochrom AG*), 1% L-glutamine (*PAN Biotech*), 1% Penicillin-Streptomycin (*Gibco*, *Thermo Fisher Scientific*) at 37 °C in a 5% CO<sub>2</sub> incubator. Cells were seeded in 10 cm cell culture dishes prior to transfection. Transfections were performed using Effectene transfection Reagent (*Qiagen*) according to the manufacturer's instruction (see below) and biosensor mGlu<sub>1</sub> constructs. 24 hours after the transfection the cultured cells were suspended in fresh DMEM-Glutamax (*Gibco*, *Thermo Fisher Scientific*) and counted. At the density of ~50.000 cells/well the cells were transferred to the black 96-well plates (*Corning*). Finally, 24 hours after the transfer and before the FRET measurements, the cells were washed twice with HBSS buffer (*Gibco*, *Thermo Fisher Scientific*) and incubated in HBSS buffer for 30 minutes.

#### **Procedure for transfection by electroporation**

For IPOne and conformational biosensors assays, IGF-CNRS Montpellier

Electroporation is a physical transfection method that uses an electrical pulse to create temporary pores in cell membranes through which substances like nucleic acids can pass into cells. The electrical pulse at an optimized voltage and only lasting a few microseconds to a millisecond is discharged through the cell

suspension in a conductive solution. This disturbs the phospholipid bilayer of the membrane and results in the formation of temporary pores. The electric potential across the cell membrane simultaneously rises to allow charged molecules like DNA to be driven across the membrane through the pores. After that, the cells are returned to growing conditions and allowed to recover (*Figure 88*).

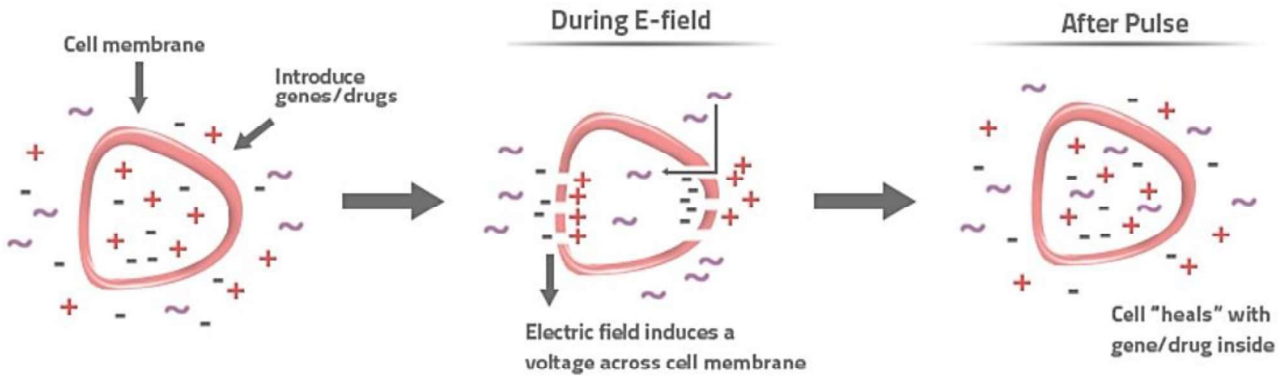


**Figure 88.** Electroporation schematic process. Figure from theory.labster.com.

First of all, the DNA mixes to transfect 20 million cells were prepared in different 1.5 ml microcentrifuge tubes as shown in the *Table 24* for each mGlu receptor tested. The plasmid solution concentration was generally 1 $\mu$ g/1 $\mu$ L (mGlu<sub>R</sub>, EAAC1 and G<sub>q</sub> top).

	mGlu <sub>1</sub>	mGlu <sub>5</sub>	mGlu <sub>4</sub>	mGlu <sub>6</sub>
<b>mGlu<sub>R</sub></b>	4 $\mu$ L (4 $\mu$ g)	1.2 $\mu$ L (1.2 $\mu$ g)	7 $\mu$ L (7 $\mu$ g)	12 $\mu$ L (12 $\mu$ g)
<b>EAAC1</b>	4 $\mu$ L (4 $\mu$ g)	4 $\mu$ L (4 $\mu$ g)	4 $\mu$ L (4 $\mu$ g)	4 $\mu$ L (4 $\mu$ g)
<b>G<sub>q</sub> top</b>	0 $\mu$ L	0 $\mu$ L	4 $\mu$ L (4 $\mu$ g)	4 $\mu$ L (4 $\mu$ g)
<b>H<sub>2</sub>O</b>	296 $\mu$ L	298.8 $\mu$ L	289 $\mu$ L	284 $\mu$ L
<b>EB5x</b>	80 $\mu$ L	80 $\mu$ L	80 $\mu$ L	80 $\mu$ L
<b>MgSO<sub>4</sub></b>	16 $\mu$ L	16 $\mu$ L	16 $\mu$ L	16 $\mu$ L

**Table 24.** Amounts of DNA solutions and buffers used in transfection of HEK293 cells per mGlu receptor subtype.

In parallel, black 96-well plates with transparent bottom (*Greiner Bio-one*) were filled with 50  $\mu$ L of poly-L-ornithine (PLO 1X, prepared from PLO 10x and PBS) (*Merck-Aldrich*) per well, and they were left in the incubator at 37 °C and 5% CO<sub>2</sub> for a minimum of 30 minutes.

Then, the cultured HEK293 cells in the dishes were observed, so as to notice their proper conditions and select those with 80% of confluence. Later, the medium of the dishes was removed, the cells were washed with 3-5 ml of PBS (*Merck-Aldrich*) and 3 ml of trypsin-EDTA (0.05%) (*Gibco, Thermo Fisher Scientific*) were added in each dish to detach the cells. Then, the dishes were left in the incubator at 37°C and 5% CO<sub>2</sub> for 5-10 minutes.

Afterwards, 7 ml of DMEM were added to each dish with trypsin and the cell suspensions were homogenized, joined and split in two *falcon* tubes. At this point, cell concentration was needed to be quantified. Thus, a sample of 10  $\mu\text{L}$  was diluted in 10  $\mu\text{L}$  of trypan blue dye, and the resulting mixture was placed into a chamber of a cell-counting slide compatible with an *EVE* Automated Cell Counter (*NanoEntek*). In parallel, the two *falcon* tubes with the cell suspension were centrifuged 5 minutes at 1000 rpm. After that, the supernatant was aspirated and, a suitable amount of electroporation buffer (EB1x) was added so as to obtain a cell suspension of 10 million cells per 100  $\mu\text{L}$  (the cell pellet is assumed to fill 1/3 of the volume).

200  $\mu\text{L}$  of the freshly prepared cell suspension were added to each microcentrifuge tube with the corresponding DNA mix; the obtained suspensions were placed in electroporation cuvettes and were electroporated with the program of 10 million cells of Gene Pulser Xcell™ Electroporation system (*Bio-Rad*). The delivered Time Constant (TC) was between 16 and 24 ms.

The living cells of each cuvette were placed in a *falcon* tube with 20 ml of DMEM (1 million cells per ml). The tubes containing the same transfected cells were joined and homogenized. Afterwards, the PLO solution from the 96-well plates was aspirated and 100  $\mu\text{L}$  of the corresponding cell suspension was added to every well of the corresponding plate. Finally, the plates were kept in the incubator at 37 °C and 5% CO<sub>2</sub> for approximately 24 hours. Between 6 and 2 hours before the experiment, the medium was removed and 100  $\mu\text{L}$  of serum-free DMEM Glutamax™ were added and the plates were kept in the incubator at 37 °C and 5% CO<sub>2</sub>.

### Procedure for lipofectamine transfection

For *IPOne* assay, *IGF-CNRS Montpellier*

Lipofection (or liposome transfection) is a technique used to inject genetic material into a cell by means of liposomes, which are vesicles that can easily merge with the cell membrane since they are both made of a phospholipid bilayer. Lipofection generally uses a positively charged (cationic) lipid (cationic liposomes or mixtures) to form an aggregate with the negatively charged (anionic) genetic material. The charged head group governs the interaction between the lipid and the phosphate backbone of the nucleic acid, and facilitates DNA condensation. The transfection complex is thought to enter the cell through endocytosis which is the process where a localized region of the cellular membrane uptakes the DNA/liposome complex by forming a membrane bound/intracellular vesicle. Once inside the cell, the complex must escape the endosomal pathway, diffuse through the cytoplasm, and enter the nucleus for gene expression (*Figure 89*).

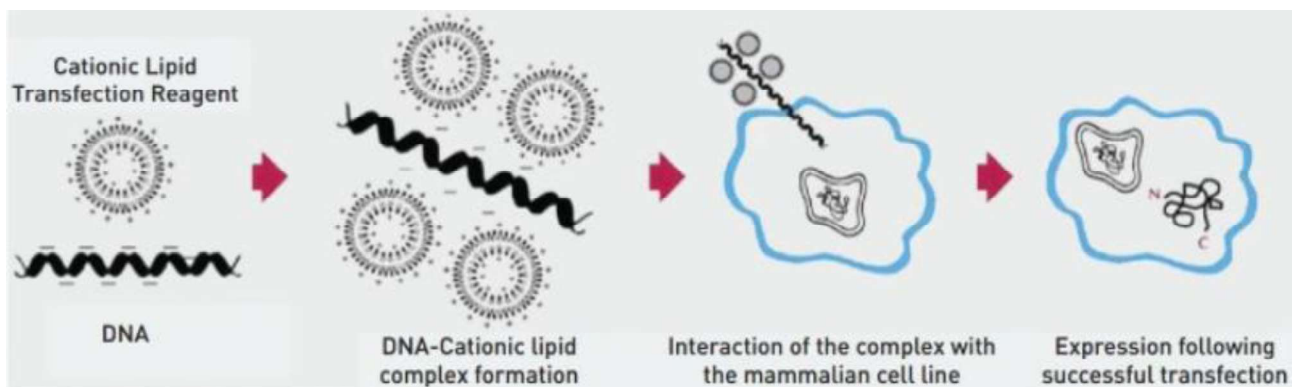


**Figure 89.** Mechanism of cationic lipid-mediated delivery. Figure from thermofisher.com

First of all, the DNA mixes in different microcentrifuge tubes were prepared as the following *Table 25* shows for each one of the mGlu receptors tested. For each well, 0.15 µg of DNA + 0.375 µl of Lipofectamine 2000 in 50 µl of Opti-MEM medium (*Gibco, Thermo Fisher Scientific*) was prepared (keeping the ratio DNA (µg)/Lipofectamine 2000 (µL) at 0.4). The plasmid solution concentration was generally 1µg/µL (mGlu<sub>R</sub>, EAAC1, G<sub>q</sub> top and empty vector pRK<sub>6</sub>).

	mGlu <sub>1</sub>	mGlu <sub>5</sub>	mGlu <sub>4</sub>	mGlu <sub>6</sub>
<b>mGlu<sub>R</sub></b>	0.040 µg	0.012 µg	0.070 µg	0.100 µg
<b>EAAC1</b>	0.040 µg	0.040 µg	0.030 µg	0.025 µg
<b>G<sub>q</sub> top</b>	0 µg	0 µg	0.030 µg	0.025 µg
<b>pRK<sub>6</sub></b>	0.070 µg	0.098 µg	0.020 µg	0 µg

**Table 25.** Amounts of DNA mixes used in transfection of HEK293 cells per mGlu receptor subtype.

Two different solutions in Opti-MEM medium (*Gibco, Thermo Fisher Scientific*) were prepared separately to be mixed later. First 0.375 µl of Lipofectamine/well were diluted in 25 µl of Opti-MEM medium/well and the mixture was left incubating 5 minutes at rt. In the meantime, each previous DNA mix was diluted in 25 µl of Opti-MEM medium/well. Both DNA mix and the lipofectamine solutions were combined and the resulting solution were incubated at least 20 minutes at rt to form the DNA-liposome complexes. This provides a total volume of 50 µl/well of the DNA complexes. In parallel, the cultured HEK293 cells were prepared and resuspended in DMEM medium to obtain a cell suspension of 1 million cells per ml. The cell resuspension procedure is the same already described above for electroporation transfection.

100 µL of the freshly prepared cell suspension were added to every well previously treated with PLO 1X solution in order to have 100000 cells/well (10 million cells/plate). Then, 50 µL of DNA/Lipofectamine complexes were added onto the cell suspension in every well of the corresponding 96-well plate (*Greiner Bio-one*). Finally, the plates were kept in the incubator at 37 °C and 5% CO<sub>2</sub> for approximately 24 hours. Between 6 and 2 hours before the experiment, the medium was removed and 100 µL of serum-free DMEM Glutamax<sup>™</sup> were added and the plates were kept in the incubator at 37 °C and 5% CO<sub>2</sub>.

#### **Procedure for induction of rat mGlu<sub>4</sub> in HEK293 cells**

*For cAMP assay, IGF-CNRS Montpellier*

24 hours before the experiment, black 96-well plates with transparent bottom (*Greiner Bio-one*) were filled with 50 µL of poly-L-ornithine (PLO 1X, prepared from PLO 10x and PBS) (*Merck-Aldrich*) per well, and they were left in the incubator at 37 °C and 5% CO<sub>2</sub> for a minimum of 30 minutes. Then, the cultured rat (r)mGlu<sub>4</sub>-HEK293 cells in the culture flasks were observed to check their proper conditions and select those with a 80% of confluence. The medium of the flask was removed, the cells were washed with 3-5 ml of PBS (*Merck-Aldrich*), and 3 ml of trypsin-EDTA (0.05%) (*Gibco, Thermo Fisher Scientific*) were added into the flask. Then, the flask was left incubating at 37°C and 5% CO<sub>2</sub> for 5 minutes to detach the cells. After that, 7 ml of DMEM medium were added and the cell suspension was collected in one tube. The cells were counted with the *EVE* Automated Cell Counter as explained above. The tube was centrifuged 5 minutes to



obtain a pellet, the medium was removed and the cell pellet was suspended in DMEM so as to obtain a cell suspension of 1 million cells/ml. 1 µg/ml of doxycycline (*Merck-Aldrich*) was finally added to induce the expression of mGlu<sub>4</sub>. The PLO from the plates was removed and 100 µL (10000 cells) of the resulting suspension were placed in each well and left approximately 24 hours at 37°C and 5% CO<sub>2</sub>.

#### **Procedure for labeling of SNAP-tag with VFT Fret-based biosensors on adherent mGlu<sub>1</sub> cells**

*For conformational biosensors assay, IGF-CNRS Montpellier*

24 hours after the transient transfection of HEK293 cells with F-ST-mGlu<sub>1</sub> (construct including a Flag and SNAP tag) by electroporation, the DMEM medium from the black non-transparent 96-well plates (*Greiner Bio-one*) was removed and the cells were washed with 100 µL of serum-free DMEM Glutamax (*Gibco, Thermo Fisher Scientific*). Then, 50 µL of 100 nM SNAP-Lumi4-Tb and 60 nM SNAP-Fluorescein in serum-free DMEM Glutamax™ were added to each well. The plates were kept incubating at 37 °C and 5% CO<sub>2</sub> for at least 1 h before performing the experiment.

#### **Procedure for effectene transfection with E and A biosensor mGlu<sub>1</sub> constructs**

*For conformational biosensors assay, MDC Berlin*

Effectene Transfection Reagent (*Qiagen*) is a non-liposomal lipid formulation that is used in conjunction with a special DNA-condensing Enhancer and optimized buffer to achieve high transfection efficiencies. The Enhancer first condenses the DNA molecules and Effectene Reagent subsequently coats them with cationic lipids providing a particularly efficient way of transferring DNA into eukaryotic cells (*Figure 90*).

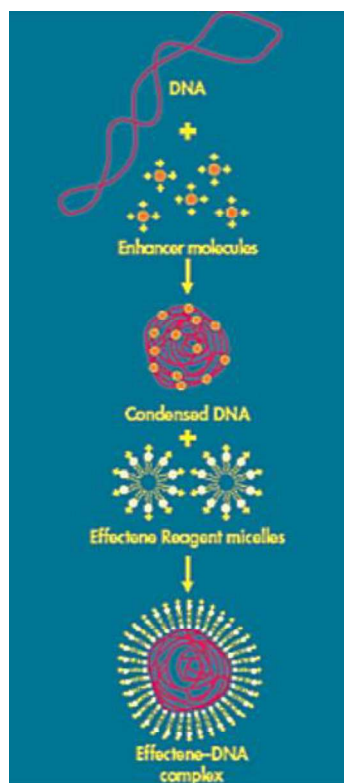


**Figure 90.** Principle of transfection with Effectene Transfection Reagent + Enhancer. Figure from “Lab 5A and 5B Overview Investigating protein sorting signals using cloning, transfection, GFP-fusion proteins, and vital stains for cellular compartments”.

First of all, the DNA mixes were prepared in different microcentrifuge tubes as shown in the *Table 26* for each mGlu<sub>1</sub> construct. All the components were added in the order they appear. The volumes used in each mix were optimized for an amount of 5 million precultured cells in 10 cm dish at 37 °C and 5% CO<sub>2</sub> for at least 6 hours. The plasmid solutions concentration was generally 1µg/µL.

10 cm dish	mGlu <sub>1</sub> receptor		note
<b>EC buffer</b>	600 µL		
<b>DNA construct</b>	4 µL (4 µg)	<i>E-</i> sensors: 2 µg D35 + 2 µg D55; <i>A-</i> sensors: 4 µg	
<b>Enhancer</b>	32 µL		<i>Incubation for 4 min at RT</i>
<b>Effectene</b>	48 µL		<i>Incubation for 10 min at RT</i>
<b>Medium to add to the complex</b>	700 µL		

**Table 26.** Amounts of DNA mixes used in transfection of HEK293 cells for mGlu<sub>1</sub> receptor.

The medium of the dishes was removed, 9 ml of fresh DMEM were added and the content of the microcentrifuge tubes was dropped entirely in each dish. Then, the dishes were left in the incubator at 37°C and 5% CO<sub>2</sub> for 24 hours.

Afterwards, the medium of the dishes was removed, the cells were washed with 3-5 ml of PBS (*Merck-Aldrich*) and 1.5 ml of trypsin- EDTA (0.05%) (*Gibco, Thermo Fisher Scientific*) were added in each dish to detach the cells. Then, the dishes were left at room temperature for less than a minute after which the trypsin was rapidly removed. At this point 4-5 ml of fresh DMEM was added and a sample of 10 µL was diluted in 10 µL of trypan blue dye to count the cell concentration. The resulting mixture was placed into a chamber of a cell-counting slide compatible with Countess II FL Automated Cell Counter (*Life Technologies*).

A suitable amount of DMEM (generally 11-12 ml) was added to the cells suspension so as to obtain a final cell suspension of ~50.000 cell/well (~5 million cells per plate). Finally, 100 µL of the resulting suspension were placed in each well and the black 96-well plates (*Corning*) were left incubating 24 hours at 37°C and 5% CO<sub>2</sub>.

## Pharmacological and biochemical assays

In the present PhD thesis, the assays used to pharmacologically characterize the compounds both in dark and upon illumination can be divided into two categories considering their different properties:

- *Endpoint functional assays*, which are based on the measurement of an accumulated biological substance (second messengers or proteins);
- *Conformational biosensors assays*, which are kinetic and based on the measurement of a differential FRET (Förster's Resonance Energy Transfer) between two fluorescent protein domains fused into two different regions of the receptor. Thus, changes on the detection of FRET between the fluorescent domains are associated to conformational changes of the GPCR that are generally linked to its activation or inactivation.

## **Endpoint functional assays**

### *IGF-CNRS Montpellier*

#### *Homogeneous Time-Resolved FRET (HTRF) technology*

The IP and cAMP accumulation assays that we used are based on Time-Resolved FRET (TR-FRET), a detection technology that combines Time-Resolved Fluorescence (TRF) with Förster's Resonance Energy Transfer, a transfer of energy between two fluorophores. Generally, lanthanides (Europium and Terbium) are used as donors and particularly by exciting at 320-340 nm a Terbium donor, which emits fluorescence at both 490 or 620 nm (between other wavelengths, *Figure 91A*). The energy of excitation can be partially transferred to a FRET acceptor in close proximity, which emits at higher wavelengths (520 or 665 nm).

As Terbium or Europium ions are only poorly fluorescent, they need to be embedded in a light-collecting "cage" to emit light more efficiently. Thereby, cryptate is used for this purpose favoring both energy collection and transfer. The cryptate-lanthanide complex is extremely stable under a wide range of chemical conditions and not subject to photo-bleaching like common fluorophores.

Acceptors are conventional fluorophores that emit in the green and red range (520 nm for fluorescein or 665 nm for d2). Terbium can be combined with both types of fluorophores (*Figure 91A*), but Europium only with red dyes (*Figure 92A*). Additionally, this fluorescence is characteristically long-lived and applying a time delay in the microsecond range (50-150  $\mu$ s) between the system excitation and fluorescence measurement allows the signal to be cleared of all non-specific short-lived emissions (*Figure 91B*).

Several TR-FRET assays are available and although all assays are based on a common technology some differences exist. These are mainly related to different donor and acceptor types, their combinations and different timings for detection start and measurement window. HTRF technology has been used in this thesis, in particular, *HTRF IP-One* and *HTRF cAMP* assay.

#### *HTRF IP-One basis*

The *HTRF IPOne Gi* assay is a competitive immunoassay to measure inositol phosphate (IP) accumulation in cells based in TR-FRET. We used an inositol phosphate (IP) antibody labeled with specific Terbium cryptate (FRET donor) that emits at 620 nm, and IP labeled with the FRET acceptor of second generation d2, based on a pigment purified from red algae, which emits at 665 nm (*Figure 91C*).

The procedure of the assay begins with an incubation of the compounds to be tested dissolved in IP-One HTRF stimulation buffer (*PerkinElmer-Cisbio*) in cells previously cultured and overexpressing the receptor we want to stimulate. This buffer contains lithium chloride that inhibits the degradation of intracellular inositol phosphate (IP) to *myo*-inositol, leading to an IP accumulation in the cytosol (*Figure 91D,E*).

Subsequent addition of d2-labelled IP and an anti IP Tb-labeled antibody in a lysis buffer produces rupture of the cell membranes (due to the lysis buffer) that liberates the cytosolic IP produced by the cell. Then, a competition between the introduced IP-d2 and the cell-produced IP is produced for the recognition of the antibody. This leads to FRET emission or a single donor emission respectively (*Figure 91C*). Therefore, the fluorescence emissions could be read to obtain the results as a ratio of fluorescence detection at 665 nm

and 620 nm (*i.e.* HTRF ratio). Afterwards, the HTRF ratios are transformed to the IP concentration with a standard curve.\*

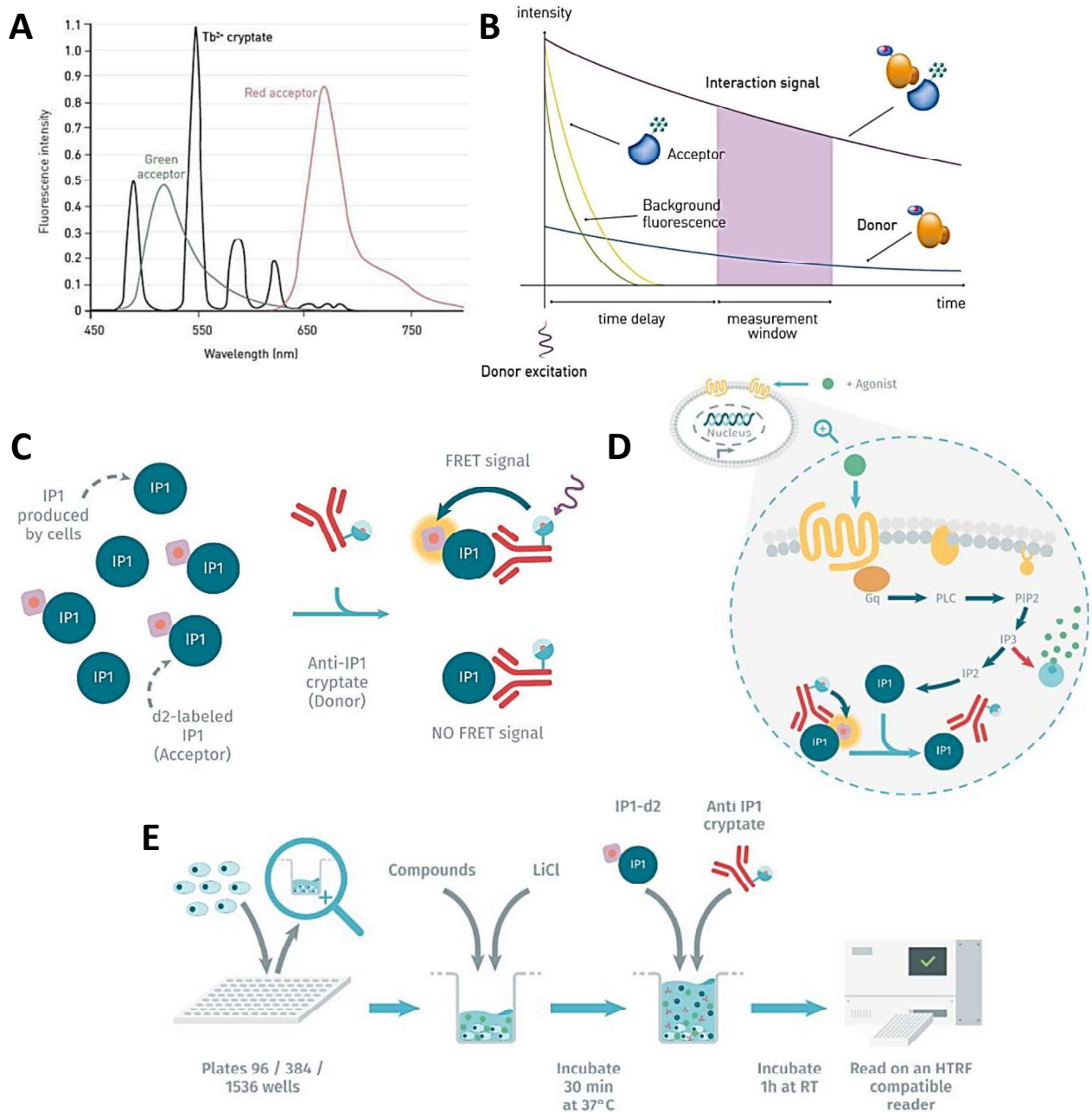


**Figure 91.** Basis of *IP-One* HTRF assay. (A) Emission spectra of the Terbium cryptate and its red and green acceptors. (B) HTRF emission is time-delayed and avoids interferences with conventional fluorescence at the measurement point. (C) Terbium-cryptate-labelled antibodies and d2-labelled IP are used, which produce FRET upon recognition. Cell-production of IP induces a competition with the introduced d2-labelled IP for the recognition of the antibody, leading a single donor emission (NO FRET signal) or FRET emission. (D) The accumulation of inositol monophosphate, after phospholipase C activation and used as a downstream readout of Gq activation signaling pathway. (E) Diagram of the procedure of *IP-One* assay.

\* See *TR-FRET Inositol phosphate one (IP1) accumulation assay: General materials and methods*

HTRF cAMP basis

The *HTRF cAMP Gi* assay is a competitive immunoassay to measure cAMP accumulation in cells. The principle is based on HTRF technology that was explained before. Particularly, native cAMP produced by cells compete with cryptate-labeled cAMP (Europium donor, *Figure 92A*) for binding to monoclonal anti-cAMP-d2 (red acceptor). The specific signal is inversely proportional to the concentration of cAMP in the standard or sample (*Figure 92B*).

Since  $G_{\alpha i/o}$  primarily inhibits the cAMP-dependent pathway by inhibiting adenylyl cyclase (AC) activity, decreasing the production of cyclic AMP from ATP, a pre-activation step to induce a high cAMP level at the beginning of the assay is needed. For this reason, Forskolin is added to activate AC and increase the intracellular concentration of cAMP (*Figure 92C*). Then, the activation of a  $G_{\alpha i/o}$ -coupled GPCR induces a decrease of the cytosolic cAMP, which is measured in this assay.

However, the normal enzymatic degradation of cAMP due to phosphodiesterase enzymes can also induce a decrease of cAMP levels. To avoid that interference, IBMX is added to the cAMP stimulation buffer, which is Glutamax DMEM. IBMX is a commonly used phosphodiesterase pan-inhibitor that prevents cAMP degradation efficiently at 500  $\mu\text{M}$  concentration.

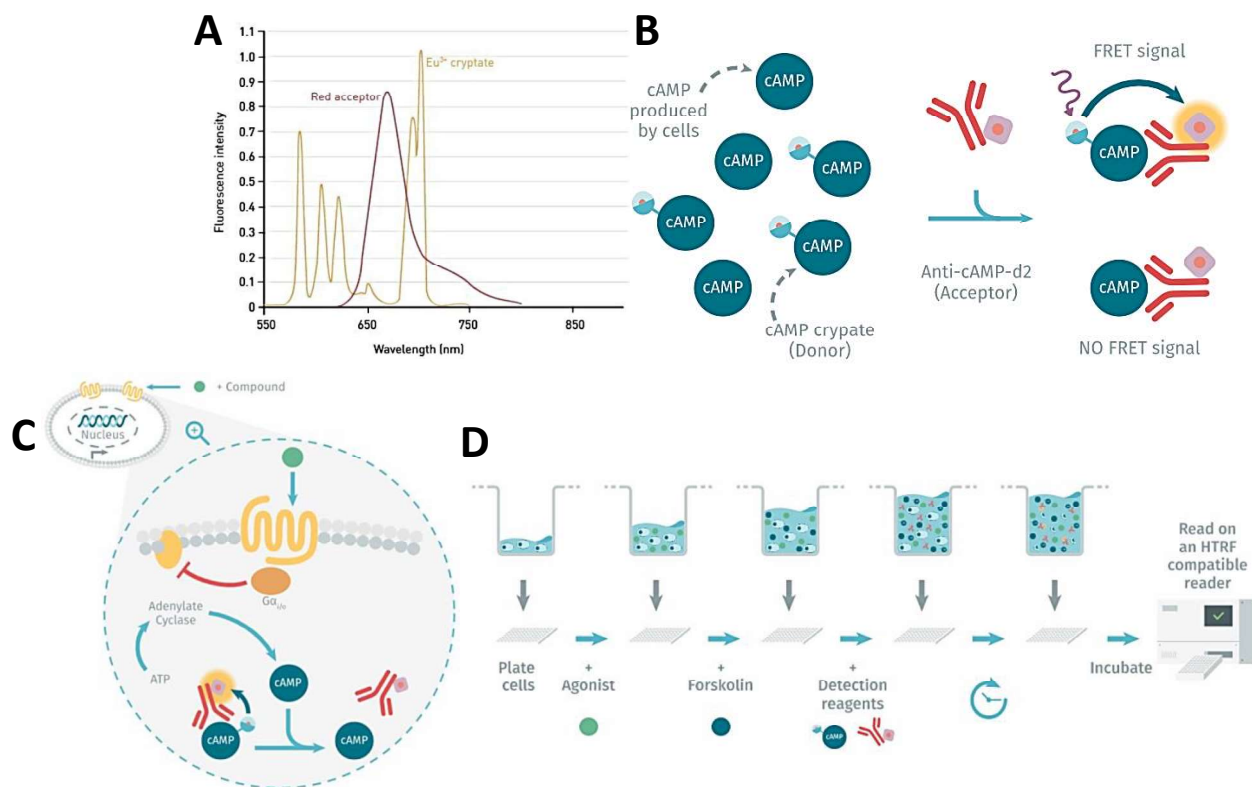


**Figure 92.** Basis of *cAMP* HTRF assay. (A) Emission spectra of the Europium cryptate and its red acceptor. (B) Europium-cryptate-labelled cAMP and cAMP-d2 antibodies are used, which produce FRET upon recognition. Cell-production of cAMP induces a competition with the introduced Europium-cryptate-labelled cAMP for the recognition of the antibody, leading a single donor emission (NO FRET signal) or FRET emission. (C) The *cAMP* HTRF assay kit detects changes of cAMP accumulation in response to  $G_i$  coupled GPCR activation or inhibition. (D) Diagram of the procedure of *cAMP* assay.

The assay procedure begins with the preparation of the compounds to be tested dissolved in cAMP stimulation buffer followed by their addition to the cells previously cultured overexpressing the receptor of interests. The cells are incubated 15 minutes with the compounds. After that, Forskolin 0.75  $\mu\text{M}$  is added in

the pre-incubated cells and the compounds are left incubating for other 15 minutes (*Figure 92D*). Subsequent addition of the labeled cAMP and d2-antibody in a lysis buffer produces rupture of the cell membranes and a competition between the introduced labelled cAMP and the cell-produced cAMP for the recognition of the antibody. This leads to FRET emission or a single donor emission respectively.

Therefore, the fluorescence emissions could be read to obtain the results as a ratio of fluorescence detection at 665 and 620 nm. As for other HTRF assays, the calculation of the fluorescence ratio (665/620 nm) minimizes possible photophysical interferences. Afterwards, the HTRF ratios are transformed to the cAMP concentration produced by the cell with a standard cAMP curve.\*

### *TR-FRET Inositol phosphate one (IP1) accumulation assay*

#### *General materials and methods*

The *IP-One HTRF Gq* kit assay (*PerkinElmer-Cisbio*) was used for the direct quantitative measurement of *myo*-inositol 1-phosphate in HEK293 cells transiently transfected with the human mGlu receptors according to the transfection methodology described above. Cells were stimulated to induce IP accumulation with various concentrations of orthosteric and/or allosteric compounds, depending on the type of the assay, in HTRF stimulation buffer (*PerkinElmer-Cisbio*) for 30 min, at 37°C and 5% CO<sub>2</sub> in both dark and under illumination conditions.

For the experiments with illumination to induce photoswitching, the *Teleopto light system* was used. Thus, black transparent-bottom 96-well plates (*Greiner Bio-one*) containing the cultured cells were placed over a single or dual wavelength LED Array (model LEDA-X and LEDA2-By respectively) connected to a LED Array Driver (model LAD-1). The light was delivered from the bottom to the solutions since the LED Array perfectly fits for 96 well-plates and each LED element comes just under each well (*Figure 93*).

Light pulses of 50/50 ms (pulse width/interval) was chosen over continuous illumination to reduce cell overheating (especially for wavelengths with higher energy such as 380 nm) and avoid a loss of robustness of the assay. Teleopto system was set at different voltages depending on the needed wavelengths to always have a light delivery of 0.12 mW/mm<sup>2</sup>. This value comes from a study carried out by Fanny Malhaire, *IGF-CNRS, Montpellier*; as a threshold power value to obtain the maximum photoswitching effect for Alloswitch-1, with the minimum damage to the cells due to overheating.

To avoid effects derived from the fast relaxation of photoisomerizable compounds in aqueous solution after the 30-min stimulation and possible interference with the fluorescence reading, the solutions of every well were removed and fresh stimulation buffer was added prior to the lysis step of the assay protocol.

After adding the fresh buffer, a solution of IP-d2 in lysis buffer and a solution of Tb-labelled anti-IP antibody (see below) in IPOne lysis buffer (*PerkinElmer-Cisbio*) were added to every well of the plate. The plate was incubated a minimum 1 hour at room temperature and TR-FRET fluorescence readings were obtained with PHERAstar FS multimode microplate reader (*BMG-Labtech*) with a delay time of 150 µs between donor excitation and fluorescence readings, as HTRF ratio (665/620).

---

\* See *TR-FRET Cyclic adenosine monophosphate (cAMP) accumulation assay: General materials and methods*

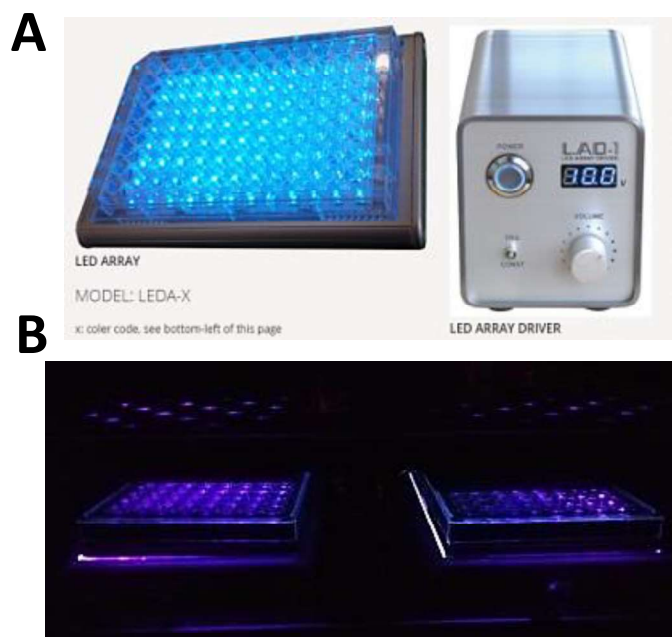


**Figure 93.** Teleopto light system used to perform the pharmacological assays under illumination conditions. (A) Main components of the system: the single wavelength LED Array (model LEDA-X) and the LED Array Driver (model LAD-1); (B) two black transparent-bottom 96-well plates containing the cultured cells placed in parallel over two LED arrays for 30-min of 380-nm illumination.

Afterwards, the HTRF ratios were transformed to the IP concentration produced by the cell with a standard IP curve (Figure 94). Then, we normalized the top and the bottom values between 0 and 100% of receptor activation with respect to a control compound pharmacologically well-characterized. The results were plotted using GraphPad Prism 8.1.1 (GraphPad Software).

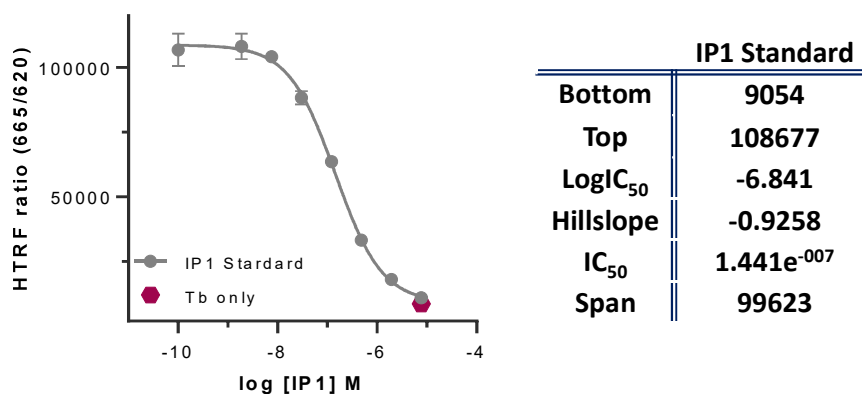


**Figure 94.** HTRF IP1 Standard curve to determine the linear dynamic range of the assay and verify that assay generated the expected IC<sub>50</sub> (~100 nM).

*Detailed procedure for single-dose screening and selectivity assay in dark and light conditions*

The single-dose screening and the selectivity assay procedures are both single dose experiments of a compound tested on four out of the eight subtypes of mGlu receptors, as PAM and NAM. To do that, we used four black plates with transparent bottom with HEK293 cells overexpressing a single mGlu subtype every three columns (two plates for dark conditions and the other two as equivalents for light conditions, Figure 95).

x2	1	2	3	4	5	6	7	8	9	10	11	12
A	HEK293 cells transfected with mGlu <sub>1</sub> (assay conditions for PAMs)			HEK293 cells transfected with mGlu <sub>5</sub> (assay conditions for NAMs)			HEK293 cells transfected with mGlu <sub>5</sub> (assay conditions for PAMs)			HEK293 cells transfected with mGlu <sub>5</sub> (for NAM and PAM controls)		
B												
C												
D												
E												
F												
G	HEK293 cells transfected with mGlu <sub>1</sub>											
H	(for PAM controls)											

x2	1	2	3	4	5	6	7	8	9	10	11	12
A	HEK293 cells transfected with mGlu <sub>4</sub> (assay conditions for PAMs)			HEK293 cells transfected with mGlu <sub>6</sub> (assay conditions for PAMs)			HEK293 cells transfected with mGlu <sub>1</sub> (assay conditions for NAMs)			HEK293 cells transfected with mGlu <sub>4</sub> (for PAM controls)		
B												
C												
D												
E												
F										HEK293 cells transfected with mGlu <sub>6</sub> (for PAM controls)		
G	HEK293 cells transfected with mGlu <sub>1</sub>											
H	(for NAM controls)											

**Figure 95.** Disposition of the different HEK293 cells transfected with different mGlu subtypes on four clear-bottom 96-well plates (*Greiner Bio-one*). One plate of each pair was placed over a LED Array and each well was illuminated from the bottom to test compound's photoswitching behavior with a light pulsed for 50/50 ms (pulse width/interval).

All the solutions of the compounds to be tested were prepared as depicted in the *Table 27* in *IP-One* stimulation buffer (*PerkinElmer-Cisbio*).

	Group I		Group III	
	mGlu <sub>1</sub>	mGlu <sub>5</sub>	mGlu <sub>4</sub>	mGlu <sub>6</sub>
<b>Compound to test as PAMs</b>	33 μM	33 μM	33 μM	33 μM
<b>Orthosteric agonist (Low dose ≈ EC<sub>20</sub>)</b>	40 nM (Quis)	3 nM (Quis)	5 nM (L-AP <sub>4</sub> )	100 nM (L-AP <sub>4</sub> )
<b>Orthosteric agonist (Saturating dose)</b>	200 μM (Quis)	30 μM (Quis)	50 μM (L-AP <sub>4</sub> )	1 mM (L-AP <sub>4</sub> )
<b>Compound to test as NAMs</b>	10 μM	33 μM		
<b>Orthosteric agonist (High dose ≈ EC<sub>80</sub>)</b>	100 μM (Glu)	100 nM (Quis)		
<b>Orthosteric agonist (Saturating dose)</b>	1 mM (Glu)	30 μM (Quis)		

**Table 27.** Concentrations of compounds used to test and orthosteric agonists for single-dose screenings and selectivity assays. Low doses were used to evaluate PAM effects, high doses to evaluate NAM effects and saturating doses as an agonist control corresponding to a full activation of mGlu receptors.



Then, the medium from clear-bottom 96-well cultured plates was removed and 70  $\mu\text{L}$  of the aforementioned solutions were distributed for each compound triply in the same plate for dark conditions. The same compound solutions were tested with three other replicates in the second plate, used to test them in parallel under light conditions.

After that, the plates were incubated at 37 °C and 5%  $\text{CO}_2$  for 30 minutes both in dark and under light conditions using the method described above. After the stimulation, the solutions of every well were removed and 70  $\mu\text{L}$  of stimulation buffer was added, then 15  $\mu\text{L}$  of the solution of IP-d2 and 15  $\mu\text{L}$  of the solution of anti-IP-Tb in HTRF lysis buffer (*PerkinElmer-Cisbio*) were added to the wells.

The plates were covered with an aluminum foil to be protected from light, and they were finally read with PHERAstar FS multimode microplate reader (*BMG-Labtech*) after 1 hour of incubation at room temperature.

#### *Detailed procedure for dose-response curves in dark and light conditions*

First of all, eight intermediated solutions of each compound were prepared to generate eight-point dose-response curves with *IP-One* stimulation buffer (*PerkinElmer-Cisbio*). The same procedure was done for the corresponding orthosteric agonists and the reference compound used as a second control. To evaluate activity of the compounds as mGlu receptor PAMs or NAMs, a solution of the corresponding orthosteric agonist with precise concentration was added to each compound and to the corresponding reference compound (*Table 27*).

Due to the poor solubility of some compounds in the *IP-One* stimulation buffer and consequent adhesion of them to the bottom of the plastic tube (*Figure 96A*), the protocol underwent some modifications until one final procedure was obtained which was thus validated.\* The latter is characterized by the following steps in the preparation of the eight concentrations of compounds to be tested:

1. Each compound solution was prepared directly in small quantities of DMSO (4-9  $\mu\text{L}$ , *Figure 96B*)
2. The pipette tips were checked after every dilution, so as not to retain and release undesired amounts of compounds into the most diluted dissolutions or take off amounts of compounds from the most concentrated solutions
3. The orthosteric agonist dilutions were prepared in *IP-One* stimulation buffer with 1% of DMSO
4. The DMSO “microdilutions” of the compounds were diluted 1:80 (to preincubate NAMs) or 1:100 with the orthosteric agonist solution in a way that the final concentration of DMSO was 1%
5. The aforementioned orthosteric agonist solution was added without mixing the resulting solution. They were mixed just before adding them to each well of the plate where the cells were placed.

Then, the medium from clear-bottom 96-well cultured plates was removed and 70  $\mu\text{L}$  of these solutions were added. Every compound solution was tested with two replicates in the same plate in dark conditions. The same compound solutions were tested with two other replicates in the second plate, used to test them in parallel under light conditions.

---

\* See Chapter 3: poor solubility of azologs **82a-b**, **83a-b**, **85** and **74b** and protocol optimization.

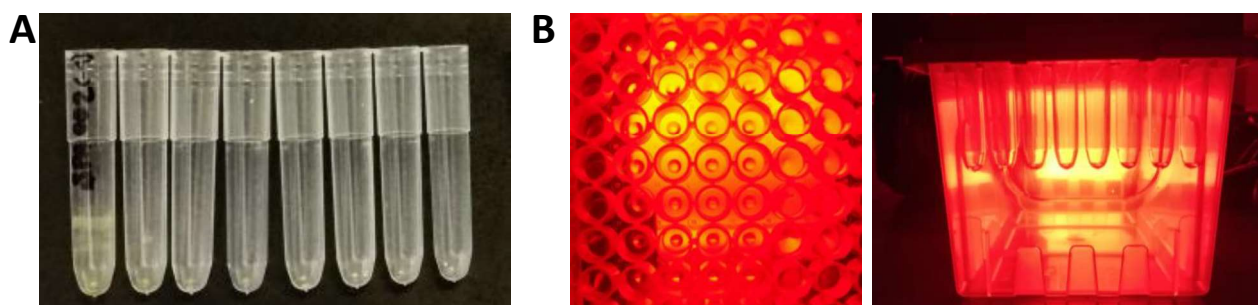


**Figure 96.** (A) Yellowish compound's residues retained on the bottom of the plastic tubes used to prepare the eight concentrations predilutions in *IP-One* stimulation buffer. (B) The DMSO eight concentrations microdilutions of the compounds to test before the addition of the orthosteric agonist solution.

After that, the plates were kept incubating at 37 °C and 5% CO<sub>2</sub> for 30 minutes both in dark and under light conditions, following the method described above. After the stimulation, we applied the lysis protocol as explained above and we waited 1 hour at room temperature before reading the plates with PHERAstar FS multimode microplate reader (*BMG-Labtech*). Additionally a standard dose response curve was run to determine the linear dynamic range of the assay [IP1 production/nM], important to verify that the assay generated accurate values of IC<sub>50</sub> (*Figure 94*).

#### *TR-FRET Cyclic adenosine monophosphate (cAMP) accumulation assay*

##### *General materials and methods*

##### *General materials and methods*

The *cAMP HTRF Gi* kit assay (*PerkinElmer-Cisbio*) was used for the direct quantitative measurement of cyclic adenosine monophosphate (cAMP) in HEK293 cells stably expressing the rmGlu<sub>4</sub> according to the expression induction protocol described above. Cells were stimulated to induce cAMP accumulation with various concentrations of orthosteric and/or allosteric compounds in HTRF stimulation buffer (serum-free DMEM Glutamax<sup>™</sup> supplemented with IBMX 500 μM)\* for 30 min at 37°C and 5% CO<sub>2</sub> in both dark and light conditions.

For these experiments, we followed a very similar method to that used with *IP-One HTRF Gq* kit assay (*PerkinElmer-Cisbio*), previously described. Indeed, the only notable difference in the protocol was the addition of Forskolin 0.75 μM in the cells for the last 15 minutes of incubation in dark and upon illumination.

Following the lysis protocol, a solution of anti-cAMP-d2 in lysis buffer and a solution of cAMP-Eu (see below) in HTRF lysis buffer (*PerkinElmer-Cisbio*) were added to every well of the plate.

The plate was incubated a minimum 1 hour at room temperature and TR-FRET fluorescence readings were obtained with PHERAstar FS multimode microplate reader (*BMG-Labtech*) with a delay time of 150 μs between donor excitation and fluorescence readings, as HTRF ratio (665/620).

Afterwards, the HTRF ratios were transformed to the cAMP concentration produced by the cell with a standard cAMP curve to determine the linear dynamic range of the assay [cAMP production/nM],

\* See *Homogeneous Time-Resolved FRET (HTRF) technology: HTRF cAMP basis*

important to verify that the assay generated accurate values of  $IC_{50}$  (Figure 97). Then, we normalized the top and the bottom values between 0 and 100% of receptor activation with respect to a control compound pharmacologically well-characterized. The results were plotted using GraphPad Prism 8.1.1 (GraphPad Software).

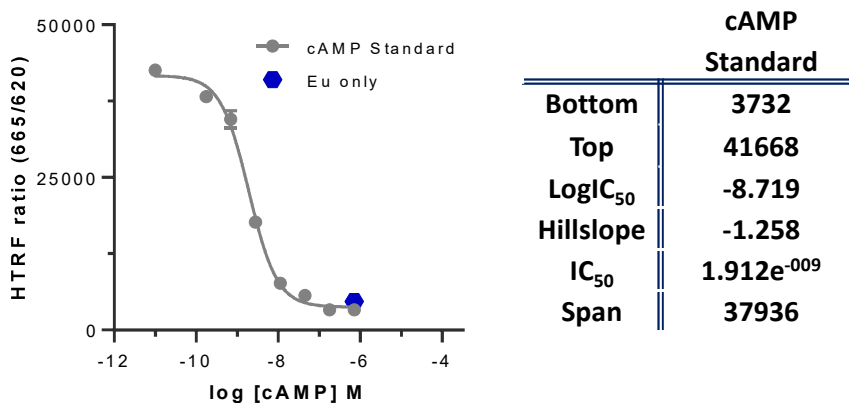


**Figure 97.** HTRF cAMP Standard curve to determine the linear dynamic range of the assay and verify that assay generated the expected  $IC_{50}$  (~3 nM).

#### Detailed procedure for dose-response curves in dark and light conditions

After 24 hours of seeding the cells and inducing mGlu<sub>4</sub> expression (see above the procedure for induction of rat mGlu<sub>4</sub>), the media was removed from plate and was replaced with 100  $\mu$ L of Glutamax medium, keeping them to incubate at 37°C for at least 2 hours before the experiment. In the meantime, eight intermediated solutions of each compound were prepared to generate eight-points dose response curves following the improved protocol extensively described in the *IP-One* section. Orthosteric agonist dilutions were prepared in cAMP stimulation buffer (DMEM Glutamax<sup>TM</sup> supplemented with IBMX 500  $\mu$ M) with 1% of DMSO. The rest of compounds were prepared directly in a small quantities of DMSO. Subsequently, these DMSO solutions were diluted 1:80 with the orthosteric agonist in the aforementioned cAMP stimulation buffer.

Once all the solutions were prepared, the medium from the plates was removed and the compounds were distributed in the plates (40  $\mu$ L per well) in triplo. Then, the plates were kept in the incubator at 37 °C and 5% CO<sub>2</sub> for 15 minutes both in dark and light conditions using the method described in the *IP-One* section. After that, 10  $\mu$ L of Forskolin 0.75  $\mu$ M were added in the preincubated cells (to reach a total 50  $\mu$ L per well) and the plates were kept in the incubator at 37 °C and 5% CO<sub>2</sub> for 15 minutes in dark and upon illumination.

After the stimulation, the solutions of every well were removed and 50  $\mu$ L of cAMP stimulation buffer was added, then 25  $\mu$ L of anti-cAMP-d2 and 25  $\mu$ L of cAMP-Eu in HTRF lysis buffer (*PerkinElmer-Cisbio*) were added to the wells. The plates were covered with an aluminum foil to be protected from light, and they were finally read with PHERAstar FS multimode microplate reader (*BMG-Labtech*) after minimum 1 hour of incubation at room temperature.

## Conformational biosensor assays

### Conformational VFT FRET-based biosensors (V sensors) assay

IGF-CNRS Montpellier

#### Basis of the conformational V FRET biosensors

The conformational VFT FRET-based biosensors assay was used to elucidate the main conformational changes at the extracellular VFT domain level. These changes are associated with the mGlu<sub>1</sub> receptor activation upon different agonists and NAMs binding.

The assay is based on the measurement of a differential time-resolved FRET (TR-FRET) between the two VFTs upon receptor activation. This TR-FRET variation is associated with a spatial distance variation between a TR-FRET pair conjugated on a SNAP-Tag (ST) fused to the N-terminal of mGlu<sub>1</sub>. Thus, the cells expressing ST-mGlu<sub>1</sub> (see above the procedure for transfection by electroporation) were labeled with the SNAP substrates O<sup>6</sup>-benzylguanine (BG)-Lumi4-Tb (100 nM in Tag-Lite buffer) as TR-FRET donor and BG-Fluorescein (Green) (60 nM in Tag-Lite buffer) as acceptor.

A high TR-FRET is measured in the basal state of mGlu<sub>1</sub>, whereas a lower TR-FRET is observed following the reorientation of the VFTs upon activation (*Figure 98*).<sup>278</sup>

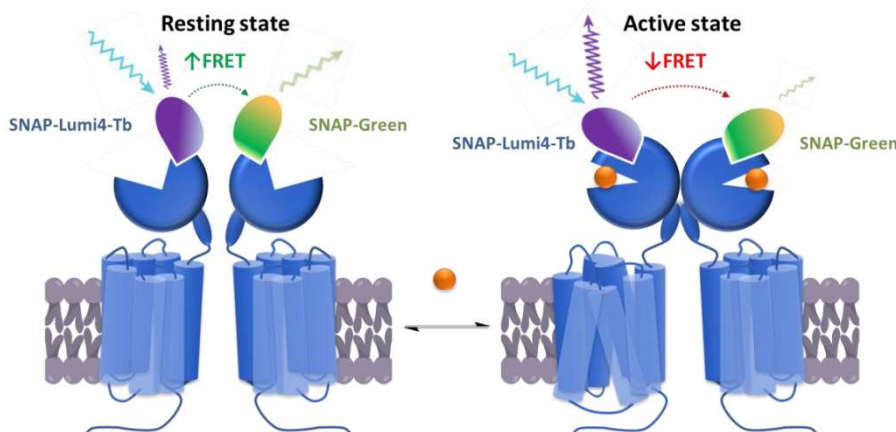


**Figure 98.** Schematic representation of VFT FRET-based biosensors (V sensors) reporting movements between VFT domains. These sensors consist in mGlu receptor modified 20-kDa SNAP-tag suicide enzyme, which is labelled with a TR-FRET acceptor (SNAP-Green (Fluorescein)) and donor (SNAP-Lumi4-Tb). The SNAP-tags are positioned strategically to sense the change of conformation occurring on receptor activation. In the open resting conformation (basal) or in the inactive conformation stabilized by a competitive antagonist, the fluorophores are in close proximity and the measured FRET is high. In the active closed conformation, stabilized by agonists, the FRET is low.

#### General materials and methods

##### The preincubated cells

After labeling (see above the procedure for labeling of SNAP-tag with VFT FRET-based biosensors on adherent mGlu<sub>1</sub> cells), the cells were washed 3 times with tag Lite Buffer and stimulated with different ligands for 30 min, at 37°C and 5% CO<sub>2</sub> in dark conditions only. The ligands solutions were prepared in Tag-

Lite buffer (*PerkinElmer-Cisbio*) and consisted of different concentrations of orthosteric agonist alone and orthosteric agonist in presence of a fixed concentration of allosteric compounds.\*

The TR-FRET measurements were performed with PHERAstar FS multimode microplate reader (*BMG-Labtech*) as described previously.<sup>278–280</sup> Briefly, the donor is excited by a laser at 337 nm, the emission fluorescent intensities were recorded at 520 nm (emission wavelength of Fluorescein (Green)) for two separate time windows (50-100  $\mu$ s as window 1, 800-900  $\mu$ s as windows 2) The results were plotted using GraphPad Prism 8.1.1 (*GraphPad Software*).

The FRET sensor values were determined by dividing the fluorescent intensities of window 1 by the intensities measured in window 2 (*Figure 99*). Kinetic FRET measurements were performed with fluorescent intensities measured every 10  $\mu$ s during 5000  $\mu$ s.

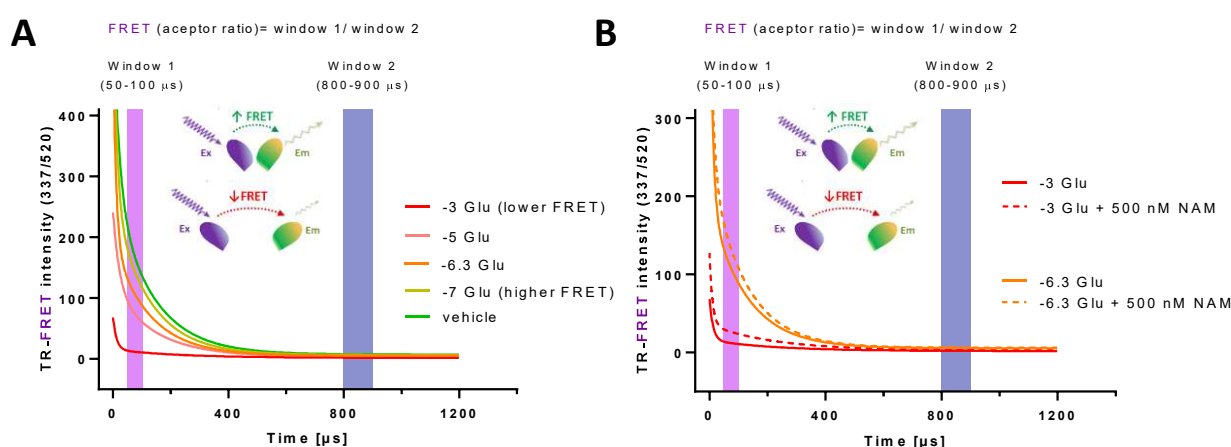


**Figure 99.** VFT FRET-based biosensors. The time windows of acceptor emission intensities used to calculate the FRET sensor values (acceptor ratio) are marked (window 1 in purple and window 2 in blue). Data are mean  $\pm$  SD of a typical experiment performed in duplicates and triplicates. (A) Decays of TR-FRET signal (acceptor emission after donor excitation) from the fluorescent-labeled mGlu<sub>1</sub> dimer in presence of the orthosteric agonist (glutamate) in different concentrations. As the glutamate concentration increases, the proportion of receptors in active form is higher and it is translated to a lower intensity of the recorded FRET signal. (B) FRET signal decays in presence of 500 nM NAM [FITM (90)]. Solid lines correspond to the samples incubated with the orthosteric agonist (glutamate) alone and the dotted lines to the samples incubating both glutamate and the negative allosteric compound (NAM). The presence of the NAM increases the FRET signal between the labeled mGlu<sub>1</sub> monomers.

*Detailed procedure for dose-response curves in dark conditions*

First of all, eleven intermediated solutions of each orthosteric agonist (glutamate or quisqualate) were prepared to generate eleven-point dose response curves in Tag-Lite buffer (*PerkinElmer-Cisbio*). Afterwards, the preincubated cells with the BG-dyes were washed three times with preheated Tag-Lite buffer to remove unbound substrate from each well and a final volume of 90  $\mu$ L of Tag-Lite buffer was added in just two rows of the plates. In the remaining six rows of each plate, 80  $\mu$ L of Tag-Lite buffer were added together with 10  $\mu$ L of NAM solutions (300- 500 nM).

\* See Chapter 4: Analysis of mGlu<sub>1</sub> NAM effect on receptor conformational changes induced by agonist for further details.

After 30 minutes of incubation at 37°C and 5% CO<sub>2</sub> each plate was read with PHERAstar FS multimode microplate reader (BMG-Labtech) recording FRET traces of single well with the following settings for decay curve monitoring mode:

- i. Focal height: 4 mm for SNAP-Fluorescein,
- ii. Positioning delay: 0.1 s
- iii. Measurement start time: 0 s
- iv. No. of flashes per well: 150
- v. Optic: Top optic
- vi. Excitation source: laser
- vii. Interval time: 10 μs
- viii. Meas. Time/flash: 5000 μs
- ix. No. of intervals: 500

These measurements represented the FRET signal recordings in the basal conditions, also called “pre-stimulation conditions”.

Subsequently, the orthosteric agonist (glutamate or quisqualate) in 10 μL of Tag-Lite buffer was added in each well as shown in *Figure 100* and the cells were incubated again 30 minutes at 37°C and 5% CO<sub>2</sub>.

x4	1	2	3	4	5	6	7	8	9	10	11	12
A	90 μL TLB + 10 μL Orthosteric agonist (Glutamate/ Quisqualate)											
B												
C	80 μL TLB + 10 μL NAM compound <sub>1/2</sub> + 10 μL Orthosteric agonist											
D												
E	(Glutamate/ Quisqualate)											
F	80 μL TLB + 10 μL NAM compound <sub>3/4</sub> + 10 μL Orthosteric agonist											
G												
H	(Glutamate/ Quisqualate)											

**Figure 100.** Arrangements of the four NAM compounds tested with the conformational VFT FRET-based biosensors assay. The eleven-points dose response curve of the orthosteric agonist only was used as reference control for each plate.

Then, each plate was read again with PHERAstar FS multimode microplate reader (BMG-Labtech) following the same protocol described above. These last measurements represented the FRET signal recordings in the so called “post-stimulation conditions”.

The complete results were plotted using GraphPad Prism 8.1.1 (GraphPad Software). Values were normalized as the percentage of response to the orthosteric agonist.

#### *Conformational intErmolecular and intrAmolecular-FRET-based biosensors (E/A sensors) assays*

##### *MDC Berlin*

##### *Basis of the conformational E/A FRET biosensors*

The conformational E-A FRET-based biosensors assays were used to study the kinetics of intErmolecular and intrAmolecular agonist-dependent activation of mGlu<sub>1</sub> receptor in presence of different negative allosteric modulators. In particular, a single fluorophore in each subunit of a GPCR dimer was placed (E-

sensor) to study intermolecular events in dimeric GPCRs, whereas both fluorophores were placed in each subunit at suitable positions to investigate intramolecular changes within the mGlu<sub>1</sub> receptor (A-sensor).

The assays are based on the measurement of a differential FRET between the cyan fluorescent protein (CFP) and the yellow fluorescent protein (YFP) after a distance variation upon receptor activation (Figure 101).

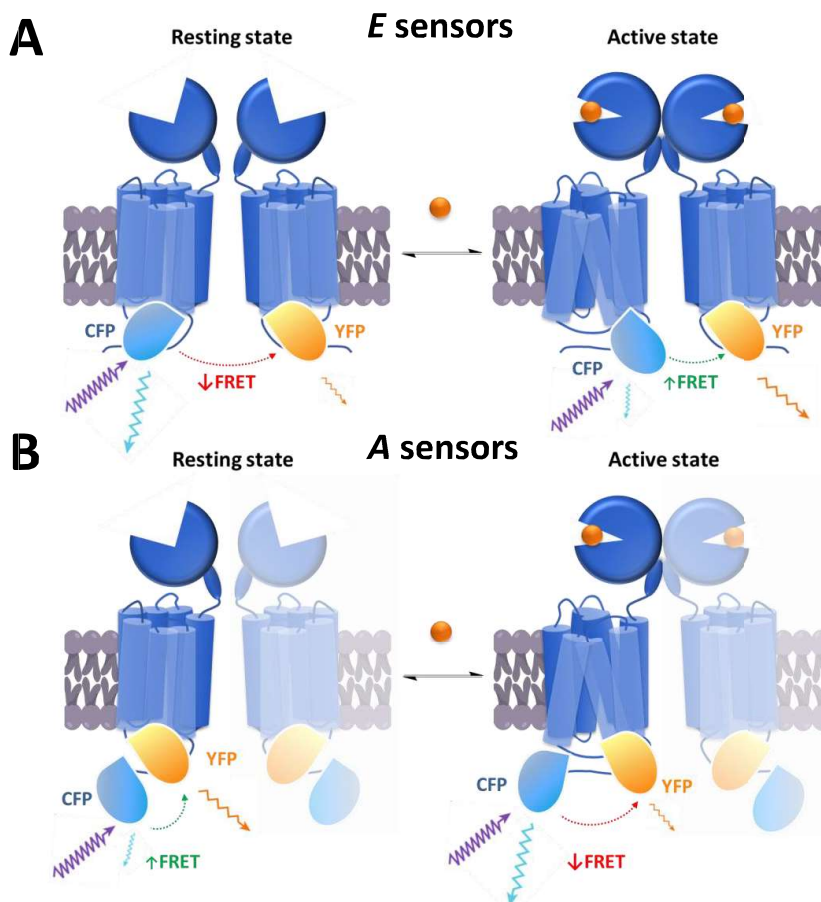


**Figure 101.** Schematic representation of E-A FRET-based biosensors reporting intermolecular and intramolecular movements of the mGlu<sub>1</sub> receptor, respectively. Two different families of sensors were previously created by incorporating cyan fluorescent protein (CFP) and yellow fluorescent protein (YFP) to two sites in the receptor.<sup>196,197</sup> (A) The E-sensor construct was composed by one mGlu<sub>1</sub> subunit labeled with a CFP and the other one labeled with a YFP, both in the second intracellular loop between Ile685 and Leu688; (B) The A-sensor construct contained two mGlu<sub>1</sub> subunits, each labeled with a YFP in the second intracellular loop and a CFP at the C-terminus.

#### General materials and methods

The transfected cells in black non-transparent 96-well plates (Corning) (see above the procedure for effectene transfection with E and A biosensor mGlu<sub>1</sub> constructs) were stimulated with various concentrations of ligands in dark conditions. The ligands were prepared in HBSS buffer (Gibco, Thermo Fisher Scientific) and consisted of orthosteric agonist alone and orthosteric agonist in presence of a fixed concentration of allosteric.\*

\* See Chapter 4: Analysis of mGlu<sub>1</sub> NAM effect on receptor conformational changes induced by agonist for further details.

The FRET measurements were performed using a Synergy Neo2 Multi-Mode Reader (*Biotek*), and data was acquired using Gen5 software (*Biotek*). Ten data points per well were measured for the baseline. After the baseline measurement, cells were stimulated manually with the ligand (glutamate) using a multichannel pipette, and ten more data points were acquired per well. For each concentration, twelve wells were used and the results were averaged.

FRET was monitored as the emission ratio of YFP to CFP. Fluorescence emissions of both donor and acceptor were corrected for spectral bleed-through as described previously.<sup>287</sup> Bleed-through is the passage of fluorescence emission in an inappropriate detection channel caused by an overlap of emission spectra, which should not be confused with the excitation and emission spectra of CFP and YFP spectral overlap that is instead one of the mandatory requirements for FRET (*Figure 102*).

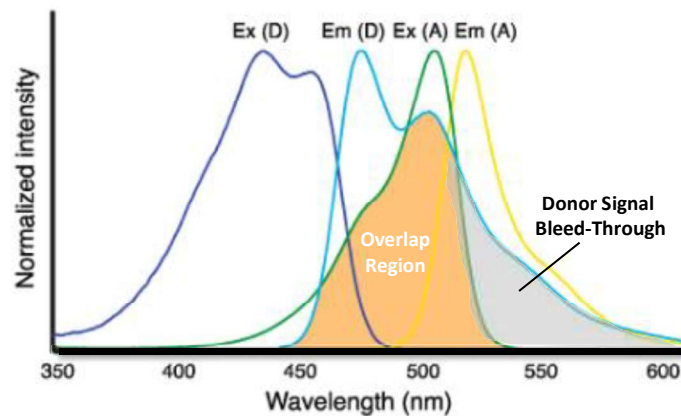


**Figure 102.** Excitation/absorption (Ex) and emission (Em) spectra of CFP donor (D) and YFP acceptor (A) FRET pair. Spectral overlap between CFP emission and YFP excitation spectra, which is essential for FRET, is highlighted in orange. Bleed-through of donor light (CFP) into the acceptor channel (YFP) is shown in gray.

In particular, bleed-through of CFP emission into the YFP channel was estimated as 36% so that the adjusted FRET ratio was calculated, for each data point of each well, using the *Equation 4*.

$$FRET = \frac{YFP}{CFP} em = \frac{YFP - 0.4 * CFP}{CFP}$$

**Equation 4.** Equation to calculate the corrected FRET channel intensity for each time point.

Afterwards, FRET changes due to different concentrations of the ligand (%  $\Delta$ FRET) were calculated relating FRET signal recordings of the basal conditions also called “pre-stimulation conditions” with those of the “post-stimulation conditions” after the addition of the orthosteric agonist (*Equation 5*).

$$\% \Delta FRET = \left( \frac{average_{post} - average_{pre}}{average_{pre}} \right) * 100$$

**Equation 5.** Equation to calculate the % $\Delta$ FRET taking into account FRET signal recordings both in the “pre-stimulation conditions” and in the “post-stimulation conditions”.

#### *Detailed procedure for dose-response curves in dark conditions*

First of all twelve intermediated solutions of the orthosteric agonist glutamate were prepared to generate twelve-points dose response curves in HBSS buffer (*Gibco, Thermo Fisher Scientific*). Afterwards, the preincubated cells were washed twice with preheated HBSS buffer to remove unbound substrate from each



well and a final volume of 90  $\mu\text{L}$  of HBSS buffer was added in just four rows of the plates. In the remaining four rows of each plate 80  $\mu\text{L}$  of HBSS buffer were added together with 10  $\mu\text{L}$  of NAM solutions (300-500 nM) 30 minutes before the first measurements so as to study the effects of the negative allosteric modulators.

After this incubation at 37°C and 5% CO<sub>2</sub> each plate was read with Synergy Neo2 Multi-Mode Reader (Biotek) recording FRET ratio  $R(t)$  (YFP/CFP) traces of single well (10 reads, Run time: 05:42).

Measurements were performed using two filter sets (Dual PMTs) for excitation and emission and dual PMTs were used for fluorescence detection. For CFP, excitation and emission bandwidth were set to 420/50 and 485/20, respectively. FRET was recorded using the second filter set, with the bandwidth settings of 420/50 and 540/25 for excitation and emission, respectively. The voltage gain for both PMTs was set to 90.

A Xenon lamp was set to high-energy mode, read height was set to 5.5 mm, and read speed was set to normal. Ten data points per well were measured for the baseline. These measurements represented the FRET signal recordings in the basal conditions, also called “pre-stimulation conditions”.

Then the orthosteric agonist glutamate in 10  $\mu\text{L}$  of HBSS buffer was added in each well as shown in *Figure 103*:

x4	1	2	3	4	5	6	7	8	9	10	11	12
A	90 $\mu\text{L}$ HBSS + 10 $\mu\text{L}$ Orthosteric agonist Glutamate											
B												
C												
D												
E	80 $\mu\text{L}$ HBSS + 10 $\mu\text{L}$ NAM compound <sub>1/2/3/4</sub> + 10 $\mu\text{L}$ Orthosteric agonist Glutamate											
F												
G												
H												

**Figure 103.** Arrangements of the four NAM compounds tested with the conformational E-A FRET-based biosensors assay. The twelve-points dose response curve of the orthosteric agonist only was used as reference control for each plate.

Rapidly, each plate was read again with Synergy Neo2 Multi-Mode Reader (Biotek) following the same protocol described above (15 reads, Run time: 08:52). Ten more data points were acquired per well and these last measurements represented the FRET signal recordings in the so called “post-stimulation conditions”.

The complete results were plotted using GraphPad Prism 8.1.1 (GraphPad Software). Values were normalized as the percentage of response to the orthosteric agonist.

## Bibliographic references

---



- (1) Brunton, L.; Lazo, J. S.; Parker, K. L. *Goodman & Gilman's- The Pharmacological Basis of Therapeutics*, 11th ed.; 1990; Vol. 1157.
- (2) Chisholm-Burns, M. A.; Wells, B. G.; Schwinghammer, T. L.; Malone, P.; Kolesar, J.; Rotschafer, J.; Dipiro, J. *Pharmacotherapy Principles & Practice*; 2010.
- (3) Deore A. B., Dhumane J. R., Wagh H. V., S. R. B. The Stages of Drug Discovery and Development Process *Amol. Asian J. Pharm. Res. Dev.* **2019**, *7* (6), 62–67. <https://doi.org/http://dx.doi.org/10.22270/ajprd.v7i6.616>.
- (4) Kramer, R. H.; Mourof, A.; Adesnik, H. Optogenetic Pharmacology for Control of Native Neuronal Signaling Proteins. *Nat. Neurosci.* **2013**, *16* (7), 816–823. <https://doi.org/10.1038/nn.3424>.
- (5) Edwards, I. R.; Aronson, J. K. Adverse Drug Reactions: Definitions, Diagnosis, and Management. *Lancet* **2000**, *356* (9237), 1255–1259. [https://doi.org/10.1016/S0140-6736\(00\)02799-9](https://doi.org/10.1016/S0140-6736(00)02799-9).
- (6) Lehár, J.; Krueger, A. S.; Avery, W.; Heilbut, A. M.; Johansen, L. M.; Price, E. R.; Rickles, R. J.; Short, G. F.; Staunton, J. E.; Jin, X.; Lee, M. S.; Zimmermann, G. R.; Borisy, A. A. Synergistic Drug Combinations Tend to Improve Therapeutically Relevant Selectivity. *Nat. Biotechnol.* **2009**, *27* (7), 659–666. <https://doi.org/10.1038/nbt.1549>.
- (7) Dimasi, J. A.; Feldman, L.; Seckler, A.; Wilson, A. Trends in Risks Associated with New Drug Development: Success Rates for Investigational Drugs. *Clin. Pharmacol. Ther.* **2010**, *87* (3), 272–277. <https://doi.org/10.1038/clpt.2009.295>.
- (8) Longley, D. B.; Johnston, P. G. Molecular Mechanisms of Drug Resistance. *J. Pathol.* **2005**, *205* (2), 275–292. <https://doi.org/10.1002/path.1706>.
- (9) Carlet, J.; Collignon, P.; Goldmann, D.; Goossens, H.; Gyssens, I. C.; Harbarth, S.; Jarlier, V.; Levy, S. B.; N'Doye, B.; Pittet, D.; Richtmann, R.; Seto, W. H.; Van Der Meer, J. W.; Voss, A. Society's Failure to Protect a Precious Resource: Antibiotics. *Lancet* **2011**, *378* (9788), 369–371. [https://doi.org/10.1016/S0140-6736\(11\)60401-7](https://doi.org/10.1016/S0140-6736(11)60401-7).
- (10) Martinez, J. L. Antibiotics and Antibiotic Resistance Genes in Natural Environments. *Sci.* **2008**, *321* (5887), 365–367. <https://doi.org/10.1126/science.1159483> ARTICLE.
- (11) Feringa, B. L. The Art of Building Small : From Molecular Switches to Motors. In *Nobel Lecture*; 2016; pp 231–259.
- (12) Velema, W. A.; Szymanski, W.; Feringa, B. L. Photopharmacology : Beyond Proof of Principle. *J. Am. Chem. Soc* **2014**, *136*, 2178–2191. <https://doi.org/10.1021/ja413063e>.
- (13) Hansen, M. J.; Velema, W. A.; De Bruin, G.; Overkleeft, H. S.; Szymanski, W.; Feringa, B. L. Proteasome Inhibitors with Photocontrolled Activity. *ChemBioChem* **2015**, *16* (17), 2053–2057. <https://doi.org/10.1002/cbic.201402237>.
- (14) Tochitsky, I.; Polosukhina, A.; Degtyar, V. E.; Gallerani, N.; Smith, C. M.; Friedman, A.; Van Gelder, R. N.; Trauner, D.; Kaufer, D.; Kramer, R. H. Restoring Visual Function to Blind Mice with a Photoswitch That Exploits Electrophysiological Remodeling of Retinal Ganglion Cells. *Neuron* **2014**, *81* (4), 800–813. <https://doi.org/10.1016/j.neuron.2014.01.003>.
- (15) Szymański, W.; Beierle, J. M.; Kistemaker, H. A. V.; Velema, W. A.; Feringa, B. L. Reversible Photocontrol of Biological Systems by the Incorporation of Molecular Photoswitches. *Chem. Rev.* **2013**, *113* (8), 6114–6178. <https://doi.org/10.1021/cr300179f>.

- (16) Beharry, A. A.; Sadvski, O.; Woolley, G. A. Azobenzene Photoswitching without Ultraviolet Light. *J. Am. Chem. Soc.* **2011**, *133* (49), 19684–19687. <https://doi.org/10.1021/ja209239m>.
- (17) Mayer, G.; Hechel, A. Biologically Active Molecules with a “Light Switch.” *Angew. Chemie - Int. Ed.* **2006**, *45* (30), 4900–4921. <https://doi.org/10.1002/anie.200600387>.
- (18) Szymanski, W.; Ourailidou, M. E.; Velema, W. A.; Dekker, F. J.; Feringa, B. L. Light-Controlled Histone Deacetylase ( HDAC ) Inhibitors : Towards Photopharmacological Chemotherapy. *Chem. - A Eur. J.* **2015**, *21*, 16517–16524. <https://doi.org/10.1002/chem.201502809>.
- (19) Gorostiza, P.; Isacoff, E. Y. Optical Switches for Remote and Noninvasive Control of Cell Signaling. *Sci.* **2008**, *322*, 395–399. <https://doi.org/10.1126/science.1166022>.
- (20) Bandara, H. M. D.; Burdette, S. C. Photoisomerization in Different Classes of Azobenzene. *Chem. Soc. Rev.* **2012**, *41* (5), 1809–1825. <https://doi.org/10.1039/c1cs15179g>.
- (21) Broichhagen, J.; Schonberger, M.; Cork, S. C.; Frank, J. A.; Marchetti, P.; Bugliani, M.; Shapiro, A. M. J.; Trapp, S.; Rutter, G. A.; Hodson, D. J.; Trauner, D. Optical Control of Insulin Release Using a Photoswitchable Sulfonylurea. *Nat. Commun.* **2014**, *5* (5116), 1–11. <https://doi.org/10.1038/ncomms6116>.
- (22) Velema, W. A.; Berg, J. P. Van Der; Hansen, M. J.; Szymanski, W.; Driessen, A. J. M.; Feringa, B. L. Optical Control of Antibacterial Activity. *Nat. Chem.* **2013**, *5*, 924–928. <https://doi.org/10.1038/nchem.1750>.
- (23) Reisinger, B.; Kuzmanovic, N.; Loffler, P.; Merkl, R.; Konig, B.; Sterner, R. Exploiting Protein Symmetry To Design Light-Controllable Enzyme Inhibitors. *Angew. Chemie - Int. Ed.* **2014**, *53*, 595–598. <https://doi.org/10.1002/anie.201307207>.
- (24) Dugave, C.; Demange, L. Cis-Trans Isomerization of Organic Molecules and Biomolecules: Implications and Applications. *Chem. Rev.* **2003**, *103* (7), 2475–2532. <https://doi.org/10.1021/cr0104375>.
- (25) Liu, R. S. H.; Asato, A. E. The Primary Process of Vision and the Structure of Bathorhodopsin: A Mechanism for Photoisomerization of Polyenes. *Proc. Natl. Acad. Sci. U. S. A.* **1985**, *82* (2), 259–263. <https://doi.org/10.1073/pnas.82.2.259>.
- (26) Matsuno-Yagi, A.; Mukohata, Y. TWO POSSIBLE ROLES OF BACTERIORHODOPSIN; A COMPARATIVE STUDY OF STRAINS OF HALOBACTERIUM HALOBIUM DIFFERING IN PIGMENTATION. *Biochem. Biophys. Res. Commun.* **1977**, *7* (1), 541–559.
- (27) Oesterhelt, D.; Stoeckenius, W. Rhodopsin-like Protein from the Purple Membrane of Halobacterium Halobium. *Nat. New Biol.* **1971**, *233*, 149–152.
- (28) Tsukamoto, H.; Terakita, A. Diversity and Functional Properties of Bistable Pigments. *Photochem. Photobiol. Sci.* **2010**, *9*, 1435–1443. <https://doi.org/10.1039/c0pp00126k>.
- (29) Banghart, M. R.; Volgraf, M.; Trauner, D. Engineering Light-Gated Ion Channels. *Biochemistry* **2006**, *45* (51), 15129–15141. <https://doi.org/10.1021/bi0618058>.
- (30) Merino, E. Synthesis of Azobenzenes: The Coloured Pieces of Molecular Materials. *Chem. Soc. Rev.* **2011**, *40* (7), 3835–3853. <https://doi.org/10.1039/c0cs00183j>.
- (31) Broichhagen, J.; Frank, J. A.; Trauner, D. A Roadmap to Success in Photopharmacology. *Acc. Chem.*

- Res. **2015**, *48* (7), 1947–1960. <https://doi.org/10.1021/acs.accounts.5b00129>.
- (32) Wagner, G.; Arion, V. B.; Brecker, L.; Krantz, C.; Mieusset, J. L.; Brinker, U. H. Controllable Selective Functionalization of a Cavitand via Solid State Photolysis of an Encapsulated Phenyl Azide. *Org. Lett.* **2009**, *11* (14), 3056–3058. <https://doi.org/10.1021/ol901122h>.
- (33) Chiba, S.; Zhang, L.; Lee, J. Y. Copper-Catalyzed Synthesis of Azaspirocyclohexadienones from Alpha-Azido-N-Arylamides under an Oxygen Atmosphere. *J. Am. Chem. Soc.* **2010**, *132* (21), 7266–7267. <https://doi.org/10.1021/ja1027327>.
- (34) Hartley, G. S. The Cis-Form of Azobenzene. *Nature* **1937**, *140*, 281–281.
- (35) Fujino, T.; Arzhantsev, S. Y.; Tahara, T. Femtosecond Time-Resolved Fluorescence Study of Photoisomerization of Trans-Azobenzene. *J. Phys. Chem. A.* **2001**, *105* (35), 8123–8129. <https://doi.org/10.1021/jp0110713>.
- (36) Satzger, H.; Root, C.; Braun, M. Excited-State Dynamics of Trans- and Cis-Azobenzene after UV Excitation in the  $\Pi\pi^*$  Band. *J. Phys. Chem. A* **2004**, *108* (30), 6265–6271. <https://doi.org/10.1021/jp049509x>.
- (37) García-Amorós, J.; Velasco, D. Recent Advances towards Azobenzene-Based Lightdriven Real-Time Information-Transmitting Materials. *Beilstein J. Org. Chem.* **2012**, *8*, 1003–1017. <https://doi.org/10.3762/bjoc.8.113>.
- (38) Asano, T.; Okada, T. Thermal Z-E Isomerization of Azobenzenes. The Pressure, Solvent, and Substituent Effects. *J. Org. Chem.* **1984**, *49* (23), 4387–4391. <https://doi.org/10.1021/jo00197a011>.
- (39) Ciccone, S.; Halpern, J. CATALYSIS OF THE CIS-TRANS ISOMERIZATION OF AZOBENZENE BY ACIDS AND CUPRIC SALTS. *Can. J. Chem.* **1959**, *37*, 1903–1910.
- (40) Beharry, A. A.; Sadovski, O.; Woolley, G. A. Photo-Control of Peptide Conformation on a Timescale of Seconds with a Conformationally Constrained, Blue-Absorbing, Photo-Switchable Linker. *Org. Biomol. Chem.* **2008**, *6* (23), 4323–4332. <https://doi.org/10.1039/b810533b>.
- (41) Cembran, A.; Bernardi, F.; Garavelli, M.; Gagliardi, L.; Orlandi, G. On the Mechanism of the Cis-Trans Isomerization in the Lowest Electronic States of Azobenzene: S<sub>0</sub>, S<sub>1</sub>, and T<sub>1</sub>. *J. Am. Chem. Soc.* **2004**, *126* (10), 3234–3243. <https://doi.org/10.1021/ja038327y>.
- (42) Cattaneo, P.; Persico, M. An Ab Initio Study of the Photochemistry of Azobenzene. *Phys. Chem. Chem. Phys.* **1999**, *1*, 4739–4743. <https://doi.org/10.1039/a905055h>.
- (43) Forman, J.; Dietrich, M.; Todd Monroe, W. Photobiological and Thermal Effects of Photoactivating UVA Light Doses on Cell Cultures. *Photochem. Photobiol. Sci.* **2007**, *6*, 649–658. <https://doi.org/10.1039/b616979a>.
- (44) Siewertsen, R.; Neumann, H.; Buchheim-Stehn, B.; Herges, R.; Näther, C.; Renth, F.; Temps, F. Highly Efficient Reversible Z-E Photoisomerization of a Bridged Azobenzene with Visible Light through Resolved S<sub>1</sub>(N $\pi^*$ ) Absorption Bands. *J. Am. Chem. Soc.* **2009**, *131* (43), 15594–15595. <https://doi.org/10.1021/ja906547d>.
- (45) Brown, E. V.; Granneman, G. R. Cis-Trans Isomerism in the Pyridyl Analogs of Azobenzene. A Kinetic and Molecular Orbital Analysis. *J. Am. Chem. Soc.* **1975**, *97* (3), 621–627. <https://doi.org/10.1021/ja00836a025>.

- (46) Gómez-Santacana, X. Design, Synthesis and Characterization of Photoswitchable Allosteric Modulators of Metabotropic Glutamate Receptors, Universitat de Barcelona, 2016.
- (47) Sueyoshi, T.; Nishimura, N.; Yamamoto, S.; Hasegawa, S. Further Evidence of Inversion Mechanism for the Cis to Trans Thermal Isomerization of 4-Dimethylaminoazobenzene Derivatives. Additivity Rule of Substituent Constants. *Chem. Lett.* **1974**, 1131–1134.
- (48) Pozhidaeva, N.; Cormier, M. E.; Chaudhari, A.; Woolley, G. A. Reversible Photocontrol of Peptide Helix Content: Adjusting Thermal Stability of the Cis State. *Bioconjug. Chem.* **2004**, *15* (6), 1297–1303. <https://doi.org/10.1021/bc049855h>.
- (49) Sadovski, O.; Beharry, A. A.; Zhang, F.; Woolley, G. A. Spectral Tuning of Azobenzene Photoswitches for Biological Applications. *Angew. Chemie - Int. Ed.* **2009**, *48* (8), 1484–1486. <https://doi.org/10.1002/anie.200805013>.
- (50) Lewis, G. E. Photochemical Reactions of Azo Compounds. I. Spectroscopic Studies of the Conjugate Acids of Cis- and Trans-Azobenzene. *J. Org. Chem.* **1960**, *25* (12), 2193–2195. <https://doi.org/10.1021/jo01082a027>.
- (51) Ide, T.; Ozama, Y.; Matsui, K. Photochemistry of Azobenzene in Sol-Gel Systems. *J. Non. Cryst. Solids* **2011**, *357* (1), 100–104. <https://doi.org/10.1016/j.jnoncrysol.2010.09.009>.
- (52) Khalaf, A. Photocyclization of Stilbenes and Stilbenoids. *Trends Photochem. Photobiol.* **2010**, *12*, 65–75. <https://doi.org/0972-4532>.
- (53) Blackburn, B. E. V; Timmons, C. J. The Photocyclisation of Stilbene Analogues. *Q. Rev. Chem. Soc.* **1969**, No. 4, 482–503.
- (54) Toro, C.; Thibert, A.; De Boni, L.; Masunov, A. E.; Hernández, F. E. Fluorescence Emission of Disperse Red 1 in Solution at Room Temperature. *J. Phys. Chem. B* **2008**, *112* (3), 929–937. <https://doi.org/10.1021/jp076026v>.
- (55) Samanta, S.; Beharry, A. A.; Sadovski, O.; McCormick, T. M.; Babalhavaeji, A.; Tropepe, V.; Woolley, G. A. Photoswitching Azo Compounds in Vivo with Red Light. *J. Am. Chem. Soc.* **2013**, *135*, 9777–9784. <https://doi.org/10.1021/ja402220t>.
- (56) Dong, M.; Babalhavaeji, A.; Samanta, S.; Beharry, A. A.; Woolley, G. A. Red-Shifting Azobenzene Photoswitches for in Vivo Use. *Acc. Chem. Res.* **2015**, *48* (10), 2662–2670. <https://doi.org/10.1021/acs.accounts.5b00270>.
- (57) Bléger, D.; Schwarz, J.; Brouwer, A. M.; Hecht, S. O -Fluoroazobenzenes as Readily Synthesized Photoswitches Offering Nearly Quantitative Two-Way Isomerization with Visible Light. *J. Am. Chem. Soc.* **2012**, *134* (51), 20597–20600. <https://doi.org/10.1021/ja310323y>.
- (58) Agnetta, L.; Bermudez, M.; Riefolo, F.; Matera, C.; Claro, E.; Messerer, R.; Littmann, T.; Wolber, G.; Holzgrabe, U.; Decker, M. Fluorination of Photoswitchable Muscarinic Agonists Tunes Receptor Pharmacology and Photochromic Properties. *J. Med. Chem.* **2019**, *62*, 3009–3020. <https://doi.org/10.1021/acs.jmedchem.8b01822>.
- (59) Samanta, S.; Qin, C.; Lough, A. J.; Woolley, G. A. Bidirectional Photocontrol of Peptide Conformation with a Bridged Azobenzene Derivative. *Angew. Chemie - Int. Ed.* **2012**, *124*, 6558–6561. <https://doi.org/10.1002/ange.201202383>.
- (60) Trads, J. B.; Katharina, H.; Matsuura, B. S.; Laprell, L.; Fehrentz, T.; Gçrldt, N.; Kozek, K. A.; Weaver, C.

- D.; Klçcker, N.; Barber, D. M.; Trauner, D. Sign Inversion in Photopharmacology : Incorporation of Cyclic Azobenzenes in Photoswitchable Potassium Channel Blockers and Openers. *Angew. Chemie - Int. Ed.* **2019**, *58*, 15421–15428. <https://doi.org/10.1002/anie.201905790>.
- (61) Maier, M. S.; Hüll, K.; Reynders, M.; Matsuura, B. S.; Leippe, P.; Ko, T.; Schäffer, L.; Trauner, D. Oxidative Approach Enables Efficient Access to Cyclic Azobenzenes. *J. Am. Chem. Soc* **2019**, *141*, 17295–17304. <https://doi.org/10.1021/jacs.9b08794>.
- (62) Fredriksson, R.; Lagerström, M. C.; Lundin, L. G.; Schiöth, H. B. The G-Protein-Coupled Receptors in the Human Genome Form Five Main Families. Phylogenetic Analysis, Paralogon Groups, and Fingerprints. *Mol. Pharmacol.* **2003**, *63* (6), 1256–1272. <https://doi.org/10.1124/mol.63.6.1256>.
- (63) Schiöth, H. B.; Lagerström, M. C. Structural Diversity of g Protein-coupled Receptors and Significance for Drug Discovery. *Nat. Rev. Drug Discov.* **2008**, *7* (4), 339–357. <https://doi.org/10.1038/nrd2518>.
- (64) Overington, J. P.; Al-lazikani, B.; Hopkins, A. L. How Many Drug Targets Are There? *Nat. Rev. Drug Discov.* **2006**, *5*, 993–996. <https://doi.org/10.1038/nrd2199>.
- (65) Sriram, K.; Insel, P. A. G Protein-Coupled Receptors as Targets for Approved Drugs:How Many Targets and How Many Drugs? *Mol. Pharmacol.* **2018**, *93*, 251–258. <https://doi.org/10.1124/mol.117.111062>.
- (66) Garland, S. L. Are GPCRs Still a Source of New Targets? *J. Biomol. Screen.* **2013**, *18* (9), 947–966. <https://doi.org/10.1177/1087057113498418>.
- (67) Bockaert, J.; Pin, J. P. Molecular Tinkering of G Protein-Coupled Receptors: An Evolutionary Success. *EMBO J.* **1999**, *18* (7), 1723–1729. <https://doi.org/10.1093/emboj/18.7.1723>.
- (68) Milligan, G.; Kostenis, E. Heterotrimeric G-Proteins: A Short History. *Br. J. Pharmacol.* **2006**, *147* (S1), S46–S55. <https://doi.org/10.1038/sj.bjp.0706405>.
- (69) Melien, Ø. Heterotrimeric G Proteins and Disease. *Methods Mol. Biol.* **2007**, *361*, 119–144. <https://doi.org/10.1385/1-59745-208-4:119>.
- (70) Ayoub, M. A. Small Molecules Targeting Heterotrimeric G Proteins. *Eur. J. Pharmacol.* **2018**, *826*, 169–178. <https://doi.org/10.1016/j.ejphar.2018.03.003>.
- (71) Jakubík, J.; Randáková, A.; El-Fakahany, E. E.; Doležal, V. Analysis of Equilibrium Binding of an Orthosteric Tracer and Two Allosteric Modulators. *PLoS One* **2019**, *14* (3), 1–19. <https://doi.org/10.1371/journal.pone.0214255>.
- (72) Wacker, D.; Stevens, R. C.; Roth, B. L. How Ligands Illuminate GPCR Molecular Pharmacology. *Cell* **2017**, *170* (3), 414–427. <https://doi.org/10.1016/j.cell.2017.07.009>.
- (73) Jeffrey Conn, P.; Christopoulos, A.; Lindsley, C. W. Allosteric Modulators of GPCRs: A Novel Approach for the Treatment of CNS Disorders. *Nat. Rev. Drug Discov.* **2009**, *8* (1), 41–54. <https://doi.org/10.1038/nrd2760>.
- (74) Christopoulos, A. Advances in G Protein-Coupled Receptor Allostery: From Function to Structure. *Mol. Pharmacol.* **2014**, *86* (5), 463–478. <https://doi.org/10.1124/mol.114.094342>.
- (75) Van Der Westhuizen, E. T.; Valant, C.; Sexton, P. M.; Christopoulos, A. Endogenous Allosteric Modulators of G Protein-Coupled Receptors. *J. Pharmacol. Exp. Ther.* **2015**, *353* (2), 246–260. <https://doi.org/10.1124/jpet.114.221606>.



- (76) Shonberg, J.; Kling, R. C.; Gmeiner, P.; Löber, S. GPCR Crystal Structures: Medicinal Chemistry in the Pocket. *Bioorganic Med. Chem.* **2015**, *23* (14), 3880–3906. <https://doi.org/10.1016/j.bmc.2014.12.034>.
- (77) Basith, S.; Cui, M.; Macalino, S. J. Y.; Park, J.; Clavio, N. A. B.; Kang, S.; Choi, S. Exploring G Protein-Coupled Receptors (GPCRs) Ligand Space via Cheminformatics Approaches: Impact on Rational Drug Design. *Front. Pharmacol.* **2018**, *9*, 1–26. <https://doi.org/10.3389/fphar.2018.00128>.
- (78) Lee, S. M.; Booe, J. M.; Pioszak, A. A. Structural Insights into Ligand Recognition and Selectivity for Classes A, B, and C GPCRs. *Eur. J. Pharmacol.* **2015**, *763*, 196–205. <https://doi.org/10.1016/j.ejphar.2015.05.013>.
- (79) Hu, G. M.; Mai, T. L.; Chen, C. M. Visualizing the GPCR Network: Classification and Evolution. *Sci. Rep.* **2017**, *7* (1), 1–15. <https://doi.org/10.1038/s41598-017-15707-9>.
- (80) Alexander, S. P. H.; Christopoulos, A.; Davenport, A. P.; Kelly, E.; Mathie, A.; Peters, J. A.; Veale, E. L.; Armstrong, J. F.; Faccenda, E.; Harding, S. D.; Pawson, A. J.; Sharman, J. L.; Southan, C.; Davies, J. A.; CGTP Collaborators. THE CONCISE GUIDE TO PHARMACOLOGY 2019/20: G Protein-Coupled Receptors. *Br. J. Pharmacol.* **2019**, *176* (S1), S21–S141. <https://doi.org/10.1111/bph.14748>.
- (81) Pándy-Szekeres, G.; Munk, C.; Tsonkov, T. M.; Mordalski, S.; Harpsøe, K.; Hauser, A. S.; Bojarski, A. J.; Gloriam, D. E. GPCRdb in 2018: Adding GPCR Structure Models and Ligands. *Nucleic Acids Res.* **2018**, *46* (D1), D440–D446. <https://doi.org/10.1093/nar/gkx1109>.
- (82) Palczewski, K.; Kumasaka, T.; Hori, T.; Behnke, C. A.; Motoshima, H.; Fox, B. A.; Le Trong, I.; Teller, D. C.; Okada, T.; Stenkamp, R. E.; Yamamoto, M.; Miyano, M. Crystal Structure of Rhodopsin: A G Protein-Coupled Receptor. *Sci.* **2000**, *289* (5480), 739–745. <https://doi.org/10.1126/science.289.5480.739>.
- (83) Cherezov, V.; Rosenbaum, D. M.; Hanson, M. A.; Rasmussen, S. G. F.; Foon, S. T.; Kobilka, T. S.; Choi, H. J.; Kuhn, P.; Weis, W. I.; Kobilka, B. K.; Stevens, R. C. High-Resolution Crystal Structure of an Engineered Human B2-Adrenergic G Protein-Coupled Receptor. *Sci.* **2007**, *318* (5854), 1258–1265. <https://doi.org/10.1126/science.1150577>.
- (84) Rosenbaum, D. M.; Cherezov, V.; Hanson, M. A.; Rasmussen, S. G. F.; Foon, S. T.; Kobilka, T. S.; Choi, H. J.; Yao, X. J.; Weis, W. I.; Stevens, R. C.; Kobilka, B. K. GPCR Engineering Yields High-Resolution Structural Insights into B2-Adrenergic Receptor Function. *Sci.* **2007**, *318* (5854), 1266–1273. <https://doi.org/10.1126/science.1150609>.
- (85) Yang, D.; Zhou, Q.; Labroska, V.; Qin, S.; Darbalaei, S.; Wu, Y.; Yuliantie, E.; Xie, L.; Tao, H.; Cheng, J.; Liu, Q.; Zhao, S.; Shui, W.; Jiang, Y.; Wang, M. W. G Protein-Coupled Receptors: Structure- and Function-Based Drug Discovery. *Signal Transduct. Target. Ther.* **2021**, *6* (7), 1–27. <https://doi.org/10.1038/s41392-020-00435-w>.
- (86) Peplow, M. Cryo-Electron Microscopy Reaches Resolution Milestone. *ACS Cent. Sci.* **2020**, *6* (8), 1274–1277. <https://doi.org/10.1021/acscentsci.0c01048>.
- (87) Huang, W.; Masureel, M.; Qu, Q.; Janetzko, J.; Inoue, A.; Skiniotis, G.; Kobilka, B. K. Structure of the Neurotensin Receptor1 in Complex with  $\beta$ -Arrestin 1. *Nature* **2020**, *579*, 303–308. <https://doi.org/10.1038/s41586-020-1953-1>.
- (88) Staus, D. P.; Hu, H.; Robertson, M. J.; Kleinhenz, A. L. W. Structure of the M2 Muscarinic Receptor –  $\beta$ -Arrestin Complex in a Lipid Nanodisc. *Nature* **2020**, *579*, 297–302. <https://doi.org/10.1038/s41586-020-1954-0>.

- (89) Hollenstein, K.; Kean, J.; Bortolato, A.; Cheng, R. K. Y.; Doré, A. S.; Jazayeri, A.; Cooke, R. M.; Weir, M.; Marshall, F. H. Structure of Class B GPCR Corticotropin-Releasing Factor Receptor 1. *Nature* **2013**, *499* (7459), 438–443. <https://doi.org/10.1038/nature12357>.
- (90) Siu, F. Y.; He, M.; De Graaf, C.; Han, G. W.; Yang, D.; Zhang, Z.; Zhou, C.; Xu, Q.; Wacker, D.; Joseph, J. S.; Liu, W.; Lau, J.; Cherezov, V.; Katritch, V.; Wang, M. W.; Stevens, R. C. Structure of the Human Glucagon Class B G-Protein-Coupled Receptor. *Nature* **2013**, *499* (7459), 444–449. <https://doi.org/10.1038/nature12393>.
- (91) Wang, C.; Wu, H.; Katritch, V.; Han, G. W.; Huang, X. P.; Liu, W.; Siu, F. Y.; Roth, B. L.; Cherezov, V.; Stevens, R. C. Structure of the Human Smoothed Receptor Bound to an Antitumour Agent. *Nature* **2013**, *497* (7449), 338–343. <https://doi.org/10.1038/nature12167>.
- (92) Doré, A. S.; Okrasa, K.; Patel, J. C.; Serrano-Vega, M.; Bennett, K.; Cooke, R. M.; Errey, J. C.; Jazayeri, A.; Khan, S.; Tehan, B.; Weir, M.; Wiggin, G. R.; Marshall, F. H. Structure of Class C GPCR Metabotropic Glutamate Receptor 5 Transmembrane Domain. *Nature* **2014**, *511* (7511), 557–562. <https://doi.org/10.1038/nature13396>.
- (93) Wu, H.; Wang, C.; Gregory, K. J.; Han, G. W.; Cho, H. P.; Xia, Y.; Niswender, C. M.; Katritch, V.; Meiler, J.; Cherezov, V.; Conn, P. J.; Stevens, R. C. Structure of a Class C GPCR Metabotropic Glutamate Receptor 1 Bound to an Allosteric Modulator. *Sci.* **2014**, *344* (6179), 58–64. <https://doi.org/10.1126/science.1249489>.
- (94) Dijksterhuis, J. P.; Petersen, J.; Schulte, G. WNT/Frizzled Signalling: Receptor-Ligand Selectivity with Focus on FZD-G Protein Signalling and Its Physiological Relevance: IUPHAR Review 3. *Br. J. Pharmacol.* **2014**, *171* (5), 1195–1209. <https://doi.org/10.1111/bph.12364>.
- (95) Guo, D.; Hillger, J. M.; IJzerman, A. P.; Heitman, L. H. Drug-Target Residence Time- A Case for G Protein-Coupled Receptors. *Med. Res. Rev.* **2014**, *34*, 856–892. <https://doi.org/10.1002/med>.
- (96) Xue, Y.; Bai, H.; Peng, B.; Fang, B.; Baell, J.; Li, L.; Huang, W.; Voelcker, N. H. Stimulus-Cleavable Chemistry in the Field of Controlled Drug Delivery. *Chem. Soc. Rev.* **2021**, *50* (8), 4872–4931. <https://doi.org/10.1039/d0cs01061h>.
- (97) Hüll, K.; Morstein, J.; Trauner, D. In Vivo Photopharmacology. *Chem. Rev.* **2018**, *118* (21), 10710–10747. <https://doi.org/10.1021/acs.chemrev.8b00037>.
- (98) Zussy, C.; Gómez-Santacana, X.; Rovira, X.; De Bundel, D.; Ferrazzo, S.; Bosch, D.; Asede, D.; Malhaire, F.; Acher, F.; Giraldo, J.; Valjent, E.; Ehrlich, I.; Ferraguti, F.; Pin, J. P.; Llebaria, A.; Goudet, C. Dynamic Modulation of Inflammatory Pain-Related Affective and Sensory Symptoms by Optical Control of Amygdala Metabotropic Glutamate Receptor 4. *Mol. Psychiatry* **2018**, *23* (3), 509–520. <https://doi.org/10.1038/mp.2016.223>.
- (99) Font, J.; López-Cano, M.; Notartomaso, S.; Scarselli, P.; Di Pietro, P.; Bresolí-Obach, R.; Battaglia, G.; Malhaire, F.; Rovira, X.; Catena, J.; Giraldo, J.; Pin, J. P.; Fernández-Dueñas, V.; Goudet, C.; Nonell, S.; Nicoletti, F.; Llebaria, A.; Ciruela, F. Optical Control of Pain in Vivo with a Photoactive MGLu5 Receptor Negative Allosteric Modulator. *Elife* **2017**, *6*, 1–20. <https://doi.org/10.7554/eLife.23545>.
- (100) Airan, R. D.; Thompson, K. R.; Fenno, L. E.; Bernstein, H.; Deisseroth, K. Temporally Precise in Vivo Control of Intracellular Signalling. *Nature* **2009**, *458* (7241), 1025–1029. <https://doi.org/10.1038/nature07926>.
- (101) Deisseroth, K. Optogenetics. *Nat. Methods* **2011**, *8* (1), 26–29. <https://doi.org/10.1038/nmeth.f.324>.

- (102) Li, X.; Gutierrez, D. V.; Hanson, M. G.; Han, J.; Mark, M. D.; Chiel, H.; Hegemann, P.; Landmesser, L. T.; Herlitze, S. Fast Noninvasive Activation and Inhibition of Neural and Network Activity by Vertebrate Rhodopsin and Green Algae Channelrhodopsin. *Proc. Natl. Acad. Sci. U. S. A.* **2005**, *102* (49), 17816–17821. <https://doi.org/10.1073/pnas.0509030102>.
- (103) Rappleye, M.; Berndt, A. Structural Basis for Ion Selectivity and Engineering in Channelrhodopsins. *Curr. Opin. Struct. Biol.* **2019**, *57*, 176–184. <https://doi.org/10.1016/j.sbi.2019.04.008>.
- (104) Deisseroth, K. Optogenetics : 10 Years of Microbial Opsins in Neuroscience. *Nat. Neurosci.* **2015**, *18* (9), 1213–1225.
- (105) Weitzman, M.; Hahn, K. M. Optogenetic Approaches to Cell Migration and Beyond. *Curr. Opin. Cell Biol.* **2014**, *30*, 112–120. <https://doi.org/10.1016/j.ceb.2014.08.004>.
- (106) Siuda, E. R.; McCall, J. G.; Al-Hasani, R.; Shin, G.; Park, S. Il; Schmidt, M. J.; Anderson, S. L.; Planer, W. J.; Rogers, J. A.; Bruchas, M. R. Optodynamic Simulation of  $\beta$ -Adrenergic Receptor Signalling. *Nat. Commun.* **2015**, *6* (8480), 1–13. <https://doi.org/10.1038/ncomms9480>.
- (107) Zheng, W.; Zhou, J.; Luan, Y.; Yang, J.; Ge, Y.; Wang, M.; Wu, B.; Wu, Z.; Chen, X.; Li, F.; Li, Z.; Vokal, S.; Guo, W.; Chen, J. F. Spatiotemporal Control of GPR37 Signaling and Its Behavioral Effects by Optogenetics. *Front. Mol. Neurosci.* **2018**, *11*, 1–11. <https://doi.org/10.3389/fnmol.2018.00095>.
- (108) Fehrentz, T.; Schönberger, M.; Trauner, D. Optochemical Genetics. *Angew. Chemie - Int. Ed.* **2011**, *50* (51), 12156–12182. <https://doi.org/10.1002/anie.201103236>.
- (109) Ellis-Davies, G. C. R. Useful Caged Compounds for Cell Physiology. *Acc. Chem. Res.* **2020**, *53* (8), 1593–1604. <https://doi.org/10.1021/acs.accounts.0c00292>.
- (110) Kaplan, J. H.; Forbush, B.; Hoffman, J. F. Rapid Photolytic Release of Adenosine 5'-Triphosphate from a Protected Analogue: Utilization by the Na:K Pump of Human Red Blood Cell Ghosts. *Am. Chem. Soc.* **1978**, *17* (10), 1929–1935.
- (111) Weinstain, R.; Slanina, T.; Kand, D.; Klán, P. Visible-to-NIR-Light Activated Release: From Small Molecules to Nanomaterials. *Chem. Rev.* **2020**, *120* (24), 13135–13272. <https://doi.org/10.1021/acs.chemrev.0c00663>.
- (112) Josa-Culleré, L.; Llebaria, A. In the Search for Photocages Cleavable with Visible Light: An Overview of Recent Advances and Chemical Strategies. *ChemPhotoChem* **2021**, *5* (4), 298–316. <https://doi.org/10.1002/cptc.202000253>.
- (113) Gienger, M.; Hübner, H.; Löber, S.; König, B.; Gmeiner, P. Structure-Based Development of Caged Dopamine D2/D3 Receptor Antagonists. *Sci. Rep.* **2020**, *10* (1), 1–9. <https://doi.org/10.1038/s41598-020-57770-9>.
- (114) WILEY-VCH Verlag GmbH & Co. KGaA, W. *Dynamic Studies in Biology Phototriggers, Photoswitches and Caged Biomolecules*; Goeldner, M., Givens, R., Eds.; 2005.
- (115) Ricart-Ortega, M.; Font, J.; Llebaria, A. GPCR Photopharmacology. *Mol. Cell. Endocrinol.* **2019**, *488*, 36–51. <https://doi.org/10.1016/j.mce.2019.03.003>.
- (116) Gómez-Santacana, X.; de Munnik, S. M.; Vijayachandran, P.; Da Costa Pereira, D.; Bebelman, J. P. M.; de Esch, I. J. P.; Vischer, H. F.; Wijtman, M.; Leurs, R. Photoswitching the Efficacy of a Small-Molecule Ligand for a Peptidergic GPCR: From Antagonism to Agonism. *Angew. Chemie - Int. Ed.* **2018**, *57* (36), 11608–11612. <https://doi.org/10.1002/anie.201804875>.

- (117) Gómez-Santacana, X.; De Munnik, S. M.; Mocking, T. A. M.; Hauwert, N. J.; Sun, S.; Vijayachandran, P.; De Esch, I. J. P.; Vischer, H. F.; Wijnmans, M.; Leurs, R. A Toolbox of Molecular Photoswitches to Modulate the CXCR3 Chemokine Receptor with Light. *Beilstein J. Org. Chem.* **2019**, *15*, 2509–2523. <https://doi.org/10.3762/bjoc.15.244>.
- (118) Leippe, P.; Koehler Leman, J.; Trauner, D. Specificity and Speed: Tethered Photopharmacology. *Biochemistry* **2017**, *56* (39), 5214–5220. <https://doi.org/10.1021/acs.biochem.7b00687>.
- (119) Rovira, X.; Trapero, A.; Pittolo, S.; Zussy, C.; Faucherre, A.; Jopling, C.; Giraldo, J.; Pin, J. P.; Gorostiza, P.; Goudet, C.; Llebaria, A. OptoGluNAM4.1, a Photoswitchable Allosteric Antagonist for Real-Time Control of MGlur4 Receptor Activity. *Cell Chem. Biol.* **2016**, *23* (8), 929–934. <https://doi.org/10.1016/j.chembiol.2016.06.013>.
- (120) Levitz, J.; Pantoja, C.; Gaub, B.; Janovjak, H.; Reiner, A.; Hoagland, A.; Schoppik, D.; Kane, B.; Stawski, P.; Schier, A. F.; Trauner, D.; Isacoff, E. Y. Optical Control of Metabotropic Glutamate Receptors. *Nat. Neurosci.* **2013**, *16* (4), 507–516. <https://doi.org/10.1038/nn.3346>.
- (121) Donthamsetti, P. C.; Winter, N.; Schönberger, M.; Levitz, J.; Stanley, C.; Javitch, J. A.; Isacoff, E. Y.; Trauner, D. Optical Control of Dopamine Receptors Using a Photoswitchable Tethered Inverse Agonist. *J. Am. Chem. Soc.* **2017**, *139* (51), 18522–18535. <https://doi.org/10.1021/jacs.7b07659>.
- (122) Keppler, A.; Gendreizig, S.; Gronemeyer, T.; Pick, H.; Vogel, H.; Johnsson, K. A General Method for the Covalent Labeling of Fusion Proteins with Small Molecules in Vivo. *Nat. Biotechnol.* **2003**, *21* (1), 86–89. <https://doi.org/10.1038/nbt765>.
- (123) Gautier, A.; Juillerat, A.; Heinis, C.; Corrêa, I. R.; Kindermann, M.; Beaufils, F.; Johnsson, K. An Engineered Protein Tag for Multiprotein Labeling in Living Cells. *Chem. Biol.* **2008**, *15* (2), 128–136. <https://doi.org/10.1016/j.chembiol.2008.01.007>.
- (124) Los, G. V.; Encell, L. P.; McDougall, M. G.; Hartzell, D. D.; Karassina, N.; Zimprich, C.; Wood, M. G.; Learish, R.; Ohana, R. F.; Urh, M.; Simpson, D.; Mendez, J.; Zimmerman, K.; Otto, P.; Vidugiris, G.; Zhu, J.; Darzins, A.; Klauert, D. H.; Bulleit, R. F.; Wood, K. V. HaloTag: A Novel Protein Labeling Technology for Cell Imaging and Protein Analysis. *ACS Chem. Biol.* **2008**, *3* (6), 373–382. <https://doi.org/10.1021/cb800025k>.
- (125) Broichhagen, J.; Damijonaitis, A.; Levitz, J.; Sokol, K. R.; Leippe, P.; Konrad, D.; Isacoff, E. Y.; Trauner, D. Orthogonal Optical Control of a G Protein-Coupled Receptor with a SNAP-Tethered Photochromic Ligand. *ACS Cent. Sci.* **2015**, *1* (7), 383–393. <https://doi.org/10.1021/acscentsci.5b00260>.
- (126) Levitz, J.; Broichhagen, J.; Leippe, P.; Konrad, D.; Trauner, D.; Isacoff, E. Y. Dual Optical Control and Mechanistic Insights into Photoswitchable Group II and III Metabotropic Glutamate Receptors. *Proc. Natl. Acad. Sci. U. S. A.* **2017**, *114* (17), E3546–E3554. <https://doi.org/10.1073/pnas.1619652114>.
- (127) Acosta-Ruiz, A.; Gutzeit, V. A.; Skelly, M. J.; Meadows, S.; Lee, J.; Parekh, P.; Orr, A. G.; Liston, C.; Pleil, K. E.; Broichhagen, J.; Levitz, J. Branched Photoswitchable Tethered Ligands Enable Ultra-Efficient Optical Control and Detection of G Protein-Coupled Receptors In Vivo. *Neuron* **2020**, *105* (3), 446–463. <https://doi.org/10.1016/j.neuron.2019.10.036>.
- (128) Berizzi, A. E.; Goudet, C. *Strategies and Considerations of G-Protein-Coupled Receptor Photopharmacology*, 1st ed.; Elsevier Inc., 2020; Vol. 88. <https://doi.org/10.1016/bs.apha.2019.12.001>.
- (129) Donthamsetti, P. C.; Broichhagen, J.; Vyklicky, V.; Stanley, C.; Fu, Z.; Visel, M.; Levitz, J. L.; Javitch, J. A.; Trauner, D.; Isacoff, E. Y. Genetically Targeted Optical Control of an Endogenous G Protein-

- Coupled Receptor. *J. Am. Chem. Soc.* **2019**, *141* (29), 11522–11530. <https://doi.org/10.1021/jacs.9b02895>.
- (130) Bahamonde, M. I.; Taura, J.; Paoletta, S.; Gakh, A. A.; Chakraborty, S.; Hernando, J.; Fernández-Dueñas, V.; Jacobson, K. A.; Gorostiza, P.; Ciruela, F. Photomodulation of G Protein-Coupled Adenosine Receptors by a Novel Light-Switchable Ligand. *Bioconjug. Chem.* **2014**, *25* (10), 1847–1854. <https://doi.org/10.1021/bc5003373>.
- (131) Duran-corbera, A.; Catena, J.; Otero-Viñas, M.; Llebaria, A.; Rovira, X. Photoswitchable Antagonists for a Precise Spatiotemporal Control of Beta2 Adrenoceptors. *J. Med. Chem.* **2020**, *63*, 8458–8470. <https://doi.org/10.1021/acs.jmedchem.0c00831>.
- (132) Gómez-Santacana, X.; Pittolo, S.; Rovira, X.; Lopez, M.; Zussy, C.; Dalton, J. A. R.; Faucherre, A.; Jopling, C.; Pin, J. P.; Ciruela, F.; Goudet, C.; Giraldo, J.; Gorostiza, P.; Llebaria, A. Illuminating Phenylazopyridines to Photoswitch Metabotropic Glutamate Receptors: From the Flask to the Animals. *ACS Cent. Sci.* **2017**, *3* (1), 81–91. <https://doi.org/10.1021/acscentsci.6b00353>.
- (133) Pittolo, S.; Gómez-Santacana, X.; Eckelt, K.; Rovira, X.; Dalton, J.; Goudet, C.; Pin, J. P.; Llobet, A.; Giraldo, J.; Llebaria, A.; Gorostiza, P. An Allosteric Modulator to Control Endogenous G Protein-Coupled Receptors with Light. *Nat. Chem. Biol.* **2014**, *10* (10), 813–815. <https://doi.org/10.1038/nchembio.1612>.
- (134) Broichhagen, J.; Johnston, N. R.; Von Ohlen, Y.; Meyer-Berg, H.; Jones, B. J.; Bloom, S. R.; Rutter, G. A.; Trauner, D.; Hodson, D. J. Allosteric Optical Control of a Class B G-Protein-Coupled Receptor. *Angew. Chemie - Int. Ed.* **2016**, *55* (19), 5865–5868. <https://doi.org/10.1002/anie.201600957>.
- (135) Broichhagen, J.; Podewin, T.; Meyer-Berg, H.; Von Ohlen, Y.; Johnston, N. R.; Jones, B. J.; Bloom, S. R.; Rutter, G. A.; Hoffmann-Röder, A.; Hodson, D. J.; Trauner, D. Optical Control of Insulin Secretion Using an Incretin Switch. *Angew. Chemie - Int. Ed.* **2015**, *54* (51), 15565–15569. <https://doi.org/10.1002/anie.201506384>.
- (136) Morstein, J.; Hill, R. Z.; Novak, A. J. E.; Feng, S.; Norman, D. D.; Donthamsetti, P. C.; Frank, J. A.; Harayama, T.; Williams, B. M.; Parrill, A. L.; Tigyi, G. J.; Riezman, H.; Isacoff, E. Y.; Bautista, D. M.; Trauner, D. Optical Control of Sphingosine-1-Phosphate Formation and Function. *Nat. Chem. Biol.* **2019**, *15* (6), 623–631. <https://doi.org/10.1038/s41589-019-0269-7>.
- (137) Morstein, J.; Dacheux, M. A.; Norman, D. D.; Shemet, A.; Donthamsetti, P. C.; Citir, M.; Frank, J. A.; Schultz, C.; Schultz, C.; Isacoff, E. Y.; Isacoff, E. Y.; Parrill, A. L.; Tigyi, G. J.; Trauner, D. Optical Control of Lysophosphatidic Acid Signaling. *J. Am. Chem. Soc.* **2020**, *142* (24), 10612–10616. <https://doi.org/10.1021/jacs.0c02154>.
- (138) Carroll, E. C.; Berlin, S.; Levitz, J.; Kienzler, M. A.; Yuan, Z.; Madsen, D.; Larsen, D. S.; Isacoff, E. Y.; Denk, W. Two-Photon Brightness of Azobenzene Photoswitches Designed for Glutamate Receptor Optogenetics. *Proc. Natl. Acad. Sci. U. S. A.* **2015**, *112* (7), E776–E785. <https://doi.org/10.1073/pnas.1416942112>.
- (139) Frank, J. A.; Yushchenko, D. A.; Fine, N. H. F.; Duca, M.; Citir, M.; Broichhagen, J.; Hodson, D. J.; Schultz, C.; Trauner, D. Optical Control of GPR40 Signalling in Pancreatic  $\beta$ -Cells. *Chem. Sci.* **2017**, *8* (11), 7604–7610. <https://doi.org/10.1039/c7sc01475a>.
- (140) Lachmann, D.; Konieczny, A.; Keller, M.; König, B. Photochromic Peptidic NPY Y4 Receptor Ligands. *Org. Biomol. Chem.* **2019**, *17*, 2467–2478. <https://doi.org/10.1039/c8ob03221a>.
- (141) Riefolo, F.; Matera, C.; Garrido-Charles, A.; Gomila, A. M. J.; Sortino, R.; Agnetta, L.; Claro, E.;

- Masgrau, R.; Holzgrabe, U.; Batlle, M.; Decker, M.; Guasch, E.; Gorostiza, P. Optical Control of Cardiac Function with a Photoswitchable Muscarinic Agonist. *J. Am. Chem. Soc.* **2019**, *141* (18), 7628–7636. <https://doi.org/10.1021/jacs.9b03505>.
- (142) Wagner, N.; Schuhmacher, M.; Lohmann, A.; Nadler, A. A Coumarin Triflate Reagent Enables One-Step Synthesis of Photo-Caged Lipid Metabolites for Studying Cell Signaling. *Chem. - A Eur. J.* **2019**, *25* (68), 15483–15487. <https://doi.org/10.1002/chem.201903909>.
- (143) Donthamsetti, P.; Quejada, J. R.; Javitch, J. A.; Vsevolod, V.; Lambert, N. A. Using Bioluminescent Resonance Energy Transfer (BRET) to Characterize Agonist-Induced Arrestin Recruitment to Modified and Unmodified G Protein-Coupled Receptors (GPCRs). *Curr Protoc Pharmacol.* **2015**, *70*, 2.14.1-2.14.14. <https://doi.org/10.1002/0471141755.ph0214s70>.
- (144) Agnetta, L.; Bermudez, M.; Riefolo, F.; Matera, C.; Claro, E.; Messerer, R.; Littmann, T.; Wolber, G.; Holzgrabe, U.; Decker, M. Fluorination of Photoswitchable Muscarinic Agonists Tunes Receptor Pharmacology and Photochromic Properties. *J. Med. Chem.* **2019**, *62* (6), 3009–3020. <https://doi.org/10.1021/acs.jmedchem.8b01822>.
- (145) Schönberger, M.; Trauner, D. A Photochromic Agonist for  $\mu$ -Opioid Receptors. *Angew. Chemie - Int. Ed.* **2014**, *53* (12), 3264–3267. <https://doi.org/10.1002/anie.201309633>.
- (146) Hauwert, N. J.; Mocking, T. A. M.; Da Costa Pereira, D.; Kooistra, A. J.; Wijnen, L. M.; Vreeker, G. C. M.; Verweij, E. W. E.; De Boer, A. H.; Smit, M. J.; De Graaf, C.; Vischer, H. F.; De Esch, I. J. P.; Wijtmans, M.; Leurs, R. Synthesis and Characterization of a Bidirectional Photoswitchable Antagonist Toolbox for Real-Time GPCR Photopharmacology. *J. Am. Chem. Soc.* **2018**, *140* (12), 4232–4243. <https://doi.org/10.1021/jacs.7b11422>.
- (147) Hauwert, N. J.; Mocking, T. A. M.; Da Costa Pereira, D.; Lion, K.; Huppelschoten, Y.; Vischer, H. F.; De Esch, I. J. P.; Wijtmans, M.; Leurs, R. A Photoswitchable Agonist for the Histamine H3 Receptor, a Prototypic Family A G-Protein-Coupled Receptor. *Angew. Chemie - Int. Ed.* **2019**, *58* (14), 4531–4535. <https://doi.org/10.1002/anie.201813110>.
- (148) Farrants, H.; Gutzeit, V. A.; Acosta-Ruiz, A.; Trauner, D.; Johnsson, K.; Levitz, J.; Broichhagen, J. SNAP-Tagged Nanobodies Enable Reversible Optical Control of a G Protein-Coupled Receptor via a Remotely Tethered Photoswitchable Ligand. *ACS Chem. Biol.* **2018**, *13* (9), 2682–2688. <https://doi.org/10.1021/acscchembio.8b00628>.
- (149) Taura, J.; Nolen, E. G.; Cabré, G.; Hernando, J.; Squarzialupi, L.; López-Cano, M.; Jacobson, K. A.; Fernández-Dueñas, V.; Ciruela, F. Remote Control of Movement Disorders Using a Photoactive Adenosine A<sub>2A</sub> Receptor Antagonist. *J. Control. Release* **2018**, *283*, 135–142. <https://doi.org/10.1016/j.jconrel.2018.05.033>.
- (150) Gómez-Santacana, X.; Dalton, J. A. R.; Rovira, X.; Pin, J. P.; Goudet, C.; Gorostiza, P.; Giraldo, J.; Llebaria, A. Positional Isomers of Bispyridine Benzene Derivatives Induce Efficacy Changes on MGLu5negative Allosteric Modulation. *Eur. J. Med. Chem.* **2017**, *127*, 567–576. <https://doi.org/10.1016/j.ejmech.2017.01.013>.
- (151) Westphal, M. V.; Schafroth, M. A.; Sarott, R. C.; Imhof, M. A.; Bold, C. P.; Leippe, P.; Dhopeshwarkar, A.; Grandner, J. M.; Katritch, V.; Mackie, K.; Trauner, D.; Carreira, E. M.; Frank, J. A. Synthesis of Photoswitchable 9-Tetrahydrocannabinol Derivatives Enables Optical Control of Cannabinoid Receptor 1 Signaling. *J. Am. Chem. Soc.* **2017**, *139* (50), 18206–18212. <https://doi.org/10.1021/jacs.7b06456>.
- (152) Banghart, M. R.; Sabatini, B. L. Photoactivatable Neuropeptides for Spatiotemporally Precise

- Delivery of Opioids in Neural Tissue. *Neuron* **2012**, *73* (2), 249–259.  
<https://doi.org/10.1016/j.neuron.2011.11.016>.
- (153) Banghart, M. R.; Williams, J. T.; Shah, R. C.; Lavis, L. D.; Sabatini, B. L. Caged Naloxone Reveals Opioid Signaling Deactivation Kinetics. *Mol. Pharmacol.* **2013**, *84* (5), 687–695.  
<https://doi.org/10.1124/mol.113.088096>.
- (154) Banghart, M. R.; He, X. J.; Sabatini, B. L. A Caged Enkephalin Optimized for Simultaneously Probing Mu and Delta Opioid Receptors. *ACS Chem. Neurosci.* **2018**, *9* (4), 684–690.  
<https://doi.org/10.1021/acscchemneuro.7b00485>.
- (155) Dolles, D.; Strasser, A.; Wittmann, H. J.; Marinelli, O.; Nabissi, M.; Pertwee, R. G.; Decker, M. The First Photochromic Affinity Switch for the Human Cannabinoid Receptor 2. *Adv. Ther.* **2018**, *1* (1), 2–7. <https://doi.org/10.1002/adtp.201700032>.
- (156) Agnetta, L.; Kauk, M.; Canizal, M. C. A.; Messerer, R.; Holzgrabe, U.; Hoffmann, C.; Decker, M. A Photoswitchable Dualsteric Ligand Controlling Receptor Efficacy. *Angew. Chemie - Int. Ed.* **2017**, *56* (25), 7282–7287. <https://doi.org/10.1002/anie.201701524>.
- (157) Prischich, D.; Gomila, A. M. J.; Milla-Navarro, S.; Sangüesa, G.; Diez-Alarcia, R.; Preda, B.; Matera, C.; Batlle, M.; Ramírez, L.; Giralt, E.; Hernando, J.; Guasch, E.; Meana, J. J.; de la Villa, P.; Gorostiza, P. Adrenergic Modulation With Photochromic Ligands. *Angew. Chemie - Int. Ed.* **2021**, *60* (7), 3625–3631. <https://doi.org/10.1002/anie.202010553>.
- (158) Ricart-Ortega, M.; Berizzi, A. E.; Catena, J.; Malhaire, F.; Muñoz, L.; Serra, C.; Lebon, G.; Goudet, C.; Llebaria, A. Development and Validation of a Mass Spectrometry Binding Assay for MGLu5 Receptor. *Anal. Bioanal. Chem.* **2020**, *412* (22), 5525–5535. <https://doi.org/10.1007/s00216-020-02772-9>.
- (159) Ricart-Ortega, M.; Berizzi, A. E.; Pereira, V.; Malhaire, F.; Catena, J.; Font, J.; Gómez-Santacana, X.; Munõz, L.; Zussy, C.; Serra, C.; Rovira, X.; Goudet, C.; Llebaria, A. Mechanistic Insights into Light-Driven Allosteric Control of GPCR Biological Activity. *ACS Pharmacol. Transl. Sci.* **2020**, *3* (5), 883–895. <https://doi.org/10.1021/acspstsci.0c00054>.
- (160) Morstein, J.; Trauner, D. New Players in Phototherapy: Photopharmacology and Bio-Integrated Optoelectronics. *Curr. Opin. Chem. Biol.* **2019**, *50*, 145–151.  
<https://doi.org/10.1016/j.cbpa.2019.03.013>.
- (161) Ray, T. R.; Choi, J.; Bandodkar, A. J.; Krishnan, S.; Gutruf, P.; Tian, L.; Ghaffari, R.; Rogers, J. A. Bio-Integrated Wearable Systems: A Comprehensive Review. *Chem. Rev.* **2019**, *119* (8), 5461–5533.  
<https://doi.org/10.1021/acs.chemrev.8b00573>.
- (162) Dieter, A.; Keppeler, D.; Moser, T. Towards the Optical Cochlear Implant: Optogenetic Approaches for Hearing Restoration. *EMBO Mol. Med.* **2020**, *12* (4), 1–16.  
<https://doi.org/10.15252/emmm.201911618>.
- (163) Paoletti, P.; Ellis-Davies, G. C. R.; Mouro, A. Optical Control of Neuronal Ion Channels and Receptors. *Nat. Rev. Neurosci.* **2019**, *20* (9), 514–532. <https://doi.org/10.1038/s41583-019-0197-2>.
- (164) Tochitsky, I.; Kienzler, M. A.; Isacoff, E.; Kramer, R. H. Restoring Vision to the Blind with Chemical Photoswitches. *Chem. Rev.* **2018**, *118* (21), 10748–10773.  
<https://doi.org/10.1021/acs.chemrev.7b00723>.
- (165) Laprell, L.; Tochitsky, I.; Kaur, K.; Manookin, M. B.; Stein, M.; Barber, D. M.; Schön, C.; Michalakis, S.; Biel, M.; Kramer, R. H.; Sumser, M. P.; Trauner, D.; Van Gelder, R. N. Photopharmacological Control

- of Bipolar Cells Restores Visual Function in Blind Mice. *J. Clin. Invest.* **2017**, *127* (7), 2598–2611. <https://doi.org/10.1172/JCI92156>.
- (166) Wegener, M.; Hansen, M. J.; Driessen, A. J. M.; Szymanski, W.; Feringa, B. L. Photocontrol of Antibacterial Activity: Shifting from UV to Red Light Activation. *J. Am. Chem. Soc.* **2017**, *139* (49), 17979–17986. <https://doi.org/10.1021/jacs.7b09281>.
- (167) Mehta, Z. B.; Johnston, N. R.; Nguyen-Tu, M. S.; Broichhagen, J.; Schultz, P.; Larner, D. P.; Leclerc, I.; Trauner, D.; Rutter, G. A.; Hodson, D. J. Remote Control of Glucose Homeostasis in Vivo Using Photopharmacology. *Sci. Rep.* **2017**, *7* (1), 1–11. <https://doi.org/10.1038/s41598-017-00397-0>.
- (168) Kniazeff, J.; Prézeau, L.; Rondard, P.; Pin, J. P.; Goudet, C. Dimers and beyond: The Functional Puzzles of Class C GPCRs. *Pharmacol. Ther.* **2011**, *130* (1), 9–25. <https://doi.org/10.1016/j.pharmthera.2011.01.006>.
- (169) Habrian, C. H.; Levitz, J.; Vyklicky, V.; Fu, Z.; Hoagland, A.; McCort-Tranchepain, I.; Acher, F.; Isacoff, E. Y. Conformational Pathway Provides Unique Sensitivity to a Synaptic MGluR. *Nat. Commun.* **2019**, *10* (1), 1–13. <https://doi.org/10.1038/s41467-019-13407-8>.
- (170) Doumazane, E.; Scholler, P.; Zwier, J. M.; Trinquet, E.; Rondard, P.; Pin, J. A New Approach to Analyze Cell Surface Protein Complexes Reveals Specific Heterodimeric Metabotropic Glutamate Receptors. *FASEB J.* **2011**, *25* (1), 66–77. <https://doi.org/10.1096/fj.10-163147>.
- (171) Huang, S.; Cao, J.; Jiang, M.; Labesse, G.; Liu, J.; Pin, J. P.; Rondard, P. Interdomain Movements in Metabotropic Glutamate Receptor Activation. *Proc. Natl. Acad. Sci. U. S. A.* **2011**, *108* (37), 15480–15485. <https://doi.org/10.1073/pnas.1107775108>.
- (172) Kniazeff, J.; Galvez, T.; Labesse, G.; Pin, J. P. No Ligand Binding in the GB2 Subunit of the GABAB Receptor Is Required for Activation and Allosteric Interaction between the Subunits. *J. Neurosci.* **2002**, *22* (17), 7352–7361. <https://doi.org/10.1523/jneurosci.22-17-07352.2002>.
- (173) Rondard, P.; Goudet, C.; Kniazeff, J.; Pin, J.; Prézeau, L. The Complexity of Their Activation Mechanism Opens New Possibilities for the Modulation of MGlu and GABA B Class C G Protein-Coupled Receptors. *Neuropharmacology* **2011**, *60* (1), 82–92. <https://doi.org/10.1016/j.neuropharm.2010.08.009>.
- (174) Pin, J. P.; Kniazeff, J.; Goudet, C.; Bessis, A. S.; Liu, J.; Galvez, T.; Acher, F.; Rondard, P.; Prézeau, L. The Activation Mechanism of Class-C G-Protein Coupled Receptors. *Biol. Cell* **2004**, *96* (5), 335–342. <https://doi.org/10.1016/j.biocel.2004.03.005>.
- (175) Møller, T. C.; Moreno-Delgado, D.; Pin, J.-P.; Kniazeff, J. Class C G Protein-Coupled Receptors: Reviving Old Couples with New Partners. *Biophys. Reports* **2017**, *3* (4–6), 57–63. <https://doi.org/10.1007/s41048-017-0036-9>.
- (176) Geng, Y.; Bush, M.; Mosyak, L.; Wang, F.; Fan, Q. R. Structural Mechanism of Ligand Activation in Human GABA B Receptor. *Nature* **2013**, *504* (7479), 254–259. <https://doi.org/10.1038/nature12725>.
- (177) Kunishima, N.; Shimada, Y.; Tsuji, Y.; Sato, T.; Yamamoto, M.; Kumasaka, T.; Nakanishi, S.; Jingami, H.; Morikawa, K. Structural Basis of Glutamate Recognition by a Dimeric Metabotropic Glutamate Receptor. *Nature* **2000**, *407*, 971–977.
- (178) Monn, J. A.; Prieto, L.; Taboada, L.; Pedregal, C.; Hao, J.; Reinhard, M. R.; Henry, S. S.; Goldsmith, P. J.; Beadle, C. D.; Walton, L.; Man, T.; Rudyk, H.; Clark, B.; Tupper, D.; Baker, S. R.; Lamas, C.; Montero, C.; Marcos, A.; Blanco, J.; Bures, M.; Clawson, D. K.; Atwell, S.; Lu, F.; Wang, J.; Russell, M.;



- Heinz, B. A.; Wang, X.; Carter, J. H.; Xiang, C.; Catlow, J. T.; Swanson, S.; Sanger, H.; Broad, L. M.; Johnson, M. P.; Knopp, K. L.; Simmons, R. M. A.; Johnson, B. G.; Shaw, D. B.; Mckinzie, D. L. Synthesis and Pharmacological Characterization of C4-Disubstituted Analogs of 1S,2S,5R,6S-2-Aminobicyclo[3.1.0]Hexane-2,6- Dicarboxylate: Identification of a Potent, Selective Metabotropic Glutamate Receptor Agonist and Determination of Agonist-Bound Huma. *J. Med. Chem.* **2015**, *58* (4), 1776–1794. <https://doi.org/10.1021/jm501612y>.
- (179) Muto, T.; Tsuchiya, D.; Morikawa, K.; Jingami, H. Structures of the Extracellular Regions of the Group II / III Metabotropic Glutamate Receptors. *Proc. Natl. Acad. Sci. U. S. A.* **2007**, *104* (10), 3759–3764.
- (180) Koehl, A.; Hu, H.; Feng, D.; Sun, B.; Zhang, Y.; Robertson, M. J.; Chu, M.; Kobilka, T. S.; Laeremans, T.; Steyaert, J.; Tarrasch, J.; Dutta, S.; Fonseca, R.; Weis, W. I.; Mathiesen, J. M.; Skiniotis, G.; Kobilka, B. K. Structural Insights into the Activation of Metabotropic Glutamate Receptors. *Nature* **2019**, *566*, 79–84. <https://doi.org/10.1038/s41586-019-0881-4>.
- (181) Lin, S.; Han, S.; Cai, X.; Tan, Q.; Zhou, K.; Wang, D.; Wang, X.; Du, J.; Yi, C.; Chu, X.; Dai, A.; Zhou, Y.; Chen, Y.; Zhou, Y.; Liu, H.; Liu, J.; Yang, D.; Wang, M. W.; Zhao, Q.; Wu, B. Structures of G<sub>i</sub>-Bound Metabotropic Glutamate Receptors MGlu2 and MGlu4. *Nature* **2021**, *594*, 583–588. <https://doi.org/10.1038/s41586-021-03495-2>.
- (182) Du, J.; Wang, D.; Fan, H.; Xu, C.; Tai, L.; Lin, S.; Han, S.; Tan, Q.; Wang, X.; Xu, T.; Zhang, H.; Chu, X.; Yi, C.; Liu, P.; Wang, X.; Zhou, Y.; Pin, J.; Rondard, P.; Liu, H.; Liu, J.; Sun, F.; Wu, B.; Zhao, Q. Structures of Human MGlu2 and MGlu7 Homo- and Heterodimers. *Nature* **2021**, *594*, 589–593. <https://doi.org/10.1038/s41586-021-03641-w>.
- (183) Pin, J.; Bettler, B. Review Organization and Functions of MGlu and GABA B Receptor Complexes. *Nature* **2016**, *540* (7631), 60–68. <https://doi.org/10.1038/nature20566>.
- (184) Tsuchiya, D.; Kunishima, N.; Kamiya, N.; Jingami, H.; Morikawa, K. Structural Views of the Ligand-Binding Cores of a Metabotropic Glutamate Receptor Complexed with an Antagonist and Both Glutamate and Gd<sup>3+</sup>. *Proc. Natl. Acad. Sci. U. S. A.* **2002**, *99* (5), 2660–2665.
- (185) Kniazeff, J.; Bessis, A.; Maurel, D.; Ansanay, H.; Prézeau, L.; Pin, J. Closed State of Both Binding Domains of Homodimeric MGlu Receptors Is Required for Full Activity. **2004**, *11* (8), 706–713. <https://doi.org/10.1038/nsmb794>.
- (186) Hlavackova, V.; Goudet, C.; Kniazeff, J.; Zikova, A.; Vol, C.; Trojanova, J.; Pin, J.; Pre, L.; Blahos, J. Evidence for a Single Heptahelical Domain Being Turned on upon Activation of a Dimeric GPCR. *EMBO J.* **2005**, *24*, 499–509. <https://doi.org/10.1038/sj.emboj.7600557>.
- (187) Rondard, P.; Pin, J. Dynamics and Modulation of Metabotropic Glutamate Receptors. *Curr. Opin. Pharmacol.* **2015**, *20*, 95–101. <https://doi.org/10.1016/j.coph.2014.12.001>.
- (188) Marshall, F. H.; Jones, K. A.; Kaupmann, K.; Bettler, B. GABA(B) Receptors - The First 7TM Heterodimers. *Trends Pharmacol. Sci.* **1999**, *20* (10), 396–399. [https://doi.org/10.1016/S0165-6147\(99\)01383-8](https://doi.org/10.1016/S0165-6147(99)01383-8).
- (189) Galvez, T.; Prézeau, L.; Milioti, G.; Franek, M.; Joly, C.; Froestl, W.; Bettler, B.; Bertrand, H. O.; Blahos, J.; Pin, J. P. Mapping the Agonist-Binding Site of GABAB Type 1 Subunit Sheds Light on the Activation Process of GABAB Receptors. *J. Biol. Chem.* **2000**, *275* (52), 41166–41174. <https://doi.org/10.1074/jbc.M007848200>.
- (190) Gassmann, M.; Shaban, H.; Sansig, G.; Haller, C.; Barbieri, S.; Humeau, Y.; Mu, M.; Kinzel, B.; Klebs, K.; Schmutz, M.; Froestl, W.; Heid, J.; Kelly, P. H.; Gentry, C.; Jaton, A.; Putten, H. Van Der; Lecourtier,

- L.; Mosbacher, J.; Cryan, J. F.; Fritschy, J.; Lu, A.; Kaupmann, K.; Bettler, B. Redistribution of GABA B(1) Protein and Atypical GABA B Responses in GABA B(2) -Deficient Mice. *J. Neurosci.* **2004**, *24* (27), 6086–6097. <https://doi.org/10.1523/JNEUROSCI.5635-03.2004>.
- (191) Galvez, T.; Duthey, B.; Kniazeff, J.; Blahos, J.; Rovelli, G.; Bettler, B.; Pre, L. Allosteric Interactions between GB1 and GB2 Subunits Are Required for Optimal GABA B Receptor Function. *EMBO J.* **2001**, *20* (9), 2152–2159.
- (192) Yin, S.; Noetzel, M. J.; Johnson, K. A.; Zamorano, R.; Jalan-sakrikar, N.; Gregory, K. J.; Conn, P. J.; Niswender, C. M. Selective Actions of Novel Allosteric Modulators Reveal Functional Heteromers of Metabotropic Glutamate Receptors in the CNS. *J. Neurosci.* **2014**, *34* (1), 79–94. <https://doi.org/10.1523/JNEUROSCI.1129-13.2014>.
- (193) Pandya, N. J.; Klaassen, R. V.; Schors, R. C. Van Der; Slotman, J. A.; Houtsmuller, A.; Smit, A. B.; Li, K. W. Group 1 Metabotropic Glutamate Receptors 1 and 5 Form a Protein Complex in Mouse Hippocampus and Cortex. *Proteomics* **2016**, *16*, 2698–2705. <https://doi.org/10.1002/pmic.201500400>.
- (194) Ferraguti, F.; Klausberger, T.; Cobden, P.; Baude, A.; Roberts, J. D. B.; Szucs, P.; Kinoshita, A.; Shigemoto, R.; Somogyi, P.; Dalezios, Y. Metabotropic Glutamate Receptor 8-Expressing Nerve Terminals Target Subsets of GABAergic Neurons in the Hippocampus. *J. Neurosci.* **2005**, *25* (45), 10520–10536. <https://doi.org/10.1523/JNEUROSCI.2547-05.2005>.
- (195) Vischer, H. F.; Castro, M.; Pin, J. EXPLORING THE BIOLOGY OF GPCRs : FROM IN VITRO TO IN VIVO G Protein – Coupled Receptor Multimers : A Question Still Open Despite the Use of Novel Approaches. *Mol. Pharmacol.* **2015**, *88*, 561–571. <https://doi.org/10.1124/mol.115.099440>.
- (196) Hlavackova, V.; Zabel, U.; Frankova, D.; Bätz, J.; Hoffmann, C.; Prezeau, L.; Pin, J. P.; Blahos, J.; Lohse, M. J. Sequential Inter- and Intrasubunit Rearrangements during Activation of Dimeric Metabotropic Glutamate Receptor 1. *Sci. Signal.* **2012**, *5* (237), 1–12. <https://doi.org/10.1126/scisignal.2002720>.
- (197) Grushevskiy, E. O.; Kukaj, T.; Schmauder, R.; Bock, A.; Zabel, U.; Schwabe, T.; Benndorf, K.; Lohse, M. J. Stepwise Activation of a Class C GPCR Begins with Millisecond Dimer Rearrangement. *Proc. Natl. Acad. Sci. U. S. A.* **2019**, *116* (20), 10150–10155. <https://doi.org/10.1073/pnas.1900261116>.
- (198) Hofmann, K. P.; Scheerer, P.; Hildebrand, P. W.; Choe, H.; Park, J. H.; Heck, M.; Ernst, O. P. A G Protein-Coupled Receptor at Work : The Rhodopsin Model. *Trends Pharmacol. Sci.* **2009**, *34* (11), 540–552. <https://doi.org/10.1016/j.tibs.2009.07.005>.
- (199) Lohse, M. J.; Hofmann, K. P. Spatial and Temporal Aspects of Signaling by G-Protein-Coupled Receptors. *Mol. Pharmacol.* **2015**, *88* (3), 572–578. <https://doi.org/10.1124/mol.115.100248>.
- (200) Lohse, M. J.; Maiellaro, I.; Calebiro, D. Kinetics and Mechanism of G Protein-Coupled Receptor Activation. *Curr. Opin. Cell Biol.* **2014**, *27* (1), 87–93. <https://doi.org/10.1016/j.ceb.2013.11.009>.
- (201) Miyawaki, A. Development of Probes for Cellular Functions Using Fluorescent Proteins and Fluorescence Resonance Energy Transfer. *Annu. Rev. Biochem.* **2011**, *80*, 357–373. <https://doi.org/10.1146/annurev-biochem-072909-094736>.
- (202) Julio-Pieper, M.; Flor, P. J.; Dinan, T. G.; Cryan, J. F. Exciting Times beyond the Brain : Metabotropic Glutamate Receptors in Peripheral and Non-Neural Tissues. *Pharmacol. Rev.* **2011**, *63* (1), 35–58. <https://doi.org/10.1124/pr.110.004036.35>.
- (203) Volk, L.; Chiu, S. L.; Sharma, K.; Huganir, R. L. Glutamate Synapses in Human Cognitive Disorders.

- Annu. Rev. Neurosci.* **2015**, *38*, 127–149. <https://doi.org/10.1146/annurev-neuro-071714-033821>.
- (204) Marx, M.; Billups, D.; Billups, B. Maintaining the Presynaptic Glutamate Supply for Excitatory Neurotransmission. *J. Neurosci. Res.* **2015**, *93*, 1031–1044. <https://doi.org/10.1002/jnr.23561>.
- (205) Danbolt, N. C. Glutamate Uptake. *Prog. Neurobiol.* **2001**, *65*, 1–105. [https://doi.org/S0301-0082\(00\)00067-8](https://doi.org/S0301-0082(00)00067-8).
- (206) Pin, J.; Colle, C. De; Bessis, A.; Acher, F. New Perspectives for the Development of Selective Metabotropic Glutamate Receptor Ligands. *Eur. J. Pharmacol.* **1999**, *375*, 277–294. <https://doi.org/S0014-2999-99-00258-7>.
- (207) Nicoletti, F.; Bockaert, J.; Collingridge, G. L.; Conn, P. J.; Ferraguti, F.; Schoepp, D. D.; Wroblewski, J. T.; Pin, J. P. Metabotropic Glutamate Receptors: From the Workbench to the Bedside. *Neuropharmacology* **2011**, *60* (7–8), 1017–1041. <https://doi.org/10.1016/j.neuropharm.2010.10.022>.
- (208) Sheffler, D. J.; Gregory, K. J.; Rook, J. M.; Conn, P. J. Allosteric Modulation of Metabotropic Glutamate Receptors. In *Advances in Pharmacology*; Elsevier Inc., 2011; Vol. 62, pp 37–77. <https://doi.org/10.1016/B978-0-12-385952-5.00010-5>.
- (209) Ménard, C.; Quirion, R. Group 1 Metabotropic Glutamate Receptor Function and Its Regulation of Learning and Memory in the Aging Brain. *Front. Pharmacol.* **2012**, *3* (182), 1–12. <https://doi.org/10.3389/fphar.2012.00182>.
- (210) D’Antoni, S.; Spatuzza, M.; Bonaccorso, C. M.; Musumeci, S. A.; Ciranna, L.; Nicoletti, F.; Huber, K. M.; Catania, M. V. Dysregulation of Group-I Metabotropic Glutamate (MGlu) Receptor Mediated Signalling in Disorders Associated with Intellectual Disability and Autism. *Neurosci. Biobehav. Rev.* **2014**, *46* (P2), 228–241. <https://doi.org/10.1016/j.neubiorev.2014.02.003>.
- (211) Frank, R. A. W.; McRae, A. F.; Pocklington, A. J.; van de Lagemaat, L. N.; Navarro, P.; Croning, M. D. R.; Komiyama, N. H.; Bradley, S. J.; Challiss, R. A. J.; Armstrong, J. D.; Finn, R. D.; Malloy, M. P.; MacLean, A. W.; Harris, S. E.; Starr, J. M.; Bhaskar, S. S.; Howard, E. K.; Hunt, S. E.; Coffey, A. J.; Ranganath, V.; Deloukas, P.; Rogers, J.; Muir, W. J.; Deary, I. J.; Blackwood, D. H.; Visscher, P. M.; Grant, S. G. N. Clustered Coding Variants in the Glutamate Receptor Complexes of Individuals with Schizophrenia and Bipolar Disorder. *PLoS One* **2011**, *6* (4), e19011. <https://doi.org/10.1371/journal.pone.0019011>.
- (212) De Bartolomeis, A.; Szumlinski, K. K. Group 1 Metabotropic Glutamate Receptors and Schizophrenia. *Wiley Interdiscip. Rev. Membr. Transp. Signal.* **2012**, *1* (1), 94–103. <https://doi.org/10.1002/wmts.15>.
- (213) Flor, P. J.; Acher, F. C. Orthosteric versus Allosteric GPCR Activation : The Great Challenge of Group-III MGluRs. *Biochem. Pharmacol.* **2012**, *84* (4), 414–424. <https://doi.org/10.1016/j.bcp.2012.04.013>.
- (214) Tora, S.; Rovira, X.; Dione, I.; Bertrand, H.; Brabet, I.; Koninck, Y. De; Doyon, N.; Pin, J.; Acher, F.; Goudet, C. Allosteric Modulation of Metabotropic Glutamate Receptors by Chloride Ions. *FASEB J.* **2015**, *29*, 4174–4188. <https://doi.org/10.1096/fj.14-269746>.
- (215) Tora, A. S.; Rovira, X.; Cao, A. M.; Cabayé, A.; Olofsson, L.; Malhaire, F.; Scholler, P.; Baik, H.; Van Eeckhaut, A.; Smolders, I.; Rondard, P.; Margeat, E.; Acher, F.; Pin, J. P.; Goudet, C. Chloride Ions Stabilize the Glutamate-Induced Active State of the Metabotropic Glutamate Receptor 3. *Neuropharmacology* **2018**, *140*, 275–286. <https://doi.org/10.1016/j.neuropharm.2018.08.011>.

- (216) Conn, P. J.; Lindsley, C. W.; Meiler, J.; Niswender, C. M. Opportunities and Challenges in the Discovery of Allosteric Modulators of GPCRs for Treating CNS Disorders. *Nat. Rev. Drug Discov.* **2014**, *13*, 692–708. <https://doi.org/10.1038/nrd4308>.
- (217) Nickols, H. H.; Conn, J. P. Development of Allosteric Modulators of GPCRs for Treatment of CNS Disorders. *Neurobiol. Dis.* **2014**, *61*, 55–71. <https://doi.org/10.1016/j.nbd.2013.09.013>.
- (218) Wood, M. R.; Hopkins, C. R.; Brogan, J. T.; Conn, P. J.; Lindsley, C. W. “Molecular Switches” on MGLuR Allosteric Ligands That Modulate Modes of Pharmacology. *Biochemistry* **2011**, *50* (13), 2403–2410. <https://doi.org/10.1021/bi200129s>.
- (219) Cho, H. P.; Garcia-Barrantes, P. M.; Brogan, J. T.; Hopkins, C. R.; Niswender, C. M.; Rodriguez, A. L.; Venable, D. F.; Morrison, R. D.; Bubser, M.; Daniels, J. S.; Jones, C. K.; Conn, P. J.; Lindsley, C. W. Chemical Modulation of Mutant MGLu1 Receptors Derived from Deleterious GRM1 Mutations Found in Schizophrenics. *ACS Chem. Biol.* **2014**, *9* (10), 2334–2346. <https://doi.org/10.1021/cb500560h>.
- (220) Garcia-Barrantes, P. M.; Cho, H. P.; Niswender, C. M.; Byers, F. W.; Locuson, C. W.; Blobaum, A. L.; Xiang, Z.; Rook, J. M.; Conn, P. J.; Lindsley, C. W. Development of Novel, CNS Penetrant Positive Allosteric Modulators for the Metabotropic Glutamate Receptor Subtype 1 (MGLu1), Based on an N-(3-Chloro-4-(1,3-Dioxoisindolin-2-Yl)Phenyl)-3-Methylfuran-2-Carboxamide Scaffold, That Potentiate Wild Type and M. *J. Med. Chem.* **2015**, *58* (20), 7959–7971. <https://doi.org/10.1021/acs.jmedchem.5b00727>.
- (221) Garcia-Barrantes, P. M.; Cho, H. P.; Blobaum, A. L.; Niswender, C. M.; Conn, P. J.; Lindsley, C. W. Lead Optimization of the VU0486321 Series of MGLu1 PAMs. Part 1: SAR of Modifications to the Central Aryl Core. *Bioorganic Med. Chem. Lett.* **2015**, *25* (22), 5107–5110. <https://doi.org/10.1016/j.bmcl.2015.10.013>.
- (222) Garcia-Barrantes, P. M.; Cho, H. P.; Metts, A. M.; Blobaum, A. L.; Niswender, C. M.; Conn, P. J.; Lindsley, C. W. Lead Optimization of the VU0486321 Series of MGLu1PAMs. Part 2: SAR of Alternative 3-Methyl Heterocycles and Progress towards an in Vivo Tool. *Bioorganic Med. Chem. Lett.* **2016**, *26* (3), 751–756. <https://doi.org/10.1016/j.bmcl.2015.12.104>.
- (223) Garcia-Barrantes, P. M.; Cho, H. P.; Blobaum, A. L.; Niswender, C. M.; Conn, P. J.; Lindsley, C. W. Lead Optimization of the VU0486321 Series of MGLu1 PAMs. Part 3. Engineering Plasma Stability by Discovery and Optimization of Isoindolinone Analogs. *Bioorganic Med. Chem. Lett.* **2016**, *26* (8), 1869–1872. <https://doi.org/10.1016/j.bmcl.2016.03.031>.
- (224) Pedro M. Garcia Barrantes. TOTAL SYNTHESIS OF GOMBAMIDE A AND ACTINOPHENANTHROLINE A. DISCOVERY, OPTIMIZATION AND CHARACTERIZATION OF NOVEL POSITIVE ALLOSTERIC MODULATORS FOR THE METABOTROPIC GLUTAMATE RECEPTOR SUBTYPE 1, Vanderbilt University, 2016.
- (225) Crupi, R.; Impellizzeri, D.; Cuzzocrea, S. Role of Metabotropic Glutamate Receptors in Neurological Disorders. *Front. Mol. Neurosci.* **2019**, *12* (20), 1–11. <https://doi.org/10.3389/fnmol.2019.00020>.
- (226) Gradini, R.; Ngomba, R.; Nicoletti, F.; Bruno, V.; Ngomba, R. T.; Gradini, R.; Battaglia, G. Metabotropic Glutamate Receptors as Drug Targets: What’s New? *Curr. Opin. Pharmacol.* **2015**, *20*, 89–94. <https://doi.org/10.1016/j.coph.2014.12.002>.
- (227) Ayoub, M. A.; Angelicheva, D.; Vile, D.; Chandler, D.; Morar, B.; Cavanaugh, J. A.; Visscher, P. M.; Jablensky, A.; Pflieger, K. D. G.; Kalaydjieva, L. Deleterious GRM1 Mutations in Schizophrenia. *PLoS One* **2012**, *7* (3). <https://doi.org/10.1371/journal.pone.0032849>.

- (228) A.R. Dalton, J.; Lans, I.; Rovira, X.; Malhaire, F.; Gómez-Santacana, X.; Pittolo, S.; Gorostiza, P.; Llebaria, A.; Goudet, C.; Pin, J.-P.; Giraldo, J. Shining Light on an MGlu5 Photoswitchable NAM: A Theoretical Perspective. *Curr. Neuropharmacol.* **2015**, *14* (5), 441–454. <https://doi.org/10.2174/1570159x13666150407231417>.
- (229) Pittolo, S.; Lee, H.; Lladó, A.; Tosi, S.; Bosch, M.; Bardia, L.; Gómez-Santacana, X.; Llebaria, A.; Soriano, E.; Colombelli, J.; Poskanzer, K. E.; Perea, G.; Gorostiza, P. Reversible Silencing of Endogenous Receptors in Intact Brain Tissue Using 2-Photon Pharmacology. *Proc. Natl. Acad. Sci. U. S. A.* **2019**, *116* (27), 13680–13689. <https://doi.org/10.1073/pnas.1900430116>.
- (230) Donthamsetti, P.; Konrad, D. B.; Hetzler, B.; Fu, Z.; Trauner, D.; Isacoff, E. Y. Selective Photoswitchable Allosteric Agonist of a G Protein-Coupled Receptor. *J. Am. Chem. Soc.* **2021**, *143* (24), 8951–8956. <https://doi.org/10.1021/jacs.1c02586>.
- (231) Galici, R.; Jones, C. K.; Hemstapat, K.; Nong, Y.; Echemendia, N. G.; Williams, L. C.; De Paulis, T.; Conn, P. J. Biphenyl-Indanone A, a Positive Allosteric Modulator of the Metabotropic Glutamate Receptor Subtype 2, Has Antipsychotic- and Anxiolytic-like Effects in Mice. *J. Pharmacol. Exp. Ther.* **2006**, *318* (1), 173–185. <https://doi.org/10.1124/jpet.106.102046>.
- (232) Engers, D. W.; Field, J. R.; Le, U.; Zhou, Y.; Bolinger, J. D.; Zamorano, R.; Blobaum, A. L.; Jones, C. K.; Jadhav, S.; Weaver, C. D.; Conn, P. J.; Lindsley, C. W.; Niswender, C. M.; Hopkins, C. R. Discovery, Synthesis, and Structure-Activity Relationship Development of a Series of N-(4-Acetamido)Phenylpicolinamides as Positive Allosteric Modulators of Metabotropic Glutamate Receptor 4 (MGlu4) with CNS Exposure in Rats. *J. Med. Chem.* **2011**, *54* (4), 1106–1110. <https://doi.org/10.1021/jm101271s>.
- (233) Hashimoto, T.; Inazawa, J.; Okamoto, N.; Tagawa, Y.; Bessho, A.; Honda, Y.; Nakanishi, S. The Whole Nucleotide Sequence and Chromosomal Localization of the Gene for Human Metabotropic Glutamate Receptor Subtype 6. *Eur. J. Neurosci.* **1997**, *9* (6), 1226–1235. <https://doi.org/10.1111/j.1460-9568.1997.tb01477.x>.
- (234) Weichert, D.; Gmeiner, P. Covalent Molecular Probes for Class A G Protein-Coupled Receptors: Advances and Applications. *ACS Chem. Biol.* **2015**, *10*, 1376–1386. <https://doi.org/10.1021/acscchembio.5b00070>.
- (235) Bossi, S.; Helleringer, R.; Galante, M.; Monlleó, E.; Trapero, A.; Rovira, X.; Daniel, H.; Llebaria, A.; McLean, H. A Light-Controlled Allosteric Modulator Unveils a Role for MGlu4 Receptors during Early Stages of Ischemia in the Rodent Cerebellar Cortex. *Front. Cell. Neurosci.* **2018**, *12* (449), 1–15. <https://doi.org/10.3389/fncel.2018.00449>.
- (236) Christopher, J. A.; Aves, S. J.; Bennett, K. A.; Doré, A. S.; Errey, J. C.; Jazayeri, A.; Marshall, F. H.; Okrasa, K.; Serrano-Vega, M. J.; Tehan, B. G.; Wiggin, G. R.; Congreve, M. Fragment and Structure-Based Drug Discovery for a Class C GPCR: Discovery of the MGlu5 Negative Allosteric Modulator HTL14242 (3-Chloro-5-[6-(5-Fluoropyridin-2-yl)Pyrimidin-4-yl]Benzonitrile). *J. Med. Chem.* **2015**, *58* (16), 6653–6664. <https://doi.org/10.1021/acs.jmedchem.5b00892>.
- (237) Bennett, K. A.; Christopher, J. A.; Tehan, B. G. *Structure-Based Discovery and Development of Metabotropic Glutamate Receptor 5 Negative Allosteric Modulators*, 1st ed.; Elsevier Inc., 2020; Vol. 88. <https://doi.org/10.1016/bs.apha.2020.03.001>.
- (238) Gómez-Santacana, X.; Rovira, X.; Dalton, J. A.; Goudet, C.; Pin, J. P.; Gorostiza, P.; Giraldo, J.; Llebaria, A. A Double Effect Molecular Switch Leads to a Novel Potent Negative Allosteric Modulator of Metabotropic Glutamate Receptor 5. *Medchemcomm* **2014**, *5* (10), 1548–1554. <https://doi.org/10.1039/c4md00208c>.

- (239) Kalgutkar, A.; Gardner, I.; Obach, R.; Shaffer, C.; Callegari, E.; Henne, K.; Mutlib, A.; Dalvie, D.; Lee, J.; Nakai, Y.; O'Donnell, J.; Boer, J.; Harriman, S. A Comprehensive Listing of Bioactivation Pathways of Organic Functional Groups. *Curr. Drug Metab.* **2005**, *6* (3), 161–225. <https://doi.org/10.2174/1389200054021799>.
- (240) Zhuo, X.; Huang, X. S.; Degnan, A. P.; Snyder, L. B.; Yang, F.; Huang, H.; Shu, Y. Z.; Johnson, B. M. Identification of Glutathione Conjugates of Acetylene-Containing Positive Allosteric Modulators of Metabotropic Glutamate Receptor Subtype 5. *Drug Metab. Dispos.* **2015**, *43* (4), 578–589. <https://doi.org/10.1124/dmd.114.061879>.
- (241) Marin, J. C. A.; Goadsby, P. J. Glutamatergic Fine Tuning with ADX-10059: A Novel Therapeutic Approach for Migraine? *Expert Opin. Investig. Drugs* **2010**, *19* (4), 555–561. <https://doi.org/10.1517/13543781003691832>.
- (242) Nyffenegger, C.; Pasquinet, E.; Suzenet, F.; Poullain, D.; Jarry, C.; Léger, J. M.; Guillaumet, G. An Efficient Route to Polynitrogen-Fused Tricycles via a Nitrene-Mediated N-N Bond Formation under Microwave Irradiation. *Tetrahedron* **2008**, *64* (40), 9567–9573. <https://doi.org/10.1016/j.tet.2008.07.055>.
- (243) Priewisch, B.; Rück-Braun, K. Efficient Preparation of Nitrosoarenes for the Synthesis of Azobenzenes. *J. Org. Chem.* **2005**, *70* (6), 2350–2352. <https://doi.org/10.1021/jo048544x>.
- (244) Banghart, M. R.; Trauner, D. A <sup>1</sup>H NMR Assay for Measuring the Photostationary States of Photoswitchable Ligands. *Methods Mol. Biol.* **2013**, *995*, 107–120. [https://doi.org/10.1007/978-1-62703-345-9\\_8](https://doi.org/10.1007/978-1-62703-345-9_8).
- (245) Vilar, B.; Busserolles, J.; Ling, B.; Laffray, S.; Ulmann, L.; Malhaire, F.; Chapuy, E.; Aissouni, Y.; Etienne, M.; Bourinet, E.; Acher, F.; Pin, J. P.; Eschalier, A.; Goudet, C. Alleviating Pain Hypersensitivity through Activation of Type 4 Metabotropic Glutamate Receptor. *J. Neurosci.* **2013**, *33* (48), 18951–18965. <https://doi.org/10.1523/JNEUROSCI.1221-13.2013>.
- (246) Wang, H.; Jiang, W.; Yang, R.; Li, Y. Spinal Metabotropic Glutamate Receptor 4 Is Involved in Neuropathic Pain. *Neuroreport* **2011**, *22* (5), 244–248. <https://doi.org/10.1097/WNR.0b013e3283453843>.
- (247) Davis, M. J.; Haley, T.; Duvoisin, R. M.; Raber, J. Measures of Anxiety, Sensorimotor Function, and Memory in Male and Female MGLuR4 <sup>-/-</sup> Mice. *Behav. Brain Res.* **2012**, *229* (1), 21–28. <https://doi.org/10.1016/j.bbr.2011.12.037>.
- (248) Davis, M. J.; Iancu, O. D.; Acher, F. C.; Stewart, B. M.; Eiwaz, M. A.; Duvoisin, R. M.; Raber, J. Role of MGLuR4 in Acquisition of Fear Learning and Memory. *Neuropharmacology* **2013**, *66*, 365–372. <https://doi.org/10.1016/j.neuropharm.2012.07.038>.
- (249) Panarese, J. D.; Engers, D. W.; Wu, Y. J.; Bronson, J. J.; Macor, J. E.; Chun, A.; Rodriguez, A. L.; Felts, A. S.; Engers, J. L.; Loch, M. T.; Emmitte, K. A.; Castelhana, A. L.; Kates, M. J.; Nader, M. A.; Jones, C. K.; Blobaum, A. L.; Conn, P. J.; Niswender, C. M.; Hopkins, C. R.; Lindsley, C. W. Discovery of VU2957 (Valigluxax): An MGLu 4 Positive Allosteric Modulator Evaluated as a Preclinical Candidate for the Treatment of Parkinson's Disease. *ACS Med. Chem. Lett.* **2019**, *10* (3), 255–260. <https://doi.org/10.1021/acsmchemlett.8b00426>.
- (250) Marino, M. J.; Hess, J. F.; Liverton, N. Targeting the Metabotropic Glutamate Receptor MGLuR4 for the Treatment of Diseases of the Central Nervous System. *Curr. Top. Med. Chem.* **2005**, *5*, 885–895.
- (251) Celli, R.; Santolini, I.; Luijtelaar, G. Van; Ngomba, R. T.; Nicoletti, F.; Celli, R.; Santolini, I.; Luijtelaar, G.

- Van; Ngomba, R. T. Targeting Metabotropic Glutamate Receptors in the Treatment of Epilepsy: Rationale and Current Status. *Expert Opin. Ther. Targets* **2019**, *23* (4), 341–351. <https://doi.org/10.1080/14728222.2019.1586885>.
- (252) Gutzeit, V. A.; Acosta-Ruiz, A.; Munguba, H.; Häfner, S.; Landra-Willm, A.; Mathes, B.; Mony, J.; Yarotski, D.; Börjesson, K.; Liston, C.; Sandoz, G.; Levitz, J.; Broichhagen, J. A Fine-Tuned Azobenzene for Enhanced Photopharmacology in Vivo. *Cell Chem. Biol.* **2021**, *28*, 1–16. <https://doi.org/10.1016/j.chembiol.2021.02.020>.
- (253) Swanson, C. J.; Bures, M.; Johnson, M. P.; Linden, A.; Monn, J. A.; Schoepp, D. D. METABOTROPIC GLUTAMATE RECEPTORS AS NOVEL TARGETS FOR ANXIETY AND STRESS DISORDERS. *Nat. Rev. Drug Discov.* **2005**, *4*, 131–144. <https://doi.org/10.1038/nrd1630>.
- (254) Kohara, A.; Takahashi, M.; Yatsugi, S.; Tamura, S.; Shitaka, Y.; Hayashibe, S.; Kawabata, S.; Okada, M. Neuroprotective Effects of the Selective Type 1 Metabotropic Glutamate Receptor Antagonist YM-202074 in Rat Stroke Models. *Brain Res.* **2008**, *1191*, 168–179. <https://doi.org/10.1016/j.brainres.2007.11.035>.
- (255) Conquet, F.; Bashirt, Z. I.; Daviest, C. H.; Daniel, H.; Ferraguti, F.; Bordi, F.; Franz-Bacon, K.; Reggiani, A.; Matarese, V.; Condé, F.; Collingridge, G. L.; Crepel, F. Motor Deficit and Impairment of Synaptic Plasticity in Mice Lacking MGluR1. *Nature* **1994**, *372* (6503), 237–243. <https://doi.org/10.1038/372237a0>.
- (256) Yohn, S. E.; Foster, D. J.; Covey, D. P.; Moehle, M. S.; Galbraith, J.; Garcia-Barrantes, P. M.; Cho, H. P.; Bubser; Blobaum, A. L.; Joffe, M. E.; Cheer, J. F.; Jones, C. K.; Lindsley, C. W.; Conn, P. J. Activation of the MGlu 1 Metabotropic Glutamate Receptor Has Antipsychotic-like Effects and Is Required for Ef Fi Cacy of M 4 Muscarinic Receptor Allosteric Modulators. *Mol. Psychiatry* **2020**, *25*, 2786–2799. <https://doi.org/10.1038/s41380-018-0206-2>.
- (257) Lavreysen, H.; Nóbrega Pereira, S.; Leysen, J. E.; Langlois, X.; Lesage, A. S. J. Metabotropic Glutamate 1 Receptor Distribution and Occupancy in the Rat Brain : A Quantitative Autoradiographic Study Using [3H]R214127. *Neuropharmacology* **2004**, *46*, 609–619. <https://doi.org/10.1016/j.neuropharm.2003.11.014>.
- (258) Beharry, A. A.; Woolley, G. A. Azobenzene Photoswitches for Biomolecules. *Chem. Soc. Rev.* **2011**, *40* (8), 4422–4437. <https://doi.org/10.1039/c1cs15023e>.
- (259) Jones, C. K.; Bubser, M.; Thompson, A. D.; Dickerson, J. W.; Turle-Lorenzo, N.; Amalric, M.; Blobaum, A. L.; Bridges, T. M.; Morrison, R. D.; Jadhav, S.; Engers, D. W.; Italiano, K.; Bode, J.; Daniels, J. S.; Lindsley, C. W.; Hopkins, C. R.; Conn, P. J.; Niswender, C. M. The Metabotropic Glutamate Receptor 4-Positive Allosteric Modulator VU0364770 Produces Efficacy Alone and in Combination with L-DOPA or an Adenosine 2A Antagonist in Preclinical Rodent Models of Parkinson’s Disease. *J. Pharmacol. Exp. Ther.* **2012**, *340* (2), 404–421. <https://doi.org/10.1124/jpet.111.187443>.
- (260) Bennouar, K. E.; Uberti, M. A.; Melon, C.; Bacolod, M. D.; Jimenez, H. N.; Cajina, M.; Kerkerian-Le Goff, L.; Doller, D.; Gubellini, P. Synergy between L-DOPA and a Novel Positive Allosteric Modulator of Metabotropic Glutamate Receptor 4: Implications for Parkinson’s Disease Treatment and Dyskinesia. *Neuropharmacology* **2013**, *66*, 158–169. <https://doi.org/10.1016/j.neuropharm.2012.03.022>.
- (261) Gobira, P. H.; Ropke, J.; Aguiar, D. C.; Crippa, J. A. S.; Moreira, F. A. Animal Models for Predicting the Efficacy and Side Effects of Antipsychotic Drugs. *Rev. Bras. Psiquiatr.* **2013**, *35*, 132–139. <https://doi.org/10.1590/1516-4446-2013-1164>.

- (262) Masuho, I.; Ostrovskaya, O.; Kramer, G. M.; Jones, C. D.; Xie, K.; Martemyanov, K. A. Distinct Profiles of Functional Discrimination among G Proteins Determine the Actions of G Protein-Coupled Receptors. *Sci. Signal.* **2015**, *8* (405), 1–16. <https://doi.org/10.1126/scisignal.aab4068>.
- (263) Satoh, A.; Nagatomi, Y.; Hirata, Y.; Ito, S.; Suzuki, G.; Kimura, T.; Maehara, S.; Hikichi, H.; Satow, A.; Hata, M.; Ohta, H.; Kawamoto, H. Discovery and in Vitro and in Vivo Profiles of 4-Fluoro-N-[4-[6-(Isopropylamino)Pyrimidin-4-yl]-1,3-Thiazol-2-yl]-N-Methylbenzamide as Novel Class of an Orally Active Metabotropic Glutamate Receptor 1 (MGLuR1) Antagonist. *Bioorg. Med. Chem. Lett.* **2009**, *19* (18), 5464–5468. <https://doi.org/10.1016/j.bmcl.2009.07.097>.
- (264) Yamasaki, T.; Fujinaga, M.; Yoshida, Y.; Kumata, K.; Yui, J.; Kawamura, K.; Hatori, A.; Fukumura, T.; Zhang, M. R. Radiosynthesis and Preliminary Evaluation of 4-[<sup>18</sup>F]Fluoro-N-[4-[6-(Isopropylamino)Pyrimidin-4-yl]-1,3-Thiazol-2-yl]-N-Methylbenzamide as a New Positron Emission Tomography Ligand for Metabotropic Glutamate Receptor Subtype 1. *Bioorganic Med. Chem. Lett.* **2011**, *21* (10), 2998–3001. <https://doi.org/10.1016/j.bmcl.2011.03.046>.
- (265) Yamasaki, T.; Fujinaga, M.; Maeda, J.; Kawamura, K.; Yui, J.; Hatori, A.; Yoshida, Y.; Nagai, Y.; Tokunaga, M.; Higuchi, M.; Suhara, T.; Fukumura, T.; Zhang, M. R. Imaging for Metabotropic Glutamate Receptor Subtype 1 in Rat and Monkey Brains Using PET with [<sup>18</sup>F]FITM. *Eur. J. Nucl. Med. Mol. Imaging* **2012**, *39* (4), 632–641. <https://doi.org/10.1007/s00259-011-1995-6>.
- (266) Fujinaga, M.; Yamasaki, T.; Yui, J.; Hatori, A.; Xie, L.; Kawamura, K.; Asagawa, C.; Kumata, K.; Yoshida, Y.; Ogawa, M.; Nengaki, N.; Fukumura, T.; Zhang, M. Synthesis and Evaluation of Novel Radioligands for Positron Emission Tomography Imaging of Metabotropic Glutamate Receptor Subtype 1 (MGLuR1) in Rodent Brain. *J. Med. Chem.* **2012**, *55* (5), 2342–2352. <https://doi.org/10.1021/jm201590g>.
- (267) Katritch, V.; Cherezov, V.; Stevens, R. C. Structure-Function of the G Protein-Coupled Receptor Superfamily. *Annu. Rev. Pharmacol. Toxicol.* **2013**, *53*, 531–556. <https://doi.org/10.1146/annurev-pharmtox-032112-135923>.
- (268) Llinas del Torrent, C.; Pérez-Benito, L.; Tresadern, G. Computational Drug Design Applied to the Study of Metabotropic Glutamate Receptors. *Molecules* **2019**, *24* (1098), 1–22. <https://doi.org/10.3390/molecules24061098>.
- (269) Wendler, T.; Schütt, C.; Näther, C.; Herges, R. Photoswitchable Azoheterocycles via Coupling of Lithiated Imidazoles with Benzenediazonium Salts. *J. Org. Chem.* **2012**, *77* (7), 3284–3287. <https://doi.org/10.1021/jo202688x>.
- (270) Weston, C. E.; Richardson, R. D.; Haycock, P. R.; White, A. J. P.; Fuchter, M. J. Arylazopyrazoles: Azoheteroarene Photoswitches Offering Quantitative Isomerization and Long Thermal Half-Lives. *J. Am. Chem. Soc.* **2014**, *136* (34), 11878–11881. <https://doi.org/10.1021/ja505444d>.
- (271) Calbo, J.; Weston, C. E.; White, A. J. P.; Rzepa, H. S.; Contreras-García, J.; Fuchter, M. J. Tuning Azoheteroarene Photoswitch Performance through Heteroaryl Design. *J. Am. Chem. Soc.* **2017**, *139* (3), 1261–1274. <https://doi.org/10.1021/jacs.6b11626>.
- (272) El-Borai, M. A.; Rizk, H. F.; El-Hefnawy, G. B.; El-Sayed, H. F.; Ibrahim, S. A. Dyeing, Color Fastness and Antimicrobial Properties of Some Mono and Disazo Disperse Dyes Derived from Thiazole Moiety. *Fibers Polym.* **2013**, *14* (12), 2061–2068. <https://doi.org/10.1007/s12221-013-2061-8>.
- (273) Garcia-Amorós, J.; Reig, M.; Cuadrado, A.; Ortega, M.; Nonell, S.; Velasco, D. A Photoswitchable Bis-Azo Derivative with a High Temporal Resolution. *Chem. Commun.* **2014**, *50* (78), 11462–11464. <https://doi.org/10.1039/c4cc05331a>.



- (274) Akwi, F. M.; Bosma, C.; Watts, P. A Facile Optimization of Diazotization and Phase Transfer Catalyzed Azo-Coupling Reactions in Microreactors. *J. Flow Chem.* **2016**, *6* (2), 73–79. <https://doi.org/10.1556/1846.2016.00003>.
- (275) Harris, M. G.; Stewart, R. Amino Group Acidity in Aminopyridines and Aminopyrimidines. *Can. J. Chem.* **1977**, *55* (21), 3800–3806. <https://doi.org/10.1139/v77-536>.
- (276) Mazik, M.; Zielinski, W. Basicity of 4-Aminopyrimidine and 2,4-Diaminopyrimidine Derivatives. *Monatshefte fur Chemie Chem. Mon.* **1996**, *127*, 587–591. <https://doi.org/10.1007/bf00817250>.
- (277) Zoltewicz, J. A.; Deady, L. W. Quaternization of Heteroaromatic Compounds: Quantitative Aspects. *Adv. Heterocycl. Chem.* **1978**, *22* (C), 71–121. [https://doi.org/10.1016/S0065-2725\(08\)60103-8](https://doi.org/10.1016/S0065-2725(08)60103-8).
- (278) Scholler, P.; Moreno-Delgado, D.; Lecat-Guillet, N.; Doumazane, E.; Monnier, C.; Charrier-Savournin, F.; Fabre, L.; Chouvet, C.; Soldevila, S.; Lamarque, L.; Donsimoni, G.; Roux, T.; Zwier, J. M.; Trinquet, E.; Rondard, P.; Pin, J. P. HTS-Compatible FRET-Based Conformational Sensors Clarify Membrane Receptor Activation. *Nat. Chem. Biol.* **2017**, *13* (4), 372–380. <https://doi.org/10.1038/nchembio.2286>.
- (279) Doumazane, E.; Scholler, P.; Fabre, L.; Zwier, J. M.; Trinquet, E.; Pin, J. P.; Rondard, P. Illuminating the Activation Mechanisms and Allosteric Properties of Metabotropic Glutamate Receptors. *Proc. Natl. Acad. Sci. U. S. A.* **2013**, *110* (15), E1416–E1425. <https://doi.org/10.1073/pnas.1215615110>.
- (280) Rovira, X.; Malhaire, F.; Scholler, P.; Rodrigo, J.; Gonzalez-Bulnes, P.; Llebaria, A.; Pin, J. P.; Giraldo, J.; Goudet, C. Overlapping Binding Sites Drive Allosteric Agonism and Positive Cooperativity in Type 4 Metabotropic Glutamate Receptors. *FASEB J.* **2015**, *29* (1), 116–130. <https://doi.org/10.1096/fj.14-257287>.
- (281) Cao, A.; Quast, R. B.; Pin, J.; Margeat, E. Allosteric Modulators Enhance Agonist Efficacy by Increasing the Residence Time of a GPCR in the Active State. *Nat. Commun.* **2021**, *12* (5426), 1–13. <https://doi.org/10.1038/s41467-021-25620-5>.
- (282) Bockenbauer, S.; Fürstenberg, A.; Yao, X. J.; Kobilka, B. K.; Moerner, W. E. Conformational Dynamics of Single G Protein-Coupled Receptors in Solution. *J. Phys. Chem. B* **2011**, *115* (45), 13328–13338. <https://doi.org/10.1021/jp204843r>.
- (283) Zhu, D.; Lu, M.; Chua, P. J.; Tan, B.; Wang, F.; Yang, X.; Zhong, G. A Highly Stereoselective Organocatalytic Tandem Aminoxylation / Aza-Michael Tetrahydro-1, 2-Oxazines. *Org. Lett* **2008**, *10* (20), 4585–4588. <https://doi.org/10.1021/ol801864c>.
- (284) Jankowiak, A.; Obijalska, E.; Kaszynski, P.; Pieczonka, A.; Young, V. G. Synthesis and Structural, Spectroscopic, and Electrochemical Characterization of Benzo[c]Quinolizinium and Its 5-Aza-, 6-Aza, and 5,6-Diaza Analogues. *Tetrahedron* **2011**, *67* (19), 3317–3327. <https://doi.org/10.1016/j.tet.2011.03.023>.
- (285) Motulsky, H.; Christopoulos, A. *Fitting Models to Biological Data Using Linear and Nonlinear Regression-*; 2003.
- (286) Gomeza, J.; Mary, S.; Brabet, I.; Parmentier, M. L.; Restituto, S.; Bockaert, J.; Pin, J. P. Coupling of Metabotropic Glutamate Receptors 2 and 4 to G Alpha 15, G Alpha 16, and Chimeric G Alpha q/i Proteins: Characterization of New Antagonists. *Mol. Pharmacol.* **1996**, *50* (4), 923–930.
- (287) Börner, S.; Schwede, F.; Schlipp, A.; Berisha, F.; Calebiro, D.; Lohse, M. J.; Nikolaev, V. O. FRET Measurements of Intracellular cAMP Concentrations and cAMP Analog Permeability in Intact Cells.

*Nat. Protoc.* **2011**, *6* (4), 427–438. <https://doi.org/10.1038/nprot.2010.198>.